Seismic Retrofit of Existing Substandard Reinforced Concrete Beam-Column Joints with Hybrid NSM Steel Bars and EB GFRP Wrap Technique

Ömer Yavuz Eski

The Faculty of Science, Agriculture & Engineering

Civil, Structural and Geospatial Engineering Discipline

Newcastle University

This dissertation is submitted for the degree of

Doctor of Philosophy in Structural Engineering

School of Engineering November 2024

DECLARATION

"I hereby declare that except where specific reference is made to the work of others, the contents of this dissertation are original and have not been submitted in whole or in part for consideration for any other degree or qualification in this, or any other university. This dissertation is my own work and contains nothing which is the outcome of work done in collaboration with others, except as specified in the text and Acknowledgements. This dissertation contains fewer than 80,000 words including appendices, bibliography, footnotes, tables, and equations and has fewer than 150 figures."

Ömer Yavuz Eski

November 2024

ACKNOWLEDGEMENTS

I am grateful to everyone who has helped me along the way to finishing this thesis. Their advice, support, and unfailing faith in my abilities have all played a role in moulding my work.

First and foremost, I want to thank my primary supervisor, Professor Dr Sean Wilkinson, for his essential direction, insightful input, and continual support. His knowledge and passion have been crucial in influencing the course of this research. I'd also like to thank my second supervisor, Dr Vladimir Vinogradov, and my external supervisor, Dr Amir Mofidi, for their intelligent recommendations, thought-provoking discussions, and encouragement, which considerably improved this thesis.

I am grateful to my family, Şükran Eski, Bahri Eski, Nermin Eski, Nazan Yılmaz, Fatih Sabri Eski, Merve Seher Eski, Recep Oğuz Eski, Tuba Eski, Rasim Furkan Yılmaz, Enes Kaan Yılmaz, Zeynep Kübra Eski, and Şükran Zümra Eski. Their encouragement through times of self-doubt, as well as their unshakable belief in me, have been my motivators. I'd like to thank my friends and coworkers for their insightful comments and stimulating debates, which helped to improve the overall quality of this work. Throughout my thesis process, Dr Sergio Serrano Blanco and Dr Sherly Christivanny Lie were with me whenever I felt mentally unwell. I would like to thank them for helping me get through this process in the best way possible. I would like to extend special thanks to Huseyin Ayan for his support and help throughout my Ph.D. process and especially during the experimental studies. I would also like to thank technicians in the SAgE group for their help during my experiments.

Finally, I am highly indebted to the State of the Republic of Türkiye and the Turkish Ministry of National Education for giving me this opportunity to complete my Ph.D., and thanks for their financial and emotional support. Please accept my heartfelt gratitude to everyone who had a role, no matter how great or small, in the completion of this thesis. This achievement would not have been possible without the collective support and contributions of each one of you.

ABSTRACT

Earthquakes are responsible for the death and injury of many thousands of people each year. These deaths primarily occur because the buildings in which they are housed do not have sufficient seismic resistance and therefore collapse killing the occupants. Although we have made tremendous progress in understanding how earthquakes impact buildings and developed building stock with very high levels of collapse resistance, in low-income countries, a considerable proportion of the building inventory still has major structural deficiencies, such as poor-quality concrete and improper detailing of reinforcement. Such deficiencies mean that these structures are still at significant risk of failure during earthquakes. To remedy this situation, it is necessary to retrofit these at-risk structures; however, to do this requires cheap and effective retrofitting technologies. Existing retrofitting techniques do exist, but they are often time-consuming to install, expensive or impractical and therefore restrict how quickly the building stock of a region can be strengthened. This study investigated the behaviour of unstrengthened and strengthened full-scale exterior reinforced concrete (RC) beam-column joints (BCJs) under cyclic load. The retrofitting schemes considered were the Externally Bonded (EB) Glass Fibre-Reinforced Polymers (GFRP) sheet, and the Near-Surface Mounted (NSM) U-shaped steel techniques. Four specimens were designed, built and tested. All four had the same initial specification, with the first specimen being a control which represented a typical connection that had been designed to an outdated Turkish building code, the second specimen was strengthened with u-shaped steel bars using the NSM method. The third specimen was retrofitted with GFRP sheets using the EB method, and the fourth specimen was strengthened using a hybrid method incorporating both of the above-mentioned techniques and developed as part of this thesis. The experimental findings showed that the retrofitted beam-column joints had significantly improved strength, had slightly improved stiffness, and the EB and hybrid methods had significantly greater energy dissipation and ductility compared to the control specimen. According to the experimental results, the specimen strengthened using the NSM method showed an increase in strength of 15.3% (but no noticeable increase in ductility) the EB method showed an increase in strength of 21.8% and an increase in ductility of 29.7%, while the hybrid method showed an increase in strength of 37.0% and an increase in ductility of 31.6%. For all retrofitted specimens, there was also a shift in the failure from the joint region to the beam ends and significantly less damage within the connection, especially for EB and hybrid methods. This change in performance (strength, ductility and shifting of plastic hinge to the beam) would protect a structure from failing due

to soft storey collapse. Finally, a finite element (FE) model was developed using ABAQUS software. This model was capable of simulating the connection loaded with a monotonic load and showed good agreement with the envelope curve of the experiments and therefore can considered to be a suitable design technique for these types of connections.

Table of Contents

DECLARATION i

ACKNOWLEDGEMENTS ii

ABSTRACT iii

Table of Contents v

List of Figures x

List of Tables xvii

Notation xix

Abbreviation xxiii

CHAPTER 1. INTRODUCTION 1

1.1 GENERAL 1

1.2 RESEARCH SIGNIFICANCE 2

1.3 PROBLEM DEFINITION 3

1.4 AIMS AND OBJECTIVES 4

1.4.1 Aim *4*

1.4.2 Objectives *4*

1.5 RESEARCH METHODOLOGY 5

1.6 THESIS LAYOUT 6

CHAPTER 2. LITERATURE REVIEW 7

2.1 GENERAL 7

2.2 SEISMIC PERFORMANCE OF EXISTING EXTERIOR RC BEAM-COLUMN JOINST 9

2.3 PARAMETERS AFFECTING SHEAR STRENGTH OF RC BEAM-COLUMN JOINST 12

2.3.1 Impact of the compressive strength of concrete *12*

2.3.2 Impact of the joint reinforcement confinement *14*

2.3.3 Impact of the column axial load *16*

2.4 STRENGTHENING TECHNIQUES 19

2.4.1 Concrete Jacketing Technique 19

2.4.2 Steel Jacketing Technique 20

2.4.3 Externally Bonded (EB) Technique 20

2.4.4 Near-Surface Mounded (NSM) Technique 22

2.5 FIBRE REINFORCED POLYMER 27

2.5.1 Mechanical Properties 28

2.6 LITERATURE REVIEW ON RETROFITTED EXTERIOR BEAM-COLUMN JOINTS 30

2.6.1 Antonopoulos and Triantafillou (2003) 31

2.6.2 Karayannis and Sirkelis (2008) 33

2.6.3 Shrestha et al. (2009) 34

2.6.4 Ilki et al. (2011) 35

2.6.5 Del Vecchio et al. (2014) 37

2.6.6 Singh et al. (2014) 37

2.6.7 Mahmoud et al. (2014) 38

2.6.8 Zamani Beydokhti and Shariatmadar (2016) 40

2.6.9 Mostofinejad and Akhlaghi (2017) 41

2.6.10 Akash and Jayasree (2018) 43

2.6.11 Saqan et al. (2018) 44

2.6.12 Wang et al. (2019) 45

2.6.13 Laseima et al. (2020) 45

2.6.14 Davodikia et al. (2021) 46

2.6.15 Sakthimurugan and Baskar (2021) 48

2.6.16 Zaferani and Shariatmadar (2022) 48

2.6.17 Hashemi and Riahi (2022) 50

2.6.18 Wang et al. (2022) 51

2.6.19 Ansari et al. (2023) 53

2.6.20 Farhang et al. (2023) *54*

2.7 SUMMARY **56**

CHAPTER 3. EXPERIMENTAL PROGRAMME **59**

3.1 GENERAL **59**

3.2 MATERIAL PROPERTIES **59**

3.2.1 Concrete *59*

3.2.1.1 Determination of physical properties of aggregates *59*

3.2.1.2 Sieve analysis of fine and coarse aggregates *64*

3.2.1.3 Properties of cement *71*

3.2.1.4 Determination of mechanical properties of concrete *71*

3.2.2 Steel *75*

3.2.3 Glass Fibre Reinforced Polymer *77*

3.2.4 Epoxy Resin *77*

3.3 DESCRIPTION OF TEST UNITS **78**

3.4 MANUFACTURE OF THE SPECIMENS **82**

3.5 STRENGTHENING APPLICATION **86**

3.5.1 Application of NSM method *87*

3.5.2 Application of EB method *91*

3.6 TEST SET-UP **95**

3.7 LOADING PROTOCOL **101**

3.8 DATA ACQUISITION SYSTEM **105**

3.8.1 Installation of Strain Gauges on Reinforcing Bars *105*

3.8.2 Installation of Target Points and Cameras *107*

3.10 SUMMARY **108**

CHAPTER 4. EXPERIMENTAL RESULTS **110**

4.1 GENERAL **110**

4.2 ANALYSIS OF TEST RESULTS 110

4.2.1 Crack Propagation and Strength 110

4.2.2 Stiffness 141

4.2.3 Ductility Ratios and Energy Dissipation Characteristic 144

4.2.4 Strain Measurements 152

4.3 SUMMARY 154

CHAPTER 5. NUMERICAL PROGRAMME 158

5.1 GENERAL 158

5.2 GEOMETRIC MODELLING, ELEMENT TYPE AND MESH 159

5.2.1 Concrete Joint, Support of Column Ends and Loading Plates 160

5.2.2 Reinforcement Bars 161

5.2.3 FRP sheets 161

5.2.4 Meshing 162

5.3 MATERIAL BEHAVIOUR 164

5.3.1 Concrete 164

5.3.2 Steel Reinforcing Bars 172

5.3.3 Fibre Reinforced Polymer 173

5.3.4 Epoxy adhesive 175

5.4 BOUNDARY CONDITIONS, CONSTRAINTS, ANALYSIS TYPE AND LOADING 176

5.5 CALIBRATION OF THE MODEL 178

5.6 NUMERICAL ANALYSIS RESULTS 180

5.7 SUMMARY 199

CHAPTER 6. CONCLUSIONS AND RECOMMENDATIONS 202

6.1 GENERAL 202

6.2 SPECIFIC CONCLUSIONS 202

6.3 RECOMMENDATIONS FOR FUTURE WORK 205

REFERENCES **207**

APPENDICES **224**

Appendix-A **224**

Appendix-B **234**

Three-Point Bending Test of Concrete ***234***

Compressive Test of Concrete ***237***

Reinforcement Tensile Test ***241***

Appendix-C **243**

Properties of SikaWrap®-930G ***243***

Properties of Sikadur®-30 ..... ***245***

Properties of Sikadur®-300 ..... ***248***

Appendix-D **251**

Calculation of the development length ***251***

Shear links design ***254***

Capacity Calculations for Column and Beam Sections ***256***

Material Models for Concrete and Steel Reinforcement for Analytical Phase ***259***

Appendix-E **266**

Appendix-F **271**

Theoretical Consideration of Shear Strength of Joints ***271***

Appendix-G **277**

Appendix-H **280**

Load-Displacement Response ***280***

Appendix-I **284**

Appendix-J **292**

List of Figures

Chapter-2

Figure 2.1. After Kocaeli earthquake (1999), damage to RC moment-framed buildings. (Sezen *et al*. 2003). 8
Figure 2.2. (a) Insufficient transverse reinforcement in the beam-column joint, (b) Inadequate transverse reinforcement in RC elements (Ince, 2024). 8
Figure 2.3. Different types of anchorages of RC joints based on the experimental studies conducted by (a) Realfonzo *et al.* (2014); (b) Padmanabham *et al.* (2022); (c) Gergely *et al.* (2000); (d) Genesio *et al.* (2010). 10
Figure 2.4. Joint conditions with different anchorage details of RC joints: (a) 180-degree angle bent beam bars; (b) 90-degree angle bent beam bars; (c) End-hook anchorage; (d) Straight bar without any hooks (Cosgun *et al*., 2020). 11
Figure 2.5. Comparison of the load-displacement relationships for J1-REF, J2, J3 and J4 (Cosgun *et al*., 2020) 12
Figure 2.6. (a) Yielding of the longitudinal reinforcement (Point B); (b) Crushing of the concrete (Point C) (Kim and LaFave, 2007). 13
Figure 2.7. Effect of concrete compressive strength on the joint shear strength for exterior joint (Parate and Kumar, 2019). 14
Figure 2.8. Effect of connection transverse reinforcement on confinement (point C): (a) Normalised joint shear stress; (b) Joint shear strain (Kim and LaFave, 2007). 15
Figure 2.9. Specimen dimensions and reinforcing details, measured in millimetres by Shafaei *et al*., (2017): (a) Specimen C1; (b) Specimen C2; (c) Specimen C3. 18
Figure 2.10. Types of FRP bars for NSM applications (De Lorenzis and Teng, 2007). 23
Figure 2.11. Variety of NSM FRP bars and minimum dimensions of grooves (Le Hoang *et al.*, 2019). 24
Figure 2.12. (a) Typical Aramid FRP (AFRP) (Kandekar and Talikoti, 2019); (b) Typical Carbon FRP (CFRP) (Günaslan *et al*., 2014); Typical Glass FRP (GFRP) (Rageh *et al*., 2022). 28
Figure 2.13. Typical stress-strain relationships for various FRPs and standard steel (Mohammadizadeh *et al.*, 2009). 28
Figure 2.14. (a) Reinforcement details; (b) Details of the FRP application process (Antonopoulos and Triantafillou, 2003). 32

Figure 2.15. (a) Test set-up and the reinforcement configuration of the specimens; (b) Strengthening scheme using CFRP sheets (Karayannis and Sirkelis, 2008). 34
Figure 2.16. (a) Reinforcement configuration; (b) Details of the FRP application (Shrestha *et al*., 2009). 35
Figure 2.17. (a) Details of reinforcement; (b) The FRP application configurations (Ilki *et al*., 2011). 36
Figure 2.18. Details of the specimen (Del Vecchio *et al*., 2014).....37
Figure 2.19. CFRP wrapping technique with details (Singh *et al*., 2014). 38
Figure 2.20. (a) Details of reinforcement and dimensions for the control specimen, J0; (b) Schematic configuration for the three groups of specimens tested (Mahmoud *et al*., 2014).39
Figure 2.21. Reinforcement details of the specimens (Zamani Beydokhti and Shariatmadar, 2016): (a) non-seismic design; (b) seismic design. 40
Figure 2.22. The application of CFRP laminates (Zamani Beydokhti and Shariatmadar, 2016). 41
Figure 2.23. (a) Reinforcement details of the specimens; (b) Specifications of all the test specimens (Mostofinejad and Akhlaghi, 2017). 42
Figure 2.24. (a) Dimensions of the beam-column joint specimen; (b) Reinforcement details of the specimen; (c) Crack pattern of BCJC specimen; (d) BCJN30 specimen; (e) BCJN45 specimen; (f) BCJN60 specimen; (g) BCJEB specimen; (h) Delamination of BCJEB specimen (Akash and Jayasree, 2018). 43
Figure 2.25. (a) Reinforcement details for each of the three specimens; Details of retrofitting: (b) Specimen SSP-2; (c) Specimen SSP-3 (Saqan *et al*., 2018). 44
Figure 2.26. Strengthening applications (Wang *et al*., 2019). 45
Figure 2.27. Specimen dimension and reinforcement specifications, (b) Retrofitting of the specimen around the joint (Laseima *et al*., 2020). 46
Figure 2.28. (a) seismic specimen; (b) non-seismic specimen; (c) Pattern of shear reinforcement of the joint core and beam by CFRP; (d) Grooves formed on the surface using the grooving method in the surface preparation process (Davodikia *et al*., 2021). 47
Figure 2.29. Details of the specimens (Sakthimurugan and Baskar, 2021). 48
Figure 2.30. (a) non-seismic designed specimen (NS); (b) seismic designed specimen (S); (c) the retrofitting designs of design (C); (d) the retrofitting designs of design (D) (Zaferani and Shariatmadar, 2022). 49

Figure 2.31. (a) Details of the reinforcement; (b) RS-SJ-FW specimen retrofitting details (Hashemi and Riahi, 2022). 50
Figure 2.32. Details of retrofitting: (a) RS-SJ-US specimen; (b) RS-FJ-FW specimen (Hashemi and Riahi, 2022). 51
Figure 2.33. Strengthening programmes (Wang *et al*., 2022). 52
Figure 2.34. (a) Reinforcement specifications, (b) The application of EB method (Ansari *et al*., 2023). 53
Figure 2.35. The NSM applications (Ansari *et al*., 2023). 54
Figure 2.36. (a) Details of the reinforcement, (b) Strengthening application, (Farhang *et al*., 2023). 55

Chapter-3

Figure 3.1. Images of the test phase for sharp sand. 61
Figure 3.2. Sieve sizes for fine and coarse aggregates. 64
Figure 3.3. Limits of the aggregate grain size distribution curve for concrete with aggregate maximum grain size of 32.0 mm (31.5 mm) (TS 802, 2016). 69
Figure 3.4. Limits of the aggregate grain size distribution curve and the granulometry of the concrete mixture. 69
Figure 3.5. (a) direct tensile test; (b) splitting tensile test; and (c) beam flexural test. 72
Figure 3.6. Three-point bending test of concrete. 73
Figure 3.7. The test equipment for concrete compression strength. 74
Figure 3.8. Stress-strain curves: (a) 8 mm diameter rebars; (b) 16 mm diameter rebars. 76
Figure 3.9. (a) The test set-up of 16 mm steel rebar, (b) Extensometer. 77
Figure 3.10. The dimension of a typical specimen (units are mm). 80
Figure 3.11. Specimen`s dimension and details (units are mm). 81
Figure 3.12. Details of beam-column joint specimens' construction. 83
Figure 3.13. Schematic representation of the specimens. 86
Figure 3.14. The application plan of the NSM method. 88
Figure 3.15. The application process of the NSM method. 89
Figure 3.16. The application plan for the EB-FRP method (units are mm). 92
Figure 3.17. The application process of the EB-FRP method. 93
Figure 3.18. (a) Hydraulic jack was used to impose an axial load on the column, (b) Hydraulic power pack. 97

Figure 3.19. Hydraulic actuators used to apply cyclic loading at the beam end. 97
Figure 3.20. Experimental set-up – schematic drawing. 98
Figure 3.21. Top and bottom support details of the column (units are mm). 99
Figure 3.22. Details of the beam end loading plates (units are mm). 100
Figure 3.23. Column ends. 101
Figure 3.24. Loading history (a) Displacement (mm), (b) Drift level (%). 102
Figure 3.25. Drift of the exterior and corner joint under cyclic loading: (a) on beam; (b) on column (Ong *et al*., 2022). 104
Figure 3.26. The locations of the strain gauges on the steel rebars. 105
Figure 3.27. The locations of the LVDTs on the column`s top and bottom end. 106
Figure 3.28. The locations of the LVDTs on the beam end. 107
Figure 3.29. (a) Checking target points using Leica Geosystems TS07; (b) The locations of the cameras. 108

Chapter-4

Figure 4.1. Crack propagation of the S1-Control for each drift ratio. 112
Figure 4.2. End of experiment pictures of S1-Control. 115
Figure 4.3. Crack propagation of the S2-NSM for each drift ratio. 117
Figure 4.4. End of experiment pictures of S2-NSM. 120
Figure 4.5. Crack propagation of the S3-EB for each drift ratio. 122
Figure 4.6. End of experiment pictures of S3-EB. 125
Figure 4.7. Crack propagation of the S4-Hybrid for each drift ratio. 127
Figure 4.8. End of experiment pictures of S4-Hybrid. 129
Figure 4.9. Hysteresis curves of the S1-Control. 130
Figure 4.10. Envelope curves of the S1-Control. 131
Figure 4.11. Hysteresis curves of the S2-NSM. 132
Figure 4.12. Envelope curves of the S2-NSM. 132
Figure 4.13. Hysteresis curves of the S3-EB. 133
Figure 4.14. Envelope curves of the S3-EB. 134
Figure 4.15. Hysteresis curves of the S4-Hybrid. 135
Figure 4.16. Envelope curves of the S4-Hybrid. 135
Figure 4.17. Hysteresis curves of the S2-NSM compared to S1-Control. 137
Figure 4.18. Hysteresis curves of the S3-EB compared to S1-Control. 137

Figure 4. 19. Hysteresis curves of the S4-Hybrid compared to S1-Control. 138
Figure 4.20. Comparison of the hysteresis curves of specimens. 138
Figure 4.21. Envelop curves of the specimens. 139
Figure 4.22. Schematic diagram of effective stiffness and energy dissipation, (Ngo *et al*., 2020). 141
Figure 4.23. Stiffness of the specimens. 142
Figure 4.24. Illustration of equivalent energy method. 144
Figure 4.25. Equivalent energy method for S1-Control. 145
Figure 4.26. Equivalent energy method for S2-NSM. 146
Figure 4.27. Equivalent energy method for S3-EB. 146
Figure 4.28. Equivalent energy method for S4-Hybrid. 147
Figure 4.29. Cross-section area method. 148
Figure 4.30. Comparison of the capacity of energy dissipation of the specimens. 149
Figure 4.31. Comparison of the capacity of cumulative energy dissipation of the specimens. 150

Chapter-5

Figure 5.1. Components of the numerical model; (a) Epoxy adhesive; (b) U-shaped steel rebar; (c) concrete part; (d) steel reinforcements; (e) FRP sheet; (f) support plate. 159
Figure 5.2. C3D8R (Eight-node brick element) (Abaqus Analysis User's Guide, 2016). 160
Figure 5.3. T3D2 (2-node, 3-dimensional truss element) (Abaqus Analysis User's Guide, 2016). 161
Figure 5.4. Shell S4R geometry (Abaqus Analysis User's Guide, 2016). 161
Figure 5.5. Fiber direction of FRP sheet. 162
Figure 5.6. Modelled specimens: (a) Concrete elements mesh; (b) Reinforcement details of joint; (c) FRP sheet element mesh; (d) Epoxy adhesive element mesh. 163
Figure 5.7. Mander model for unconfined concrete with phases (Mander *et al*., 1988). 166
Figure 5.8. Crack opening with fracture energy of concrete (Björnström *et al*., 2006). 168
Figure 5.9. Tension softening model: (a) Linear function (Karlsson and Sorensen, 2006); (b) Bilinear function (Hillerborg, 1985); and (c) Exponential function (Cornelissen *et al*., 1986). 168
Figure 5.10. Response of concrete to a uniaxial loading condition: (a) Compression, (b) Tension (Lubliner *et al*., 1989). 169

Figure 5.11. The uniaxial compressive stress-inelastic strain relationship for concrete according to CDP constitutive model; (b) Definition of damage parameter in CDP model for uniaxial compression damage. 171
Figure 5.12. (a) Definition of damage parameter for uniaxial tension damage; (b) Relationship of stress–crack opening for concrete in tension. 171
Figure 5.13. Bilinear stress-strain model of steel (CEB-FIP, 2011). 172
Figure 5.14. A unidirectional fibre reinforced lamina and principal material axes (Taranu *et al*., 2012). 173
Figure 5.15. Normal stress-separation relationship of the interface (Rezazadeh and Barros, 2014). 175
Figure 5.16. Computational simulation of boundary conditions and applied loading to the specimens. 178
Figure 5.17. Load-displacement response of finite element analysis for varying viscosity parameter values. 179
Figure 5.18. Comparison with experimental and numerical results. 180
Figure 5.19. FEA output of S1-Control of shear behaviour (4.62% Drift Ratio): (a) Concrete compressive damage; (b) SDEG (stiffness degradation variable); (c) PE (plastic strain); (d) Reinforcement Mises stress; (e) Concrete tensile damage; (f) Concrete tensile damage (experiment). 185
Figure 5.20. FEA output of S1-Control of shear behaviour (5.77% Drift Ratio): Reinforcement Mises stress. 186
Figure 5.21. FEA output of S2-NSM of shear behaviour (4.62% Drift Ratio): (a) Concrete compressive damage; (b) SDEG (stiffness degradation variable); (c) PE (plastic strain); (d) Reinforcement Mises stress; (e) Concrete tensile damage; (f) Concrete tensile damage (experiment). 187
Figure 5.22. FEA output of S2-NSM (4.62% Drift Ratio): (a) Epoxy Mises stress; (b) U-shaped steel Mises stress. 188
Figure 5.23. FEA output of S2-NSM: (a) Reinforcement Mises stress (2.31% Drift Ratio); (b) U-shaped steel Mises stress (after 1.54% Drift Ratio-28mm deflection). 189
Figure 5.24. FEA output of S4-Hybrid of shear behaviour (5.77% Drift Ratio): (a) Concrete compressive damage; (b) SDEG (stiffness degradation variable); (c) PE (plastic strain); (d) Reinforcement Mises stress; (e) Concrete tensile damage; (f) Concrete tensile damage (experiment). 190

Figure 5.25. FEA output of S4-Hybrid (5.77% Drift Ratio): (a) HSNMTCRT (matrix tensile initiation criterion); (b) the experimental observation; (c) HSNFTCRT (fibre tensile initiation criterion); (d) HSNFCCRT (fibre compressive initiation criterion); (e) HSNMCCRT (matrix compressive initiation criterion). 191
Figure 5.26. FEA output of S4-Hybrid (5.77% Drift Ratio): (a) Epoxy Mises stress; (b) U-shaped steel Mises stress. 192
Figure 5.27. FEA output of S4-Hybrid of shear behaviour (1.54% Drift Ratio): Reinforcement Mises stress. 192
Figure 5.28. Comparison with numerical model and experimental results for Tensile Damage Evolution for S1-Control. 194
Figure 5.29. Comparison with numerical model and experimental results for Tensile Damage Evolution for S2-NSM. 196
Figure 5.30. Comparison with numerical model and experimental results for Tensile Damage Evolution for S4-Hybrid. 198

List of Tables

Chapter-2

Table 2.1. Comparison of Strengthening Techniques for RC Beam-Column Joints 26
Table 2.2. Typical characteristics of carbon, glass, and aramid fibres (Mohammadizadeh *et al.*, 2009).....29

Chapter-3

Table 3.1. The weights of fine sand.....61
Table 3.2. The weights of sharp sand.....61
Table 3.3. The physical property values obtained for fine sand and sharp sand.....62
Table 3.4. The weights of coarse aggregate-1.....63
Table 3.5. The weights of coarse aggregate-2.....63
Table 3.6. The physical property values for coarse aggregate-1 and coarse aggregate-2.....64
Table 3.7. Cumulative passing of fine and coarse aggregates. 67
Table 3.8. Determination of the percentage for the concrete mixture. 68
Table 3.9. Calculation of aggregate dry weights. 70
Table 3.10. Calculation of aggregate dry surface saturation weights. 70
Table 3.11. Calculation of water absorbed by fine and coarse aggregates for 1 m3 concrete. 70
Table 3.12. Quantities for 1 m3 concrete mixture. 71
Table 3.13. The result of concrete tensile strength. 74
Table 3.14. The result of concrete compressive strength. 75
Table 3.15. Steel reinforcement properties. 76
Table 3.16. The retrofitting technique specifications. 79
Table 3.17. Properties of Sikadur®30 (at 23 °C) based on the product datasheets. 90
Table 3.18. Properties of SikaWrap 930G based on the product datasheets. 91
Table 3.19. Properties of Sikadur®300 (7 days and 23 °C) based on the product datasheets. 92
Table 3.20. The displacement values for each step. 103

Chapter-4

Table 4.1. The capacities of the specimens for both directions and the drift ratios at which they reach their capacities. 136
Table 4.2. Comparison of the lateral strength capacity of the specimens. 139

Table 4.3. Stiffness values of the specimens. 143
Table 4.4. Comparison of ductility ratios. 147
Table 4.5. Comparison of the capacity of energy dissipation values of the specimens. 150
Table 4.6. Comparison of the capacity of cumulative energy dissipation values of the specimens..... 151
Table 4.7. Performance of strain gauges during the experiments. 152

Chapter-5

Table 5.1. Utilised values of the parameters related to the Concrete Damage Plasticity (CDP) model. 165
Table 5.2. Stress and strain values for ϕ8 reinforcing steel in ABAQUS. 173
Table 5.3. Stress and strain values for ϕ16 reinforcing steel in ABAQUS. 173
Table 5.4. Orthotropic elastic properties of the composite used in the jacket (Hahn and Tsai, 1980). 174
Table 5.5. Orthotropic damage initiation properties of the composite used in the jacket (Hahn and Tsai, 1980). 174
Table 5.6. Maximum displacements and loads obtained from experimental and computational tests. 182

Notation

Chapter-2

A_g	=	The gross cross-sectional area of the column
f_{ck} (f_c`)	=	The characteristic compressive strength of concrete
a_f	=	The width of the FRP/steel bar
b_f	=	The height of the FRP/steel bar
d_f	=	The groove size

Chapter-3

D_{max}	=	The maximum aggregate size
δ_A	=	Apparent specific gravity
δ_{DS}	=	Dry specific gravity
δ_S	=	Specific gravity
δ_C	=	Specific gravity of cement
δ_W	=	Specific gravity of water
S	=	Water absorption rate
C	=	The content of cement;
W	=	The water content;
$V_{aggregate}$	=	The total volume of aggregates
V_{air}	=	The volume of air
V_{cement}	=	The volume of cement
V_{water}	=	The volume of water
$W_{aggregate,\ DS}$	=	Dry weights of aggregate
$W_{aggregate,\ S}$	=	Dry surface saturation weights of aggregate
f_{cm}	=	The target compressive strength of concrete
f_{cc}	=	The norm strength of concrete
f_{ctk}	=	The characteristic tensile strength of concrete
$f`_{ctk}$	=	The characteristic tensile strength of concrete using the split cylinder test
$f``_{ctk}$	=	The characteristic tensile strength of concrete using the flexural test
M_b	=	The maximum bending moment
I	=	The area moment of inertia of cross-section

y	=	the vertical distance from the neutral axis to where the stress is being calculated
f_{sy}	=	The yield strength of steel reinforcement
f_{su}	=	The ultimate strength of steel reinforcement
ε_{sy}	=	The yield strain of steel reinforcement
ε_{su}	=	The ultimate strain of steel reinforcement
E_s	=	The elasticity modulus (Young`s modulus) of steel reinforcement
ε_{sh}	=	The strain at the onset of strain hardening of steel reinforcement
$\varepsilon_{s,\,max}$	=	The strain corresponding to maximum stress of steel reinforcement
f_{ctd}	=	The design tensile strength of concrete
f_{ct}	=	The tensile strength of concrete at the time of testing
f_{yd}	=	The design strength of the reinforcement
f_{ywk}	=	The yield strength of the transverse reinforcement
A_{sw}	=	The total area of transverse reinforcement
f_{yk}	=	The minimum yield strength of the reinforcement
ϕ	=	The diameter of steel reinforcement
l_b	=	The development length of deformed bars
δ	=	The vertical displacement of the beam-end
L	=	The distance from the loading point to the column face

Chapter-4

F_{imax}^{+}	=	The peak strength in the push direction
F_{imax}^{-}	=	The peak strength in the pull direction
X_i^{+}	=	The displacement corresponding to F_{imax}^{+}
X_i^{-}	=	The displacement corresponding to F_{imax}^{-}
$K_{eff,i}$	=	The effective stiffness
E_{ID}	=	Hysteretic energy dissipation per cycle
μ	=	The ductility ratio
Δu	=	Beam tip displacement at the load step corresponding to 20% reduction in ultimate load
Δy	=	The displacement of the reduced stiffness equivalent elasto-plastic yield

Chapter-5

ψ	=	The dilation angle
μ	=	The viscosity parameter
ϵ	=	The flow potential eccentricity
K_c	=	the second stress invariant on the tensile meridian to that on the compressive meridian
v	=	Poisson's ratio
$\gamma_{conrete}$	=	Density of plain unreinforced concrete
f_{b0}/f_{c0}	=	The ratio of the compressive strength under biaxial loading to uniaxial compressive strength
f_{b0}	=	The biaxial compressive strength of concrete
f_{c0}	=	The uniaxial compressive strength of concrete
$\varepsilon_c^{pl,h}$	=	Plastic hardening strain in compression
$\varepsilon_c^{in,h}$	=	Inelastic compression strain
$\varepsilon_t^{pl,h}$	=	Plastic hardening strain in tension
$\varepsilon_t^{in,h}$	=	Inelastic tension strain
ω_c	=	The crack opening displacement at which stress can no longer be transferred
G_f	=	The fracture energy of concrete
d_c	=	The compression damage parameter;
d_t	=	The tension damage parameter
σ_c	=	The nominal compressive stress
σ_t	=	The post-peak concrete strength in tension
σ_{cu}	=	The ultimate compressive strength of the unconfined cylinder specimen
σ_{tu}	=	The ultimate tensile strength of the unconfined cylinder specimen
σ_{c0}	=	The concrete stress in elastic region
$\varepsilon_{c,\ elastic}$	=	The concrete strain in elastic region
ε_c	=	The nominal compressive strain
ε_{cu}	=	The strain of the unconfined cylinder specimen
ω_t	=	The recovery parameters in tension
ω_c	=	The recovery parameters in compression
E_0	=	The initial elastic stiffness

ε_{cr}	=	The cracking strain
E_L	=	The modulus of elasticity in the directions parallel to the fibre
E_T	=	The modulus of elasticity in the directions perpendicular to the fibre
G	=	The shear modulus
$\sigma_L^{f,t}$	=	The tensile strength of the materials in the direction parallel to the fibre orientation
$\sigma_L^{f,c}$	=	The compressive strength of the materials in the direction parallel to the fibre orientation
$\sigma_T^{f,t}$	=	The tensile strength of materials in the direction perpendicular to the fibre orientation
$\sigma_T^{f,c}$	=	The compressive strength of materials in the direction perpendicular to the fibre orientation
τ_{LT}^{f}	=	In-plane shear failure strength
G_f	=	Longitudinal tensile and compressive fracture energy
G_m	=	Transverse tensile and compressive fracture energy

Abbreviation

FRP	=	Fibre Reinforced Polymers
CFRP	=	Carbon Fibre Reinforced Polymers
AFRP	=	Aramid Fibre Reinforced Polymers
GFRP	=	Glass Fibre Reinforced Polymers
BFRP	=	Basalt Fibre Reinforced Polymers
EB	=	Externally Bonded
NSM	=	Near Surface Mounded
RC	=	Reinforced Concrete
ACI	=	American Concrete Institute
TEC	=	Turkish Earthquake Code
BS	=	British Standard
TS	=	Turkish Standard
ISO	=	International Organization for Standardization
ASTM	=	American Society for Testing and Materials
BCJ	=	Beam Column Joint
EDM	=	Electrical Discharge Machining
LVDT	=	Linear Variable Differential Transformer
CSA	=	Canadian Standards Association
CDP	=	Concrete Damage Plasticity

CHAPTER 1. INTRODUCTION

1.1 GENERAL

Earthquakes are one of the most costly and deadly natural hazards that societies face. Historically, countless earthquakes have been responsible for the death and injury of thousands of people and the collapse of numerous buildings around the world. Whereas events like the 2011 Christchurch and Tohoku earthquakes have shown that modern seismic design does offer good protection from these events there are many existing reinforced concrete (RC) buildings (in both high and low income countries) that have not been built to the latest code. In fact, in low income countries a considerable proportion of the building inventory have major structural deficiencies such as poor quality of concrete, insufficient flexural strength, and improper reinforcement detailing (Helal, 2012; Goksu *et al.,* 2014; and Barbosa *et al.,* 2017) that leave these structures susceptible to failures during earthquakes.

The Kahramanmaras (2023) earthquake profoundly impacted 11 provinces in Turkey, resulting in significant damage to numerous buildings and the deaths of many people. Based on on-site investigations conducted in these provinces, the causes of structural damage in reinforced concrete buildings aged 6–26 years were evaluated in relation to design and material defects. The primary factors contributing to the structural damages were inadequate stirrups in structural elements, short column, strong beam-weak column, infill wall failures, soft story type collapse, substandard concrete quality, and steel reinforcement corrosion (Turan *et al*., 2024 and Vuran *et al*., 2024).

Post-Earthquake surveys show that most of the catastrophic failures leading to building collapse and the deaths of occupants occured due to insufficient capacity of the beam-column connections (Zhao *et al.,* 2009 and Gautam & Chaulagain, 2016). Therefore, in such buildings constructed to conform to old building codes, beam-column connections generally do not have sufficient transverse steel reinforcement in the junction area, the beam reinforcement has inadequate anchorage, and/or the strong column-weak beam criterion has not been implemented. In these cases, these joints are vulnerable to brittle failure due to the earthquake producing large shear stresses in the column-beam junction (Ghobarah and Said, 2002) resulting in fracture that may lead to collapse (Sakthimurugan and Baskar, 2021).

After a major earthquake, public structures such as schools, hospitals, libraries, and courthouses play a pivotal role in maintaining services to citizens such as providing

accommodation to the affected communities or caring for the injured. As such these structures should have the most current level of seismic protection irrespective of their age. For this reason, existing structural deficiencies of public buildings should be effectively addressed.

1.2 RESEARCH SIGNIFICANCE

It is widely recognised that beam-column connections are crucial in the moment-resisting of RC frame structures during earthquakes. The current codes include a comprehensive description of the appropriate design and detailing of joint shear reinforcement. Nevertheless, it is also widely recognised that numerous pre-existing buildings built to previous codes, lack shear reinforcement, particularly in the joint regions. Reinforced concrete beam-column connections are generally the most susceptible components during an earthquake and many experience shear damage at the joint (Fayaz *et al*., 2022). Therefore, there is a requirement for practicable and effective methods to retrofit reinforced concrete beam-column connections that are not detailed to current seismic design codes.

Many conventional reinforcing methods for structural strengthening are documented in the literature. Some of these procedures are critiqued for being time-consuming, labour-intensive, and involving complicated details. Reinforcement of essential buildings, such as schools, is particularly time sensitive. To avoid disrupting education and training, such structures must be reinforced quickly and effectively. Furthermore, after a major earthquake, public structures such as schools, hospitals, libraries, and courthouses play a pivotal role in maintaining services to citizens such as providing accommodation to the affected communities or caring for the injured. As such, these structures should have the most current level of seismic protection irrespective of their age. For this reason, it is essential that existing structural deficiencies in public buildings should be effectively addressed.

Externally Bonded (EB) and Near Surface Mounded (NSM) methods are two of the most widely used reinforcement techniques (Akbarzadeh ve Maghsoudi, 2010 and Zhou *et al*., 2013). Many studies have investigated the EB FRP reinforcement process in recent years due to its high strength-to-weight ratio, superior corrosion resistance, and ease of installation. Many experimental investigations have demonstrated the effectiveness of FRP reinforcement in improving the seismic resistance of inadequate beams and columns (Lee ve Lopez, 2020 and Vahidpour *et al*., 2022). Likewise, the first experimental investigation of the NSM approach was carried out using CFRP strips in grooves drilled into concrete specimens (Blaschko and

Zilch, 1999). Several experimental studies have been conducted to evaluate the flexural behaviour of RC beams reinforced with NSM bars or strips made of FRP materials (e.g., Al-Mahmoud *et al*., 2009; El-Hacha and Gaafar, 2011; Badawi and Soudki, 2009; and Singh *et al*., 2014). By using these two methods, element-wise reinforcements have been performed and their effectiveness has been proved. However, there are still not enough studies for critical areas such as beam-column joints.

1.3 PROBLEM DEFINITION

Earthquake forces generate large shear forces in the joint area, as well as oblique primary tensile stresses, which cause cracking and eventually disperse the concrete in the joint area. To handle these stresses in an appropriate way, extra stirrups should be employed in the joint area. When reviewing earthquake regulations, it is advised that some of the extra reinforcement utilised in the reinforcing zone at the column's end be continued in the joint area. However, because it is difficult to install the stirrups needed by the codes in this zone, it is frequently overlooked, and no stirrups are installed in the joint zone. As a result, the bulk of current buildings' beam-column junctions are severely inadequate in terms of earthquake resistance.

In a conventional moment-resisting frame system, three categories of beam-column connections can be identified: interior, exterior, and corner. External beam-column connections are deemed the most crucial elements during seismic events for the following reasons (Fayaz *et al*., 2022):

- Since the external joints are located at the edge or corners of the building, they are under the direct effect of earthquake forces. In this case, the beams and columns at these joints are subjected to larger bending moments and shear forces compared to the interior joints.
- External beam-column connections are essential for the structural stability. If these joints are damaged, the structural system of the structure is severely weakened, and this may cause the overall collapse of the structure.
- In external joints, beams are connected to columns only on one side and the other side is free. This causes the forces on the joint to be distributed over a smaller area and the stress at the joint is greater. In internal joints, the forces are absorbed by the columns on both sides along the beam and a better force distribution is achieved.

- In external corner joints, the direction of earthquake forces encountered by beams and columns is more complex. Forces along two different axes act on the joint, making the design and performance of the joint more critical.
- The ductility (deformation capacity) of external joints is generally lower than that of internal joints. This increases the likelihood of the joint experiencing a sudden failure during an earthquake.

For these reasons, exterior beam-column joints should be specially considered in moment resisting frame systems and extra attention ought to be taken in the design to ensure that these joints provide adequate strength and ductility against earthquake forces.

It is necessary to develop easy, economical, and effective methods to increase the bearing capacity of the joints and to prevent sudden collapse in earthquakes. It is also important that the retrofitting is carried out quickly without evacuating the buildings and without disturbing the occupants. To prevent collapse due to joint failure, the basic principle is to ensure the formation of a joint in the beam without significant damage to the joints. If this is achieved, a ductile behaviour is achieved.

The improved performance of reinforced concrete joints presents significant challenges and practical obstacles. Reinforced concrete and steel jackets for retrofitting have been extensively utilised for decades. Nonetheless, these techniques have faced criticism for their labour difficulty, extended implementation period, and challenging details. Furthermore, the application of RC jackets augments the size and self-weight of structural components, resulting in architectural complications.

1.4 AIMS AND OBJECTIVES

1.4.1 Aim

To develop and validate a numerical design procedure for increasing the shear strength of RC beam-column joints strengthened with steel bars and GFRP sheets.

1.4.2 Objectives

(i) To determine the current deficiencies in exterior RC beam-column joint, what are the important mechanism that lead to these deficiencies.

(ii) To review current state-of-the-art retrofitting technologies and assess the efficiency, effectiveness, and practicality of them and to propose a potential method of improving them.

(iii) To develop an experimental programme to determine the best retrofitting strategy.

(iv) To test a number of specimens to determine the increase in performance that can be achieved by different retrofitting techniques.

(v) To develop a finite element model of the best retrofitting technique with the aim of checking the feasibility of a future parametric study as part of the development of a design procedure.

1.5 RESEARCH METHODOLOGY

A review of the existing literature was conducted to investigate the behaviour of deficient joints as well as the effectiveness of retrofitting procedures. To achieve the aims described above, two methodologies were used: experimental and numerical (finite element method) investigations.

Experiments were conducted to assess the impact of various strengthening methods; (EB) and (NSM) were tested. The project includes the manufacture and testing of four external RC beam-column joints. Two types of loads were used in the tests. The first is a constant axial load operating on the top section of the column, while the second is a reverse cyclic load applied to the beam end. Variables investigated in this experimental investigation include the type of strengthening approach used.

The efficacy of the suggested reinforcement strategy was thoroughly examined through comprehensive analyses of both global and local structural behaviour, including load-displacement response, crack propagation patterns, and deformation characteristics. Furthermore, detailed evaluations were conducted on failure modes (such as joint shear failure, and beam flexural failure), strength capacity under cyclic loading, stiffness degradation across various drift levels, ductility ratio as a measure of deformation capacity, and energy dissipation characteristics.

A finite element analysis was performed to evaluate the strengthening techniques used in this project. This research entailed developing a finite element model for beam-column connections using ABAQUS software to predict the behaviour of the tested specimens. The model's findings were validated by comparing them to those of the experimental study.

In conclusion, a numerical model was established to ascertain the joint shear strength of beam-column connections for both unstrengthened and strengthened examples.

1.6 THESIS LAYOUT

The thesis comprises seven chapters. Each chapter contains the following contents:

- Chapter 1 introduced the role of existing reinforced concrete frames subjected to cyclic loading and the importance of this study.
- In Chapter 2, the seismic performance of existing reinforced concrete exterior beam-column joints is reviewed as are the various existing studies investigating their performance. The various collapse mechanism of external joints observed in recent earthquakes are presented together with the various mechanisms that lead to inadequate performance. Experimental retrofitting research is also reviewed together with the various advantages and disadvantages of the different methods.
- Chapter 3 describes details of the experimental programme followed, e.g. material properties, manufacturing of the specimens, strengthening phases of the specimens, instrumentation, test setup and loading procedures.
- Chapter 4 presents the results and findings of the experimental studies. Including load-displacement graphs, drift ratio, and an assessment of the specimen behaviour including changes in stiffness, energy dissipation capacities and ductility ratios together with the reinforcement strains of the joints during the test.
- Chapter 5 presents a comprehensive overview of finite element modelling through the utilisation of ABAQUS software. This includes the various types of elements, material constitutive models, as well as the geometry and boundary conditions. The findings from the experiments presented in Chapter 4 were used to validate the present findings.
- Chapter 6 contains the conclusions from this research, and recommendations for further research.

CHAPTER 2. LITERATURE REVIEW

2.1 GENERAL

The subsequent evaluations of structures that collapsed as a result of the earthquake (Kocaeli, Turkey, 1999; Kahramanmaras, Turkey, 2023) established that inadequate building techniques were responsible for the adverse consequences. An aftermath survey of these events uncovered many examples of residential and commercial buildings that had collapsed and had been constructed with insufficient seismic detailing. This chapter will review the various mechanisms that lead to inadequate performance as well as current-state-of-the-art strengthening techniques with a view of informing an experimental programme that can provide the data to develop better strengthening techniques.

According to Mertol & Tunc (2023) and Ince (2024), a study conducted after the earthquake in Kahramanmaras region of Turkey in 2023 revealed that the structures that had collapsed or suffered significant damage were built between the period from 1975 to 2000. It was confirmed that the design and construction of these structures did not completely adhere to the seismic codes in effect at that time. The collapsed buildings and their damage patterns indicate various deficiencies in the construction process. These include inadequate development length, violation of bending stirrup ends at 135^{o}, deficiencies in construction materials, insufficient reinforcement ratio, inadequate transverse reinforcement, lack of transverse reinforcement in the connection, corrosion, insufficient shear capacity, short column design, soft and weak story, noncompliance with confinement zones, strong beam-weak column, discontinuous frames, and issues related to building inspection. Their study showed that buildings in this event most often experienced collapse or damage due to insufficient joint resistance. This emphasised the significant negative impact of insufficient beam-column connections on the seismic response of reinforced concrete framed buildings.

Figure 2.1 illustrates an instance of structural deterioration in beam-column joints in standard RC framed structures following the Kocaeli earthquake in 1999. The figure reveals that while the beam and column components were undamaged, the joints suffered severe damage. As shown in this picture of a building under construction, it is useful to place transverse reinforcement at the beam-column joints because the transverse reinforcement along the column protects the integrity of the joint. In addition, as a result of the inspection carried out after the Kahramanmaras earthquake, it is shown in Figure 2.2 (a) that there is no transverse reinforcement in the beam-column joint area and in Figure 2.2 (b) that there is insufficient

transverse reinforcement in the reinforced concrete elements. Ince (2024) stated that when an element lacks sufficient shear capacity, it leads to brittle shear failure instead of ductile behaviour. Ductile behaviour refers to the capacity to undergo deformation. In order to achieve ductile behaviour in reinforced concrete buildings, it is crucial for structural elements to fully utilise their capacity without experiencing brittle failure. Therefore, it is essential that reinforced concrete parts like as columns, beams, and column-beam connections possess adequate strength and ductility to achieve their full shear capacity. Hence, to ensure ductile behaviour, it is crucial to have appropriate and adequate transverse reinforcement details.

Figure 2.1. After Kocaeli earthquake (1999), damage to RC moment-framed buildings. (Sezen *et al*. 2003).

(a) (b)

Figure 2.2. (a) Insufficient transverse reinforcement in the beam-column joint, (b) Inadequate transverse reinforcement in RC elements (Ince, 2024).

2.2 SEISMIC PERFORMANCE OF EXISTING EXTERIOR RC BEAM-COLUMN JOINST

Various studies have confirmed that the failure mechanism and seismic response of reinforced concrete joints are significantly influenced by the type of anchorage for beam bars (Pampanin *et al.* 2002; Akguzel and Pampanin 2010; Hassan 2011; Shayanfar *et al.* 2016; De Risi and Verderame 2017).

Figure 2.3 (a) shows that in RC beam-column joints with 90° hooks, once diagonal cracking occurs, the joint core will resist more load due to stabilised diagonal struts. This can lead to a hardening behaviour in this region when the principal tensile stress in the joint area reaches its maximum value, corresponding to more severe diagonal cracks. The failure mechanism of RC beam-column joints featuring 180° hooks (see in Figure 2.3 (b)), differs significantly from those featuring 90° hooks bent inward. Specifically, the joint behaviour transitions to a "concrete wedge" brittle failure mechanism (Pampanin *et al.*, 2002) once diagonal cracking occurs, as a result of the interaction between diagonal shear cracks and stress concentration at the hook anchorage location (shown in Figure 2.3 (b)). For RC beam-column joints where 90° hooks are bent away from the joint region, as depicted in Figure 2.3 (c), the failure process is almost the same as those with 180° hooks. In this type of beam bar anchoring connections, the column cover may fracture due to the first shear crack propagating along the longitudinal bars of the beam.

Hence, the diagonal concrete struts in the joint core are unable to be transfer their load, leading to an early joint failure compared to RC joints with longitudinal bars bent inwards. The lack of an effective node in joints with 90°-hooks bent away or 180°-hooks hinders the activation and development of the diagonal compression strut. For RC beam-column connections where the beam's longitudinal bars end at the joint area with a short development length, as depicted in Figure 2.3 (d), the bond mechanism between the concrete and the beam's longitudinal bars is crucial. The fracture initiates in the anchorage length of the bar, around the midpoint of the column's depth. This detail could cause the bond to fail before the diagonal compressive strut mechanism is fully developed. Therefore, the maximum joint strength is anticipated to be lower than that of reinforced concrete joints with 90° hooks bent inward.

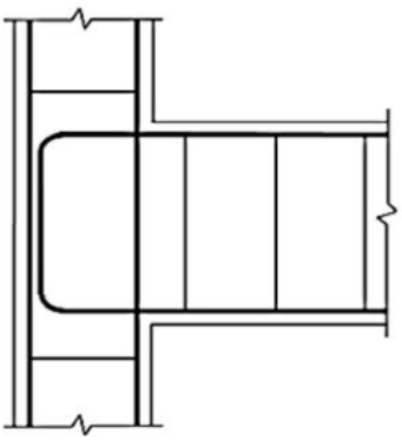

(a) Beam bars bent in the joint area

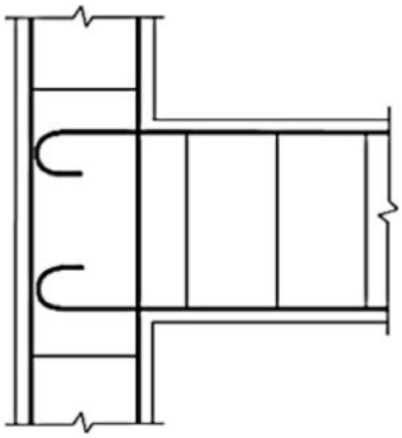

(b) End-hook anchorage

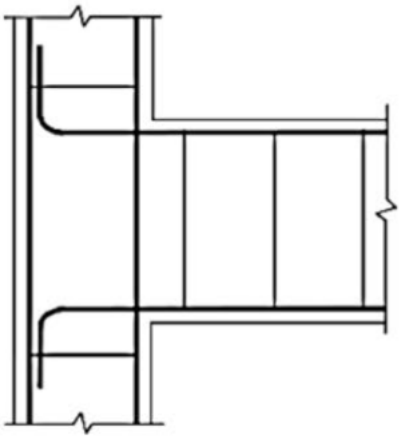

(c) Beam bars bent away from joint area

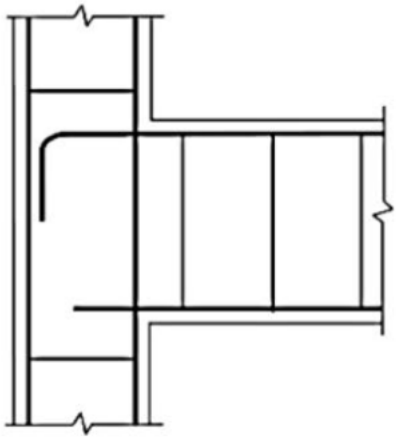

(d) A short embedment length in joint area

Figure 2.3. Different types of anchorages of RC joints based on the experimental studies conducted by (a) Realfonzo *et al.* (2014); (b) Padmanabham *et al.* (2022); (c) Gergely *et al.* (2000); (d) Genesio *et al.* (2010).

Cosgun *et al.* (2020) investigated the effect of anchorage of longitudinal beam reinforcement on the performance of the joint in their study. The test programme considered three distinct elements: the longitudinal reinforcement of the beam anchored within the joint using hooks at an angle of 90 degrees, hooks at an angle of 180 degrees, and a straight bar without any hooks (shown in Figure 2.4). To replicate the state of connections in deficient reinforced concrete buildings that are already in existence, each test specimen was manufactured using low strength concrete and plain bars. For the initial set of experiments, four specimens of RC beam-column joints at a 2/3 scale were subjected to quasi-static load application and displacement control to evaluate the performance of the joints featuring the previously mentioned anchorage details.

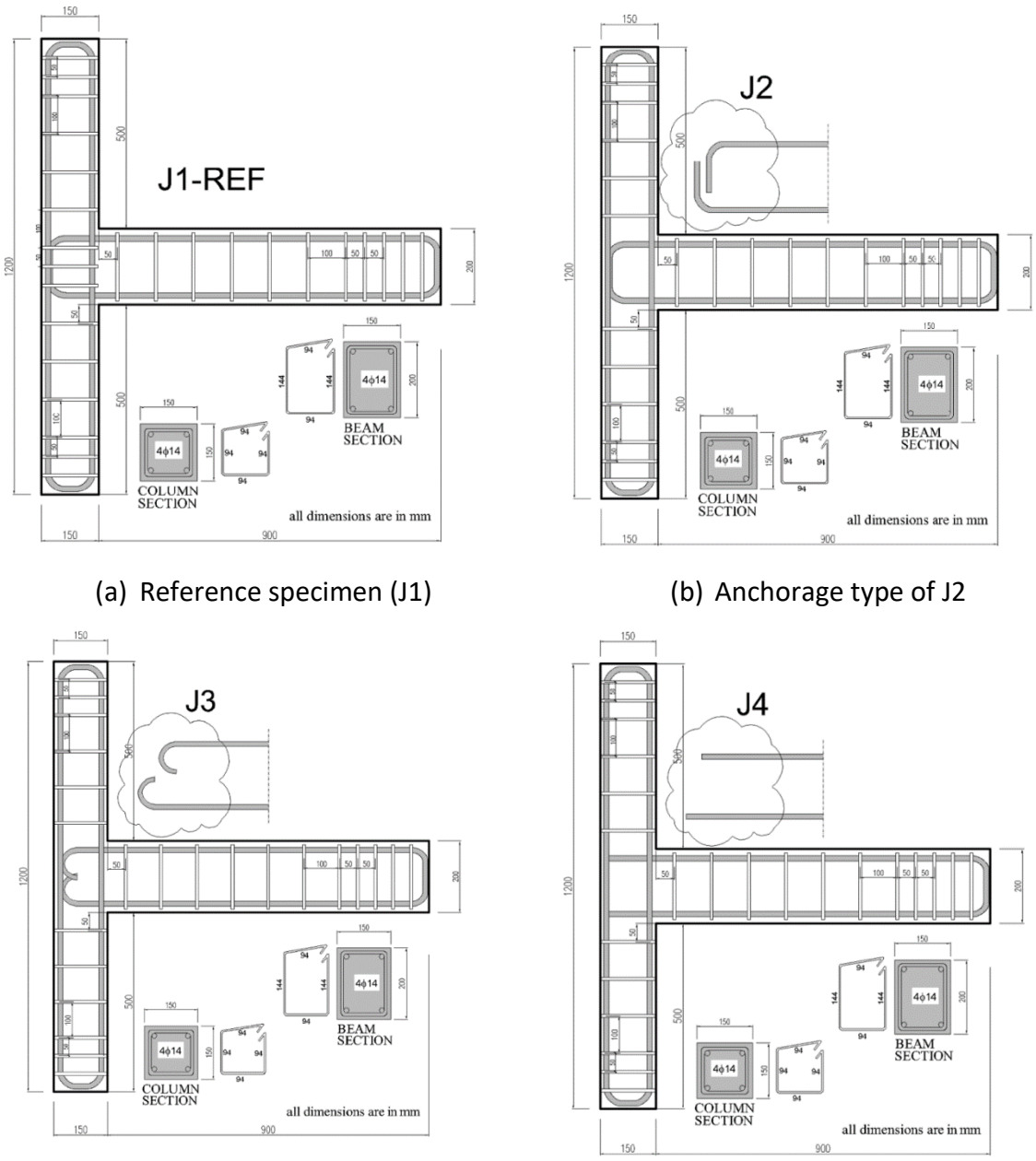

(a) Reference specimen (J1) (b) Anchorage type of J2

(c) Anchorage type of J3 (d) Anchorage type of J4

Figure 2.4. Joint conditions with different anchorage details of RC joints: (a) 180-degree angle bent beam bars; (b) 90-degree angle bent beam bars; (c) End-hook anchorage; (d) Straight bar without any hooks (Cosgun *et al*., 2020).

The load was applied in a cyclically inverted manner. A comparison was made between the specimens' responses in terms of load-drift and displacement hysteretic behaviour (illustrated in Figure 2.5). According to this graph, the bearing capacity of specimen J1 is approximately 13 kN, 8 kN for specimen J2, 7 kN for specimen J3, and 5 kN for specimen J4. The detrimental impact of the deficient anchorage details on the seismic performance of the joints was discovered to be extremely significant.

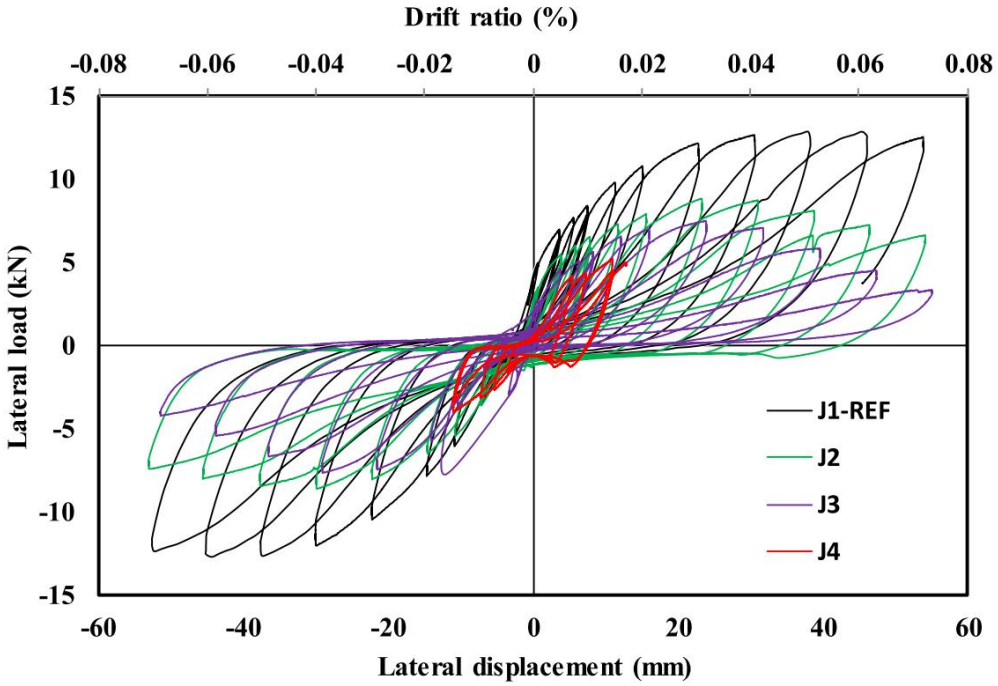

Figure 2.5. Comparison of the load-displacement relationships for J1-REF, J2, J3 and J4 (Cosgun *et al*., 2020)

2.3 PARAMETERS AFFECTING SHEAR STRENGTH OF RC BEAM-COLUMN JOINST

The type of connection and the progression of the failure modes have an impact on the shear performance (and hence capacity) of beam-column junctions. Experimental studies have revealed key characteristics that influence the behaviour of unconfined external beam-column junctions, either directly or indirectly. Kim and LaFave (2007), Hassan (2011), Tran (2016), and Parate & Kumar (2019) investigated the effect of various factors on joint behaviour under cyclic loading, such as the column axial load to column capacity ratio, concrete compressive strength, reinforcement confinement within the joint, beam reinforcement ratio, and joint aspect ratio. In the following section, the impact of three of those parameters—namely the compressive strength of concrete, the joint reinforcement confinement, and the column axial load—are thoroughly examined.

2.3.1 Impact of the compressive strength of concrete

Kim and LaFave (2007) developed a database of experimental investigations on RC joints to investigate the impact of compressive strength of concrete on joint response. The study examined a wide range of concrete compressive strengths, ranging from 19 to 89 MPa, for exterior joints. Three important points, A, B and C, were identified in relation to the joint

reaction. Point A marks the onset of diagonal cracking on connections, point B represents the yielding of longitudinal reinforcement bars, and point C denotes the crushing of concrete.

As shown in Figure 2.6, the joint shear stress is positively influenced by the compressive strength of the concrete at both Point B and Point C. A corresponding degree of correlation is noted between the compressive strength of the concrete and the joint shear stress at both Point B and Point C, covering all joint types and failure modes under consideration. Furthermore, by enhancing the load-bearing capacity of the beam, bars within the joint region and the column and beam compression zone, an increase in concrete strength also enhances the resistance of the joint.

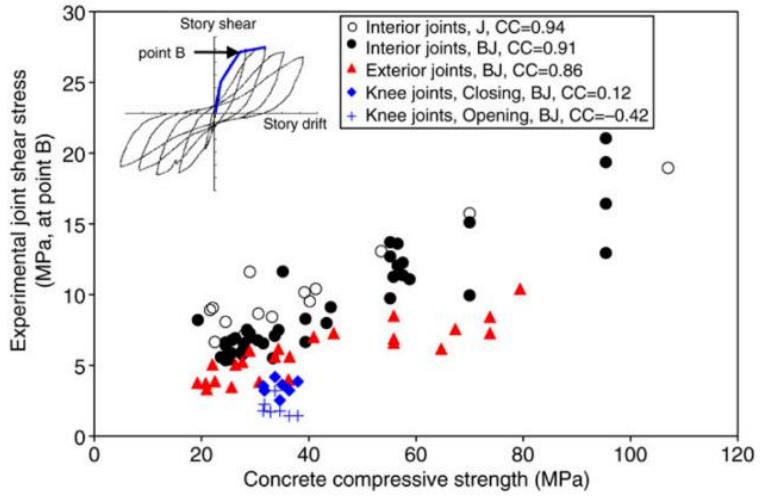

(a)

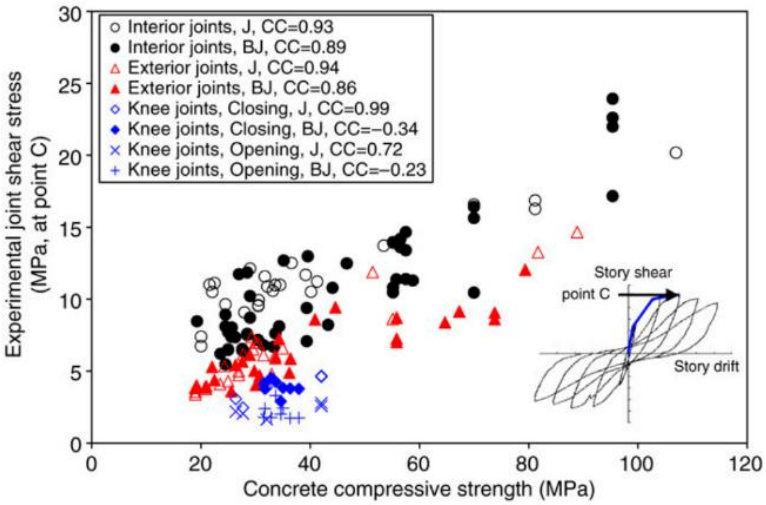

(b)

Figure 2.6. (a) Yielding of the longitudinal reinforcement (Point B); (b) Crushing of the concrete (Point C) (Kim and LaFave, 2007).

Parate and Kumar (2019) examined the shear strength at the beam-column joint for various codes. While holding all other parameters constant, they examined the impact of four distinct compressive strengths of concrete (20, 40, 60, and 80 MPa) on the shear strength of the joint. It was observed that as the compressive strength of the concrete increased, so did the predictions of the code for joint shear strength (as illustrated in Figure 2.7). The external joint experienced a relative change in joint shear strength between codes ranging from 22% to 47% in response to changes in concrete compressive strength.

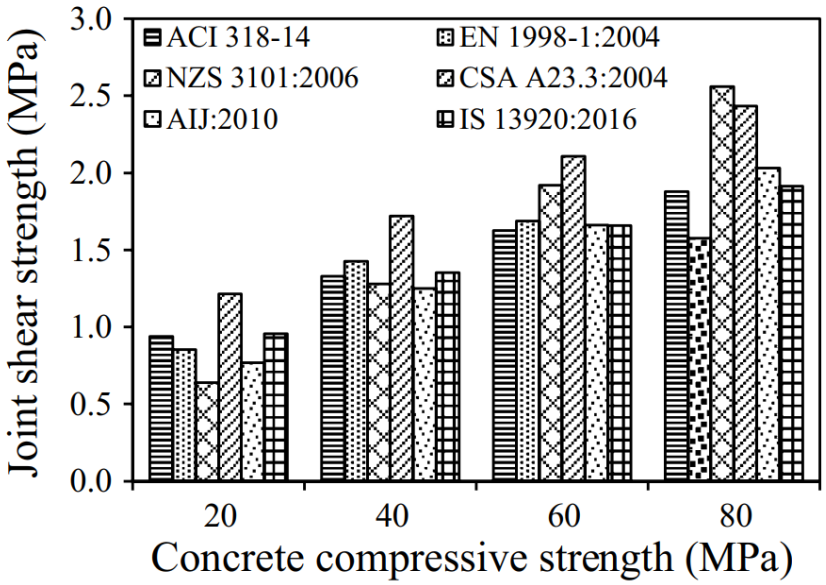

Figure 2.7. Effect of concrete compressive strength on the joint shear strength for exterior joint (Parate and Kumar, 2019).

2.3.2 Impact of the joint reinforcement confinement

A joint confinement index was proposed by Bonacci and Pantazopoulou (1993) to investigate the possible effect of joint transverse reinforcement on joint shear-resistance. This index is calculated by multiplying the volumetric joint transverse reinforcement ratio with the joint transverse reinforcement yield stress, and then dividing the result by the concrete compressive strength. In this study, the confinement by longitudinal beam, longitudinal column, and joint transverse reinforcement was calculated using the idea proposed by Bonacci and Pantazopoulou (1993). The volumetric column reinforcement ratio was calculated by dividing the total volume of the longitudinal column reinforcement within the joint panel by the volume of the joint panel, defined as the product of the column's width, depth, and the beam's height. This study calculated the volumetric beam reinforcement ratio by dividing the total volume of the beam reinforcement (inside the joint panel) by the product of the beam

width, column depth, and beam height. The volumetric ratio of joint transverse reinforcement was determined by dividing the entire volume of the joint transverse reinforcement, situated between the upper and lower beam reinforcements, by the product of the width, depth, and spacing between the upper and lower beam reinforcements. Confinement by reinforcement refers to the normalisation of the product of each volumetric reinforcement ratio and reinforcement yield stress by the compressive strength of concrete (Kim and LaFave, 2007).

Kim and LaFave (2007) performed a study utilising the aforementioned joint confinement index. Figure 2.8 illustrates that the correlation coefficients for the influence of joint transverse reinforcement on joint shear stress and strain at Point C for exterior connections with J-type failure were 0.70 and 0.74, respectively. The findings indicate a correlation between the degree of joint transverse reinforcement and the joint shear strength of external joints of the J-failure type. In this instance, both the longitudinal reinforcement of the joint and the beam are contained within the elastic range. In all other instances, no relationship seems to exist between the joint transverse reinforcement index and the joint shear stress.

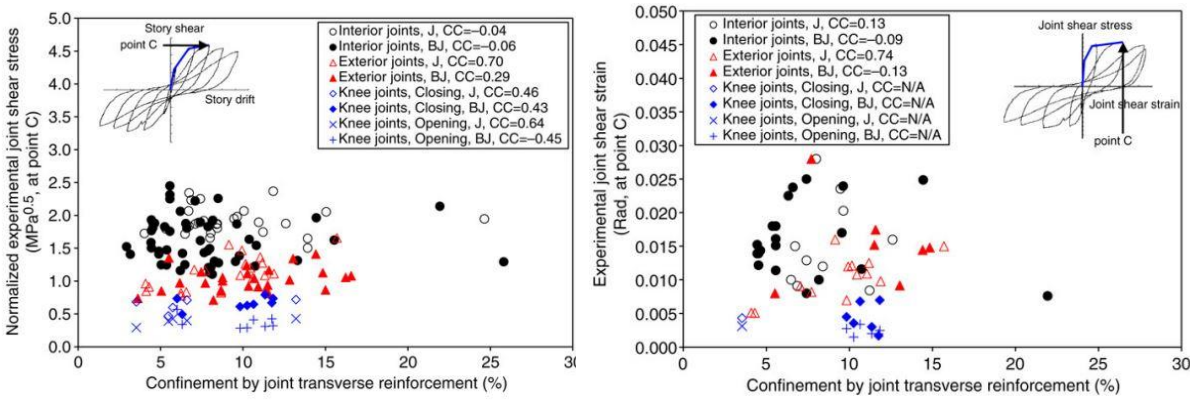

(a) (b)

Figure 2.8. Effect of connection transverse reinforcement on confinement (point C): (a) Normalised joint shear stress; (b) Joint shear strain (Kim and LaFave, 2007).

2.3.3 Impact of the column axial load

The relationship between the axial load level applied to the column and the shear strength of RC beam column connections is complicated because of the numerous variables that control the shear resistance of these joints. Pantelides *et al.* (2002), Haach *et al.* (2014), and Shafaei *et al.*, (2017) investigated the effect of column axial load on the beam-column joint in their studies. Their studies are reviewed in detail below.

A study was conducted by Pantelides *et al.* (2002) to investigate the behaviour of four half-scale RC exterior joints in shear-critical mode. Due to the fact that the specimens were designed for use in buildings developed during the 1960s, they were unable to adhere to the most recent seismic design standards. The longitudinal reinforcement in the beam was augmented to avoid premature deterioration of the beam, resulting in a shear failure mode in the joint. No transverse reinforcement was present in the joint core, and the longitudinal reinforcement bars of the beam were not sufficiently anchored in the connection.

Specimens of beam column joints were exposed to cyclic quasi-static loading at the beam end. At the top of the columns, a uniform axial compressive force of $0.1f_c`A_g$ was applied to the initial two specimens and $0.25f_c`A_g$ was applied to the remaining specimens. Each of the four specimens failed due to the development of cracks in the joint which in turn limited the joint`s shear capacity. A negligible degree of variation was detected in the maximal lateral load experienced by each specimen. The impact of column axial load compression on the strength with respect to cyclic load capacity was not significant. However, a clear distinction can be observed in the displacement ductility of specimens subjected to $0.1f_c`A_g$ axial load versus those subjected to $0.25f_c`A_g$ axial load. The ductility of the specimens exposed to the lesser axial load was 1.69 times greater than that of the beam column exterior joints subjected to the higher column compression. The relatively brittle nature of the specimens subjected to a $0.25f_c`A_g$ axial load is confirmed by the lower drift ratio at ultimate displacement in comparison to the specimens subjected to a $0.1f_c`A_g$ axial load.

Haach *et al.*, (2014) tested three exterior beam column joints with identical geometrical properties by applying varying levels of axial loads to the columns. They also compared the obtained results with certain theoretical approaches for predicting failure. The geometrical qualities of three outside beam-column connections are evaluated by subjecting them to a variety of column axial loads. The experimental results clearly showed that the joint strength is significantly impacted by the axial load of the column structures. And also, the observed

cracking pattern indicated that increased column axial stresses resulted in reduced ductility of the joint, delayed deformation of the transverse reinforcement, and caused cover rupture on the outer side of the joint.

Shafaei *et al.*, (2017) conducted an experiment to analyse the seismic behaviour of exterior reinforced concrete (RC) beam-column junctions with typical features found in mid-rise RC frame buildings in developing nations like Iran, built before the 1970s. Three half-scale external RC beam-column joints underwent testing with incremental lateral cyclic loading. The tested specimens consisted of one unit with seismic reinforcement detailing following ACI 318-11 criteria, and two units with non-seismic reinforcement detailing typical of 1970s construction practices in underdeveloped countries like Iran. Two typical deficiencies were examined in the non-seismic units: the absence of transverse steel hoops and insufficient bond capacity of the beam's bottom reinforcing bars in the joint region. The test results indicated that specimens lacking seismic detailing exhibited considerable reductions in strength and stiffness relative to the seismically detailed specimen. This was mostly attributable to joint shear failure or bond failure of the beam's bottom reinforcement bars. The specimens without seismic detailing demonstrated a 30% reduction in average strength and ductility, and a 60% decline in energy dissipation capability relative to the specimen with seismic detailing. The dimensions and reinforcing features of the specimen are depicted in Figure 2.9.

Moreover, El-Naqeeb *et al*. (2022) examined the impact of column axial stress level on connection strength by means of the nonlinear finite element analysis program ABAQUS. The research is based on a verified model of a tested exterior beam-column connection. Multiple connections have been simulated given different degrees of column axial stress and varying concrete strengths. This work demonstrates that raising the axial stress level in the column causes a postponement in the onset of joint fractures and enhances the strength of the joint. Nevertheless, the axial stress level of the column greatly enhances the shear strength of the joint, up to a specific threshold that is determined by the strength of the concrete. Beyond this threshold, a decrease in the joint strength is indicated. Thus, the degree of improvement in the joint capacity under various axial stress levels should be directly proportional to the uniaxial strength of the concrete. The influence of raising the axial stress level on the shear strength of the joint is particularly evident when using medium or high-strength concrete.

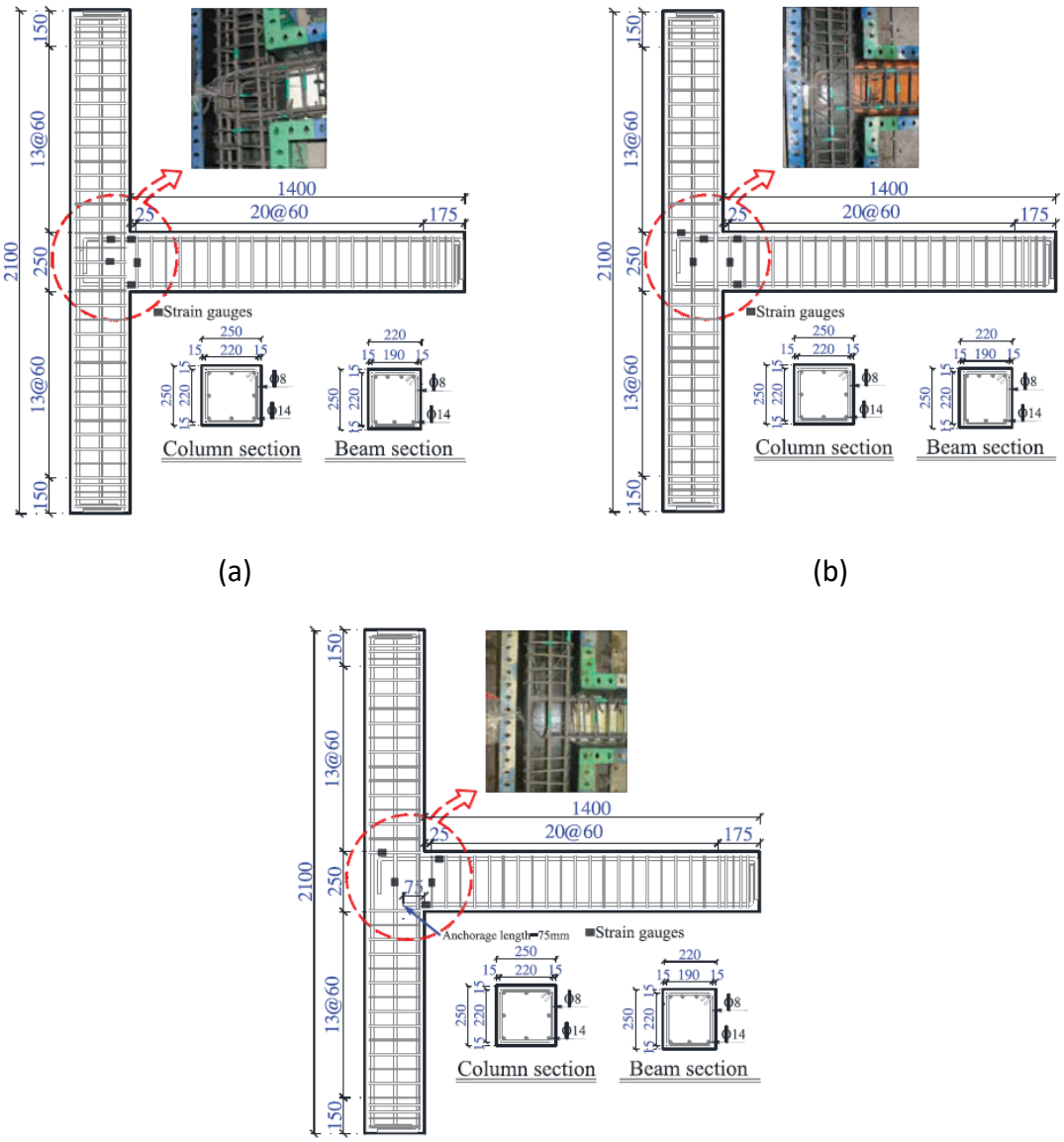

Figure 2.9. Specimen dimensions and reinforcing details, measured in millimetres by Shafaei *et al.*, (2017): (a) Specimen C1; (b) Specimen C2; (c) Specimen C3.

2.4 STRENGTHENING TECHNIQUES

Earthquake engineering has a long history of needing to strengthen structures after they have been completed (retrofit). This is because each new earthquake, reveals previously unknown deficiencies in regional construction practices. Furthermore, many low-income countries lack the expertise to implement good code based seismic engineering practice even when good codes exist, or they lack the necessary regulatory enforcement to ensure that what is required by the codes is actually implemented. Some of the different methods are concrete jacketing, steel jacketing, Externally Bonded, Near Surface Mounded techniques etc. and the more usual ones are now described with a view of determining the best for further investigation.

2.4.1 Concrete Jacketing Technique

Concrete jacketing is a widely used technique to enhance the strength of RC beam column joints by the application of a new layer of concrete and additional reinforcement around the joint. Surface preparation is the initial step in the process, which includes the roughening of the current concrete and the removal of defective sections to ensure a strong bond between the previous and new concrete. To enhance the shear and flexural strength, as well as the ductility, of the joint, additional longitudinal and transverse reinforcement, such as stirrups or ties, is incorporated. An additional layer of high-strength concrete is then placed to surround the reinforcement. However, despite its successful improvement of the structural capacity and seismic performance of the joint, this approach has several disadvantages. A key drawback is the substantial enlargement in the cross-sectional area, which might constrict the available space and disrupt architectural elements or current mechanical systems. Furthermore, the use of concrete jacketing introduces a significant amount of dead weight to the structure, which needs to be taken into consideration during the entire design process. Additionally, this technique is laborious and time-consuming, frequently necessitating elaborate formwork and prolonged curing periods (Karayannis *et al.*, 2008). Furthermore, inadequate workmanship during the process of surface preparation or incorrect adhesion between the old and new concrete might result in diminished efficacy or premature failure. Finally, the enlarged dimensions of the joint might have an adverse impact on the visual appeal of the building, thereby rendering this approach less appropriate for constructions where visual appeal is a primary factor.

2.4.2 Steel Jacketing Technique

Steel jacketing is a technique employed to augment the structural integrity of beam-column connections by enclosing the joint with steel plates or sections. This jacket is formed by bolting or welding these steel components together and securing them to the existing concrete at the joints. This approach offers the benefit of achieving substantial enhancements in shear strength and ductility without extensive enlargement of the cross-sectional area, rendering it appropriate for situations with limited space allocation. Nevertheless, steel jacketing has several drawbacks. A major issue of concern is corrosion (Engindeniz *et al*., 2005), especially in humid or seaside atmospheres. Failure to adequately protect the steel with paints or maintenance can result in corrosion and a gradual loss of its structural integrity, therefore undermining the efficacy of the jacket. Fire protection poses an additional obstacle, since steel becomes weaker at elevated temperatures, requiring the application of fireproofing techniques like coatings or wraps. However, this might escalate the expenses and complexity of the design. Furthermore, the effectiveness of steel jacketing heavily relies on the implementation of appropriate anchorage and detailing (Engindeniz *et al*., 2005). Insufficient anchorage can lead to inefficient weight transfer, slippage, or even overall failure of the jacket. The installation of steel jacketing necessitates skilled technicians, particularly for welding or bolting, and errors in these procedures might diminish the overall efficacy of the reinforcement. Finally, while steel jacketing is generally faster to install than concrete jacketing, the presence of steel plates can still impact the aesthetics of the structure and may require additional finishes or cladding to achieve a desirable appearance.

2.4.3 Externally Bonded (EB) Technique

The Externally Bonded (EB) method is a structural engineering approach that strengthens and rehabilitates existing structures by applying external reinforcement. This technique utilises composite materials, usually Fibre Reinforced Polymers (FRP), to improve the load-carrying capacity, stiffness, and durability of structural components such concrete beams, columns, slabs, and walls.

The main aim of the EB approach is to strengthen faults or inadequacies in current structures. Structures can deteriorate over time owing to ageing, environmental exposure, higher loads, or changes in usage demands (Frangopol and Soliman, 2019). The EB approach provides a practical option to strengthen these structures, allowing them to comply with current design standards and support increased loads without requiring substantial renovation.

Furthermore, the EB approach is crucial for repairing and rehabilitating deteriorated or damaged structures (Li *et al.*, 2021). Engineers can restore structural integrity, reduce cracking, and prevent further deterioration by using composite materials like Fibre Reinforced Polymers (FRP) as external reinforcement on damaged parts. This method helps prolong the lifespan of the structure, reducing the necessity for expensive and intrusive repairs or replacements. The EB technique is used to reinforce structures in situations like seismic retrofitting or improving resilience to environmental elements such as corrosion or severe weather (Sbahieh *et al*., 2022)**.** Engineers can customise the strengthening solution by selectively using external reinforcement to enhance the structure's resilience to harsh circumstances and potential threats.

The key consideration in this method is proper surface preparation to ensure adequate bonding between the existing structure and the FRP materials. This typically involves cleaning the surface to remove dirt, grease, oil and loose particles. Any existing coatings, sealants, or surface irregularities that may affect bonding are addressed. FRP materials, such as CFRP or GFRP sheets, strips, or fabrics, are then applied to the prepared surface using suitable adhesive systems. Pressure is applied using rollers or hand tools to ensure close contact between the FRP and the substrate and to remove trapped air or voids. The FRP materials are laid in multiple layers, typically with overlapping edges to ensure uniform coverage and optimum load transfer. Despite its many advantages, the Externally Bonded (EB) method also has some disadvantages. The pros and cons of this technique are described below.

Advantages of the EB method:

In comparison to traditional methods such as steel jacketing or concrete overlay, the EB approach provides a faster and more efficient way to strengthen structure elements such as beams, columns, beam-column connections, and shear walls. This can reduce the downtime of the structure while minimising disturbance to occupants or activities.

Carbon fibre reinforced polymers (CFRP), aramid fibre reinforced polymers (AFRP), and glass fibre reinforced polymers (GFRP) are examples of high-strength reinforcement materials that, according to Laseima *et al*. (2020), can substantially improve the structural performance and load-bearing capacity of beam-column joints. This enables the implementation of greater design loads or enhanced resistance against external forces, including wind and seismic loads.

It has been investigated by researchers through experimental studies that EB strengthening increases the ductility and durability of structural elements such as beams, columns, beam-column joints, making them more resistant to earthquake loads and environmental factors (e.g., Karayannis and Sirkelis, 2008; Zamani Beydokhti and Shariatmadar, 2016; Lee and Lopez, 2020; and Vahidpour *et al*., 2022). The use of corrosion resistant reinforcing materials reduces the risk of deterioration and extends the service life of the structure.

The EB approach is non-invasive to the current structure as it consists of placing reinforcement materials around rather than inside the joint. This lessens the necessity for disruptive construction activities like demolition or excavation and lowers the risk of harm to nearby building elements.

The EB method can be applied on a wide range of structural elements. It can also be applied to different types of structures, such as concrete, steel or masonry. This versatility makes the method suitable for retrofitting existing structures with various design constraints.

Disadvantages of the EB FRP method:

The effectiveness of the EB method depends on the bond between the reinforcement materials and the existing structure. Poor surface preparation, inadequate adhesive application, or environmental factors can compromise the bond quality, leading to reduced strengthening effectiveness or premature failure (Tatar and Milev, 2021).

The compatibility between the reinforcement materials and the existing structure must be carefully evaluated to ensure optimal performance and durability. Differences in material properties, coefficient of thermal expansion, or stiffness can lead to compatibility issues and potential long-term problems, such as delamination or debonding (Tatar and Hamilton, 2016 and Tatar and Milev, 2021).

The cost-effectiveness of the EB technique in comparison to standard strengthening methods is determined by factors such as building size, design complexity, and availability of experienced labour and specialised materials. Initial costs may be elevated, particularly for extensive projects or constructions facing distinctive obstacles.

2.4.4 Near-Surface Mounded (NSM) Technique

Recently, NSM FRP bars have emerged as an effective option for enhancing the flexural and shear strength of inadequate concrete, masonry, and timber elements.

Figure 2.10 depicts that the NSM FRP reinforcement bar may consist of round, square, rectangular, or oval rods, as well as strips. For the sake of brevity, the term "bars" is used to refer to all cross-sectional configurations, while "strips" is reserved for thin narrow strips. Different cross-sectional geometries offer a variety of advantages and practical application options. For instance, square bars optimise the sectional area for a specified square groove dimension, while round bars are more accessible and facilitate easier anchoring in prestressing applications. Narrow strips optimise the surface area to cross-sectional area ratio for a specified volume, thereby reducing the likelihood of debonding, but necessitate a thicker cover for a given cross-sectional area (De Lorenzis and Teng, 2007).

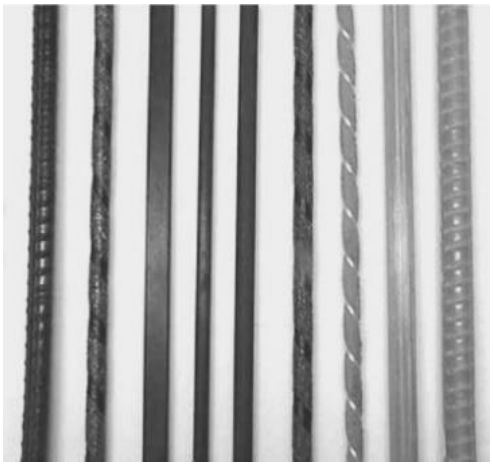

Figure 2.10. Types of FRP bars for NSM applications (De Lorenzis and Teng, 2007).

The term 'near' is used to differentiate this structural retrofitting technique from those employing FRP composites with external bonds. As shear or flexural reinforcement, FRP bars are utilised in the NSM strengthening technique. Embedment is achieved by cutting a groove into the surface of the to be reinforced member along the intended direction and to the intended width and depth. Epoxy or cement substance fills in part the groove. The paste is then forced to flow around the bar and totally fill the area between the bar and the groove by means of the FRP bars with round, square or rectangular cross sections being inserted in the grooves and lightly pressed. The surface is then levelled once more once the grooves have filled with more paste. The groove should be dimensioned to guarantee sufficient adhesive around the bars; typical groove dimensions for various types of FRP bar are referenced (Abdullah, 2016). For FRP round bars, the minimum dimension of the grooves should be at least 1.5 times the diameter of the FRP bars, as shown in Figure 2.11. The minimum groove dimension for FRP rectangular bars is $3.0a_f \times 1.5b_f$ (where a_f and b_f are the width and height

of the FRP/steel bar, respectively) provided by Le Hoang *et al.*, (2019). To prevent overlapping of tensile tensions around FRP bars, the distance between grooves on FRP bars should be greater than twice the groove's depth. To minimise debonding failure of FRP bars, a clear edges distance four times the depth of the NSM groove should be provided (ACI 440.1R-15, 2015).

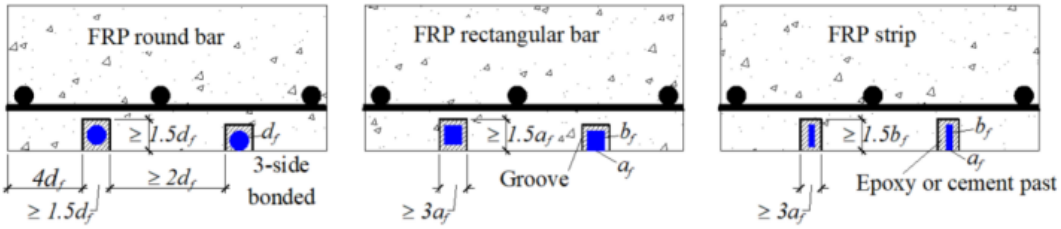

Figure 2.11. Variety of NSM FRP bars and minimum dimensions of grooves (Le Hoang *et al.*, 2019).

Although the Near Surface Mounted (NSM) approach offers many benefits, it also comes with drawbacks. Below are the pros and cons of this method.

Advantages of the NSM method:

Nanni *et al*., (1999) claimed that The NSM strengthening method may be more advantageous than externally bonded reinforcing (EBR) methods in specific circumstances due to its superior reinforcement anchoring systems, resistance to external corrosion, and reduced surface preparation and installation time.

First, EBR cannot mobilise the maximum tensile strength of FRP materials because of their premature debonding, according to previous research (Spadea *et al*., 1998). Several anchorage systems have been proposed (Khalifa *et al*., 1999) to increase the efficacy of the EBR technique. The NSM retrofitting technique enables the anchoring of FRP reinforcing rods/strips into RC members to achieve reliable anchorage.

A further benefit of NSM embedment is that it considerably decreases the likelihood of damage caused by vandalism, fire, mechanical damage, and ageing. When these composites are subjected to high and low temperatures, their reinforcing performance can be negatively impacted and decrease considerably (Di Tommaso *et al*., 2001).

Disadvantages of the NSM method:

The NSM approach is limited in its application to existing structures, especially those with restricted access or space constraints. Adding NSM FRP retrofitting to existing concrete elements might be difficult in constructions with limited access to the concrete surface or where drilling slots for rod insertion is not possible due to structural or architectural constraints.

Ensuring adequate anchorage of the FRP rods or bars within the concrete matrix is crucial for the effectiveness of the NSM method. However, achieving proper bonding and anchorage may be challenging, especially in deteriorated or poorly consolidated concrete substrates. Factors such as surface contamination, inadequate surface preparation, or insufficient concrete cover can compromise the bond between the FRP reinforcement and the surrounding concrete (Hosen *et al*., 2015).

Inadequate bonding between FRP rods or bars and the concrete substrate increases the danger of delamination or debonding over time. This might happen owing to poor surface preparation, insufficient adhesive penetration, or cyclic loading conditions. Delamination compromises the effectiveness of the strengthening intervention and can result in reduced structural performance or premature failure of the reinforced element (Su *et al*., 2022).

In addition, Table 2.1 shows the advantages and disadvantages of the techniques mentioned above.

Table 2.1. Comparison of Strengthening Techniques for RC Beam-Column Joints

Technique	Advantages	Disadvantages
Concrete Jacketing	-Significantly improves shear/flexural strength and ductility. - Uses familiar materials (concrete, rebar). - Long-term durability if properly executed.	- Bulky: Increases member size, affecting aesthetics/space. - Labor-intensive: Requires formwork, curing, and skilled workmanship. - Adds dead load to the structure. - Risk of poor bond between old/new concrete.
Steel Jacketing	- Space-efficient: Minimal cross-section increase. - Rapid installation (bolting/welding). - High shear/ductility enhancement.	- Corrosion risk, especially in humid environments. - Requires fireproofing (additional cost). - Anchorage failures if poorly detailed. - Aesthetic concerns (may need cladding).
EB FRP	- Lightweight: No significant dead load. - Corrosion-resistant (CFRP/GFRP). - Fast installation, minimal disruption. - Versatile (applicable to concrete/steel/masonry).	- Debonding risk if surface prep/adhesive fails. - Material costs (CFRP > steel/concrete). - Low fire resistance (polymer matrix). - Limited ductility compared to steel.
NSM FRP	- High bond strength (embedded in grooves). - Protected from vandalism/environment. - Minimal aesthetic impact. - Better anchorage than EB FRP.	- Grooving complexity: Requires precise execution. - Limited applicability in confined spaces. - Delamination risk if bonding is inadequate. - Higher skill requirement for installation.

2.5 FIBRE REINFORCED POLYMER

Fibre Reinforced Polymer (FRP), also known as Fibre Reinforced Plastic, is a composite material composed of a polymer matrix and high-strength fibres. This combination produces a material with enhanced mechanical properties, including high strength and stiffness, while remaining lightweight.

Fibre-reinforced polymers can be produced in multiple configurations, including structural shapes, reinforcing bars, deformation systems such as externally wound fibres and sand coatings, along with fabric coverings for both structural and non-structural elements (GangaRao *et al*., 2007). FRP composites are produced by combination fibres with polymers, either through the saturation and curing of polymer layers or by adhering prefabricated laminates. Three commercially accessible kinds of fibre-reinforced polymers (FRPs) for retrofitting are aramid FRP (AFRP), carbon FRP (CFRP), and glass FRP (GFRP).

Aramid FRP (AFRP): Aramid fibres, commonly known in the market as Kevlar, are illustrated in Figure 2.12 (a). The structure of Aramid fibre is inherently anisotropic and typically exhibits a yellow hue. Aramid fibres are costlier than glass, exhibiting moderate stiffness and suitability for tensile applications (such as cables and tendons), however demonstrating weaker compressive strength. Aramids possess higher tensile strength, significant stiffness, high modulus, and low weight and density (Günaslan *et al*., 2014).

Carbon FRP (CFRP): Carbon fibres exhibit anisotropic properties. Carbon fibre, depicted in Figure 2.12 (b), is manufactured at 1300°C. Carbon fibres provide high strength, exceptional creep resistance, chemical resistance, low conductivity, low density, and a high elastic modulus. The disadvantages of carbon fibres are their high cost and anisotropic nature, coupled with low compressive strength (Günaslan *et al*., 2014).

Glass FRP (GFRP): Glass fibres, as depicted in Figure 2.12 (c), exhibit isotropic properties and are the most commonly utilised filaments. Various types of glass fibres are utilised in GFRP, with the predominant varieties being E-glass (electrical), S-glass (high strength), and C-glass (alkali-resistant) (Günaslan *et al*., 2014). The characteristic properties of glass fibres are high strength, low cost when compared to other FRPs (Meikandaan and Murthy, 2017), and good water resistance and resistance to chemicals.

(a) (b) (c)

Figure 2.12. (a) Typical Aramid FRP (AFRP) (Kandekar and Talikoti, 2019); (b) Typical Carbon FRP (CFRP) (Günaslan *et al*., 2014); Typical Glass FRP (GFRP) (Rageh *et al*., 2022).

2.5.1 Mechanical Properties

The mechanical properties of FRP composites are determined by the proportion of fibres and matrix materials, the manufacturing process, the mechanical properties of constituent materials, and the orientation of the fibres within the matrix. Fibres may be designed as ''Continuous Form'' (aligned and continuous fibres are generally straight and long as well as parallel to one another) or as ''Woven Form'' (fibres produced in a cloth form and providing strength in multiple directions) or as ''Chopped Form'' (fibres are typically irregularly and discontinuously arranged and short, also known as fibreglass) (Abbood *et al*., 2021). Figure 2.13 illustrates the comparative behaviour of FRP and steel under tensile stresses, highlighting that the stiffness of CFRP exceeds that of GFRP and AFRP in the stress-strain relationships. CFRP and GFRP are utilised in advanced applications for the retrofitting of concrete structures. The typical material properties of carbon, glass, and aramid fibre-reinforced polymers (FRP) are given in Table 2.2.

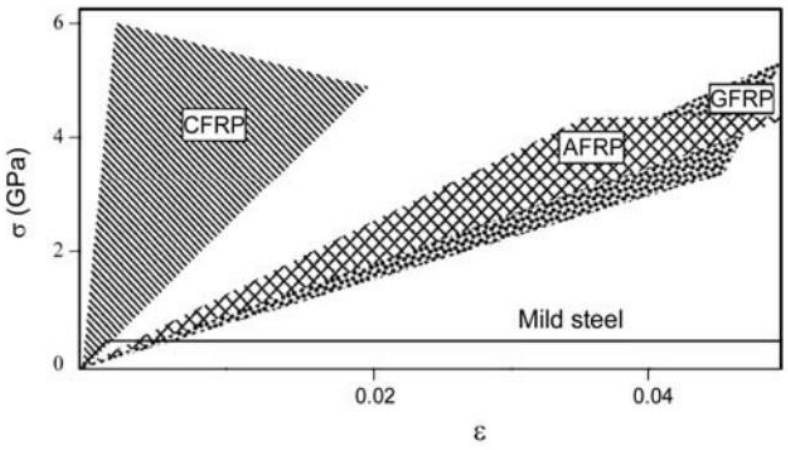

Figure 2.13. Typical stress-strain relationships for various FRPs and standard steel (Mohammadizadeh *et al.*, 2009).

Table 2.2. Typical characteristics of carbon, glass, and aramid fibres (Mohammadizadeh *et al.*, 2009).

Type of fibre	Thickness	Ultimate tensile strength	Elastic modulus	Ultimate tensile elongation
	mm	MPa	GPa	%
Carbon	0.10 – 0.25	2100 - 6000	215 - 700	0.2 – 2.3
Glass	0.06 – 0.30	1900 - 4800	70 - 90	3.0 – 5.5
Aramid	0.10 – 0.30	2900 - 4100	70 - 130	2.5 – 5.0

2.6 LITERATURE REVIEW ON RETROFITTED EXTERIOR BEAM-COLUMN JOINTS

Strengthening RC beam-column connections is a difficult task with numerous practical problems. Various methods applicable to concrete elements have also been used to make connections, the most typical of which is the fabrication of RC or steel jackets Alcocer and Jirsa (1993). RC jackets and some steel jackets, such as steel "cages," necessitate extensive work and artistic craftsmanship. Furthermore, concrete jackets expand the size and weight of structural members. Steel plates that are flat or corrugated have also been tested (Ghobarah *et al.,* 1997; Aboutaha *et al.,* 1999; and Campione *et al.,* 2015). In addition to corrosion protection, these elements necessitate particular attachment via the use of epoxy adhesives in conjunction with bolts or special grouting. Since these strengthening techniques are time-consuming, require a lot of labour, and lead to an enhance in the size of the structural elements, alternative strengthening methods have been researched by Hollaway and Leeming (1999).

EB and NSM methods are two of the most used types of strengthening techniques (Akbarzadeh and Maghsoudi, 2010; Zhou *et al.,* 2013). Many studies have looked at the process of EB FRP retrofitting in recent years because of its high strength-to-weight ratio, superior corrosion resistance, and ease of installation. Many experimental investigations have demonstrated the effectiveness of FRP retrofitting in improving the seismic resistance of inadequate beams and columns (e.g., Chen and Teng, 2003; Mofidi and Chaallal, 2014; Venkateswarlu and Natarajan, 2015; del Rey Castillo *et al*., 2018; Mai *et al*., 2018; Lee and Lopez, 2020; and Vahidpour *et al*., 2022).

The NSM technique was first employed in Finland in the 1940s to strengthen a bridge deck slab by inserting steel bars into grooves (Asplund, 1949). The first experimental investigation on the NSM approach was carried out utilising CFRP strips in grooves carved into concrete specimens (Blaschko and Zilch, 1999). Several experimental studies have been conducted to evaluate the flexural behaviour of RC beams reinforced with NSM bars or strips made of FRP materials (e.g., Al-Mahmoud *et al*., 2009; El-Hacha and Gaafar, 2011; Badawi and Soudki, 2009; and Singh *et al*., 2014). FRP retrofitting has several advantages, including high strength, lightweight, corrosion resistance, and potentially great durability, but it is expensive and not widely available. Furthermore, FRP bars have low ductility. Steel bars, on the other hand, are widely available, less expensive, and exhibit appropriate ductility, long-term durability, and bond performance (Rahal and Rumaih, 2011)**.** Garrity (2001) employed NSM strengthening

applying steel bars on arch bridges. Almusallam *et al.* (2013) studied the experimental and numerical behaviour of RC beams enhanced in flexure using NSM steel or GFRP bars and discovered that NSM bars increased RC beam flexural capacity. In addition, mounting of steel bars inside the groove on concrete beams and columns, to improve their flexural capacity, has been observed in previous investigations (Hosen *et al.,* 2014; Hasan *et al.,* 2016; Alavi-Dehkordi *et al.,* 2019; and Askandar and Mahmood, 2019). Moreover, the preparation of U-shaped or L-shaped FRP bars is not possible in the laboratory and field environment. These different shapes of FRP bars must be prepared by the manufacturer. Steel is employed as a reinforcing material due to its economic feasibility. It offers a cost-effective and structurally efficient solution. In addition, it can be given a shape and implemented effortlessly in the field area.

A comprehensive review of existing literature related to the topic reveals that NSM bars/strips and EB FRP jacket techniques are generally applied separately on RC beam-column joints. There are not enough studies in the literature on the NSM and EB FRP jacketing hybrid methods applied on RC beam-column connections. Retrofitting strategy using EB, NSM and EB+NSM around the beam-column joints are examined in detail below.

2.6.1 Antonopoulos and Triantafillou (2003)

Antonopoulos and Triantafillou (2003) conducted an extensive experimental study on reinforced concrete joints reinforced with fibre-reinforced polymer (FRP) under cyclic loading. An investigation was conducted on the impact of characteristics including the FRP ratio, mechanical anchorage, and joint reinforcement on the effectiveness of the evaluated retrofitting procedures. This study involved 18 tests on two-thirds scale exterior RC shear deficient sub-assemblages. Each specimen was identical in size and reinforcing configuration and were intended to be shear deficient, simulating a substandard RC beam-column connection. Two specimens were equipped with one shear reinforcement in the joint, whereas the remaining specimens had no joint shear reinforcement. Additionally, 3 out of 16 specimens without transverse reinforcement in the connection had a transverse beam on one side to replicate the confinement provided by the transverse elements meeting at the joint.
The characteristics of the specimens that were tested are displayed in Figure 2.14 (a). The specimens were reinforced utilising glass and carbon FRP sheets and strips with varying amounts of FRP reinforcement on the beam column joints (see in Figure 2.14 (b)). The results highlight the crucial function of mechanical anchorages in preventing premature debonding.

They also provide valuable insights into a variety of characteristics, including the area fraction of FRP, FRP distribution between the beam and column, column axial load, internal joint steel reinforcement, early damage, carbon versus glass fibres, and sheets versus strips.

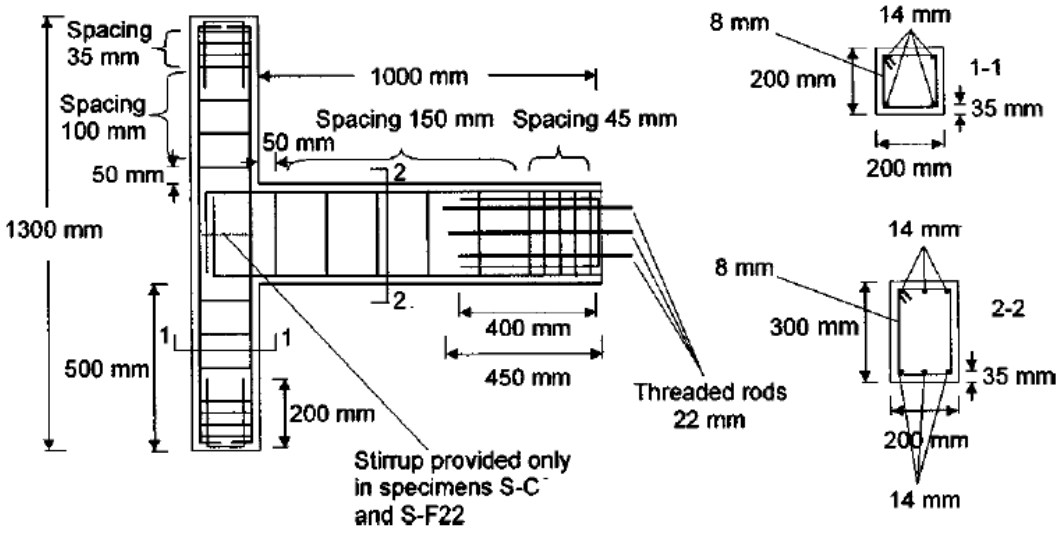

(a)

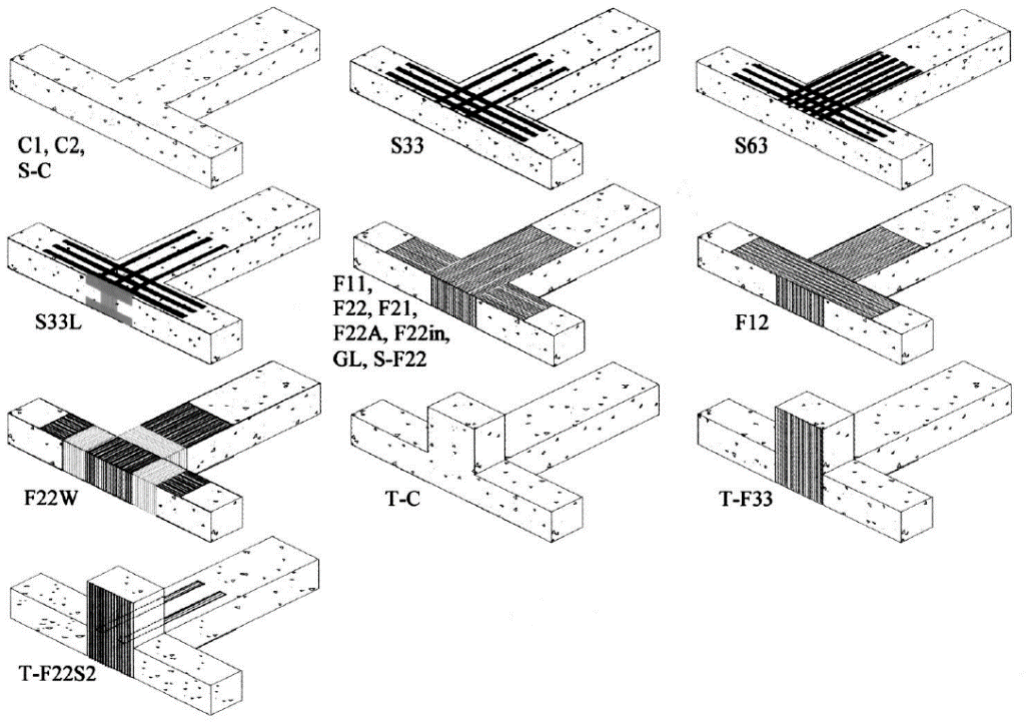

(b)

Figure 2.14. (a) Reinforcement details; (b) Details of the FRP application process (Antonopoulos and Triantafillou, 2003).

2.6.2 Karayannis and Sirkelis (2008)

Findings from an experimental study on exterior RC connections retrofitted with a combination of CFRP and epoxy resin were presented by Karayannis and Sirkelis (2008). The specimens that were not reinforced were divided into two groups: one lacking transverse reinforcement (Group A) and the other using transverse reinforcement in the joint (Group B). Figure 2.15 (a) displays the setup and the reinforcement plan for the unstrengthened specimens in Group A. Group B specimens were the same as those in Group A, but they had additional transverse reinforcement in the form of four 8 mm transverse reinforcements added to the connection area.

Two specimens from each group were first exposed to moderate cyclic stresses. The third specimen was reinforced using CFRP sheets before the application of any loads. The CFRP sheets were applied to restrict the critical zones of both the column and the beam, as well as the joint zone, in accordance with the configuration depicted in Figure 2.15 (b).

In this study, the average concrete compressive strength specimens were 36.4MPa (cylinder strength), and the steel bars used were of grade S500. The CFRP sheets were utilised the SikaWrap® Hex 230 C and Sikadur®330 (epoxy based impregnating resin and adhesive). The CFRP sheets have a thickness of 0.12mm and the primary fibre direction is 0 degrees (unidirectional).

The proposed reinforcement technique significantly improved load-bearing capacity, energy absorption, and ductility, while also changing the failure mode from connection failure to flexural hinging in the beam. The test findings indicated that the seismic response of specimens exposed to significant damage might be regained by fixing the damaged joint utilising epoxy injection. Furthermore, the energy absorption and strength exceeded those of the control specimen. The test found that the Carbon Fibre Reinforced Polymer (CFRP) impact on shear strength is influenced by the existence of connection reinforcement.

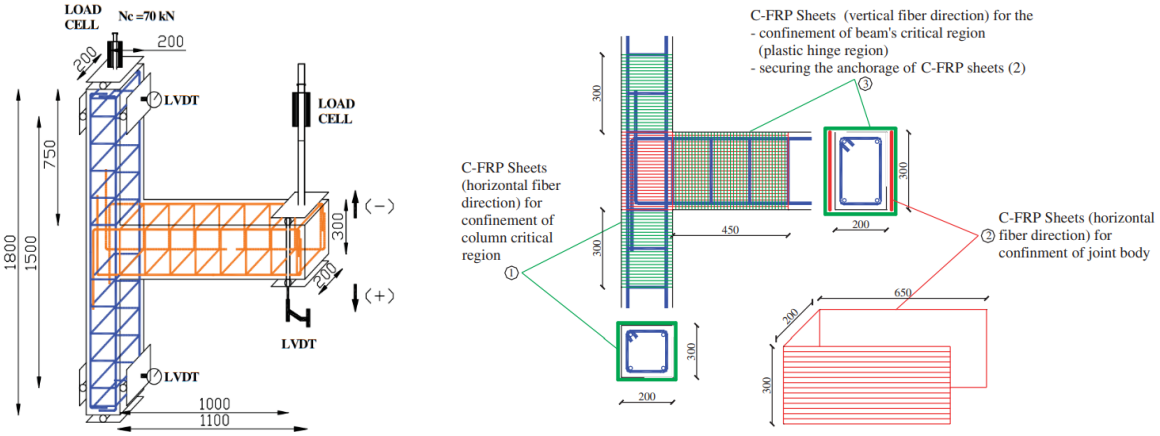

(a) (b)

Figure 2.15. (a) Test set-up and the reinforcement configuration of the specimens; (b) Strengthening scheme using CFRP sheets (Karayannis and Sirkelis, 2008).

2.6.3 Shrestha et al. (2009)

Experimental findings of exterior RC connections strengthened with FRP composites were examined by Shrestha *et al.* (2009). Two sets of external connections were examined. The initial group had a monotonic load and included three connections (one control and two strengthened with FRP), whereas the second group was tested with cyclic loading and included two connections (one control and one reinforced with FRP). FRP sheets and strip were used to reinforced of the specimens. The reinforcement configuration and the application scheme are shown in Figure 2.16 (a) and (b). In their setup, hinge supports were attached to both ends of the column and anchored to a rigid testing apparatus. The column was exposed to an axial load of 180 kN (equivalent to 8% of the column's gross axial load capacity and indicative of a typical floor load) via a hydraulic jack connected to one end of the column via a system of high-strength Macalloy bars.

Tests showed that FRP effectively improved the load-carrying capacity and deformation of these joints once exposed to either cyclic or monotonic loads. Furthermore, the tests facilitated a deep understanding of the strength and behaviour of FRP. Wrapping beams or columns at the ends of the FRP strengthening prevented full debonding of the FRP. However, it was recognised that preventing localised debonding of the FRP at the shear cracks is necessary to improve the efficiency of the FRP strengthening. The FRP strain data showed that the full potential of the FRP was not achieved due to the gradual separation of the FRP strips.

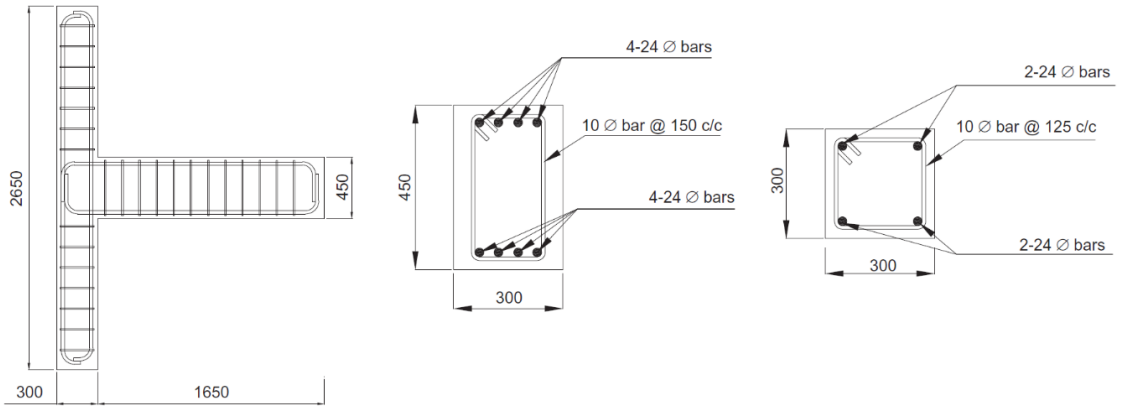

(a)

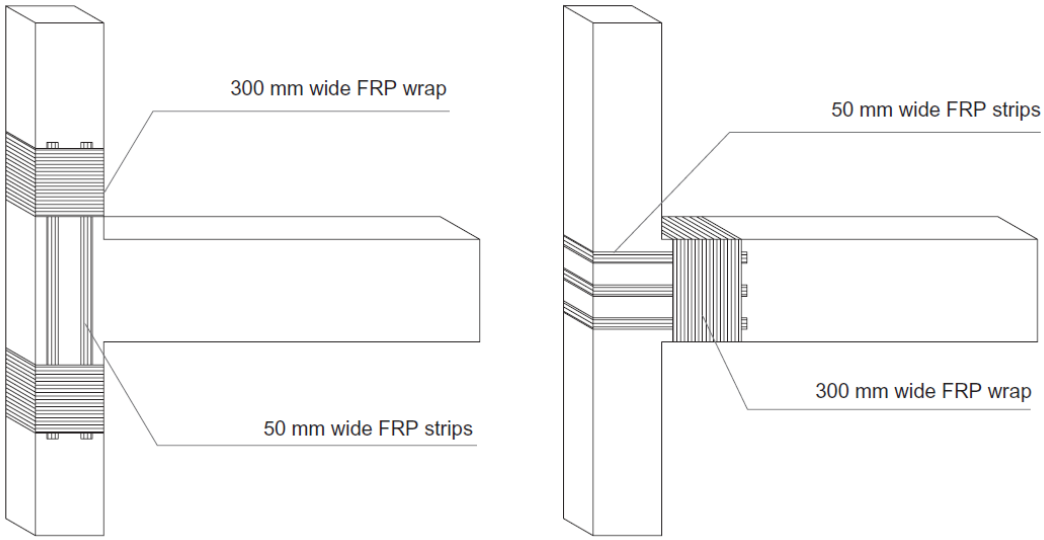

(b)

Figure 2.16. (a) Reinforcement configuration; (b) Details of the FRP application (Shrestha *et al*., 2009).

2.6.4 Ilki et al. (2011)

The behaviour of FRP reinforced connections utilising smooth bars and low-strength concrete (the mean measured cylinder strength was 8.3 MPa for the testing days) was investigated by Ilki *et al.* (2011). The dimension of specimens and reinforcement information are illustrated in Figure 2.17 (a). Two series of eight exterior joints at full scale were constructed, each lacking transverse reinforcement in the connection zone. The tested specimens comprised a column, an in-plane beam, a transverse beam, and a slab. They were exposed to a cyclic load at the beam end in addition to a constant column axial load. The application of the FRP and the reinforcement scheme are illustrated in Figure 2.17 (b).

The joint core was enveloped by the first piece, which is a square FRP sheet; the second piece was affixed diagonally to piece 1 in order to provide adequate anchorage for piece 1 to the specimen. It was concluded that using FRP sheets alone was insufficient to prevent the longitudinal bars of the beam from slipping. The implementation of FRP sheets as a retrofit for junctions after welding rehabilitation of anchorage bars resulted in a substantial postponement of strength degradation.

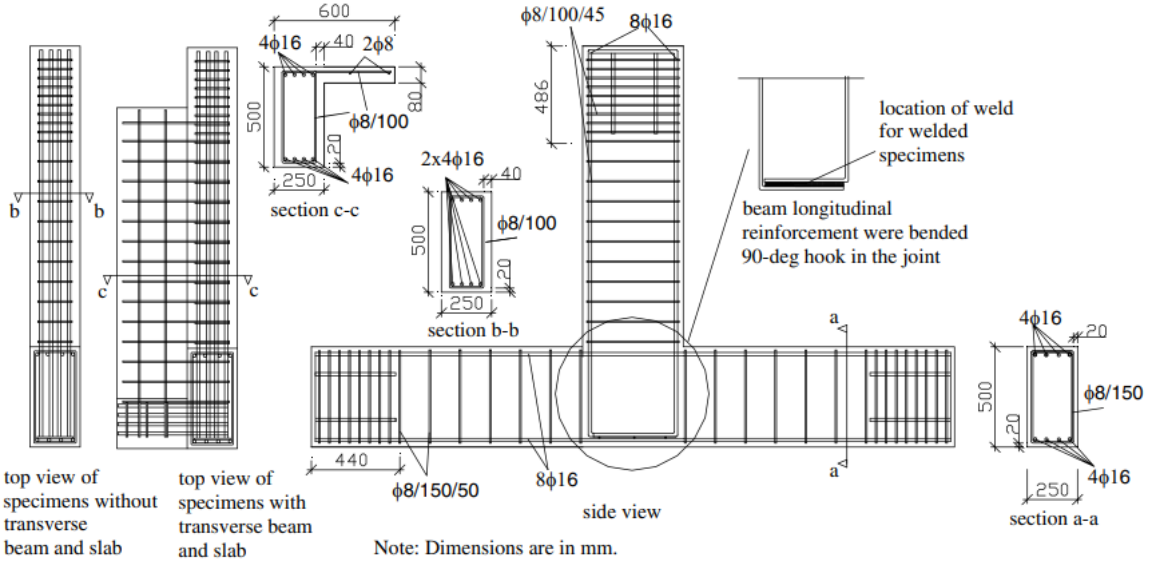

(a)

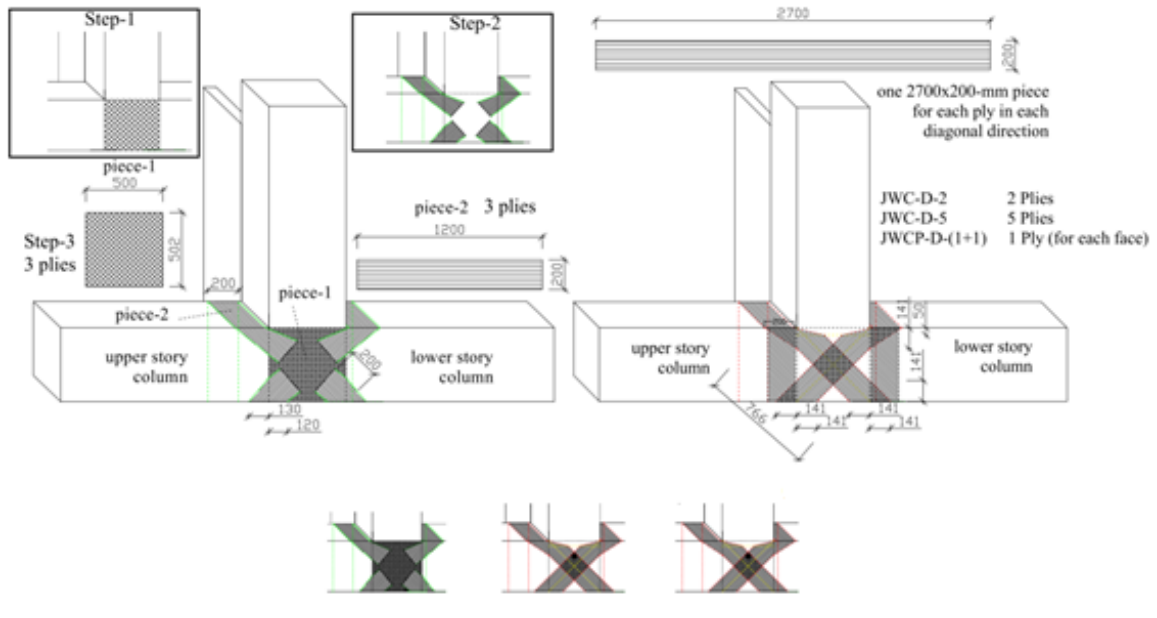

(b)

Figure 2.17. (a) Details of reinforcement; (b) The FRP application configurations (Ilki *et al.*, 2011).

2.6.5 Del Vecchio et al. (2014)

Six beam-column corner junctions were tested under lateral loads by Del Vecchio *et al*. (2014). Their specimens were built without transverse reinforcement at the connection zone to ensure shear failure would happen at the core see in Figure 2.18. This research investigated the behaviour of unconfined joints that do not comply with current seismic codes and the effectiveness of externally bonded FRPs as a retrofitting method. Their findings indicated that all the reinforcement techniques employed were effective in enhancing strength compared to the control group prior to the sheets being detached.

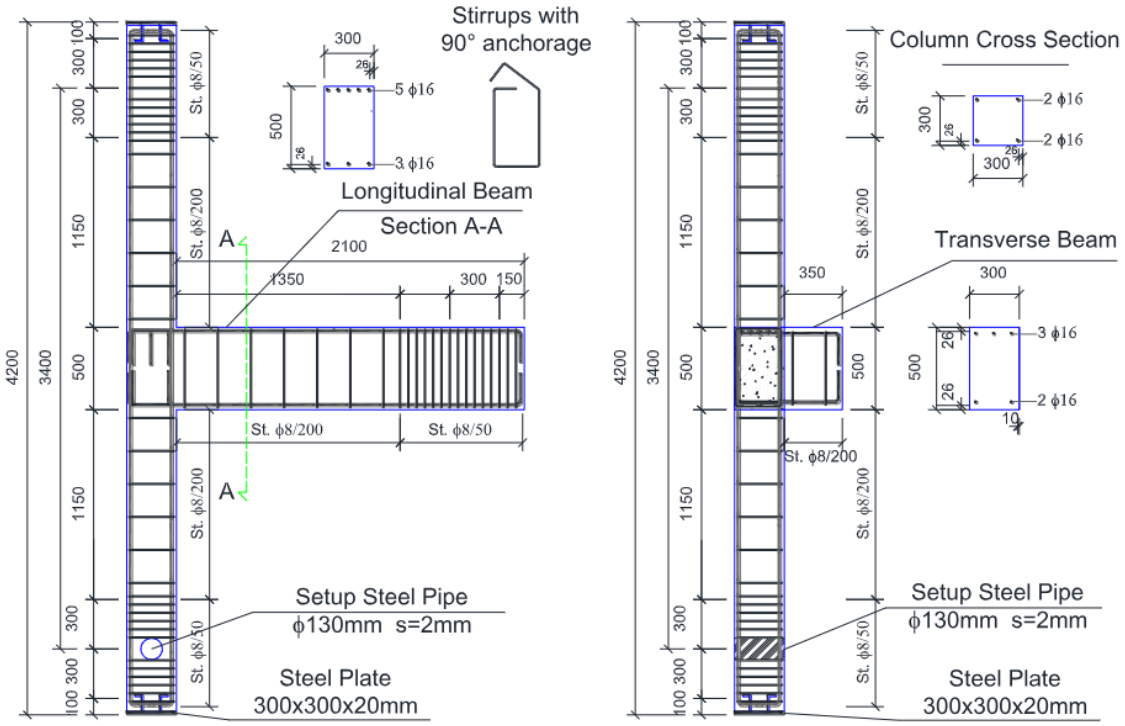

Figure 2.18. Details of the specimen (Del Vecchio *et al*., 2014).

2.6.6 Singh et al. (2014)

Singh *et al*. (2014) demonstrated the impact of retrofitting beam-column junctions with CFRP jackets on their strength after undergoing three distinct stress levels. Nine RC beam-column junctions were evaluated in the presence of static loads. CFRP reinforcement has been applied to beam-column junctions that have been subjected to three distinct levels of stress (see in Figure 2.19). The garments are presented in two layers, arranged in an L-shape and oriented at a 45-degree angle to the joint. In comparison to the control beams, the ultimate load-bearing capacity of the retrofitted beams increases by 7–12%, and the yield load for each of these exterior beam-column connections rises by 15%. Compared to stress level 1, the

stiffness up to the first fracture load was increased by 17.36% and 26.94% for stress levels 2 and 3, respectively.

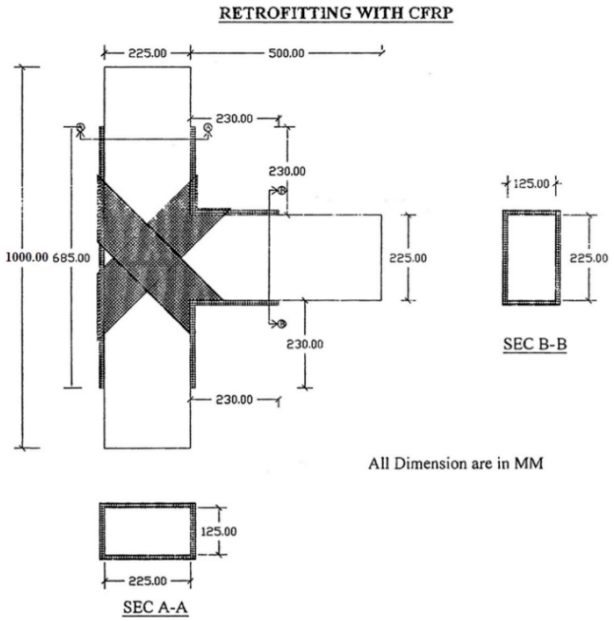

Figure 2.19. CFRP wrapping technique with details (Singh *et al*., 2014).

2.6.7 Mahmoud et al. (2014)

This work describes experimental research on the structural behaviour of RC exterior beam-column junctions that were repaired using CFRP (Mahmoud *et al.*, 2014). The current experimental programme involves testing ten half-scale specimens separated into three groups, each representing a different probable flaw, together with a detailed control specimen. The identified issues are the lack of transverse reinforcement in the connection core, inadequate bond length for the main reinforcement of the beam, and a poorly spliced implanted column at the joint (see in Figure 2.20 (a)). Three distinct strengthening methods were employed to repair the damaged beam-column junctions, which included externally bonded (EB) CFRP sheets and strips, as well as near surface mounted (NSM) CFRP strips are shown in Figure 2.20 (b). The failure mode, such as ultimate capacity, mode of failure, initial stiffness, ductility, and the ultimate strain in the reinforcing steel and CFRP, were assessed and compared between the control group and the CFRP reinforced specimens. The test findings indicated that the suggested CFRP reinforcement configurations were the most suitable option for retrofitting the initial two flaws based on the analysed failure criteria. The third group's results demonstrated that reinforcing the joint with NSM strip technique improved the structural performance of specimens compared to the control specimen. In

contrast, strengthening the joints with EB CFRP strips and sheets did not restore the joints' capacity.

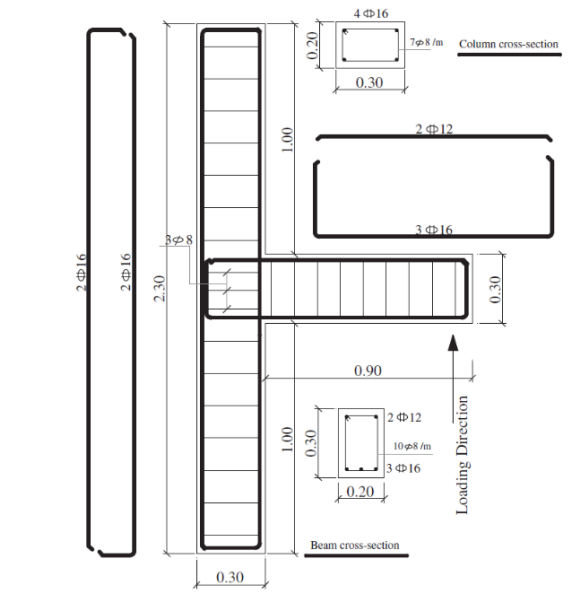

(a)

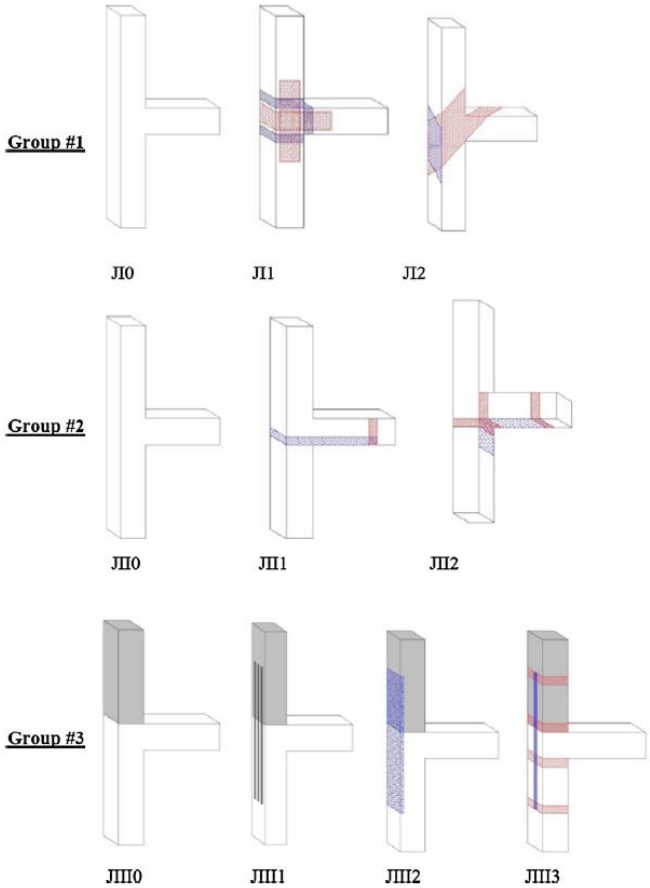

(b)

Figure 2.20. (a) Details of reinforcement and dimensions for the control specimen, J0; (b) Schematic configuration for the three groups of specimens tested (Mahmoud *et al*., 2014).

2.6.8 Zamani Beydokhti and Shariatmadar (2016)

This study aims to provide the findings of an experimental analysis on the performance of shear-deficient external beam-column connections that were repaired using carbon-fibre-reinforced polymers (CFRPs) (Zamani Beydokhti and Shariatmadar, 2016). The joints lacked transverse reinforcement, so they are referred to as non-seismic (NS) joints illustrated in Figure 2.21 (a). Four NS-grade joints were subjected to reversed cyclic loads and compared with one Seismic joint (S-grade specimen) shown in Figure 2.21 (b). The experimental programme consisted of three distinct phases: the damaging phase, the repairing phase, and the retesting phase. During the third step of the test, the repaired specimens were retested until they attained their maximum capacity. Findings are compared based on strength, ductility, energy dissipation, and stiffness deterioration. The joints' repair-ability performance level was determined by assessing the damage index. Repairing joints with CFRP laminates is not feasible when damage exceeds the repair-ability performance threshold. CFRP laminates do not enhance the seismic performance of damaged beam-column junctions in this scenario. The joints investigated in this study will be repaired up to a maximum of 1.5% story drift ratio. The application of CFRP sheets for the retrofitting of specimens is illustrated in Figure 2.22.

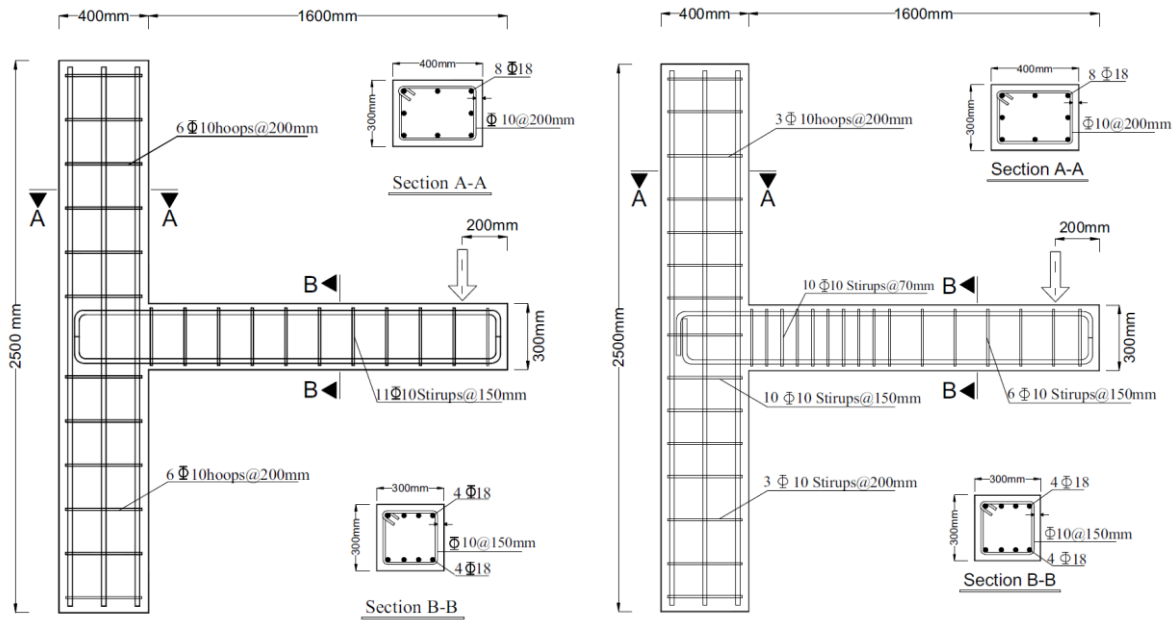

Figure 2.21. Reinforcement details of the specimens (Zamani Beydokhti and Shariatmadar, 2016): (a) non-seismic design; (b) seismic design.

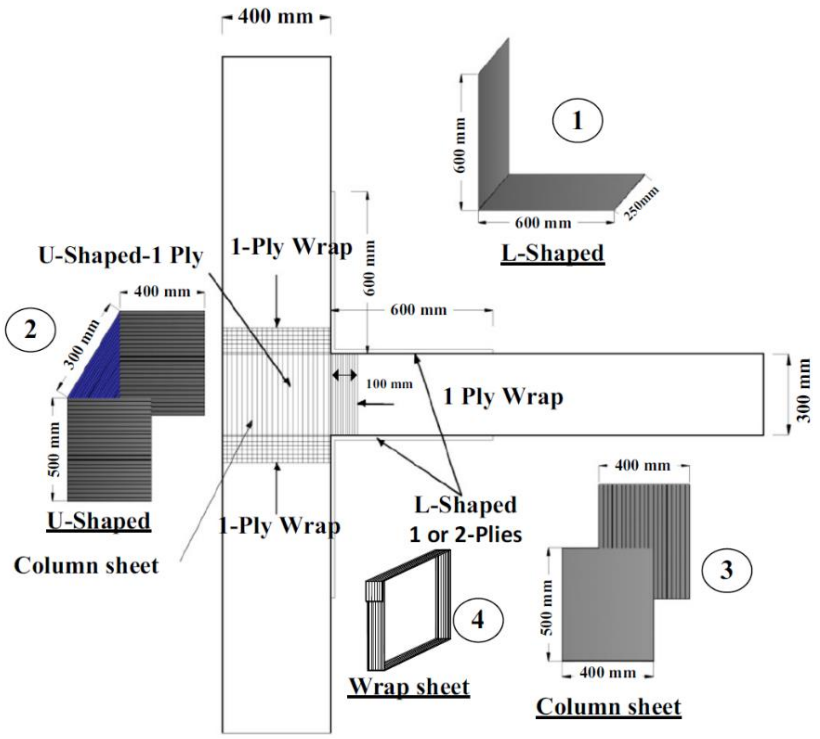

Figure 2.22. The application of CFRP laminates (Zamani Beydokhti and Shariatmadar, 2016).

2.6.9 Mostofinejad and Akhlaghi (2017)

Six half-scale RC beam-column subassemblies were built for this study lacking any transverse reinforcement in the joint area by Mostofinejad and Akhlaghi (2017) (see in Figure 2.23 (a)). They aimed to examine how genetically modified (GM) materials impact the seismic performance of outside RC beam-column connections that lack strength but are reinforced with CFRP sheets using the externally bonded reinforcement on grooves (EBROG) approach. The study also examines how well FRP fans can avoid splitting failure of the concrete cover. The retrofitting methods are depicted in Figure 2.23 (b). The study found that using the EBROG approach along with FRP fans at the end of FRP sheets completely prevented debonding. It was possible to postpone brittle shear failure of the beam-column joints and move the beam plastic hinge away from the column interface in certain situations. Furthermore, utilising CFRP composites through the EBROG approach significantly improved the seismic capacity of the test specimens in terms of strength, stiffness, ductility, pinching width ratio, and energy dissipation.

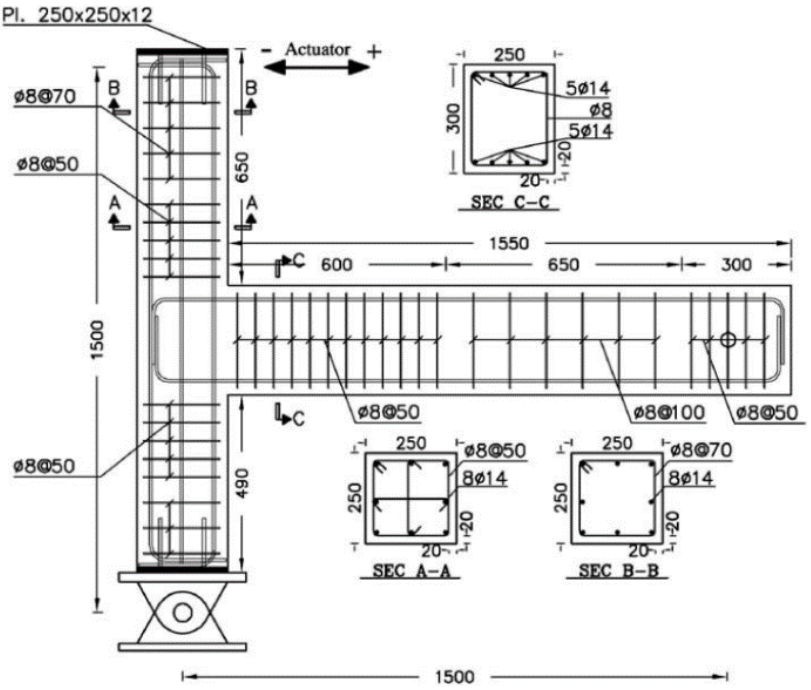

(a)

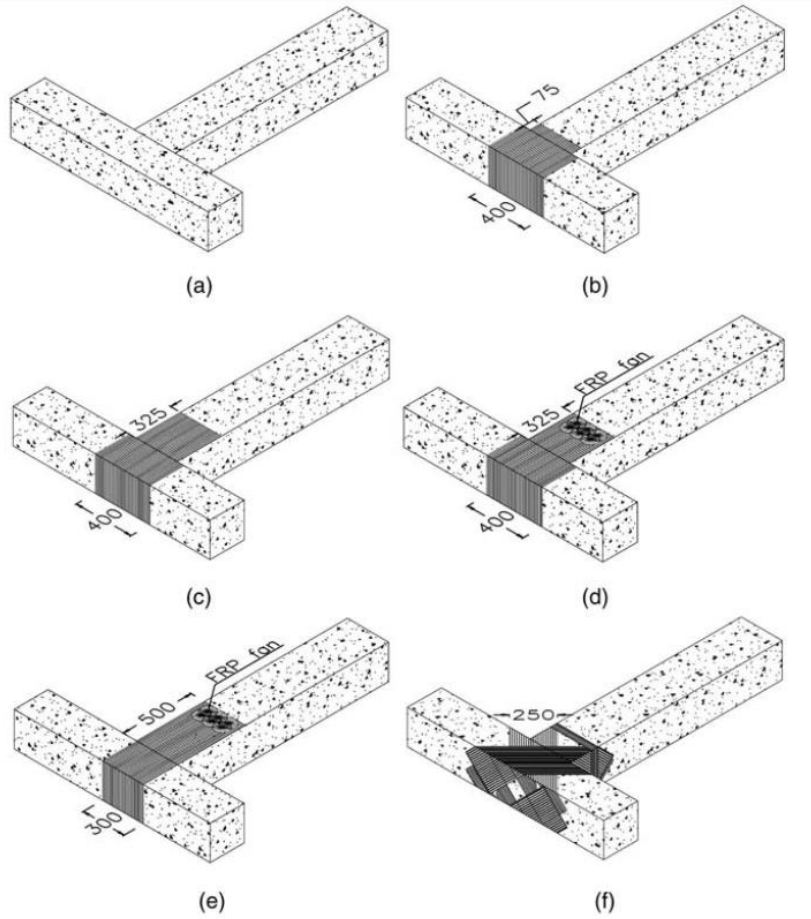

(b)

Figure 2.23. (a) Reinforcement details of the specimens; (b) Specifications of all the test specimens (Mostofinejad and Akhlaghi, 2017).

2.6.10 Akash and Jayasree (2018)

A method is proposed by Akash and Jayasree (2018) in this study for retrofitting exterior beam-column junctions of reinforced concrete columns (RCC) using Near Surface Mounted (NSM) GFRP strips and externally bonded GFRP sheet in various orientations (30°, 45°, and 60°) (as illustrated in Figure 2.24). Every specimen was exposed to reverse cyclic loading testing. The assessment of beam-column junctions encompassed an examination of their stiffness degradation, energy absorption, ductility, and strength. The results indicate that all of the above properties were substantially improved in the NSM retrofitted specimens with a 30° orientation.

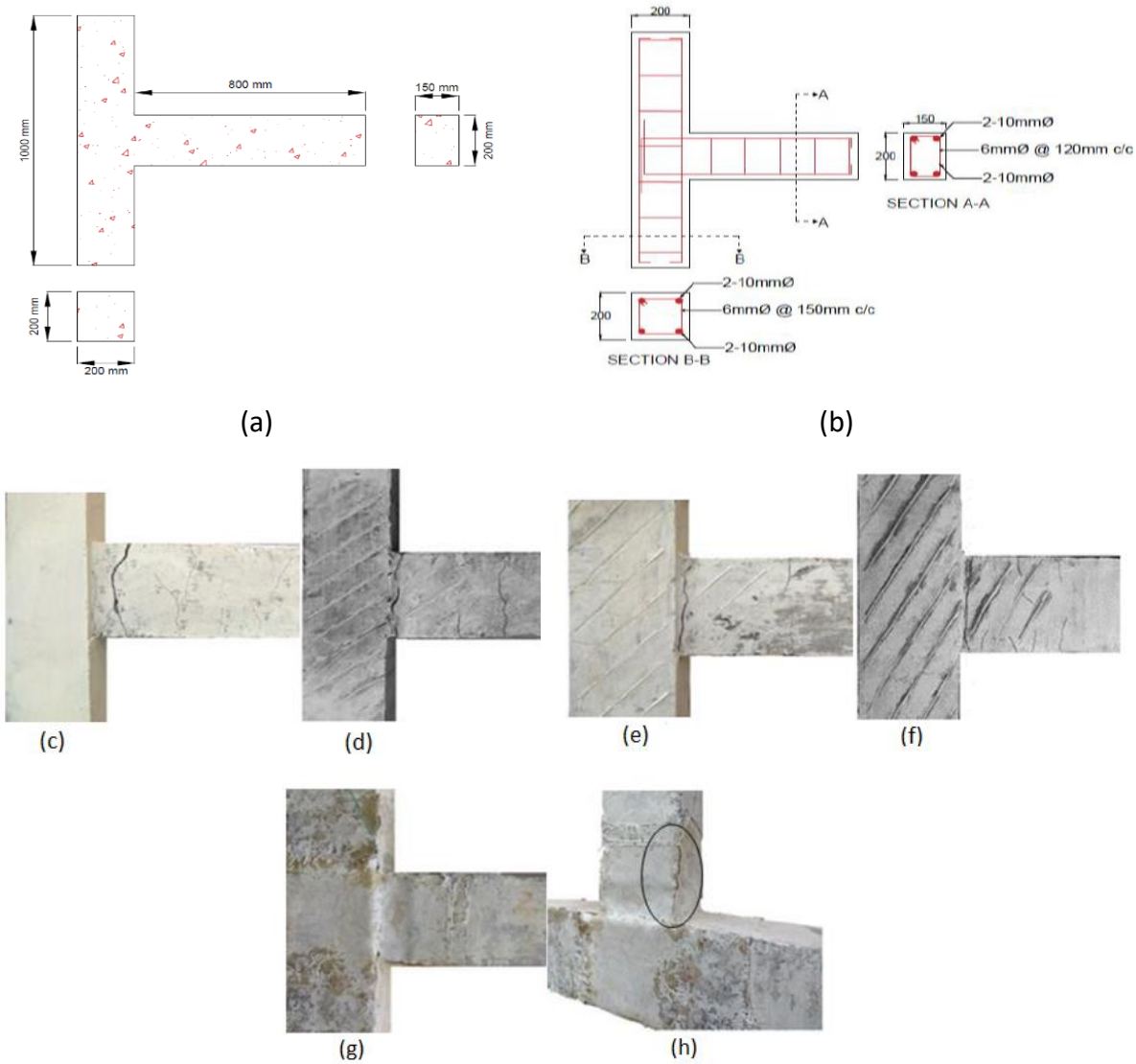

Figure 2.24. (a) Dimensions of the beam-column joint specimen; (b) Reinforcement details of the specimen; (c) Crack pattern of BCJC specimen; (d) BCJN30 specimen; (e) BCJN45 specimen; (f) BCJN60 specimen; (g) BCJEB specimen; (h) Delamination of BCJEB specimen (Akash and Jayasree, 2018).

2.6.11 Saqan et al. (2018)

An experimental study was conducted to assess the seismic behaviour of rigid frames reinforced with EB CFRP sheet and NSM CFRP bars by Saqan *et al.* (2018). Three rigid frame specimens were tested under cyclic loading. All three examples were the same size and had the same internal reinforcement shown in Figure 2.25 (a). One specimen was utilised as a control, while the other two specimens were reinforced using CFRP fabric and NSM bars to achieve the same capacity at initial yielding. CFRP wraps were utilised to secure the primary CFRP sheets and NSM bars on the reinforced specimens and to hinder the debonding of the FRP reinforcement. The retrofitting methods for specimen SSP-2 and SSP-3 are given in Figure 2.25 (b) and (c), respectively. The test findings showed that both methods delay the point at which the internal steel reinforcement starts to give way, leading to higher flexural strength in the structures, increased energy absorption, and less stiffness loss. Results indicated that reinforcing with CFRP fabric leads to less cracking, more energy dissipation, and less strength loss post-yielding compared to reinforcing with NSM bars, which results in higher ultimate strength.

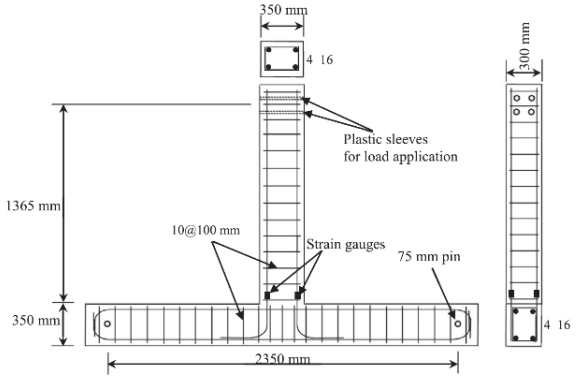

(a)

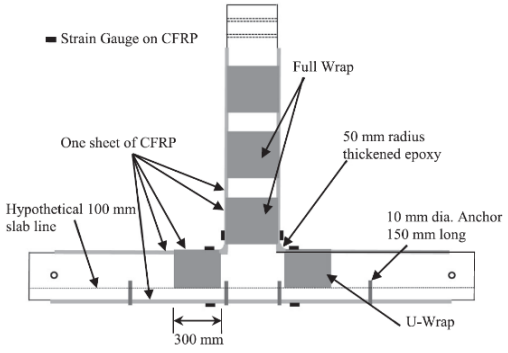

(b) Specimen SSP-2

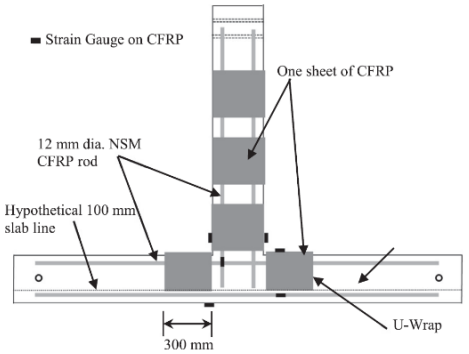

(c) Specimen SSP-3

Figure 2.25. (a) Reinforcement details for each of the three specimens; Details of retrofitting: (b) Specimen SSP-2; (c) Specimen SSP-3 (Saqan *et al.*, 2018).

2.6.12 Wang et al. (2019)

This study presents an experimental investigation aimed at strengthening earthquake-prone RC beam-column connections using CFRP, as conducted by (Wang *et al*., 2019). Testing was conducted on six exterior RC beam-column connection specimens to determine an efficient strategy for enhancing the seismic performance of these joints in relation to their lateral strength and ductility. The six specimens at a 2/3 scale consisted of one specimen without seismic design (ND), one specimen with seismic design (D), and four specimens labelled as "NDSL", "NDSC", "NDSB", and "NDSB2" retrofitted using various methods. Figure 2.26 depicts the application of the strengthening methods.

These schemes investigated the use of EB CFRP sheets and NSM CFRP strips for strengthening. The test findings demonstrated that incorporating CFRP reinforcement can greatly enhance the seismic performance of a structurally weak beam column connections. The utilisation of NSM CFRP strips in beams and joints efficiently shifts the plastic hinge away from the joint area, resulting in a ductile failure mode (beam flexural failure), showcasing the efficacy of this seismic retrofit technique.

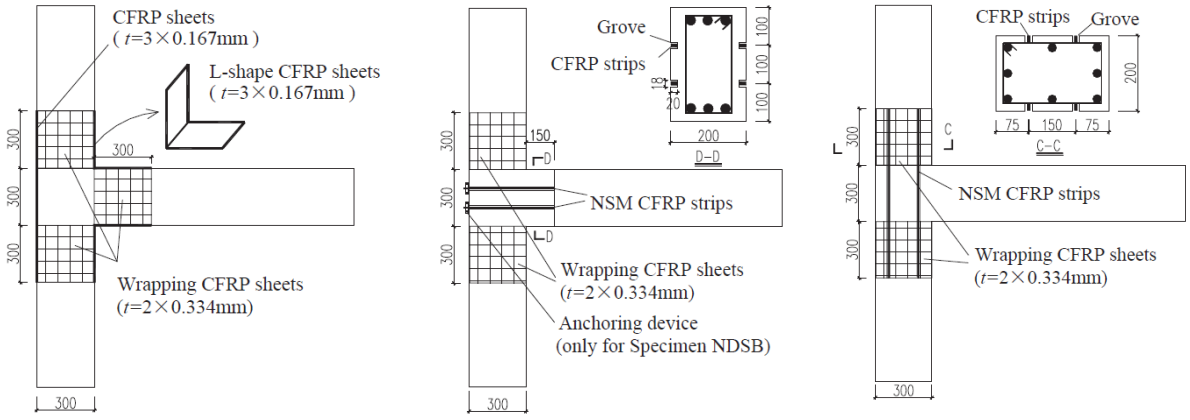

(a) NDSL (b) NDSB & NDSB2 (c) NDSC

Figure 2.26. Strengthening applications (Wang *et al*., 2019).

2.6.13 Laseima et al. (2020)

This research was investigated the seismic performance of full-scale outside reinforced concrete (RC) beam-column joints that have been upgraded with externally bonded CFRP by Laseima *et al.* (2020). Two comparable RC beam column junctions were constructed and tested without transverse reinforcement at the joints illustrated in Figure 2.27 (a).

The connections were subjected to cyclic loading with controlled displacement to evaluate their seismic performance. The initial junction was inspected as the control specimen, and the subsequent specimen was reinforced with CFRP sheets depicted in Figure 2.27 (b). The column and beam's square shape near the joint area was altered to squircle segments with rounded edges. The experimental results show that energy dissipation, strength, and ductility capacity are significantly enhanced by 61.8%, 208.9%, and 61.8%, respectively, as a result of retrofitting beam-column junctions with CFRP. This demonstrates that CFRP is suitable for retrofitting. The debonding potential of the CFRP reduced and the restricting influence of the CFRP rose due to the transition from square to squircle segments in the beam and column. The experimental results were confirmed by employing a 3D nonlinear finite element (FE) model.

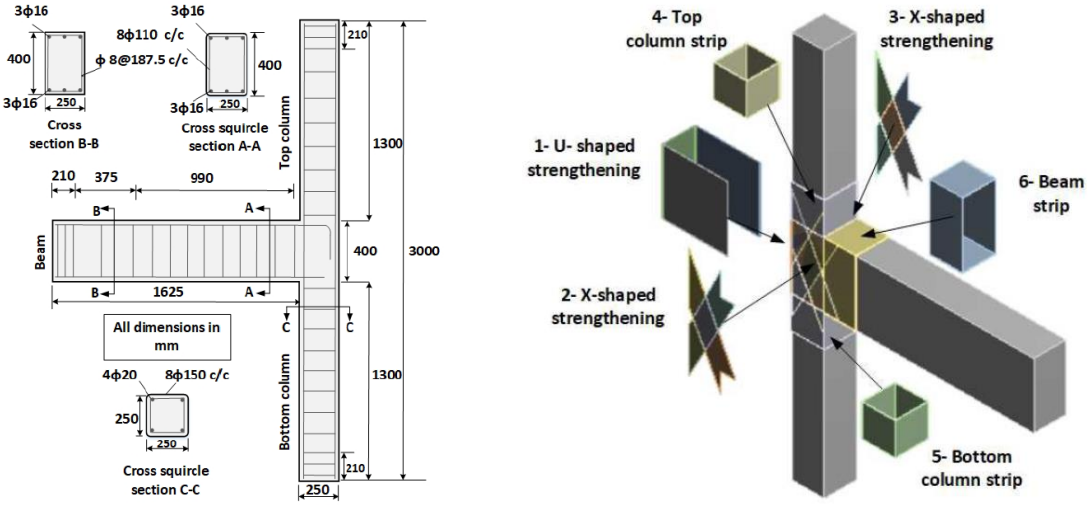

(a) (b)

Figure 2.27. Specimen dimension and reinforcement specifications, (b) Retrofitting of the specimen around the joint (Laseima *et al*., 2020).

2.6.14 Davodikia et al. (2021)

Davodikia *et al.* (2021) utilised the grooving method to apply CFRP composites and examined its effectiveness in preventing the separation of FRP composites during shear strengthening of RC beam-column joints. Four scaled exterior concrete beam-column junctions were constructed in the laboratory for this study. There are two control specimens, one with special seismic characteristics following ACI requirements and the other without seismic information shown in Figure 2.28 (a) and (b). Both retrofitted specimens do not have seismic features and are retrofitted using CFRP composites. One specimen has CFRP composites applied on the

concrete surface conventionally, whereas another specimen has CFRP composites installed on the concrete surface using the grooving method illustrated in Figure 2.28 (c) and (d).

The specimens were exposed to cyclic loading with progressively increasing amplitudes. The findings were evaluated by analysing hysteretic curves, envelope curves, energy dissipation, stiffness degradation, and cracking patterns. The findings indicated that the approach used eradicates the separation problem and led to a notable enhancement in load-bearing capacity, ductility, and energy dissipation.

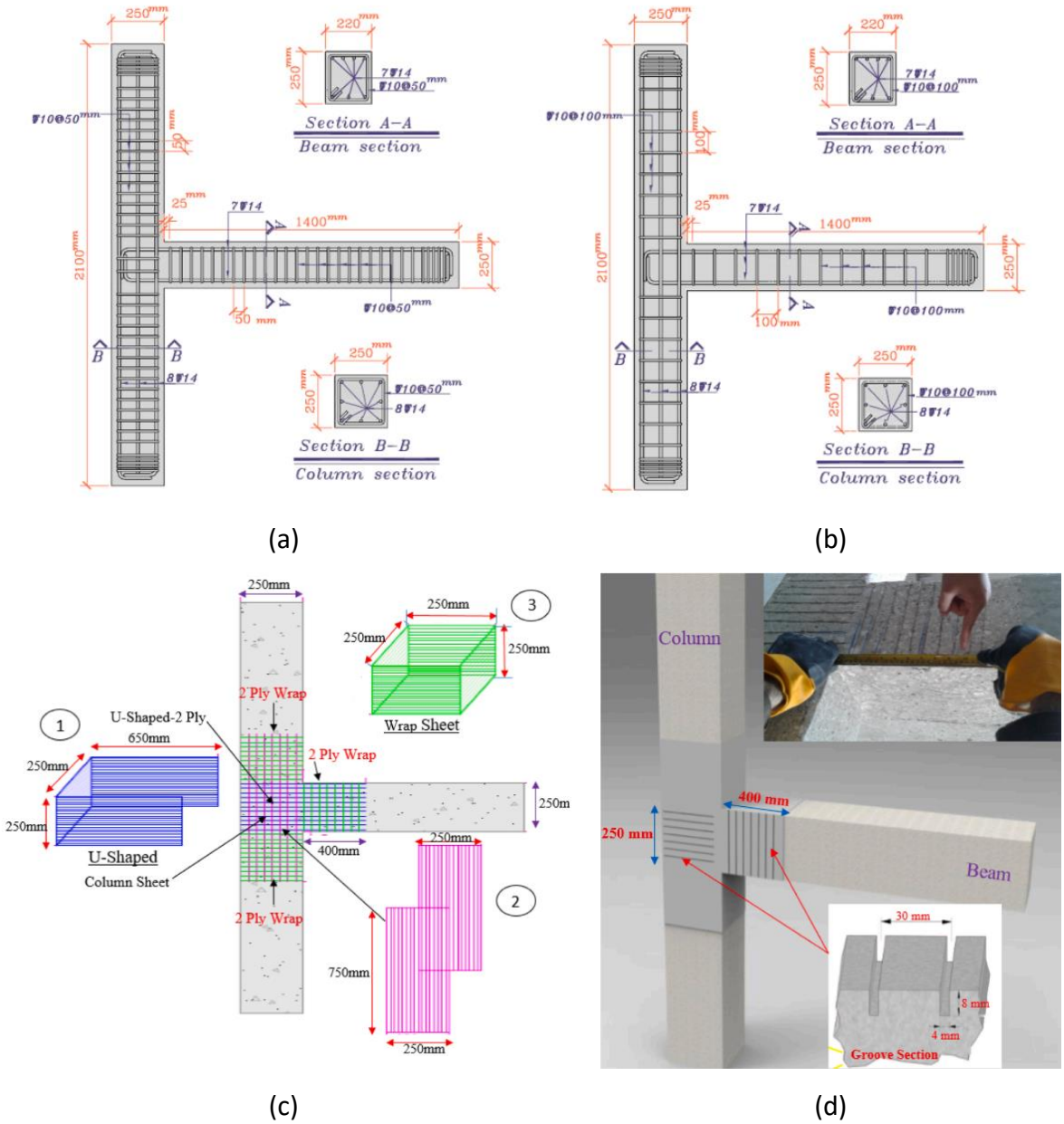

Figure 2.28. (a) seismic specimen; (b) non-seismic specimen; (c) Pattern of shear reinforcement of the joint core and beam by CFRP; (d) Grooves formed on the surface using the grooving method in the surface preparation process (Davodikia *et al.*, 2021).

2.6.15 Sakthimurugan and Baskar (2021)

Sakthimurugan and Baskar (2021) carried out in two stages with a total of 19 beam column connection specimens. Three connections were examined as control specimens, the other eight joints were preloaded with 50% of average ultimate load of control specimens and strengthened afterwards in the first stage of work, and the last eight joints were preloaded with 60% of average ultimate load, thereby inducing a certain level of damage. The dimension and details of the reinforcement are depicted in Figure 2.29. These specimens were reinforced utilising Basalt FRP (BFRP) material. Additionally, the beam-column joints were modelled using ANSYS software, and the numerical analysis demonstrated that BFRP enhanced the performance of the strengthened specimens. The ANSYS results closely aligned with the experimental results.

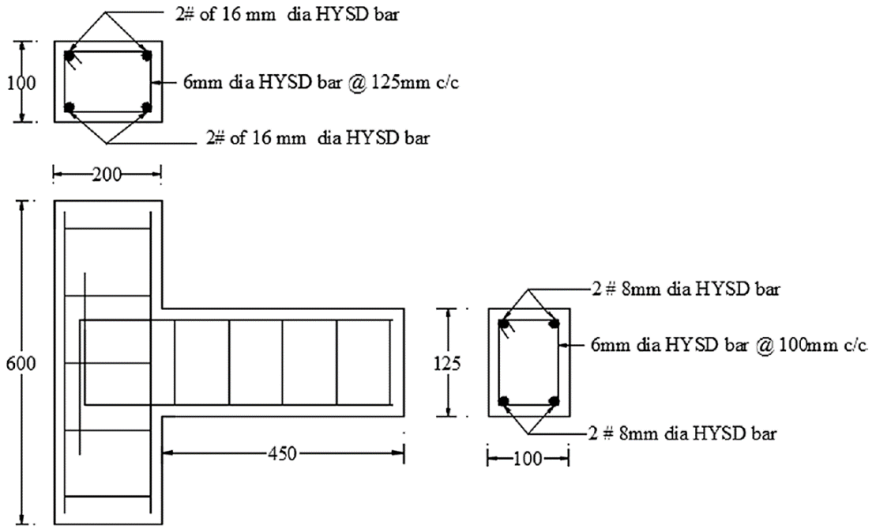

Figure 2.29. Details of the specimens (Sakthimurugan and Baskar, 2021).

2.6.16 Zaferani and Shariatmadar (2022)

Experiments were conducted in this research to examine the repair and retrofitting of external RC beam-column junctions utilising FRP composites by Zaferani and Shariatmadar (2022). In the development of the examined joints, the seismic design details for the panel zone are disregarded (see in Figure 2.30 (a) and (b)). The programme evaluation was conducted in three phases. Initially, the specimens were subjected to varying degrees of harm through loading. The damaged specimens were subsequently strengthened and repaired using FRP composites and the NSM and hybrid EBR + NSM techniques illustrated in Figure 2.30 (c) and (d). In conclusion, the retrofitted joints underwent cyclic loading until they ceased to function. The objective of this research was to examine the impact of the retrofitting techniques that were

implemented on the strength, rigidity, and ductility of compromised RC joints. In pursuit of this objective, a total of eight RC beam column connections were cast and evaluated, comprising seven non-seismically designed (NS) joints and one seismically designed (S) joint. A comparison was made between the experimental outcomes obtained for the strength, reduction of stiffness, and cumulative dissipated energy of the NS specimen and the S specimen. The outcomes demonstrated that the hybrid retrofitting techniques that were suggested are capable of restoring the depleted capacities of connections and may even elevate them to levels surpassing those of the seismic control specimen.

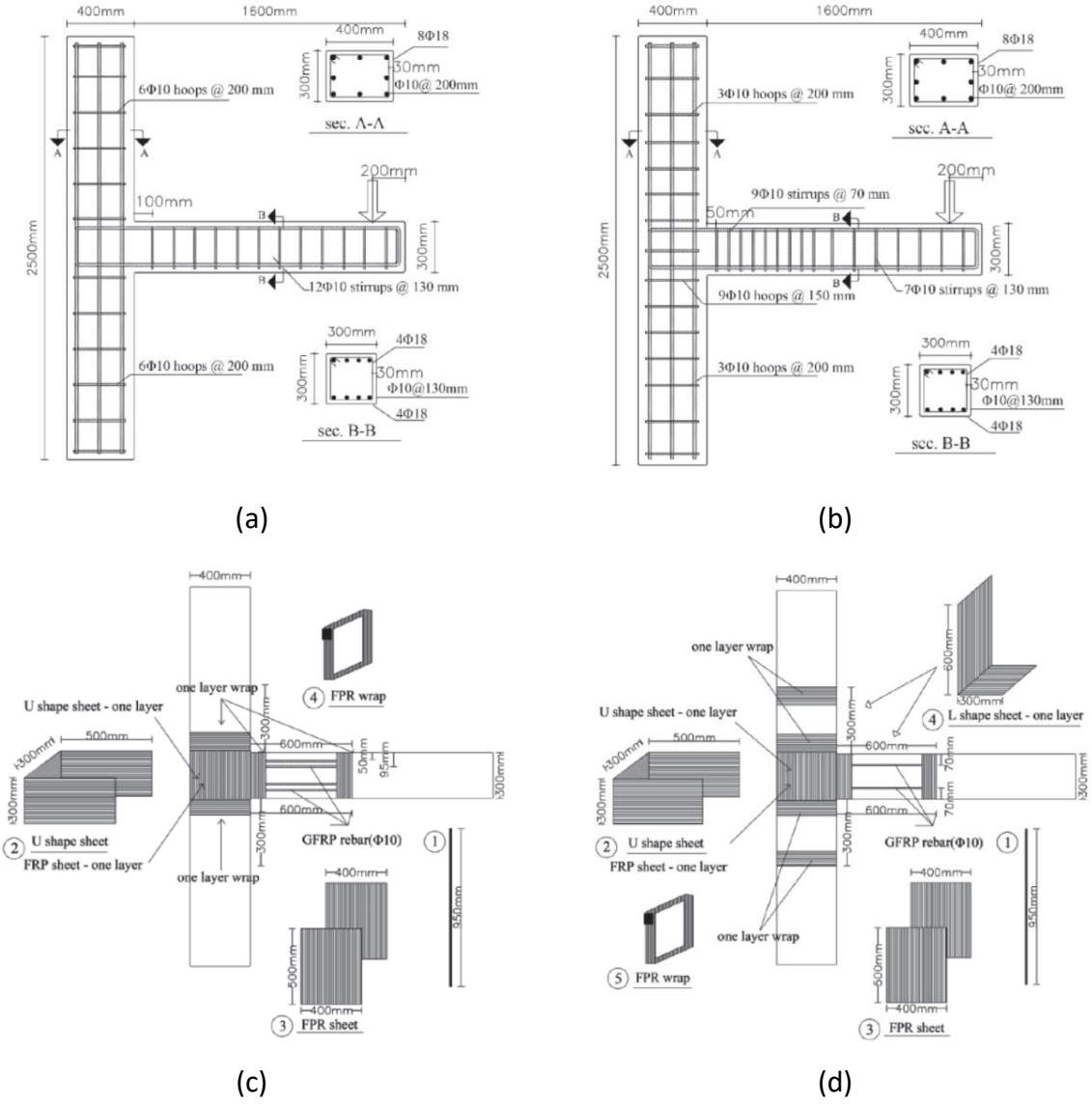

Figure 2.30. (a) non-seismic designed specimen (NS); (b) seismic designed specimen (S); (c) the retrofitting designs of design (C); (d) the retrofitting designs of design (D) (Zaferani and Shariatmadar, 2022).

2.6.17 Hashemi and Riahi (2022)

An experimental study was conducted to assess three reinforcement techniques for RC beam-column junctions involving NSM steel bars and CFRP strips under cyclic loads by Hashemi and Riahi (2022). These solutions enhance the strength of joints and avoid the creation of plastic hinges near the column while minimising damage to the floor slab. Specimens of a reinforced concrete beam-column connection from an intermediate moment-resisting frame were built at half scale, along with a control specimen. The details of reinforcement and the strengthening schemes are shown in Figure 2.31 (a) and (b) and Figure 2.32 (a) and (b). The tests were conducted under cyclic loading in accordance with the guidelines outlined in ACI 374.1-05, while maintaining a constant axial load on the column, to analyse their seismic performance. The experimental findings revealed that the suggested ways could enhance joint capacity by up to 30% compared to the control specimen. Additionally, two of the strategies increased joint ductility by eliminating the plastic hinge from the joint core. Furthermore, the modified specimens showed a 100% improvement in energy dissipation and exhibited reduced pinching hysteresis behaviour. To prevent debonding of CFRP strips, it is necessary to enhance the penetration depth of the strips into the core material based on the observation in one of the specimens. The anchorage method of the additional steel rebar inside the joint core was effective in transferring forces to the column correctly.

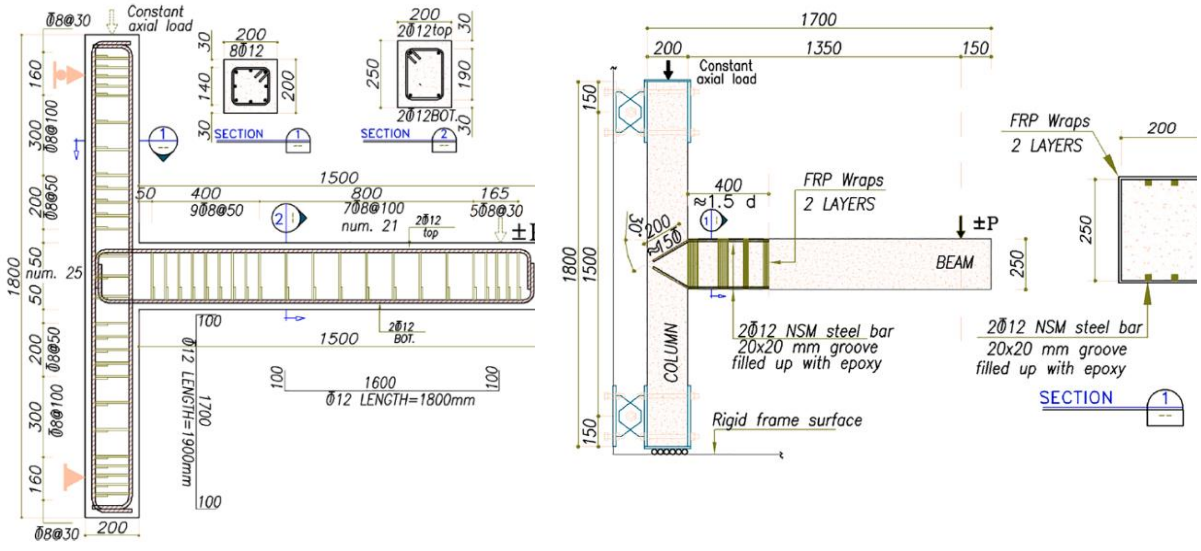

(a) (b)

Figure 2.31. (a) Details of the reinforcement; (b) RS-SJ-FW specimen retrofitting details (Hashemi and Riahi, 2022).

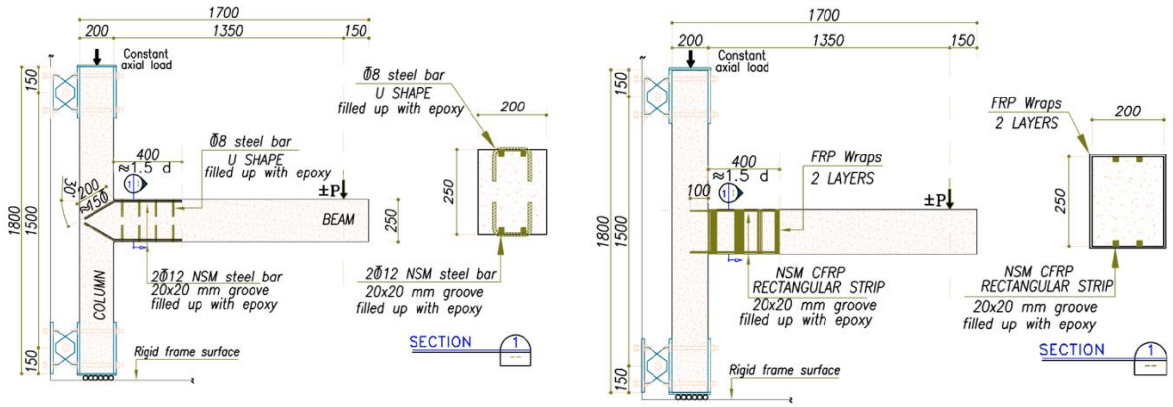

(a) (a)

Figure 2.32. Details of retrofitting: (a) RS-SJ-US specimen; (b) RS-FJ-FW specimen (Hashemi and Riahi, 2022).

2.6.18 Wang et al. (2022)

Wang *et al.* (2022) investigated an experimental study and numerical modelling using ANSYS software on the behaviour of RC beam-column connections with three series of exterior joints using EB CFRP jackets to improve the shear capacity under steady axial and a quasi-static cyclic load. The reinforcement phases utilised in this study are shown in Figure 2.33.

The characteristics include the CFRP reinforcement ratio and arrangement, transverse beam-to-joint panel width ratio, transverse beam-to-joint panel height ratio, transverse beam position, and number of transverse beams. A new dimensionless index, termed "strengthening efficiency," was introduced to assess the residual effect of a CFRP-strengthening system weakened by transverse beams compared to the increase in joint shear capacity relative to the one-way counterpart. The findings from 44 nonlinear finite element models, validated against experimental data, demonstrated the efficacy of the CFRP strengthening method across a broad spectrum of parameters. The distinct variations in the functions of the parameters were uncovered, and the underlying causes of these variances were examined. The shear mechanism of the joint panels retrofitted with CFRP was analysed using the proposed strut-and-tie model. According to their results, the strengthening efficiencies of 3D connections ranged from 25.3% to 87.5%. The findings validated the efficacy of the CFRP fortification method across a considerable range of parameters examined; however, the contribution of transverse beams to the CFRP was found to be detrimental. Relocating the transverse beams away from the interior edge of the joint panel resulted in a significant increase in the strengthening efficiency of the vertical sheets.

The course of fracture propagation in the joint panel and the strain distributions in the vertical sheets both corroborated this result.

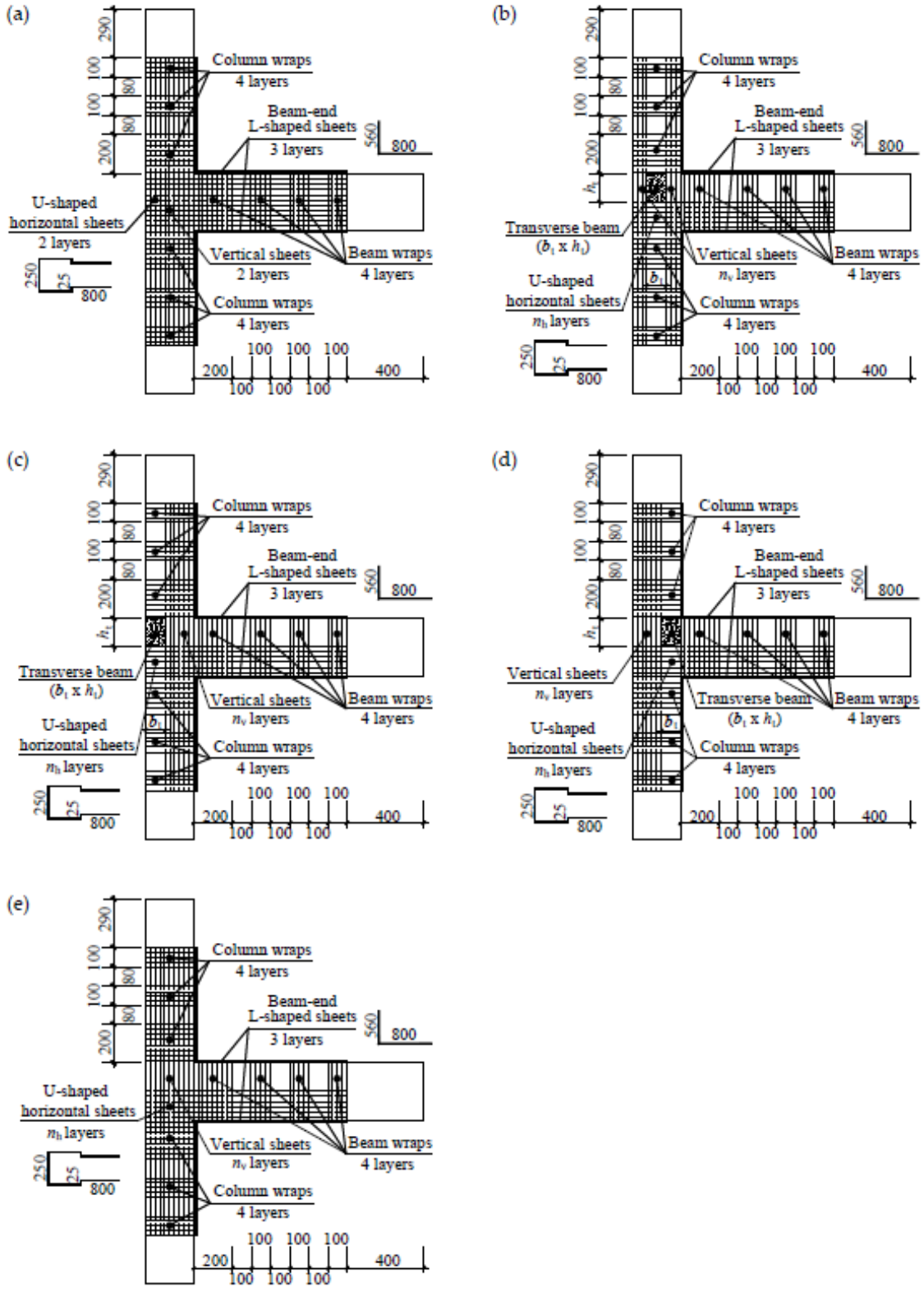

Figure 2.33. Strengthening programmes (Wang *et al*., 2022).

2.6.19 Ansari et al. (2023)

This study examines the performance of external RC beam-column connections reinforced with CFRP sheets when subjected to reversed cyclic loads (Ansari *et al*., 2023). The aim of this study is to compare two different strengthening strategies. One specimen was reinforced using the external bonding reinforcement (EBR) method, while the other two specimens were reinforced using manually fabricated FRP bars with the NSM method. One example contained only side bars, whereas the other utilised L-shaped bars along with side bars for reinforcement. FRP rods were created manually using cores made of wood or steel, which were then wrapped with CFRP sheets of varying widths. The behaviour of the reinforced specimens was compared to a reference specimen without reinforcement. The details of reinforcement and the application of EB method are illustrated in Figure 2.34 (a) and (b), respectively. In addition, Figure 2.35 (a) and (b) indicates the application schemes of the NSM technique. The findings indicate that utilising manually produced FRP bars with NSM technology, particularly on both sides of the specimen, is more efficient in reinforcing the outer beam-column joints than the EBR approach. Additionally, the specimen including solely side NSM rebars exhibited superior energy-based characteristics, but the specimen with both L-shaped and side NSM rebars performed better in load capacity-based parameters.

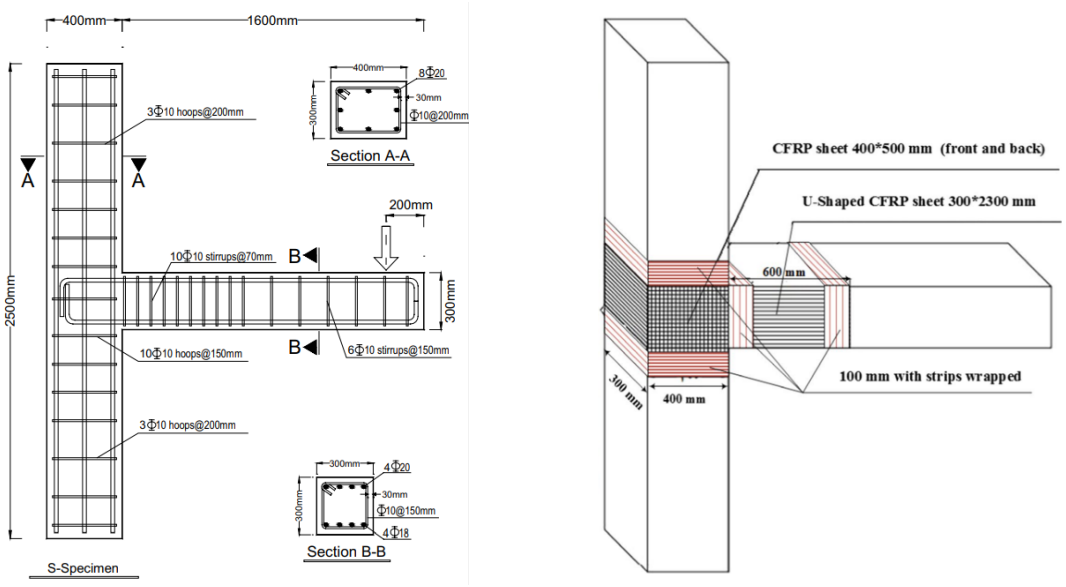

(a) (b)

Figure 2.34. (a) Reinforcement specifications, (b) The application of EB method (Ansari *et al*., 2023).

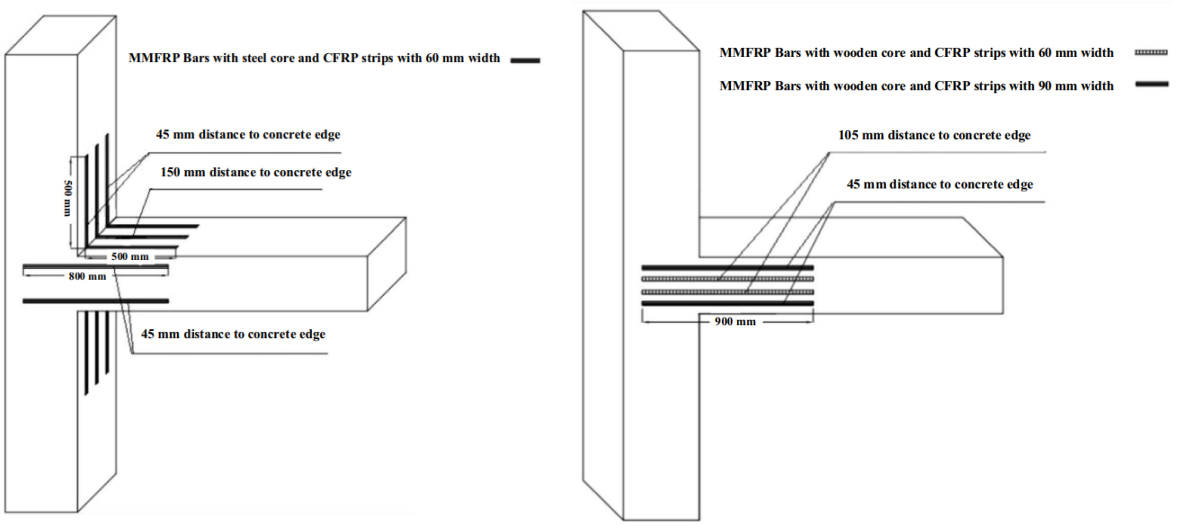

(a) (b)

Figure 2.35. The NSM applications (Ansari *et al*., 2023).

2.6.20 Farhang et al. (2023)

The numerical and experimental investigations were conducted on the CFRP shear strengthening of full-scale RC 3D exterior beam-column joints exposed to a combination of reversed lateral stresses and the absence of transverse rebars at their joint core by Farhang *et al.* (2023).

In this study, concrete with 12 MPa (average compressive strength) was used to investigate the effectiveness of various retrofitting techniques on beam-column connections. A control beam-column joint was constructed without any reinforcement, while two joints were reinforced using specified patterns of single-layer and three-layer CFRP sheets (as depicted in Figure 2.36). Following this, cyclic load–displacement, failure mode, ductility, secant stiffness, energy dissipation, and energy absorption curves were calculated and compared for each specimen. Following this, the experimental specimens were modelled using the finite-element method in ABAQUS and subjected to non-linear analysis; the resulting analytical results were then compared to the experimental ones. During an alternative stage of the research, adjustments were made to the specific concrete compressive strength, the beam longitudinal tensile reinforcement ratio, and the compressive axial force exposed to the column. These modifications resulted in the generation of eight simulated numerical specimens, which underwent non-linear analysis and were subsequently compared. In addition to preventing shear diagonal failure at the rear of the column-transverse beam joint, the strengthened

specimens improved lateral load capacity by 11 to 15%, energy absorption by 10 to 20%, and energy dissipation by 2.2 times in comparison to the control specimens with the same parameters. Furthermore, it was noted that augmenting the specific compressive strength of concrete from 12 to 30 MPa resulted in a 31% average increase in lateral load capacity and a 46% average increase in absorbed energy. Conversely, an applied axial force that was doubled caused an 11% average decrease in lateral load capacity.

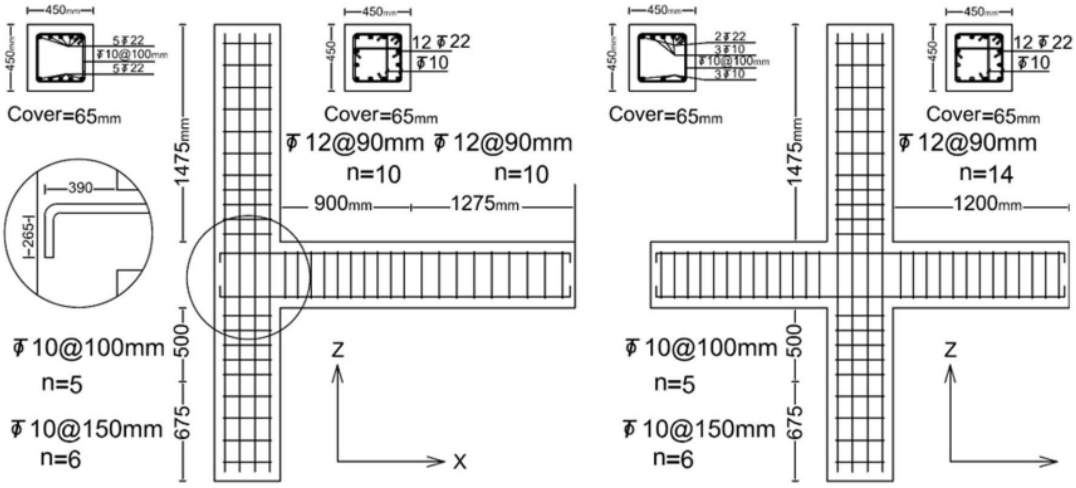

(a)

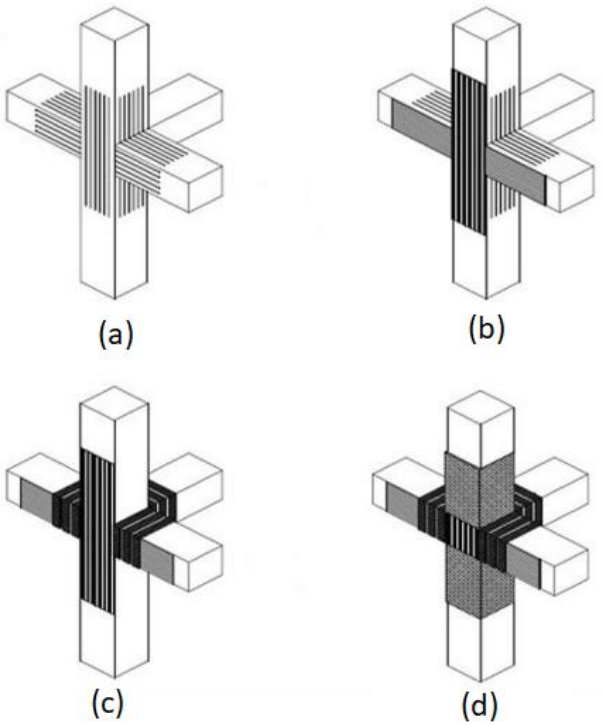

(b)

Figure 2.36. (a) Details of the reinforcement, (b) Strengthening application, (Farhang *et al.*, 2023).

The reviewed studies highlight critical advancements, challenges, and trends in strengthening exterior RC beam-column joints using various retrofitting techniques. Key takeaways include:

Common Retrofitting Methods:

- Externally Bonded (EB) FRP (e.g., CFRP sheets/strips) is widely adopted for its high strength-to-weight ratio, corrosion resistance, and ease of installation, but faces challenges like debonding and dependency on anchorage.
- Near-Surface Mounted (NSM) techniques (steel bars or FRP strips) improve flexural capacity and ductility while minimizing member size changes, though they require precise groove preparation.
- Hybrid EB+NSM systems show superior performance in restoring strength and ductility compared to individual methods. However, studies on hybrid EB+NSM applications for joints are still limited.

Performance Enhancements:

- Retrofitted joints exhibit 20–200% increases in load capacity, energy dissipation, and ductility, with failure modes shifting from brittle joint shear to ductile beam hinging
- Anchorage innovations (e.g., EBROG grooves, FRP fans) mitigate debonding, enhancing strain utilization.

Material and Practical Considerations:

- Low-strength concrete poses challenges but can be effectively retrofitted with multi-layer CFRP or NSM steel.
- Steel reinforcements remain cost-effective for NSM due to ductility and availability, while FRP offers lightweight alternatives.

2.7 SUMMARY

Based on the literature review and existing understanding of the seismic behaviour of shear-deficient externally reinforced concrete beam-column connections, the following conclusions can be made:

Reinforced concrete beam-column joints in existing older buildings are particularly vulnerable to shear failure when subjected to seismic activities. This vulnerability is well-documented through a combination of experimental beam-column joint tests and post-earthquake field reports, which consistently highlight the structural inadequacies in these critical regions.

Several crucial factors influence the performance of external reinforced concrete beam-column joints, including the ratio of the axial load on the column to axial strength, the compressive strength of the concrete, and the confinement supplied by the shear reinforcement in the joint.

Existing reinforced concrete structures are often classified into three primary areas of structural deficiency: columns, beams, and the integrated frame system that combines these components. Every individual component provides a crucial function in maintaining the stability and strength of a building, and any vulnerability in these areas may compromise the overall structural integrity of the construction. Among these deficiencies, probably the most widespread and critical problem is the absence of confinement in the beam column joint. The primary cause of this particular deficiency can be attributed to the lack or inadequate transverse reinforcement, such as stirrups or ties, which are crucial for providing confinement.

In order to improve the seismic performance of exterior RC beam-column connections, several rehabilitation techniques, including steel and reinforced concrete jacketing, have been explored and integrated into the construction process. These methods are called traditional techniques and are associated with numerous difficulties in practical applications. These retrofitting techniques are time-consuming, require a lot of labour, and lead to an increase in the size of structural elements and gravity loads imposed on the building. Of the various new methods reviewed, two methods stand out as worthy of further investigation. These are the EB and NSM methods. Neither method is perfect because both methods have some disadvantages and therefore need further research.

Both NSM and EB are effective in improving the seismic performance of beam-column joints, especially in structures that were not originally designed to meet modern seismic codes; however, NSM can suffer from inadequate bonding between the new reinforcement and the concrete, while the EB method can suffer debonding/delamination of the FRP. There are few studies on the use of these two methods together; and current research just presents the results of experiments without suggesting a design method. In this thesis, a hybrid method is

developed by combining EB and NSM methods to see if it can overcome these shortcomings followed by a method of numerically simulating the behaviour of this type of joint and, hence facilitating their design.

CHAPTER 3. EXPERIMENTAL PROGRAMME

3.1 GENERAL

In the last chapter it was demonstrated that there are many buildings with inadequate seismic resistance and that these buildings need to be strengthened using a retrofitting technique.

This chapter describes the experimental investigation conducted on exterior RC beam-column connections that were exposed to cyclic loading in order to determine the optimal retrofitting strategy. The equipment for testing and loading procedure, the properties of the materials used in the construction and strengthening method, and the details on the manufacturing of the beam-column joint specimens are provided. The instrumentation utilised for strain measurement, global and local deformation, and load, as well as the equations employed to analyse the experimental data, are also given in this chapter.

3.2 MATERIAL PROPERTIES

3.2.1 Concrete

This thesis focuses on old school buildings in Turkey and the specimens were designed according to Turkish Earthquake Code (TEC 1998). According to current research, the concrete strength in existing school buildings is below 20 MPa (Inel *et al.*, 2008; Kanıt and Altın, 2010; Bilgin, 2015), but according to the TEC 1998, the minimum compressive strength of concrete should be 20 MPa. In this study, the beam-column connection specimens were designed and built with normal-weight concrete, targeting a concrete cylinder compressive strength of 20 MPa and using a maximum aggregate size of 20 mm as this represents the best baseline to establish current capacity of these sorts of buildings.

Within the scope of this study, concrete was prepared in laboratory conditions and the physical properties of aggregates need to be determined before designing concrete. In this section, specific gravity, dry specific gravity, apparent specific gravity, and water absorption rate of fine and coarse aggregates are calculated and sieve analysis is carried out.

3.2.1.1 Determination of physical properties of aggregates

EN 1907-6:2022 is a European standard that specifies the methods for determining the physical properties of aggregates used in concrete design. Aggregates are a key component in concrete, influencing its strength, durability, and overall performance. The physical properties (mentioned above) of aggregates defined by this standard are essential in ensuring the quality and performance of the concrete mix. The procedure outlined in the next paragraph was

followed for fine and sharp sand and the values obtained. The pycnometer method was used to determine the physical properties of fine sand and sharp sand. The volume of the pycnometer is 1000ml.

Samples of 500 grams of both fine materials were taken and soaked in water for 24 hours. The excess water on the water saturated materials was removed and the material is saturated to dry surface with the help of a dryer. Sufficiently dried fine aggregates were placed into the cone-shaped container in 3 stages and 25 metal rod impacts were made at each stage. The filled container was turned upside down and divided into two by tapping with a spatula. The saturated material on the dry surface maintains its shape when the container is turned upside down without the grains holding on to each other as required by the specification. There is almost complete collapse, but the top is still visible, and the slopes have a specific angle. After this procedure, the weight of the material saturated on the dry surface was measured (A). The material is then placed in the pycnometer and water is added. The water and material were thoroughly mixed with the help of a metal rod and the lid of the pycnometer was tightly closed. Additional water was added to the pycnometer and wipe off the foam with a napkin. At the end of these procedures, the weight of the pycnometer, water and material was recorded (B). Then the pycnometer and the weight of the water were measured together (C). Finally, the dry weight of the material was measured after 24 hours in the oven at (110 ± 5)°C (D). Materials were measured using a Mettler PM4600 Deltarange Balance. The range of this device is 0.01g for measurements of 600g and below and 0.1g for measurements above this value. The weights for fine sand and sharp sand are given in Table 3.1 and Table 3.2 respectively. Some images of the test phase are shown in Figure 3.1. The same procedures were repeated for the fine sand. Specific gravity, dry specific gravity, apparent specific gravity, and water absorption rate can be calculated using Equation (3.1), (3.2), (3.3) and (3.4), respectively. The physical property values obtained for fine sand and sharp sand were illustrated in Table 3.3.

$$\text{Specific Gravity} = \left[\frac{A}{A-(B-C)}\right] \tag{3.1}$$

$$\text{Dry Specific Gravity} = \left[\frac{D}{A-(B-C)}\right] \tag{3.2}$$

$$\text{Apparent Specific Gravity} = \left[\frac{D}{D-(B-C)}\right] \tag{3.3}$$

$$\text{Water Absorption Rate} = \left[\frac{(A-D)}{D}\right] \times 100 \quad (3.4)$$

Table 3.1. The weights of fine sand.

Material	A	B	C	D
Fine Sand	Weight of saturated & surface dry fine sand	Weight of pycnometer+saturated & surface dry fine sand+water	Weight of pycnometer+water	Weight of oven dry fine sand
	(g)	(g)	(g)	(g)
	484	1639	1341	477.97

Table 3.2. The weights of sharp sand.

Material	A	B	C	D
Sharp Sand	Weight of saturated & surface dry sharp sand	Weight of pycnometer+saturated & surface dry sharp sand+water	Weight of pycnometer+water	Weight of oven dry sharp sand
	(g)	(g)	(g)	(g)
	425	1597	1341	419

(a) Saturated sharp sand

(b) Saturated & surface dry sharp sand

Figure 3.1. Images of the test phase for sharp sand.

(c) Pycnometer + water

(d) Pycnometer + saturated & surface dry sharp sand + water

Figure 3.1. Images of the test phase for sharp sand (continue).

Table 3.3. The physical property values obtained for fine sand and sharp sand.

Material	**Dry Specific Gravity**	**Specific Gravity**	**Apparent Specific Gravity**	**Water Absorption Rate**
	δ_{DS}	δ_S	δ_A	S
	kg/m^3	kg/m^3	kg/m^3	%
Fine Sand	2570	2602	2656	1.26
Sharp Sand	2479	2515	2571	1.43

The following instruction was followed for coarse aggregate-1 and coarse aggregate-2 and the values were obtained. Coarse aggregate-1 represents aggregates 10 mm gravel while coarse aggregate-2 stands for aggregates 20 mm gravel.

Samples of 500 grams of both coarse materials were taken and soaked in water for 24 hours. After the water in the aggregates was drained, their surfaces were dried properly with the help of a napkin. After these procedures, the weight of the saturated surface dry aggregate in air was measured first (W_1). Then the weight of the saturated aggregate suspended in water with the basket was measured (W_2) and then the weight of the basket suspended in water was measured (W_3). Finally, the dry weight of the material was measured after 24 hours in the oven at (110 ± 5)°C (W_4). The weights for coarse aggregate-1 and coarse aggregate-2 are given in Table 3.4 and Table 3.5 respectively. The same procedures were repeated for the coarse aggregate-2. Specific gravity, dry specific gravity, apparent specific gravity and water

absorption rate can be calculated using Equation (3.5), (3.6), (3.7) and (3.8), respectively. The physical property values obtained for coarse aggregate-1 and coarse aggregate-2 were given in Table 3.6.

$$\text{Specific Gravity} = \left[\frac{W_1}{W_1-(W_2-W_3)}\right] \quad (3.5)$$

$$\text{Dry Specific Gravity} = \left[\frac{W_4}{W_1-(W_2-W_3)}\right] \quad (3.6)$$

$$\text{Apparent Specific Gravity} = \left[\frac{W_4}{W_4-(W_2-W_3)}\right] \quad (3.7)$$

$$\text{Water Absorption Rate} = \left[\frac{(W_1-W_4)}{W_4}\right] \times 100 \quad (3.8)$$

Table 3.4. The weights of coarse aggregate-1.

Material	**W_1**	**W_2**	**W_3**	**W_4**
Coarse Aggregate-1	Weight of saturated surface dry aggregate in air	Weight of saturated suspended in water with basket	Weight of basket suspended in water	Weight of oven dry aggregate
	(g)	(g)	(g)	(g)
	500	367.12	68.14	486.2

Table 3.5. The weights of coarse aggregate-2.

Material	**W_1**	**W_2**	**W_3**	**W_4**
Coarse Aggregate-2	Weight of saturated surface dry aggregate in air	Weight of saturated suspended in water with basket	Weight of basket suspended in water	Weight of oven dry aggregate
	(g)	(g)	(g)	(g)
	500	375.08	68.14	488.36

Table 3.6. The physical property values for coarse aggregate-1 and coarse aggregate-2.

Material	Dry Specific Gravity	Specific Gravity	Apparent Specific Gravity	Water Absorption Rate
	δ_{DS}	δ_S	δ_A	S
	kg/m^3	kg/m^3	kg/m^3	%
Coarse Aggregate-1	2419	2487	2597	2.84
Coarse Aggregate-2	2530	2590	2692	2.38

3.2.1.2 Sieve analysis of fine and coarse aggregates

For the sieve analysis of fine and coarse aggregates to be used for the concrete designed within the scope of this study, analyses were carried out in accordance with BS-1377-2-1990 regulation. Sieve sizes in accordance with this regulation were used during the analysis phase.

Sieve analysis results of aggregates used in concrete design are shown in Appendix-A Table A1, Table A2, Table A3, Table A4 and granulometry curves are illustrated in Appendix-A Figure A1, Figure A2, Figure A3 and Figure A4 for fine sand, sharp sand, coarse aggregate-1 and coarse aggregate-2, respectively. In these granulometry curves, the log-10 scale is used only for the X-axis. Furthermore, Figure 3.2 shows the sieve sizes used in the sieve analyses.

(a) Sieve sizes for fine aggregates

(b) Sieve sizes for coarse aggregates

Figure 3.2. Sieve sizes for fine and coarse aggregates.

Within the scope of this thesis, TS 802-2016 regulation is used for concrete design and calculations are made for C20 concrete. For the concrete to be used, D_{max} is the maximum aggregate size in the concrete and this value is determined as 20mm.

Determination of the percentage for the concrete mixture, suitable slump values, water content value depending on the maximum aggregate size, water/cement ratio, and exposure classes in the regulation were taken into consideration before the concrete design. All figures and tables used in the concrete design phase are given in Appendix-A.

Within the scope of this study, it is aimed to design the compressive strength of concrete as 20 MPa. For this purpose, the target compressive strength (f_{cm}) for f_{ck}=20 MPa was determined as 26 MPa by using the Table A5. For the determination of the water cement ratio, the water/cement ratio was calculated as 0.59 for f_{cm} =26 MPa by using the Equation (3.9) below in the non-air-entrained concrete graph using Figure A5.

$$\text{The ratio of water/cement} = y = 1{,}1318e^{-0.025x} \tag{3.9}$$

where *x* refers to f_{cm}.

In Table A6, the slump value for columns, beams and reinforced concrete structures is given as minimum 50 mm and maximum 100 mm. For this study, the slump value is targeted to be between 80-100 mm and the amount of water was determined as 202 kg/m^3 for the maximum aggregate size of 20 mm (D_{max}=20 mm) in Figure A6.

In order to determine the maximum water cement ratio and minimum amount of cement at the concrete design stage, XC1 (due to carbonation corrosion) was selected for C20/25 concrete grade from the exposure class in Table A7 and the maximum water cement ratio was determined as 0.70 and the minimum cement amount was determined as 250 kg.

In this study, another method for determining the amount of cement in concrete, the Graf method, was utilized. The Graf formula is a formula that explicitly takes into account the effect of the mechanical strength of the cement. This formula is shown in Equation (3.10).

$$f_{cm} = \frac{f_{cc}}{K_G}\left(\frac{C}{W}\right)^2 \tag{3.10}$$

In this formula, f_{cc} is the norm strength of concrete (N/mm^2), f_{cm} is the target compressive strength, *C* is the content of cement, *W* is the water content, the *KG* value varies between 4

and 10 and is independent of the age of the concrete (Akman, 1990). The cement content was found to be 361.35 kg by accepting a *KG* value of 4.

The amounts of fine and coarse aggregates in the mixture are determined with the help of unit volume equation. The total volume of aggregates in the mixture ($V_{aggregate}$) is found. Fine and coarse aggregates forming the mixture fine aggregates separately by using their % values in the mixture (all-in-aggregate) volumes are determined. The volumes of the aggregates are multiplied by their unit volume weights to determine their weights. Calculations 1 m^3 made for concrete which is given in Equation (3.11).

$$V_{concrete} = V_{cement} + V_{water} + V_{aggregate} + V_{air} = 1\ m^3 \quad (3.11)$$

The total air content for non-air entrained concrete corresponding to the maximum aggregate size of the aggregates in Figure A7 was found to be 2%.

Air quantity in volume; $1m^3 \times \frac{2}{100} = 0.02\ m^3$ is considered.

For a 1 m^3 concrete design, the cement volume is found to be 0.1147 m^3 using the cement specific gravity (δ_C) of 3150 kg/m^3 for a cement content of 361.35 kg. Likewise, for the water volume, the specific gravity of water (δ_W) is assumed to be 1000 kg/m^3 and the volume of water is calculated as 0.2020 m^3 for 202 kg.

Separate volumes of the fine and coarse aggregates that make up the aggregate were determined. Using Equation (3.11), the equation to obtain the aggregate volume is written as follows.

$$V_{aggregate} = 1\ m^3 - (V_{cement} + V_{water} + V_{air})$$

$$V_{aggregate} = 1\ m^3 - (0.1147\ m^3 + 0.2020\ m^3 + 0.02\ m^3)$$

$$V_{aggregate} = 0.6633\ m^3$$

Calculations were made to obtain the appropriate mixture in accordance with the data obtained from sieve analysis. Cumulative passing of fine and coarse aggregates and determination of the percentage for the concrete mixture are shown in Table 3.7 and Table 3.8, respectively.

Table 3.7. Cumulative passing of fine and coarse aggregates.

Sieve Size	Cumulative passing (%)			
	Fine Sand	Sharp Sand	Coarse Aggregate-1	Coarse Aggregate-2
28	100	100	100	100
20	100	100	100	82.13
14	100	100	100	39.42
10	100	100	92.16	4.49
6.3	100	100	37.32	0.17
5	99.89	99.50	20.49	0.02
3.35	99.20	92.80	6.97	0
2	98.48	80.76	3.13	0
1.18	97.89	71.37	1.65	0
0.6	86.59	59.30	0.13	0
0.425	64.67	53.04	0.05	0
0.212	16.97	30.92	0.04	0
0.15	7.50	17.45	0.03	0
0.063	0.08	0.48	0	0

Table 3.8. Determination of the percentage for the concrete mixture.

Sieve Size	Percentage				
	Fine Sand	**Sharp Sand**	**Coarse Aggregate-1**	**Coarse Aggregate-2**	**Reached Value for mixture**
	10	**15**	**35**	**40**	**100**
(mm)	%	%	%	%	%
28	10	15	35	40	100
20	10	15	35	32.85	92.85
14	10	15	35	15.77	75.77
10	10	15	32.26	1.80	59.05
6.3	10	15	13.06	0.07	38.13
5	9.99	14.93	7.17	0.01	32.09
3.35	9.92	13.92	2.44	0	26.28
2	9.85	12.11	1.10	0	23.06
1.18	9.79	10.71	0.58	0	21.07
0.6	8.66	8.89	0.04	0	17.60
0.425	6.47	7.96	0.02	0	14.44
0.212	1.70	4.64	0.01	0	6.35
0.15	0.75	2.62	0.01	0	3.38
0.063	0.01	0.07	0	0	0.08

Accordingly, the granulometry curve of the mixture formed by using 10% fine sand, 15% sharp sand, 35% coarse aggregate-1, and 40% coarse aggregate-2 by volume is within the limits of use and close to the ideal granulometry which is shown in Figure 3.3. In addition, care should be taken to ensure that the prepared mixing curve is between the 3rd and 4th zones. The desired limits and the yellow line representing the granulometry of the mixture are presented in Figure 3.4.

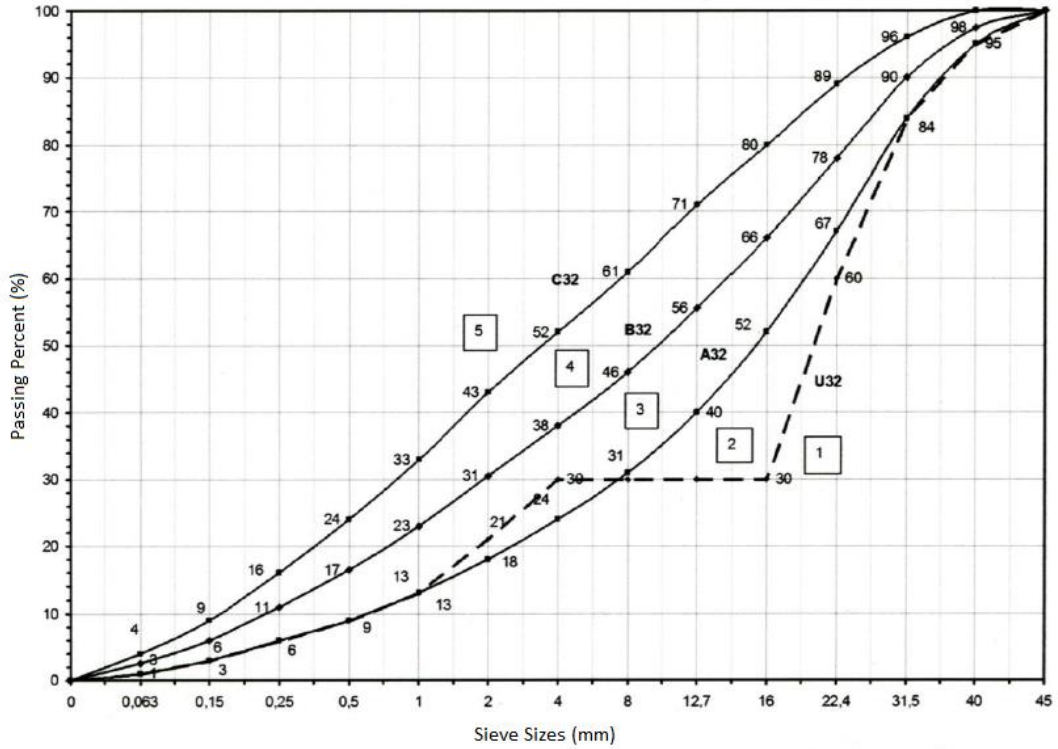

Figure 3.3. Limits of the aggregate grain size distribution curve for concrete with aggregate maximum grain size of 32.0 mm (31.5 mm) (TS 802, 2016).

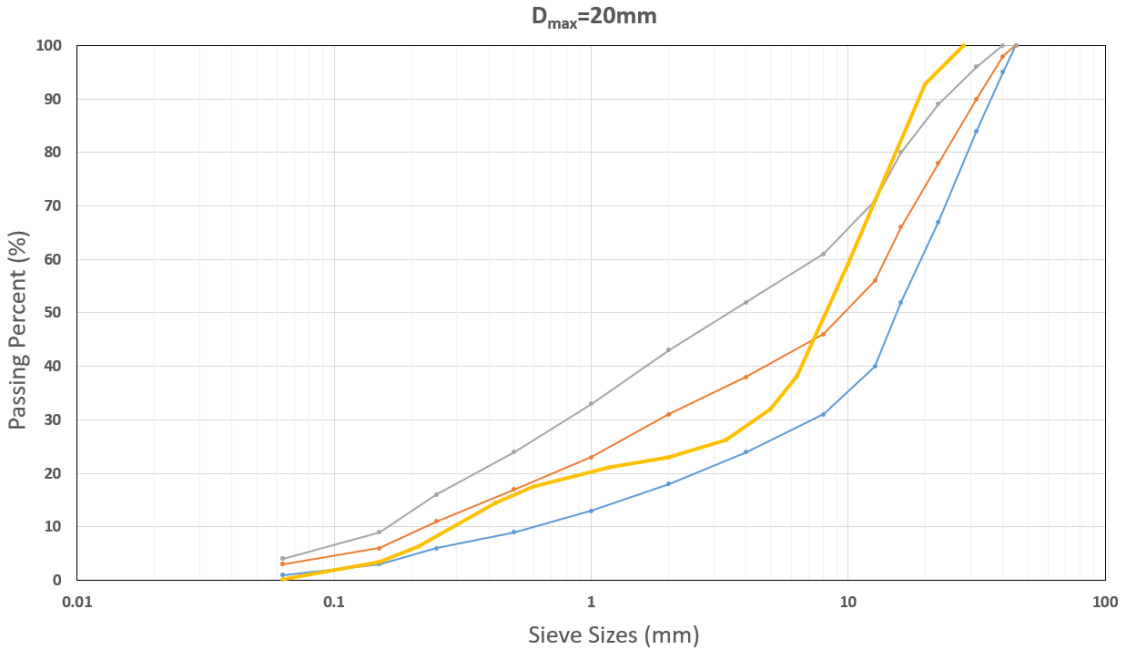

Figure 3.4. Limits of the aggregate grain size distribution curve and the granulometry of the concrete mixture.

After determining the volume of aggregates in the concrete mixture, separate weights of the fine and coarse aggregates that make up the aggregate are determined using Equation (3.12)

and Equation (3.13). Dry weights of aggregate and dry surface saturation weights of aggregate are depicted in Table 3.9 and Table 3.10, respectively.

$$W_{aggregate,\ DS} = \delta_{DS} \times V_{aggregate} \tag{3.12}$$

$$W_{aggregate,\ S} = \delta_{S} \times V_{aggregate} \tag{3.13}$$

Table 3.9. Calculation of aggregate dry weights.

Material	**Weight of aggregates ($W_{aggregate,\ DS}$)**	**Unit**
Fine Sand	170.46	kg
Sharp Sand	246.64	kg
Coarse Aggregate-1	561.57	kg
Coarse Aggregate-2	671.25	kg

Table 3.10. Calculation of aggregate dry surface saturation weights.

Material	**Weight of aggregates ($W_{aggregate,\ S}$)**	**Unit**
Fine Sand	172.59	kg
Sharp Sand	250.22	kg
Coarse Aggregate-1	577.36	kg
Coarse Aggregate-2	687.16	kg

The amount of excess water is obtained using the water absorption rates for the weights calculated for each aggregate using the data in Table 3.9. This calculated water should be subtracted from the total amount of water used. Otherwise, the excess water will cause errors in the calculation of the concrete mixture. The moisture content of the aggregates was determined before casting and given in Table 3.3 and Table 3.6 on the previous pages and the amount of excess water for 1 m^3 concrete was calculated and presented in Table 3.11.

Table 3.11. Calculation of water absorbed by fine and coarse aggregates for 1 m3 concrete.

Material	**Amount of water absorbed**	**Unit**
Fine Sand	2.15	litre
Sharp Sand	3.53	litre
Coarse Aggregate-1	15.94	litre
Coarse Aggregate-2	16.00	litre
Total Absorbed Water	37.62	litre

As a result of the calculations and corrections, the quantities in Table 3.12 were obtained for 1 m^3 concrete mixture. The water cement ratio for the concrete mix prepared for this study was calculated as 0.56 (water=202/cement=361.35).

Table 3.12. Quantities for 1 m3 concrete mixture.

Material	**Type**	**Quantity (kg/m^3)**
Cement	Portland Cement 32.5R	361.35
Water	City water	164.38
Fine sand	Yellow building sand	172.59
Sharp sand	Washed concreting sand	250.22
Coarse Aggregate-1	10 mm washed gravel	577.36
Coarse Aggregate-2	20 mm washed gravel	687.16
		2213.07

3.2.1.3 Properties of cement

Portland Cement 32.5R (BS EN 197-1 CEM II) was used in the mixtures. The physical, chemical, and mechanical properties of the cement provided by the manufacturer are given in Appendix-A Table A8.

3.2.1.4 Determination of mechanical properties of concrete

To assess the concrete properties, rectangular beam (100 mm × 100 mm × 500 mm) for the tensile test and cylinders (100 mm diameter × 200 mm length) for the compressive test were prepared and cured in the water container in the laboratory for seven days.

Tensile test of concrete : Many laboratory studies have evaluated the tensile strength of concrete using three main methods: direct tensile tests; splitting tensile tests; and beam flexural tests (Rashid *et al*., 2002 and Lu and Li, 2011). The methods are shown in Figure 3.5.

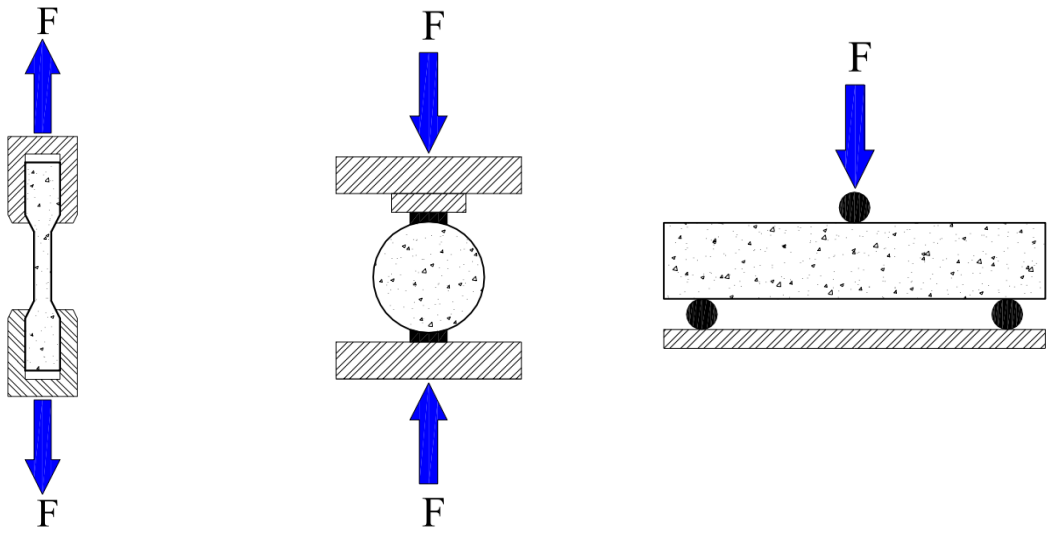

(a) (b) (c)

Figure 3.5. (a) direct tensile test; (b) splitting tensile test; and (c) beam flexural test.

The tensile strength f_{ctk} can approximately be obtained by dividing the tensile strength values obtained from the split cylinder test ($f_{ctk}^{`}$) by 1.5 and the tensile strength values from the flexural test result ($f_{ctk}^{``}$) by 2.0 (TS 500, 2000). The relationship between the three methods mentioned above is as follows;

$$f_{ctk} = \frac{f_{ctk}^{`}}{1.5} = \frac{f_{ctk}^{``}}{2}$$

In this project, the beam flexural test method was used to obtain the tensile strength of concrete.

Three-point bending test of concrete: Samples of concrete were tested in a three-point bending test (see in Figure 3.6). The samples tested were 100 mm × 100 mm in cross-section and 500 mm in length. The flexural tests were carried out in an Instron 5585H testing machine at a clear span of 400 mm. The samples were constantly loaded at a rate of 1 mm/min.

Figure 3.6. Three-point bending test of concrete.

According to the test results the bending strength was determined using Equation (3.14);

$$f_{ctk}^{``} = \frac{M_b \times y}{I} \tag{3.14}$$

where *Mb* is the maximum bending moment (N), I is the area moment of inertia of cross-section (mm^4), and y is the vertical distance from the neutral axis to where the stress is being calculated (mm).

During the concrete pouring process carried out within the scope of this thesis, 3 beam samples were taken for each specimen, and the samples were cured in water for 7 days. All samples were tested at the end of 28 days. All values after the test and the averaged values are given in Table 3.13. In Table 3.13, the tensile strength of the concrete was calculated 1.80 MPa (average value obtained after 28 days) and the Coefficient of Variation (CoV) was calculated 12.27%. Details of concrete tensile test values are given in Appendix-B**.**

Table 3.13. The result of concrete tensile strength.

	28-Day Result (MPa)		
Specimen-1	*ST11*	2.16	**2.11**
	ST12	2.15	
	ST13	2.02	
Specimen-2	*ST21*	1.69	**1.72**
	ST22	1.77	
	ST23	1.7	
Specimen-3	*ST31*	1.68	**1.59**
	ST32	1.38	
	ST33	1.72	
Specimen-4	*ST41*	1.75	**1.79**
	ST42	1.68	
	ST43	1.93	
Average			**1.80**

Compression test of concrete: The compression tests were carried out using an Impact brand automatic console cube and cylinder compression testing machine which is compression range 0 to 2000 kN. The test equipment is shown in Figure 3.7.

Figure 3.7. The test equipment for concrete compression strength.

9 cylindrical samples (100 mm diameter × 200 mm length) were prepared for each specimen in order to ascertain the compressive strength of concrete. The samples were then cured in water for 7 days. The compressive strength of the concrete cylinder is illustrated in Table 3.14

for the test day, 28 days, and 7 days. Details of concrete compressive test values are given in Appendix-B**.**

Table 3.14. The result of concrete compressive strength.

	7-Day Result (MPa)			**28-Day Result (MPa)**			**Test-Day Result (MPa)**		
Specimen-1	*S11*	13.14	**13.06**	*S14*	23.61	**23.89**	*S17*	24.23	**24.69**
	S12	13.27		*S15*	24.24		*S18*	24.37	
	S13	12.76		*S16*	23.81		*S19*	25.47	
Specimen-2	*S21*	12.5	**12.19**	*S24*	21.88	**22.77**	*S27*	22.65	**24.11**
	S22	11.85		*S25*	23.75		*S28*	25.04	
	S23	12.22		*S26*	22.68		*S29*	24.63	
Specimen-3	*S31*	12.09	**12.60**	*S34*	21.27	**21.91**	*S37*	22.42	**23.88**
	S32	12.95		*S35*	22.08		*S38*	24.56	
	S33	12.75		*S36*	22.38		*S39*	24.66	
Specimen-4	*S41*	12.94	**12.56**	*S44*	23.33	**23.60**	*S47*	24.79	**24.71**
	S42	12.66		*S45*	24.33		*S48*	24.62	
	S43	12.09		*S46*	23.15		*S49*	24.72	
Average			**12.60**			**23.04**			**24.35**

In Table 3.14, the compressive strength of the concrete was calculated 24.35 MPa (average value obtained on the test day) and the Coefficient of Variation (CoV) was calculated 1.72%.

In this study, a cylinder sample of concrete was tested to measure the strain of concrete. Two strain gauges were attached to this specimen and the data was recorded on a computer during the test. The data obtained as a result of the test and the graphs are shown in Appendix B Figure B2. As a result of this test, the data obtained from the strain gauges were averaged and the stress corresponding to the maximum stress was calculated as 0.00235 mm/mm.

3.2.2 Steel

Two different diameters of grade B420C deformed steel bars were used as longitudinal, transverse, and u-shaped reinforcement. The transverse and u-shaped reinforcement bars were 8 mm in diameter while 16 mm bars were used as longitudinal reinforcement. The average values of yield strength (f_{sy}), yield strain (ε_{sy}), ultimate strength (f_{su}), ultimate strain (ε_{su}) and elastic modulus (E_s) of the steel reinforcement obtained from three samples are given in Table 3.15 and stress-strain curve for 8 mm and 16 mm steel reinforcement are illustrated in Figure 3.8 (a) and (b), respectively. Details of steel reinforcement tensile test values are given in Appendix-B**.**

Table 3.15. Steel reinforcement properties.

Bar size	f_{sy}	ε_{sy}	f_{su}	ε_{su}	ε_{sh}	E_s
mm	MPa	mm/mm	MPa	mm/mm	mm/mm	MPa
8	502	0.00249	578	0.103	0.0299	201283
16	471	0.00237	581	0.114	0.0218	198963

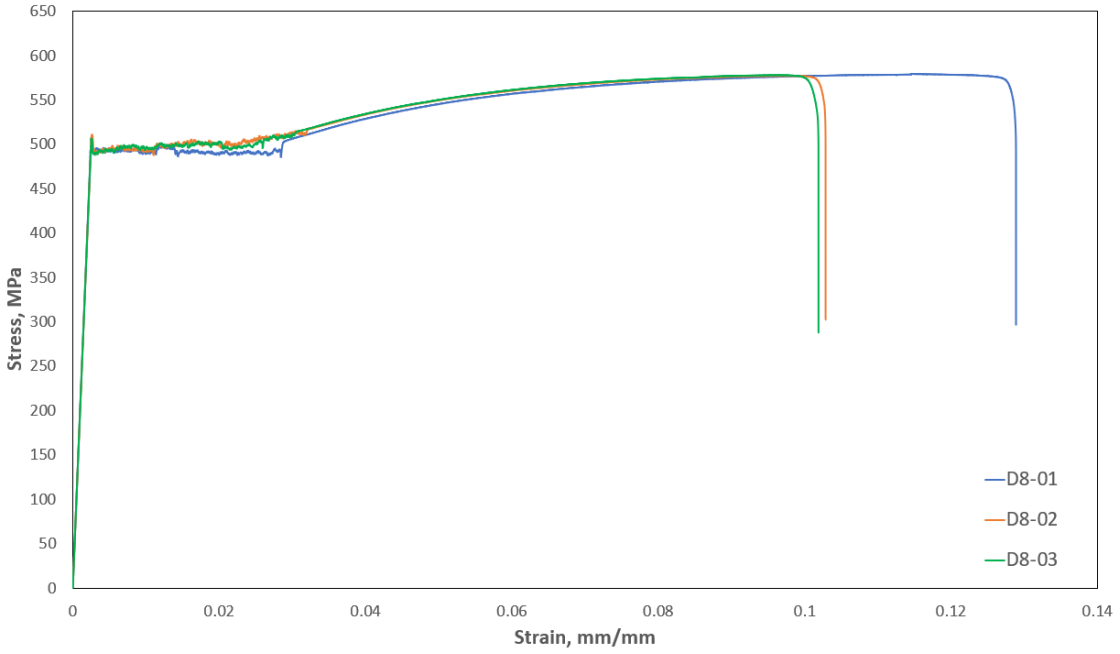

(a)

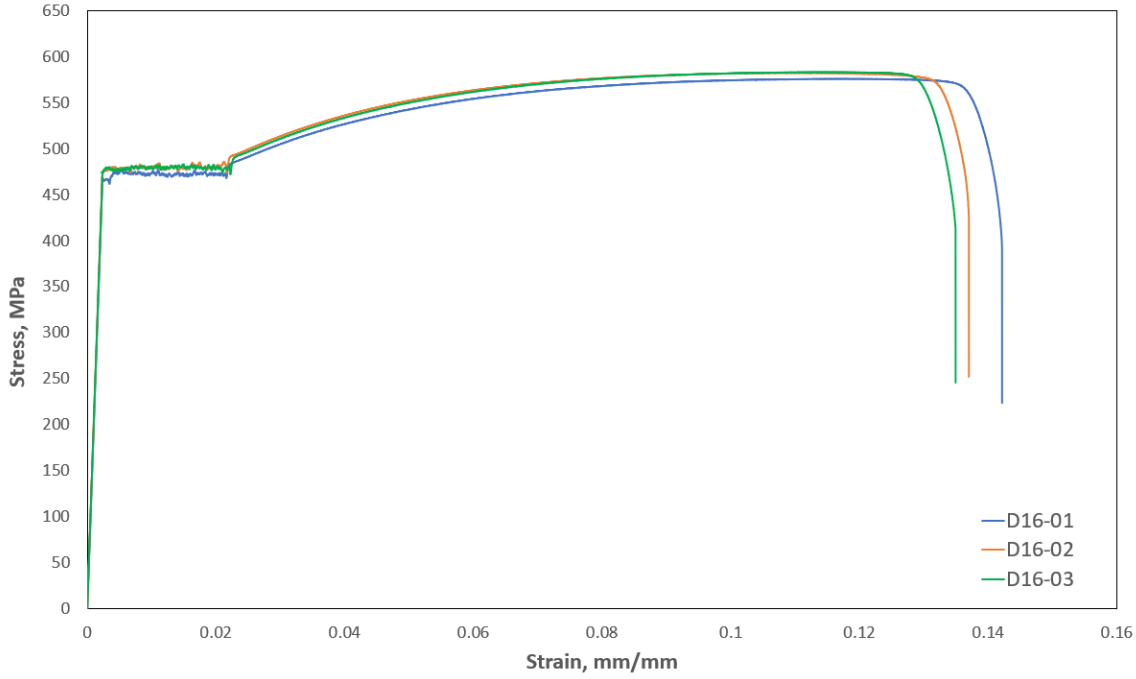

(b)

Figure 3.8. Stress-strain curves: (a) 8 mm diameter rebars; (b) 16 mm diameter rebars.

The tensile tests were carried out on an Instron testing machine with a capacity of 250 kN. The samples were constantly loaded at a rate of 10 mm/min. An extensometer was used to obtain the measurement of deformation (strain) values. The samples were 1000 mm length and tested in accordance with ISO 15630-1, ISO 6892-1, ASTM A370 and TS 708 standards. The test set-up for 16 mm steel reinforcement and extensometer are shown in Figure 3.9 (a) and (b), respectively.

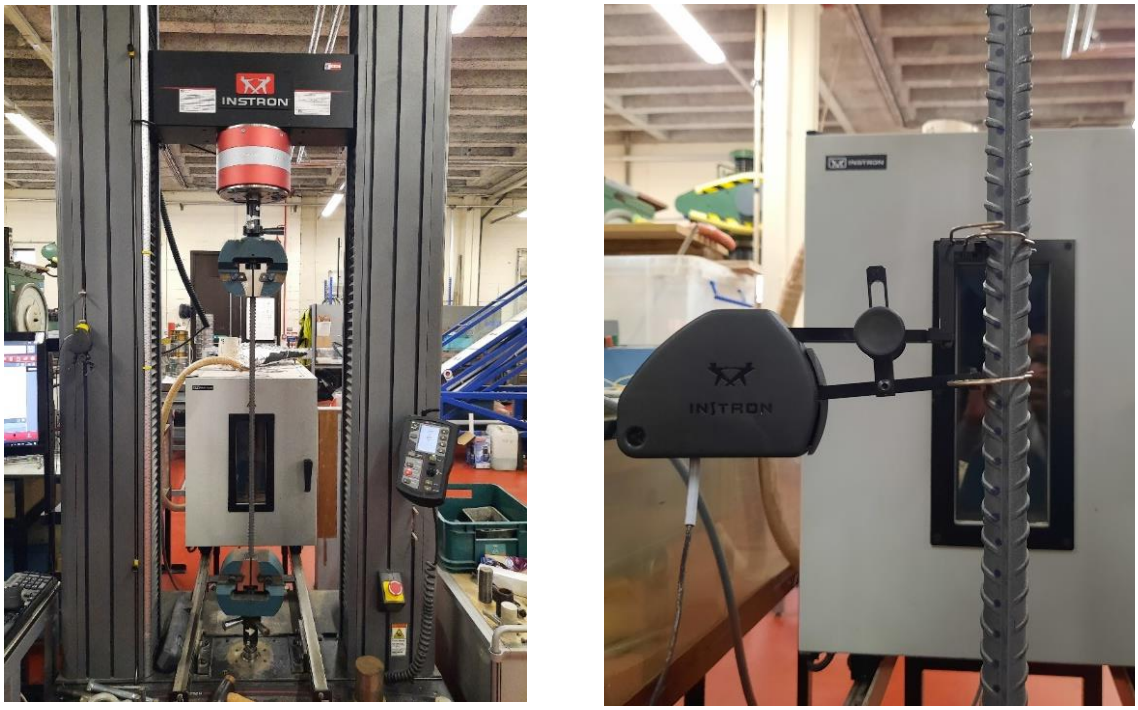

(a) (b)

Figure 3.9. (a) The test set-up of 16 mm steel rebar, (b) Extensometer.

3.2.3 Glass Fibre Reinforced Polymer

Glass fibre reinforced polymer (GFRP), consisting of a unidirectional woven glass fibre fabric, SikaWrap® 930G, was utilised for strengthening. The manufacturer provides the following properties: The tensile strength=1500 MPa, the tensile modulus of elasticity=70,000 MPa, the strain (laminate elongation at rupture) = 2.14%, fabric width=600 mm, and the thickness of the fibre fabric= 0.363 mm. Further information can be found in Appendix-C Figure C1.

3.2.4 Epoxy Resin

In this project, two different types of epoxies were used namely Sikadur®30 for NSM method and Sikadur®300 for EB method. The properties given below for Sikadur®30 and Sikadur®300 were provided by the manufacturer.

Sikadur®30 (Sika Corporation, Lyndhurst, NJ, USA), an epoxy adhesive, was used to bond the retrofitting materials to the concrete substrate. Sikadur®30 has two components, namely component A and component B. Component A is white in colour, while component B is black. These two components are mixed in a ratio of 3:1 until a uniform light grey colour is achieved. The density is 1.65 kg/L at 23^{o}C after mixing. The compressive strength is 75 MPa, the tensile strength is 26 MPa, the shear strength is 18 MPa, and tensile modulus of elasticity is 11,200 MPa, and modulus of elasticity in compression of the adhesive is 9,600 MPa.

Sikadur®300 an epoxy-based impregnating/laminating resin, was used in this project to bond the retrofitting materials to the concrete substrate and SikaWrap® structural strengthening fabrics. Sikadur®300 has two components, namely component A (resin) and component B (hardener). Component A is amber in colour, while component B is pale yellow. These two components are mixed in a ratio of 100:34,5 by weight. The density is 1.16 kg/L at 23^{o}C after mixing. The tensile strength= 45 MPa, tensile modulus of elasticity= 3500 MPa, flexural modulus= 2800 MPa, and elongation at break of the adhesive= 1,5%.

Further information can be found in Appendix-C Figure C2 for Sikadur®30 and Figure C3 for Sikadur®300.

3.3 DESCRIPTION OF TEST UNITS

A total of four full-scale exterior RC beam-column joint specimens were designed and constructed according to TEC (1998). The column height is 1800 mm and the beam length measured from the face of the column is 1500 mm. Both the column and the beam have cross-sectional dimensions of 250 mm × 300 mm. The dimension of a typical specimen is illustrated in Figure 3.10. These dimensions were chosen as they are the smallest sizes that could realistically occur in a building (i.e. full-scale experiment) and small enough so they could be tested in the Heavy Structures Laboratory at Newcastle university. All specimens were designed without any transverse steel reinforcement in the joint region (see Figure 3.11). The beam reinforcement comprises 3φ16 top and bottom longitudinal bars and φ8/50/100 mm transverse bars. The column reinforcement includes 6φ16 longitudinal bars and φ8/50/100 mm transverse bars. The transverse bars spacing in beams and columns was determined as 100 mm. However, the spacing of the transverse rebars in the columns has been reduced to 50 mm to provide sufficient shear strength in the region where the support conditions will

occur at the ends of the columns. Likewise, the transverse rebars spacing of the beams has been decreased to 50 mm to supply adequate shear strength in the region where the load will be given at the end of the beam. The concrete clear cover of columns and beams is 30 mm. The 16 mm longitudinal steel rebars, the 8 mm transverse steel rebars and the U-shaped steel rebars in the beams and columns all have a minimum yield stress of 420 MPa. Mechanical characteristics of steel bars used in RC beam-column joints are presented in Table 3.15 above.

Anchorage is achieved by extending the reinforcing bars a distance of l_b beyond the point of maximum stress in the bar. This length, known as the development length, can be calculated for deformed bars using Equation (3.15) in TS 500 (2000).

$$l_b = \left(0.12 \times \frac{f_{yd}}{f_{ctd}} \times \varphi\right) \tag{3.15}$$

When the above equation is applied for φ16 and C20, the development length was calculated as 701 mm and is shown in Appendix-D Table D1.

TEC (1998) regulation was used for the calculation of the anchorage length at the beam-column junction. Formulas for minimum anchorage length values are shown in Appendix-D Figure D1. In this study, the anchorage length was used as 754 mm and is shown in detail in Appendix-D Figure D2. In addition, shear link spacing design and the capacity calculations of the specimens using the XTRACT software for beams and columns are given in Appendix-D.

All the specimens have the same steel reinforcement detailing which is shown in Figure 3.11 and differ only in their retrofitting technique. The S1 specimen had no retrofitting and was used as a control, while the S2, S3 and S4 specimens used different retrofitting techniques. The retrofitting technique specifications for the specimens are outlined in Table 3.16.

Table 3.16. The retrofitting technique specifications.

Specimen Name	Description	Extra bars	Wrap
S1	Control	None	None
S2	NSM method	U-shaped steel bars	None
S3	EB method	None	GFRP Sheet
S4	Hybrid method	U-shaped steel bars	GFRP Sheet

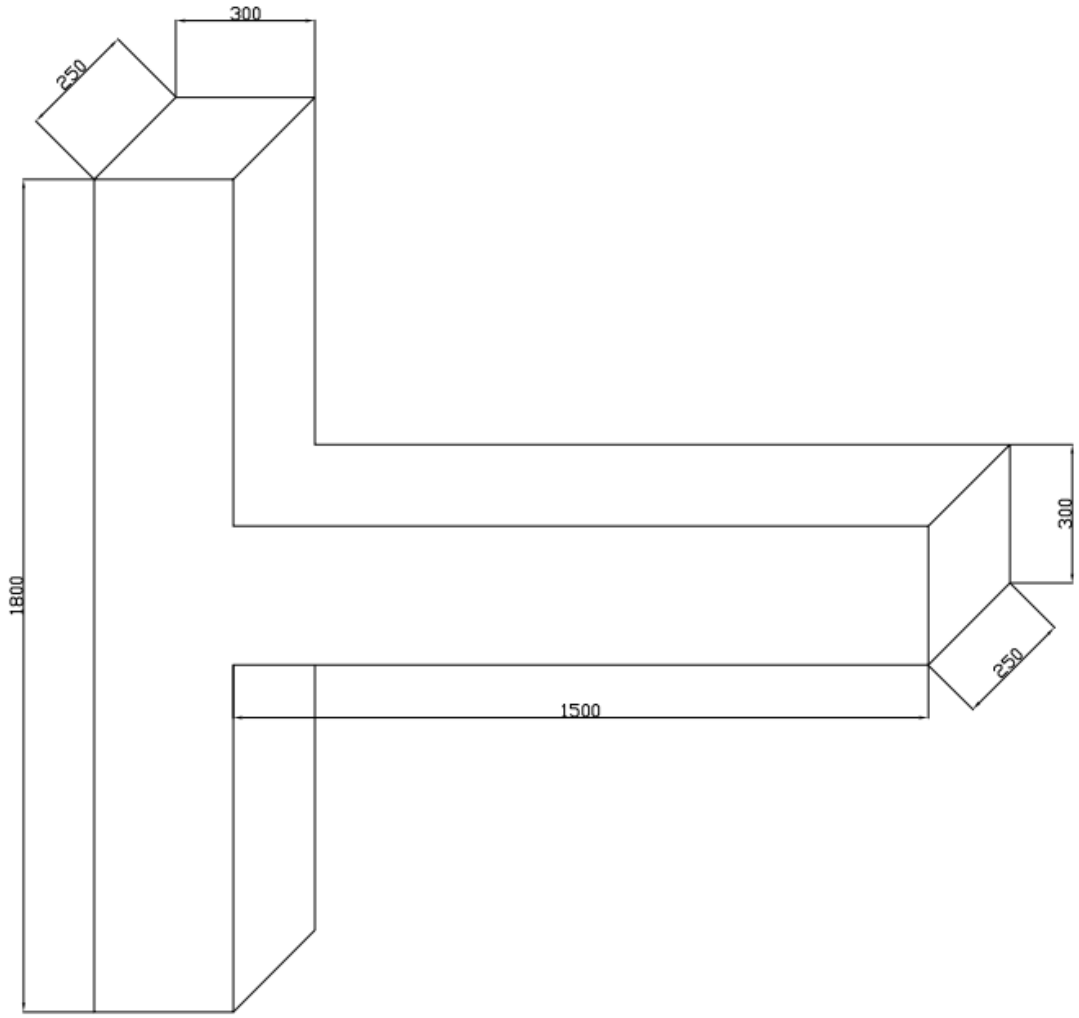

Figure 3.10. The dimension of a typical specimen (units are mm).

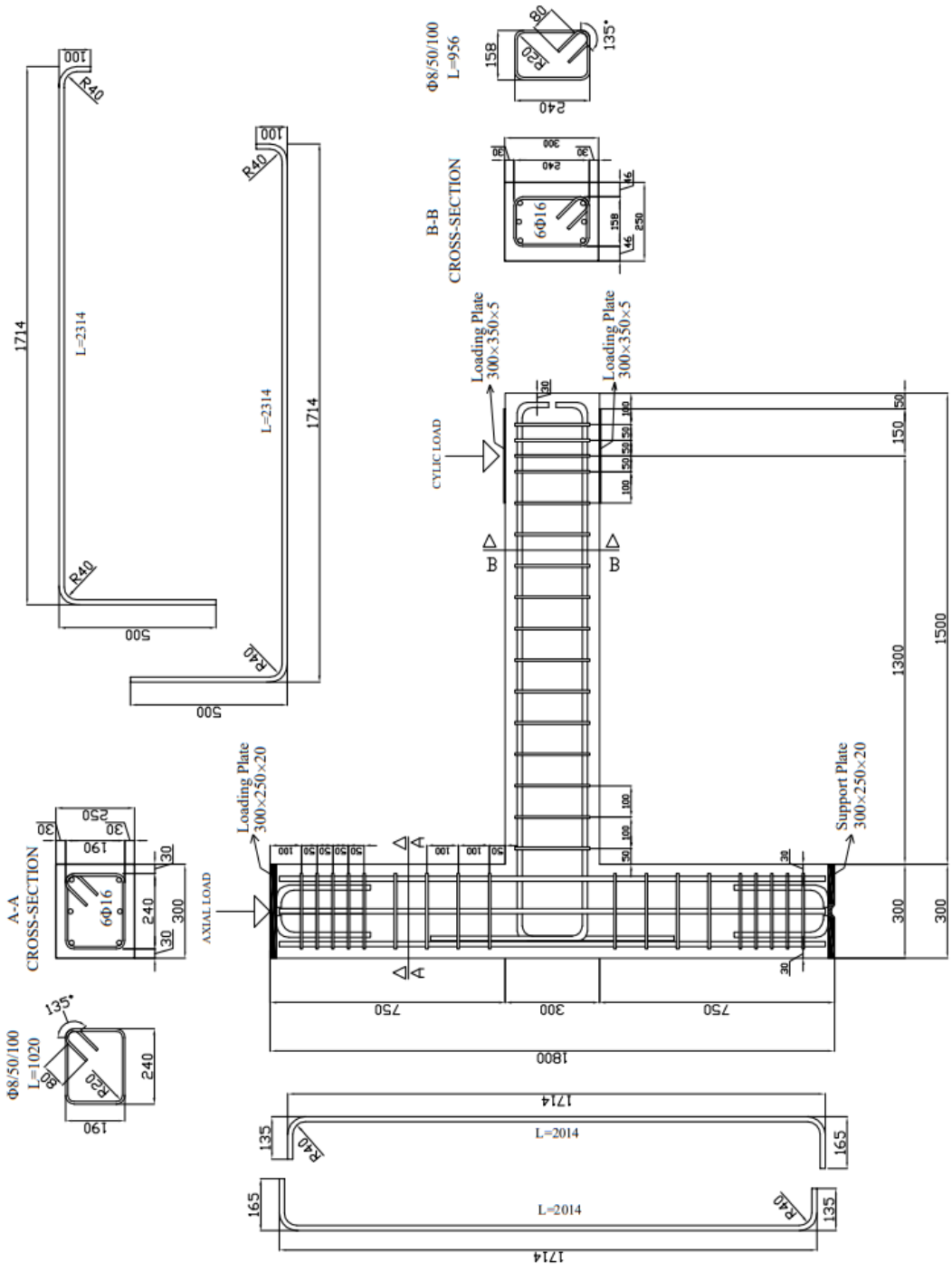

Figure 3.11. Specimen`s dimension and details (units are mm).

3.4 MANUFACTURE OF THE SPECIMENS

The four concrete beam/column test specimens were horizontally cast utilising a reusable hardwood mould designed for efficient assembly and disassembly post-casting. The base and sides of the mould were made from 18 mm hardwood plywood, with the sides supported by 47 mm × 100 mm rectangular wooden blocks (see Figure 3.12 (a)). The inside of the moulds was then thoroughly coated with Ronseal Trade Polyurethane Varnish (see Figure 3.12 (b)). The purpose of this is to ensure that the concrete is easily separated from the mould. After that, the gaps between the plywood sheets were sealed using silicon to prevent bleeding of concrete that may occur during casting.

The construction of the rebar cage of the columns and beams was performed separately. Before tying the transverse and longitudinal reinforcements, they were bent in accordance with the project (see Figure 3.12 (c) and (d)). To construct each reinforcing cage, the longitudinal bars were connected to the two end transverse reinforcements and all necessary transverse reinforcements were placed between them. The intermediate transverse reinforcements were then tied to the longitudinal bars (see Figure 3.12 (e) and (f)). Next, the beam cage was positioned perpendicular to the column cage in the joint area and tied together (see Figure 3.12 (g)). Once the column and beam cages were joined into a single beam-column joint reinforcement cage, strain gauges were instrumented to the steel bars (see Figure 3.12 (h)). The locations of the strain gauges on the steel rebars and all the steps involved in the application of the strain gauges are shown in Appendix-E Figures E1. Afterwards, steel plates were placed on the top and bottom of the column (see Chapter 3.6). In addition, steel hooks, two at the column ends and one at the beam end, were placed in the steel cage prior to concreting to ensure proper handling of the test specimen (see Figure 3.12 (i) and (j)). Finally, commercially available spacers were utilised to ensure the appropriate cover distance between the mould and the reinforcing bars. The concrete was poured and subjected to mechanical vibration during the pouring process to eliminate voids (see Figure 3.12 (k)). Demoulding the specimen, specimens after casting, samples taken during the concrete pouring process, and curing process of the samples are given in Figure 3.12 (l), (m), (n)and (o), respectively.

(a) Preparation of formworks

(b) Vanishing of formworks

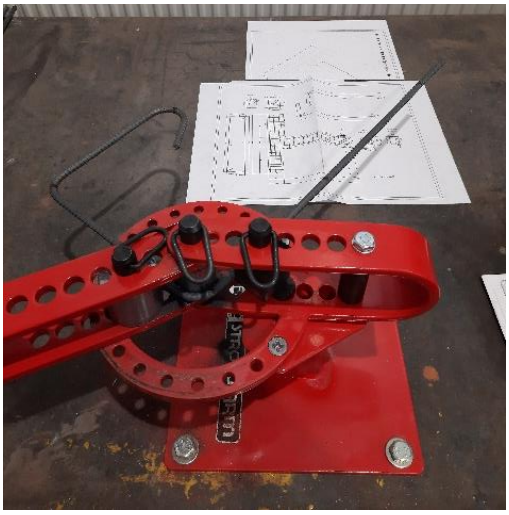

(c) Bending of transverse rebars

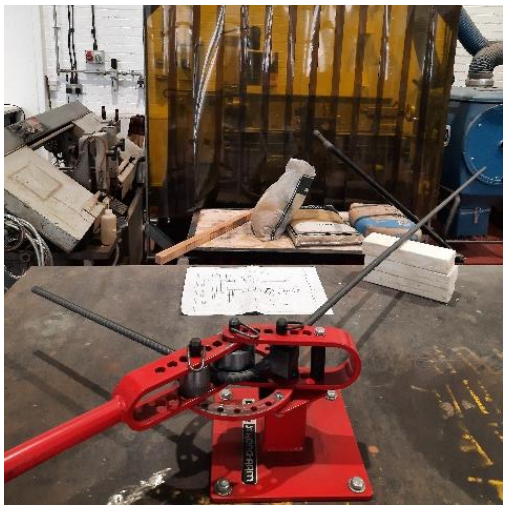

(d) Bending of longitudinal rebars

(e) Tying of the column reinforcements

(f) Tying of the beam reinforcements

Figure 3.12. Details of beam-column joint specimens' construction.

(g) Combining column and beam reinforcements

(h) Installation of the strain gauges (Phases of the installation of strain gauges were given in Appendix-E.)

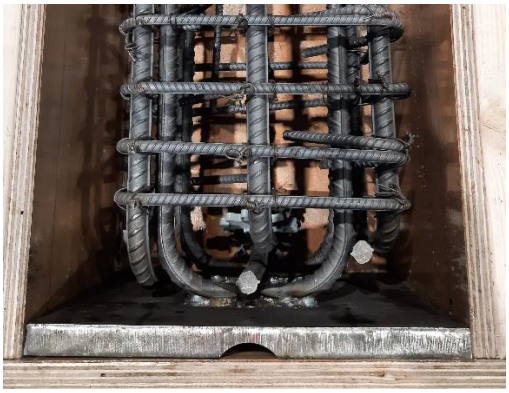

(i) Column lower end detail (sketch of the support details were given in Chapter 3.6)

(j) Column upper end detail (sketch of the support details were given in Chapter 3.6)

(k) Pouring concrete

(l) Demoulding the specimen

Figure 3.12. Details of beam-column joint specimens' construction (continue).

(m) Specimens after casting

(n) Samples taken during the concrete pouring process

(o) Curing process of the samples

Figure 3.12. Details of beam-column joint specimens' construction (continue).

3.5 STRENGTHENING APPLICATION

In this project, S1-Control had no retrofitting and acted as the control, while S2-NSM, S3-EB and S4-Hybrid employed different retrofitting specifications. The schematic representation of the specimens is shown in Figure 3.13. In addition, the shear capacity of the beam-column joint calculated by theoretical approaches using these methods is given in Appendix-F.

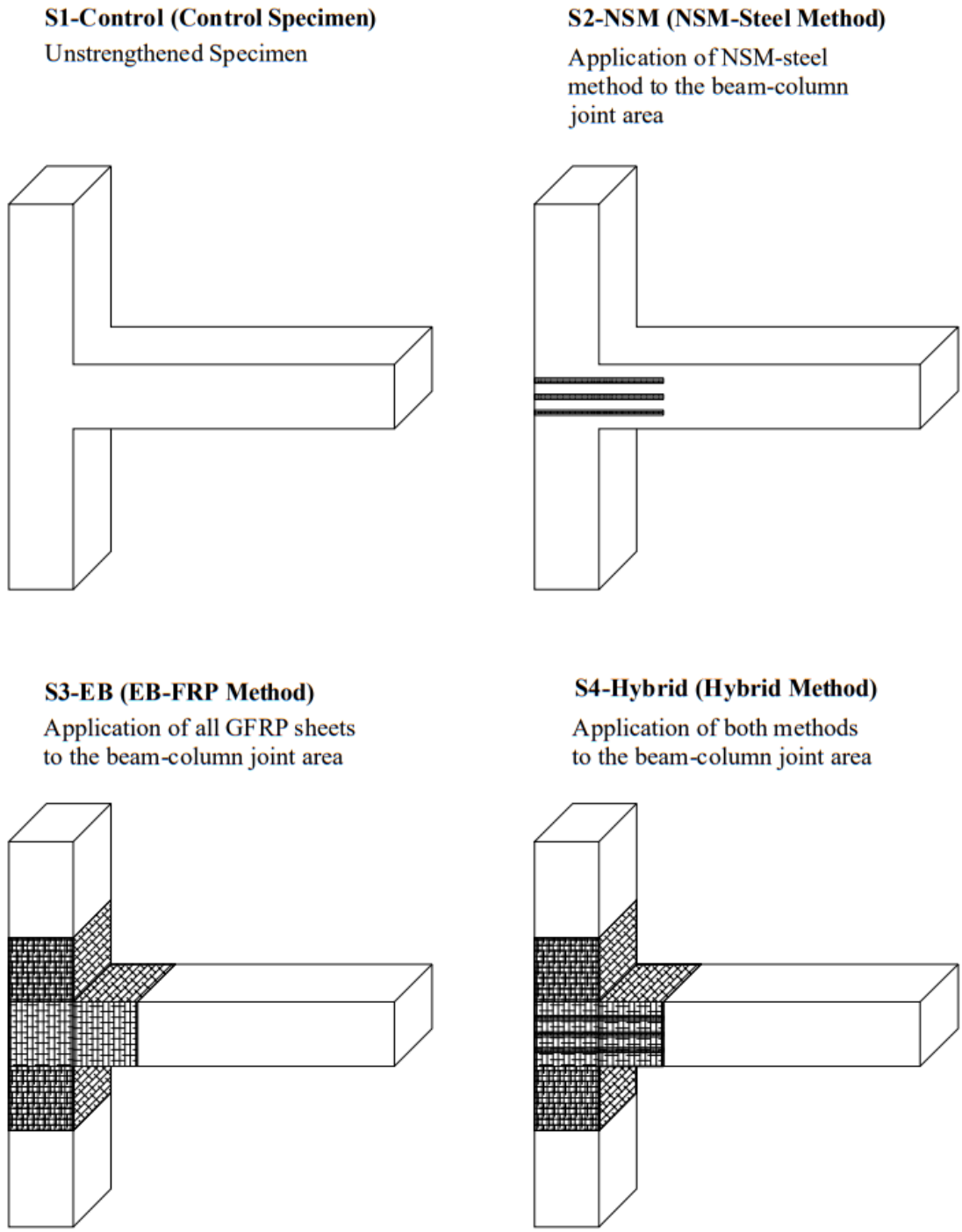

Figure 3.13. Schematic representation of the specimens.

3.5.1 Application of NSM method

In the NSM-steel method, reinforcing bars were inserted into grooves cut into the concrete cover of the beam-column connections and bonded with an epoxy adhesive filler. (The groove's depth must be less than the cover to prevent damage to the existing reinforcement). Within the scope of this project, implementation phases were followed in the dimensions shown in Figure 3.14. Before the grooves are opened, reference drawings were made on the concrete surface according to the dimensions shown in Figure 3.15 (a). Retrofitting started with a cutting groove of 25 mm × 25 mm in the concrete cover of the specimens. In addition, the groove`s dimension was calculated as 3×diamater of U-shaped bar (Hassan and Rizkalla, 2004). Furthermore, the distances between the grooves are based on Le Hoang *et al.* (2019).

The grooves were made using a special concrete saw with two diamond blades (Hilti DC-SE20 wall chaser which has a maximum cut depth of 40 mm and a maximum cut width of 46 mm) in Figure 3.15 (b) and (c). A hammer and hand chisel were used to remove any remaining concrete lugs and to roughen the surfaces of the grooves, as shown in Figure 3.15 (d). The grooves were properly cleaned with a wire brush and a high-pressure air jet shown in Figure 3.15 (e) and (f). Steel bars were bonded to the concrete using epoxy resin. In this project, Sikadur®30 (Sika Corporation, Lyndhurst, NJ, USA), an epoxy adhesive, was used to bond the retrofitting materials to the concrete substrate. The mixing ratios and properties of this product are described in detail below. To ensure the epoxy achieved full strength, the specimens were allowed to cure for one week.

Sikadur®30 has two components, namely component A and component B. Component A is white in colour, while component B is black illustrated in Figure 3.15 (g) and (h). These two components were mixed in a ratio of 3:1 until a uniform light grey colour was achieved. The density was 1.65 kg/L at 23^{o}C after mixing. The bond strength according to DIN EN 24624 (1992) is 21 MPa with steel and 4 MPa with concrete. The compressive, tensile, shear strength, and tensile modulus of elasticity and modulus of elasticity in compression of the adhesive are illustrated in Table 3.17.

To ensure that the method was practical on site (i.e. the epoxy did not flow out of the grooves), the specimen was lifted into its correct orientation before application of the epoxy. Firstly, the groove was half-filled with epoxy and then the steel bar was placed inside the groove and lightly pressed. This forced the epoxy to flow around the inserted steel bar. The position of

the rebar was visually checked, and the rest of the groove was then filled with epoxy adhesive filler and the surface was levelled see Figure 3.15 (i) and (j).

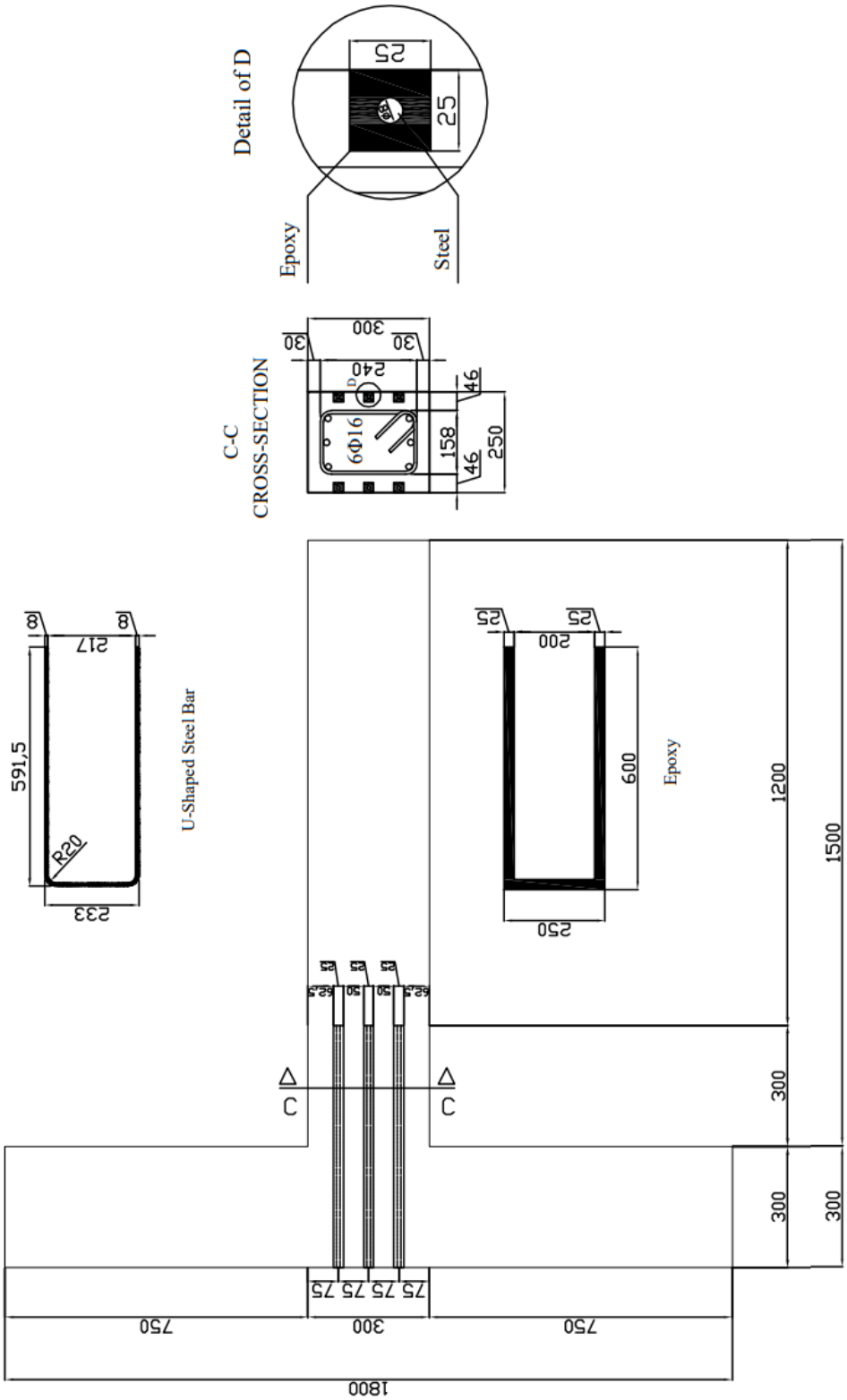

Figure 3.14. The application plan of the NSM method.

(a) The reference drawings before cutting the grooves for the NSM method.

(b) Hilti DC-SE20 wall chaser and diamond blades

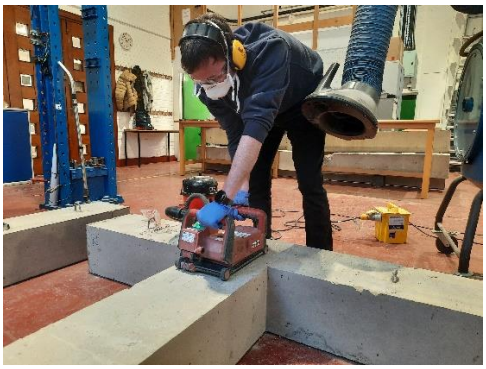

(c) Cutting grooves using reference drawings with Hilti DC-SE20.

(d) Use a hammer and a hand chisel to remove any remaining concrete lugs and to roughen the surfaces of the grooves.

(e) Cleaning the grooves with a wire brush.

(f) Cleaning the grooves with a high-pressure air jet.

Figure 3.15. The application process of the NSM method.

(g) Component A, which is white in colour, is mixed with component B, which is black.

(h) These two components are mixed in a ratio of 3:1 until a uniform light grey colour is achieved.

(i) Filling the grooves halfway with epoxy and then inserting the steel bar into the groove and pressing it gently.

(j) Filling the groove with epoxy adhesive and levelling the surface.

Figure 3.15. The application process of the NSM method (continue).

Table 3.17. Properties of Sikadur®30 (at 23 °C) based on the product datasheets.

Characteristic	**Sikadur®30**
Compressive strength (MPa)	75
Tensile strength (MPa)	26
Shear strength (MPa)	18
Tensile modulus of elasticity (MPa)	11,200
Modulus of elasticity in compression (MPa)	9,600

3.5.2 Application of EB method

Two of the specimens were strengthened via bonding of FRP to the outside of the specimen. The application process for this is given in Figure 3.16. Detailed information on this procedure is given in Appendix-F (see page 271). Appendix-F gives detailed information about the number of layers of fabrics, especially in the column-beam joints. For this study, the application processes of GFRP fabrics were adopted from those in the literature (Zamani Beydokhti and Shariatmadar 2016; Laseima *et al.* 2020). However, a simpler and more efficient way was finally selected for the application of fibre-reinforced polymer (FRP) fabrics to strengthen beam-column joints. The chosen method prioritizes speed and ease of installation, making it highly suitable for situations where rapid retrofitting is needed, such as in post-earthquake repairs or in projects where minimizing disruption to building occupants is critical.

Before the application of the FRP, the material in the form of fabric was cut in sizes suitable for the areas where they will be applied in the specimens and made ready. The edges of the members where the fibre polymer will wrap at 90° were rounded arc with a radius of 20 mm to prevent stress concentration. The sharpness in the areas where the fibre polymer was applied was smoothed and the surface was cleaned of dust with an air compressor. After application, to ensure the epoxy achieved full strength, the specimens were allowed to cure for one week. For this project, SikaWrap 930G (GFRP), consisting of a unidirectional woven glass fibre fabric, was used because it is more accessible and economical compared to other forms of advanced composites available. The tensile strength, the tensile modulus of elasticity, tensile strain, and thickness of the fibre fabric are given in Table 3.18.

Table 3.18. Properties of SikaWrap 930G based on the product datasheets.

Characteristic	**SikaWrap 930G**
Tensile strength (MPa)	1500
Tensile modulus (MPa)	70,000
Tensile strain (mm/mm)	0.0214
Thickness (mm)	0.363

Sikadur®300 an epoxy-based impregnating/laminating resin, was used in this project to bond the retrofitting materials to the concrete substrate and SikaWrap® structural strengthening fabrics. Sikadur®300 has two components, namely component A (resin) and component B (hardener). Component A is amber in colour, while component B is pale yellow. These two components were mixed in a ratio of 100:34,5 by weight. An electric single mixer (maximum

300 rpm) with a spiral paddle was used to mix. Components A and B were continuously mixed for 4 minutes until a uniform light-yellow colour was achieved. The density was 1.16 kg/L at 23°C after mixing. The tensile strength, tensile modulus of elasticity, flexural modulus, and elongation at break of the adhesive are given in Table 3.19.

The application process of the EB-FRP method is shown in Figure 3.17.

Table 3.19. Properties of Sikadur®300 (7 days and 23 °C) based on the product datasheets.

Characteristic	Sikadur®300
Tensile strength (MPa)	45
Tensile modulus (MPa)	3500
Flexural modulus (MPa)	2800
Elongation at break (%)	1,5

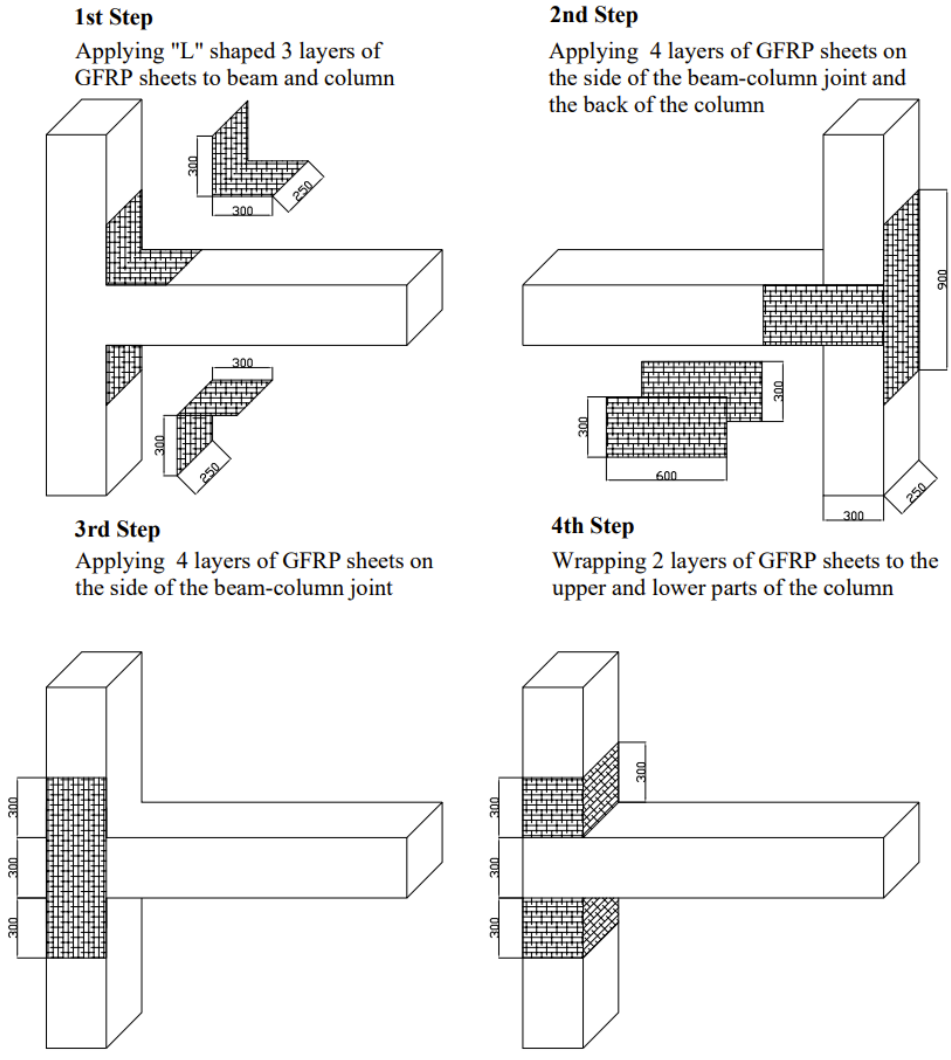

Figure 3.16. The application plan for the EB-FRP method (units are mm).

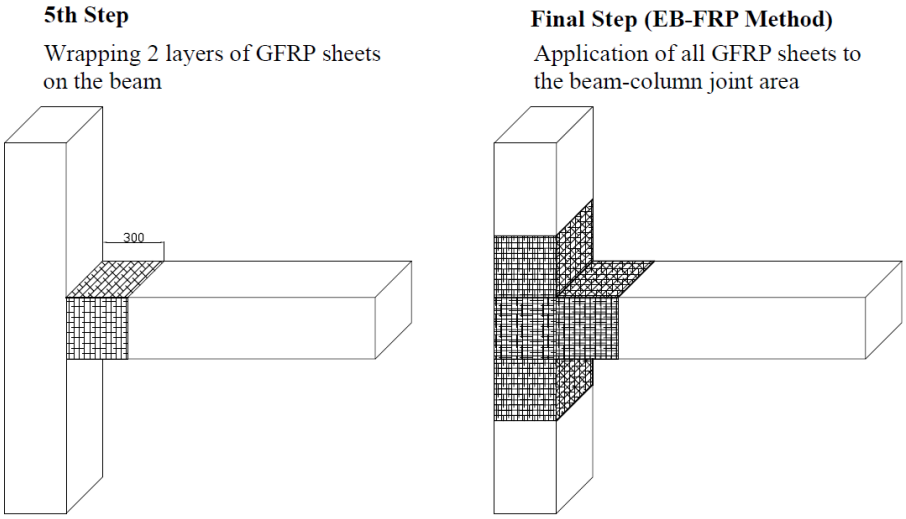

Figure 3.16. The application plan for the EB-FRP method (units are mm) (continue).

The implementation steps shown in Figure 3.16 is an additive process. The final step is the view after the EB method was applied.

(a) Rounding of the corners to prevent stress concentration

(b) Removing dust from the surface with an air compressor

Figure 3.17. The application process of the EB-FRP method.

(c) Preparation of GFRP fabrics

(d) Mixing Sikadur 300 adhesive material

(e) Application of the adhesive material

(f) Uniform distribution of the adhesive material

(g) Application completed column-beam joint

Figure 3.17. The application process of the EB-FRP method (continue).

3.6 TEST SET-UP

Two separate forces were applied to the test rig. First, the column was exposed to a constant axial load, and then a cyclic load was applied to the beam end. A hydraulic jack (see in Figure 3.18 (a)) with a capacity of 20 tonnes was used for the axial load. For the cyclic load, hydraulic actuators of 50 tonnes and 20 tonnes capacity with ± 150 mm stroke, shown in Figure 3.19 (a) and (b), were used to apply pushing and pulling forces to the beam end. Figure 3.20 shows schematic diagrams of the test setup.

As shown in Figure 3.21, a 20 mm thick steel plate was used at the upper and lower ends of the column and 4 × 16 mm ribbed reinforcements were welded onto these steel plates. The bottom plate onto which the column will be placed was previously prepared by wire electrical discharge machining (EDM) technique to fit on a 50 mm diameter steel roller (see detail C in Figure 3.21). The procedure for the top plate, see detail B in Figure 3.21, was repeated and these plates were fixed with steel cages before pouring the concrete. Additionally, a steel plate 20 mm thick, 600 mm long, and 250 mm wide was fixed to the strong floor for support of the column bottom end (see detail C in Figure 3.21).

This study specifically examines the exterior column-beam joint regions on the ground floor of an existing three-story school building designed according to TEC 1998. The beam-column joints are critical structural elements, particularly in seismic zones, as they are prone to shear and bond failures during earthquakes. Since school buildings must prioritize life safety, assessing the performance of these joints is essential for evaluating the structure's seismic resilience. The ground floor was selected for analysis because it typically experiences the highest seismic demands due to its position at the base of the structure. Exterior joints are of particular concern because they often lack the confinement provided by adjacent structural elements (unlike interior joints), making them more vulnerable to damage. By focusing on this region, the study aims to identify potential weaknesses in shear resistance, and reinforcement detailing common issues in Turkish construction.

In the experimental setup, a hydraulic jack (Enerpac brand) which was being controlled by the Enerpac ZE40 hydraulic power pack (see in Figure 3.18 (b)) was utilized to apply a constant axial compressive load of 168 kN to the column. This load was carefully selected to simulate the service-level gravitational load that the ground-floor column would typically experience in the actual three-story school building. The magnitude of 168 kN corresponds to the cumulative dead and live loads transferred from the upper floors (second and third levels)

onto the column, representing realistic structural demands under normal operating conditions.

The ultimate capacity of the column is derived by summing the individual capacities of the concrete section and longitudinal steel and it can be calculated using Equation (3.16).

$$N = (f_{ck} \times A_g) + (f_{yk} \times A_{st}) \quad (3.16)$$

where, f_{ck} denotes characteristic compressive strength of the concrete (measured on cylinders), A_g signifies the gross cross-sectional area of the column, f_{yk} stands for the characteristic yield strength of the longitudinal reinforcement, A_{st} indicates total cross-sectional area of the longitudinal steel.

When calculating the column capacity using Equation (3.16) below, the bearing capacity of the reinforcement can be neglected since it is quite low compared to the concrete, and only the effect of the concrete was calculated in this study. In this project, approximately 10% of the column capacity was tried to be used, but the hydraulic oil pump used could be adjusted to 168 kN and this value was approximately 9.74%.

$$N = 9.74\% \times (23MPa \times (250mm \times 300mm)) = 168000 = 168\ kN$$

In this calculation, for f_{ck}, the 28-day average compressive strength (23 MPa (see Table 3.14)) was used while $A_g(250mm \times 300mm)$ was obtained by multiplying the width and length of the column.

During the test, the hydraulic pump (see in Figure 3.18 (b)) was set to provide constant oil pressure to the actuator, and therefore a constant load was subjected to the column. To ensure that this was the case, the pressure in the hydraulic unit was measured with a bourdon gauge.

For the cyclic loading applied to the beam end, manual operation of the hydraulic pumps was employed to apply push and pull forces. The loading was stopped upon reaching the target displacement value for each cycle, which was precisely monitored using Linear Variable Differential Transformers (LVDTs) installed at the beam end. Throughout the test, load cells mounted on the pump ends enabled real-time load measurement, while the LVDTs provided continuous displacement monitoring. All measurement data, including both load and displacement values, were recorded simultaneously in a computerised data acquisition system for subsequent analysis. In addition, the connection at the beam end is illustrated in Figure 3.22.

(a)

(b)

Figure 3.18. (a) Hydraulic jack was used to impose an axial load on the column, (b) Hydraulic power pack.

(a)
Hydraulic actuator with 50 tonnes capacity

(b)
Hydraulic actuator with 20 tonnes capacity

Figure 3.19. Hydraulic actuators used to apply cyclic loading at the beam end.

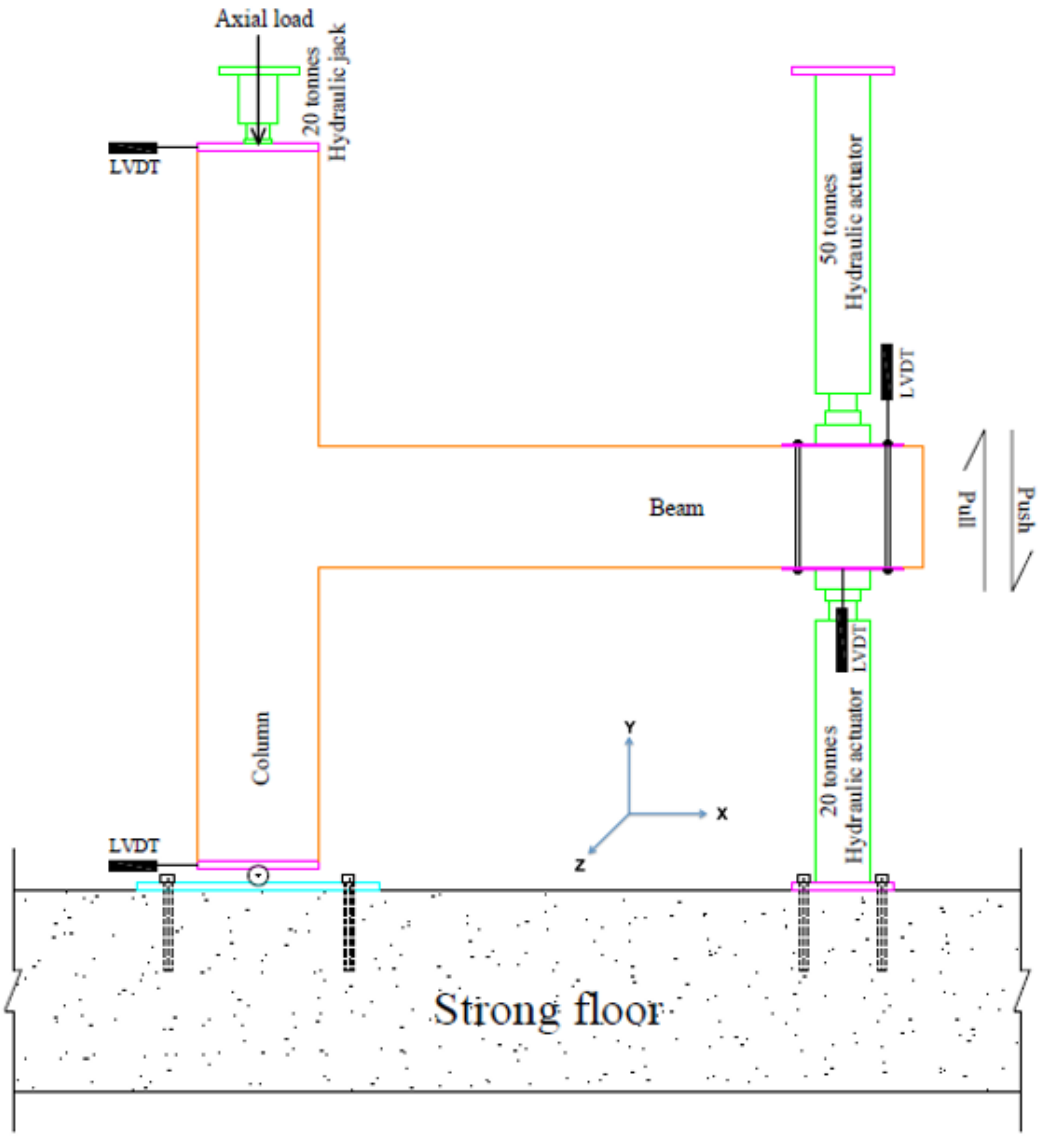

Figure 3.20. Experimental set-up – schematic drawing.

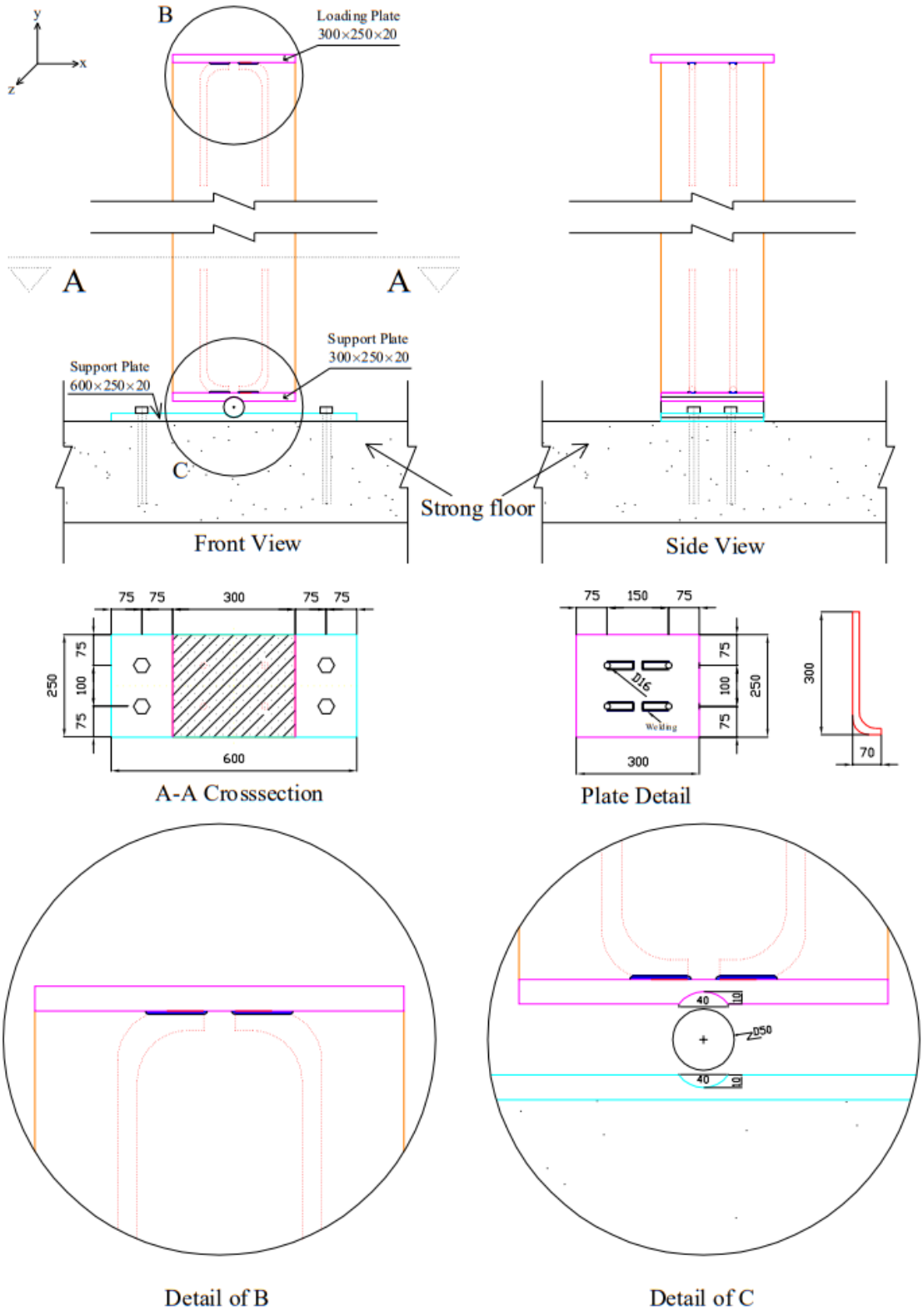

Figure 3.21. Top and bottom support details of the column (units are mm).

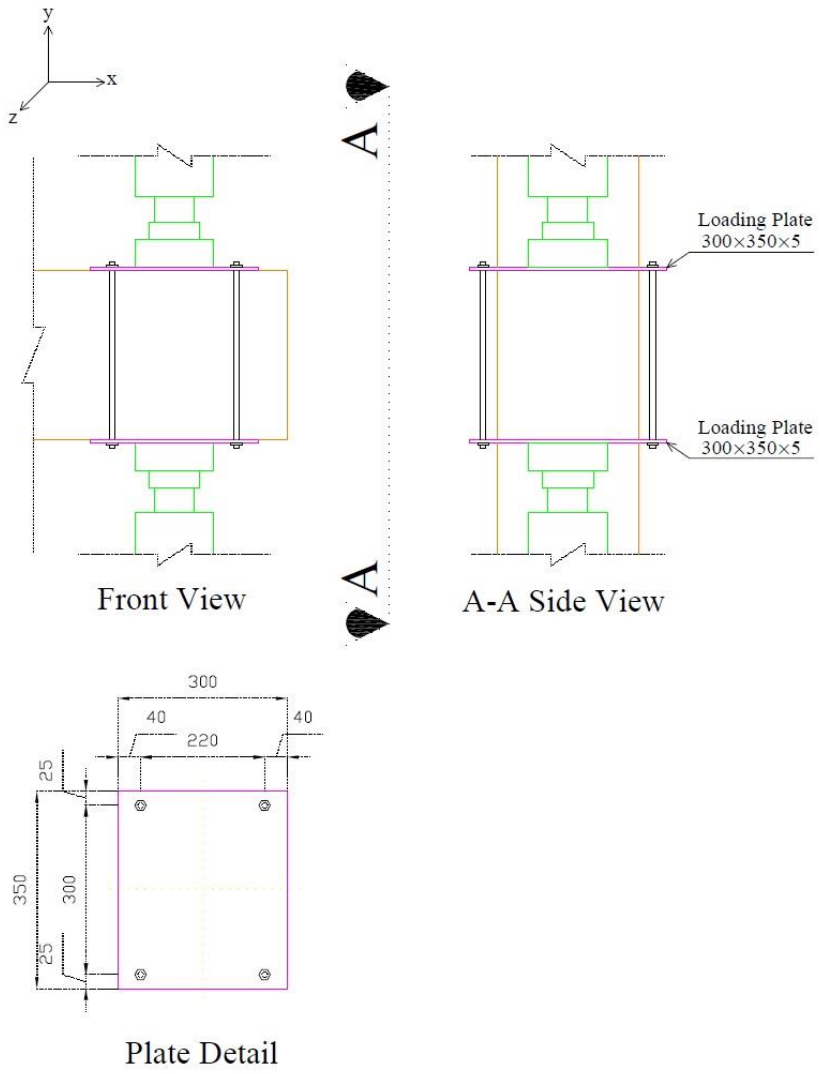

Figure 3.22. Details of the beam end loading plates (units are mm).

In addition, detailed drawings of the test frames are presented in Appendix-G Figure G1, Figure G2, and Figure G3.

The upper end of the column was restricted from horizontal movement, while rotation was permitted ($U_x = U_z = 0$). The lower end, the column was restrained from both horizontal and vertical movement, but rotations were allowed, creating hinged boundary conditions ($U_x = U_y = U_z = 0$). The column ends are illustrated in Figure 3.23.

(a)
Column bottom end

(b)
Column top end

Figure 3.23. Column ends.

3.7 LOADING PROTOCOL

The control specimen (and subsequent specimens before retrofitting) was designed to undergo shear failure within the joint, without reaching the maximum bending capacity of the beam section.

Testing shear-deficient beam-column connections, according to Wong (2005), requires the implementation of displacement control based on the inter-story drift ratio. One benefit of employing drift ratio-based displacement control is that it permits assessment of the shear capacity of a joint long after joint shear fractures have formed in both diagonal directions, without causing substantial joint strength degradation caused by excessive cyclic loading. According to the recommendation in ACI 374.2-13 clause 5.2, it is adequate to undergo a minimum of two cycles at each deformation level in order to cause damage proportional to the number of cycles at a particular drift level. In addition, average loading rates were of the order of between 1 cycle per minute for low loads to 1 cycle per 3 minutes for higher loads in this study.

In this study, displacement was gradually increased to reach specific inter-story drift ratios of 0.015%, 0.023%, 0.077%, 0.15%, 0.23%, 0.39%, 0.62%, 0.92%, 1.54%, 2.31%, 3.85%, 4.62%, 5.77%, 6.54%, and 7.31%, as shown in Figure 3.24. The inter-story drift ratio given above is calculated using Equation (3.16) with the distance L being 1300mm (see Figure 3.11).

$$\text{Inter-story drift ratio} = \delta / L \qquad (3.16)$$

where δ is the vertical displacement of the beam-end and L is the distance from the loading point to the column face (L= 1300 mm). In addition, the displacement values at the point of loading for each cycle are given in Table 3.20.

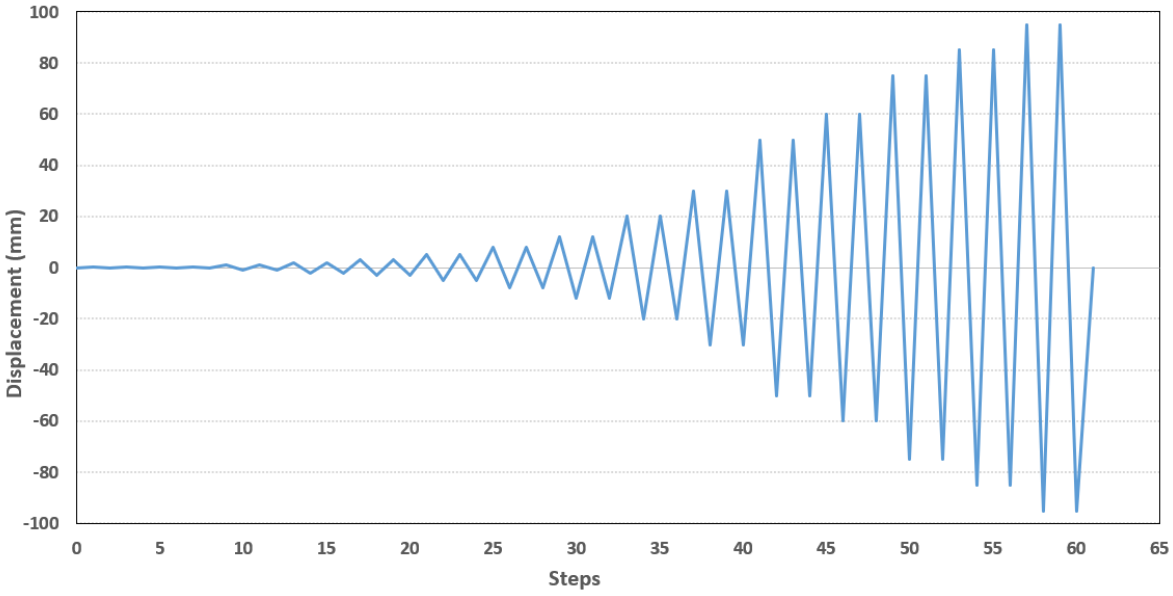

(a)

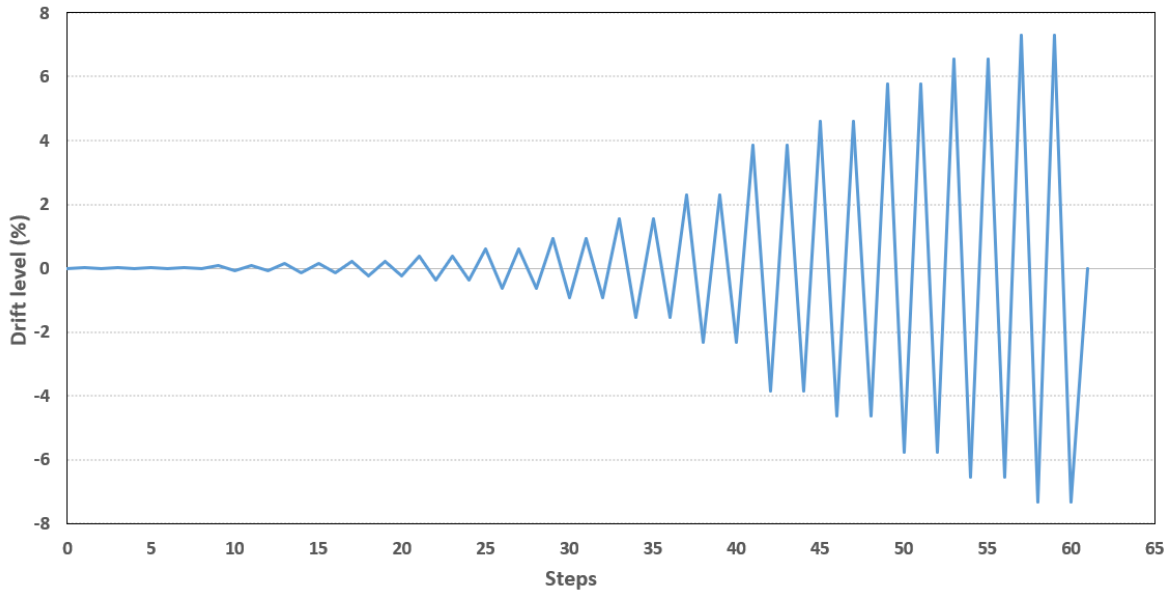

(b)

Figure 3.24. Loading history (a) Displacement (mm), (b) Drift level (%).

Table 3.20. The displacement values for each step.

Step	Displacement (mm)	Step	Displacement (mm)
0	0	31	12
1	0.2	32	-12
2	-0.2	33	20
3	0.2	34	-20
4	-0.2	35	20
5	0.3	36	-20
6	-0.3	37	30
7	0.3	38	-30
8	-0.3	39	30
9	1	40	-30
10	-1	41	50
11	1	42	-50
12	-1	43	50
13	2	44	-50
14	-2	45	60
15	2	46	-60
16	-2	47	60
17	3	48	-60
18	-3	49	75
19	3	50	-75
20	-3	51	75
21	5	52	-75
22	-5	53	85
23	5	54	-85
24	-5	55	85
25	8	56	-85
26	-8	57	95
27	8	58	-95
28	-8	59	95
29	12	60	-95
30	-12	61	0

Ong *et al.* (2022) indicated that the loading can be applied either at the end of the column or the end of the beam (see in Figure 3.25). By applying load at the tip of the beam, it is possible to eliminate the need to consider the P-Δ effect on the flexural requirement of the beam-column joint. The experimental study conducted by Adibi *et al*. (2017) revealed a significant P-Δ effect in the load-displacement curves of both the beam-column joints with and without retrofitting. Nevertheless, the testing process will become excessively intricate to account for the P-Δ effect, as it would necessitate the use of a horizontally moving and consistently vertical hydraulic jack at the top of the column within the testing frame (Ruiz-Pinilla *et al.*, 2017). Due

to its insignificance when a low axial force is applied to the end of a column or when specimens have low column slenderness, the P-Δ effect is generally disregarded in most testing procedures of the external joints. The differences in the improvement of the seismic characteristics between the presence of the P-Δ effect and its absence is minor, as confirmed by Adibi *et al*. (2017).

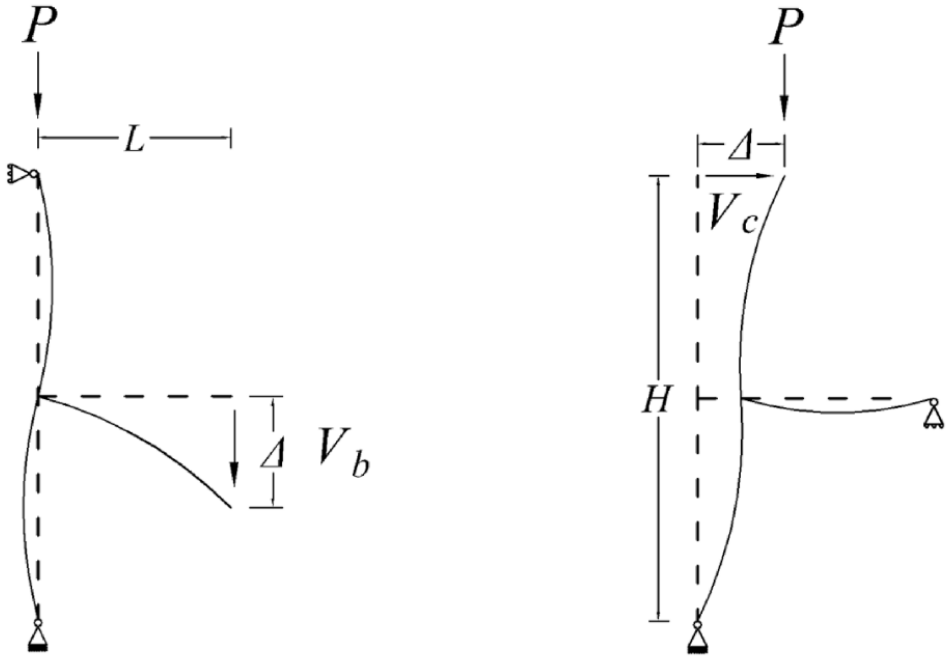

(a) (b)

Figure 3.25. Drift of the exterior and corner joint under cyclic loading: (a) on beam; (b) on column (Ong *et al*., 2022).

3.8 DATA ACQUISITION SYSTEM

Before the test, the measurements of all strain gauges (10mm, 120 ohm, 2.02 gauge factor from Micro Measurements), LVDTs (LSC series and Penny and Giles brand), and load cells (Sensotec 150k) were connected to a National Instruments NI 9219 module in a NI cDAQ-9178 chassis. Throughout the test, the data was then logged simultaneously using National Instruments LabView software with a sample rate of 1 Hz and was synchronised using time stamps. The purpose of installing the instruments was to quantify the strain and displacements that were generated.

3.8.1 Installation of Strain Gauges on Reinforcing Bars

Strain gauges were installed to two longitudinal bars situated on one side of the beam and column to quantify the strain variation. In addition, one strain gauge was affixed to one side of the stirrup on the beam. Additionally, for Specimen 2, three additional strain gauges were implemented on one side of the U-shaped steel. Figure 3.26 depicts the positioning of strain gauges. Figure 3.26 (a) refers to Specimen 1, 3 and 4 while Figure 3.26 (b) represents to Specimen 2. The application steps of the strain gauges are shown visually in Appendix-E Figure E1.

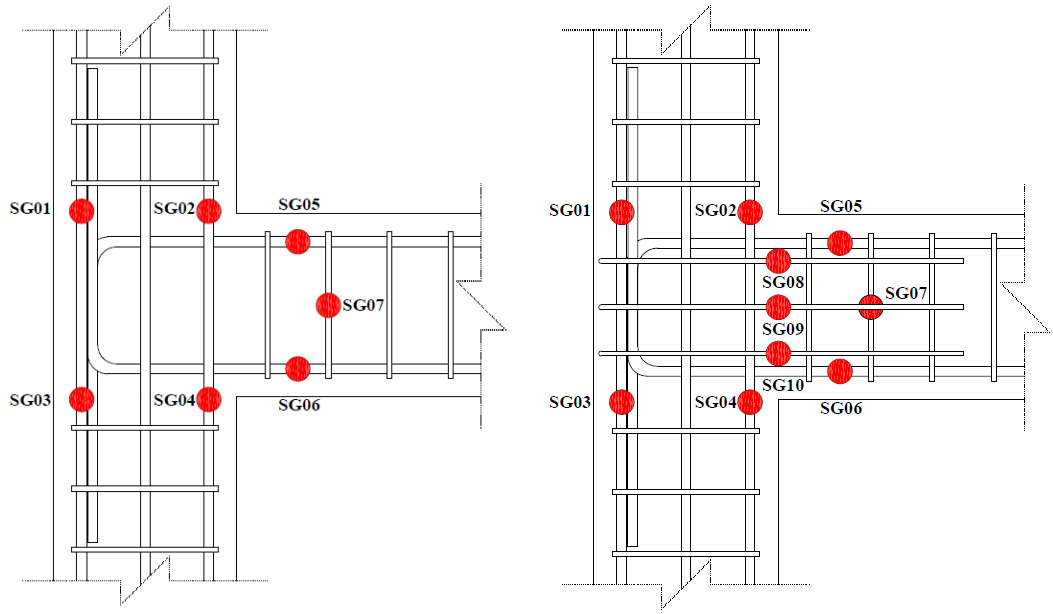

(a) Specimen 1, 3 and 4 (b) Specimen 2

Figure 3.26. The locations of the strain gauges on the steel rebars.

Before the strain gauges were implemented to the reinforcement rebars, the existing cables on the strain gauges were replaced with Teflon cables (330-FTE 100' STD SILVER-PLATED CU

TWISTED WIRE) that are resistant to the heat of concrete hydration and water in the concrete. Moreover, the cable joints were protected with a heat shrink.

M-Prep conditioner A, M-Prep neutralizer 5A, 200 Catalyst, M-bond 200 Adhesive, and M-Coat JA used for bonding the strain gauges are illustrated in Appendix-E Figure E2 and Figure E3, respectively. In addition, the properties of the strain gauge (C4A-06-125SL-350/29P) used in this study are shown in Appendix-E Figure E4.

Each specimen was equipped with LVDTs at four different locations to monitor displacement. Two LVDTs (LSC series brand) were placed on the top and bottom surfaces of the column end (x-axis direction), while two LVDTs (Penny and Giles brand) were installed on the top and bottom of the beam end (y-axis direction). All LVDTs are shown in Figure 3.27 and Figure 3.28.

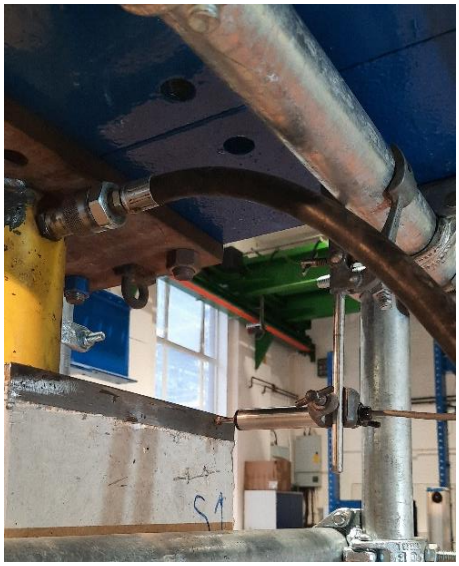

(a) LVDT location at the top surface of the column

(b) LVDT location at the bottom surface of the column

Figure 3.27. The locations of the LVDTs on the column`s top and bottom end.

(a) LVDT location at the top of the beam

(b) LVDT location at the bottom of the beam

Figure 3.28. The locations of the LVDTs on the beam end.

3.8.2 Installation of Target Points and Cameras

Six different cameras (4 × Canon EOS 6D Mark II (6240 × 4160 (26.2 effective megapixels)), Canon EOS 700D (5184 × 3456 (18.0 effective megapixels)), Canon EOS 50D (4752 × 3168 (15.1 megapixels)), and Canon EOS 4000D (5184 × 3456 (18.0 effective megapixels))) were used during the experiments to accurately investigate the deformations. In addition, fixed target points were determined and marked before the experiments. After the specimen to be tested was prepared, target points were installed at specific points on the specimen. The positions of these target points were determined and noted using Leica Geosystems TS07 shown in Figure 3.29 (a). Two total stations were utilised to check the target points for each side of the specimen in this project.

During the experiment, the cameras were positioned around the specimen under test where the best view could be obtained. A full circle of photographs around the specimen were taken before the start of the experiment, every 20 cycles and at the end of the experiment. In all other steps, photographs were taken of a single face (see Figure 3.29 (b)) and saved on the SD card inside the cameras. Care was taken to ensure that fixed target points and variable target points on the test specimen remained in the frame of the photograph.

(a) (b)

Figure 3.29. (a) Checking target points using Leica Geosystems TS07; (b) The locations of the cameras.

3.10 SUMMARY

In this section, the experimental setup used to investigate the seismic performance of exterior RC (reinforced concrete) beam-column joints subjected to cyclic loading is described in detail and design calculations of the joint shear capacity are presented. These specimens were designed considering typical beam-column connection details as specified in TEC, 1998.

The materials used for the specimens, such as concrete, steel, glass fibre reinforced polymer (GFRP) and epoxy resin, are described in detail.

Four identical specimens were prepared for this study, one control specimen and three reinforced specimens. The other three identical specimens were strengthened with two strengthening technologies adapted from promising technologies described in the literature, and the characteristics of the strengthening techniques used were described. These are the Near Surface Mount (NSM) method, in which steel bars are embedded in grooves drilled in the concrete, the Externally Bonded (EB) method, which involves the application of GFRP sheets and a hybrid of the two.

The test setup in which specimens were subjected to a combination of axial loading and reverse cyclic loading is described in detail. The loading protocol is described in detail,

including displacement levels and drift ratios. It also covers the instrumentation used during the test, such as strain gauges attached to the reinforcing bars, target points, and cameras used to record deformations.

In the next chapter, an experimental protocol was developed, and all specimens were tested, and the results are presented.

CHAPTER 4. EXPERIMENTAL RESULTS

4.1 GENERAL

This chapter provides the experimental findings of beam-column junctions in both unreinforced and reinforced concrete junctions. The report includes the damages identified and the propagation of damage observed during the testing. The displacement data used in the calculations presented in this section are the data collected during the experiment from the displacement meters (LVDTs) placed on each specimen. These displacement data are given below in response to the load acting on the beam end. The specimens are examined to compare their performance and determine the effect of the suggested strengthening method by assessing the strength, stiffness, ductility ratios, energy dissipation characteristics, and strain measurements at critical locations in the joint area.

4.2 ANALYSIS OF TEST RESULTS

4.2.1 Crack Propagation and Strength

Analysis of Crack Propagation:

Damages in the specimens are generally determined by measuring the width of the cracks in the joint or beam. For each specimen, crack measurements were performed during the experiment after each step. Crack measurements could not be performed in cases where the joint region had completely disintegrated (high drift ratios). For the different experiments, cracks in the push direction (positive direction) are marked in red, and cracks in the pull direction (negative direction) are marked in blue e.g., Figure 4.1 (h). At the end of each loading step, the experiments were paused, and the measurements were repeated. During the experimental pause, the specimens did not show any signs of relaxation. The values measured in these analyses are the distances perpendicular to the crack width for the largest width along that crack. Damage assessment was investigated after the step at which the first crack started and the damage in the first cycle was analysed for each drift ratio. These cracks are labelled with the name of the step at which the crack occurred and are presented in crack diagrams with their corresponding widths. For specimens S1 and S2, damages at the beam-column joint were considered, while for specimens S3 and S4, damages on the whole beam were focused. The cracks are drawn to approximate scale. Since the crack measurements were terminated at 4.62% drift ratio and beyond, only the cracks are shown in the drawings without the crack names.

Below, drawings and photographs are shown for each specimen, S1-Control, S2-NSM, S3-EB and S4-Hybrid respectively, and the crack values measured on the drawings are shown.

Damage Investigations of S1-Control Specimen:

When the damage diagrams of the first specimen were examined, the first hairline cracks were detected at a 0.23% drift ratio in the push direction in the joint region. At a 0.39% drift ratio, it was observed that hairline cracks were formed in both push and pull directions in the corners where the beam and the column were joined in the joint region. At a 0.62% drift ratio, crack formation continued where the beam was connected to the column, and had a width of 0.4 mm. At a 0.92% drift ratio, shear cracks of approximately 45 degrees started to form in the beam-column joint area, and it was observed that both push and pull bending cracks were formed on the beam at the same drift ratio. At a drift ratio of 1.54%, intersecting shear cracks were observed in the joint area, and the width of the shear crack in the pushing direction was 1.15 mm in the area where the beam was connected to the column. For the same drift ratio, it was observed that additional flexural cracks formed on the beam. At a 2.31% drift ratio, the shear cracks in the joint area were observed to progress, and the width of the crack formed in the previous drift ratio in the push direction at the connection of the beam to the column was measured at 1.3 mm. In addition, the crack number 29 at the beam-column junction was 0.5 mm. When the specimen was examined at a 3.85% drift ratio, it was found that severe crack damage had started to occur in the junction area, and this value was 2.3 mm. In addition, cracks numbered 33 and 39 in the upper corner where the beam is connected to the column were measured as 1.15 mm and 1.75 mm, respectively. For drift ratios of 4.62%, 5.77%, and 6.54%, it was observed that serious deformations occurred both in the areas where the beam was connected to the column and in the beam-column joint area. Damages such as the disintegration of concrete on both sides of the specimen and the formation of severe cracks on the back face of the column had started.

Figure 4.1 provides damage photographs and drawings of the S1-Control specimen for drift ratios of 0.23%, 0.39%, 0.62%, 0.92%, 1.54%, 2.31%, 3.85%, 4.62%, 5.77%, and 6.54%. Moreover, Figure 4.2 displays post-test photographs of the S1-Control specimen to provide a clearer understanding of the damages.

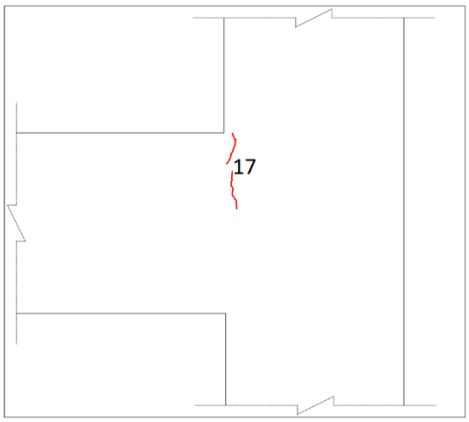

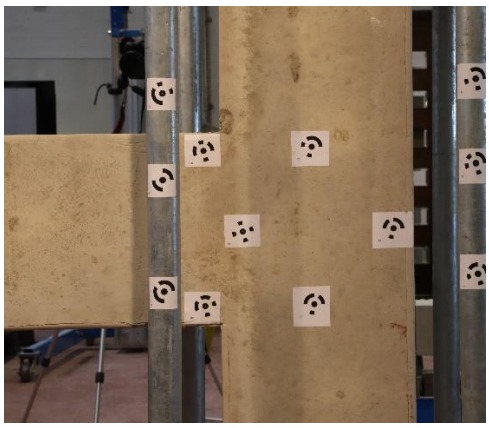

(a) Drift ratio: 0.23%, Displacement: 3 mm

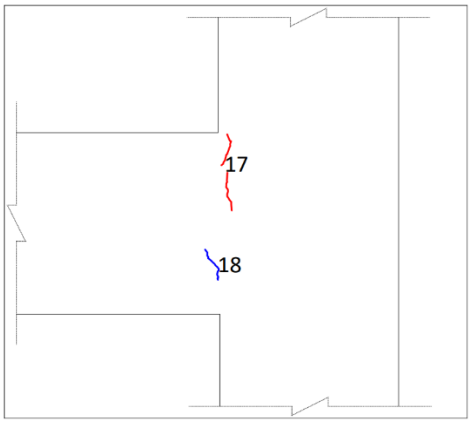

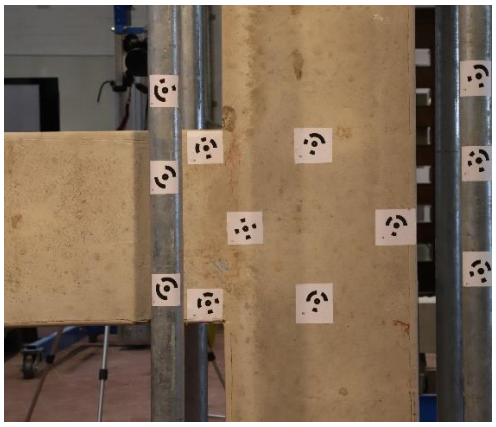

(b) Drift ratio: 0.39%, Displacement: 5 mm

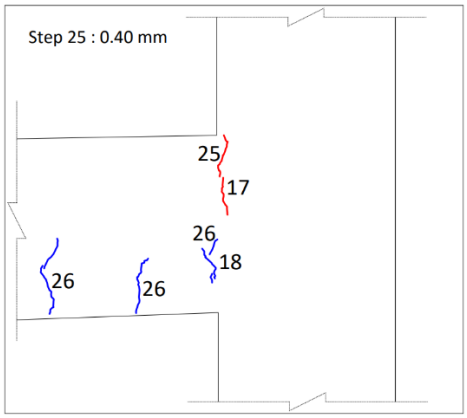

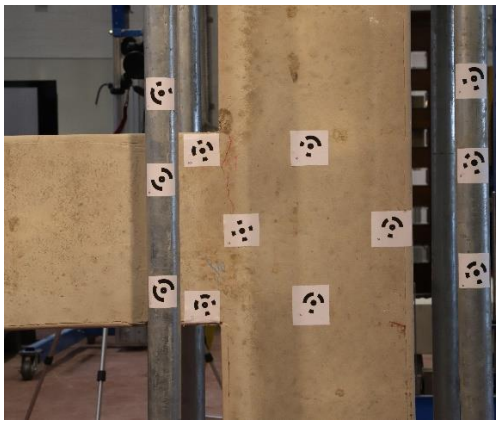

(c) Drift ratio: 0.62%, Displacement: 8 mm

Figure 4.1. Crack propagation of the S1-Control for each drift ratio.

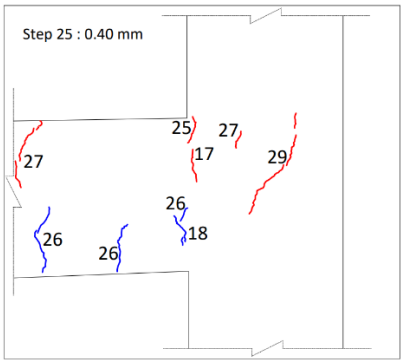

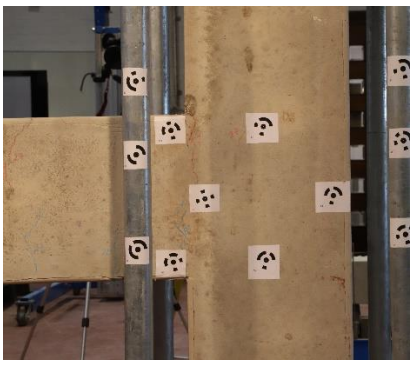

(d) Drift ratio: 0.93%, Displacement: 12 mm

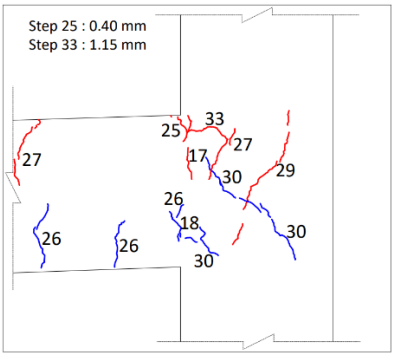

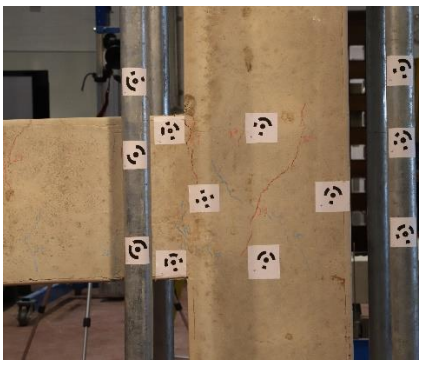

(e) Drift ratio: 1.54%, Displacement: 20 mm

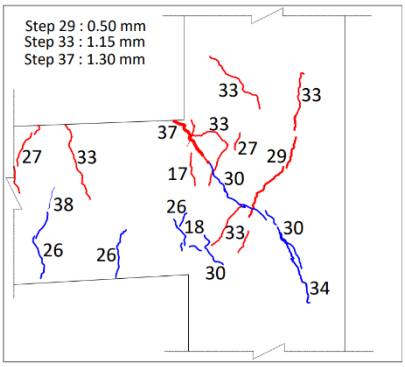

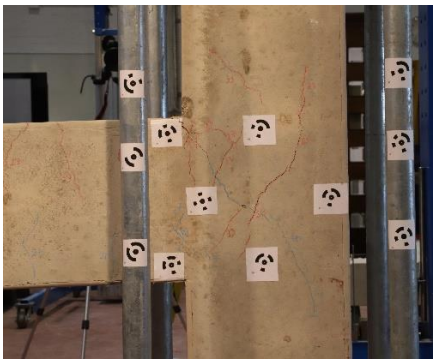

(f) Drift ratio: 2.31%, Displacement: 30 mm

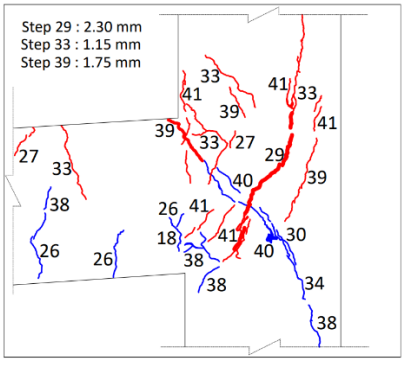

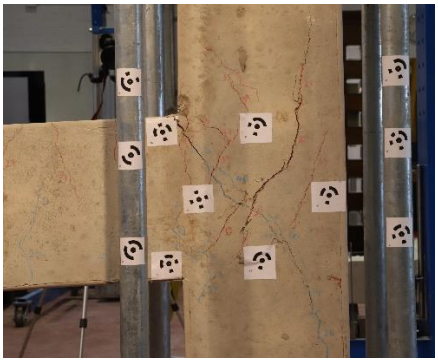

(g) Drift ratio: 3.85%, Displacement: 50 mm

Figure 4.1. Crack propagation of the S1-Control for each drift ratio (continue).

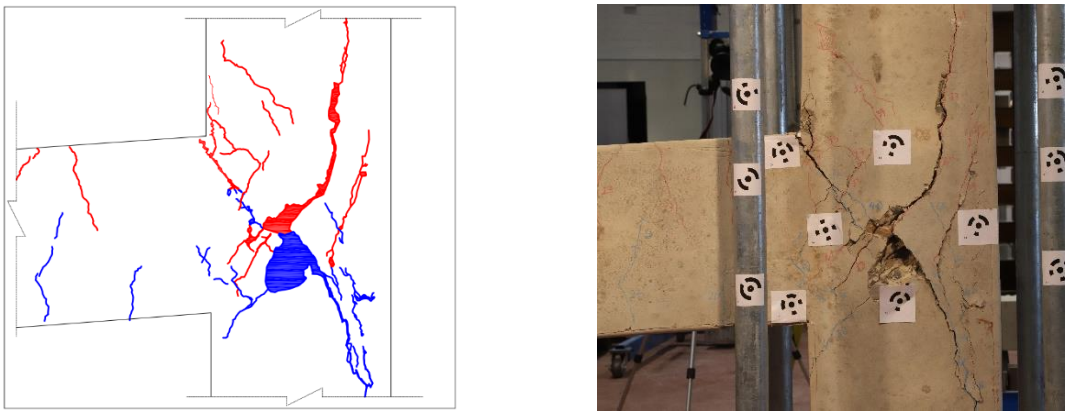

(h) Drift ratio: 4.62%, Displacement: 60 mm

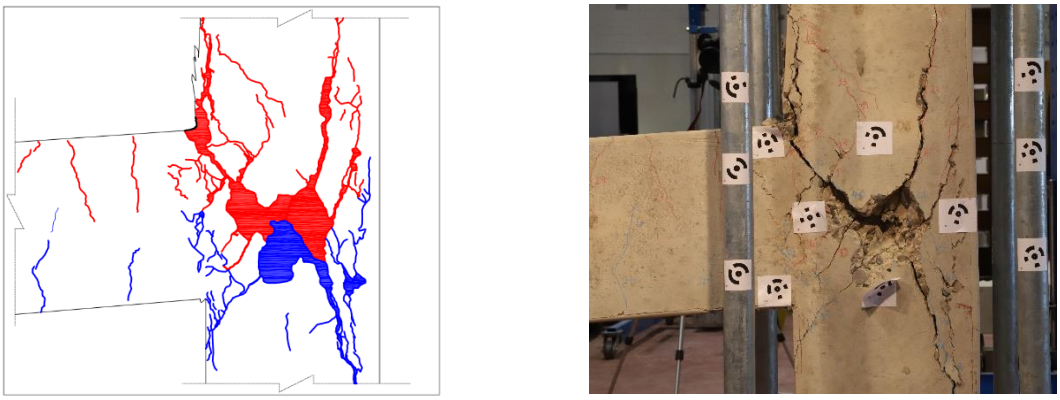

(i) Drift ratio: 5.77%, Displacement: 75 mm

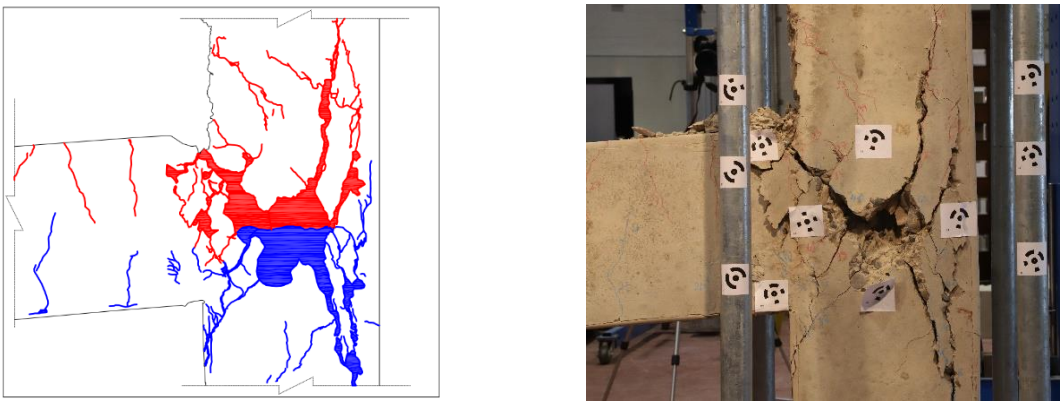

(j) Drift ratio: 6.54%, Displacement: 85 mm

Figure 4.1. Crack propagation of the S1-Control for each drift ratio (continue).

(a)

(b)

(c)

(d)

(e)

(f)

Figure 4.2. End of experiment pictures of S1-Control.

Damage Investigations of S2-NSM specimen:

When the damage diagrams of the second specimen strengthened with the NSM technique were examined, the first hairline cracks were detected in the beam region in the pulling direction at a 0.39% drift ratio. At a 0.62% drift ratio, crack formation continued in the region where the beam was connected to the column, and at the same drift ratio, it was observed that flexural crack number 25 had formed on the beam. At a 0.92% drift ratio, the length and width of the cracks formed at the previous drift ratio remained constant, but flexural cracks were observed to form on the beam in both pushing and pulling directions. 1.54% and 2.31% shear cracks were observed in the joint area, and cracks with a width of 0.3 mm in pushing and 0.6 mm in pulling were observed in the area where the beam was connected to the column. For the same drift ratio, extra flexural cracks were observed on the beam. When the specimen with a 3.85% drift ratio was examined, it was observed that the shear cracks continued to progress slightly in the joint area. However, in the region where the beam is connected to the column, it was observed that the crack number 23 reached 1.3 mm in the pushing direction. In addition, severe cracks were observed, especially on the beam at the end of the reinforced area, and this value was calculated as 5 mm (crack number 37). When the damages occurred at 4.62%, 5.77%, and 6.54% drift ratios were carefully examined, it was observed that no serious deformations occurred in the beam-column joint area. This study did not observe the damage between concrete and epoxy reported in the literature. Conversely, the epoxy and concrete worked well together, and no separation between the surfaces was observed. At these drift ratios, it is clearly seen that the damage is transferred from the beam-column joint to the beam. Damage such as spalling and rupture of concrete, especially on the beam, occurred on both sides of the specimen. In addition, at the end of the experiment, it was determined that a concrete rupture and serious cracks occurred behind the column.

Damage photographs and drawings of the S2-NSM specimen are shown in Figure 4.3 for 0.39%, 0.62%, 0.92%, 1.54%, 2.31%, 3.85%, 4.62%, 5.77%, and 6.54% drift ratios. Furthermore, for specimen S2-NSM, post-test photographs are given in Figure 4.4 which clearly show that damage occurred in the concrete (rather than the concrete epoxy interface) and therefore did not lead to debonding of the retrofitted reinforcing bars within the connection as reported in the literature.

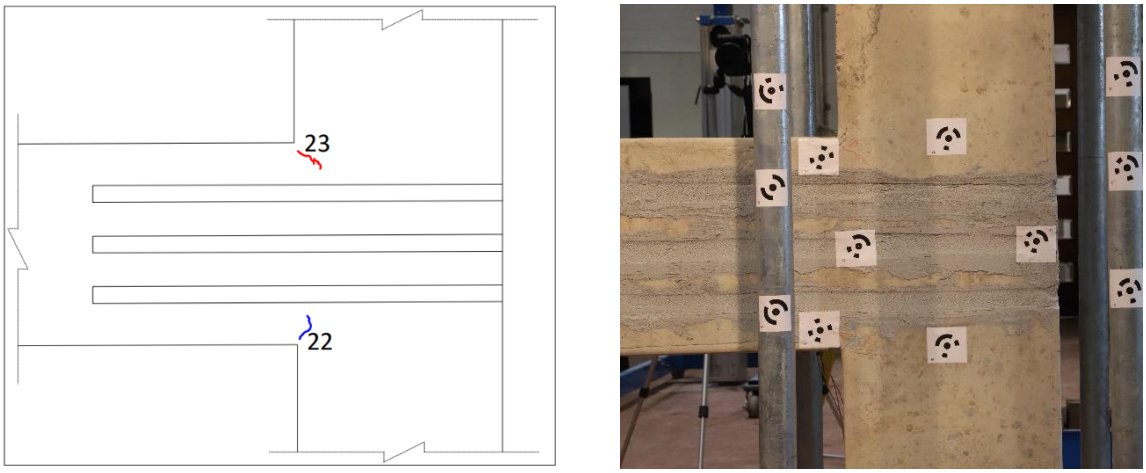

(a) Drift ratio: 0.39%, Displacement: 5 mm

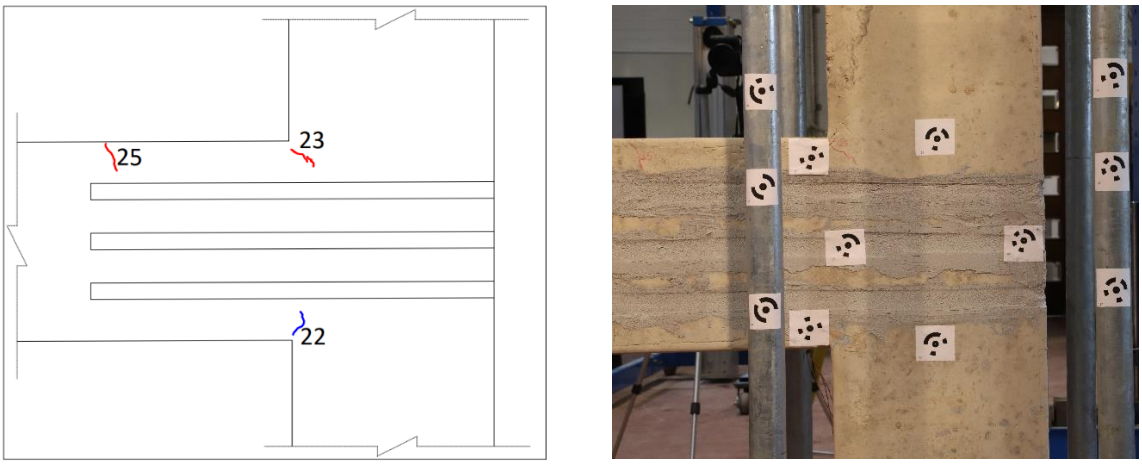

(b) Drift ratio: 0.62%, Displacement: 8 mm

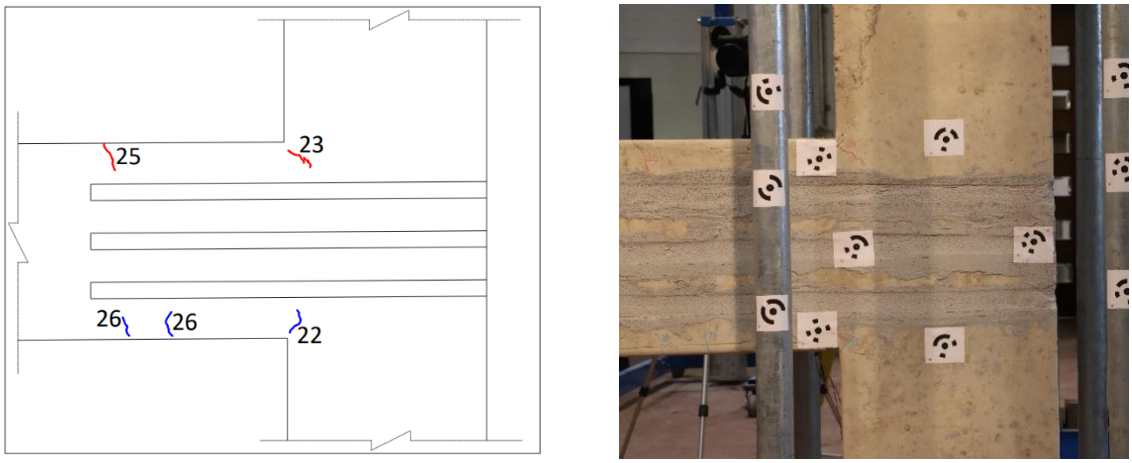

(c) Drift ratio: 0.92%, Displacement: 12 mm

Figure 4.3. Crack propagation of the S2-NSM for each drift ratio.

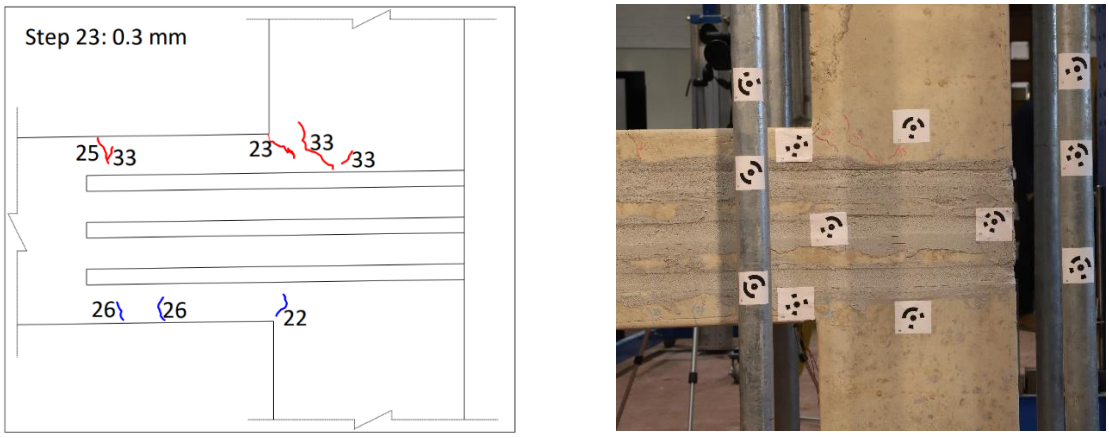

(d) Drift ratio: 1.54%, Displacement: 20 mm

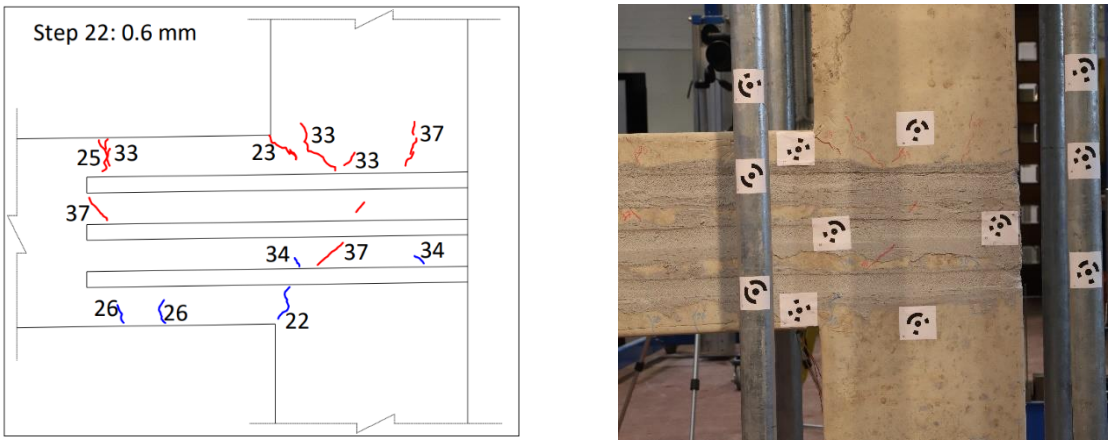

(e) Drift ratio: 2.31%, Displacement: 30 mm

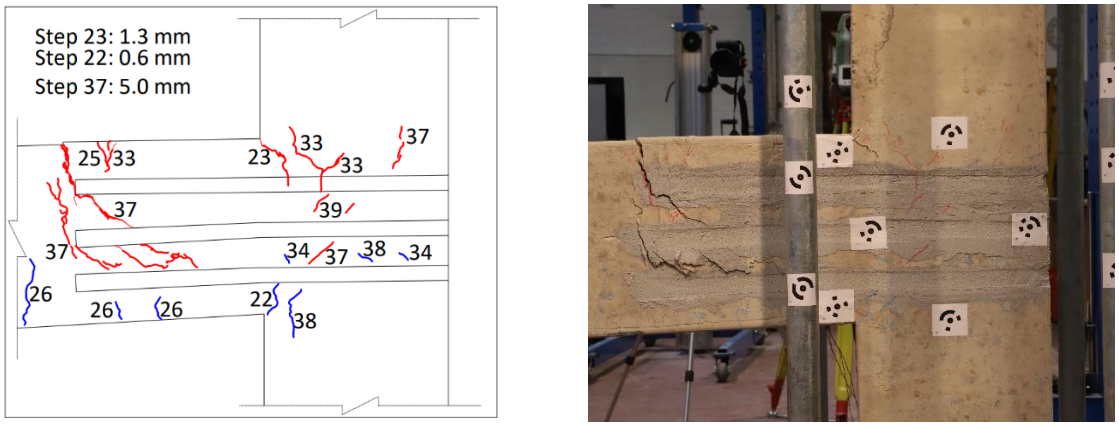

(f) Drift ratio: 3.85%, Displacement: 50 mm

Figure 4.3. Crack propagation of the S2-NSM for each drift ratio (continue).

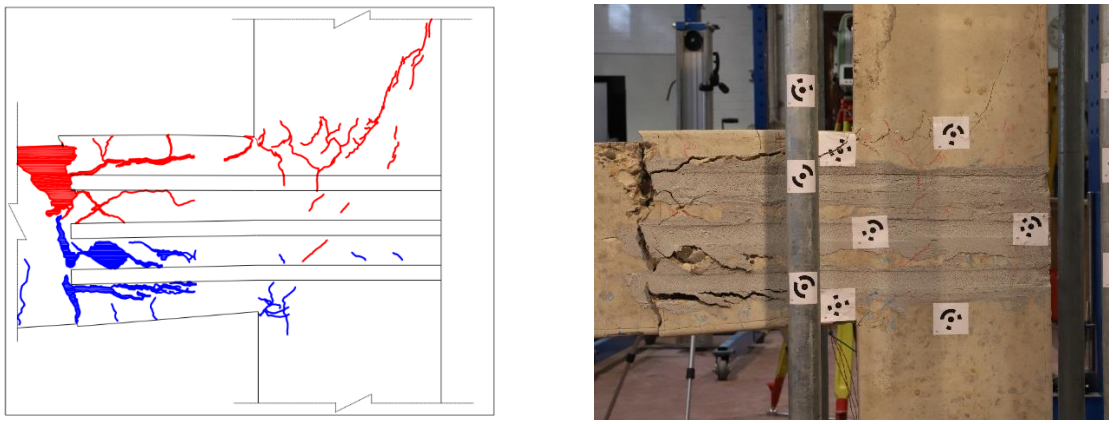

(g) Drift ratio: 4.62%, Displacement: 60 mm

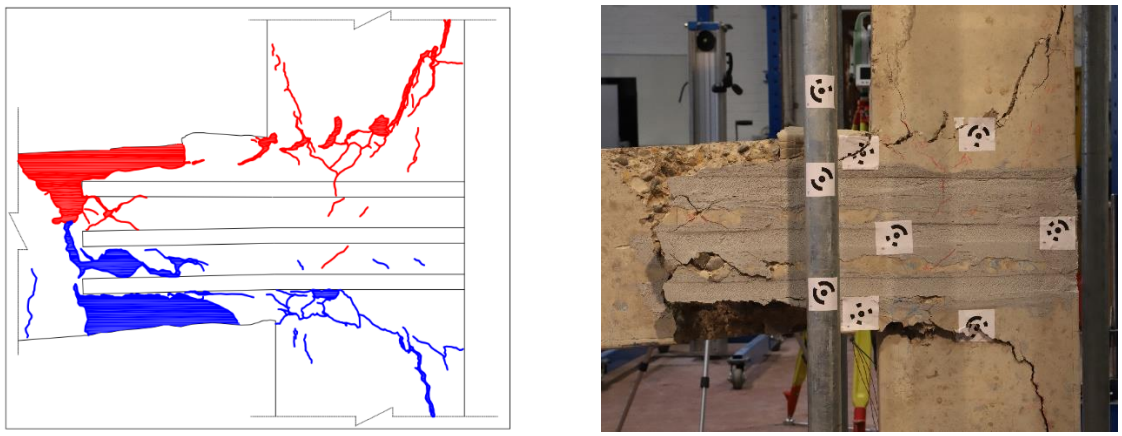

(h) Drift ratio: 5.77%, Displacement: 75 mm

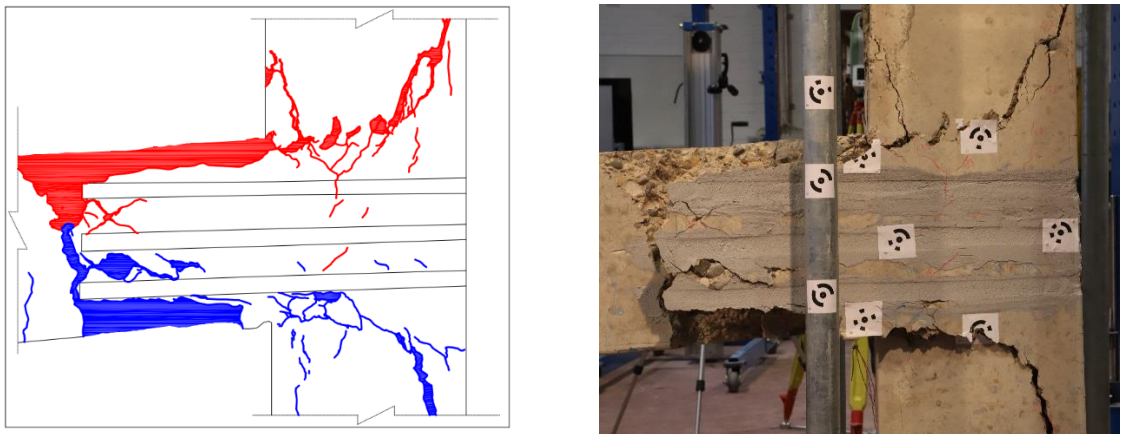

(i) Drift ratio: 6.54%, Displacement: 85 mm

Figure 4.3. Crack propagation of the S2-NSM for each drift ratio (continue).

(a)

(b)

(c)

(d)

(e)

(f)

Figure 4.4. End of experiment pictures of S2-NSM.

Damage Investigations of S3-EB specimen:

When the damage diagrams of the third specimen strengthened with the EB technique were examined, the first hairline cracks were detected at a drift ratio of 0.92% in the push direction on the beam. Flexural cracks formed on the beam in both push and pull directions at a drift ratio of 1.54%. At a 2.31% drift ratio, in addition to the cracks formed at the previous drift ratio, it was determined that cracks started to form on the beam near the area where the retrofit ended. When the specimen with a 3.846% drift ratio was examined, it was observed that a serious crack with a width of 2 mm (crack number 41) was formed at the top of the beam in the push direction. 4.62%, 5.77%, and 6.54% drift ratios, no deformations were observed in the beam-column joint area. At a 7.31% drift ratio, severe damages such as disintegration and rupture of the concrete on the beam occurred on both sides of the specimen. Additionally, when the specimen was carefully examined after the experiment, it was found that the beam reinforcement was deformed due to bending in the beam area where the At a 2.31% drift ratio, in addition to the cracks formed at the previous drift ratio, it was determined that cracks started to form on the beam near the area where the retrofit ended. The EB technique used for the third specimen was found to be particularly effective in the beam-column joint area. It was observed that the damage transferred from the beam-column joint to the beam at the end of the retrofit. In addition, as a result of the examination made at the end of the experiment, it was determined that there were tears in the GFRP fabric at the top and bottom of the beam at the end of the retrofit.

Figure 4.5 presents damaged images and sketches of the S3-EB specimen at various drift ratios: 0.92%, 1.54%, 2.31%, 3.85%, 4.62%, 5.77%, 6.54%, and 7.31%. Furthermore, to enhance comprehension of the extent of damage to specimen S3-EB, visual documentation of the specimen post-test is presented in Figure 4.6.

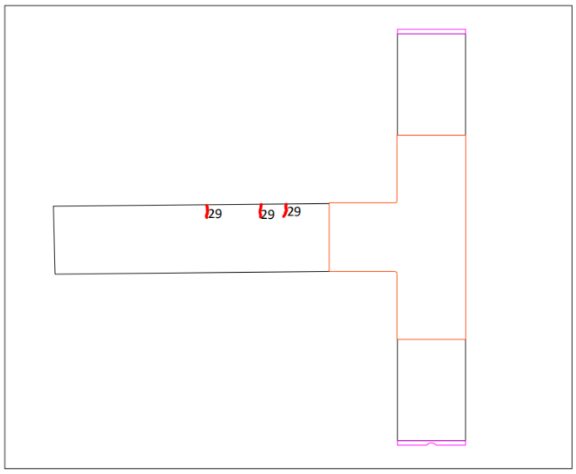

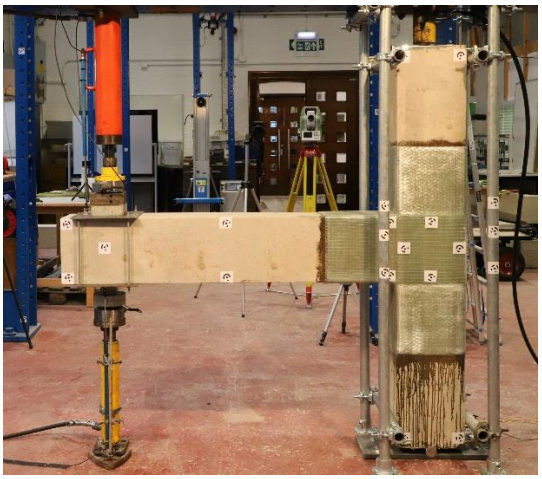

(a) Drift ratio: 0.92%, Displacement: 12 mm

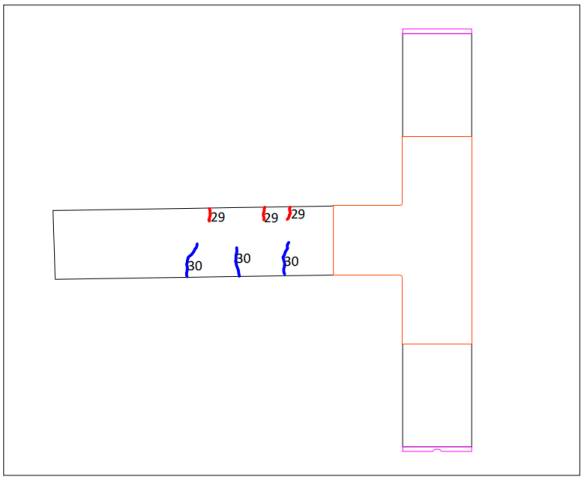

(b) Drift ratio: 1.54%, Displacement: 20 mm

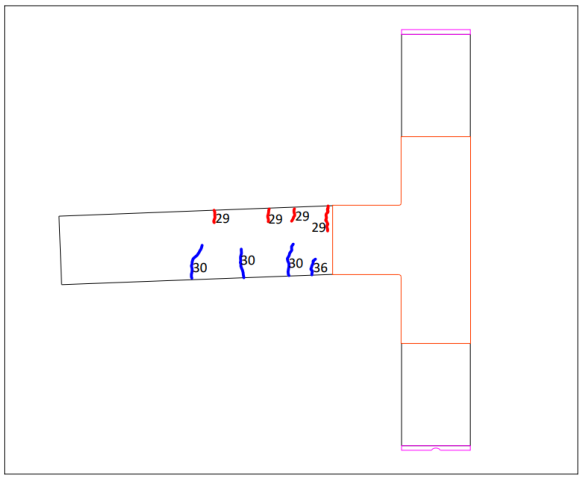

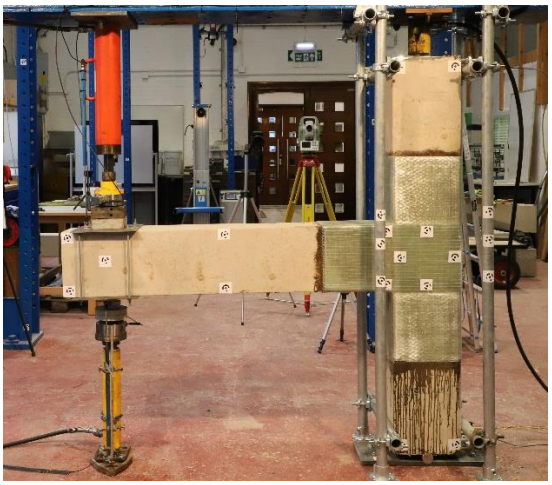

(c) Drift ratio: 2.31%, Displacement: 30 mm

Figure 4.5. Crack propagation of the S3-EB for each drift ratio.

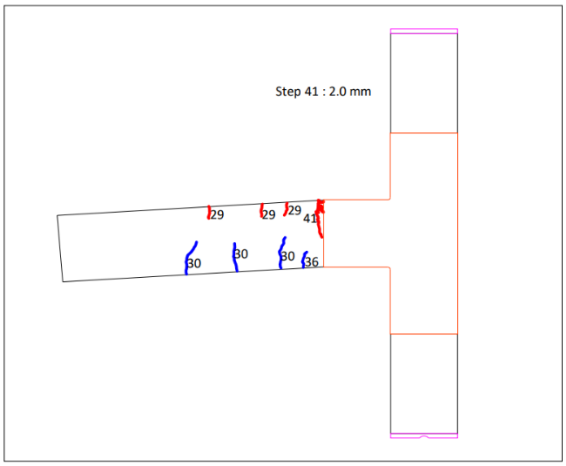

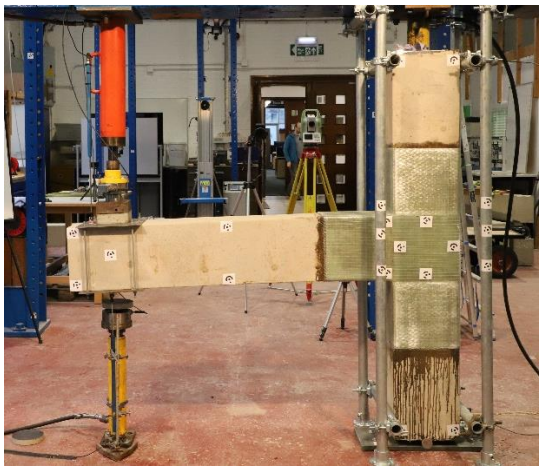

(d) Drift ratio: 3.85%, Displacement: 50 mm

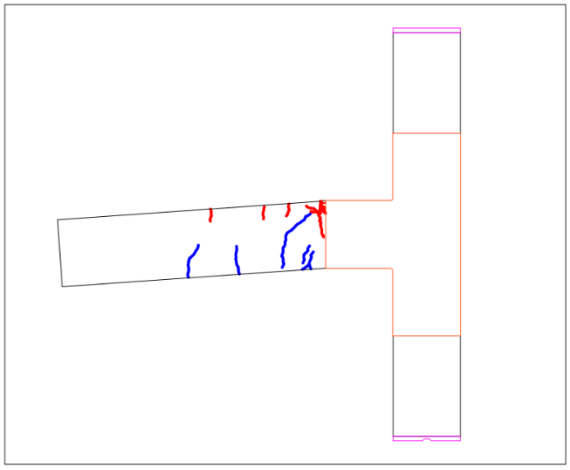

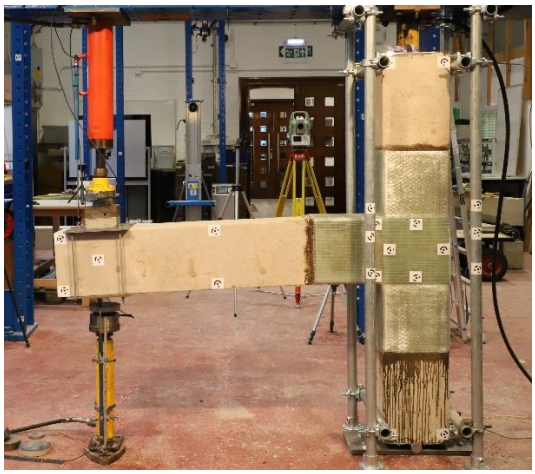

(e) Drift ratio: 4.62%, Displacement: 60 mm

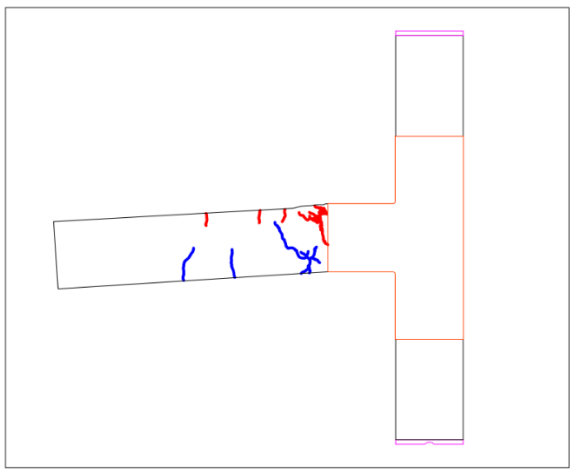

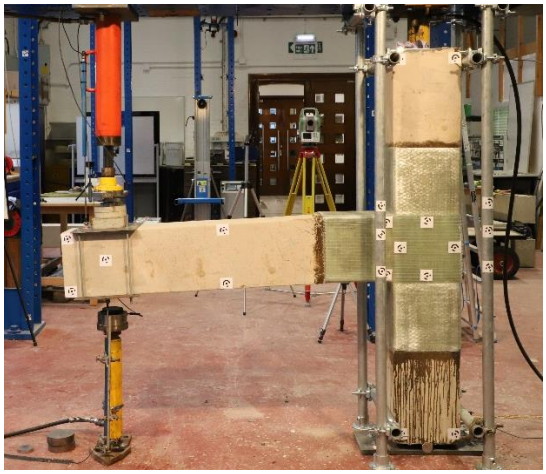

(f) Drift ratio: 5.77%, Displacement: 75 mm

Figure 4.5. Crack propagation of the S3-EB for each drift ratio (continue).

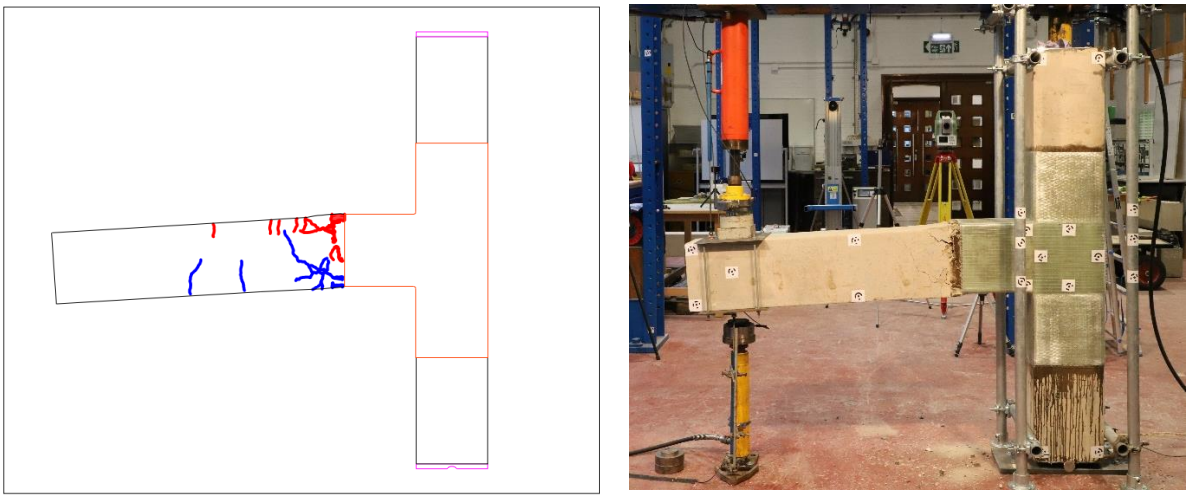

(g) Drift ratio: 6.54%, Displacement: 85 mm

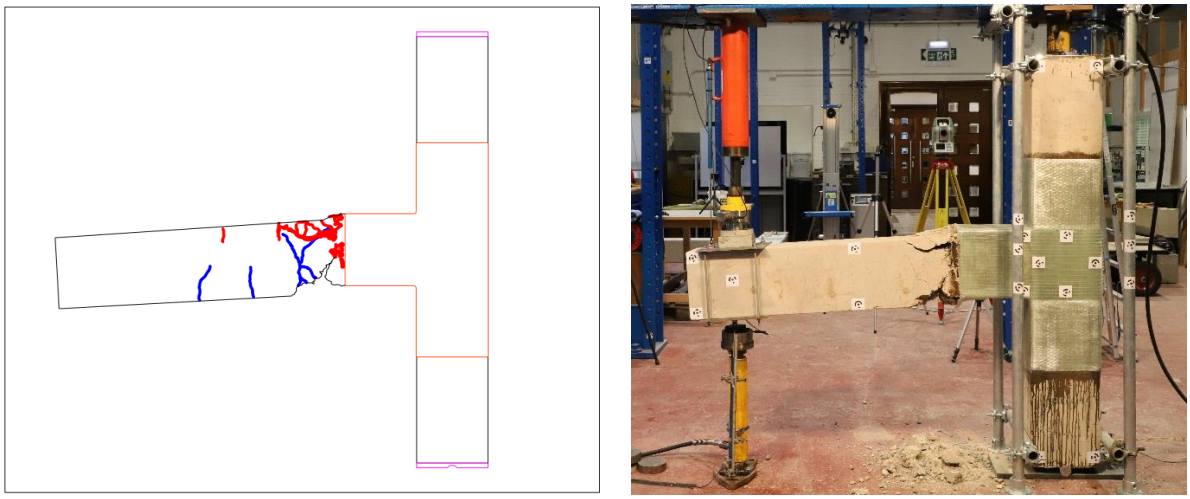

(h) Drift ratio: 7.31%, Displacement: 95 mm

Figure 4.5. Crack propagation of the S3-EB for each drift ratio (continue).

(a)

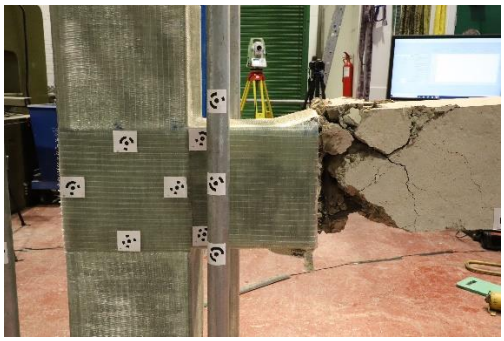

(b)

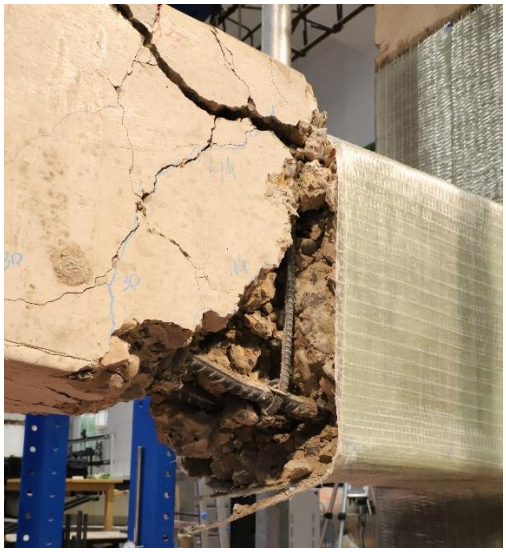

(c)

(d)

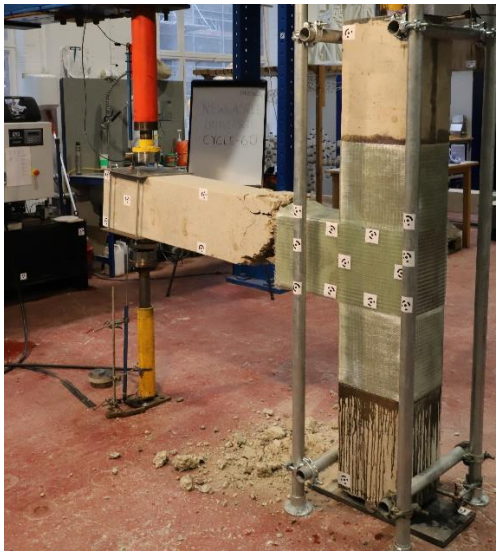

(e)

(f)

Figure 4.6. End of experiment pictures of S3-EB.

Damage Investigations of S4-Hybrid specimen:

When the damage diagrams of the fourth specimen reinforced with the NSM+EB technique were examined, the first hairline cracks were detected at a 0.92% drift ratio in the push direction on the beam. At the 1.54% drift ratio, it was observed that flexural cracks occurred on the beam in both pushing and pulling directions. At a 2.31% drift ratio, in addition to the cracks formed at the previous drift ratio, it was determined that cracks started to form on the beam near the area where the retrofit ended. Examining the specimen with a 3.85% drift ratio revealed the formation of a serious crack at the top of the beam in the pushing direction, measuring 3 mm in width (crack number 41). 4.62% and 5.77% drift ratios, no deformations were observed in the beam-column joint area. At the 5.77% drift ratio, serious damages such as disintegration and rupture of the concrete on the beam occurred on both sides of the specimen. The S4-Hybrid specimen had a safety issue due to the torsion that occurred during loading at the end of the beam during the test phase. Therefore, it could not reach high drift ratios as in the other specimens. Therefore, the experiment was stopped, and the available data were analysed.

When the specimen was carefully examined after the test, it was found that the beam reinforcements were deformed due to bending in the beam area where the retrofit ended. In the hybrid method used for the fourth specimen, it was found that similar damages occurred as in the third specimen, and therefore the EB technique was more effective. In addition, this specimen did not develop the damage that occurred in the second specimen reinforced with NSM. It was found that the combination of NSM and EB techniques prevented the damage in the beam-joint area and transferred all the damage to the beam. Moreover, the inspection conducted after the experiment revealed the presence of tears in the GFRP fabric located at both the top and bottom of the beam where retrofit was applied.

Damage photographs and drawings of the S4-Hybrid specimen are given in Figure 4.7 for 0.92%, 1.54%, 2.31%, 3.85%, 4.62%, and 5.77% drift ratios. In addition, for a clearer understanding of the damage of the S4-Hybrid specimen, photographs of the specimen after the experiment are shown in Figure 4.8.

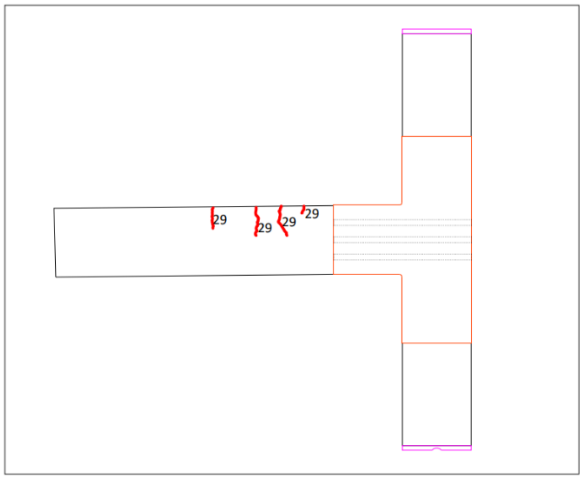

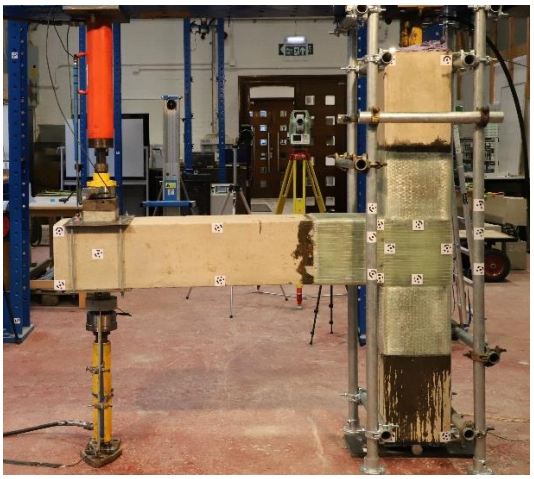

(a) Drift ratio: 0.92%, Displacement: 12 mm

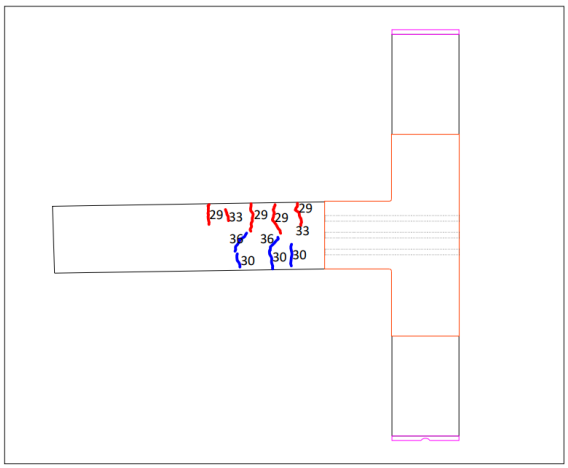

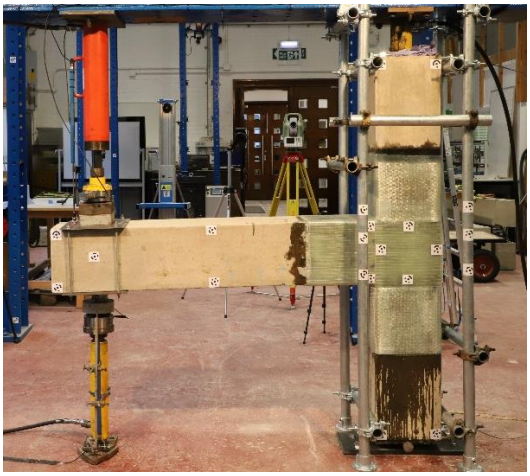

(b) Drift ratio: 1.54%, Displacement: 20 mm

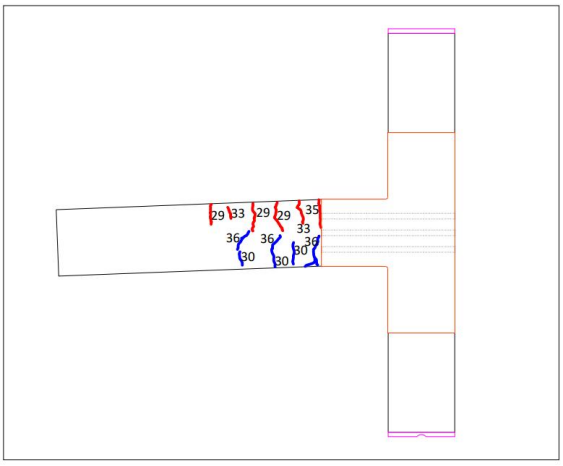

(c) Drift ratio: 2.31%, Displacement: 30 mm

Figure 4.7. Crack propagation of the S4-Hybrid for each drift ratio.

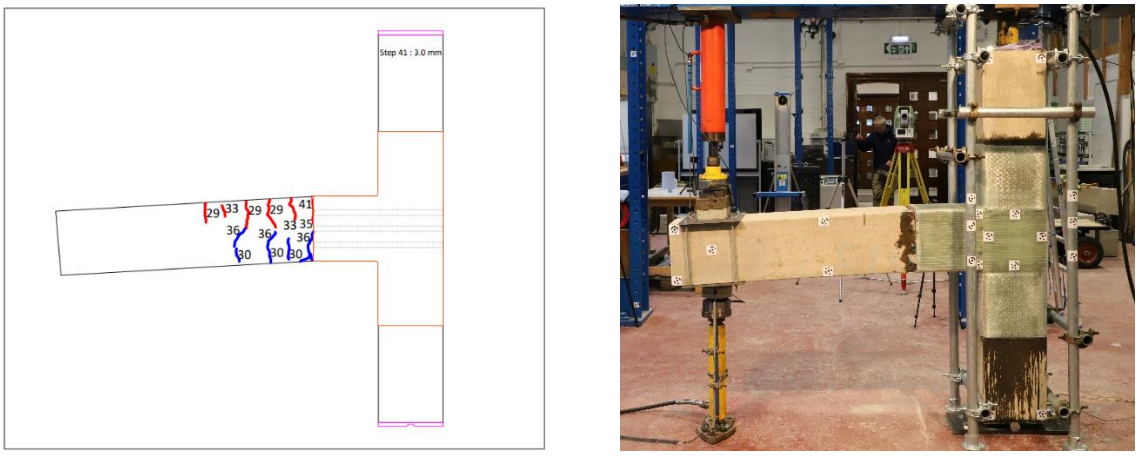

(d) Drift ratio: 3.85%, Displacement: 50 mm

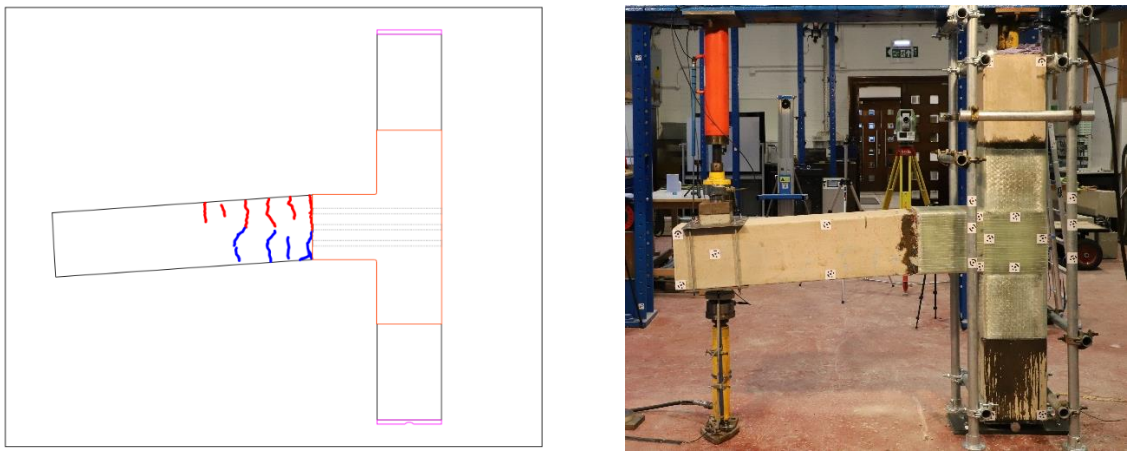

(e) Drift ratio: 4.62%, Displacement: 60 mm

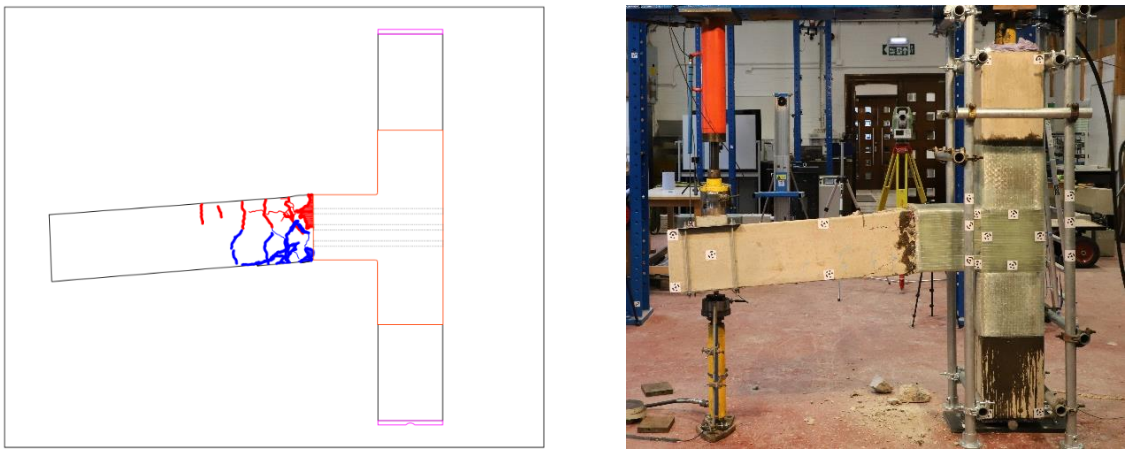

(f) Drift ratio: 5.77%, Displacement: 75 mm

Figure 4.7. Crack propagation of the S4-Hybrid for each drift ratio (continue).

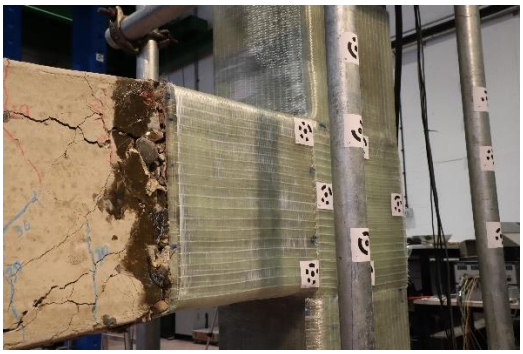

(a)

(b)

(c)

(d)

Figure 4.8. End of experiment pictures of S4-Hybrid.

Strength of the Specimens:

In this section, the load-displacement results of the specimens are presented. For each specimen, envelope curves were prepared and analysed using the displacement values at the loading point at the end of the beam and the loads corresponding to these values. The loads were obtained from the load cells connected to the end of the pumps and recorded on a computer throughout the experiment. The failure mechanisms, damage conditions and crack development of the specimens will be discussed in the following sections. In the graphs presented in this section, the horizontal limits expressed by the dashed line indicate the load required for the beam to reach the yield moment. This yield moment was calculated theoretically and is given in Appendix-D (page 251).

The load-displacement graph and envelope curve of the first specimen (S1-Control), which is also described as the reference specimen, are given in Figure 4.9 and Figure 4.10.

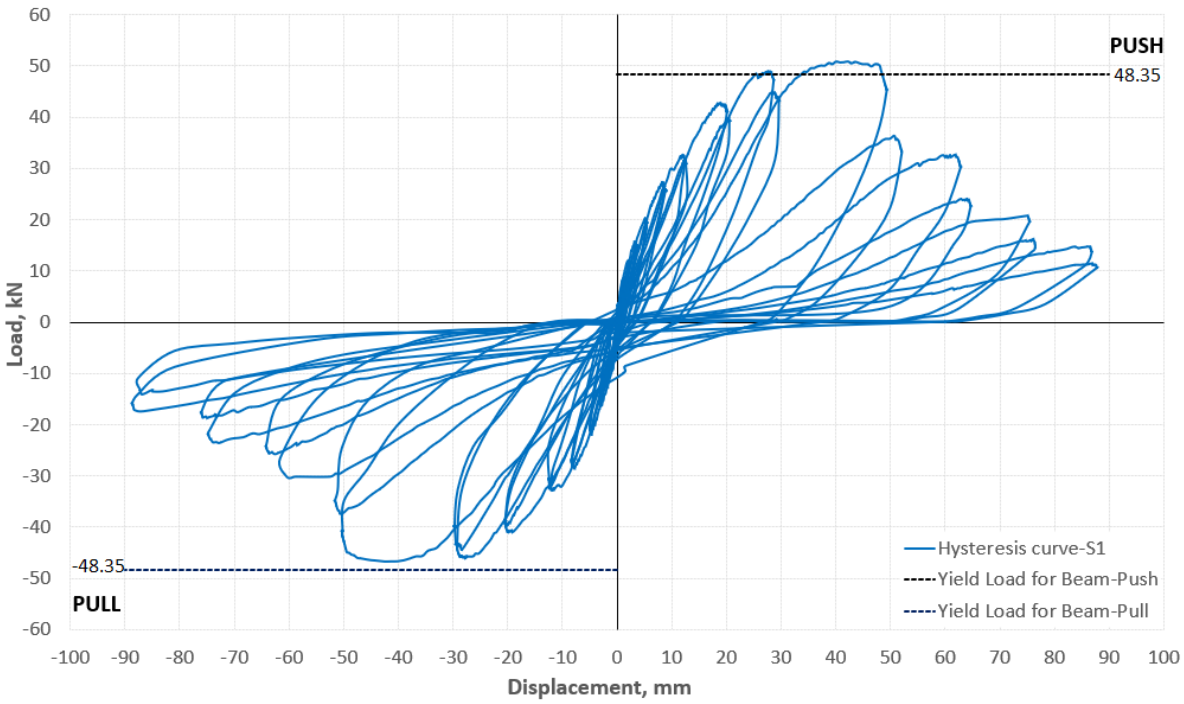

Figure 4.9. Hysteresis curves of the S1-Control.

In Figure 4.10, the red continuous line represents the envelope curve in the direction of pushing while the blue line stands for the envelope curve in the direction of pulling.

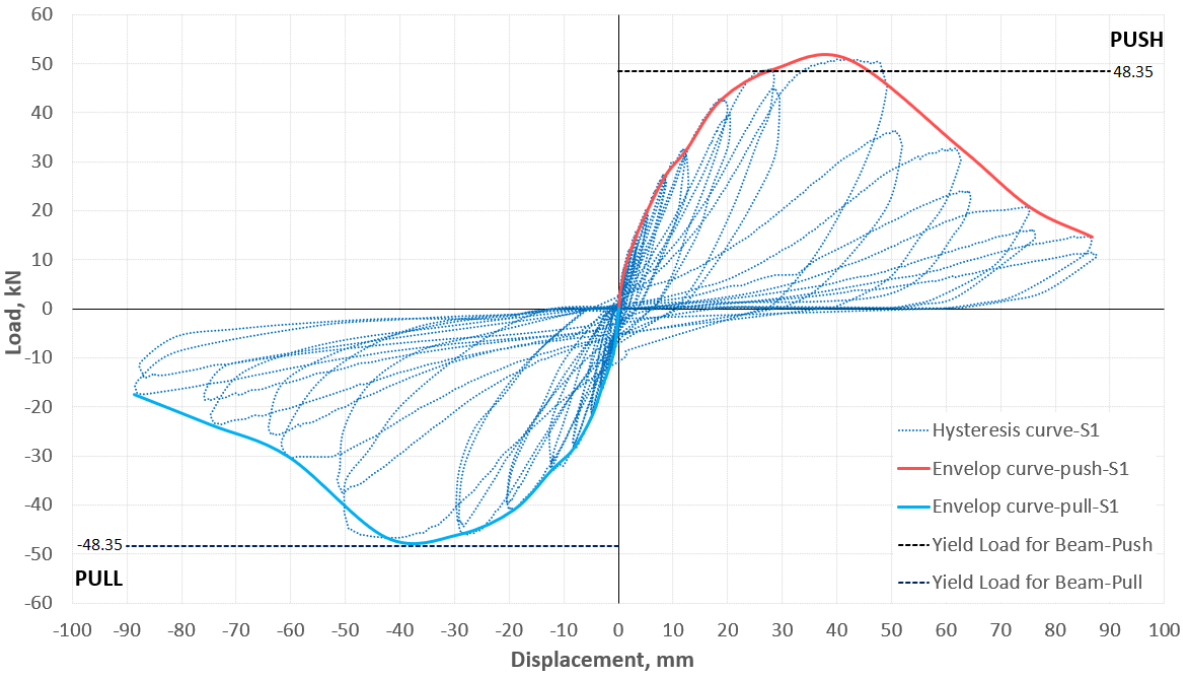

Figure 4.10. Envelope curves of the S1-Control.

When the test results of the first specimen (S1-Control) was analysed, the load capacity (max load) of the specimen was measured as 50.8 kN at 42.2 mm displacement (3.85% drift ratio) in the push (positive) direction and 46.8 kN at 42.5 mm displacement (3.85% drift ratio) in the pull (negative) direction. In the second cycle (60 mm displacement), the highest load obtained was 24.0 kN at 64.6 mm displacement (4.62% drift ratio) in the push (positive) direction and 25.8 kN at 64.1 mm displacement (4.62% drift ratio) in the pull (negative) direction. Between the cycle when the specimen reached the maximum load and the second cycle, the decrease in strength was about 52.7% in the positive direction and about 44.9% in the negative direction. During the experiment, it was observed that the load required for the beam to reach the theoretically calculated yield moment was reached in the pushing direction but not in the pulling direction.

The load-displacement graph and envelope curve of the second specimen (S2-NSM) are given in Figure 4.11 and Figure 4.12.

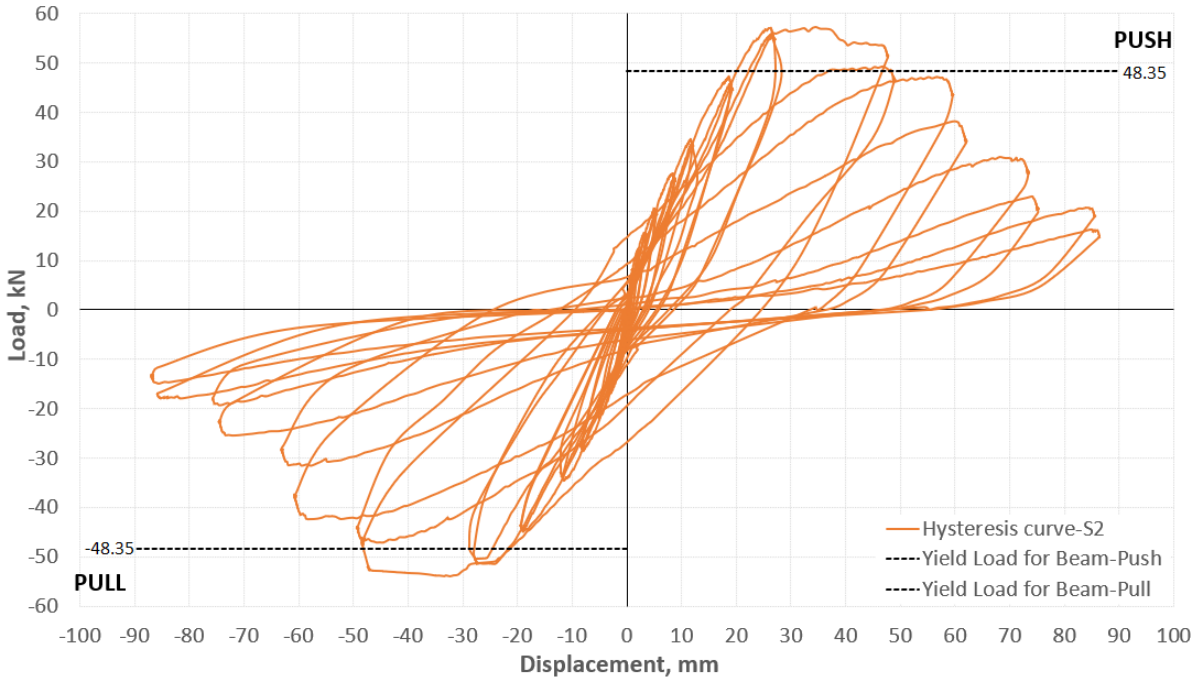

Figure 4.11. Hysteresis curves of the S2-NSM.

In Figure 4.12, the red continuous line represents the envelope curve in the direction of pushing while the blue line stands for the envelope curve in the direction of pulling.

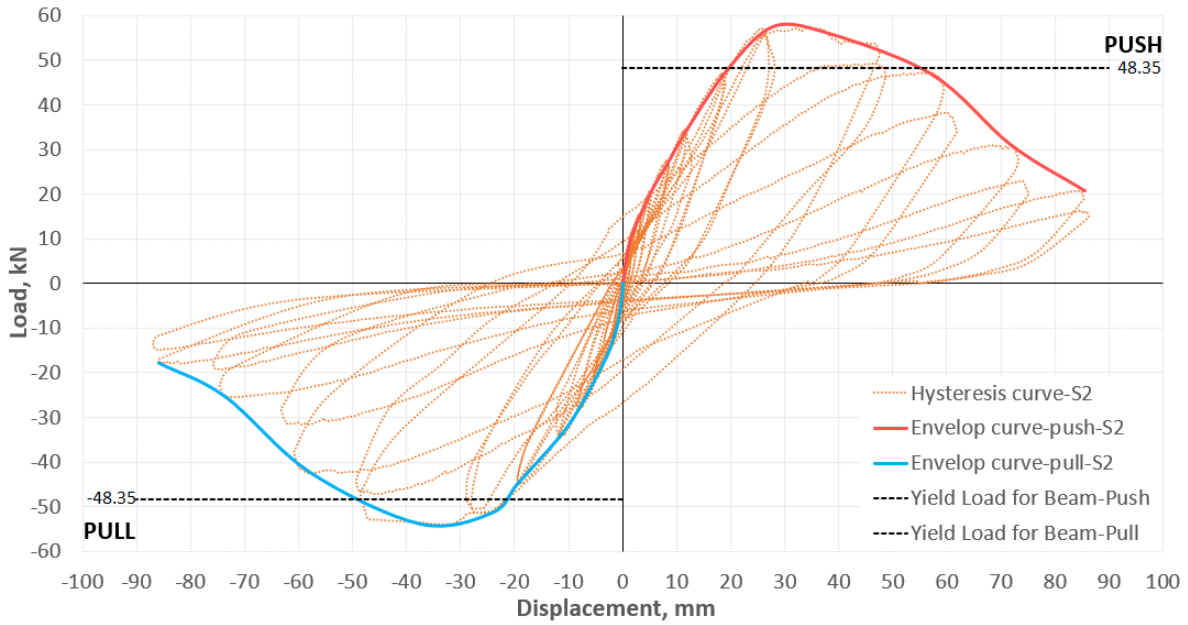

Figure 4.12. Envelope curves of the S2-NSM.

When the test results of the second specimen (S2-NSM) was analysed, the load capacity of the specimen was measured as 57.4 kN at 34.4 mm displacement (3.85% drift ratio) in the push (positive) direction and 53.9 kN at 37.6 mm displacement (3.85% drift ratio) in the pull

(negative) direction. In the second cycle of 60 mm displacement cycle, the highest load obtained was 38.6 kN at 62 mm displacement (4.62% drift ratio) in the push (positive) direction and 31.5 kN at 63.2 mm displacement (4.62% drift ratio) in the pull (negative) direction. Between the cycle when the specimen reached the maximum load and the second cycle in 60 mm displacement, the decrease in strength was about 33.3% in the positive direction and about 41.6% in the negative direction. During the experiment, it was observed that the load required for the beam to reach the theoretically calculated yield moment was reached in the pushing and pulling direction.

The load-displacement graph and envelope curve of the third specimen (S3-EB) are given in Figure 4.13 and Figure 4.14.

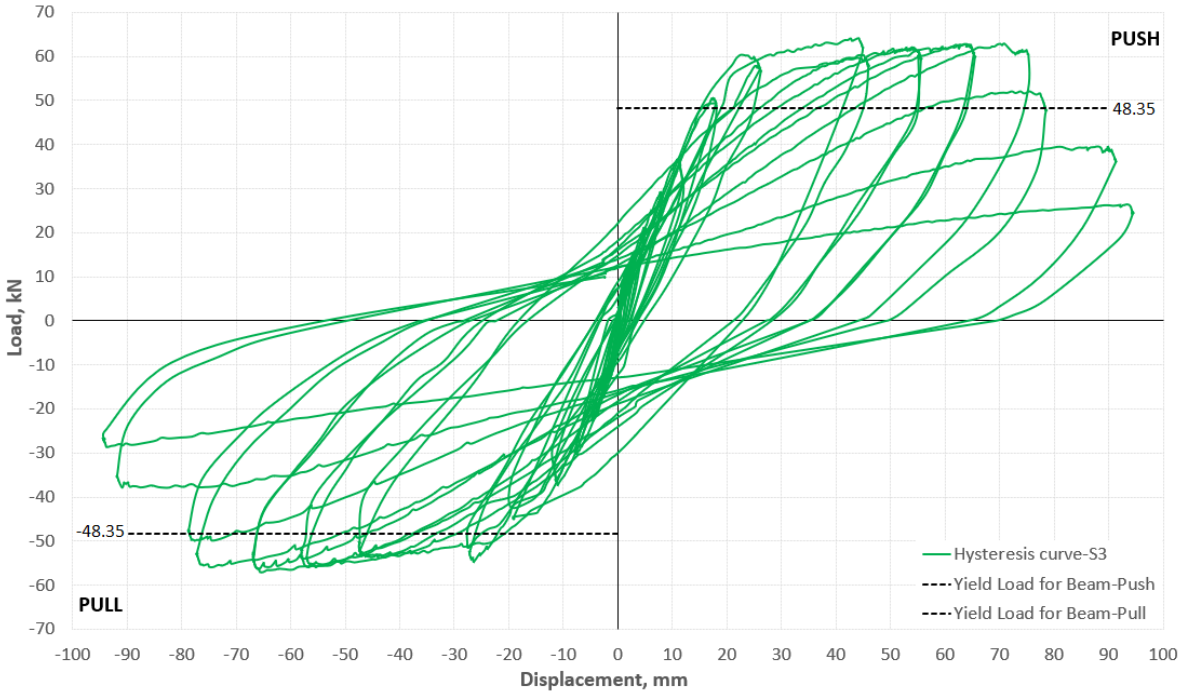

Figure 4.13. Hysteresis curves of the S3-EB.

In Figure 4.14, the red continuous line represents the envelope curve in the direction of pushing while the blue line stands for the envelope curve in the direction of pulling.

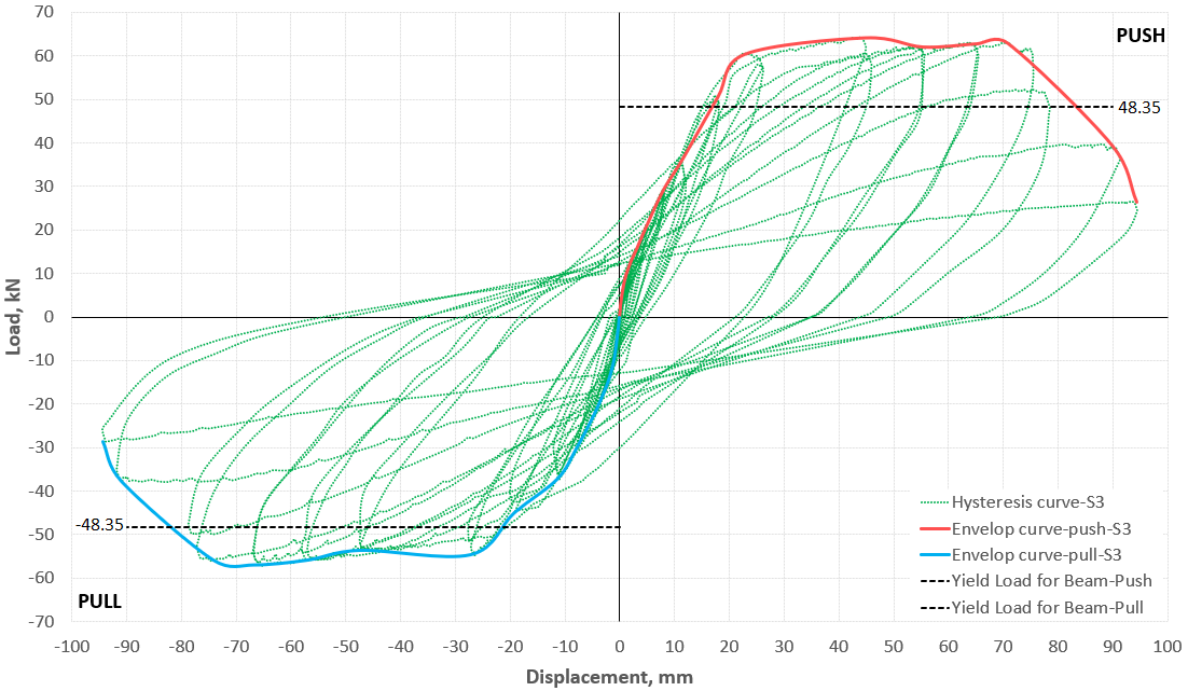

Figure 4.14. Envelope curves of the S3-EB.

When the test results of the third specimen (S3-EB) was analysed, the load capacity of the specimen was measured as 64.2 kN at 44.9 mm displacement (3.85% drift ratio) in the push (positive) direction and 57 kN at 66.9 mm displacement (5.77% drift ratio) in the pull (negative) direction. In the second cycle of 60 mm displacement cycle, the highest load obtained was 62.1 kN at 55.6 mm displacement (4.62% drift ratio) in the push (positive) direction and 55.1 kN at 58.1 mm displacement (4.62% drift ratio) in the pull (negative) direction. Between the cycle when the specimen reached the load capacity and the second cycle, the decrease in strength was about 3.3% in the positive direction and about 3.4% in the negative direction. During the experiment, it was observed that the load required for the beam to reach the theoretically calculated yield moment was reached in the pushing and pulling direction.

The load-displacement graph and envelope curve of the fourth specimen (S4-Hybrid) are given in Figure 4.15 and Figure 4.16.

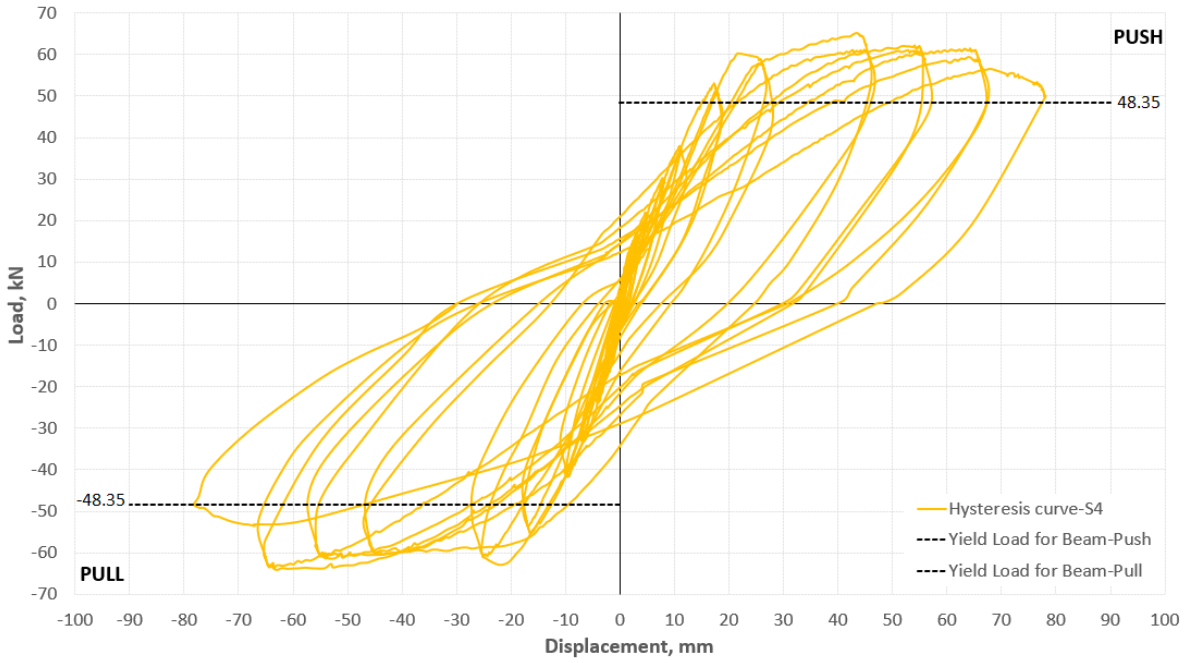

Figure 4.15. Hysteresis curves of the S4-Hybrid.

In Figure 4.16, the red continuous line represents the envelope curve in the direction of pushing while the blue line stands for the envelope curve in the direction of pulling.

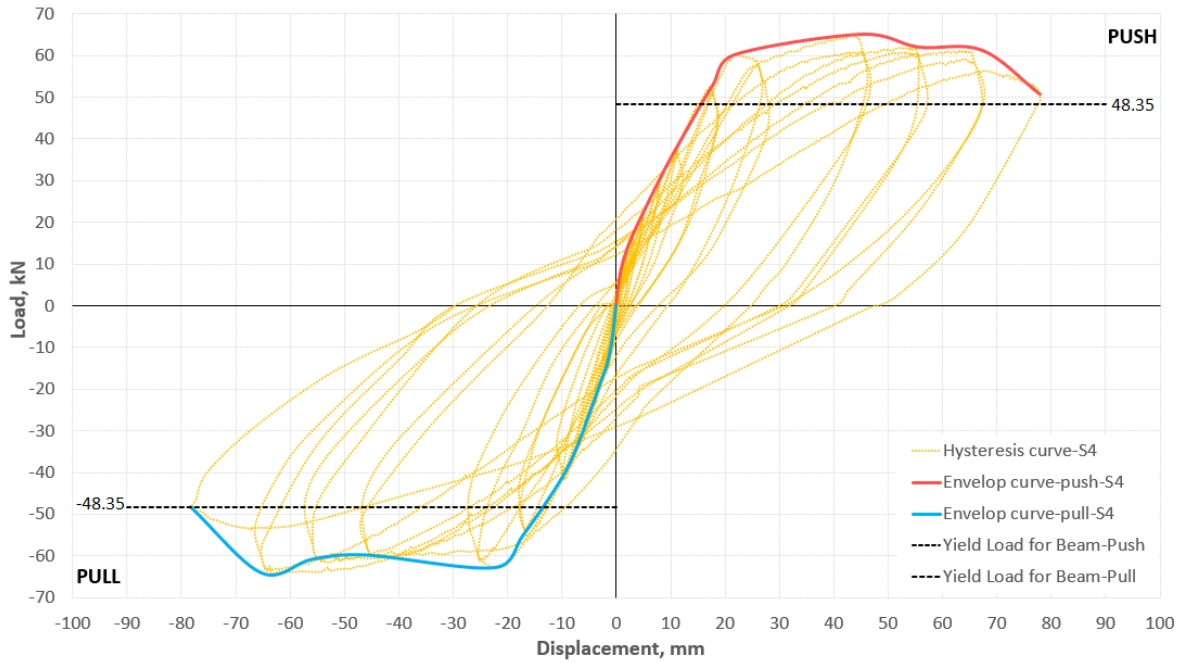

Figure 4.16. Envelope curves of the S4-Hybrid.

When the test results of the fourth specimen (S4-Hybrid) was analysed, the load capacity of the specimen was measured as 65.1 kN at 45.1 mm displacement (3.85% drift ratio) in the

push (positive) direction and 64.1 kN at 65.2 mm displacement (5.77% drift ratio) in the pull (negative) direction. In the second cycle (60 mm displacement), the maximum load obtained was 59.3 kN at 66.9 mm displacement (5.77% drift ratio) in the push (positive) direction and 63.4 kN at 66.5 mm displacement (5.77% drift ratio) in the pull (negative) direction. Between the cycle when the specimen reached the load capacity and the 60 mm displacement cycle, the decrease in strength was about 8.9% in the positive direction and about 1.0% in the negative direction. During the experiment, it was observed that the load value required for the beam to reach the theoretically calculated yield moment was reached in the pushing and pulling direction.

A summary of the test results for both directions and the displacement ratios at which they reached their capacities are presented in Table 4.1.

Table 4.1. The capacities of the specimens for both directions and the drift ratios at which they reach their capacities.

Specimen Name	**Capacity in Push Direction**	**Drift Ratio**	**Capacity in Pull Direction**	**Drift Ratio**	**Decrease in strength in the second cycle (60 mm displacement)**	
	kN	**%**	**kN**	**%**	**Push (%)**	**Pull (%)**
S1-Control	50.8	3.85	46.8	4.62	52.8	44.9
S2-NSM	57.4	3.85	53.9	4.62	33.3	41.6
S3-EB	64.2	3.85	57	5.77	3.3	3.4
S4-Hybrid	65.1	3.85	64.1	5.77	8.9	1.0

The load-displacement response obtained in the experiments are given in Appendix-G.

Comparison of Strength Capacity:

In this section, firstly, the load-displacement graphs of the strengthened specimens are shown by comparing each of the specimens with the control specimen, and then the behaviour of all specimens is shown on a single graph and the effect of strengthening is examined. The load-displacement graphs and envelope curves of the specimens are presented in Figure 4.17, Figure 4.18, Figure 4. 19, Figure 4.20, and Figure 4.21.

In Figure 4.17, Figure 4.18, Figure 4. 19, and Figure 4.20, the black dotted line represents S1-Control, the orange line S2-NSM, the green line S3-EB and the yellow line S4-Hybrid,

respectively. In Figure 4.21, the blue line represents S1-Control, the orange line S2-NSM, the green line S3-EB and the yellow line S4-Hybrid, respectively.

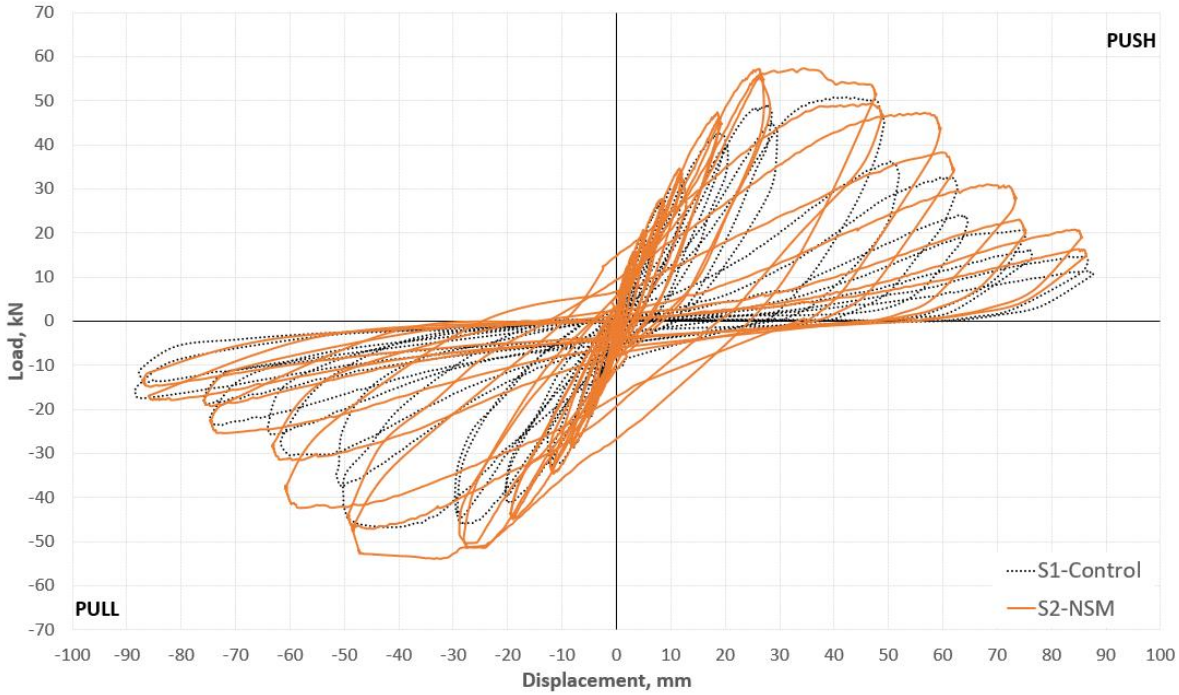

Figure 4.17. Hysteresis curves of the S2-NSM compared to S1-Control.

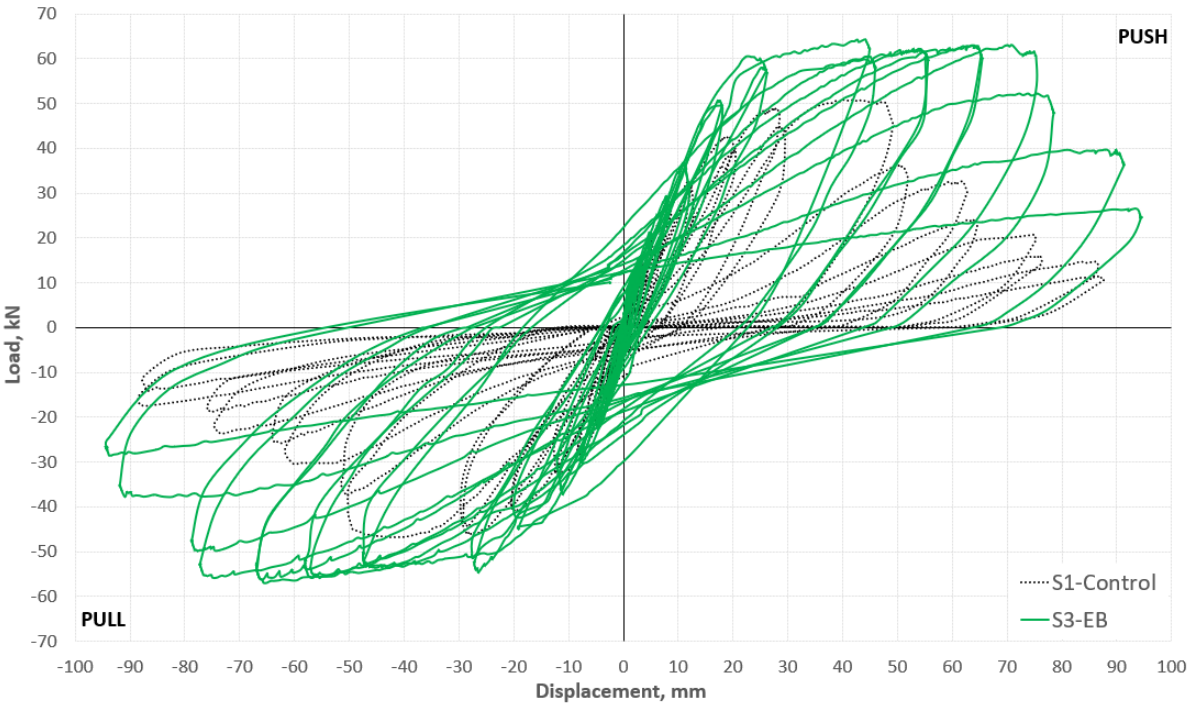

Figure 4.18. Hysteresis curves of the S3-EB compared to S1-Control.

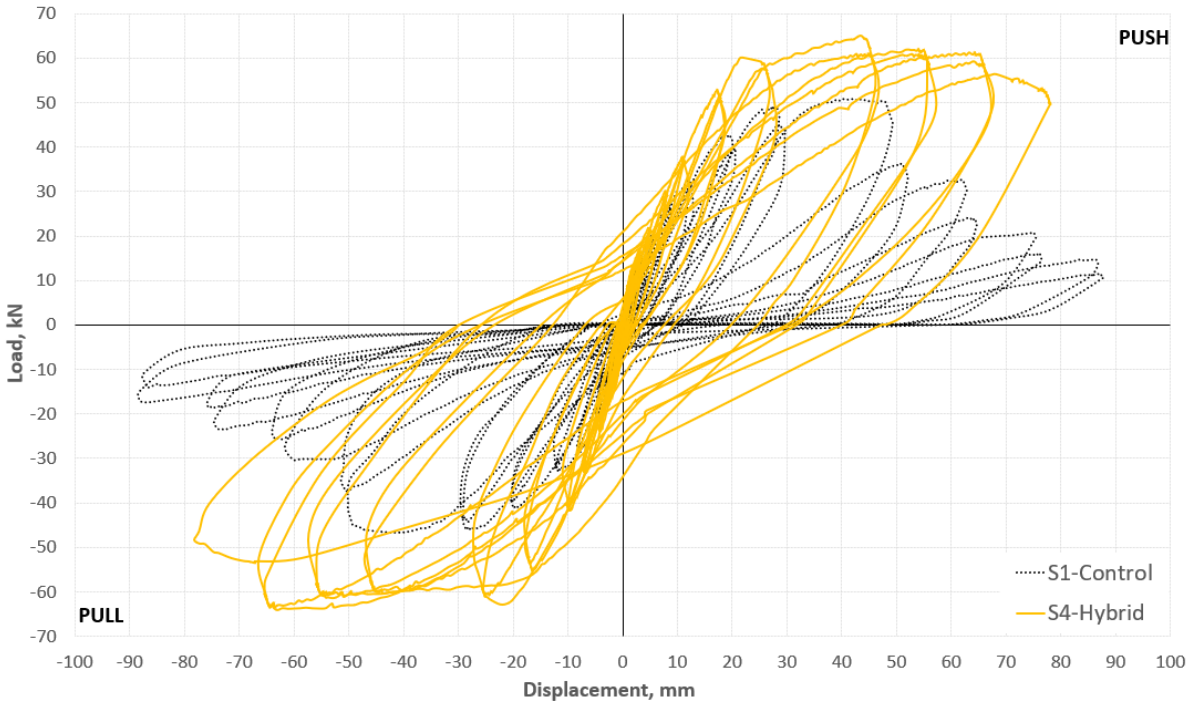

Figure 4. 19. Hysteresis curves of the S4-Hybrid compared to S1-Control.

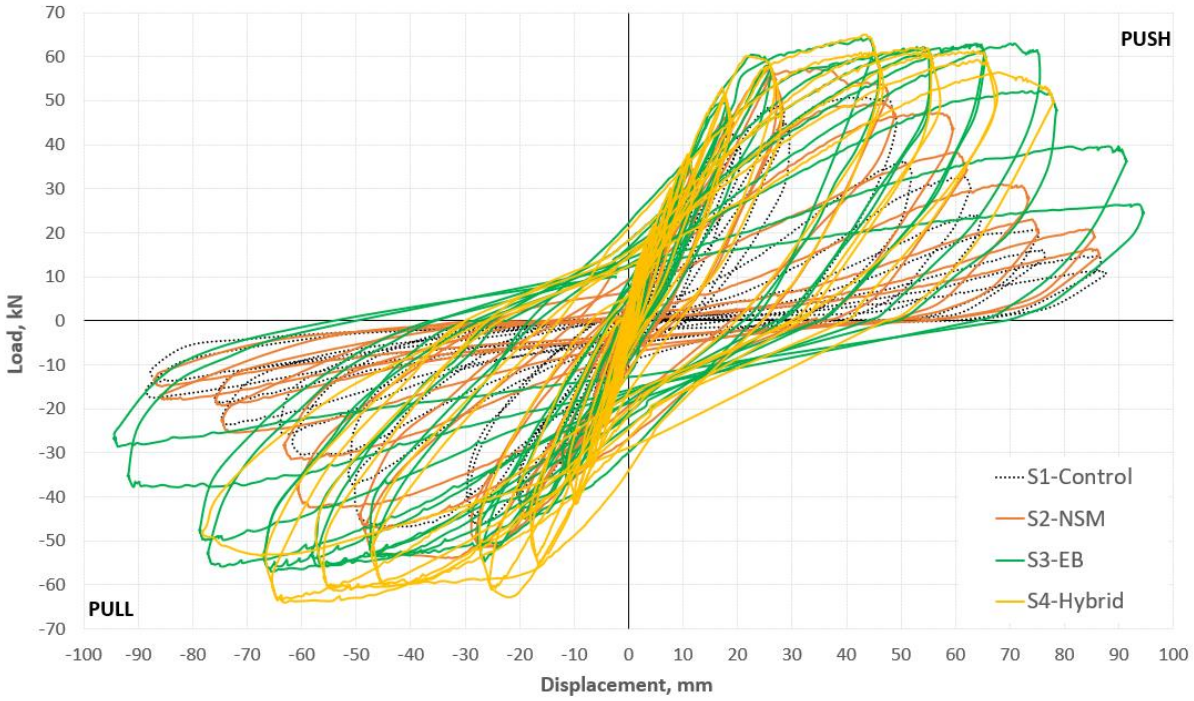

Figure 4.20. Comparison of the hysteresis curves of specimens.

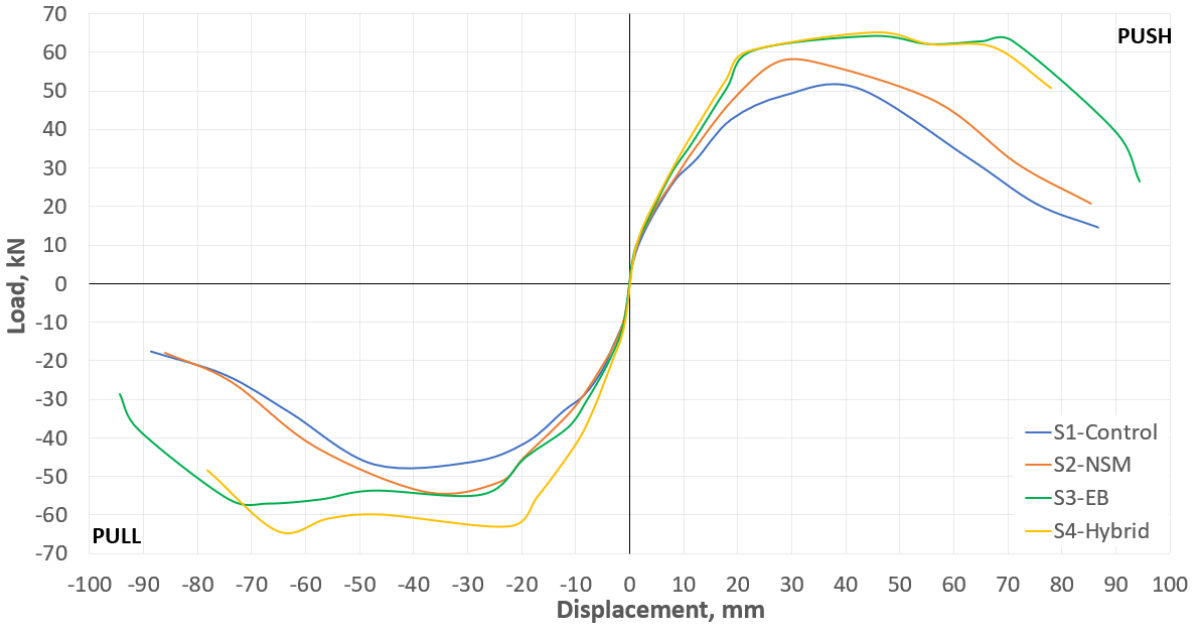

Figure 4.21. Envelop curves of the specimens.

Table 4.2 shows the maximum values for pushing and pulling below.

Table 4.2. Comparison of the lateral strength capacity of the specimens.

Specimen Name	F^{+}_{max} (Pushing) (kN)	F^{-}_{max} (Pulling) (kN)	Difference Pushing (%)	Difference Pulling (%)
S1-Control	50.8	-46.8	-	-
S2-NSM	57.4	-53.9	12.9	15.3
S3-EB	64.2	-57	26.4	21.8
S4-Hybrid	65.1	-64.1	28.1	37

When Table 4.2 is carefully analysed and the maximum push and pull values obtained from the test results are taken into consideration, it is seen that the S2-NSM specimen has a capacity increase of 12.9% for push and 15.3% for pull. Likewise, S3-EB specimen has 26.4% capacity increase for pushing and 21.8% capacity increase for pulling, while S4-Hybrid specimen has 28.1% capacity increase for pushing and 37% capacity increase for pulling.

Based on the results given in Table 4.2, in the push direction between S3-EB and S4-Hybrid specimens, there is no significant difference in the strength reduction; however, in the pull direction the S4-Hybrid specimen shows a 12% (64.1/57) increase in strength compared to the

S3-EB specimen. In terms of strength reduction, the hybrid method maintained 58% (37/64.1) of the maximum capacity at 60mm in the pull direction while the EB method had only 37% (21.8/57) of the original capacity (i.e. the hybrid method has a 57% (58/37) greater residual capacity than the EB method).

It is difficult to know the exact reason for the improved performance in the hybrid specimen. As both specimens failed in the beam and the beams in the two specimens had the same specification it could be down to variability between samples and therefore, they can be considered to have the same design capacity. Alternatively, looking at the crack diagrams of the two specimens, the failure mechanism may be bond failure. In the Figure 4.5, the cracks in the EB specimen propagate into the section of the beam that is wrapped in FRP which would reduce the bond. In the case of the hybrid method, the cracks are less and there is also more reinforcement so for the same amount of debonding there will be a greater moment as there is more steel.

4.2.2 Stiffness

Comparison Stiffness of the Joint:

Stiffness is one of the most important parameters for structures. Stiffness is the ability of a structure to resist deformation when exposed to external forces. It is a measure of the amount of force required to cause a certain amount of deformation in the structure (Murty *et al*., 2012). Figure 4.22 depicts the schematic diagram of effective stiffness and energy dissipation.

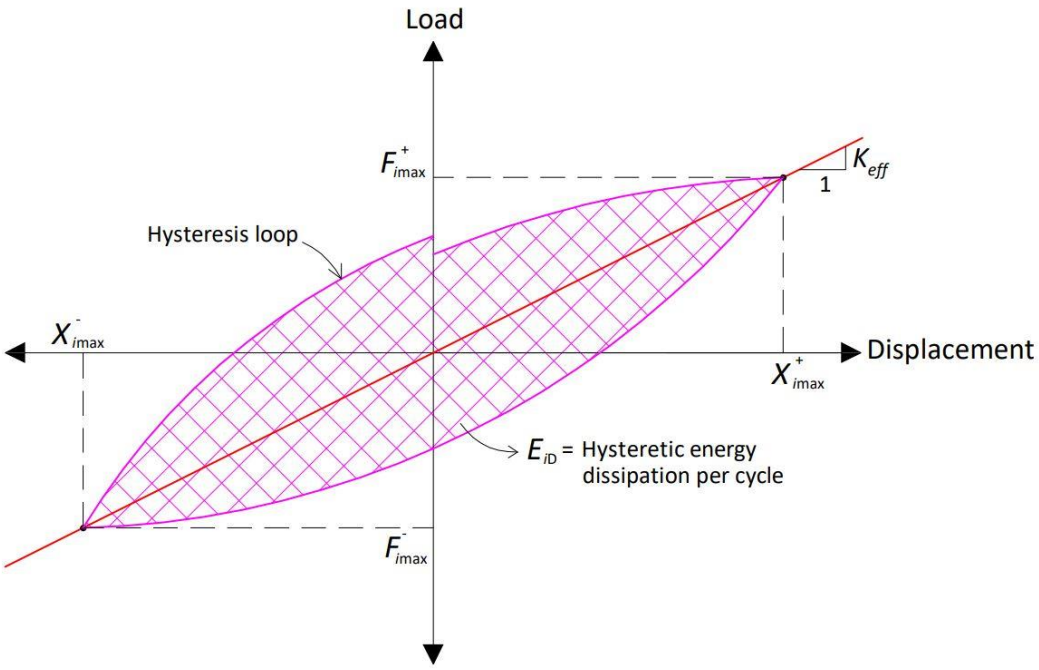

Figure 4.22. Schematic diagram of effective stiffness and energy dissipation, (Ngo *et al*., 2020).

As the cracks propagated in the beam-column joint, the vertical stiffness of the beam gradually decreased with increasing displacement. In the present research, the effective stiffness can be calculated using Equation (4.1) (Realfonzo *et al*., 2014).

$$K_{eff,i} = \frac{F^{+}_{imax} + F^{-}_{imax}}{X^{+}_{i} + X^{-}_{i}} \quad (4.1)$$

where, F^{+}_{imax} and F^{-}_{imax} are the peak strength in the push and pull direction in the ith cycle, respectively; and X^{+}_{i} and X^{-}_{i} are the displacement corresponding to F^{+}_{imax} and F^{-}_{imax}, respectively. The effective stiffness (K_{eff}) values are given in Table 4.3 and shown graphically in Figure 4.23. The values given in Table 4.3 are the effective stiffness values obtained in the first cycle at each drift ratio. In Figure 4.23, the blue line represents S1-Control, the orange line S2-NSM, the green line S3-EB and the yellow line S4-Hybrid, respectively.

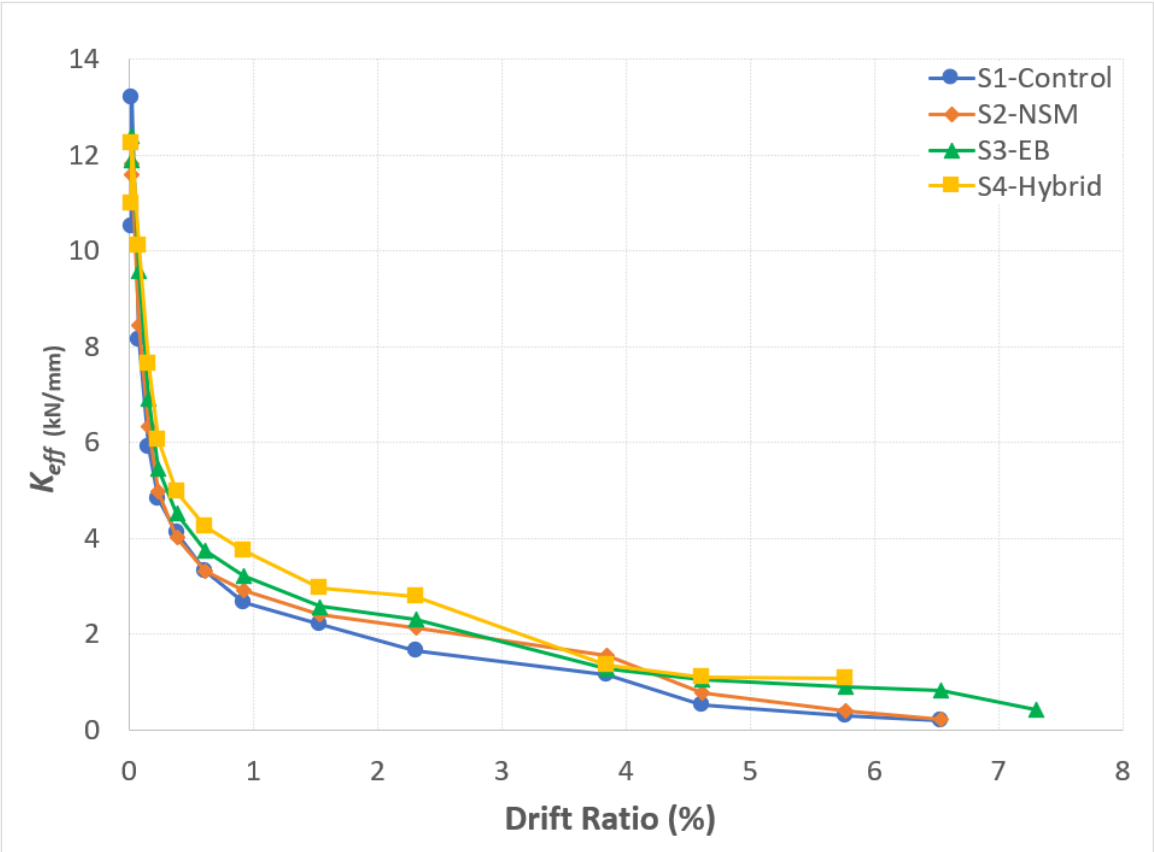

Figure 4.23. Stiffness of the specimens.

Compared with the initial stiffness of all specimens, the stiffness of all specimens decreased until the end of the experiment due to cracks, bending in the beam longitudinal reinforcement and rupture in the FRP material. Unreinforced and reinforced specimens show decreasing stiffness during the experiment. The decrease in the stiffness of all specimens continued until approximately 0.077% drift ratio. After this, differences started to be observed. As can be seen in Figure 4.23, it can be said that the S4-Hybrid specimen is stiffer than the other specimens. In the stiffness curves of S3-EB and S4-Hybrid specimens, it can clearly be seen that they are stiffer at other drift ratios except 3.85% drift ratio. The reason for this loss of stiffness for these two specimens is thought to be the sudden rupture of the FRP material in the beam wrapping area. Using the values of 5.77% drift ratio towards the end of the experiment, the reduction in stiffness of all specimens is 97.1% for S1-Control specimen, 96.6% for S2-NSM specimen, 92.4% for S3-EB specimen, and 90.3% for S4-Hybrid specimen compared to their initial stiffness. The reduction in specimen stiffness is consistent with the damage mechanisms and distribution presented in the damage investigations.

Table 4.3. Stiffness values of the specimens.

		K_{eff} (kN/mm)			
Drift Ratio (%)	**Displacement (mm)**	**S1-Control**	**S2-NSM**	**S3-EB**	**S4-Hybrid**
0.015	0.2	10.5	11.6	11.9	11
0.023	0.3	13.2	11.8	12.4	12.2
0.077	1	8.2	8.5	9.6	10.1
0.15	2	5.9	6.3	6.9	7.6
0.23	3	4.8	5	5.5	6.1
0.39	5	4.1	4.0	4.5	5
0.62	8	3.3	3.3	3.7	4.2
0.92	12	2.7	2.9	3.2	3.8
1.54	20	2.2	2.4	2.6	3
2.31	30	1.6	2.1	2.3	2.8
3.85	50	1.2	1.6	1.3	1.4
4.62	60	0.5	0.8	1.1	1.1
5.77	75	0.3	0.4	0.9	1.1
6.54	85	0.2	0.2	0.8	-
7.31	95	-	-	0.4	-

4.2.3 Ductility Ratios and Energy Dissipation Characteristic

Comparison ductility ratios of the Joint:

The displacement ductility coefficient μ is s significant parameter for evaluating the ductility performance of beam-column connections as defined in Equation (4.2) (Bayrak and Sheikh, 1998).

$$\mu = \frac{\Delta_u}{\Delta_y} \tag{4.2}$$

where μ is the ductility ratio, Δ_u is the ultimate displacement value, and Δ_y is the yield displacement. By idealizing the envelope curve according to the equivalent energy method, yield displacement and yield horizontal load-bearing capacity values were obtained. The final displacement value was determined as the displacement value corresponding to a 20% (Truong *et al.,* 2017 and Shen *et al.,* 2022) reduction of the horizontal load-bearing capacity. As shown in Figure 4.24, the regions Area-1 and Area-1` had the same areas as Area-2 and Area-2`, respectively.

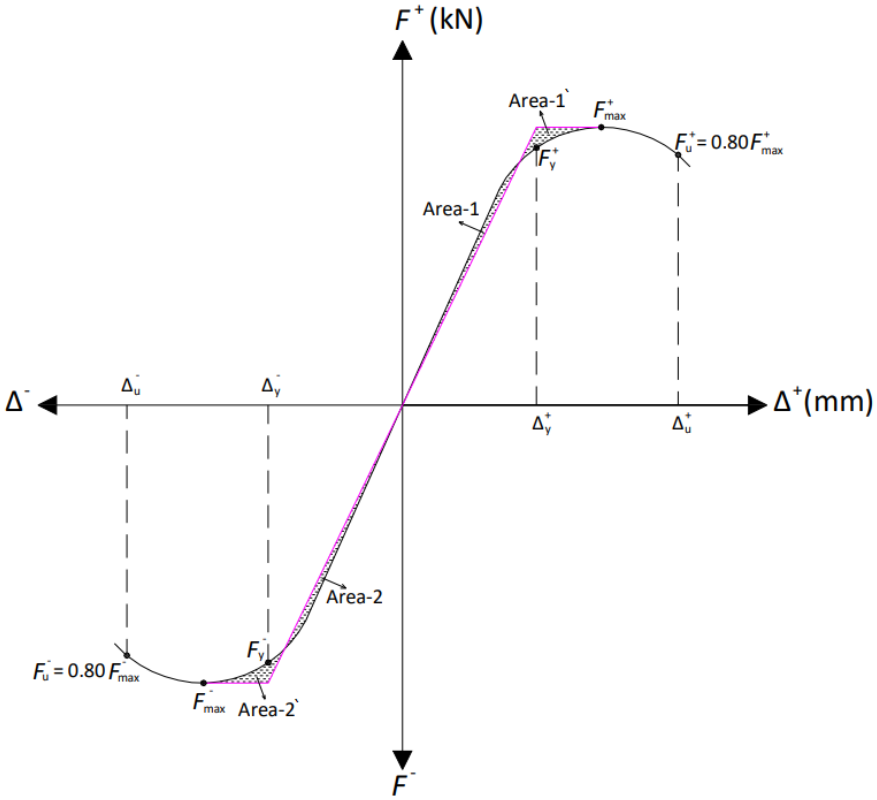

Figure 4.24. Illustration of equivalent energy method.

The calculation steps of the values calculated using the equivalent energy method for each specimen are given in Figure 4.25, Figure 4.26, Figure 4.27, and Figure 4.28. The calculated values are also shown in Table 4.4. The area calculations in the equivalent energy method for S1-Control are shown in detail and the same calculation steps are followed for the other specimens.

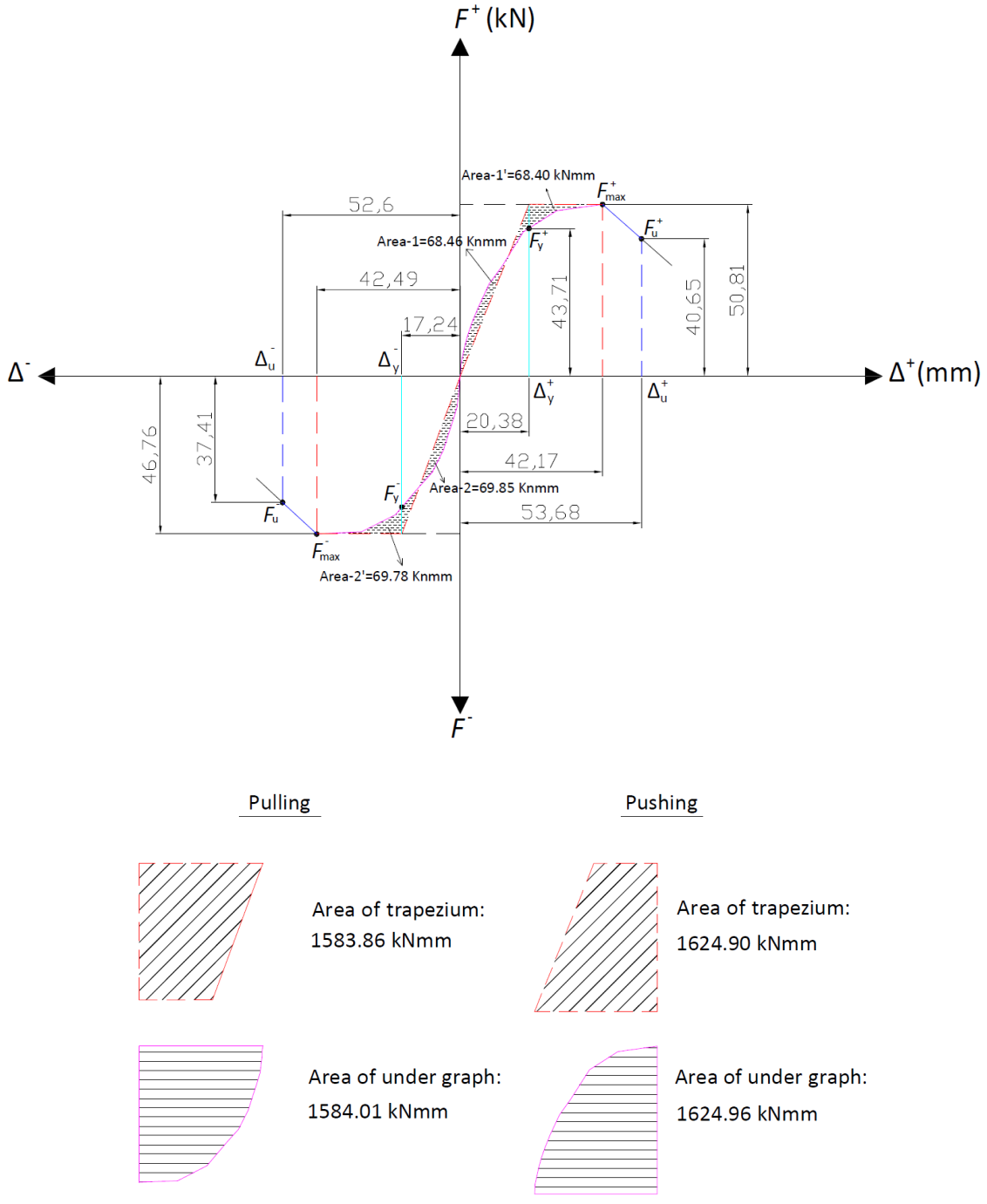

Figure 4.25. Equivalent energy method for S1-Control.

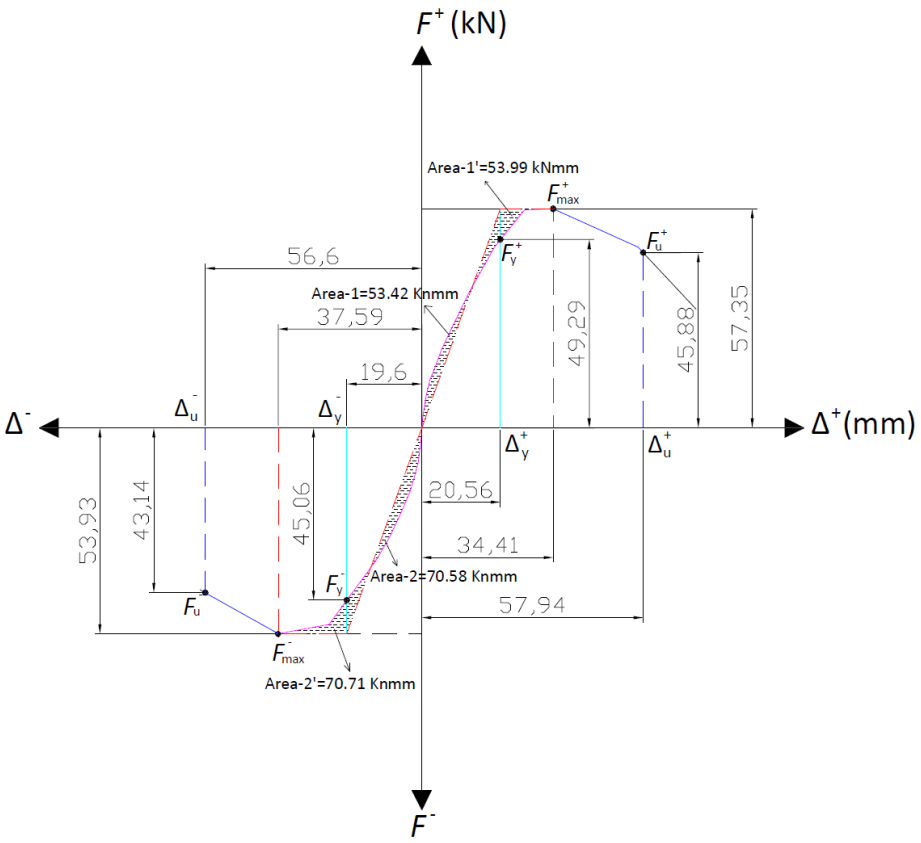

Figure 4.26. Equivalent energy method for S2-NSM.

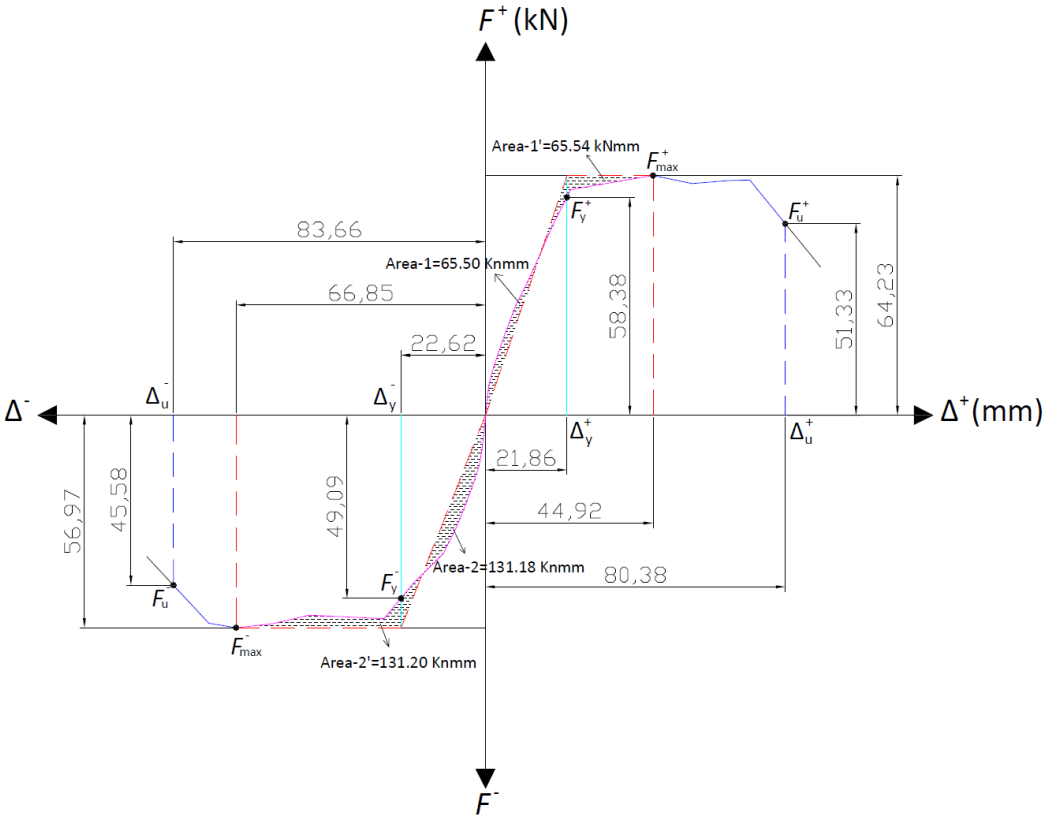

Figure 4.27. Equivalent energy method for S3-EB.

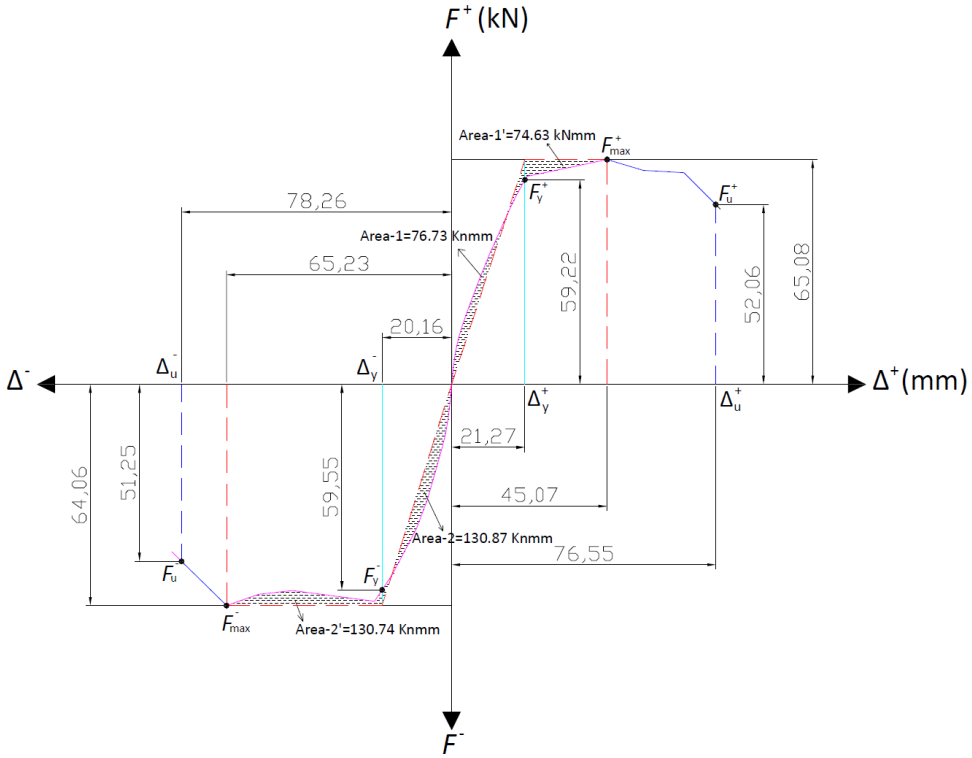

Figure 4.28. Equivalent energy method for S4-Hybrid.

Table 4.4. Comparison of ductility ratios.

Specimen Name	Push				Pull				$\mu_{average}$	Percentage change from Control
	F_y^+	Δ_y^+	Δ_u^+	μ_{push}	F_y^-	Δ_y^-	Δ_u^-	μ_{pull}		
	kN	mm	mm	-	kN	mm	mm	-	-	%
S1-Control	43.71	20.38	53.68	2.63	37.41	17.24	52.6	3.05	2.84	-
S2-NSM	49.29	20.56	57.94	2.82	45.06	19.6	56.6	2.89	2.85	0.37
S3-EB	58.38	21.86	80.38	3.68	49.09	22.62	83.66	3.70	3.69	29.7
S4-Hybrid	59.22	21.27	76.55	3.60	59.55	20.16	78.26	3.88	3.74	31.6

Table 4.4 shows that there is a very small difference between S1-Control and S2-NSM specimens in terms of the ratio of ductility considering the $\mu_{average}$ values. For S2-NSM, this value is 0.37%. However, for S3-EB and S4-Hybrid specimens, there is a significant increase in ductility. When these specimens are compared with the control specimen, the values for S3-EB and S4-Hybrid specimens are 29.7% and 31.6%, respectively. As a result, it has been observed that there is an increase in the ductility ratio when the strengthening methods are used together.

Comparison Energy Dissipation of the Joint:

For the calculation of the energy for each cycle, the cross-sectional area method (Liu *et al.*, 2021), shown visually in Figure 4.29, was used. In this method, taking the counterclockwise direction as the axis of rotation, multiply the height of each point by the difference of the distances of the previous and next points from the axis. This process is repeated for all points and the values are summed to obtain twice the cross-sectional area in Equation (4.3).

$$Area = \frac{1}{2}\sum \{y_n(x_{n-1} - x_{n+1})\} \tag{4.3}$$

In this study, two cycles were used for each drift ratio. The values given in Table 4.5 are the average values for each drift ratio and shown graphically in Figure 4.30. In addition, the values of cumulative energy dissipation are given in Table 4.6 and illustrated graphically in Figure 4.31.

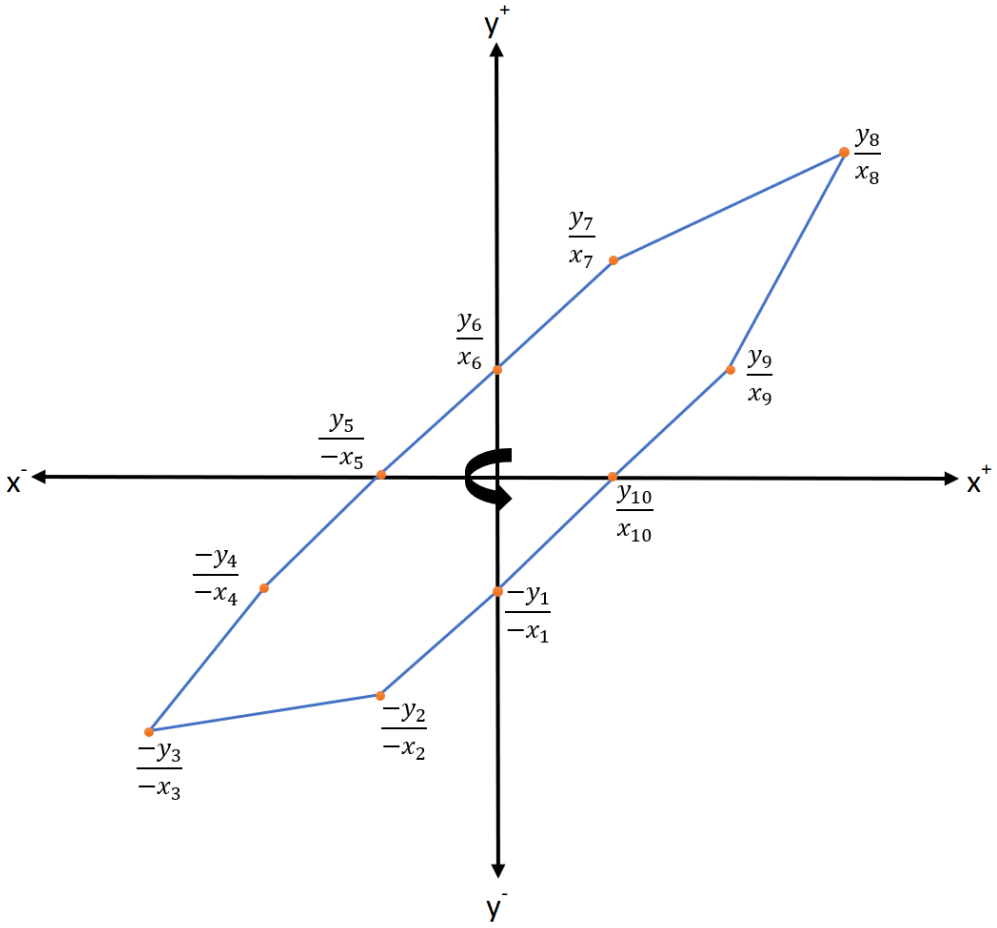

Figure 4.29. Cross-section area method.

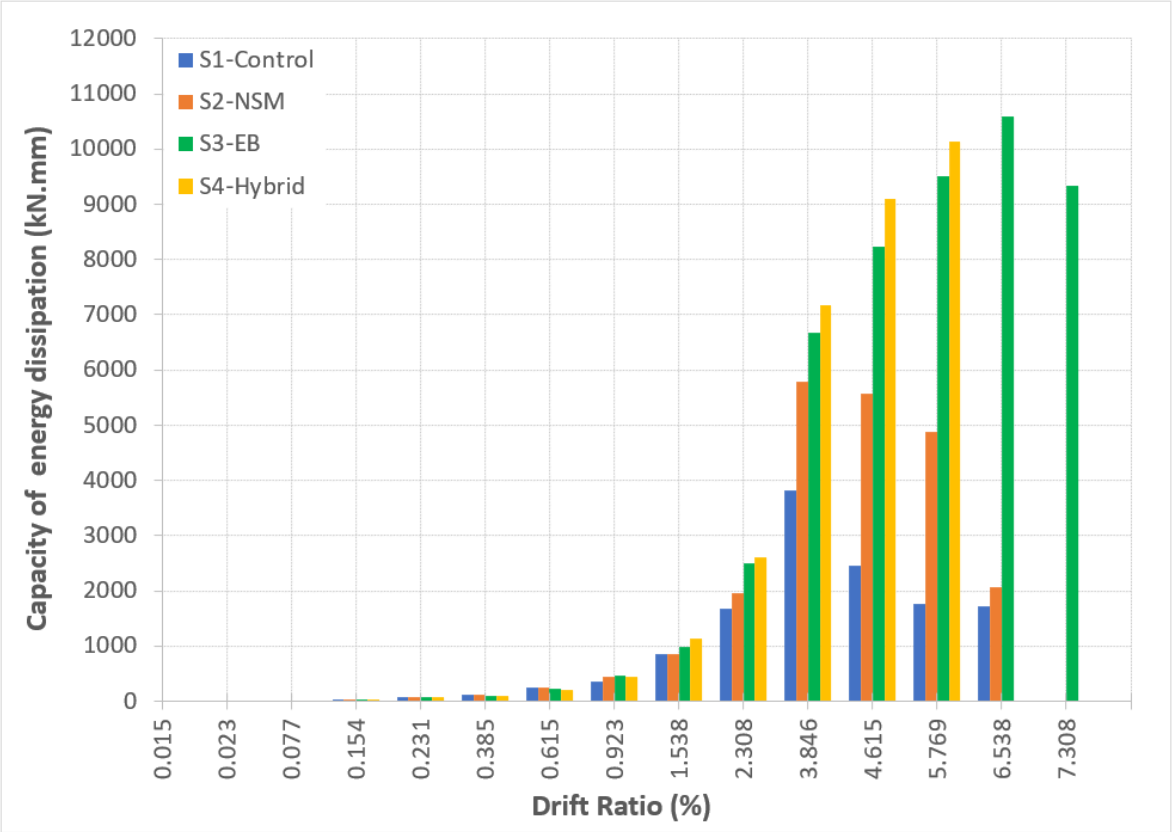

Figure 4.30. Comparison of the capacity of energy dissipation of the specimens.

As can be seen in Figure 4.30, the energy dissipated by the specimens with reinforcement with the joint is higher than that of the unreinforced specimens. It is clearly seen that both strengthening methods are effective, but the effectiveness of the strengthening application with FRP stands out in this respect. The highest energy dissipation capacity for S1-Control and S2-NSM specimens was 3.85% drift ratio. After this value, both specimens were weaker than the others in terms of energy absorption. Especially the energy dissipation capacity of the control specimen decreased dramatically. However, although there was a slight decrease in the next drift ratios (4.62% and 5.77%) in the S2-NSM specimen, it was similar to the value of maximum energy capacity. In this context, it can be seen that the specimen reinforced with NSM-steel in the joint area absorbed more energy than the control specimen. A closer examination of the S2-NSM specimen reveals that after a drift ratio of 5.77%, its energy dissipation capacity significantly decreases by approximately 42%. The reason for this is thought to be the formation of serious shear cracks along the column surface around the joint area. When S3-EB specimen is analysed, it reached its maximum energy capacity at 6.54% drift ratio and after this value, a decrease in energy capacity was observed. When it comes to the S4-Hybrid specimen, it reached the maximum energy dissipation capacity at 5.77% drift ratio.

Table 4.5. Comparison of the capacity of energy dissipation values of the specimens.

		Capacity of energy dissipation (kN.mm)			
Drift Ratio (%)	**Displacement (mm)**	**S1-Control**	**S2-NSM**	**S3-EB**	**S4-Hybrid**
0.015	0.2	0.5	0.4	0.3	0.5
0.023	0.3	1.1	1.6	0.9	0.7
0.077	1	15.4	14.4	9.1	8.2
0.15	2	37	33.9	33.6	31.9
0.23	3	66.4	68	64.7	67.2
0.39	5	121.6	126.7	105.8	96.4
0.62	8	241.5	257.2	224.2	206.6
0.92	12	345.5	450.8	463.9	435.2
1.54	20	860.4	851.3	981.8	1135
2.31	30	1681.6	1963.0	2507.6	2613.8
3.85	50	3813.4	5787.9	6682.5	7169.6
4.62	60	2449.8	5563.9	8237.1	9096.4
5.77	75	1770.3	4873.6	9507.8	10144
6.54	85	1728.4	2057.1	10599.7	No Data
7.31	95	-	-	9334.43	-

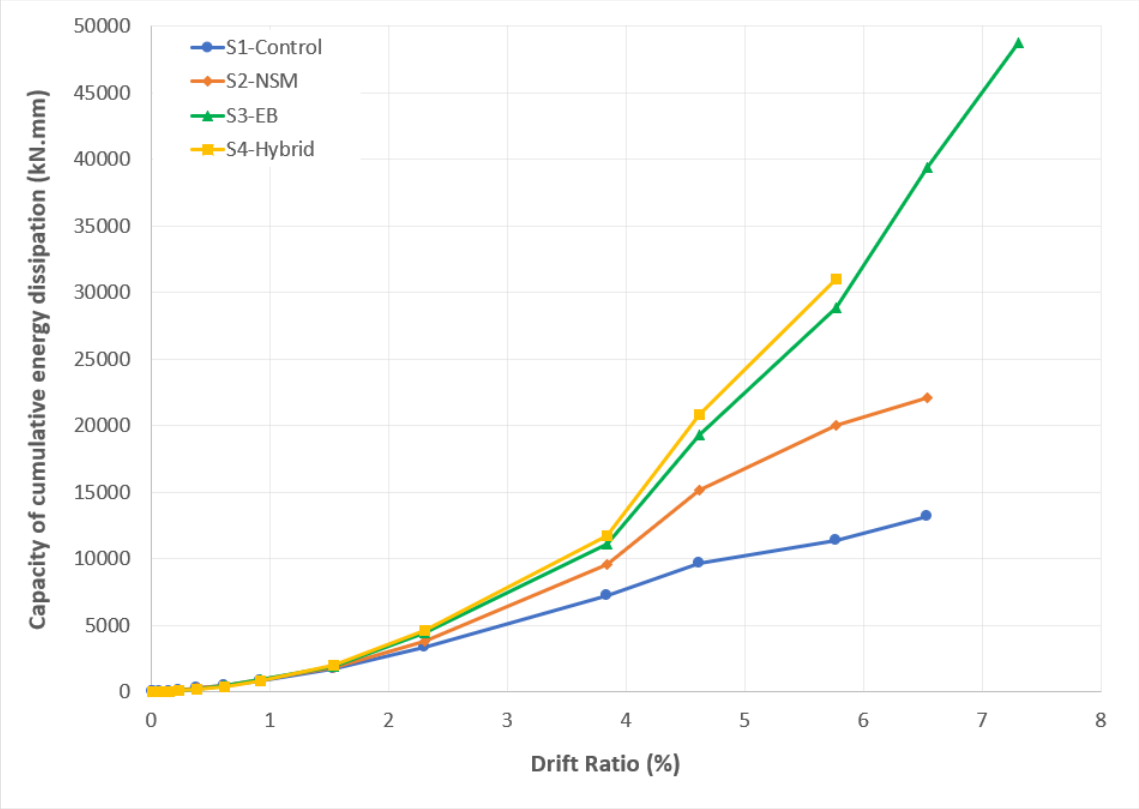

Figure 4.31. Comparison of the capacity of cumulative energy dissipation of the specimens.

When the graph in Figure 4.31 is analysed, the total energy dissipated by the specimens with reinforcing in the joint is higher than the unreinforced specimens. When the strengthened specimens are compared with the control specimen, it can be seen that there is a significant difference. Especially after 2.31% drift ratio, here, serious differences start to occur in terms of total energy dissipation capacity. For S3-EB and S4-Hybrid specimens, a significant increase is observed after 3.85% drift ratio compared to the other two specimens.

When all specimens are evaluated at 5.77% drift ratio, the increase in the total energy dissipation of the specimens obtained by the retrofitting application is 43% for the second specimen, 60.4% and 63.2% for the third and fourth specimens, respectively. From this point of view, it is seen that the cumulative energy dissipation of specimens without transverse reinforcement in the joint area and therefore without sufficient confinement can be increased by 40~45% with NSM application and by 60~65% with FRP application. In this context, it is concluded that the wrapping effect in the joint area greatly increases the energy dissipation capacity.

Table 4.6. Comparison of the capacity of cumulative energy dissipation values of the specimens.

		Capacity of cumulative energy dissipation (kN.mm)			
Drift Ratio (%)	**Displacement (mm)**	**S1-Control**	**S2-NSM**	**S3-EB**	**S4-Hybrid**
0.015	0.2	0.5	0.4	0.3	0.5
0.023	0.3	1.6	2	1.2	1.2
0.077	1	17.4	16.3	10.3	9.4
0.15	2	54.0	50.2	43.9	41.3
0.23	3	120.4	118.2	108.5	108.5
0.39	5	242	244.8	214.4	204.9
0.62	8	483.5	502.0	438.5	411.5
0.92	12	828.9	952.9	902.4	846.7
1.54	20	1689.3	1804.1	1884.2	1981.7
2.31	30	3370.9	3767.1	4391.8	4595.5
3.85	50	7184.3	9555.1	11074.3	11765.1
4.62	60	9634.1	15118.9	19311.4	20861.5
5.77	75	11404.4	19992.5	28819.2	31005.5
6.54	85	13132.8	22049.6	39418.9	No Data
7.31	95	-	-	48753.3	-

4.2.4 Strain Measurements

In this section, the data obtained from strain gauges during the experiment are discussed. The locations of the strain gauges are shown in Section 3.8.1 and the application of these devices to the reinforcement is detailed in Appendix-E Figure E1. Seven strain gauges were used for S1-Control, S3-EB, and S4-Hybrid specimens, while 10 strain gauges were used for S2-NSM. In this study, reinforcements with a diameter of 8 mm for transverse reinforcement and 16 mm for longitudinal reinforcement were used and the yield strengths of these reinforcements are given in Section 3.2.4. The yield strain for ϕ8 is 0.00249 mm/mm while the yield strain for ϕ16 is 0.00237 mm/mm. Considering these values, all strain gauges were carefully examined and the drift ratio where the reinforcement yielded was determined (see Table 4.7).

Table 4.7. Performance of strain gauges during the experiments.

Specimen Name	Gauge No	Location	Max strain	Yield (Y/N)	Drift Ratio (%) at yield
S1-Control	SG01	Column	0.05153	Yes	2.31
	SG02	Column	-	Failed	-
	SG03	Column	0.00023	No	-
	SG04	Column	0.00161	No	-
	SG05	Beam	0.05192	Yes	5.77
	SG06	Beam	0.05174	Yes	5.77
	SG07	Beam	-	Failed	-
S2-NSM	SG01	Column	0.00036	No	-
	SG02	Column	0.05033	Yes	5.77
	SG03	Column	0.00018	No	-
	SG04	Column	0.00119	No	-
	SG05	Beam	0.05184	Yes	2.31
	SG06	Beam	0.05226	Yes	2.31
	SG07	Beam	0.05192	Yes	5.77
	SG08	Joint	0.02036	Yes	1.54
	SG09	Joint	0.00244	No	-
	SG10	Joint	0.05256	Yes	1.54
S3-EB	SG01	Column	0.00041	No	-
	SG02	Column	0.00073	No	-
	SG03	Column	0.00013	No	-
	SG04	Column	0.00075	No	-
	SG05	Beam	0.00287	Yes	2.31
	SG06	Beam	0.01116	Yes	3.85
	SG07	Beam	0.00039	No	-
S4-Hybrid	SG01	Column	8.56E-05	No	-
	SG02	Column	0.00066	No	-
	SG03	Column	8.56E-05	No	-
	SG04	Column	0.00068	No	-
	SG05	Beam	0.00233	No	-
	SG06	Beam	0.01629	Yes	3.85
	SG07	Beam	0.00057	No	-

The results given in Table 4.7 and Figure 3.26 in section 3.8.1, where the locations of the strain gauges are shown, are evaluated together and commented below for each specimen.

For the S1-Control specimen, the strain gauge SG01 shows that the reinforcement yielded at step 40, i.e., cycle 20. This value corresponds to the second cycle of the 2.31% drift ratio. SG02 was probably damaged, and no data could be obtained. SG03 and SG04 showed no yielding of the reinforcement during the experiment. When strain gauges SG05 and SG06 were analysed, it was found that the reinforcement with strain gauge SG05 yielded at step 50 (5.77% drift ratio in the first cycle at pulling direction), while the reinforcement with strain gauge SG06 yielded at step 52 (5.77% drift ratio in the second cycle at pulling direction). When the strain gauge of SG07 was probably damaged, and no data could be obtained.

For the S2-NSM specimen, it was observed that the reinforcements did not yield throughout the experiment in SG01, SG03 and SG04 gauges, but SG02 gauge yielded at step 49, i.e., cycle 25. This value corresponds to the first cycle of the 5.77% drift ratio. When SG05 and SG06 strain gauges on the beam bottom and top reinforcement were analysed, it was found that the reinforcement with strain gauge SG05 yielded at step 37 (2.31% drift ratio in the first cycle at pushing direction), while the reinforcement with strain gauge SG06 yielded at step 38 (2.31% drift ratio in the first cycle at pulling direction). When the strain gauge of SG07 was analysed, it was observed that this reinforcement yielded at step 49 (5.77% drift ratio in the first cycle at pushing direction). When it comes to the results of strain gauges SG08, SG09 and SG10, which were added to the S2-NSM specimen, were examined, it was observed that there was no yielding in the u-shaped reinforcement in the centre of the beam-column joint (strain gauge SG09). However, it was found that the reinforcement with strain gauge SG08 yielded at step 33 (1.54% drift ratio in the first cycle at pushing direction) and strain gauge SG10 yielded at step 34 (1.54% drift ratio in the first cycle at pulling direction).

For the S3-EB specimen, it was observed that the reinforcements did not yield throughout the experiment in SG01, SG02, SG03, and SG04 gauges. In the same way, strain gauge SG07, which was placed on the transverse reinforcement in the beam element, was also found not to yield. When SG05 and SG06 strain gauges on the beam top and bottom reinforcement were analysed, it was found that the reinforcement with strain gauge SG05 yielded at step 37 (2.31% drift ratio in the first cycle at pushing direction), while the reinforcement with strain gauge SG06 yielded at step 42 (3.85% drift ratio in the first cycle at pulling direction).

For the S4-Hybrid specimen, it was determined that the reinforcements did not yield throughout the experiment in SG01, SG02, SG03, and SG04 gauges. Likewise, strain gauge SG07, which was placed on the transverse reinforcement in the beam element, was also found not to yield. Once SG05 and SG06 strain gauges on the beam top and bottom reinforcement were analysed, it was found that the reinforcement with strain gauge SG05 did not yield during the experiment while the reinforcement with strain gauge SG06 yielded at step 42 (3.85% drift ratio in the first cycle at pulling direction).

In addition, detailed information on strain gauges is described in Appendix-I.

4.3 SUMMARY

This chapter provides the experimental results of unreinforced and reinforced concrete beam-column junctions. The efficacy of the suggested retrofitting strategy is examined by analyses of global and local behaviour, failure modes, strength, stiffness, ductility ratio, and characteristics of energy dissipation. The following findings from the experiment are based on the observed damage and hysteretic behaviour of the specimens considered.

1. In the unreinforced specimen (S1-Control), the test findings verified the structural failure of beam-column connections that were inadequately specified and built in accordance with the Turkish Earthquake Code (TEC 1998). The specimens exhibited a failure mechanism highlighted by shear damage to the joints, showing as a combination of local deformation and diagonal cracks.
2. When the unreinforced specimen was examined, it was observed that the first hairline damage occurred in the beam region at 0.23% drift ratio in the early stages of loading. At 0.39% drift ratio, the first crack started to form in the beam-column joint region and lasted until 0.92%. At 0.92% drift ratio, 45-degree shear cracks started to form in the joint area, and severe cracks occurred in this area at 3.85% drift ratio. For drift ratios of 4.62%, 5.77%, and 6.54%, it was observed that serious deformations occurred both in the areas where the beam was connected to the column and in the beam-column junction area. Once the damage diagrams of the second specimen strengthened with the NSM technique were examined, the first hairline cracks were detected in the beam region in the pulling direction at a 0.39% drift ratio. Shear cracks were observed at the drift ratios of 1.54% and 2.31% in the joint area. When the damages occurred at 4.62%,

5.77%, and 6.54% drift ratios were carefully examined, it was observed that no serious deformations occurred in the beam-column joint area. This study did not observe the damage between concrete and epoxy reported in the literature, but rather the epoxy kept the introduced steel bonded to the concrete, leading to crushing of the concrete. At these drift ratios, it is clearly seen that the damage is transferred from the beam-column joint to the beam. When the third specimen reinforced with the EB method was examined, the first hairline cracks were detected on the beam in the push direction at a 0.92% drift ratio. Flexural cracks developed on the beam in both push and pull orientations at a drift ratio of 1.54%. Cracks began to form on the beam near the area where the retrofit ended at a 2.31% drift ratio, in addition to the cracks that were already formed at the previous drift ratio. When the specimen with a 3.85% drift ratio was examined, it was observed that a serious crack was formed at the top of the beam in the push direction. 4.62%, 5.77%, and 6.54% drift ratios; no deformations were observed in the beam-column joint area. Severe damages, including disintegration and rupture of the concrete on the beam, were observed on both sides of the specimen at a 7.31% drift ratio; however, only minimal debonding of the FRP was observed. Analysis of the damage diagrams of the fourth specimen reinforced using the NSM+EB approach revealed the presence of initial hairline cracks at a drift ratio of 0.92% in the push direction on the beam. At a drift ratio of 1.54%, flexural cracks were detected on the beam in both the pushing and pulling directions. At a 2.31% drift ratio, in addition to the cracks formed at the previous drift ratio, it was determined that cracks started to form on the beam near the area where the retrofit ended. Examining the specimen with a 3.85% drift ratio revealed the formation of a serious crack at the top of the beam in the pushing direction. 4.62% and 5.77% drift ratios, no deformations were observed in the beam-column joint area. At the 5.77% drift ratio, serious damages such as disintegration and rupture of the concrete on the beam occurred on both sides of the specimen. The combination of methods employed for the fourth specimen revealed comparable damage to those observed in the third specimen, thereby indicating the effectiveness of wrapping when the two methods were used together. Furthermore, this specimen did not exhibit the same level of damage as the second specimen equipped with NSM reinforcement. The integration of NSM and EB approaches was shown to effectively mitigate damage in the beam-joint region and transmit all damage to the beam. Unfortunately, the post-experiment

inspection detected tears in the GFRP fabric at both the top and bottom sides of the beam wherever retrofit was added; however, these were less than the EB method.

3. There has been a significant improvement in the global performance of S2-NSM, S3-EB and S4-Hybrid compared to the original (S1) connection. The S2-NSM specimen has a capacity increase of 12.9% for push and 15.3% for pull. Likewise, the S3-EB specimen has a 26.4% capacity increase for pushing and a 21.8% capacity increase for pulling, while the S4-Hybrid specimen has a 28.1% capacity increase for pushing and a 37% capacity increase for pulling. In light of these results, the most successful strengthening technique was the S4-Hybrid specimen in terms of capacity; however, the EB method also showed a significant increase in capacity.
4. The energy dissipation levels of the strengthened specimens are much higher compared to the control specimen, particularly at drift levels of 2.31% or higher. For instance, the energy absorbed by the strengthened specimens at a 3.85% drift ratio was 9555 kN-mm (S2-NSM), 11074 kN-mm (S3-EB), and 11765 kN-mm (S4-Hybrid). These values represent increases of 33%, 54%, and 63%, respectively, over the corresponding values for the control specimen (S1-Control).
5. Experiments indicate that both control and retrofitted specimens exhibit a declining trend in stiffness. All specimens exhibited a uniform decline in stiffness until reaching a drift ratio of around 0.077%, beyond which variations became apparent. The S4-Hybrid specimen exhibits higher stiffness compared to the other specimens. It is evident from the stiffness curves of S3-EB and S4-Hybrid specimens that they exhibit higher stiffness for drift ratios other than 3.85%. The decrease in stiffness observed in these two specimens is believed to be caused by the abrupt failure of the FRP material at the beam-wrapping region. Based on the 5.77% drift ratio values observed at the conclusion of the experiment, the stiffness of all specimens decreased by 97.1% for the S1-Control specimen, 96.64% for the S2-NSM specimen, 92.4% for the S3-EB specimen, and 90.3% for the S4-Hybrid specimen, in comparison to their initial stiffness. The reduction in specimen stiffness is consistent with the damage mechanisms and distribution presented in the damage observations.
6. No significant difference exists between S1-Control and S2-NSM specimens in terms of the ductility ratio. For S2-NSM, the average value of μ was 0.37%, while the ductility of S3-EB and S4-Hybrid specimens were 29.7% and 31.6%, respectively, representing a significant increase.

In conclusion, the EB and hybrid retrofitting strategies showed significantly better performance in terms of strength and ductility and slightly better in terms of stiffness. Of the 3 techniques, hybrid was shown to be the best; however, only marginally so. The next chapter develops a finite element model that can simulate the behaviour of the control specimen and the specimen that adopted the hybrid retrofitting strategy as the basis for designing these connections.

CHAPTER 5. NUMERICAL PROGRAMME

5.1 GENERAL

This chapter provides a comprehensive account of the development of nonlinear three-dimensional finite element (FE) models that simulate the behaviour of exterior, reinforced concrete beam-column joints under monotonic static loading. The finite element models are constructed using the comprehensive FE software ABAQUS and then verified by comparing them with the experimental results presented in the previous section.

Within the scope of this study, the envelope curves obtained as a result of monotonic static loading and the envelope curves obtained from experiments as a result of cyclic loading are compared. The reason for using non-linear monotonic static loading in the modelling is that dynamic analysis increases the computational cost (Ridwan, 2016). In addition, most engineers (especially true in Turkey) use a quasi-static load approach to calculate design seismic forces. In this method, seismic forces are reduced by a response modification factor (R in the Turkish Earthquake Code (TEC 1998)- behaviour factor q, in Eurocode 2 (EN1992-1-1 2004)). This factor is dependent on the structural framing system and the ductility of the connections. The ductility of the connections is defined in the codes as the rotation of the connection at ultimate load divided by the rotation of the connection at first yield and these values are obtained by a pushover test (i.e. non-linear monotonic loading). In the literature there are many examples of researchers used monotonic static loading in numerical analysis using envelope curves obtained under cyclic loads (Najafgholipour *et al*. 2017; Diro and Kabeta 2020; Najafgholipour and Arabi 2021; and Abdelwahed *et al*. 2021). In these studies, very meaningful results were obtained using this approach, and similar deformations were obtained on the specimens.

The purpose of the model is both as a tool to provide insight into the experimental results and to demonstrate the feasibility of a predictive tool for future analysis of similar connections with the aim of providing design guidance.

The numerical analyses showed that the static loading of the specimen (S1-Control), the specimen reinforced with NSM (S2-NSM) and the hybrid specimen (S4-Hybrid) using numerical simulations were close to the experimental results.

Following the validation of the models, the main response characteristics investigated include the overall hysteresis curve, joint deformation, and crack pattern. Based on the experimental

and numerical results, the effectiveness of the used strengthening techniques for RC beam-column connections is evaluated in the next section.

5.2 GEOMETRIC MODELLING, ELEMENT TYPE AND MESH

The implemented 3D finite element models explicitly include the concrete beam-column junction, embedded longitudinal and transverse reinforcement bars, FRP sheets, epoxy adhesive, and steel loading plates. Figure 5.1 displays the reinforced concrete beam-column junction, FRP sheets, epoxy adhesive, and support plates as three-dimensional geometric entities, with the embedded reinforcement bars shown as one-dimensional entities.

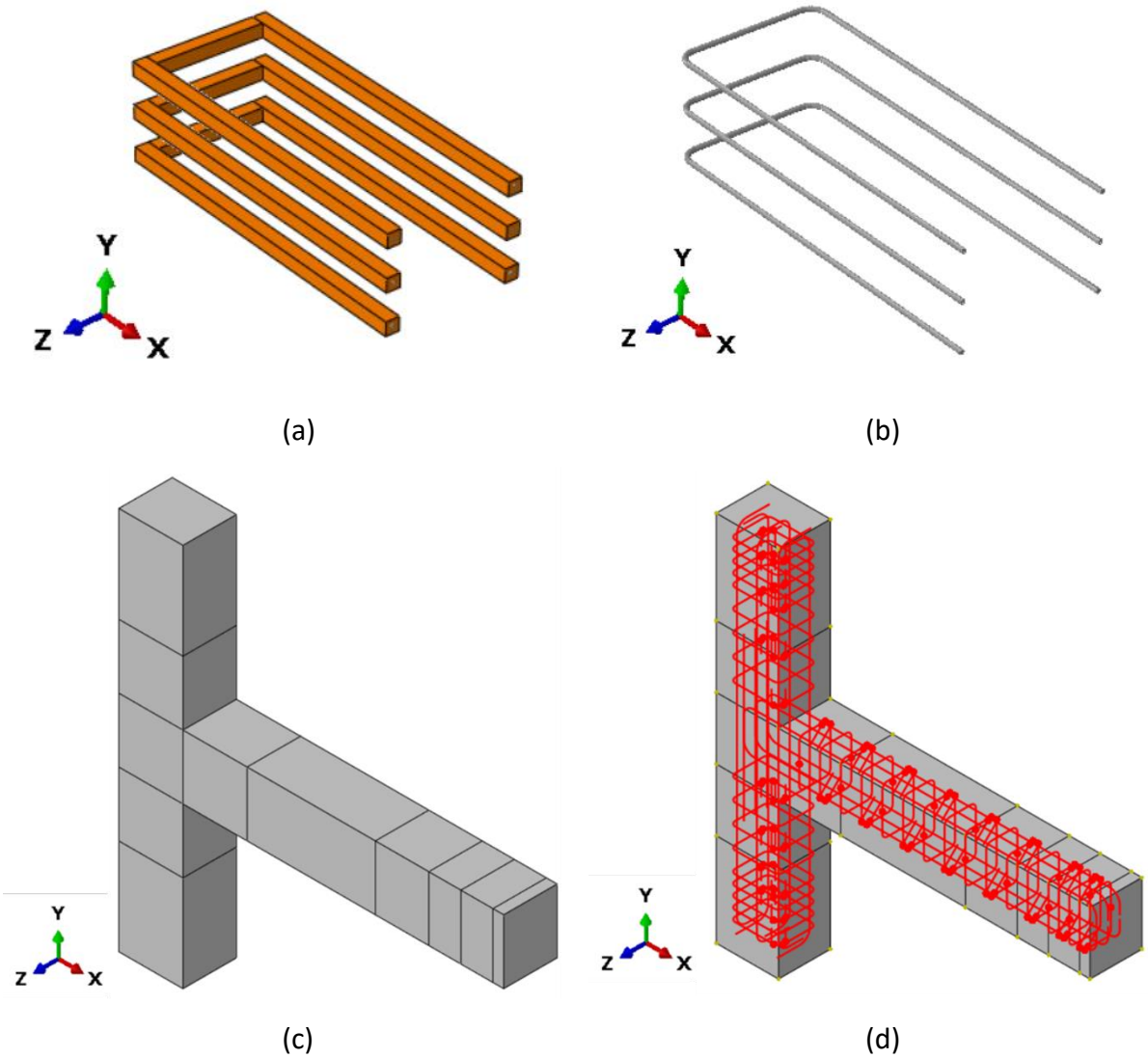

Figure 5.1. Components of the numerical model; (a) Epoxy adhesive; (b) U-shaped steel rebar; (c) concrete part; (d) steel reinforcements; (e) FRP sheet; (f) support plate.

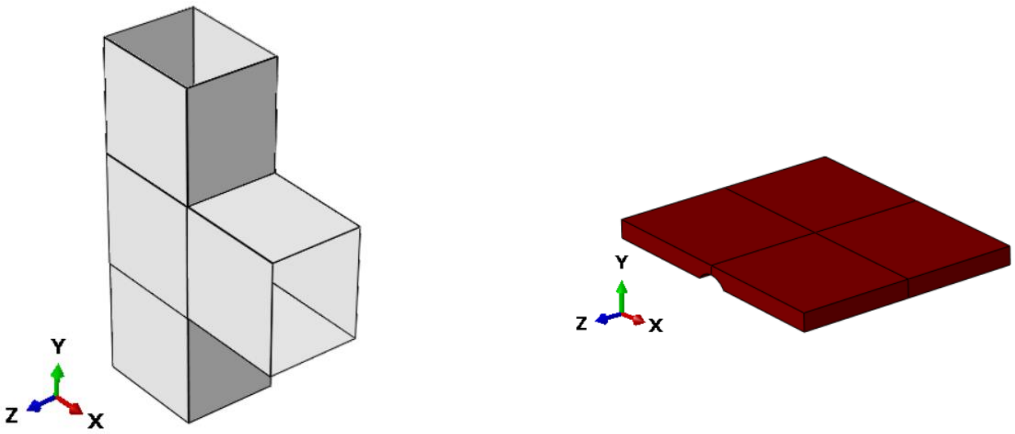

(e) (f)

Figure 5.1. Components of the numerical model; (a) Epoxy adhesive; (b) U-shaped steel rebar; (c) concrete part; (d) steel reinforcements; (e) FRP sheet; (f) support plate (continue).

5.2.1 Concrete Joint, Support of Column Ends and Loading Plates

In the finite element analysis modelling, the footings, slabs, columns, and beams can be approximated in terms of material and represented using C3D8R (8-node linear brick element with reduced integration and hourglass control) elements in Abaqus. The node has the capability to simulate and calculate plastic deformation, crushing and cracking values. Figure 5.2 shows the shape and node locations for C3D8R element to model concrete beam-column joint in ABAQUS (Abaqus Analysis User's Guide, 2016). These first order brick elements possess three translational degrees of freedom at each node, enabling them to handle trilinear stress fluctuations. Furthermore, the usage of reduced integration helps to minimise the incidents of shear and volumetric locking (Ridwan, 2016). In this study, C3D8R element was used for concrete of the beam-column connection part of the specimen. In addition, for the loading plates and support of column ends were represented using discrete parts.

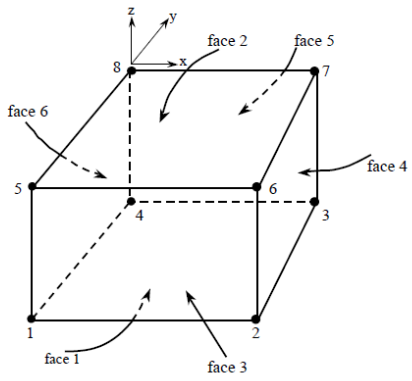

Figure 5.2. C3D8R (Eight-node brick element) (Abaqus Analysis User's Guide, 2016).

5.2.2 Reinforcement Bars

In Abaqus, using one-dimensional elements to model reinforcement bars is suitable because the cross-sectional dimensions of the reinforcement bars are much smaller compared to their length. T3D2 is a 2-node truss element that only resists axial forces (tension or compression) and is computationally efficient, making it ideal for modelling rebar when bending and torsion are not significant. The choice of element should align with the specific analysis requirements, balancing the need for accuracy with computational efficiency.

An investigation was undertaken by Gebreyohaness (2013) to identify the appropriate element type for modelling reinforcing bars. T3D2 elements exhibited a superior agreement with actual findings while requiring less computational resources. Therefore, the T3D2 truss element shown in Figure 5.3 is employed to represent the reinforcing bar in present study.

Figure 5.3. T3D2 (2-node, 3-dimensional truss element) (Abaqus Analysis User's Guide, 2016).

5.2.3 FRP sheets

In Abaqus, FRP sheets are modelled using by 4-noded linear elastic S4R shell element depicted in Figure 5.4. The element has three-degrees of freedom at each node: translations in the nodal x, y, and z directions. The bond between FRP and concrete was simulated using tie model because no separation between concrete and FRP material was observed during the experiment. This model gives appropriate results with a good correlation with the experimental test results. In addition, the fibre direction of FRP sheet is depicted in Figure 5.5. Moreover, the laminate was modelled using ABAQUS composite modeller and the layup is presented in Appendix-J.

Figure 5.4. Shell S4R geometry (Abaqus Analysis User's Guide, 2016).

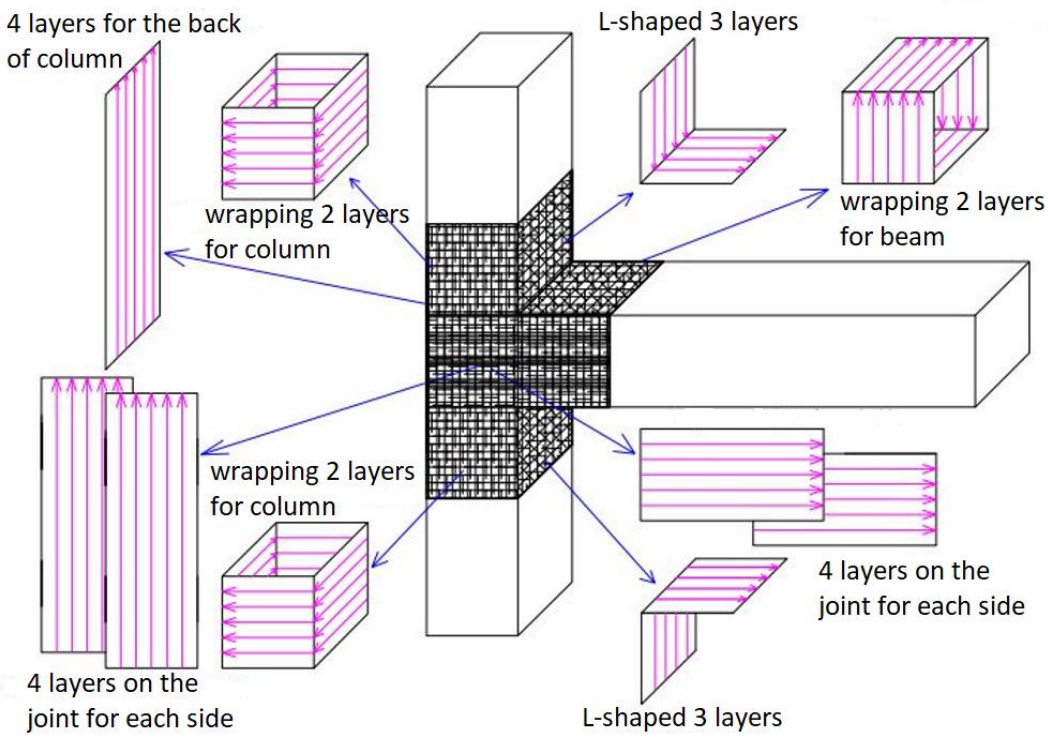

Figure 5.5. Fiber direction of FRP sheet.

5.2.4 Meshing

Meshing in Abaqus is a critical step in the finite element method (FEM) for model accuracy and computational efficiency.

Mesh quality has a direct impact on the meaningful and accurate interpretation of results. A bad mesh can give inaccurate results, which can lead to incorrect interpretations and faulty engineering decisions. In summary, meshing in Abaqus is a process that directly affects model accuracy, solution stability and computational efficiency. Meshing ensures accurate representation of geometry and material behaviour, which increases the reliability of results. An appropriate mesh is critical to the success of engineering analyses. Details of the mesh used for concrete, steel reinforcement, epoxy, and fibre-glass sheeting are given in section 5.5. In this thesis, 12.5 mm and 25 mm mesh was selected for concrete elements, a 12.5 mm for epoxy and a 25 mm for FRP sheets while a 10 mm mesh was chosen for steel rebars.

In the control model (S1-control), the total number of elements are 103816 (97920 linear hexahedral elements of type C3D8R for concrete, 5896 linear line elements of type T3D2 for steel bars). In the S2-NSM specimen, the total number of elements are 104230 (97920 linear hexahedral elements of type C3D8R for concrete (96576) and epoxy (1344), 6310 linear line elements of type T3D2 for steel bars (5896) and u-shaped steel bars (414)).

In the hybrid model (S4-Hybrid), the total number of elements are 106222 (97920 linear hexahedral elements of type C3D8R for concrete (96576) and epoxy (1344), 6310 linear line elements of type T3D2 for steel bars (5896) and u-shaped steel bars (414), and 1992 linear quadrilateral elements of type S4R for FRP sheets). The meshing approach used for the models is shown in Figure 5.6.

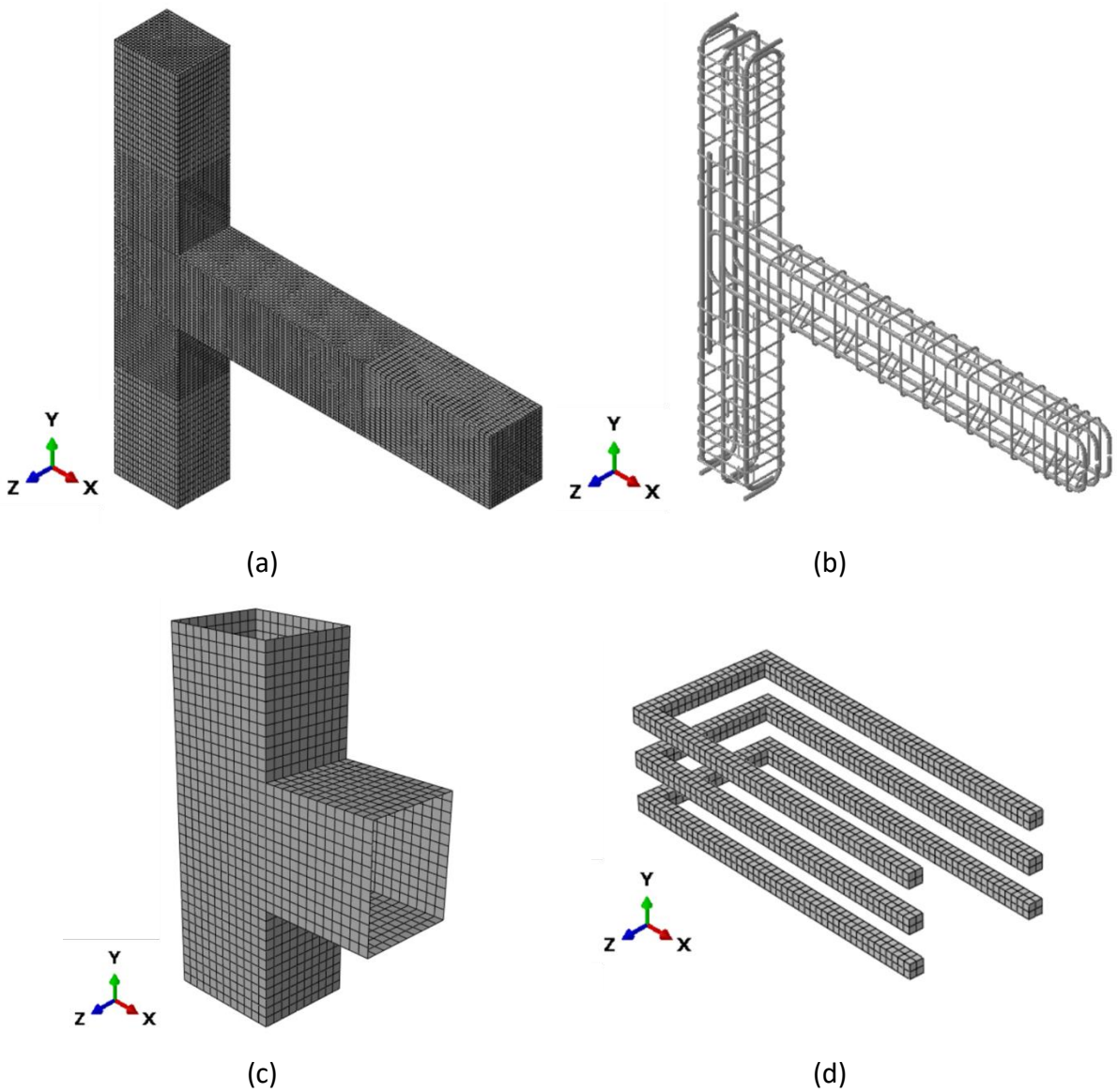

Figure 5.6. Modelled specimens: (a) Concrete elements mesh; (b) Reinforcement details of joint; (c) FRP sheet element mesh; (d) Epoxy adhesive element mesh.

5.3 MATERIAL BEHAVIOUR

5.3.1 Concrete

Plastic Behaviour of Concrete:

The Concrete Damaged Plasticity (CDP) model is one of the most widely used models in Abaqus for simulating the behaviour of concrete (Ridwan, 2016). It accounts for the plasticity and damage mechanisms that occur in concrete under compressive and tensile loading. It is suitable for static and dynamic loading, including cyclic loading in seismic analysis, and is commonly used for simulating the response of reinforced and plain concrete structures such as beams, columns, beam and column joints, and slabs. The Concrete Damage Plasticity (CDP) model was used for plain concrete in this research.

The CDP model was developed on the yield functions that Lubliner *et al.* (1989) proposed and were subsequently modified by Lee and Fenves (1998). It integrates both plasticity and damage mechanics to represent the behaviour of concrete. It allows the material to undergo plastic (irreversible) deformations and simultaneously accounts for the degradation of the material's stiffness due to cracking (tensile damage) and crushing (compressive damage). The ABAQUS documentation provides a comprehensive explanation of the CDP model (Abaqus Online Documentation, 2006).

The CDP model involves many input parameters to extend the uniaxial stress-strain characteristics of concrete to the three-dimensional stress space. Main parameters considered in this study are the dilation angle (ψ), flow potential eccentricity (ϵ), ratio of the compressive strength under biaxial loading to uniaxial compressive strength (f_{b0}/f_{c0}), ratio of the second stress invariant on the tensile meridian to that on the compressive meridian (K_c), viscosity parameter (μ) (Abaqus Analysis User's Guide, 2016). These are explained at the following:

- Dilation angle, which defines the direction of plastic flow through the incremental plastic strain vector. The dilation angle (ψ) in the Concrete Damage Plasticity model falls within the specified range of 31° to 42° (Bilal *et al*., 2023). In this study, the dilation angle (ψ) was calculated as 32° using Equation (5.1) proposed by Trimarentra *et. al* (2018).

$$\psi = \left[0.117 \times f_c^{`} + 28.965\right]^{\circ} \quad (5.1)$$

where $f_c^{`}$ is the compressive strength of concrete and this value is 24.35 MPa in this study.

- The flow potential eccentricity (ϵ) defines the shape of the flow potential function, and the default value in ABAQUS is 0.1.
- The ratio of the compressive strength under biaxial loading to uniaxial compressive strength (f_{b0}/f_{c0}); According to Lubliner *et al.* (1989), this value is between 1.10 and 1.16, and the default value in ABAQUS is 1.16.
- The yield stress ratio (K_c) controls the relative shape of the yield surface in the deviatoric plane. It defines the ratio of the tensile meridian yield stress to the compressive meridian yield stress. The value of this parameter is between 0.5 and 1.0. When the ratio (K_c) is equal to 1, the stress becomes independent of the third deviatoric stress invariant. The default value of K_c in ABAQUS is 0.667 (Abaqus Analysis User's Guide, 2016).
- This viscosity parameter (μ) is used to introduce rate dependency into the model, helping with convergence in problems where the concrete undergoes severe damage or where the solution would otherwise be unstable. In the literature, no single value or method for choosing it (without calibration) exists. Existing studies have chosen the viscosity parameter via calibration and the results examples of recommended values are as follows: 0.001 by Dere and Koroglu (2017), 0.007985 by Najafgholipour *et al*. (2017), 0.0005 by Demir *et. al,* (2018), 0.0058 by Raza *et al.* (2019), 0.01 by Diro and Kabeta (2020), and 0.0001-0.008 by Abdelwahed *et al*. (2021). In this study, the viscosity parameter was calibrated and chosen as 0.003 and the detailed calibration procedure is explained in section 5.5.

The CDP parameters for modelling in this study are given in Table 5.1.

Table 5.1. Utilised values of the parameters related to the Concrete Damage Plasticity (CDP) model.

Dilation angle, (ψ)	Eccentricity, (ϵ)	f_{b0}/f_{c0}	K_c	Viscosity parameter, (μ)
32°	0.1	1.16	0.667	0.003 (calibrated)

According to EN1992-1-1 section 3.1.3(4) the value of Poisson's ratio (v) may be taken equal to v = 0.2. Moreover, the concrete's unit weight is specifically defined in EN1991-1-1 Annex A. Density of plain unreinforced concrete can be taken equal to $\gamma_{concrete}$ = 2400 kg/m^3.

Concrete in Compression:

The stress-strain relationship of concrete under uniaxial compression can be characterised by three distinct areas, namely the elastic (orange line), hardening (blue line), and softening (red line) phases as shown in Figure 5.7. Under uniaxial compression, concrete initially exhibits a linear-elastic response until the applied compressive stress reaches 30-40% of its maximum strength. Following that, the stress-strain curve enters the hardening phase, during which concrete stress increases until it reaches its maximum compressive strength, while tangential stiffness gradually declines from its initial value (specified by Young's modulus for concrete) to zero. Once the ultimate compressive stress is reached, the material response enters the softening region. This part of the stress-strain curve occurs beyond the point where tangential stiffness becomes zero and is characterized by a rapid decline in concrete strength as it softens and loses its load-bearing capacity.

Mander unconfined concrete model was used in the numerical study. In Appendix-D, the stress-strain relationship of the concrete compressive load was explained in detail.

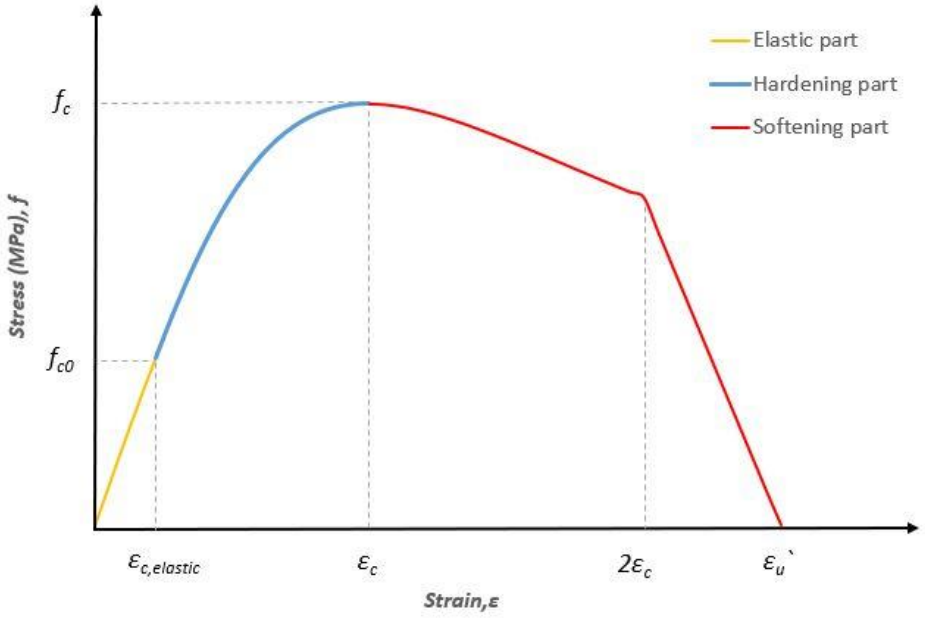

Figure 5.7. Mander model for unconfined concrete with phases (Mander *et al*., 1988).

Figure 5.7 depicts the elastic linear part of the concrete stress-strain behaviour, which is calculated using the expression in Equation (5.2).

$$f_{c0} = E_c \times \varepsilon_{c,elastic} \tag{5.2}$$

Here, f_{c0} represents the concrete stress in elastic part, $\varepsilon_{c,elastic}$ denotes the concrete strain within this elastic region, and E_c is the concrete`s modulus of elasticity. In this research, the value of f_{c0} was calculated using $0.4f_c$ (TS 500, 2000), defining the behaviour of concrete up to 40% of its strength in the elastic region was significant in determining the effective elastic modulus. And the elastic modulus of concrete was calculated using the Equation 5.2.

The hardening part between f_{c0} and f_c where the stress continues along the ascending branch up to the peak concrete strength f_c at ε_c. Uniaxial compressive behaviour can be defined by either experimental tests or existing constitutive models, such as those proposed by Mander *et al.* (1988) for unconfined concrete.

The softening part is where the stress has a decreasing trend after the peak of f_c. When looking at the Figure 5.7, it can be seen that the hardening zone of unconfined concrete is approximately parabolic until $2\varepsilon_c$. Conversely, the softening region demonstrates a linear behaviour until ε_u`. Within the scope of this study, the concrete strain at peak stress (ε_c) was measured using a strain gauges concrete cylinder and plotting the stress versus strain graph. The stress-strain graph together with the details of this testing is given in Appendix-B Figure B2. The final value for ε_c adopted for this study was 0.0024.

Concrete in Tension:

The definition of the formation of micro-cracks to macro cracks in finite element analysis is frequently referred to as tension softening, and it is conducted by introducing a crack opening law. The crack opening law is usually expressed in terms of fracture energy, but it can also be characterised using a stress-strain or stress-displacement relationship (see Figure 5.8). The fracture energy (G_f) is a material characteristic that describes the amount of energy required to open a unit area of a crack, resulting in a stress-free crack (Malm, 2006). The fracture energy of concrete can be calculated using the Remmel (1998) method as given in Equation (5.3) and according to Bangash (2001), it ranges from 50 to 200 N/m for ordinary concrete.

$$G_f = 65 \times \ln\left(1 + \frac{f_c}{10}\right) \tag{5.3}$$

where f_c is the concrete compressive strength.

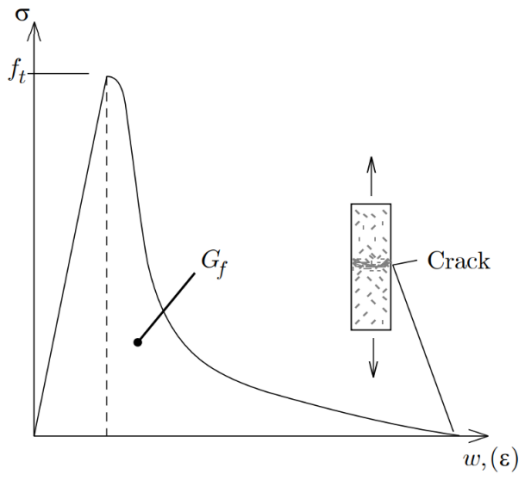

Figure 5.8. Crack opening with fracture energy of concrete (Björnström *et al*., 2006).

The region under the unloading phase of the σ-ω graph in Figure 5.8 represents the fracture energy. In this work, G_f was computed using Equation (5.3) as 0.08021 N/mm.

Various methodologies can be implemented to describe the brittle behaviour of concrete through the concepts of fracture energy. The optimal method is to characterise tensile cracking by a linear approximation, where a linear reduction in strength occurs post-cracking, as seen in Figure 5.9 (a) (Karlsson and Sorensen, 2006). The brittle behaviour of concrete under tension can be defined more comprehensively by a bilinear function, as demonstrated by Hillerborg (1985) and illustrated in Figure 5.9 (b). A more precise approach to characterising brittle behaviour is to employ an exponential expression, as experimentally demonstrated by Cornelissen *et al.* (1986) and illustrated in Figure 5.9 (c).

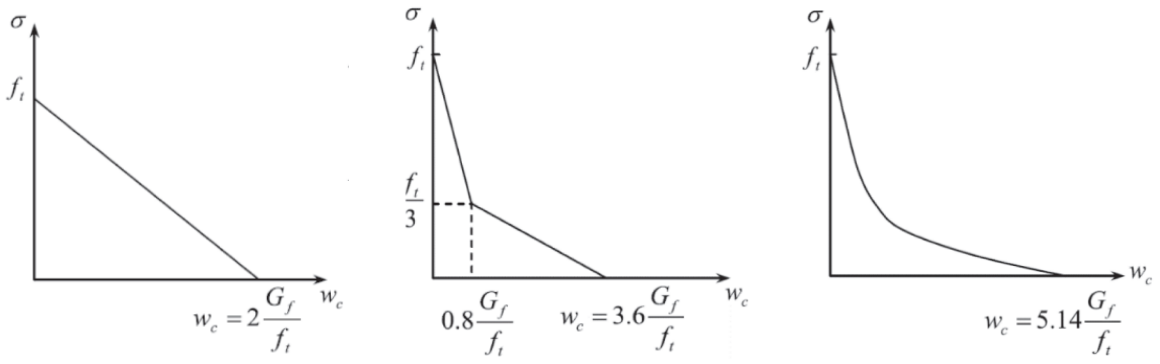

(a) (b) (c)

Figure 5.9. Tension softening model: (a) Linear function (Karlsson and Sorensen, 2006); (b) Bilinear function (Hillerborg, 1985); and (c) Exponential function (Cornelissen *et al*., 1986).

In Figure 5.9, f_t is the concrete tensile strength, ω_c is the crack opening displacement at which stress can no longer be transferred.

Earij *et al*. (2017) argued that using the bi–linear and exponential tension stiffening laws (shown in Figure 5.9), has no effect on the predicted post–peak load– deflection response providing that the same G_f value is used. The tail of the exponential law is 1.5 longer than that of Hillerborg (1985) bi–linear law; yet, the predicted response remains unaffected. To this end, the numerical response predicted with either of the bi–linear curves shown in Figure 5.9 is expected to be similar. Hence, the bi–linear tension softening model of Hillerborg (1985) was chosen due to its wide use in the computational modelling of concrete.

Defining compressive behaviour and tension stiffening:

Defining compressive behaviour and tension stiffening are illustrated in Figure 5.10 (a) and (b), respectively. Two hardening variables are used to independently characterise the damage states in compression and tension. These are denoted by $\varepsilon_c^{pl,h}$ and $\varepsilon_t^{pl,h}$, which represent equivalent plastic strains in compression and tension, respectively.

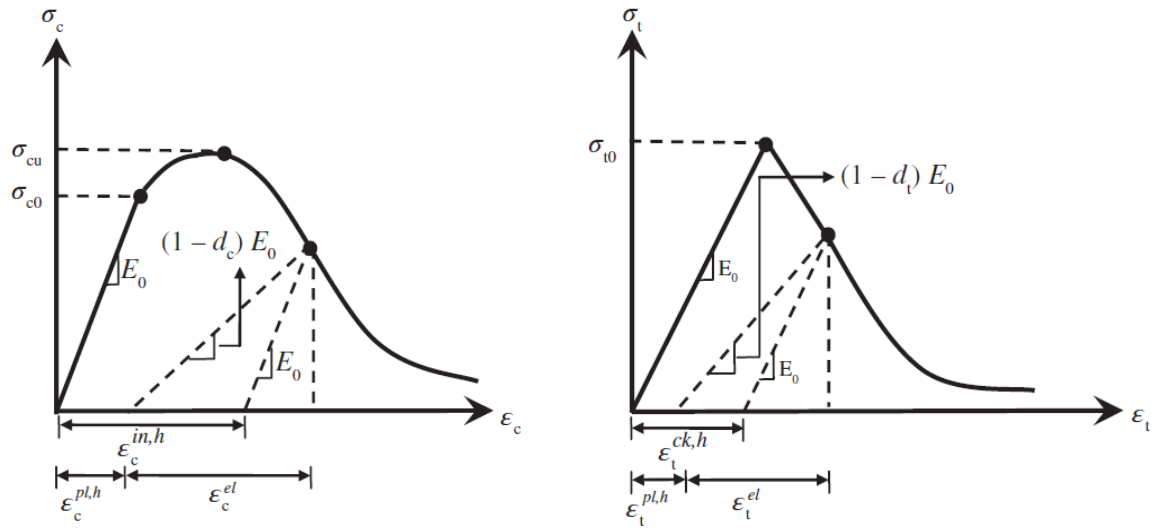

(a) (b)

Figure 5.10. Response of concrete to a uniaxial loading condition: (a) Compression, (b) Tension (Lubliner *et al*., 1989).

As illustrated in Figure 5.10 (a), the plastic hardening strain in compression $\varepsilon_c^{pl,h}$ was a critical factor in the determination of the relationship between the damage parameters and the

compressive strength of concrete in Equation (5.4) - (5.7) (Abaqus Analysis User's Guide, 2016).

$$\sigma_c = (1 - d_c) \times E_0 \times \left(\varepsilon_c - \varepsilon_c^{pl,h}\right) \tag{5.4}$$

$$\varepsilon_c^{in,h} = \varepsilon_c - \frac{\sigma_c}{E_0} \tag{5.5}$$

$$\varepsilon_c^{pl,h} = \varepsilon_c - \frac{\sigma_c}{E_0} \times \left(\frac{1}{1-d_c}\right) \tag{5.6}$$

$$\varepsilon_c^{pl,h} = \varepsilon_c^{in,h} - \frac{d_c}{(1-d_c)} \times \frac{\sigma_c}{E_0} \tag{5.7}$$

where $\varepsilon_c^{in,h}$ is the inelastic compression strain, $\varepsilon_c^{pl,h}$ is the plastic hardening strain in compression, and E_0 is the initial elastic stiffness.

As given in Figure 5.10 (b), in concrete damage plasticity models, the plastic hardening strain in tension $\varepsilon_t^{pl,h}$ was derived in Equation (5.8) - (5.11) (Abaqus Analysis User's Guide, 2016).

$$\sigma_t = (1 - d_t) \times E_0 \times \left(\varepsilon_t - \varepsilon_t^{pl,h}\right) \tag{5.8}$$

$$\varepsilon_t^{in,h} = \varepsilon_t - \frac{\sigma_t}{E_0} \tag{5.9}$$

$$\varepsilon_t^{pl,h} = \varepsilon_t - \frac{\sigma_t}{E_0} \times \left(\frac{1}{1-d_t}\right) \tag{5.10}$$

$$\varepsilon_t^{pl,h} = \varepsilon_t^{in,h} - \frac{d_t}{(1-d_t)} \times \frac{\sigma_t}{E_0} \tag{5.11}$$

where $\varepsilon_t^{in,h}$ is the inelastic tension strain, $\varepsilon_t^{pl,h}$ is the plastic hardening strain in tension. The CDP models calculated using a value of strain at maximum stress of ε_c=0.0024. Using this value the uniaxial compressive stress-inelastic strain relationship for concrete is shown in Figure 5.11 (a).

Damage is usually characterised by the degradation of stiffness and the damage parameters in both direction (d_c) and tension (d_t) are assumed to be functions of the plastic strains, temperature, and field variables (Abaqus Analysis User's Guide, 2016) and could be determined using Equation (5.12) and Equation (5.13) for compression and tension damage parameter, respectively. These parameters can take values starting from 0 representing the undamaged material up to 1 which represents the total loss of strength as shown in Figure 5.11 (b) for compression. Moreover, the tension damage parameter is given in Figure 5.12 (a).

$$d_c = 1 - \frac{\sigma_c}{\sigma_{cu}} \tag{5.12}$$

$$d_t = 1 - \frac{\sigma_t}{\sigma_{tu}} \tag{5.13}$$

here, σ_c and σ_t represent the post-peak concrete strengths corresponding to the inelastic strain in compression and tension, respectively while σ_{cu} and σ_{tu} denote the ultimate strengths of concrete in compression and tension, respectively.

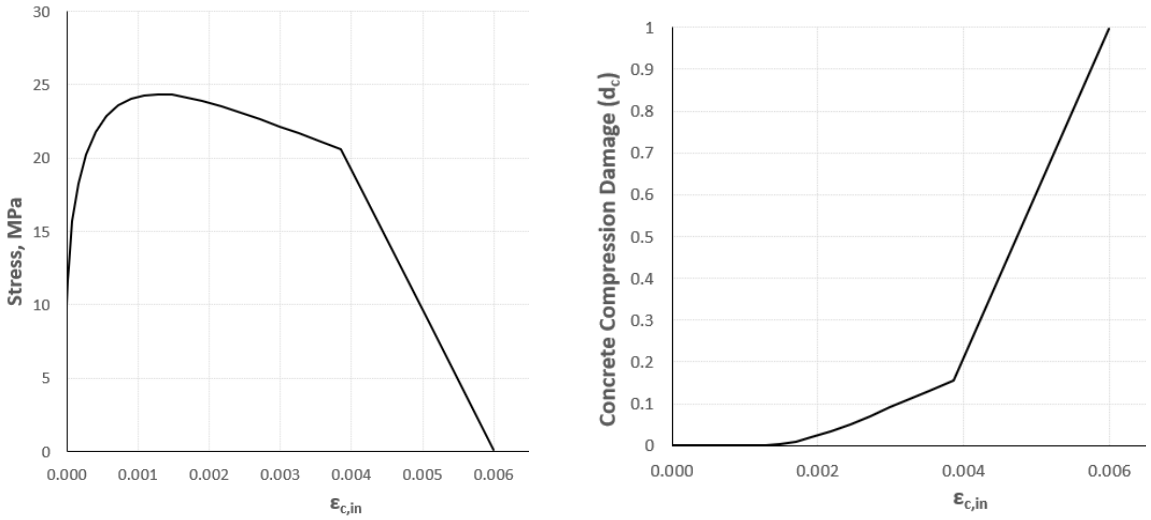

(a) (b)

Figure 5.11. The uniaxial compressive stress-inelastic strain relationship for concrete according to CDP constitutive model; (b) Definition of damage parameter in CDP model for uniaxial compression damage.

Relationship of stress–crack opening for concrete in tension is given in Figure 5.12 (b).

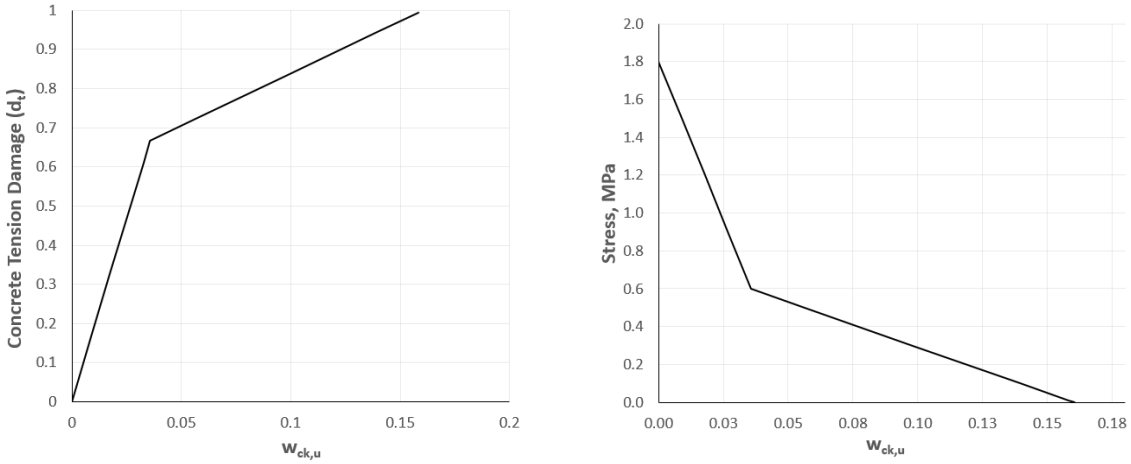

(a) (b)

Figure 5.12. (a) Definition of damage parameter for uniaxial tension damage; (b) Relationship of stress–crack opening for concrete in tension.

In Figure 5.12, unit of $w_{ck,u}$ is mm. In addition, the concrete model data used in the Abaqus software are given in detail in Appendix-J.

5.3.2 Steel Reinforcing Bars

The behaviour of reinforcing steel beyond its yield point was characterized using the von Mises yield criterion combined with an isotropic hardening response. A bilinear stress-strain model of steel, which was employed in CEB-FIP (2011), was selected for use in this study. This stress-strain model is shown in Figure 5.13. Young's modulus for ϕ8 and ϕ16 rebar are E_s=201283MPa and E_s=198963MPa, respectively. Poisson's ratio and reinforcement density can be taken as 0.3 and 7.85E-09 tonne/mm^3, respectively (EN1993-1-1, 2005). In this study, the measured values were used for yield strength (f_{sy}), yield strain (ε_{sy}), ultimate strength (f_{su}), ultimate strain (ε_{su}) of steel, these values were obtained from tensile test of steel. The stress-strain data were subsequently converted into true stress and logarithmic plastic strain format using Equations (5.14), (5.15) and (5.16) as outlined in the Abaqus Analysis User's Guide (2016). In addition, the stress-strain data of the steel for modelling are given in Table 5.2 and

Table 5.3 for ϕ8 and ϕ16, respectively.

$$True\ Strain = \ln(1 + \varepsilon_s) \tag{5.14}$$

$$True\ Stress = Engineering\ Stress \times e^{True\ Strain} \tag{5.15}$$

$$Effective\ Plastic\ Strain = Total\ Strain - Elastic\ Strain \tag{5.16}$$

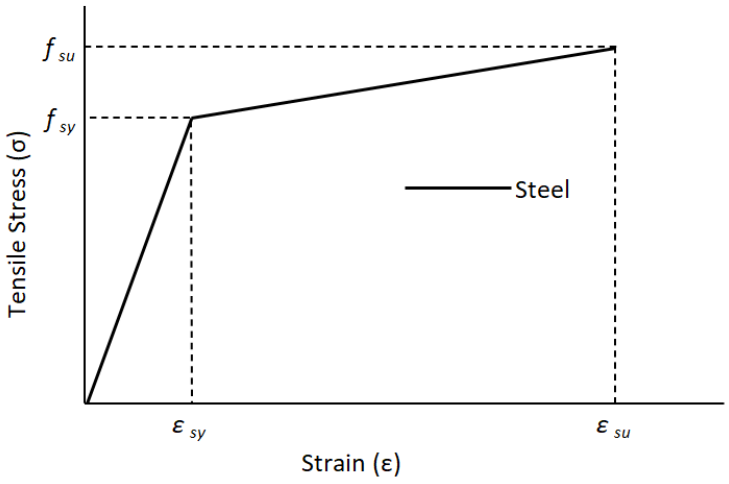

Figure 5.13. Bilinear stress-strain model of steel (CEB-FIP, 2011).

Table 5.2. Stress and strain values for ϕ8 reinforcing steel in ABAQUS.

	Engineering Stress (MPa)	Engineering Strain	True Stress (MPa)	True Strain	Effective True Stress (MPa)	Effective Plastic True Strain
	σ	ε	σ	ε	σ	ε
	0	0	0	0	-	-
Yield	502	0.002490	503.25	0.002487	503.250	0.0000
Ultimate	578	0.103	637.53	0.09803	637.534	0.09554

Table 5.3. Stress and strain values for ϕ16 reinforcing steel in ABAQUS.

	Engineering Stress (MPa)	Engineering Strain	True Stress (MPa)	True Strain	Effective True Stress (MPa)	Effective Plastic True Strain
	σ	ε	σ	ε	σ	ε
	0	0	0	0	-	-
Yield	471	0.002370	472.12	0.0023672	472.116	0.0000
Ultimate	581	0.114	647.23	0.10796	647.234	0.10559

5.3.3 Fibre Reinforced Polymer

The FRP jacket was modelled as a laminar orthotropic material. The data required for the modelling of the GFRP used in this project was not provided by the manufacturer, so the data provided by Hahn and Tsai (1980) was used. The elastic properties of the materials were defined as listed in Table 5.4, where E_L and E_T are the modulus of elasticity in the directions parallel and perpendicular to the fibre (see Figure 5.14), v is the Poisson`s ratio and G is the shear modulus. The FRP jacket was modelled using the shell element (S4R) with four nodes and reduced integration.

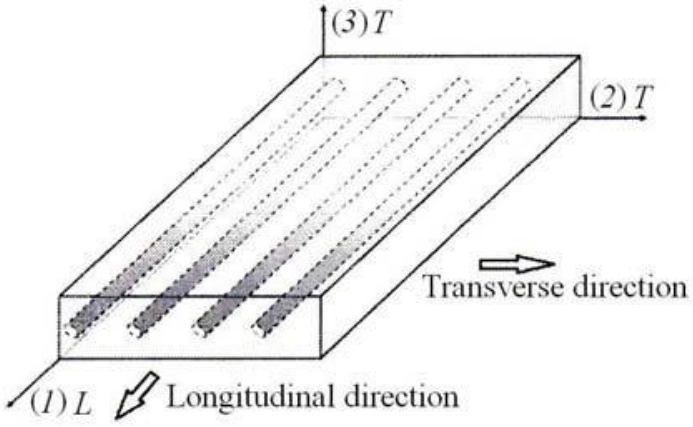

Figure 5.14. A unidirectional fibre reinforced lamina and principal material axes (Taranu *et al*., 2012).

The unidirectional composite exhibits varying properties along the material axis orientations. Consequently, this category of composites is orthotropic, exhibiting axes 1, 2, and 3 as axes of symmetry (see Figure 5.14). The unidirectionally fibre-reinforced composite parts exhibit the highest strength in the longitudinal direction, while the material characteristics in the transverse directions (2, 3) are practically uniform due to the random fibre distribution in the cross-section. Therefore, a unidirectional composite can be regarded as transversely isotropic, meaning it is isotropic in the 2-3 plane (Taranu *et al*., 2012).

Table 5.4. Orthotropic elastic properties of the composite used in the jacket (Hahn and Tsai, 1980).

E_L (MPa)	E_T (MPa)	v_{TT}	G_{LT} (MPa)	G_{TT} (MPa)	G_{TT} (MPa)
38600	8270	0.26	4140	4140	3100

The subscript "L" denotes longitudinal direction (or fibre direction), and the subscript "T" represents the two transverse directions orthogonal to the fibre direction. The damage initiation and evolution behaviour are also assumed to be orthotropic (Hashin, 1980). Table 5.5 lists the tensile and compressive strength of the materials in the direction parallel to the fibre orientation, $\sigma_L^{f,t}$ and $\sigma_L^{f,c}$; the tensile and compressive strength of materials in the direction perpendicular to the fibre orientation, $\sigma_T^{f,t}$ and $\sigma_T^{f,c}$; and in-plane shear failure strength, τ_{LT}^{f}. The superscripts "t" and "c" refer to tension and compression, respectively. The fracture energies of the fibre and matrix are assumed to be G_f = 12.5 N/mm (Longitudinal tensile and compressive fracture energy) and G_m = 1.0 N/mm (Transverse tensile and compressive fracture energy), respectively (Abaqus Analysis User's Guide, 2016).

Table 5.5. Orthotropic damage initiation properties of the composite used in the jacket (Hahn and Tsai, 1980).

$\sigma_L^{f,t}$(MPa)	$\sigma_L^{f,c}$(MPa)	$\sigma_T^{f,t}$(MPa)	$\sigma_T^{f,c}$(MPa)	τ_{LT}^{f}(MPa)
1062	610	31	118	72

It is also necessary to evaluate the damage criteria for fibre composite materials. Hashin Damage Criteria in ABAQUS are widely used for modelling failure in fibre-reinforced composite materials. These criteria were developed by Hashin (1980) to account for different failure modes in composite materials, specifically in fibre-dominated and matrix-dominated regions. ABAQUS uses these factors to estimate damage onset and development in composite

laminates. The Hashin failure criteria identifies four primary forms of failure in fibre-reinforced composites:

- HSNFTCRT (fibre tensile initiation criterion)
- HSNFCCRT (fibre compressive initiation criterion)
- HSNMTCRT (matrix tensile initiation criterion)
- HSNMCCRT (matrix compressive initiation criterion)

Each of these failure modes has its own criteria based on stresses and strains in the material. For each of these variables indicating the satisfaction of an initiating criterion in a damage mode, a value below 1.0 signifies non-satisfaction of the criterion, whilst a value of 1.0 or greater signifies satisfaction of the criterion (Abaqus Analysis User's Guide, 2016).

5.3.4 Epoxy adhesive

The adhesive was modelled using cubic elements (C3D8R) with eight nodes, three degrees of freedom per node, and reduced integration. A perfect plasticity model with no hardening was employed to simulate the behaviour of the epoxy adhesive, as represented in Figure 5.15. The epoxy used in this study has a density of 1.65 kg/l, a tensile strength of 26 N/mm², and a Young's modulus of 11,200 N/mm², according to the Sikadur®30 product data sheet. Colombi and Poggi (2006) reported that the elongation at failure and Poisson's ratio are 0.01 and 0.3, respectively.

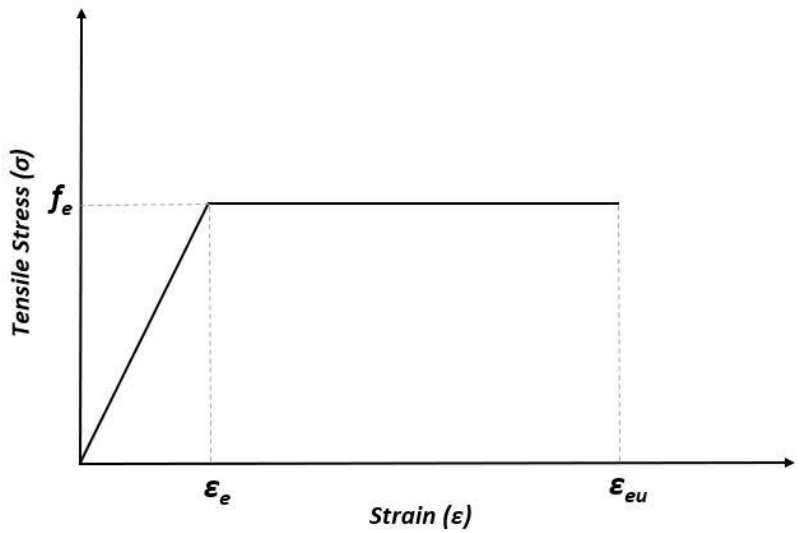

Figure 5.15. Normal stress-separation relationship of the interface (Rezazadeh and Barros, 2014).

5.4 BOUNDARY CONDITIONS, CONSTRAINTS, ANALYSIS TYPE AND LOADING

During specimen manufacturing, it is necessary to determine the boundary conditions between the concrete and the steel plates mounted at the upper and lower ends of the column. In this study, tie constraints were used between the concrete and the steel plates. With this constraint, the members maintain a complete bond and act in a consistent way throughout the analysis. Boundary conditions simulating the test forces were applied to the concrete sections at the upper and lower ends of the column. For this purpose, reference points are assigned to the midpoints of the plates at the top and bottom ends of the column. Using the interaction segment in the Abaqus software, it is necessary to establish an interaction between this point and the plates. For this interaction, Rigid Body is selected in the Type section and the relationship between the reference point and the plates is established. The purpose of this is to ensure that the loads or constraints defined at these points are transferred to the entire plate. Therefore, the horizontal movement of the reference point at the upper plate of the column is constrained ($U_x = U_z = 0$), thus simulating the vertical axial loading applied during the test. Likewise, the lower plate, both horizontal and vertical translation of the reference point to which the column lower end section ($U_x = U_y = U_z = 0$) are constrained. A constant axial force of 168kN was applied to the upper steel plate and monotonic loading was applied to the beam loading plate using the displacement-controlled approach.

The tie constraint used between the steel plates used in the column end areas and the concrete was also used between the beam end and the loading plate. Other surfaces where tie constraints were used are between the epoxy-concrete and FRP sheet-concrete surfaces. This is because, as far as observed in the experiments, there was no debonding due to the adhesive material between these concrete surfaces during the test and these surfaces moved together. Therefore, bond-slip relationships were not used in this study. The embedded region technique was utilised to link the degrees of freedom of the truss elements simulating embedded reinforcing bars and the degrees of freedom of the brick elements in the surrounding concrete. Utilising this constraint, a region of the model will be embedded in another region in a way that they will both have the same degrees of freedom. In addition, this method was used between u-shaped reinforcements and epoxy. In this technique, the embedded element is selected as the embedded region (steel rebars) whereas the other element is selected as the host region (concrete/ epoxy).

In the literature, researchers have used different approaches such as ABAQUS explicit or monotonic static loading. Although ABAQUS software provides a similar approach to explicit analyses, Ridwan (2016) stated that the inertia effect in the calculation phase and the calculations are computationally very expensive and therefore take a long time. When the studies of Ridwan (2016) and Yimer and Aure (2021) were examined, they showed the comparison of the envelope curves of the experimental results and numerical analysis results. On the other hand, when the studies by Najafgholipour *et al*. (2017), Diro and Kabeta (2020), Najafgholipour and Arabi (2021), and Abdelwahed *et al*. (2021) are examined, the envelope curves obtained from the experimental studies and the envelope curves obtained as a result of monotonic static loading in numerical analysis are compared and the models are verified. It can be seen from their work that they obtained close and meaningful results when comparing the cyclic loading envelope curves obtained from experiments with the help of monotonic static loading from numerical modelling. For this reason, analyses were performed under monotonic static loading within the scope of this thesis.

In the loading step, a constant axial force of 168kN was applied to the upper column as the first step and then the monotonic loading was implemented to the beam loading plate using the displacement-controlled approach as the second step. Loading steps and boundary conditions are given in Figure 5.16. In the analyses performed using the displacement control on the beam loading plate, this value is 85 mm for the S1-Control specimen, the S2-NSM specimen and the S4-Hybrid specimen.

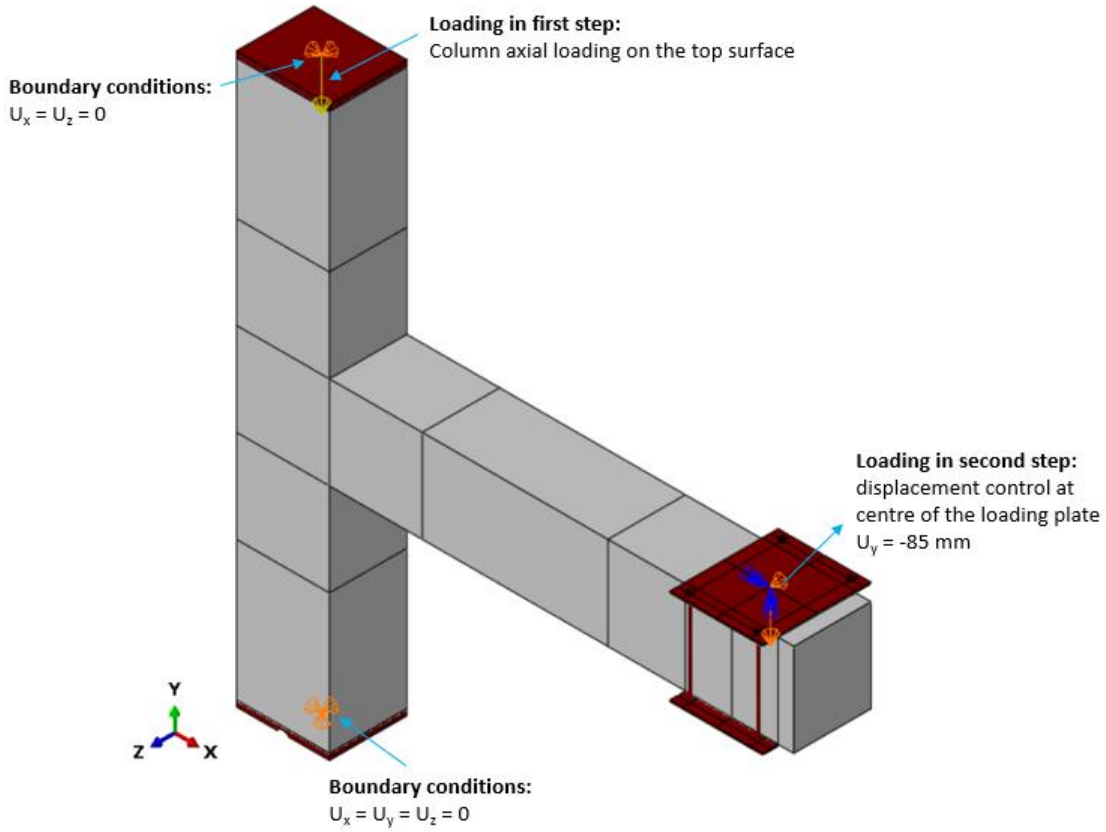

Figure 5.16. Computational simulation of boundary conditions and applied loading to the specimens.

5.5 CALIBRATION OF THE MODEL

This study examines the influence of factors in the constitutive equations of a damage plasticity model and calibrates the model by presenting the impacts of various logical values of the viscosity parameter and doing a mesh sensitivity analysis.

Najafgholipour *et al*. (2017) proposed the introduction of visco-plastic regularity into the numerical model as a method to enhance the rate-dependent plastic damage model by introducing uniqueness to the increasing stress field in the constitutive equations. It was demonstrated that the considerate selection of the viscosity parameter and its integration into the model produces a relaxation time for the visco-plastic system of equations, ensuring convergence in the softening regime. However, varying the viscosity parameter in monotonic loading scenarios does not significantly affect the behaviour of concrete materials under uniaxial compression or tension (Lee, 1996). The study conducted by Lee (1996) demonstrated that optimal results are achieved with lower viscosity parameter values relative to the simulated time of analysis. A variety of guidelines and recommendations were proposed by

many scientists to determine the optimal viscosity parameter values in the CDP model, based upon the type of the predominant internal actions and the extent of nonlinearity present in different issues (Wosatko *et al.* 2015 and Ren *et al.* 2015). Figure 5.17 illustrates the effects of incorporating extra relaxation time for the visco-plastic system on the analytical outcomes utilising various viscosity parameter values.

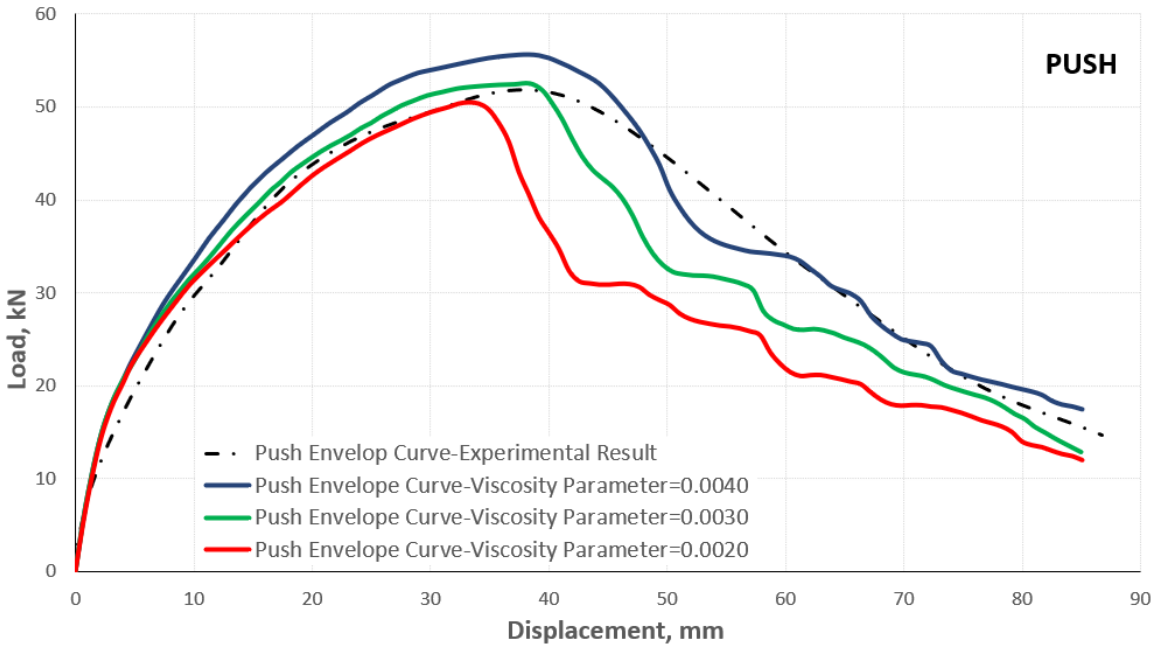

Figure 5.17. Load-displacement response of finite element analysis for varying viscosity parameter values.

In this work, viscosity parameter was chosen by choosing a value that best fitted the experimental results for the S1 control specimen and then this value was held constant for the subsequent simulations (S2-NSM and S4-Hybrid). In Figure 5.17, the result of three identical simulations for the S1 control specimen, but using different values of viscosity; namely, 0.0040, 0.0030, and 0.0020 are presented. This figure indicates that the variations in the responses occur mainly in the softening region and to a much lesser extent in the hardening zones. From Figure 5.17**,** it can be seen that 0.003 gives the best response up to peak load, but underestimates the softening region of the response, while 0.004 is slightly too stiff and too strong before peak load, but has a better fit after this point. It could be argued that since the cylinders used to obtain the concrete properties were not the same as the ones cast when the original test specimens were made that the concrete in the new cylinders may be slightly softer than the concrete used in the test specimens and therefore a better choice; however, the peak stress of the new cylinders was matched to the measured peak stress of the original

concrete cylinders and therefore the peak load is too high when viscosity = 0.004 is used. Conversely, using viscosity = 0.003 gives a better simulated response up to peak load and a softer (conservative) response after this value. For this reason, a viscosity value of 0.003 has been adopted for all simulations ss it is a better match up to peak load and has a conservative response after this.

In this study, for the concrete a 12.5 mm mesh was adopted for around the connection and 25 mm mesh for the concrete beam and column outside the joint as shown in Figure 5.6 (a). This non-uniform mesh was chosen because it produced results that matched the envelope curve reproduced the crack patterns and the propagation of the cracks. Further mesh refinements were deemed computationally too expensive for no significant improvement in the results.

5.6 NUMERICAL ANALYSIS RESULTS

The adopted finite element analysis results of the RC beam-column joints (mesh size = 12.5mm & 25mm and viscosity= 0.003) under vertical loading are provided through force-displacement curves, ultimate loads, displacements, and cracking patterns that monitor the shear behaviour of the connections. Figure 5.18 (a), (b), and (c) illustrate the comparison between the force-displacement curves predicted by simulation and the experimental results of exterior connection specimens for S1-Control, S2-NSM, and S4-Hybrid, respectively.

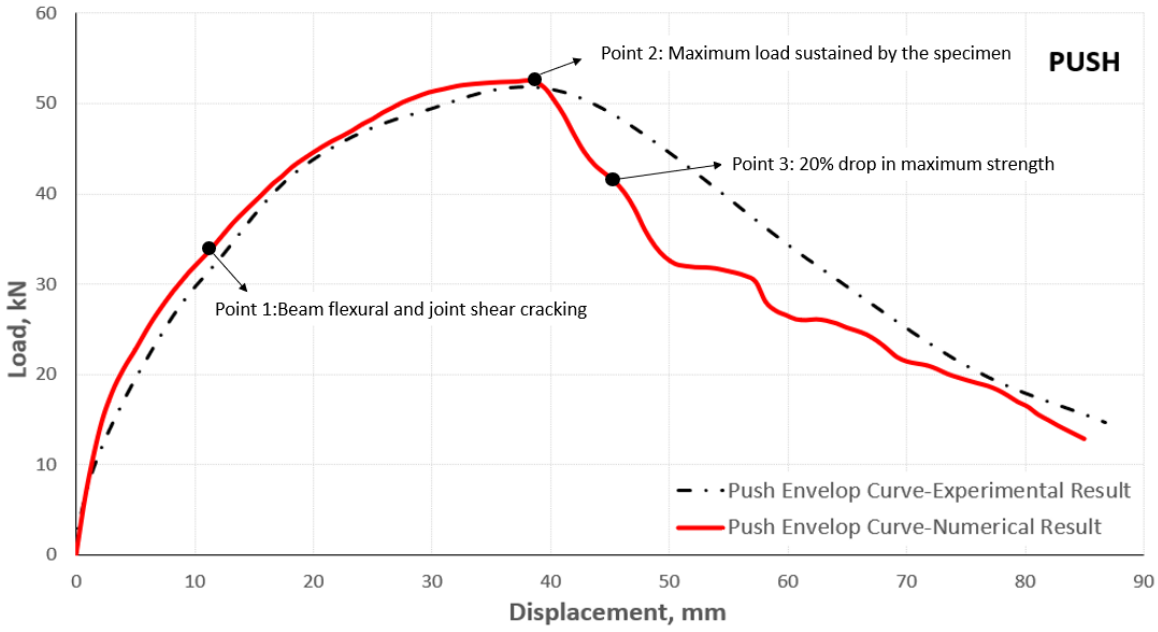

(a) S1-Control

Figure 5.18. Comparison with experimental and numerical results.

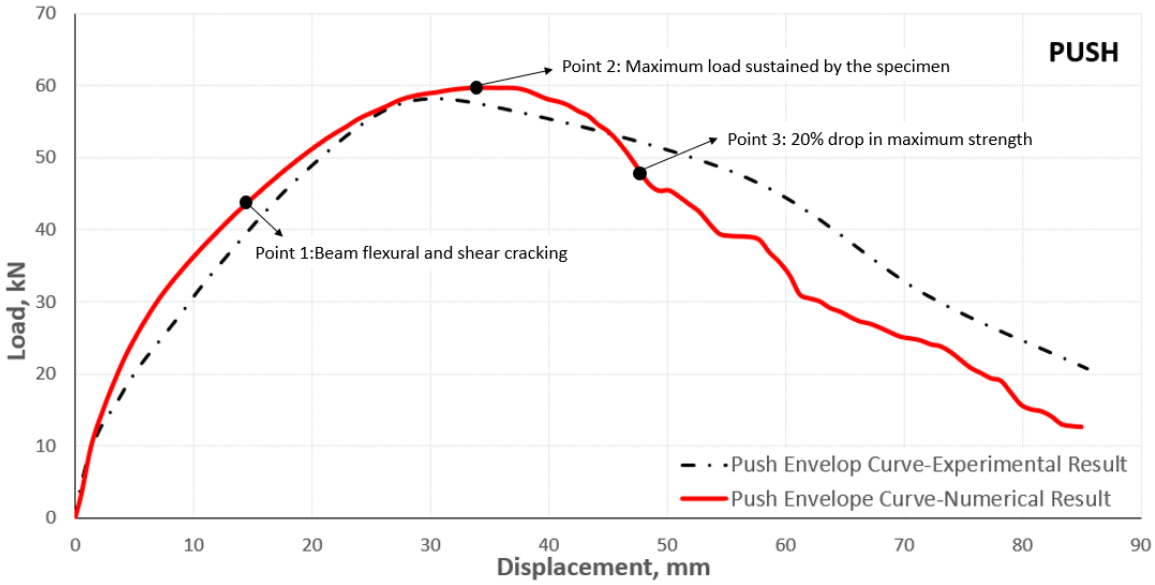

(b) S2-NSM

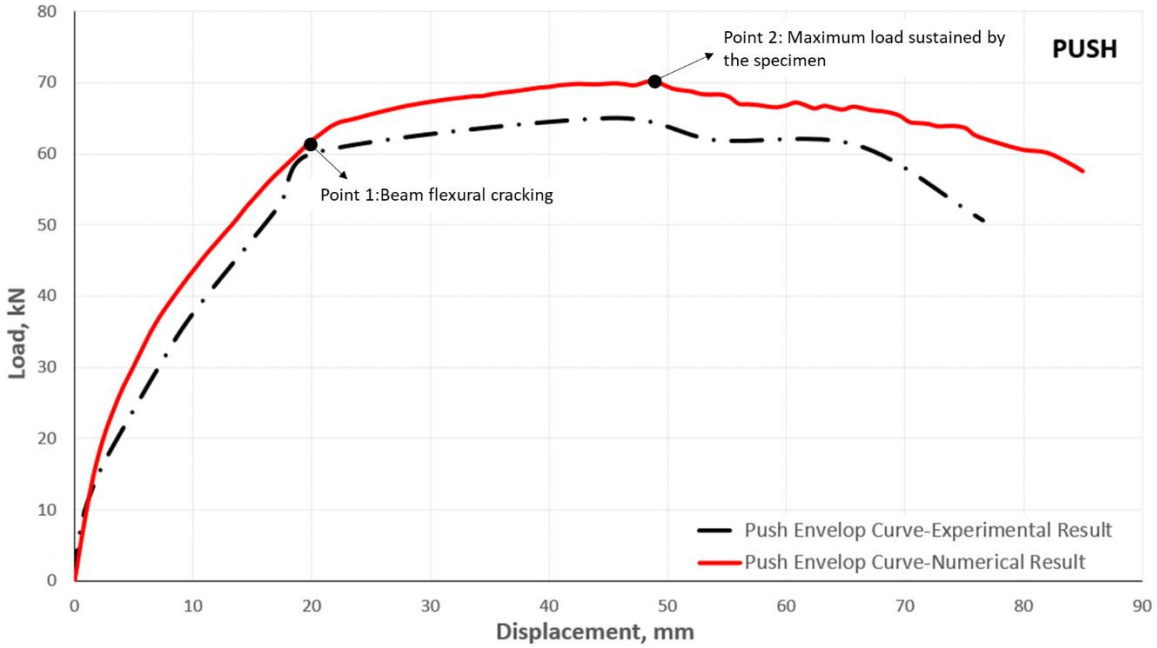

(c) S4-Hybrid

Figure 5.18. Comparison with experimental and numerical results (continue).

Table 5.6. depicts the maximum loads and displacements predicted by the numerical simulation and the experimental test findings. To describe the overall model accuracy and the corresponding average overestimation or underestimate of FEA, the error (%) is assessed according to the relations established by Behnam *et al*. (2018), as defined in Equation (5.17).

$$\text{Error } (\%) = \left|\frac{\text{FEA result} - \text{Test result}}{\text{Test result}}\right| \times 100 \qquad (5.17)$$

Table 5.6. Maximum displacements and loads obtained from experimental and computational tests.

Specimen Name	Loading Direction	Experimental results		FEA results		Prediction	
		Maximum load	Displacement at maximum load	Maximum load	Displacement at maximum load	Error for max load	Error for max displacement
		(kN)	(mm)	(kN)	(mm)	(%)	(%)
S1-Control	**Push**	50.8	42.2	52.5	38.4	3.4	9.0
S2-NSM	**Push**	57.4	34.4	59.8	34.0	4.1	1.2
S4-Hybrid	**Push**	65.1	45.1	70.2	48.8	7.8	8.2

From a numerical perspective (see Table 5.6), the FEA results closely approximate the experimental data. The maximum load prediction errors ranged from 3.4% to 7.8%, indicating a good correlation between the simulation and actual behaviour. The displacement predictions at peak load showed higher variability, with errors of 9.0% for the control, 1.2% for the NSM specimen, and 8.2% for the hybrid specimen. In general, the FEA model performed close to the experiments in predicting the behaviour of the control specimen and the retrofitted specimens with all errors being less than 10%. The biggest difference between experimental and simulated results was for the S4 hybrid specimen. This example is the most complex containing retrofitted steel bars and fibreglass wrapping and therefore it is not unexpected that a slightly poorer fit was obtained. Another reason for this difference in behaviour could be the material properties adopted for the fibreglass were not directly measured but rather manufacturers values were used, which is a potential source of inaccuracy.

The finite element analysis indicates that the initial response exhibits slightly more stiffness compared to the test results. This may result from the influence of certain assumed variables, including the selection of concrete tensile and compressive properties, as well as uncertainties associated with experimental procedures, such as potential material deficiencies. Additionally, natural differences between responses obtained from cyclic loading in experiments and monotonic loading in the presented analysis may also contribute to the comparatively limited initial stiffness response of finite element analysis relative to testing.

In Figure 5.18 (a), (b) and (c), Point 1 shows the measurable beam flexural and joint shear cracking for the control specimen (S1), for NSM specimen (S2) the beam flexural and shear

cracking, and for the hybrid specimen (S4) the beam flexural cracking. Point 2 shows the ultimate strength of the specimens and finally Point 3 shows where the ultimate strength dropped by 20% (Shen *et al.,* 2022) in the control specimen (S1) and NSM specimen (S2).

The precision of the numerical model in representing joint shear behaviour is assessed through five output parameters that comprehensively characterise overall joint shear behaviour, including concrete tensile damage (DAMAGET), compressive damage (DAMAGEC), reinforcement output stress, plastic strain (PE) for cracking pattern, and stiffness degradation variable (SDEG). The CDP model accurately represents the nonlinear behaviour of concrete under both tensile and compressive forces. An important and complex element of using damage plasticity models is the precise characterisation of damage in the constitutive model.

DAMAGET refers to the Tensile Damage Variable. It is a key parameter used in damage mechanics to track the evolution of damage in materials subjected to tensile loading. This variable helps in simulating the degradation and failure of materials when they experience tensile forces, especially in materials where fracture or cracking is the primary mode of failure. DAMAGET specifically refers to the damage that occurs due to tensile stresses in the material. It is used to model how a material progressively loses its ability to carry tensile loads due to the growth of micro-cracks or voids when subjected to tension.

DAMAGEC stands for the Compressive Damage Variable. It is used to model the reduction in material stiffness when a material experiences compressive stresses beyond its elastic or plastic limit, leading to progressive failure. It is important for capturing material behaviours like crushing or compaction in materials that fail under compression, such as concrete, foam, and other brittle or quasi- brittle materials.

The maximum principal plastic strain value is the primary signal of fracture initiation in the concrete damage plasticity model. Cracks develop when the maximum principal plastic strain is positive, with their orientation regarded perpendicular to the maximum principal plastic strains. Consequently, to clarify the direction of cracking, the output of the maximum principal plastic strains is examined.

SDEG refers to the stiffness degradation variable, a key indicator of material damage and failure in simulations. It tracks the progression of material damage by measuring how much the stiffness of a material has degraded due to the damage model being used. The SDEG variable ranges from 0 to 1. If SDEG is equal to zero, it means the material is undamaged (no

stiffness degradation) has occurred. If SDEG is 1, the material is fully damaged, meaning the material has lost all stiffness and is considered to have completely failed.

Figure 5.19 illustrates concrete damage in both tension and compression, alongside reinforcing Von-Mises stress output, stiffness degradation, and plastic strain (cracking pattern) at five important points of joint shear behaviour relevant to S1-Control.

For the S1-Control specimen, the damage and stresses of the beam at a displacement of 60 mm (drift ratio = 4.62%) were analysed. As shown in Figure 5.19, the concrete tensile damage occurred on the beam and caused severe damage around the joint. Furthermore, the compressive damage to the joint core occurred. At this stage, no yielding of the beam longitudinal bars was observed. Measurable flexural cracks in the beam and severe shear cracks in the joint are clearly visible and confirm the experimental observations reported at this stage. In addition, plastic strain and stiffness degradation in the joint area are clearly visible.

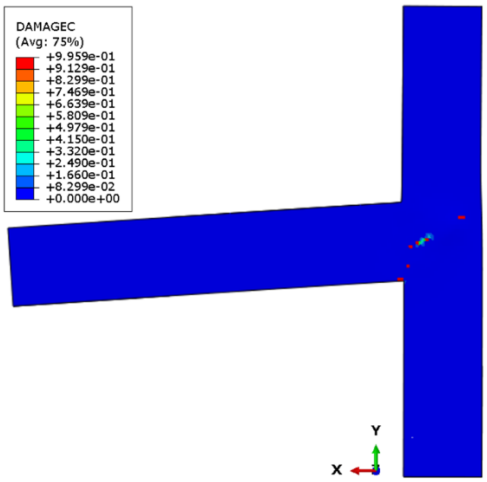

(a)

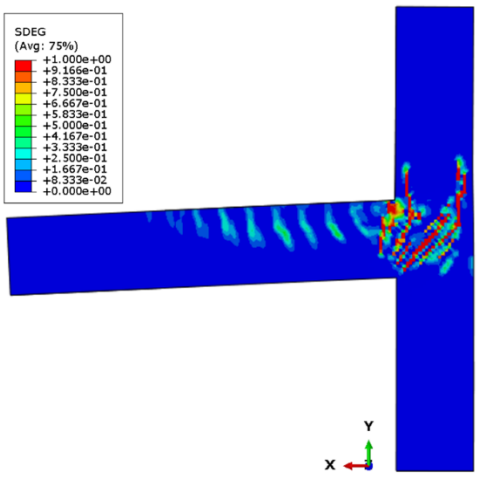

(b)

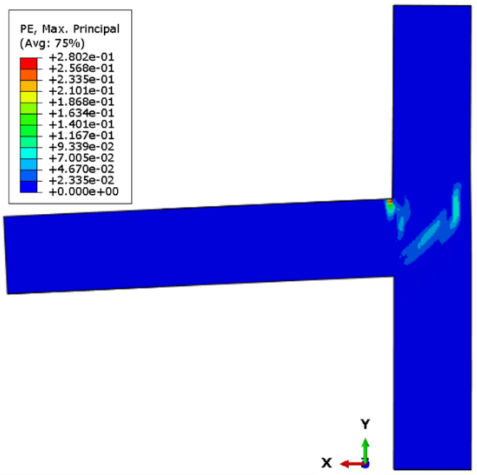

(c)

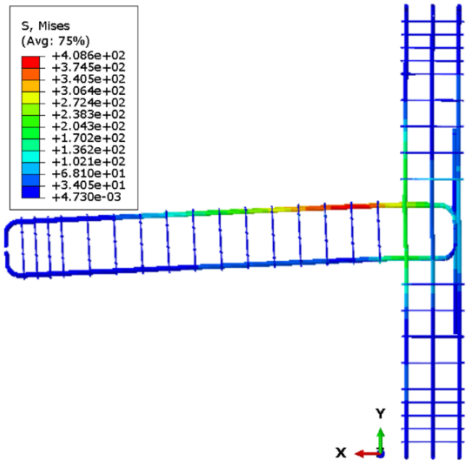

(d)

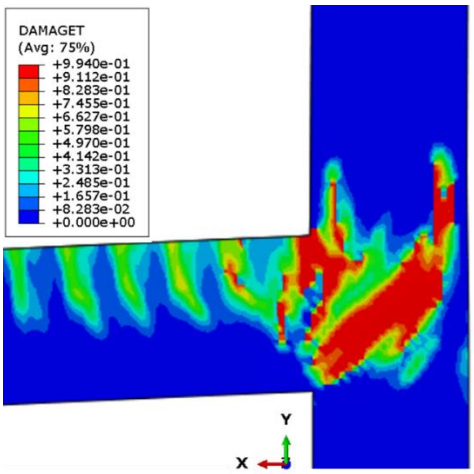

(e)

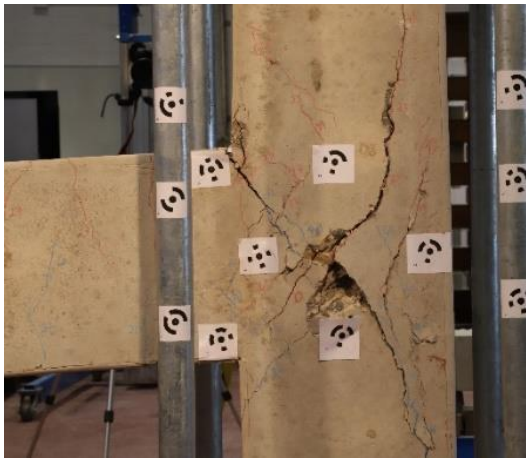

(f)

Figure 5.19. FEA output of S1-Control of shear behaviour (4.62% Drift Ratio): (a) Concrete compressive damage; (b) SDEG (stiffness degradation variable); (c) PE (plastic strain); (d) Reinforcement Mises stress; (e) Concrete tensile damage; (f) Concrete tensile damage (experiment).

According to the experimental results, the beam longitudinal bars (strain gauge number: SG05) yielded at a 5.77% drift ratio. In the numerical model, the bars yielded at a 5.77% drift ratio as well (see Figure 5.20). Therefore, it can be said that the results of the numerical analyse is in good agreement with the experimental result.

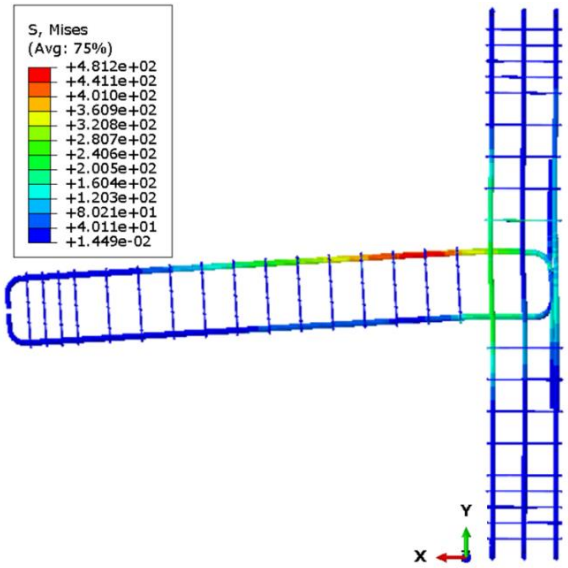

Figure 5.20. FEA output of S1-Control of shear behaviour (5.77% Drift Ratio): Reinforcement Mises stress.

Figure 5.21 illustrates concrete damage in both tension and compression, alongside reinforcing Von-Mises stress output, stiffness degradation, and plastic strain (cracking pattern) at five important points of joint shear behaviour relevant to S2-NSM.

For specimen S2-NSM, the damage and stresses of the beam at a displacement of 60 mm (drift ratio = 4.62%) were presented. As shown in Figure 5.21, the concrete compressive failure occurred on the joint. Concrete tensile damage was also observed in the form of a serious crack at the top of the beam at the end of the strengthening. Flexural cracks were also observed on the beam. At this stage, yielding of the beam longitudinal bars occurred. Moreover, plastic strain and stiffness degradation on the beam and connection are clearly visible. The damage and stresses confirmed the reported experimental observations. In the retrofit technique used, significant shear cracks are observed where the reinforcement ends (see Figure 5.21 (e) and (f)).

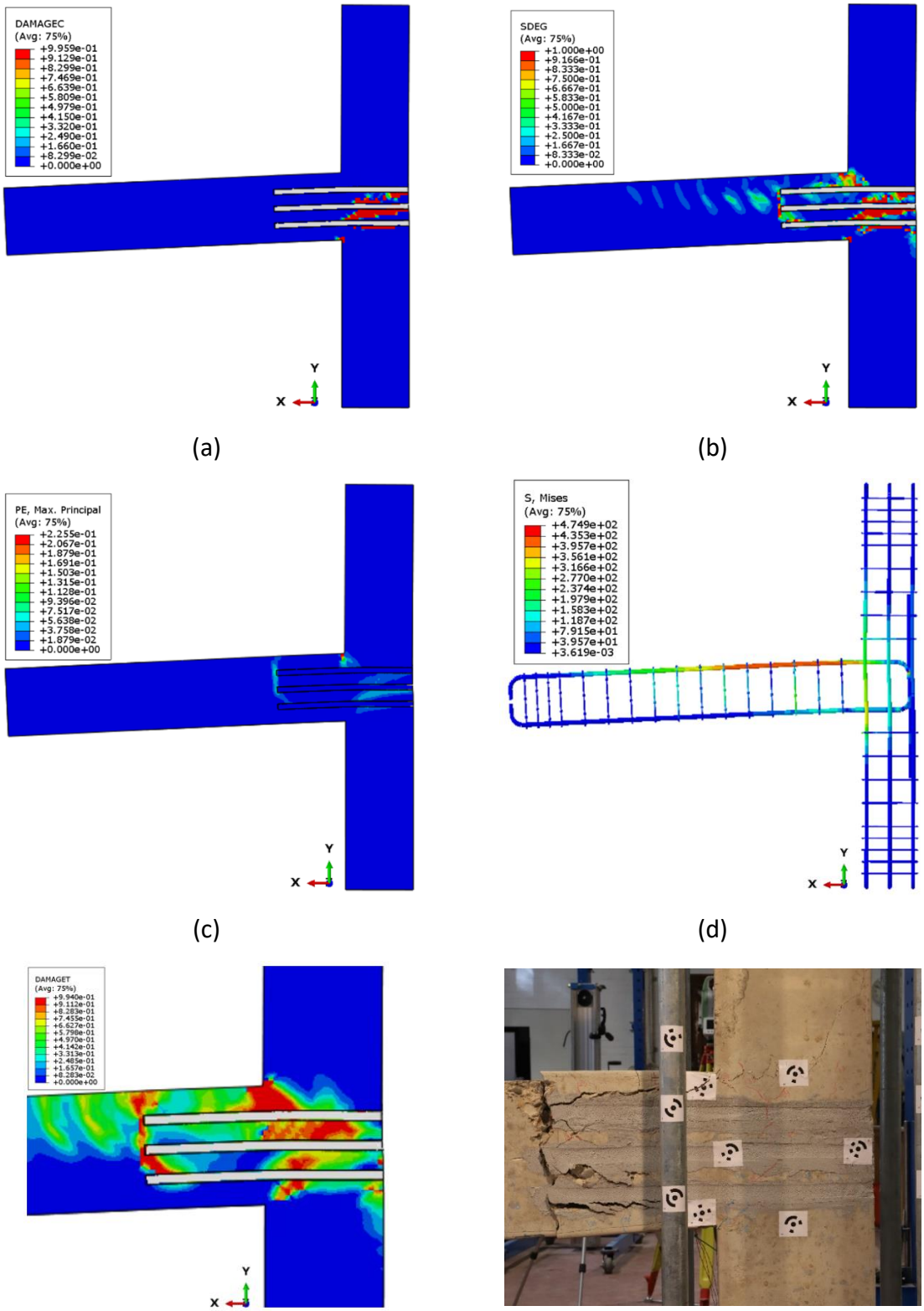

Figure 5.21. FEA output of S2-NSM of shear behaviour (4.62% Drift Ratio): (a) Concrete compressive damage; (b) SDEG (stiffness degradation variable); (c) PE (plastic strain); (d) Reinforcement Mises stress; (e) Concrete tensile damage; (f) Concrete tensile damage (experiment).

Analysing the epoxy results, it is clear that the epoxy material was damaged (see Figure 5.22 (a)). The maximum stress for the epoxy material was 26 MPa, and the epoxy material was in the plastic region of the constitutive model in the numerical analysis (see Figure 5.15). When it comes to u-shaped steel in the epoxy material, the results of the analysis show that these bars had yielded (see Figure 5.22 (b)).

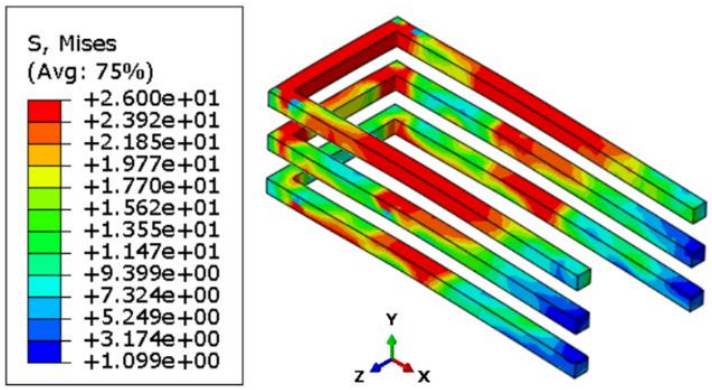

(a)

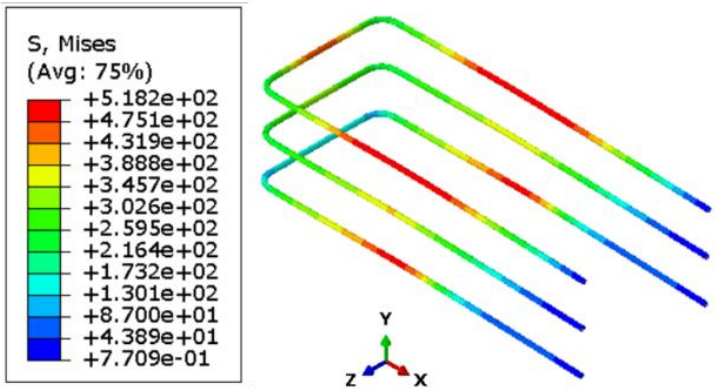

(b)

Figure 5.22. FEA output of S2-NSM (4.62% Drift Ratio): (a) Epoxy Mises stress; (b) U-shaped steel Mises stress.

According to the experimental results, the beam longitudinal bars (strain gauge number: SG05) yielded at a 2.31% drift ratio. In the numerical model, the bars yielded at a 2.31% drift ratio as well (see Figure 5.23 (a)). When it comes to U-shaped steel bar, it yielded at a 1.54% drift ratio in the experiment. However, in the numerical model, the top of the U-shaped steel bar yielded after a 2.15% drift ratio (approximately 28mm deflection) (see Figure 5.23 (b)). Therefore, it can be said that the numerical analysis results and experimental results are in agreement.

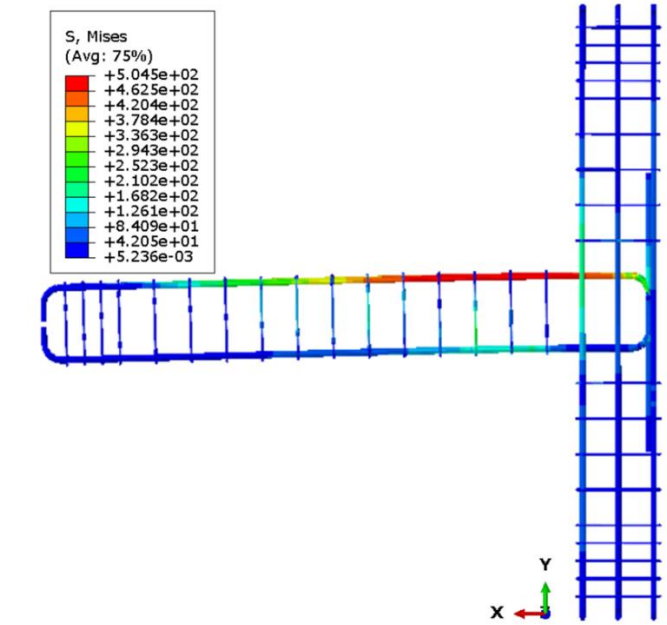

(a)

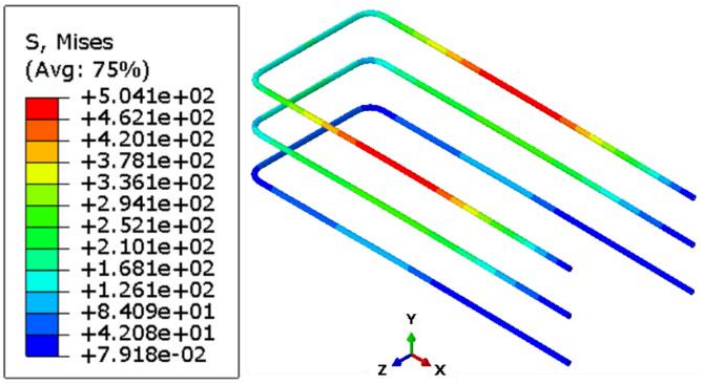

(b)

Figure 5.23. FEA output of S2-NSM: (a) Reinforcement Mises stress (2.31% Drift Ratio); (b) U-shaped steel Mises stress (after 1.54% Drift Ratio-28mm deflection).

Figure 5.24 illustrates concrete damage in both tension and compression, alongside reinforcing Von-Mises stress output, stiffness degradation, and plastic strain (cracking pattern) at five important points of joint shear behaviour relevant to S4-Hybrid.

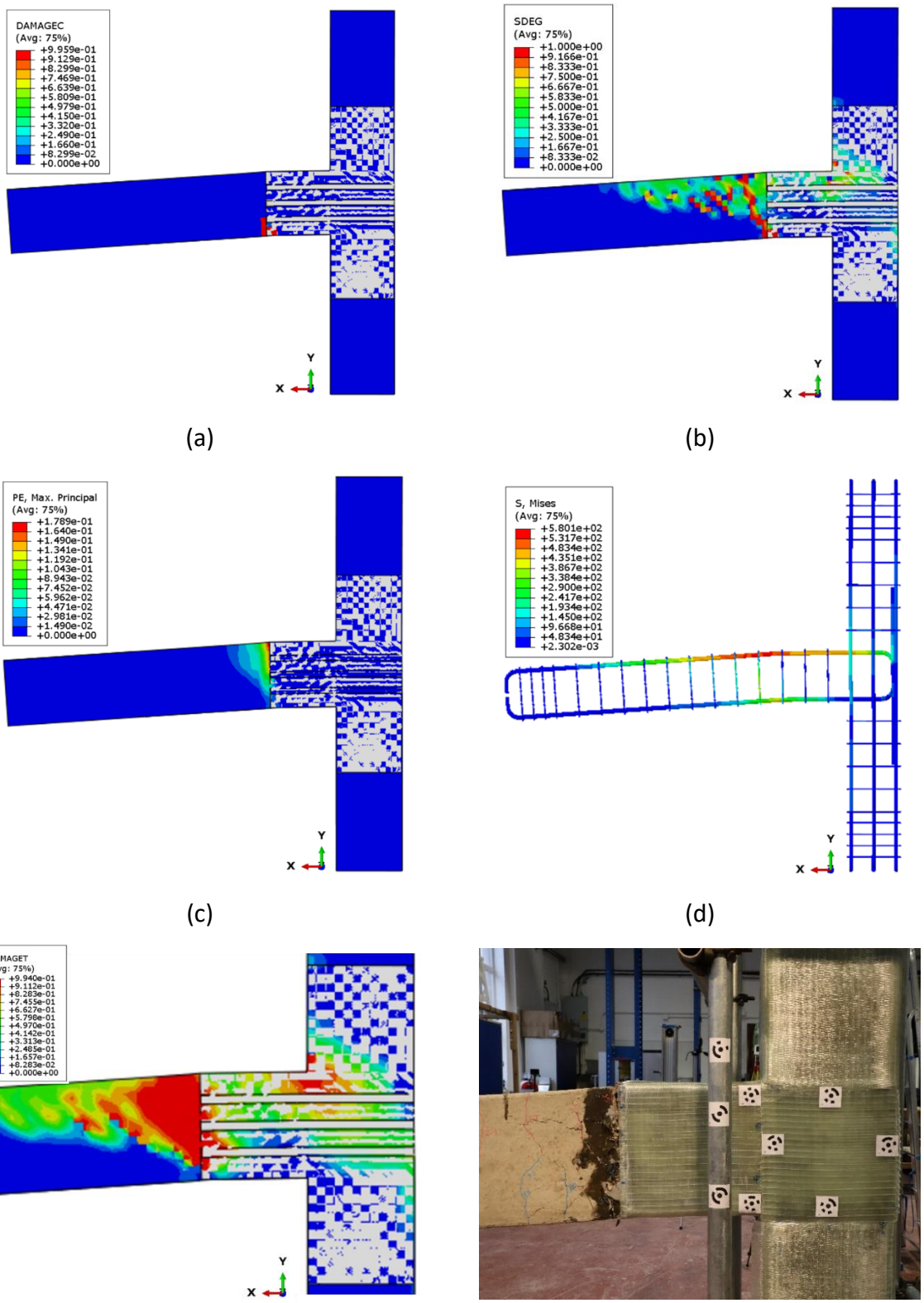

Figure 5.24. FEA output of S4-Hybrid of shear behaviour (5.77% Drift Ratio): (a) Concrete compressive damage; (b) SDEG (stiffness degradation variable); (c) PE (plastic strain); (d) Reinforcement Mises stress; (e) Concrete tensile damage; (f) Concrete tensile damage (experiment).

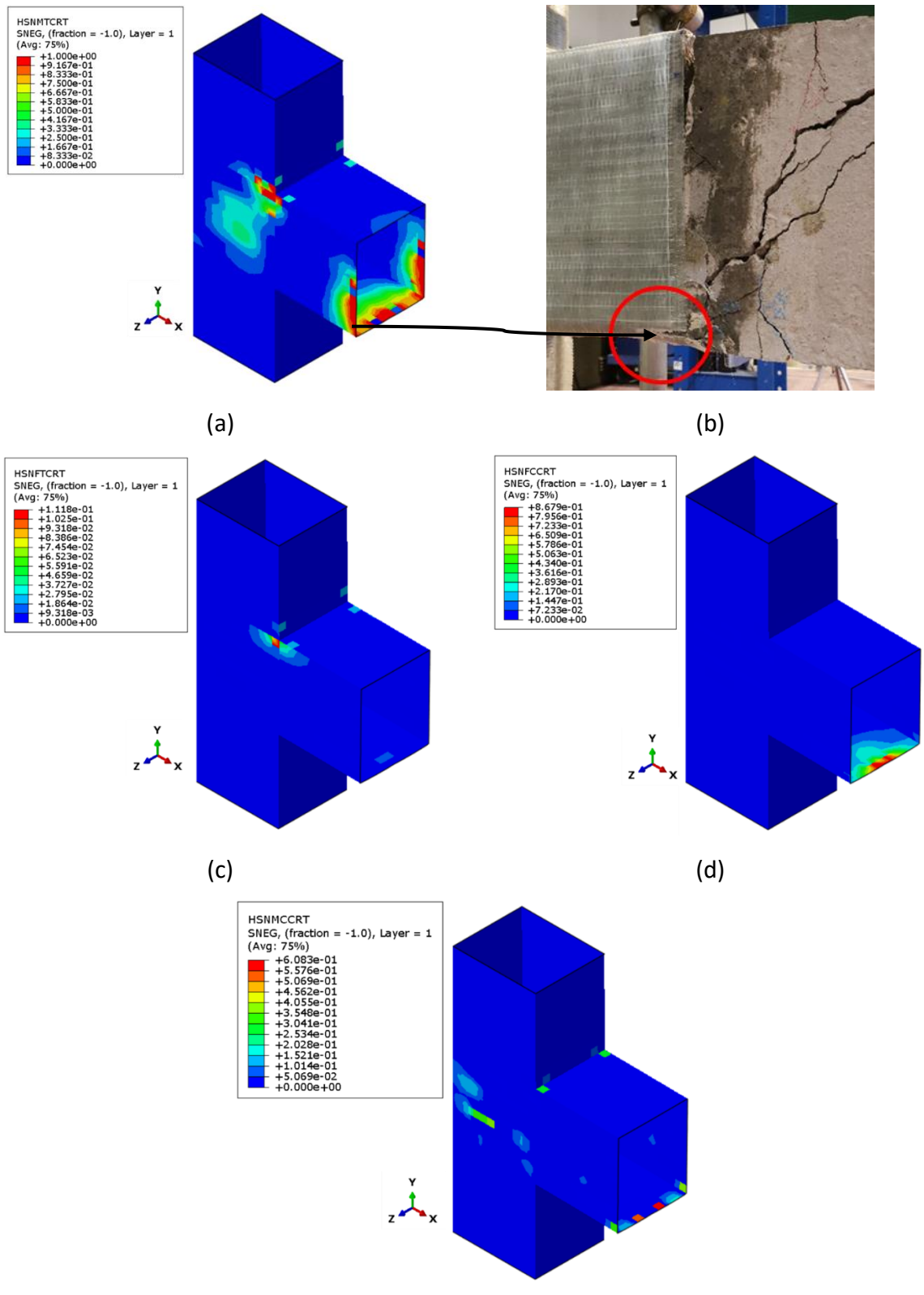

Figure 5.25. FEA output of S4-Hybrid (5.77% Drift Ratio): (a) HSNMTCRT (matrix tensile initiation criterion); (b) the experimental observation; (c) HSNFTCRT (fibre tensile initiation criterion); (d) HSNFCCRT (fibre compressive initiation criterion); (e) HSNMCCRT (matrix compressive initiation criterion).

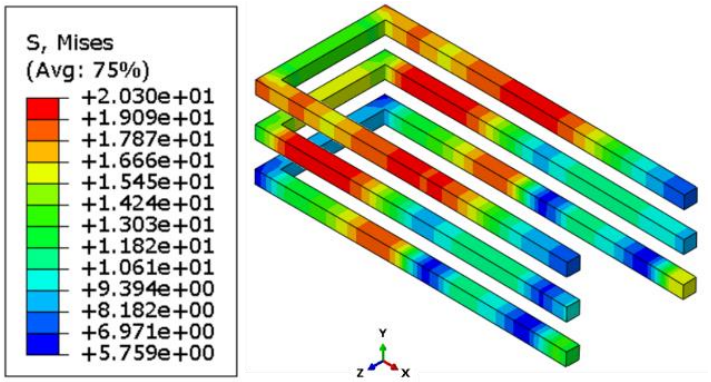

(a)

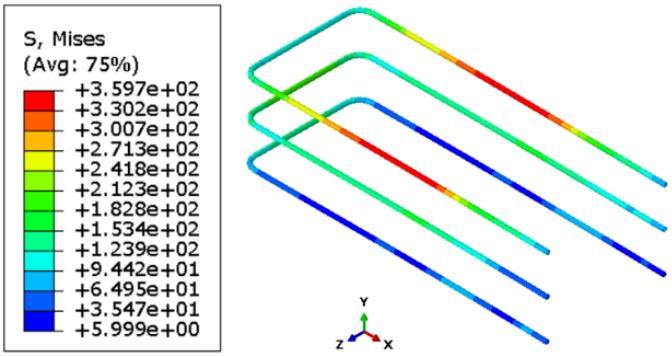

(b)

Figure 5.26. FEA output of S4-Hybrid (5.77% Drift Ratio): (a) Epoxy Mises stress; (b) U-shaped steel Mises stress.

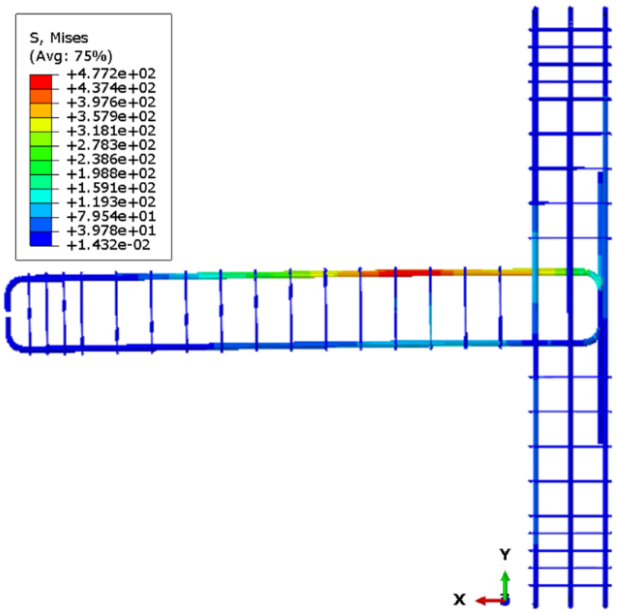

Figure 5.27. FEA output of S4-Hybrid of shear behaviour (1.54% Drift Ratio): Reinforcement Mises stress.

For specimen S4-Hybrid, the damage and stresses of the beam at a displacement of 75 mm (drift ratio = 5.77%) were analysed. As shown in Figure 5.24, the concrete compressive failure occurred on the bottom of beam and at the end of the strengthening. Concrete tensile damage was also observed in the form of a serious crack at the top of the beam at the end of the strengthening. Flexural cracks were also observed on the beam. At this stage, yielding of the beam longitudinal bars occurred. Moreover, plastic strain and stiffness degradation on the beam are clearly visible. The damage and stresses confirmed the reported experimental observations. The strengthening techniques used transferred the damage from the joint area to the beam side and strengthened the joint area against shearing.

When Figure 5.25 (a) and (b) are examined, it is clearly seen that the FRP sheet meets the HSNMTCRT criterion and reaches a value of 1. When the criterion reaches a value of 1, it means that the material's matrix is no longer able to withstand the tensile stresses, resulting in failure. This means that tensile forces destroyed the matrix material, causing ruptures. However, in Figure 5.25 (c), (d) and (e), it is seen that the Hashin damage criteria are not met and therefore no damage occurred. The results shown in Figure 5.25 are given for Layer-1. This is because it is the most critical layer where concrete and FRP sheet come into contact.

Analysing the epoxy results, it is clear that the epoxy material was not damaged (see Figure 5.26 (a)). The maximum stress for the epoxy material was 21.2 MPa, and the epoxy material was still in the elastic region of the constitutive model in the numerical analysis (see Figure 5.15). When it comes to u-shaped steel in the epoxy material, the results of the analysis show that these bars did not yield (see Figure 5.26 (b)).

According to the experimental results, the longitudinal bars in the beam (strain gauge number: SG05) did not yield at a 1.54% drift ratio, whereas they did in the numerical model. This is because, the strain gauges on the bar were glued closer to the joint area (Figure 3.26) than the location of yielding in the numerical model, at the location of the strain gauge in the numerical model, the steel had not yielded, this is likely due to the fibreglass confining the concrete at this location and thus preventing the concrete from cracking and hence locally reducing the strains (see Figure 5.27).

In addition, the concrete crack propagation of the S1-Control, the S2-NSM, and the S4-Hybrid specimens are shown in detail for each drift ratio in Figure 5.28, Figure 5.29, and Figure 5.30, respectively.

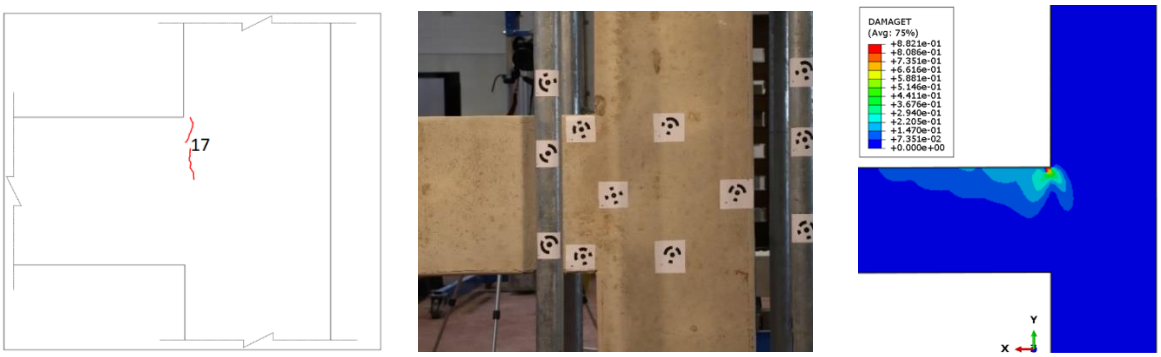

(a) Drift ratio: 0.23%, Displacement: 3 mm

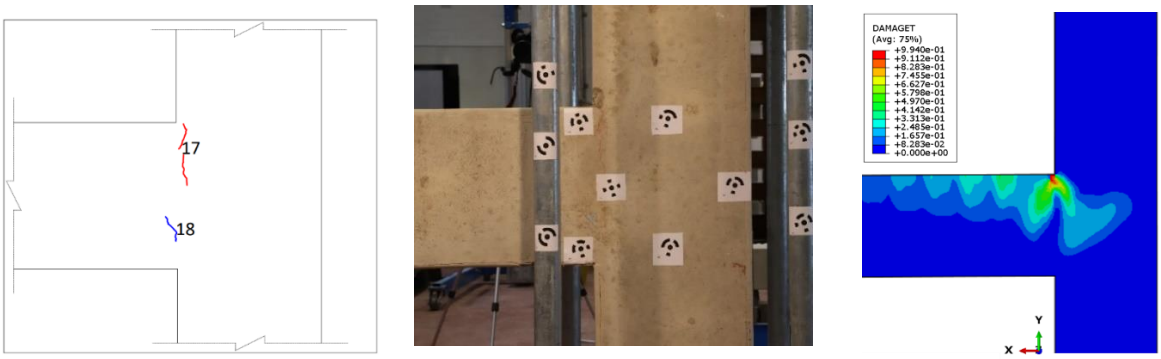

(b) Drift ratio: 0.39%, Displacement: 5 mm

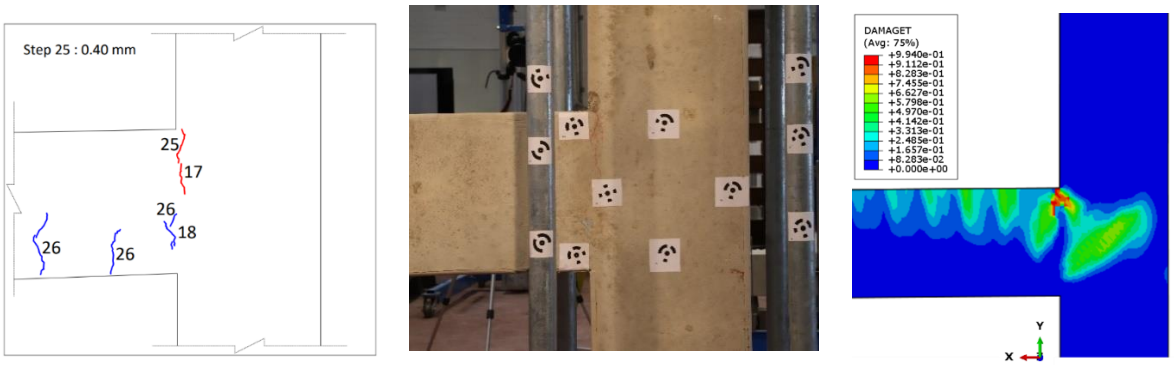

(c) Drift ratio: 0.62%, Displacement: 8 mm

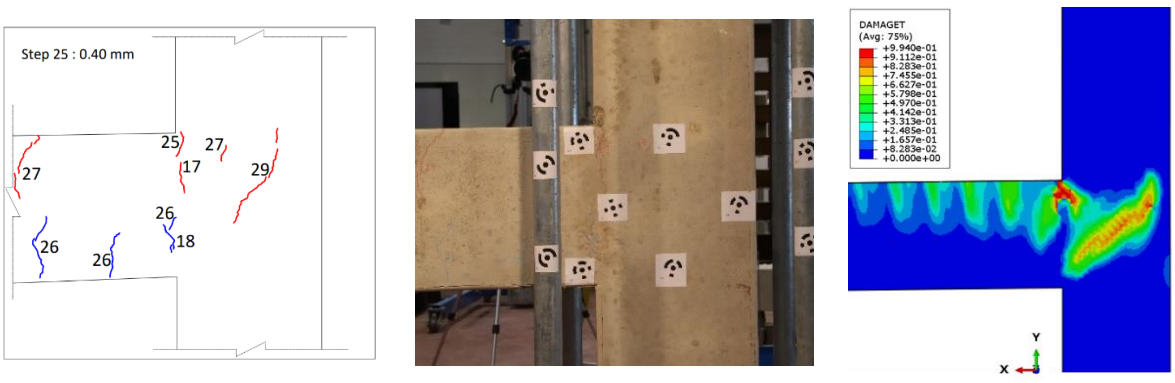

(d) Drift ratio: 0.92%, Displacement: 12 mm

Figure 5.28. Comparison with numerical model and experimental results for Tensile Damage Evolution for S1-Control.

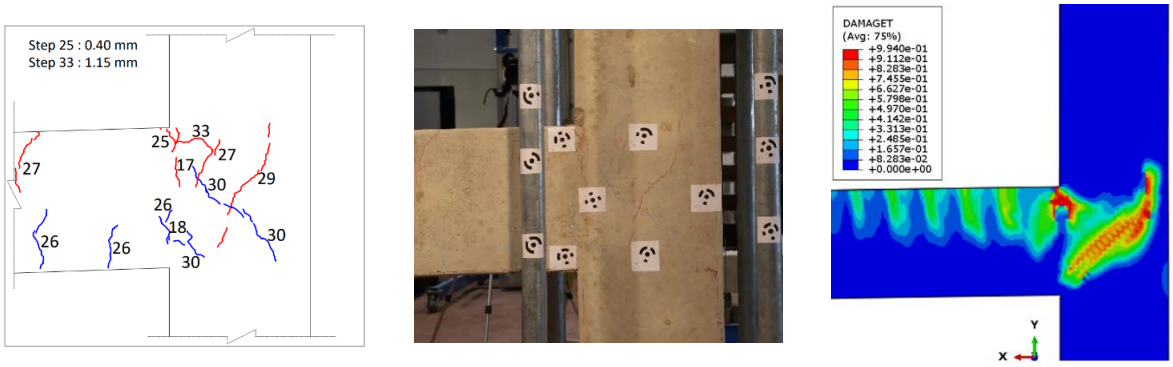

(e) Drift ratio: 1.54%, Displacement: 20 mm

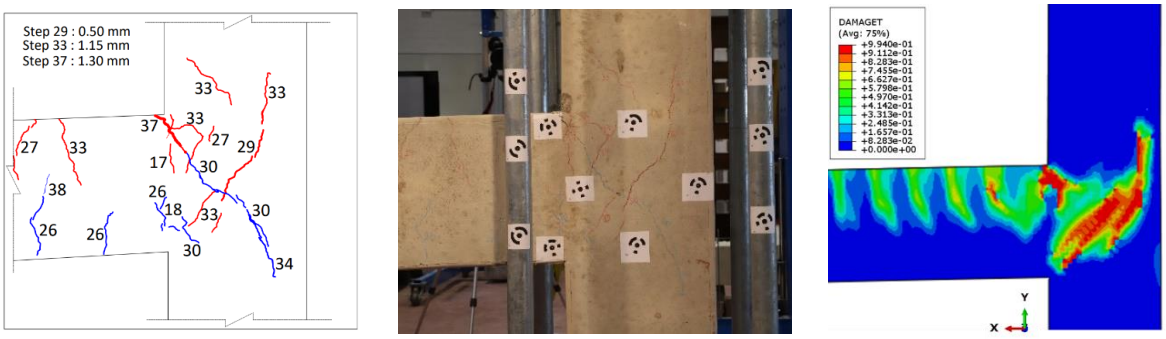

(f) Drift ratio: 2.31%, Displacement: 30 mm

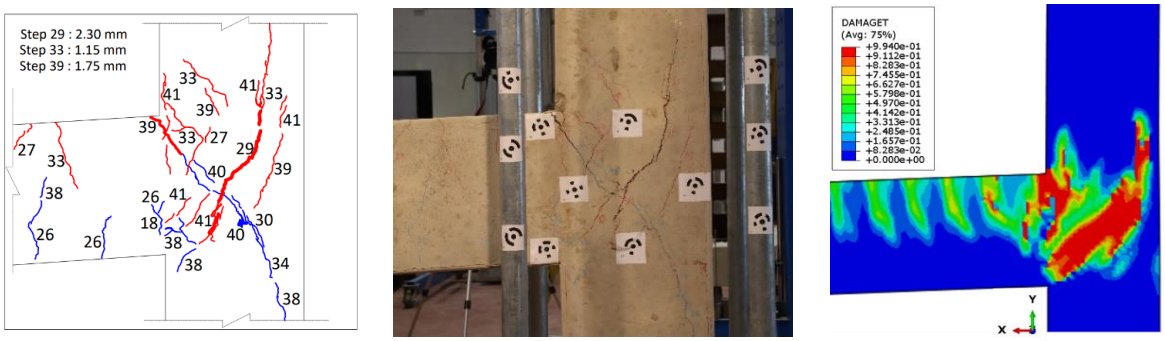

(g) Drift ratio: 3.85%, Displacement: 50 mm

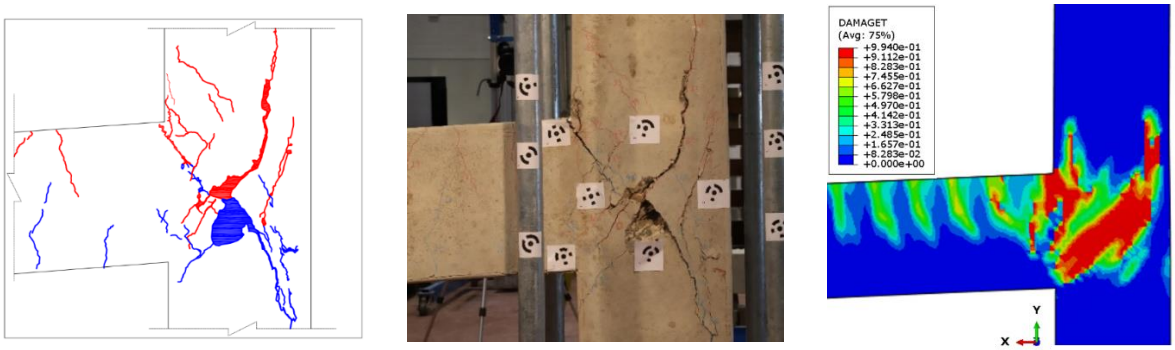

(h) Drift ratio: 4.62%, Displacement: 60 mm

Figure 5.28. Comparison with numerical model and experimental results for Tensile Damage Evolution for S1-Control (continue).

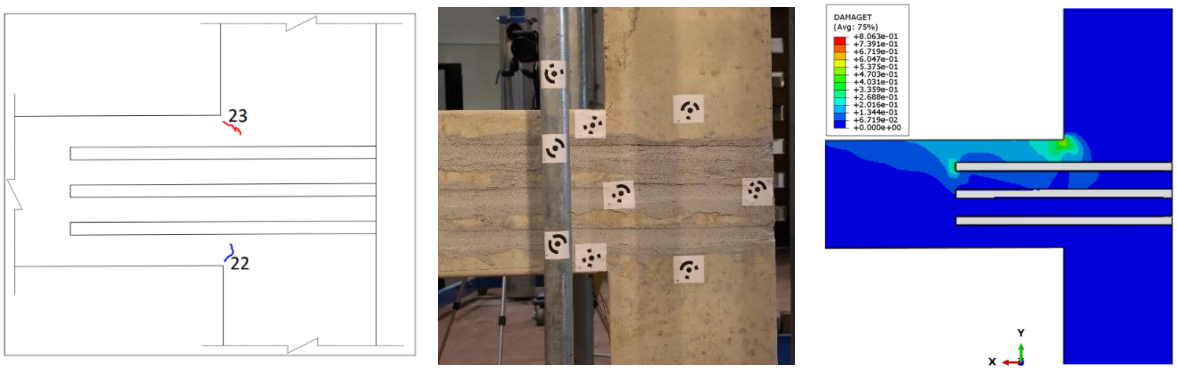

(a) Drift ratio: 0.39%, Displacement: 5 mm

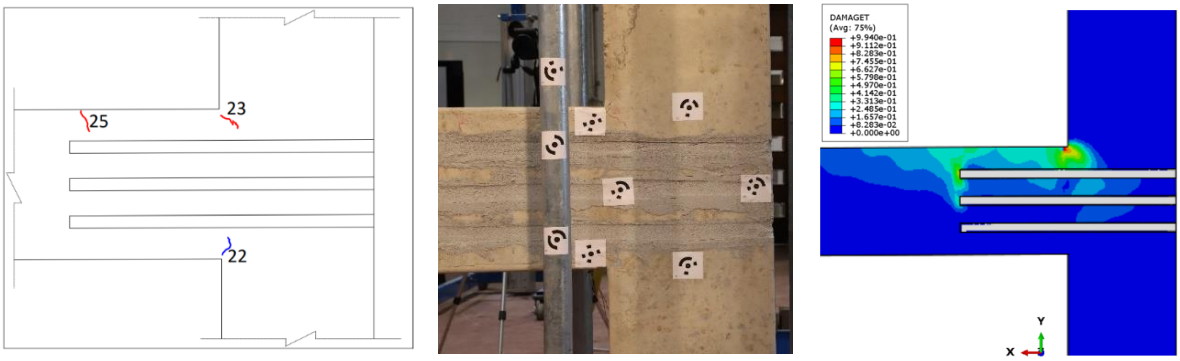

(b) Drift ratio: 0.62%, Displacement: 8 mm

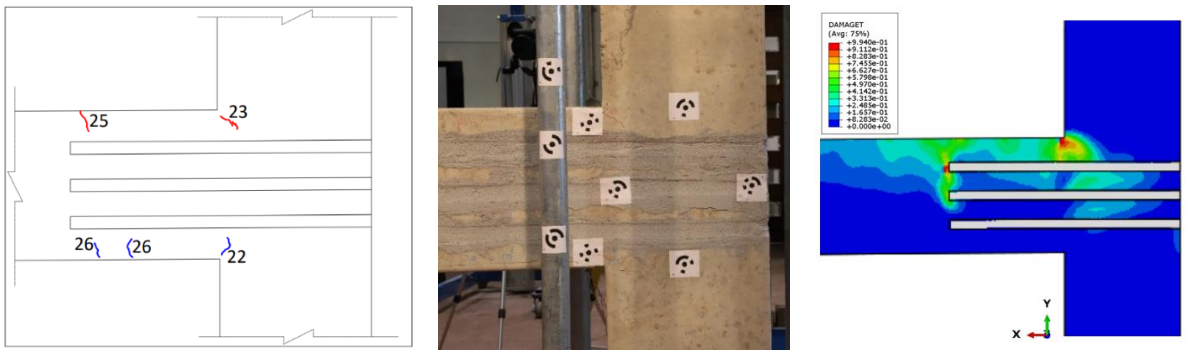

(c) Drift ratio: 0.92%, Displacement: 12 mm

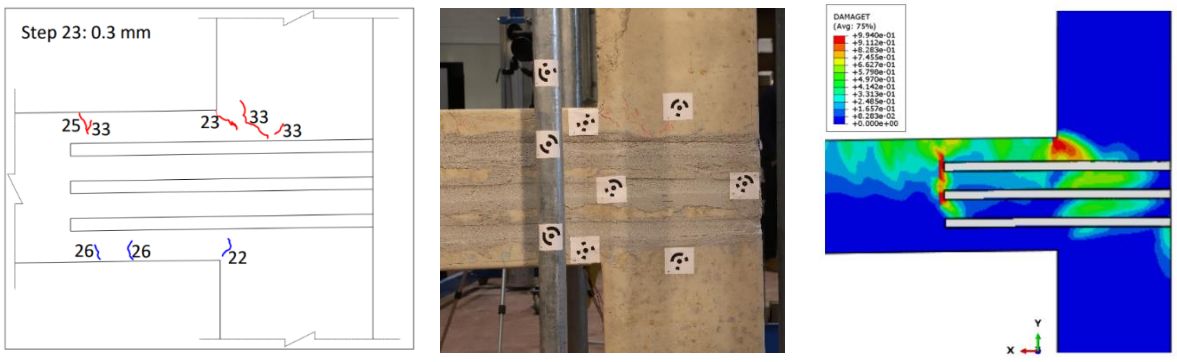

(d) Drift ratio: 1.54%, Displacement: 20 mm

Figure 5.29. Comparison with numerical model and experimental results for Tensile Damage Evolution for S2-NSM.

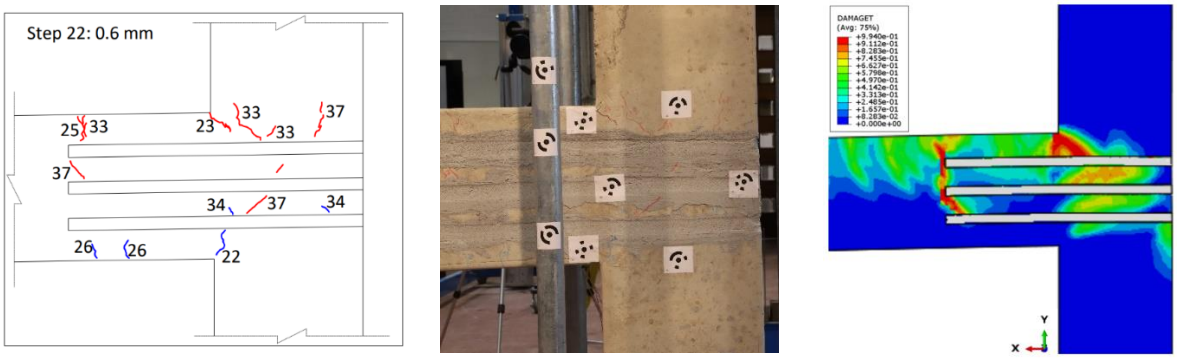

(e) Drift ratio: 2.31%, Displacement: 30 mm

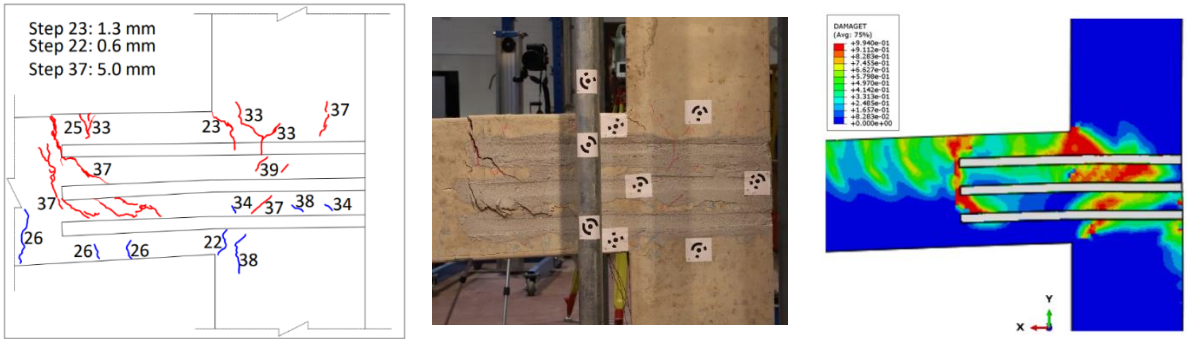

(f) Drift ratio: 3.85%, Displacement: 50 mm

(g) Drift ratio: 4.62%, Displacement: 60 mm

Figure 5.29. Comparison with numerical model and experimental results for Tensile Damage Evolution for S2-NSM (continue).

(a) Drift ratio: 0.92%, Displacement: 12 mm

(b) Drift ratio: 1.54%, Displacement: 20 mm

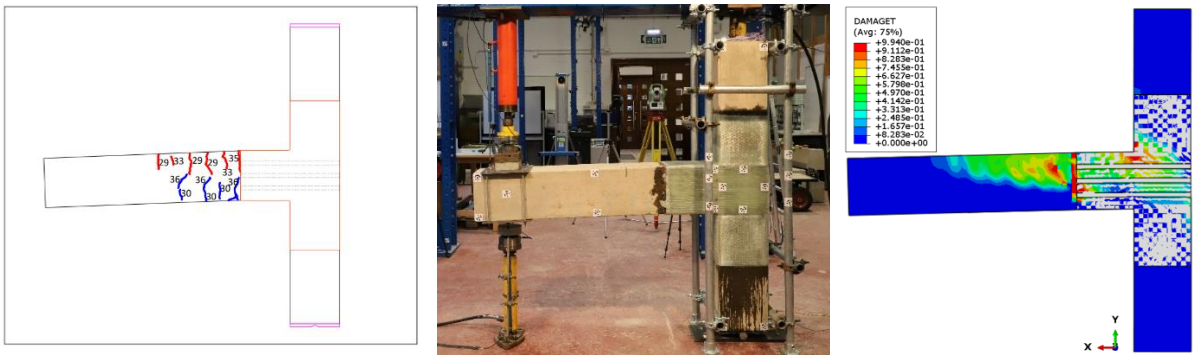

(c) Drift ratio: 2.31%, Displacement: 30 mm

(d) Drift ratio: 3.85%, Displacement: 50 mm

Figure 5.30. Comparison with numerical model and experimental results for Tensile Damage Evolution for S4-Hybrid.

(e) Drift ratio: 4.62%, Displacement: 60 mm

(f) Drift ratio: 5.77%, Displacement: 75 mm

Figure 5.30. Comparison with numerical model and experimental results for Tensile Damage Evolution for S4-Hybrid (continue).

5.7 SUMMARY

The numerical modelling program successfully demonstrated the viability of using Finite Element Analysis (FEA) to simulate the behaviour of reinforced concrete beam-column joints strengthened with different retrofitting techniques. The use of ABAQUS software allowed for an in-depth understanding of the structural performance under monotonic static loads and validated the findings from the experimental program.

The purpose of the model is both as a tool to provide insight into the experimental results and as a predictive tool for future analysis of similar connections.

From a numerical perspective, the FEA results closely approximate the experimental data. The maximum load prediction errors ranged from 3.4% to 7.8%, indicating a good correlation between the simulation and actual behaviour. The displacement predictions at peak load showed higher variability, with errors of 9.0% for the control, 1.2% for the NSM specimen, and

8.2% for the hybrid specimen. In general, the FEA model performed close to the experiments in predicting the behaviour of the control specimen and the retrofitted specimens.

The Concrete Damage Plasticity (CDP) model, when combined with other constitutive material models, accurately represented the tensile softening and compressive hardening and softening behaviour of concrete, as well as the nonlinear response of steel reinforcements. Modifying factors such as mesh size was tested for convergence and viscosity was investigated for optimising the ability of the model to accurately simulate both flexural and shear failure processes. The model calibration process proved essential for accurately replicating the experimental results.

For the control specimen (S1), the numerical model effectively captured the brittle failure mechanism resulting from insufficient reinforcement in the joint region. Likewise, for the NSM-reinforced specimen (S2), the results were very close to the crack propagation obtained from the experiments, and it was concluded that the effect of using NSM was not as effective as in the experiments. Conversely, for the hybrid retrofitted specimen (S4), the FEA accurately predicted the improved performance, with the retrofitted joint demonstrating a more ductile failure pattern and increased energy absorption capabilities.

In the numerical modelling, especially when the epoxy results are examined, it is clearly seen that the epoxy material for S2-NSM has passed the plastic limit. It was also found that the u-shaped steel reinforcement yielded as in the experiments. When the S4-hybrid model was analysed, it was clearly seen that the severe damage in the experiments occurred at the end of the EB reinforcement. It appears that the EB technique prevents the damage seen in the NSM technique due to wrapping. According to the results of the numerical analysis of the S4-hybrid specimen, it is likely that the epoxy remains in the elastic zone and the u-shaped reinforcements do not yield.

The FEA results were able to predict the cracking patterns and failure modes observed during experimental testing. In the unstrengthened specimen (S1), cracks initiated in the beam-column joint region due to shear forces, leading to a brittle failure mechanism. On the other hand, for the retrofitted specimens, particularly the hybrid retrofitted joint (S4), the FEA model predicted the failure at the beam ends rather than the joint itself, indicating the effectiveness of the retrofitting strategy in shifting the failure location and improving the overall seismic resilience of the joint.

The force-displacement curves generated through FEA closely matched those obtained from the experiments. This confirms that the model accurately predicts the structural performance, especially in terms of load-carrying capacity, stiffness degradation, and ductility.

Overall, the FEA model demonstrated high reliability in simulating the nonlinear behaviour of concrete joints, supporting its use for evaluating retrofitted structures.

CHAPTER 6. CONCLUSIONS AND RECOMMENDATIONS

6.1 GENERAL

This research focused on developing a retrofitting solution for seismically deficient reinforced concrete (RC) beam-column joints. An initial literature review highlighted the critical factors affecting joint performance and offered potential retrofitting strategies, namely: Near Surface Mounted (NSM) steel bars and Externally Bonded (EB) Glass Fibre-Reinforced Polymer (GFRP) sheets. Although promising solutions, a number of deficiencies remained. An experimental programme was conducted to determine and test these potential solutions. Four specimens were tested, namely 1) an unretrofitted control, 2) NSM, 3) EB, and 4) a hybrid of the two which is proposed as part of this thesis. Of these specimens, the EB and hybrid methods were found to offer good seismic performance. A potential method to design the retrofitting details for these types of joints was investigated using ABAQUS software to simulate the performance of the hybrid retrofitting technique. This model showed a good correlation with the experimental results, demonstrating that it is possible to design a simple and effective retrofit for substandard beam column connections in reinforced concrete buildings.

6.2 SPECIFIC CONCLUSIONS

This research had a number of objectives in the development of the retrofitting strategy and the success of these is described here:

Determine the factors affecting joint performance:

A comprehensive review of the literature revealed several crucial factors that influence the performance of external reinforced concrete beam-column joints, including the ratio of the axial load to axial capacity of the column, the compressive strength of the concrete, and the confinement supplied by the shear reinforcement in the joint.

Identify potential solutions that may be able to provide sufficient strength:

Many methods were reviewed with the most promising being NSM and EB which are effective in improving the seismic performance of beam-column joints, especially in structures that were not originally designed to meet modern seismic codes; however, NSM can suffer from inadequate bonding between the new reinforcement and the concrete, while the EB method can suffer debonding/delamination of the FRP. There are few studies on the use of these two methods together; and current research do not offer a design method. In this thesis, a hybrid method was developed by combining EB and NSM methods to overcome these shortcomings

followed by a method of numerically simulating the behaviour of this type of joint and, hence facilitating their design.

Developing an experimental programme to determine the best retrofitting strategy:

Specimens were designed considering typical beam-column connection details as specified in TEC, 1998.

The materials used for the specimens, such as concrete, steel, glass fibre reinforced polymer (GFRP) and epoxy resin, were described in detail.

The study used four identical specimens: one control and three strengthened specimens (S1-control, S2-NSM, S3-EB and S4-Hybrid). The remaining three specimens were identical to the control (before retrofit) and were subsequently reinforced using two technologies improved from promising technologies discussed in the literature. Additionally, the characteristics of the strengthening procedures used were detailed. These are the Near Surface Mount (NSM) method, in which steel bars are embedded in grooves drilled in the concrete, the Externally Bonded (EB) method, which involves the application of GFRP sheets and a hybrid of the two.

The test setup in which specimens were subjected to a combination of axial loading and reverse cyclic loading was described in detail as was the loading protocol, including displacement levels and drift ratios. The test procedure also described the instrumentation used during the test, such as strain gauges attached to the reinforcing bars, target points, and cameras used to record deformations.

To test a number of specimens to determine the increase in performance that can be achieved by different retrofitting techniques:

There has been a significant improvement in the global performance of S2-NSM, S3-EB and S4-Hybrid. The S2-NSM specimen has a capacity increase of 12.9% for push and 15.3% for pull. Likewise, S3-EB specimen has 26.4% capacity increase for pushing and 21.8% capacity increase for pulling, while S4-Hybrid specimen has 28.1% capacity increase for pushing and 37% capacity increase for pulling. In the light of these results, the most successful strengthening techniques was the S4-Hybrid specimen in terms of capacity; however, the EB method also shows a significant increase in capacity.

The energy dissipation levels of the strengthened specimens were much higher than those of the control specimens, particularly at drift levels of 2.31% or higher. For instance, the energy

absorbed by the strengthened specimens at 3.85% drift ratio was 9555 kN-mm (S2-NSM), 11074 kN-mm (S3-EB), and 11765 kN-mm (S4-Hybrid). These values represent increases of 33%, 54%, and 63%, respectively, over the corresponding values for the control specimen (S1-Control).

No significant difference improvements exist between the S2-NSM S1 and the Control and specimens in terms of the ductility ratio, For S2-NSM, the average value of μ was 0.37%, meaning no significant increase in energy dissipation for this retrofitting technique. The ductility of S3-EB and S4-Hybrid specimens were μ=29.7% and μ=31.6%, representing a significant increase. From the experimental programme, it is clear that both the EB and Hybrid are sufficient for retrofitting these types of connections, while the NSM method does not give enough extra capacity and ductility to warrant its use. Without performing the retrofit on site, it is not possible to determine if the extra capacity that the hybrid method offers is worth the extra expense and effort over the EB method; however, there is some extra capacity and ductility that may make this worthwhile. Furthermore, the final drift of the hybrid method was not found due to safety concerns in the experiment and so the benefits of the hybrid method may be even greater that was found in this experimental programme. Recommendations on how to determine the best method are given later.

To develop a finite element model of the best retrofitting technique with the aim of checking the feasibility of a future parametric study as part of the development of a design procedure:

The FEA program using ABAQUS effectively demonstrated its capability to simulate the behaviour of RC beam-column connections strengthened with different retrofitting methods. The analysis replicated the structural performance under monotonic loads both in terms of loads, drifts (both total drift and drift to yielding), crack patterns and crack propagation, and failure mechanisms. The model accurately predicted the maximum load-bearing capacity in the push direction, and the estimates for maximum displacement were within 1%-9% of the experimental values. The Concrete Damage Plasticity (CDP) model, combined with constitutive material models, effectively captured the tensile softening and compressive behaviour of concrete, as well as the nonlinear response of steel reinforcement. Adjustments to mesh size and viscosity played a crucial role in optimizing the model's ability to simulate both flexural and shear failures.

The FEA model successfully simulated the different failure mechanisms observed in both unstrengthened and retrofitted specimens. For the control specimen (S1), it accurately predicted a brittle failure caused by insufficient joint reinforcement. In contrast, the hybrid retrofitted specimen (S4) showed improved performance, with a more ductile failure pattern and greater energy absorption. The analysis matched the observed experimental cracking patterns and failure modes, where unstrengthened joints failed at the joint region due to shear forces, while retrofitted joints, particularly the hybrid ones, showed failure at the beam ends. This shift in failure location indicated the effectiveness of the retrofitting strategy in enhancing seismic resilience.

The force-displacement curves generated by the FEA model closely matched the experimental data, confirming its reliability in predicting load-carrying capacity, stiffness degradation, and ductility. Overall, the model demonstrated strong accuracy in capturing the nonlinear behaviour of concrete joints and supports its use for assessing retrofitted structures.

6.3 RECOMMENDATIONS FOR FUTURE WORK

Based on the findings from this research, the following recommendations are proposed for future work:

Although the hybrid retrofitting method was the best at increasing capacity and ductility, it was only marginally better than the EB method and required more effort to apply; however, due to safety concerns, testing was terminated early when the beam started to twist. In a real building, this twisting would have been prevented by the slab and so it is possible that the hybrid method could have even greater benefits as a retrofitting solution. This should be investigated. Furthermore, the literature suggests that there are cases where EB suffers from delamination (which was not the case in this thesis), therefore it is recommended that a more comprehensive test programme is conducted to see where, or if, the hybrid method is significantly better than EB.

Although the hybrid retrofitting method has proven effective in laboratory settings, further pilot projects in actual buildings are necessary to assess its practical applicability. Implementing the method in real-world seismic retrofitting projects would provide valuable feedback and help address any logistical or practical challenges that may arise during large-scale applications.

Further investigation into the use of different FRP materials, such as carbon or aramid fibres, in the EB technique could provide insights into achieving better structural performance in different sized beam column connection. Additionally, varying the diameter and placement of NSM steel bars could lead to optimized designs that further enhance load-bearing capacity and energy dissipation.

The long-term performance of NSM and EB-retrofitted joints, particularly under environmental conditions such as moisture, temperature fluctuations, and chemical exposure, remains largely unexplored. Investigating the durability of these retrofitting methods under such conditions would ensure their reliability for real-world applications.

The FEA framework established in this study can be utilised for further research on different retrofitting materials and techniques, as well as for other structural elements. Moreover, it provides a strong foundation for developing design guidelines for engineers seeking cost-effective and efficient retrofitting solutions.

Three FE models were produced, and so it is recommended that a parametric study is conducted where a comprehensive set of FE models are developed with different sized members, different concrete strength (especially lower than 20MPa as this is often the case in Turkey where substandard building have been constructed) with different unretrofitted specifications and different quantities of retrofitting materials (e.g. U bars and fiberglass) with a view of producing retrofitting design guidelines.

The ABAQUS software used in the numerical modelling in this software applied a monotonic load. While this is sufficient for producing designs of buildings using a code-based approach a more representative test would be to use an explicit solver and apply cyclic dynamic loads. This was beyond the scope of this thesis as this type of analysis is numerically more intensive and can have convergence issues. It is therefore recommended that a numerical programme using an explicit solve be conducted to see if the entire experimental force displacement curve can be replicated and whether this can lead to a better numerical design procedure.

REFERENCES

ABAQUS, 2006. Abaqus Online Documentation: Version 6.6-1, Dassault Systèmes Simulia Corp.; Providence, RI, USA.

ABAQUS, 2016. Abaqus Analysis User's Guide, Dassault Systèmes Simulia Corp.; Providence, RI, USA.

Abbood, I. S., aldeen Odaa, S., Hasan, K. F., & Jasim, M. A., 2021. Properties evaluation of fiber reinforced polymers and their constituent materials used in structures–A review. *Materials Today: Proceedings*, *43*, 1003-1008.

Abdelwahed, B. S., Kaloop, M. R., & El-Demerdash, W. E., 2021. Nonlinear numerical assessment of exterior Beam-Column connections with Low-Strength concrete. *Buildings*, *11*(11), 562.

Abdullah, A. H., 2016. NSM FRP reinforcement for strengthening reinforced concrete beams-overview. *ZANCO Journal of Pure and Applied Sciences*, 28(2).

Aboutaha, R.S., Engelhardt, M.D., Jirsa, J.O. and Kreger, M.E., 1999. Rehabilitation of shear critical concrete columns by use of rectangular steel jackets. *Structural Journal*, *96*(1), pp.68-78.

ACI-318, 2011, Building code requirements for structural concrete, American Concrete Institute, Michigan, USA.

ACI 318 Committee, 2014. Building Code Requirements for Structural Concrete (ACI 318- 14) and Commentary (ACI 318R-14), *American Concrete Institute (ACI)*, Farmington Hills, MI, USA.

ACI Committee 374, 2013. Guide for testing reinforced concrete structural elements under slowly applied simulated seismic loads. American Concrete Institute.

ACI 440.1R-15, 2015. Guide for the Design and construction of structural concrete reinforced with Fiber-Reinforced Polymer (FRP) bars. *American Concrete Institute*.

Adibi, M., Marefat, M. S., Esmaeily, A., Arani, K. K., and Esmaeily, A., 2017. Seismic retrofit of external concrete beam-column joints reinforced by plain bars using steel angles prestressed by cross ties. *Engineering Structures*, *148*, 813-828.

Akash, S. and Jayasree, S., 2018. Effect of Near Surface and Externally Bonded Retrofitting on Exterior Beam-Column Joint. *International Journal of Engineering and Advanced Technology (IJEAT)*. ISSN: 2249-8958, Volume-8, Issue- 4C.

Akbarzadeh, H., and Maghsoudi, A. A., 2010. Experimental and analytical investigation of reinforced high strength concrete continuous beams strengthened with fibre reinforced polymer. *Materials & Design*, *31*(3), 1130-1147.

Akguzel, U. and Pampanin, S., 2010. Effects of variation of axial load and bidirectional loading on seismic performance of GFRP retrofitted reinforced concrete exterior beam-column joints. *Journal of Composites for Construction*, *14*(1), pp.94-104.

Akman, M.S., 1990. Yapı Malzemeleri, İ.T.Ü. İnşaat Fakültesi Matbaası, 162 s, İstanbul.

Alavi-Dehkordi, S., Mostofinejad, D., & Alaee, P., 2019. Effects of high-strength reinforcing bars and concrete on seismic behaviour of RC beam-column joints. *Engineering Structures*, *183*, 702-719.

Alcocer, S.M. and Jirsa, J.O., 1993. Strength of reinforced concrete frame connections rehabilitated by jacketing. *ACI structural journal*, *90*(3).

Al-Mahmoud, F., Castel, A., François, R. and Tourneur, C., 2009. Strengthening of RC members with near-surface mounted CFRP rods. *Composite structures*, *91*(2), pp.138-147.

Almusallam, T.H., Elsanadedy, H.M., Al-Salloum, Y.A. and Alsayed, S.H., 2013. Experimental and numerical investigation for the flexural strengthening of RC beams using near-surface mounted steel or GFRP bars. *Construction and Building Materials*, *40*, pp.145-161.

Ansari, A., Shariatmadar, H. and Beydokhti, E.Z., 2023. Comparison Between EBR Method and a NSM New Technique for Strengthening Concrete Beam–Column Joints. *Iranian Journal of Science and Technology, Transactions of Civil Engineering*, pp.1-15.

Antonopoulos, C.P. and Triantafillou, T.C., 2003. Experimental Investigation of FRP Strengthened RC Beam-Column Joints. *Journal of Composites for Construction*, 7: (1): 39- 49.

Askandar, N., and Mahmood, A., 2019. Comparative investigation on torsional behaviour of RC beam strengthened with CFRP fabric wrapping and near-surface mounted (NSM) steel bar. *Advances in Civil Engineering*.

Asplund, S.O., 1949, January. Strengthening bridge slabs with grouted reinforcement. In *Journal Proceedings* (Vol. 45, No. 1, pp. 397-406).

ASTM A370-14: Standard Test Methods and Definitions for Mechanical Testing of Steel Products.

Badawi, M. and Soudki, K., 2009. Flexural strengthening of RC beams with prestressed NSM CFRP rods–experimental and analytical investigation. *Construction and Building Materials*, *23*(10), pp.3292-3300.

Bangash, M.Y.H., 2001. *Manual of numerical methods in concrete* (pp. 70-85). London: Thomas Telford.

Barbosa, A., Fahnestock, L., Fick, D., Gautam, D., Soti, R., Wood, R., Moaveni, B., Stavridis, A., Olsen, M. and Rodrigues, H., 2017. Performance of medium-to-high rise reinforced concrete frame buildings with masonry infill in the 2015 Gorkha, Nepal, Earthquake. *Earthquake Spectra*, 33 (1_suppl), pp. 197-218.

Bayrak, O., & Sheikh, S. A., 1998. Confinement reinforcement design considerations for ductile HSC columns. *Journal of Structural Engineering*, *124*(9), 999-1010.

Behnam, H., Kuang, J. S., and Samali, B., 2018. Parametric finite element analysis of RC wide beam-column connections. *Computers & Structures*, *205*, 28-44.

Bilal, K. A., Mahamid, M., Hariri-Ardebili, M. A., Tort, C., and Ford, T., 2023. Parameter selection for concrete constitutive models in finite element analysis of composite columns. *Buildings*, *13*(7), 1759.

Bilgin, H., 2015. Seismic performance evaluation of an existing school building in Turkey. Challenge *Journal of Structural Mechanics*, 1(4), 161-167.

Björnström, J., Ekström, T. and Hassanzadeh, M., 2006. Dammsäkerhet: spruckna betongdammar: översikt och beräkningsmetoder (in Swedish).

Blaschko, M. and Zilch, K., 1999. Rehabilitation of concrete structures with CFRP strips glued into slits. In *Proceedings of the twelfth international conference of composite materials, ICCM* (Vol. 12).

Bonacci, J., and Pantazoupoulou, S., 1993. Parametric investigation of joint mechanics. *Structural Journal*, 90(1), 61-71.

British Standards Institution (BSI), 1990. Methods of test for Soils for civil engineering purposes, Part 2: Classification tests, BS 1377-2:1990.

BS EN 12390-3, 2019. Testing Hardened Concrete. Compressive Strength of Test Specimens. *British Standard Institution, London*, *16*.

BS EN 12390-5, 2019. Testing hardened concrete Part 5: Flexural strength of test specimens. *BSI Standards Publication, London*.

BS EN 197-1, 2011. Cement-Part 1: Composition, specifications and conformity criteria for common cements. *London: European Committee for Standardisation*.

Campione, G., Cavaleri, L., and Papia, M., 2015. Flexural response of external RC beam–column joints externally strengthened with steel cages. *Engineering Structures*, *104*, 51-64.

Canadian Standards Association (CSA)., 2002. Design and construction of building components with fibre-reinforced polymers. CSA 5806-02, Toronto.

CEB-FIP, 2011. Model Code 2010. Final draft *fib*, *CEB-FIP*.

Chadwell, C.B. and Imbsen, R.A., 2004. XTRACT Cross Sectional Analysis of Structural Components. *Imbsen and Associates Inc., Sacramento*.

Chen, J.F. and Teng, J.G., 2003. Shear capacity of FRP-strengthened RC beams: FRP debonding. *Construction and Building Materials*, *17*(1), pp.27-41.

Colombi, P., and Poggi, C., 2006. An experimental, analytical, and numerical study of the static behaviour of steel beams reinforced by pultruded CFRP strips. *Composites Part B: Engineering*, 37(1), 64-73.

Concrete Society., 2004. Design guidance for strengthening concrete structures using fibre composite materials. Concrete Society Technical Rep. No. 55, London.

Cornelissen, H., Hordijk, D. and Reinhardt, H., 1986. Experimental determination of crack softening characteristics of normalweight and lightweight. *Heron*, *31*(2), pp.45-46.

Cosgun, C., Turk, A.M., Mangir, A., Cosgun, T. and Kiymaz, G., 2020. Experimental behaviour and failure of beam-column joints with plain bars, low-strength concrete and different anchorage details. *Engineering Failure Analysis*, *109*, p.104247.

Davodikia, B., Saghafi, M.H. and Golafshar, A., 2021, December. Experimental investigation of grooving method in seismic retrofit of beam-column external joints without seismic details using CFRP sheets. In *Structures* (Vol. 34, pp. 4423-4434). Elsevier.

Dere, Y., & Koroglu, M. A. 2017. Nonlinear FE modeling of reinforced concrete. *International Journal of Structural and Civil Engineering Research*, 6(1), 71-74.

del Rey Castillo, E., Griffith, M. and Ingham, J., 2018. Seismic behaviour of RC columns flexurally strengthened with FRP sheets and FRP anchors. *Composite Structures*, *203*, pp.382-395.

De Lorenzis, L., & Teng, J. G., 2007. Near-surface mounted FRP reinforcement: An emerging technique for strengthening structures. *Composites Part B: Engineering*, *38*(2), 119-143.

Del Vecchio, C., Di Ludovico, M., Balsamo, A., Prota, A., Manfredi, G. and Dolce, M., 2014. Experimental investigation of exterior RC beam-column joints retrofitted with FRP systems. *Journal of Composites for Construction*, *18*(4), p.04014002.

Demir, A., Ozturk, H., Edip, K., Stojmanovska, M., Bogdanovic, A. and Seismology, E., 2018. Effect of viscosity parameter on the numerical simulation of reinforced concrete deep beam behaviour. *The Online Journal of Science and Technology*, *8*(3), pp.50-56.

De Risi, M.T. and Verderame, G.M., 2017. Experimental assessment and numerical modelling of exterior non-conforming beam-column joints with plain bars. *Engineering Structures*, *150*, pp.115-134.

DIN, E., 1992. 24624. *Paints and Varnishes-Pull-off Test for Adhesion*.

Diro, G. A., & Kabeta, W. F., 2020. Finite element analysis of key influence parameters in reinforced concrete exterior beam column connection subjected to lateral loading. *European Journal of Engineering and Technology Research*, 5(6), 689-697.

Di Tommaso, A., Neubauer, U., Pantuso, A., & Rostasy, F. S., 2001. Behaviour of adhesively bonded concrete-CFRP joints at low and high temperatures. *Mechanics of Composite materials*, *37*, 327-338.

Earij, A., Alfano, G., Cashell, K., & Zhou, X., 2017. Nonlinear three–dimensional finite–element modelling of reinforced–concrete beams: Computational challenges and experimental validation. *Engineering Failure Analysis*, 82, 92-115.

El-Hacha, R. and Gaafar, M., 2011. Flexural strengthening of reinforced concrete beams using prestressed, near-surfacemounted CFRP bars. *PCI journal*, *56*(4).

El-Naqeeb, M., El-Metwally, S., & Abdelwahed, B., 2022. Strength of exterior beam-column connections considering column axial stress: numerical investigation. *Jordan Journal of Civil Engineering*, *16*(2).

Engindeniz, M., Kahn, L. F., and Abdul-Hamid, Z., 2005. Repair and strengthening of reinforced concrete beam-column joints: State of the art. *ACI structural journal*, *102*(2), 1.

EN1097-6:2022 – Standard, EN 1097-6:2022, Tests for mechanical and physical properties of aggregates – Part 6: Determination of particle density and water absorption.

EN1991-1-1: 2002: Eurocode 1: Actions on structures - Part 1-1: General actions - Densities, self-weight, imposed loads for buildings.

EN1992-1-1: 2004 Eurocode 2: Design of concrete structures - Part 1-1: General rules and rules for buildings.

EN1993-1-1:2005 Eurocode 3: Design of steel structures. BS EN, 1(1).

Fayaz, Q., Kaur, G. and Bansal, P.P., 2022. Numerical modelling of seismic behaviour of an exterior RC beam column joint strengthened with UHPFRC and CFRP. *Arabian Journal for Science and Engineering*, pp.1-16.

Farhang, K., Farahbod, F., Nezamabadi, M. F., & Mansouri, B., 2023. Shear strengthening of RC 3D exterior beam-column joints with CFRP sheets an experimental and numerical study. *Asian Journal of Civil Engineering*, 1-21.

Frangopol, D.M. and Soliman, M., 2019. Life-cycle of structural systems: recent achievements and future directions. In *Structures and infrastructure systems* (pp. 46-65). Routledge.

GangaRao, H.V.S., Taly, N. and Vijay, P.V., 2007. Reinforced Concrete Design with FRP Composites. Boca Raton: CRC Press.

Garrity, S.W., 2001, June. Near-surface reinforcement of masonry arch highway bridges. In *Proceedings of the 9th Canadian masonry symposium*.

Gautam, D. and Chaulagain, H., 2016. Structural performance and associated lessons to be learned from world earthquakes in Nepal after 25 April 2015 (MW 7.8) Gorkha earthquake. *Engineering Failure Analysis*, *68*, pp.222-243.

Gebreyohaness, A., 2013. *Seismic Assessment of Pre-1936 Dual RC Wall-Riveted Steel Frame Buildings* (Doctoral dissertation, ResearchSpace@ Auckland).

Genesio, G., Eligehausen, R., Sharma, A. and Pampanin, S., 2010. Experimental and numerical study towards a deformation-based seismic assessment of substandard exterior RC beam-column joints. In *Proceedings of the 7th Int. Conf. on Fracture Mechanics of Concrete and Concrete Structures (FRAMCOS-7), Jeju, Korea*.

Gergely, J., Pantelides, C.P. and Reaveley, L.D., 2000. Shear strengthening of RCT-joints using CFRP composites. *Journal of composites for construction*, *4*(2), pp.56-64.

Ghobarah, A. and Said, A., 2002. Shear strengthening of beam-column joints. *Engineering structures*, *24*(7), pp.881-888.

Ghobarah, A., Aziz, T.S. and Biddah, A., 1997. Rehabilitation of reinforced concrete frame connections using corrugated steel jacketing. *Structural Journal*, *94*(3), pp.282-294.

Goksu, C., Yilmaz, H., Chowdhury, S., Orakcal, K. and Ilki, A., 2014. The Effect of Lap Splice Length on the Cyclic Lateral Load Behavior of RC Members with Low-Strength Concrete and Plain Bars. *Advances in Structural Engineering*, 17 (5), pp. 639-658.

Günaslan, S. E., Karaşin, A., & Öncü, M. E., 2014. Properties of FRP materials for strengthening. *International Journal of Innovative Science, Engineering & Technology*, *1*(9), 656-660.

Haach, V.G., De Cresce El Debs, A.L.H. and El Debs, M.K., 2014. Influence of high column axial loads in exterior R/C beam-column joints. *KSCE Journal of Civil Engineering*, *18*, pp.558-565.

Hafezolghorani, M., Hejazi, F., Vaghei, R., Jaafar, M.S.B. and Karimzade, K., 2017. Simplified damage plasticity model for concrete. *Structural engineering international*, *27*(1), pp.68-78.

Hahn, H.T. and Tsai, S. W., 1980. Introduction to composite materials. CRC Press, Boca Raton.

Hasan, Q.F., Tekeli, H. and Demir, F., 2016. NSM Rebar and CFRP laminate strengthening for RC columns subjected to cyclic loading. *Construction and Building Materials*, *119*, pp.21-30.

Hashemi, S. M., & Riahi, H. T., 2022. Seismic performance of reinforced concrete beam-column joints strengthened with NSM steel bars and NSM CFRP strips. In *Structures* (Vol. 39, pp. 57-69).

Hashin, Z., 1980. Failure criteria for unidirectional fiber composites. *J Appl Mech* 47(2):329-334.

Hassan, T. and Rizkalla, S., 2004. Bond mechanism of NSM FRP bars for flexural strengthening of concrete structures. ACI Structural journal, 101(6), pp.830-839.

Hassan, W.M., 2011. *Analytical and experimental assessment of seismic vulnerability of beam-column joints without transverse reinforcement in concrete buildings*. University of California, Berkeley.

Helal, Y., 2012. *Seismic Strengthening of Deficient Exterior RC Beam-Column Sub-Assemblages Using Posttensioned Metal Strips*. Ph.D. Dissertation, University of Sheffield.

Hillerborg, A., 1985. The theoretical basis of a method to determine the fracture energy GF of concrete. *Materials and structures*, *18*, pp.291-296.

Hollaway, L. C., & Leeming, M. (Eds.)., 1999. *Strengthening of reinforced concrete structures: Using externally bonded FRP composites in structural and civil engineering*. Elsevier.

Hosen, M. A., Jumaat, M. Z., Darain, K. M. U., Obaydullah, M., & Islam, A. S., 2014. Flexural strengthening of RC beams with NSM steel bars. In *Proceedings of the International Conference on Food, Agriculture and Biology (FAB-2014), Kuala Lumpur, Malaysia*.

Hosen, M.A., Jumaat, M.Z., Islam, A.B.M.S., Kamruzzaman, M., Huda, M.N. and Soeb, M.R., 2015. Eliminating concrete cover separation of NSM strengthened beams by CFRP end anchorage. *Struct. Eng. Mech*, *56*(6), pp.899-916.

Ilki, A., Bedirhanoglu, I., & Kumbasar, N., 2011. Behaviour of FRP-retrofitted joints built with plain bars and low-strength concrete. *Journal of Composites for Construction*, *15*(3), 312-326.

Ince, O., 2024. Structural damage assessment of reinforced concrete buildings in Adıyaman after Kahramanmaraş (Türkiye) Earthquakes on 6 February 2023. *Engineering Failure Analysis*, *156*, p.107799.

Inel, M., Ozmen, H. B., and Bilgin, H., 2008. Seismic performance evaluation of school buildings in Turkey. *Struct. Eng*. Mech, 30(5), 535-558.

ISO 15630-1, 2019. Steel for the Reinforcement and Prestressing of Concrete—Test Methods—Part 1: Reinforcing Bars, Rods and Wire.

ISO 6892-1, 2019. Metallic materials -Tensile testing - Part 1: Method of test at room temperature.

Kandekar, S., and Talikoti, R., 2019. Strength and Durability Study of Aramid Fibers in Retrofitting of Reinforced Concrete Structure. *Fibers*,7,11.

Kanıt, R., and Altın, M., 2010. A Method for the cost estimation in strengthening school buildings in Turkey.

Karayannis, C. G., and Sirkelis, G. M., 2008. Strengthening and rehabilitation of RC beam–column joints using carbon-FRP jacketing and epoxy resin injection. *Earthquake Engineering & Structural Dynamics*, *37*(5), 769-790.

Karayannis, C. G., Chalioris, C. E., and Sirkelis, G. M., 2008. Local retrofit of exterior RC beam–column joints using thin RC jackets—An experimental study. *Earthquake Engineering & Structural Dynamics*, *37*(5), 727-746.

Karlsson, B.I., Sorensen, E.P., 2006. ABAQUS: Analysis user's manual version 6.5. Pawtucket, Rhode Island: Hibbitt Publication.

Khalifa, A., Alkhrdaji, T., Nanni, A., and Lansburg, S., 1999. Anchorage of surface mounted FRP reinforcement. *CONCRETE INTERNATIONAL-DETROIT-*, *21*, 49-54.

Kim, J. and LaFave, J.M., 2007. Key influence parameters for the joint shear behaviour of reinforced concrete (RC) beam–column connections. *Engineering structures*, *29*(10), pp.2523-2539.

Laseima, S. Y., Mutalib, A. A., Osman, S. A., and Hamid, N. H., 2020. Seismic Behaviour of Exterior RC Beam-Column Joints Retrofitted using CFRP Sheets. *Latin American Journal of Solids and Structures*, *17*.

Lee, J., 1996. Theory and implementation of plastic-damage model for concrete structures under Cyclic and Dynamic Loading, Ph.D. Thesis (in English), University of California, Berkeley, USA.

Lee, J., and Fenves, G. L., 1998. Plastic-damage model for cyclic loading of concrete structures. *Journal of engineering mechanics*, *124*(8), 892-900.

Lee, J. and Lopez, M., 2020. Application of frictional bond-slip model to large-scale FRP-strengthened T-beams with U-wraps. *International Journal of Concrete Structures and Materials*, *14*(1), p.1.

Le Hoang, T. T., Masuya, H., Yoshimori, K., and Yokoyama, H., 2019. Flexural Behaviour of RC Beams Strengthened with FRP Bars by Near-Surface Mounted Method. *International Journal of Structural and Civil Engineering Research,* Vol. 8, No. 4.

Li, D., Zhou, J. and Ou, J., 2021. Damage, non-destructive evaluation, and rehabilitation of FRP composite-RC structure: A review. *Construction and Building Materials*, *271*, p.121551.

Liu, Q., Duan, Q., Zhao, P., Ren, H., Duan, H., Liu, G., ... & Qin, L., 2021. Summary of calculation methods of engineering earthwork. In *Journal of Physics: Conference Series* (Vol. 1802, No. 3, p. 032002). IOP Publishing.

Lubliner, J., Oliver, J., Oller, S., and Onate, E., 1989. A plastic-damage model for concrete. *International Journal of solids and structures*, *25*(3), 299-326.

Lu, Y. B., & Li, Q. M., 2011. About the dynamic uniaxial tensile strength of concrete-like materials. *International journal of impact engineering*, *38*(4), 171-180.

Mahmoud, M.H., Afefy, H.M., Kassem, N.M. and Fawzy, T.M., 2014. Strengthening of defected beam–column joints using CFRP. *Journal of advanced research*, *5*(1), pp.67-77.

Mai, A.D., Sheikh, M.N. and Hadi, M.N., 2018. Investigation on the behaviour of partial wrapping in comparison with full wrapping of square RC columns under different loading conditions. *Construction and Building Materials*, *168*, pp.153-168.

Mander, J. B., Priestley, M. J., and Park, R., 1988. Theoretical stress-strain model for confined concrete. *Journal of structural engineering*, *114*(8), 1804-1826.

Malm, R., 2006. *Shear cracks in concrete structures subjected to in-plane stresses. Lic* (Doctoral dissertation, Thesis, Royal Institute of Technology (KTH), Stockholm).

Meikandaan, T. P., & Murthy, A. R., 2017. Flexural behaviour of RC beam wrapped with GFRP sheets. *International Journal of Civil Engineering and Technology*, *8*(2).

Mertol, H.C., Tunç, G., Akış, T., Kantekin, Y. and Aydın, İ.C., 2023. Investigation of RC Buildings after 6 February 2023, Kahramanmaraş, Türkiye Earthquakes. *Buildings*, *13*(7), p.1789.

Mofidi, A. and Chaallal, O., 2014. Tests and design provisions for reinforced-concrete beams strengthened in shear using FRP sheets and strips. *International Journal of Concrete Structures and Materials*, *8*, pp.117-128.

Mohammadizadeh, M. R., Fadaei, M. J., and Rounagh, H. R., 2009. Improving torsional behaviour of reinforced concrete beams strengthened with carbon fibre reinforced polymer composite. *Iranian Polymer Journal*, 18, 4(16), 315-327.

Mohr, O., 1900. Welche umstande bedingen die elastizitatsgrenze und den bruch eines materials. Zeitschrift des Vereins deutscher Ingenieure.

Mostofinejad, D. and Akhlaghi, A., 2017. Experimental investigation of the efficacy of EBROG method in seismic rehabilitation of deficient reinforced concrete beam–column joints using CFRP sheets. *Journal of Composites for Construction*, *21*(4), p.04016116.

Murty, C. V. R., Goswami, R., Vijayanarayanan, A. R., and Mehta, V., 2012. Earthquake behaviour of buildings. Gujarat State Disaster Management Authority, Gandhinagar, 53, 79.

Nanni, A., Alkhrdaji, T., Barker, M., Chen, G., Mayo, R., and Yang, X., 1999. Overview of testing to failure program of a highway bridge strengthened with FRP composites. In *Proceedings of fourth international symposium on non-metallic (FRP) reinforcement for concrete structures (FRPRCS-4)* (pp. 69-75). Farmington Hills, Mich.: American Concrete Institute.

Ngo, T. T., Pham, T. M., & Hao, H., 2020. Ductile and dry exterior joints using CFRP bolts for moment-resisting frames. In *Structures* (Vol. 28, pp. 668-684). Elsevier.

Najafgholipour, M. A., & Arabi, A. R., 2021. Finite-element study on the behaviour of exterior reinforced concrete beam-to-column connections with transverse reinforcement in the joint panel. *Practice Periodical on Structural Design and Construction*, *26*(1), 04020050.

Najafgholipour, M. A., Dehghan, S. M., Dooshabi, A., & Niroomandi, A., 2017. Finite element analysis of reinforced concrete beam-column connections with governing joint shear failure mode. *Latin American Journal of Solids and Structures*, *14*(7), 1200-1225.

Ong, C. B., Chin, C. L., Ma, C. K., Tan, J. Y., Awang, A. Z., and Omar, W., 2022. Seismic retrofit of reinforced concrete beam-column joints using various confinement techniques: A review. *In Structures*, 42, 221-243, Elsevier.

Padmanabham, K., Rambabu, K. and Sairam, K., 2022. Modelling Studies of Retrofitted Anchorage System in Exterior Beam Column Joint by Supplementary Steel. *Saudi J Civ Eng*, *6*(9), pp.215-234.

Pampanin, S., Calvi, G.M. and Moratti, M., 2002, September. Seismic behaviour of RC beam-column joints designed for gravity loads. In *12th European conference on earthquake engineering* (Vol. 726, pp. 1-10).

Pantelides, C.P., Clyde, C. and Reaveley, L.D., 2002. Performance-based evaluation of reinforced concrete building exterior joints for seismic excitation. *Earthquake spectra*, *18*(3), pp.449-480.

Parate, K. and Kumar, R., 2019. Shear strength criteria for design of RC beam–column joints in building codes. *Bulletin of Earthquake Engineering*, *17*, pp.1407-1493.

Paulay, T., and Priestley, M. J. N., 1992. Seismic design of reinforced concrete and masonry buildings, Wiley, New York.

Rageh, B.O., El-Mandouh, M.A., Elmasry, A.H. and Attia, M.M., 2022. Flexural behaviour of RC beams strengthened with gfrp laminate and retrofitting with novelty of adhesive material. *Buildings*, *12*(9), p.1444.

Rahal, K.N. and Rumaih, H.A., 2011. Tests on reinforced concrete beams strengthened in shear using near surface mounted CFRP and steel bars. *Engineering Structures*, *33*(1), pp.53-62.

Rashid, M. A., Mansur, M. A., and Paramasivam, P., 2002. Correlations between mechanical properties of high-strength concrete. *Journal of materials in civil engineering*, *14*(3), 230-238.

Raza, A., Khan, Q. U. Z., & Ahmad, A., 2019. Numerical Investigation of Load-Carrying Capacity of GFRP-Reinforced Rectangular Concrete Members Using CDP Model in ABAQUS. *Advances in Civil Engineering*, 2019(1), 1745341.

Realfonzo, R., Napoli, A. and Pinilla, J.G.R., 2014. Cyclic behaviour of RC beam-column joints strengthened with FRP systems. *Construction and Building Materials*, *54*, pp.282-297.

Remmel, G., 1994. Tensile and shear behavior of high strength concrete members (in German), Deutscher Ausschuss für Stahlbeton.

Ren, W., Sneed, L. H., Yang, Y., & He, R., 2015. Numerical simulation of prestressed precast concrete bridge deck panels using damage plasticity model. *International Journal of Concrete Structures and Materials*, *9*, 45-54.

Rezazadeh, M., and Barros, J., 2014. A new hybrid methodology according to near surface mounted carbon fiber reinforced polymer technique for the flexural strengthening of reinforced concrete beams. *Journal of Reinforced Plastics and Composites*, *33*(21), 1993-2009.

Ridwan, R., 2016. Reinforced concrete beam-column joints strengthened in shear with embedded bars. UK: University of Birmingham; PhD Thesis.

Ruiz-Pinilla, J. G., Pallarés, F. J., Gimenez, E., and Calderón, P. A., 2014. Experimental tests on retrofitted RC beam-column joints underdesigned to seismic loads. General approach. *Engineering Structures*, *59*, 702-714.

Saqan, E.I., Rasheed, H.A. and Alkhrdaji, T., 2018. Evaluation of the seismic performance of reinforced concrete frames strengthened with CFRP fabric and NSM bars. *Composite Structures*, *184*, pp.839-847.

Sakthimurugan, K., and Baskar, K., 2021. Evaluation of efficacy of basalt textile fabric on retrofitting of damaged reinforced concrete external beam–column joints. *Innovative Infrastructure Solutions*, *6*(2), 1-12.

Sbahieh, S., Rabie, M., Ebead, U. and Al-Ghamdi, S.G., 2022. The mechanical and environmental performance of fiber-reinforced polymers in concrete structures: Opportunities, challenges, and future directions. *Buildings*, *12*(9), p.1417.

Sezen, H., Whittaker, A. S., Elwood, K. J., and Mosalam, K. M., 2003. Performance of reinforced concrete buildings during the August 17, 1999, Kocaeli, Turkey earthquake, and seismic design and construction practise in Turkey. *Engineering Structures*, *25*(1), 103-114.

Shafaei, J., Hosseini, A., Marefat, M.S., Ingham, J.M. and Zare, H., 2017. Experimental evaluation of seismically and non-seismically detailed external RC beam-column joints. *Journal of Earthquake Engineering*, *21*(5), pp.776-807.

Shayanfar, J., Bengar, H.A. and Niroomandi, A., 2016. A proposed model for predicting nonlinear behavior of RC joints under seismic loads. *Materials & Design*, *95*, pp.563-579.

Shen, X., Li, B., Chen, Y. T., and Tizani, W., 2022. Experimental and numerical study on reinforced concrete beam-column joints with diagonal bars: Effects of bonding condition and diameter. In *Structures* (Vol. 37, pp. 905-918). Elsevier.

Shrestha, R., Smith, S.T. and Samali, B., 2009. Strengthening RC beam–column connections with FRP strips. *Proceedings of the Institution of Civil Engineers-Structures and Buildings*, *162*(5), pp.323-334.

Sikadur®-300. Epoxy impregnating / laminating resin for SikaWrap® structural strengthening fabrics. Available online: https://gbr.sika.com/dam/dms/gb01/c/sikadur_-300.pdf (accessed on 27 January 2024).

Sikadur®-30. Thixotropic epoxy adhesive for bonding reinforcement. Available online: https://gbr.sika.com/content/dam/dms/gb01/w/sikadur_-30.pdf (accessed on 21 January 2024).

SikaWrap 930G. Woven unidirectional glass fibre fabric, designed for structural strengthening applications as part of the Sika® strengthening system. Available online: https://gbr.sika.com/dam/dms/gb01/w/sikawrap_-930_g.pdf (accessed on 27 January 2024).

Singh, S.B., Reddy, A.L. and Khatri, C.P., 2014. Experimental and parametric investigation of response of NSM CFRP-strengthened RC beams. *Journal of Composites for Construction*, *18*(1), p.04013021.

Singh, V., Bansal, P. P., Kumar, M., and Kaushik, S. K., 2014. Experimental studies on strength and ductility of CFRP jacketed reinforced concrete beam-column joints. *Construction and Building Materials*, *55*, 194-201.

Spadea, G., Bencardino, F., and Swamy, R. N., 1998. Structural behaviour of composite RC beams with externally bonded CFRP. *Journal of Composites for Construction*, *2*(3), 132-137.

Su, M., Gong, S., Liu, Y. and Peng, H., 2022. Flexural behavior of RC beams strengthened with fully or partially prestressed near-surface mounted FRP strips: An experimental investigation. *Engineering Structures*, *262*, p.114345.

Talaat, A., Emad, A., Tarek, A., Masbouba, M., Essam, A., & Kohail, M., 2021. Factors affecting the results of concrete compression testing: A review. *Ain Shams Engineering Journal*, *12*(1), 205-221.

Taranu, N., Hohan, R. and Bejan, L., 2012. Longitudinal stiffness characteristics of unidirectional fibre reinforced polymeric composites subjected to tension. *Buletinul Institutului Politehnic din lasi. Sectia Constructii, Arhitectura*, *58*(2), p.49.

Tatar, J. and Hamilton, H.R., 2016. Implementation of bond durability in the design of flexural members with externally bonded FRP. *Journal of Composites for Construction*, *20*(3), p.04015072.

Tatar, J. and Milev, S., 2021. Durability of externally bonded fiber-reinforced polymer composites in concrete structures: A critical review. *Polymers*, *13*(5), p.765.

Tran, M.T., 2016. Influence factors for the shear strength of exterior and interior reinforced concrete beam-column joints. *Procedia engineering*, *142*, pp.63-70.

Trimarentra, K., Piscesa, B., Attard, M.M. and Samani, A.K., 2018. Evaluation of codes of practice and modelling of high strength circular concrete-filled-steel-tube. *13th International Conference on Steel, Space and Composite Structures*, Perth, Australia.

TS 500, 2000. Requirements for design and construction of reinforced concrete structures, TSE (Turkish Standards Institute), Ankara, Turkey.

TS 708, 2010. Steel for the reinforcement of concrete – Reinforcing steel, TSE (Turkish Standards Institute), Ankara, Turkey.

TS 802-2016, 2016. Calculation Principles of Concrete Mix Design (in Turkish), Turkish Standardization Institute, Ankara.

Turan, A. I., Celik, A., Kumbasaroglu, A., and Yalciner, H., 2024. Assessment of reinforced concrete building damages following the Kahramanmaraş earthquakes in Malatya, Turkey (February 6, 2023). *Engineering Science and Technology, an International Journal*, *54*, 101718.

Turkish Earthquake Code (TEC-1998), 1998. Specifications for buildings to be built in seismic areas. Ministry of Public Works and Settlement. Ankara, Turkey (in Turkish).

Turkish Earthquake Code (TEC-2007), 2007. Specifications for buildings to be built in seismic areas. Ministry of Public Works and Settlement. Ankara, Turkey (in Turkish).

Truong, G. T., Dinh, N. H., Kim, J. C., and Choi, K. K., 2017. Seismic performance of exterior RC beam–column joints retrofitted using various retrofit solutions. *International Journal of Concrete Structures and Materials*, *11*, 415-433.

Vahidpour, M., Kheyroddin, A. and Kioumarsi, M., 2022. Experimental investigation on flexural capacity of reinforced concrete beams strengthened with 3D-fiberglass, CFRP and GFRP. *International Journal of Concrete Structures and Materials*, *16*(1), pp.1-20.

Venkateswarlu, C. and Natarajan, C., 2015. Performance Assessment of RC Beams with CFRP and GFRP Sheets. In *Advances in Structural Engineering: Materials, Volume Three* (pp. 1987-2000). Springer India.

Vuran, E., Serhatoğlu, C., Timurağaoğlu, M. Ö., Smyrou, E., Bal, İ. E., & Livaoğlu, R., 2024. Damage observations of RC buildings from 2023 Kahramanmaraş earthquake sequence and discussion on the seismic code regulations. *Bulletin of Earthquake Engineering*, 1-30.

Wang, B., Wu, X., Liu, Q., Wu, Y., Huang, F., Xu, L., Wu, X. and Deng, Y., 2022. Effectiveness and efficiency of externally bonded CFRP sheets for shear strengthening of RC beam-column joints. *Polymers*, *14*(7), p.1347.

Wang, G.L., Dai, J.G. and Bai, Y.L., 2019. Seismic retrofit of exterior RC beam-column joints with bonded CFRP reinforcement: An experimental study. *Composite Structures*, *224*, p.111018.

Wong, H. F., 2005. *Shear strength and seismic performance of non-seismically designed reinforced concrete beam-column joints*. Hong Kong University of Science and Technology (Hong Kong).

Wosatko, A., Pamin, J., & Polak, M. A., 2015. Application of damage–plasticity models in finite element analysis of punching shear. *Computers & Structures*, *151*, 73-85.

Yimer, M. A., & Aure, T. W., 2022. Numerical investigation of reinforced concrete and steel fiber-reinforced concrete exterior beam-column joints under cyclic loading. *Iranian Journal of Science and Technology, Transactions of Civil Engineering*, *46*(3), 2249-2273.

Zaferani, M.J. and Shariatmadar, H., 2022. Repair and retrofitting of external RC beam-to-column joints using the hybrid NSM+ EBR method. *Engineering Structures*, *263*, p.114370.

Zamani Beydokhti, E. and Shariatmadar, H., 2016. Strengthening and rehabilitation of exterior RC beam–column joints using carbon-FRP jacketing. *Materials and Structures*, *49*, pp.5067-5083.

Zhao, B., Taucer, F. and Rossetto, T., 2009. Field investigation on the performance of building structures during the 12 May 2008 Wenchuan earthquake in China. *Engineering Structures*, *31*(8), pp.1707-1723.

Zhou, Y., Gou, M., Zhang, F., Zhang, S., & Wang, D., 2013. Reinforced concrete beams strengthened with carbon fibre reinforced polymer by friction hybrid bond technique: Experimental investigation. *Materials & Design*, *50*, 130-139.

APPENDICES

Appendix-A

In this section, the results of the analyses of the materials used for concrete, the necessary tables and figures used in concrete design are given. In addition, information about cement (provided by the manufacturer) is given.

Table A1, Table A2, Table A3, and Table A4 shows the sieve analysis results for fine sand, sharp sand, coarse aggregate-1, and coarse aggregate-2, respectively.

Table A1. Sieve analysis results for fine sand.

Description	***Sieve Size***	***Weight retained***	***Weight retained***	***Cumulative weight retained***	***Cumulative passing***	***Cumulative passing***
	(mm)	***(g)***	***(%)***	***(g)***	***(g)***	***(%)***
Fine sand	6.3	0	0	0	486.93	100
	5	0.54	0.11	0.54	486.39	99.89
	3.35	3.34	0.69	3.88	483.05	99.20
	2	3.52	0.72	7.40	479.53	98.48
	1.18	2.85	0.59	10.25	476.68	97.89
	0.6	55.03	11.30	65.28	421.65	86.59
	0.425	106.75	21.92	172.03	314.90	64.67
	0.212	232.26	47.70	404.29	82.64	16.97
	0.15	46.12	9.47	450.41	36.52	7.50
	0.063	36.12	7.42	486.53	0.40	0.08
	Pan	0.40	0.08	486.93	0	0
	Total	486.93	100	-	-	-

Table A2. Sieve analysis results for sharp sand.

Description	***Sieve Size***	***Weight retained***	***Weight retained***	***Cumulative weight retained***	***Cumulative passing***	***Cumulative passing***
	(mm)	***(g)***	***(%)***	***(g)***	***(g)***	***(%)***
Sharp sand	6.30	0	0	0	547.90	100
	5.00	2.72	0.50	2.72	545.18	99.50
	3.35	36.72	6.70	39.44	508.46	92.80
	2.00	65.97	12.04	105.41	442.49	80.76
	1.18	51.45	9.39	156.86	391.04	71.37
	0.60	66.16	12.08	223.02	324.88	59.30
	0.43	34.25	6.25	257.27	290.63	53.04
	0.21	121.22	22.12	378.49	169.41	30.92
	0.15	73.80	13.47	452.29	95.61	17.45
	0.06	92.98	16.97	545.27	2.63	0.48
	Pan	2.63	0.48	547.90	0	0
	Total	547.9	100	-	-	-

Table A3. Sieve analysis results for coarse aggregate-1.

Description	***Sieve Size***	***Weight retained***	***Weight retained***	***Cumulative weight retained***	***Cumulative passing***	***Cumulative passing***
	(mm)	***(g)***	***(%)***	***(g)***	***(g)***	***(%)***
Coarse Aggregate-1	14.00	0	0	0	1404.98	100
	10.00	110.15	7.84	110.15	1294.83	92.16
	6.30	770.50	54.84	880.65	524.33	37.32
	5.00	236.50	16.83	1117.15	287.83	20.49
	3.35	189.93	13.52	1307.08	97.90	6.97
	2.00	53.88	3.83	1360.96	44.02	3.13
	1.18	20.80	1.48	1381.76	23.22	1.65
	0.60	21.42	1.52	1403.18	1.80	0.13
	0.43	1.11	0.08	1404.29	0.69	0.05
	0.21	0.18	0.01	1404.47	0.51	0.04
	0.15	0.07	0.005	1404.54	0.44	0.03
	0.06	0.44	0.03	1404.98	0	0
	Pan	0.00	0.00	1404.98	0	0
	Total	1404.98	100	-	-	-

Table A4. Sieve analysis results for coarse aggregate-2.

Description	***Sieve Size***	***Weight retained***	***Weight retained***	***Cumulative weight retained***	***Cumulative passing***	***Cumulative passing***
	(mm)	***(g)***	***(%)***	***(g)***	***(g)***	***(%)***
Coarse Aggregate-2	28	0	0	0	2924.04	100
	20	522.41	17.87	522.41	2401.63	82.13
	14	1249.10	42.72	1771.51	1152.53	39.42
	10	1021.20	34.92	2792.71	131.33	4.49
	6.3	126.48	4.33	2919.19	4.85	0.17
	5	4.20	0.14	2923.39	0.65	0.02
	3.35	0.65	0.02	2924.04	0	0
	2	0	0	2924.04	0	0
	1.18	0	0	2924.04	0	0
	0.6	0	0	2924.04	0	0
	0.425	0	0	2924.04	0	0
	0.212	0	0	2924.04	0	0
	0.15	0	0	2924.04	0	0
	0.063	0	0	2924.04	0	0
	Pan	0	0	2924.04	0	0
	Total	2924.04	100	-	-	-

Figure A1, Figure A2, Figure A3, and Figure A4 shows the granulometry curve of fine sand, sharp sand, coarse aggregate-1, and coarse aggregate-2, respectively.

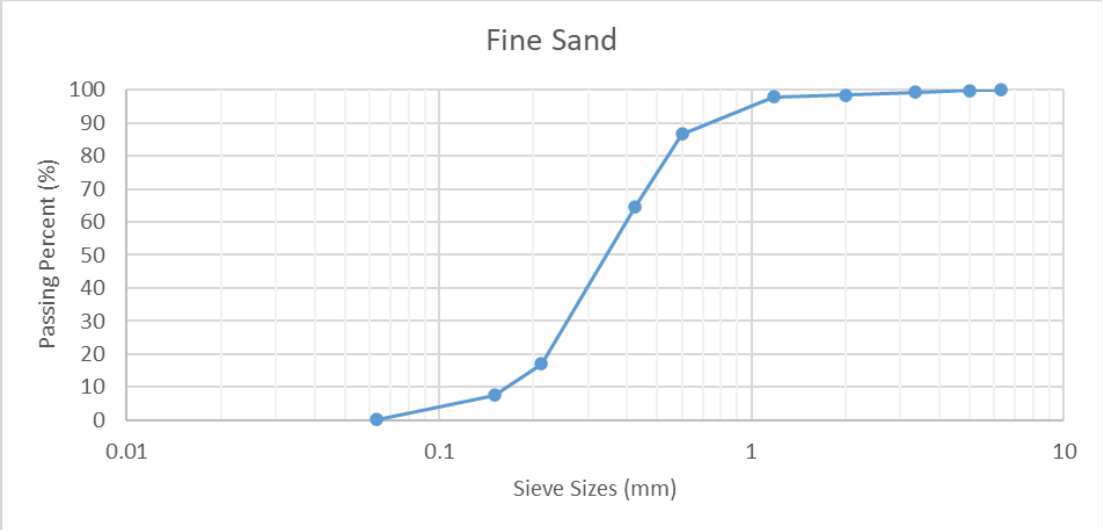

Figure A1. The granulometry curve of fine sand

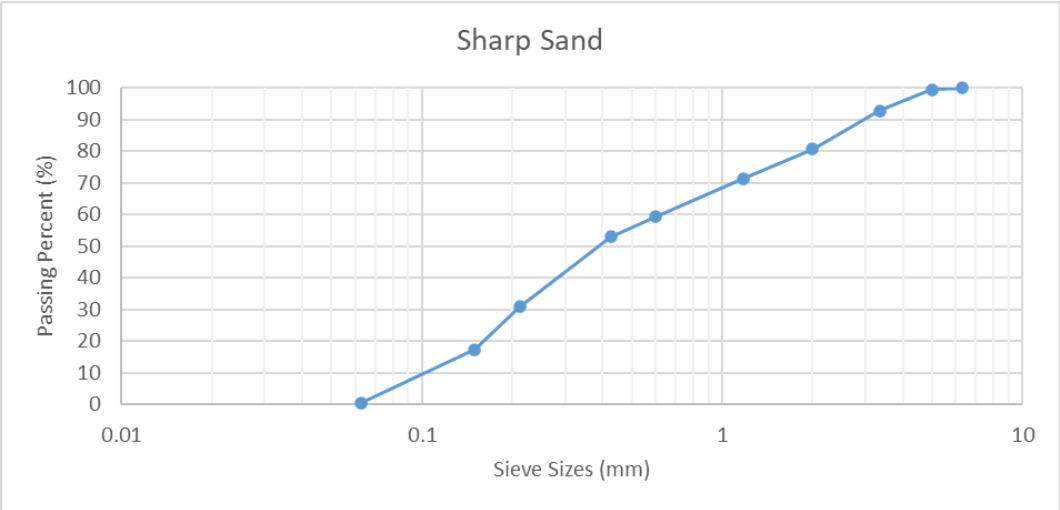

Figure A2. The granulometry curve of sharp sand

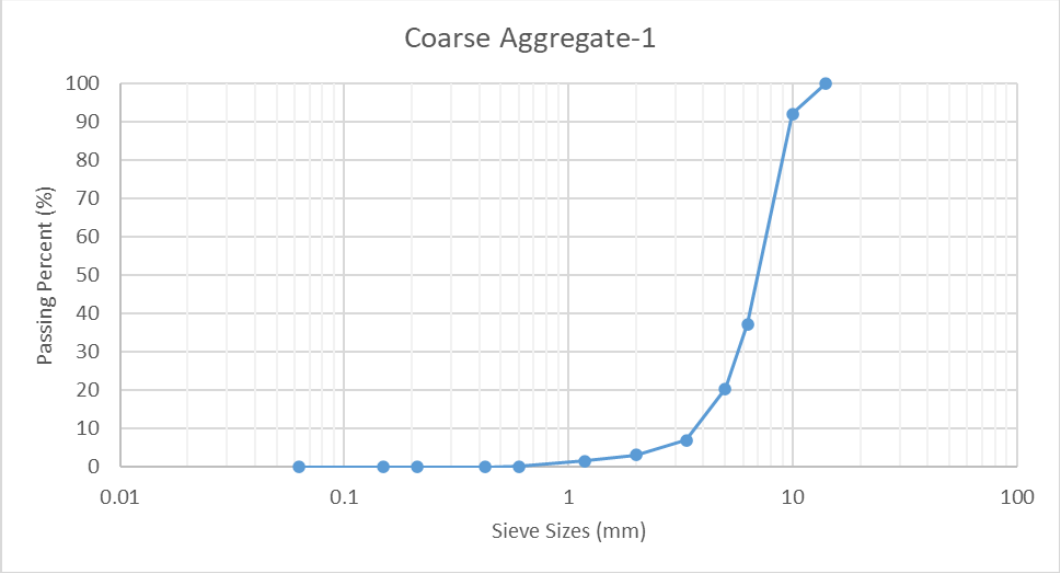

Figure A3. The granulometry curve of coarse aggregate-1.

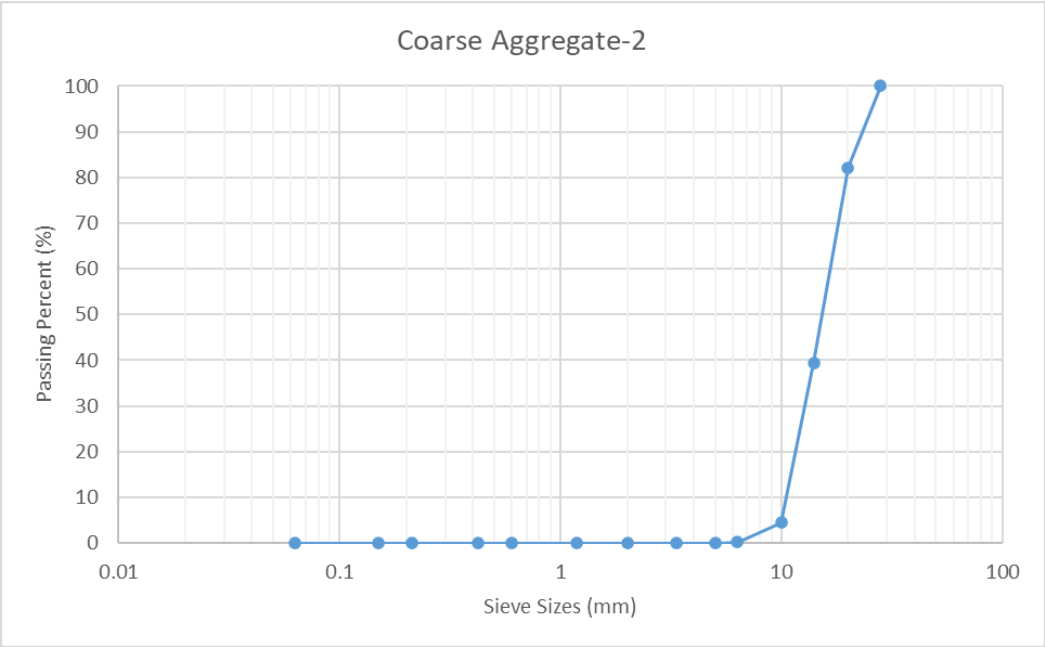

Figure A4. The granulometry curve of coarse aggregate-2.

Table A5, Table A6, and Table A7 shows the determination of the percentage for the concrete mixture, suitable slump values for various structural elements, and according to the exposure classes maximum permissible water/cement ratio, minimum cement dosage, minimum air content (%) and concrete class, respectively.

Table A5. Determination of the percentage for the concrete mixture (TS 802, 2016).

Concrete Grade	Characteristic compressive strength, f_{ck} (MPa)		Target compressive strength, f_{cm} (Average cylinder/equivalent cube compressive strength) (MPa)		
	Characteristic cylinder (150x300) (mm) compressive strength, f_{ck} (MPa)	Equivalent cube (150x150x150) (mm) compressive strength, f_{ck} (MPa)	If the standard deviation is known	If the standard deviation is unknown	
				(150x300) (mm) cylinder	(150x150x150) (mm) cube
C14/16	14	16	$f_{cm} = f_{ck} + 1{,}48\sigma$	18	20
C16/20	16	20		20	24
C18/22	18	22		22	26
C20/25	20	25		26	31
C25/30	25	30		31	36
C30/37	30	37		36	43
C35/45	35	45		43	53
C40/50	40	50		48	58
C45/55	45	55		53	63
C50/60	50	60		58	68
C55/67	55	67		63	75
C60/75	60	75		68	83
C70/85	70	85		78	93
C80/95	80	95		88	103
C90/105	90	105		98	113
C100/115	100	115		108	123

Table A6. Suitable slump values for various structural elements (TS 802, 2016).

Building elements	Slump Values, (mm)	
	Minimum	Maximum
Reinforced concrete foundation walls and piers	30	80
Unreinforced concrete foundations, caissons, and substructure walls	30	80
Beams, columns, reinforced concrete shear walls, tunnel side and arch concretes	50	100
Concrete slab	30	80
Tunnel base coating concretes	20	50
Mass concrete for dams	20	50

Table A7. According to the exposure classes maximum permissible water/cement ratio, minimum cement dosage, minimum air content (%) and concrete class (TS 802, 2016).

Exposure classes	Type of exposure	Maximum water/cement ratio	Minimum strength class	Minimum cement content (kg/m^3)	Minimum air content (%)	Other conditions
X0	No risk of corrosion or harmful effects	-	C12/15 C16/20	-	-	-
XC1	Due to carbonation corrosion	0.70	C20/25	250	-	-
XC2		0.65	C25/30	260	-	
XC3		0.60	C25/30	270	-	
XC4		0.55	C30/37	280	-	
XS1	Sea water effect (chloride effect)	0.55	C30/37	300	-	-
XS2		0.50	C35/45	320	-	
XS3		0.45	C35/45	320	-	
XD1	Sea water except chloride	0.55	C30/37	300	-	-
XD2		0.50	C35/45	320	-	
XD3		0.45	C35/45	320	-	
XF1	Effect of freeze-thaw	0.60	C25/30	280	-	TS 706 EN 12620+A11 in accordance with the standard freeze-thaw with durability aggregate
XF2		0.55	C25/30	300	4.0 [a)]	
XF3		0.50	C25/30	300	4.0 [a)]	
XF4		0.50	C30/37	320	4.0 [a)]	
XM1	Abrasion effect	0.55	C30/37	300	-	
XM2		0.55	C30/37	320	-	
XM3		0.45	C35/45	320	-	
XA1	Hazardous chemical environment	0.60	C25/30	280	-	Sulfate-resistant cement [b)]
XA2		0.50	C35/45	320	-	
XA3		0.45	C35/45	320	-	

a For non-weather-exposed concrete, the concrete performance shall be determined by appropriate test method in comparison with concrete with proven resistance to freezing/thawing for the relevant impact class.

b In exposure classes XA2 and XA3, sulfate resistant cement must be used if the dominant effect is caused by sulfate . In case of classification of cement in terms of resistance to sulfates, cement classified as medium and high resistant should be used in XA2 exposure class (if applicable in XA1 exposure class) and high strength cement should be used in XA3 exposure class.

Figure A5, Figure A6, and Figure A7 shows the relationship between compressive strength and water/cement ratio in air-entrained and non-air-entrained concrete, different largest aggregate grain size and different concrete using naturally formed aggregate approximate mix water of concrete without chemical admixture and non-air entrained for slump values quantities, depending on the largest grain size of the aggregate and climatic conditions, the concrete mixture total air contents to be used in the calculations, respectively.

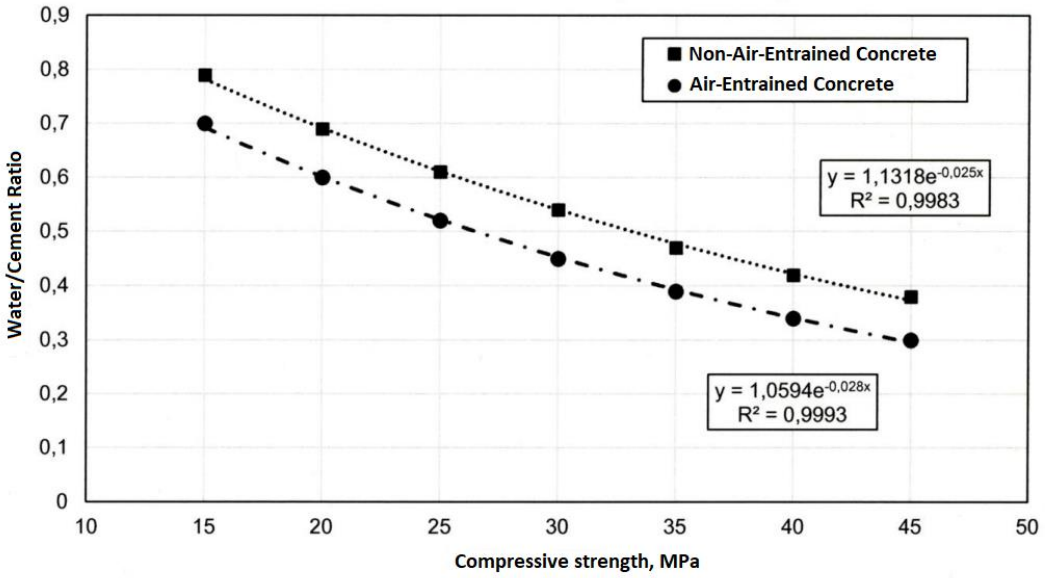

Figure A5. Relationship between compressive strength and water/cement ratio in air-entrained and non-air-entrained concrete (TS 802, 2016).

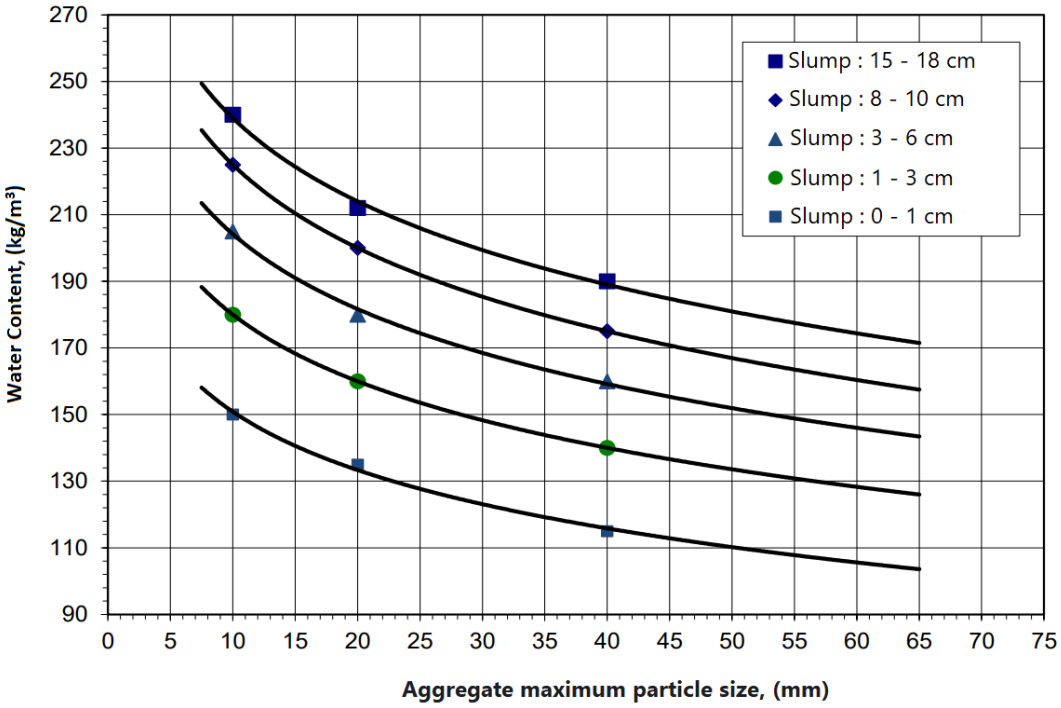

Figure A6. Different largest aggregate grain size and different concrete using naturally formed aggregate approximate mix water of concrete without chemical admixture and non-air entrained for slump values quantities (TS 802, 2016).

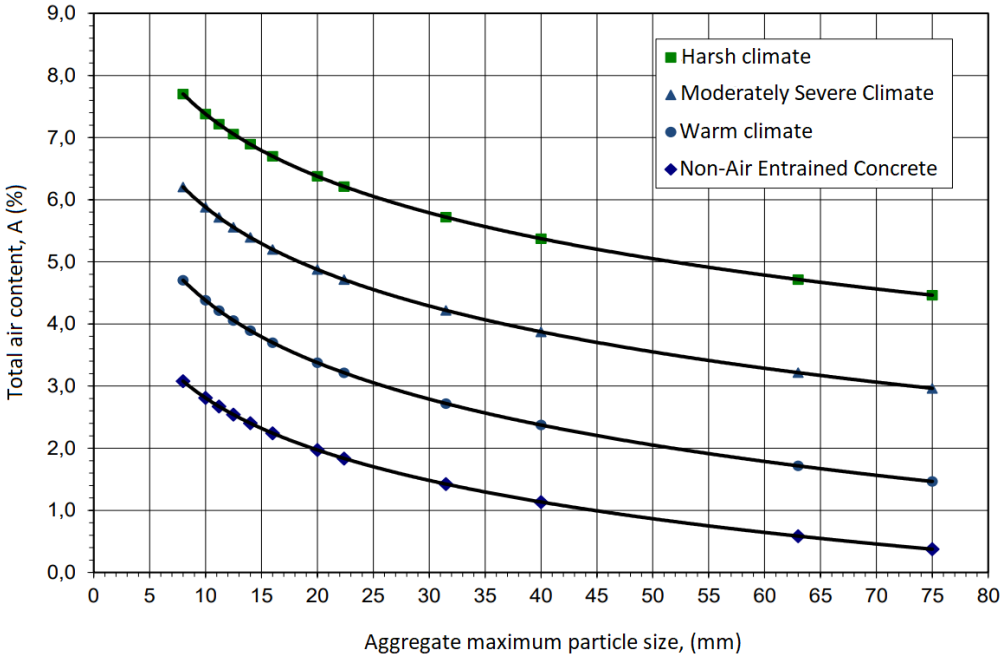

Figure A7. Depending on the largest grain size of the aggregate and climatic conditions, the concrete mixture total air contents to be used in the calculations (TS 802, 2016).

Table A8 shows the physical, chemical, and mechanical properties of PC 32.5R Cement (provided by the manufacturer).

Table A8. Physical, chemical, and mechanical properties of PC 32.5R Cement (provided by the manufacturer).

Cement Despatch Quality															
Date	Sample ID	Despatch Point	Compressive Strength			Cement Physical Characteristics						Colour			
			2CSA	28CSA	Prism Maker	Prism Density	R45	BLAINE	CONS	EXPAC	SETINI	L*	a*	b*	DeltaE
			MPa	MPa	-	g/cm^2	%	g/mm^2	%	mm	min	-	-	-	-
03.01.2023 08:18	CLD23000089	Paper Bag	13.6	34.9	SS	2.21	21.1	432	25.3	1	120	64.91	0.6	9.7	3.1
09.01.2023 07:19	CLD23000363	Paper Bag	16	34.5	PB	2.36	22.7	459	25.2	2	230				
17.01.2023 08:24	CLD23000512	Paper Bag	15.2	37.6	MS	2.22	24.6	415	25.1	3	365				
18.01.2023 08:44	CLD23000534	Paper Bag	17.1	38.2	MS	2.19	20.55	480	25.6		355	64.99	0.4	8.5	2.3
23.01.2023 08:34	CLD23000676	Paper Bag	14.1	35	CH	2.21	22.6	455	25.2	1	330				
26.01.2023 08:00	CLD23000740	Paper Bag	19.6	39.1	CH	2.2	16.7	559	25.2		390	66.68	0.3	9.3	4.1
30.01.2023 08:00	CLD23000890	Paper Bag	14.6	35.9	SS	2.23	22.25	414	24.2	2	230	65.01	0	7.7	2
01.02.2023 08:00	CLD23000926	Paper Bag	16	37.3	SS	2.24	19.4	300	25.6		240				
08.02.2023 08:00	CLD23001124	Plastic Bag	14.9	35.7	SS	2.25	25.9	392	25.6		245				
13.02.2023 08:00	CLD23001285	Plastic Bag	16.3	34.6	CH	2.2	21	400	25.7	1	200	66.87	-0.3	6.4	3.8
15.02.2023 12:00	CLD23001343	Plastic Bag	15.2	34.4	CH	2.25	19.5	376	24.6		165				
20.02.2023 09:00	CLD23001733	Plastic Bag	14.1	34.3	CH	2.24	27.3	386	24.5	2	180				
22.02.2023 09:00	CLD23001814	Plastic Bag	13.9	36.3	CH	2.28	28.1	365	24.4		280	64.78	-0.1	6.9	1.7
27.02.2023 09:00	CLD23002150	Plastic Bag	16	38	SS	2.24	24	438	24.4	1	120	64.85	0.4	7.7	1.8
01.03.2023 08:00	CLD23002313	Plastic Bag	14.9	35.6	SS	2.16	24.2	434	24.2		245				
06.03.2023 08:52	CLD23002667	Plastic Bag	13	37.5	PB	2.24	29.85	370	24.1	2	340	64.18	0.6	8.2	1.6
08.03.2023 07:17	CLD23002770	Paper Bag	14.8	36.5	PB	2.21	35.1	501	23.9		280				
13.03.2023 10:00	CLD23003169	Paper Bag	13.3	36.2	PB	2.21	25.15	525	23.7	3	350	64.91	0.2	7.6	1.9
15.03.2023 08:00	CLD23003295	Plastic Bag	12.8	45.7	PB	2.23	30.4	353	23.8		400				
20.03.2023 08:30	CLD23003622	Paper Bag	14.6	36.7	CH	2.21	25.8	375	23.7	1	360				
22.03.2023 08:33	CLD23003759	Plastic Bag	10.8	27.4	CH	2.2	32.35	355	23.6		275	63.93	0.3	7.8	1
27.03.2023 09:00	CLD23004264	Paper Bag	14.6	34.2	SS	2.24	21.4	441	24.4	1	295	65.09	0.3	7.6	2
29.03.2023 08:38	CLD23004366	Paper Bag	13.6	34.9	SS	2.24	18.2	515	24.4		165				
03.04.2023 13:39	CLD23004793	Paper Bag	14.9	38.9	SS	2.23	19.6	504	25.5	1	225				
04.04.2023 08:06	CLD23004859	Plastic Bag	16.3	40.3	SS	2.25	23.75	510	25.8	1	226	64.17	0.2	7.4	1.1
10.04.2023 09:02	CLD23005413	Plastic Bag	14.7	35.8	SS	3	23.6	392	25	1	224	63.12	0.2	7.5	0.4
12.04.2023 14:31	CLD23005492	Paper Bag	16.3	39.2	SS	2.22	20	411	25.3	1	200				
17.04.2023 08:30	CLD23005891	Paper Bag	16.9	39.4	CH	2.22	17.8	469	26.3	2	197				
18.04.2023 09:21	CLD23006054	Paper Bag	15.5	37.3	CH	2.27	18	462	25.8	1	194	64.04	0.3	7.6	1
24.04.2023 08:00	CLD23006558	Paper Bag	13.6	35.1	SS	2.25	24	451	24.3	1	212	65.71	0.4	8	2.8
26.04.2023 08:00	CLD23006661	Plastic Bag	15.9	39.2	SS	2.29	22.3	390	24.5	1	217				
01.05.2023 07:27	CLD23007157	Plastic Bag	19.5	43.6	PB	2.24	18.05	534	26	1	226				
03.05.2023 08:00	CLD23007237	Paper Bag	20.1	44.2	PB	2.2	20.2	455	25	1	221	62.85	-0.1	7.3	0.3
09.05.2023 08:11	CLD23007748	Paper Bag	18.7	41.8	MS	2.22	27.5	331	25	1	200				
10.05.2023 08:00	CLD23007872	Plastic Bag	19.7	44.5	MS	2.26	19.8	409	26.8	1	229	61.91	0	7	1.2
15.05.2023 06:48	CLD23008358	Plastic Bag	17.6	40.2	CH	2.21	21.1	528	25.5	1	201				
16.05.2023 06:55	CLD23008543	Paper Bag	14.6	35.8	CH	2.21	26.45	562	25	1	200	62.62	0	6.9	0.6
22.05.2023 12:05	CLD23008955	Plastic Bag	19	40.4	MS	2.15	18.7	429	25	2	210	62.93	0.1	7	0.3
24.05.2023 08:01	CLD23009111	Plastic Bag	16.7	42.5	MS	2.2	26.3	322	25.2		195				
29.05.2023 08:32	CLD23009401	Paper Bag	19.8	43.2	PB	2.13	16.3	499	26.5	0	151				
31.05.2023 09:00	CLD23009511	Plastic Bag	14	40.2	PB	2.25	23.75	582	26	0	230	62.2	0	7.1	0.9
05.06.2023 09:00	CLD23009923	Plastic Bag	17.2	40.4	PB	2.21	21.5	382	26.5	1	182				
07.06.2023 08:00	CLD23010003	Paper Bag	17	42.6	PB	2.27	22.5	361	25.8	1	188	62.09	-0.1	6.8	1.1
12.06.2023 09:29	CLD23010497	Plastic Bag	15.1	34.5	CH	2.2	23.75	396	25.5	0	185				
19.06.2023 14:15	CLD23011215	Paper Bag	17.1	42.2	SS	2.23	25.9	344	25.5	2	340	63.08	0.1	6.9	0.3
21.06.2023 08:35	CLD23011387	Plastic Bag	15	40.8	SS	2.24	30.8		25.5		315				
27.06.2023 08:51	CLD23011973	Plastic Bag	17.8	40.1	CH	2.24	20.4	395	26	0	282				
28.06.2023 08:13	CLD23012051	Paper Bag	22.1	53.9	CH	2.23	17.15	332	26.3	0	306	60.6	-0.2	7.2	2.5
03.07.2023 07:44	CLD23012565	Plastic Bag	20.9	51.1	MS	2.66	21.3	314							
05.07.2023 08:08	CLD23012642	Paper Bag	20.4	52.3	MS	2.28	20.6	315				60.27	-0.1	6.9	2.9
10.07.2023 09:00	CLD23013112	Plastic Bag	17.5	44.7	SS	2.25	20.15	357	25.2	0	295				
12.07.2023 08:27	CLD23013287	Paper Bag	20.5	48.5	SS	2.24	18.4	359	25.2		305	61.39	-0.2	7.2	1.7
17.07.2023 14:43	CLD23013656	Paper Bag	13.3	32.3	MS	2.24	24.8	387				63.69	0.1	7.9	0.9

Table A8. Physical, chemical, and mechanical properties of PC 32.5R Cement (provided by the manufacturer) (continue).

Cement Despatch Quality																										
Date	Sample ID	Despatch Point	Chemistry		XRF Quality											XRD Quality										
			LOI	Cr6 I	SiO2	Al2O3	Fe2O3	CaO	MgO	SO3	K2O	Na2O	Cl	EqNa2O	% LST	CaOf	Alite	Belite	Aluminate	Anhyd	Hemi	Gypsum
			%	ppm	%	%	%	%	%	%	%	%	%	%	%		%	%	%	%	%	%
03.01.2023 08:18	CLD23000089	Paper Bag	11.11	0	18.21	4.72	2.79	63.19	1.41	3.03	0.64		0.063	0.56	17.73	0.74	51.7	9.7	7.6	1.7	1.8	0.9
09.01.2023 07:19	CLD23000363	Paper Bag	10.68		18.15	4.75	2.71	63.55	1.41	3.05	0.65	0.14	0.063	0.57	18.84	0.72	50.2	9.4	7.7	1.7	2.1	0.9
17.01.2023 08:24	CLD23000512	Paper Bag	9.82		18	4.67	2.74	63.11	1.31	3.01	0.64	0.12	0.061	0.54	15.37	0.75	51.8	11.8	6.2	1.9	1.6	0.8
18.01.2023 08:44	CLD23000534	Paper Bag	11.19		18.1	4.65	2.76	63.51	1.33	3.11	0.65	0.12	0.062	0.54	18.45	0.51	52.3	8.5	7	1.9	2	1
23.01.2023 08:34	CLD23000676	Paper Bag	10.68		18.71	4.72	2.75	64.19	1.36	3.31	0.66	0.13	0.061	0.56	16.37	0.37	54.7	8.3	6.6	1.6	2.2	0.9
26.01.2023 08:00	CLD23000740	Paper Bag	11.88		18.55	4.81	2.72	64.31	1.36	3.45	0.67	0.12	0.067	0.56	17.66	0.57	54.4	5.9	7.7	2	2.2	1
30.01.2023 08:00	CLD23000890	Paper Bag	11.76		18.18	4.62	2.73	64.51	1.3	3.26	0.64	0.11	0.054	0.53	15.23	0.5	56.3	7	6.2	2	2.2	1
01.02.2023 08:00	CLD23000926	Paper Bag	11.45		18.04	4.57	2.65	64.75	1.28	3.23	0.64	0.11	0.056	0.53	16.2	0.68	54.9	7.5	6	2	2.3	1.1
08.02.2023 08:00	CLD23001124	Plastic Bag	12.01		17.34	4.39	2.68	64.33	1.25	2.8	0.63	0.1	0.052	0.51	20.69	0.62	49	9.6	5.3	1.7	2.1	1
13.02.2023 08:00	CLD23001285	Plastic Bag	12.68		17.47	4.41	2.63	64.79	1.28	3.06	0.65	0.11	0.057	0.54	21.19	0.95	49.8	8.6	5.2	1.7	1.9	0.9
15.02.2023 12:00	CLD23001343	Plastic Bag	12.68		17.39	4.34	2.76	65.02	1.33	3.2	0.64	0.1	0.052	0.52	19.13	0.49	51.3	8.1	4.3	1.8	2.4	1.1
20.02.2023 09:00	CLD23001733	Plastic Bag	9.94		18.29	4.61	2.88	64.48	1.39	2.96	0.66	0.11	0.058	0.54	19.86	0.64	50.1	10.1	5.1	1.7	1.7	1
22.02.2023 09:00	CLD23001814	Plastic Bag	10		18.39	4.61	2.71	64.16	1.46	2.98	0.65	0.12	0.048	0.54	16.91	0.58	53.5	9.7	5.7	2.1	1.6	0.8
27.02.2023 09:00	CLD23002150	Plastic Bag	10.91		18.24	4.57	2.72	64	1.47	2.91	0.64	0.11	0.055	0.54	17.64	1.18	54.6	6.8	5.8	1.6	2	0.9
01.03.2023 08:00	CLD23002313	Plastic Bag	11.09		18.52	4.61	2.73	63.96	1.54	2.81	0.65	0.11	0.053	0.54	17.48	1	52.1	10.6	5.2	1.6	1.6	0.8
06.03.2023 08:52	CLD23002667	Plastic Bag	10.63	0	18.75	4.72	2.88	65.01	1.44	2.92	0.66	0.12	0.082	0.55	19.12	2.15	50.3	9.5	5	1.9	1.6	1.2
08.03.2023 07:17	CLD23002770	Paper Bag	11.52		18.52	4.61	2.69	64.29	1.42	2.9	0.63	0.12	0.068	0.53	16.54	1.12	54.8	7.4	5.2	1.6	2.2	1
13.03.2023 10:00	CLD23003169	Paper Bag	11.12		18.3	4.5	2.96	63.08	1.42	3.09	0.62	0.12	0.06	0.53	19.61	1.24	49.1	11.4	4.3	1.9	1.7	1
15.03.2023 08:00	CLD23003295	Plastic Bag	10.32		18.76	4.58	3.01	63.96	1.44	3.04	0.62	0.12	0.062	0.54	18.66	1.14	48.9	13.2	4.6	1.6	1.8	0.7
20.03.2023 08:30	CLD23003622	Paper Bag	10		18.65	4.39	2.86	64.12	1.4	3.04	0.55	0.12	0.046	0.49	17.17	0.81	58.3	5.8	3.4	2	2	0.8
22.03.2023 08:33	CLD23003759	Plastic Bag	10.98		18.5	4.46	2.84	63.84	1.33	2.9	0.6	0.12	0.08	0.51	20.28	1.34	46.7	13.7	3.9	1.8	1.7	1
27.03.2023 09:00	CLD23004264	Paper Bag	10.75		18.78	4.55	2.85	63.74	1.62	3.25	0.62	0.13	0.091	0.54	17.16	1.25	53.8	8.6	4.6	1.5	2.2	1.1
29.03.2023 08:38	CLD23004366	Paper Bag	11.87		18.11	4.41	2.69	63.59	1.47	3.35	0.61	0.13	0.084	0.53	21.02	1.52	49.2	8.6	4.5	2.4	2.3	1
03.04.2023 13:39	CLD23004793	Paper Bag	10.27		18.43	4.51	2.8	63.6	1.56	3.25	0.62	0.13	0.07	0.53	18.56	1.44	50.3	11	4.5	2.1	1.8	0.9
04.04.2023 08:06	CLD23004859	Paper Bag	9.92		18.45	4.48	2.84	63.89	1.68	3.32	0.63	0.13	0.061	0.55	17.27	1.33	53	9.6	4.9	2.4	1.7	0.9
10.04.2023 09:02	CLD23005413	Plastic Bag	8.89		18.94	4.6	2.89	63.42	1.53	3.02	0.64	0.13	0.076	0.55	14.11	1.68	52.9	13.1		1.6	1.4	0.9
12.04.2023 14:31	CLD23005492	Paper Bag	9.44		18.57	4.5	2.92	63.08	1.52	2.96	0.63	0.13	0.065	0.54	17.47	1.4	51.7	10.3	3.9	2.4	1.8	0.7
17.04.2023 08:30	CLD23005891	Paper Bag	10.04		18.37	4.49	2.9	63.11	1.48	3.08	0.63	0.13	0.065	0.54	16.22	1.03	54.9	54.9	3.8	2.1	1.9	0.8
18.04.2023 09:21	CLD23006054	Paper Bag	10.47		18.19	4.47	2.89	63.2	1.43	3	0.62	0.13	0.067	0.54	16.83	0.98	53	9.3	3.7	2.1	2	0.9
24.04.2023 08:00	CLD23006558	Paper Bag	10.91		18.19	4.54	2.77	63.72	1.5	3.01	0.64	0.13	0.057	0.55	20.31	1.26	49.8	9.6	5	2.1	1.7	1.1
26.04.2023 08:00	CLD23006651	Plastic Bag	8.95	0	18.91	4.61	2.85	64	1.5	3.04	0.63	0.14	0.068	0.56	16.33	1.67	52.2	11.2	5.2	2.1	1.9	0.6
01.05.2023 07:27	CLD23007157	Plastic Bag	8.53		19.04	4.6	2.86	64.22	1.49	3.21	0.64	0.14	0.084	0.56	13.63	2.06	55.9	10.1	4.4	1.8	1.8	0.7
03.05.2023 08:00	CLD23007237	Paper Bag	8.87		18.71	4.54	2.81	64.1	1.42	3.13	0.63	0.15	0.071	0.57	14.24	1.71	55.7	10.3	4.5	1.9	1.8	0.5
09.05.2023 08:11	CLD23007748	Paper Bag	8.94		18.79	4.6	2.78	64.01	1.45	3	0.64	0.16	0.087	0.58	15.18	2.09	54.4	10.6	4.7	1.7	1.7	0.6
10.05.2023 08:00	CLD23007872	Plastic Bag	9.24		18.58	4.52	2.87	63.76	1.43	2.91	0.61	0.15	0.067	0.55	16.88	1.68	54.4	8.8	4.3	2	2	0.7
15.05.2023 06:48	CLD23008358	Plastic Bag	9.39		18.44	4.6	2.76	64.13	1.49	3.19	0.65	0.15	0.079	0.58	15.16	1.49	54.7	10	4.4	1.6	2	0.8
16.05.2023 06:55	CLD23008543	Paper Bag	9.44		19.05	4.71	2.74	64.25	1.53	3.04	0.62	0.15	0.083	0.56	16.65	1.43	51.3	12.1	4.6	1.9	1.9	0.7
22.05.2023 12:05	CLD23008955	Plastic Bag	9.1		18.5	4.54	2.82	63.34	1.47	3.04	0.62	0.15	0.072	0.56	14.72	1.41	55.8	9.8	4.4	1.7	1.7	0.7
24.05.2023 08:01	CLD23009111	Plastic Bag	7.49		19.35	4.74	2.87	64.12	1.53	2.96	0.63	0.15	0.069	0.57	10.73	1.5	57.7	11.2	4.7	1.5	1.7	0.6
29.05.2023 08:32	CLD23009401	Paper Bag	10.06		18.1	4.44	2.69	64.25	1.47	3.19	0.61	0.15	0.074	0.55	15.03	0.99	55	10.1	4.4	1.7	1.8	0.9
31.05.2023 09:00	CLD23009511	Plastic Bag	8.32	0	18.65	4.56	2.88	62.8	1.66	3.82	0.62	0.17	0.082	0.58	13.62	1.35	53.7	11.5	4	2.6	1.8	1.1
05.06.2023 09:00	CLD23009923	Plastic Bag	8.69		18.48	4.56	2.82	63.36	1.55	2.69	0.61	0.15	0.064	0.55	15.81	1.37	53.2	10.9	4.3	1.7	1.9	0.7
07.06.2023 08:00	CLD23010003	Paper Bag	8.89		18.69	4.59	2.85	63.84	1.65	2.62	0.61	0.15	0.064	0.55	15.52	1.82	52.1	12.1	4.2	1.5	1.9	0.7
12.06.2023 09:29	CLD23010497	Plastic Bag	9.33		18.48	4.54	2.71	63.35	1.57	2.92	0.62	0.16	0.08	0.56	16.89	1.16	51.4	11.7	4.3	1.8	2	0.8
19.06.2023 14:15	CLD23011215	Paper Bag	9.15		18.85	4.54	2.78	63.98	1.52	2.86	0.6	0.15	0.059	0.54	14.89	1.25	58.4	7.2	3.4	1.9	1.7	0.9
21.06.2023 08:35	CLD23011387	Plastic Bag	7.03		19.16	4.69	2.87	63.44	1.63	3.03	0.62	0.16	0.077	0.57	11.19	1.31	57.6	12.4	4.7	1.8	1.3	0.6
27.06.2023 08:51	CLD23011973	Plastic Bag	9.38		18.61	4.52	2.76	63.63	1.51	3.06	0.62	0.16	0.082	0.56	17.39	1.63	53.7	9.3	4.2	2.1	1.9	0.8
28.06.2023 08:13	CLD23012051	Paper Bag	6.13		19.64	4.8	3.09	63.84	1.64	2.93	0.62	0.19	0.08	0.6	9.22	1.98	59.1	12.2	5.1	1.5	1.2	0.7
03.07.2023 07:44	CLD23012565	Plastic Bag	6.01	0.18	19.31	4.71	3.09	63.4	1.57	3.14	0.64	0.16	0.067	0.58	10.18	2.37	55.6	13	5	2.3	1.4	0.5
05.07.2023 08:08	CLD23012642	Paper Bag	5.61		19.59	4.73	3.12	63.56	1.66	3.16	0.63	0.16	0.069	0.58	10.25	2.24	55.8	13.1	4.9	2.3	1.5	0.4
10.07.2023 09:00	CLD23013112	Plastic Bag	6.65		18.92	4.61	3.33	62.68	1.54	2.91	0.61	0.16	0.059	0.56	10.97	1.31	55.4	13.9	4.8	1.7	1.3	0.5
12.07.2023 08:27	CLD23013287	Paper Bag	6.24		19.36	4.71	3.14	63.46	1.6	3.19	0.63	0.18	0.076	0.59	11.12	1.62	55.4	12.9	4.9	2.2	1.5	0.4
17.07.2023 14:43	CLD23013656	Paper Bag	8.43		18.83	4.63	3.09	63.03	1.45	3.19	0.62	0.16	0.063	0.57	15.1	1.94	47.3	15.8	5.1	2.1	1.7	0.7

Appendix-B

In this section, the test results of the samples taken from each specimen are given in detail as the concrete tensile test (three-point bending test) and the concrete compressive test (cylinder compressive test), respectively. In addition, information on the test results of the rebars used for the steel cage is given.

Three-Point Bending Test of Concrete

$$\sigma = \frac{M}{W}$$

$$\sigma = f_{ctk}^{``} = \frac{\left(\frac{F \times L}{4}\right)}{\left(\frac{b \times h^2}{6}\right)}$$

$$f_{ctk} = \frac{f_{ctk}^{`}}{1.5} = \frac{f_{ctk}^{``}}{2} \text{ (TS 500, 2000)}$$

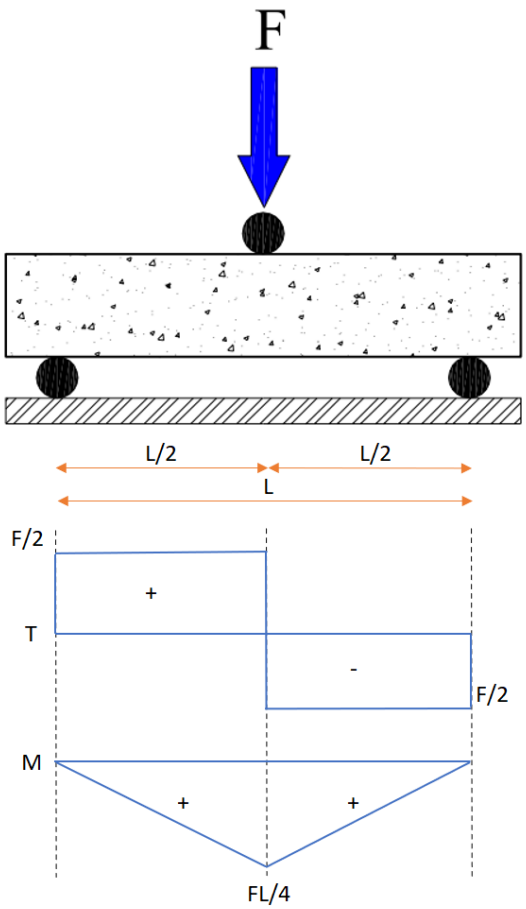

Figure B1. Three-point bending test of concrete and diagram of shear and moment.

Specimen-1 (Control Specimen)

Three-point bending test (BS EN 12390-5:2019)

Casting date: 06/12/2023 Test date:03/01/2024

Age: 28 days

Sample Name	**ST11**	**ST12**	**ST13**
Pace rate (mm/min)	1	1	1
Weight (g)	11210	11190	11200
Width (mm)	100	100	100
Thick (mm)	100	100	100
Length (mm)	500	500	500
Test length (mm)	400	400	400
Density (kg/m^3)	2242	2238	2240
Max Load (N)	7194.3	7155.0	6716.9
$f_{ctk}^{``}$ **(MPa)**	4.32	4.29	4.03
f_{ctk} **(MPa)**	2.16	2.15	2.02
$f_{ctk,average}$ **(MPa)**	2.11		

Specimen-2 (NSM)

Three-point bending test (BS EN 12390-5:2019)

Casting date: 08/12/2023 Test date:05/01/2024

Age: 28 days

Sample Name	**ST21**	**ST22**	**ST23**
Pace rate (mm/min)	1	1	1
Weight (g)	11190	11170	11180
Width (mm)	100	100	100
Thick (mm)	100	100	100
Length (mm)	500	500	500
Test length (mm)	400	400	400
Density (kg/m^3)	2238	2234	2236
Max Load (N)	5647.5	5913.8	5653.9
$f_{ctk}^{``}$ **(MPa)**	3.39	3.55	3.40
f_{ctk} **(MPa)**	1.69	1.77	1.70
$f_{ctk,average}$ **(MPa)**	1.72		

Specimen-3 (EB)

Three-point bending test (BS EN 12390-5:2019)

Casting date: 11/12/2023 Test date:08/01/2024

Age: 28 days

Sample Name	**ST31**	**ST32**	**ST33**
Pace rate (mm/min)	1	1	1
Weight (g)	11195	11180	11190
Width (mm)	100	100	100
Thick (mm)	100	100	100
Length (mm)	500	500	500
Test length (mm)	400	400	400
Density (kg/m^3)	2239	2236	2238
Max Load (N)	5588.7	4592.4	5740.2
$f_{ctk}^{``}$ **(MPa)**	3.35	2.76	3.44
f_{ctk} **(MPa)**	1.68	1.38	1.72
$f_{ctk,average}$ **(MPa)**	1.59		

Specimen-4 (Hybrid)

Three-point bending test (BS EN 12390-5:2019)

Casting date: 13/12/2023 Test date:10/01/2024

Age: 28 days

Sample Name	**ST41**	**ST42**	**ST43**
Pace rate (mm/min)	1	1	1
Weight (g)	11280	11160	11090
Width (mm)	100	100	100
Thick (mm)	100	100	100
Length (mm)	500	500	500
Test length (mm)	400	400	400
Density (kg/m^3)	2256	2232	2218
Max Load (N)	5833.2	5609.4	6427.6
$f_{ctk}^{``}$ **(MPa)**	3.5	3.37	3.86
f_{ctk} **(MPa)**	1.75	1.68	1.93
$f_{ctk,average}$ **(MPa)**	1.79		

Compressive Test of Concrete

Specimen-1 (Control Specimen)

Cylinder compressive test (BS EN 12390-3:2009)

Casting date: 06/12/2023 Test date:13/12/2023

Age: 7 days

Sample Name	**S11**	**S12**	**S13**
Pace rate (kN/s)	2.4	2.4	2.4
Weight (g)	3726	3745	3691
Diameter (mm)	103	103	103
Height (mm)	200	200	197
Density (kg/m^3)	2235.88	2247.28	2248.61
Max Load (kN)	109.4	110.5	106.3
f_{ck} (MPa)	13.14	13.27	12.76
$f_{ck,average}$ (MPa)	13.06		

Casting date: 06/12/2023 Test date:03/01/2024

Age: 28 days

Sample Name	**S14**	**S15**	**S16**
Pace rate (kN/s)	2.4	2.4	2.4
Weight (g)	3537	3584	3570
Diameter (mm)	102	102	103
Height (mm)	199	201	201
Density (kg/m^3)	2175.16	2182.14	2131.61
Max Load (kN)	192.8	198.0	198.3
f_{ck} (MPa)	23.61	24.24	23.81
$f_{ck,average}$ (MPa)	23.89		

Casting date: 06/12/2023 Test date:20/02/2024

Age: 76 days

Sample Name	**S17**	**S18**	**S19**
Pace rate (kN/s)	2.4	2.4	2.4
Weight (g)	3539	3512	3558
Diameter (mm)	102	102	102
Height (mm)	201	197	201
Density (kg/m^3)	2154.74	2181.72	2166.31
Max Load (kN)	198.0	199.0	208.0
f_{ck} (MPa)	24.23	24.37	25.47
$f_{ck,average}$ (MPa)	24.69		

Specimen-2 (NSM)

Cylinder compressive test (BS EN 12390-3:2009)

Casting date: 08/12/2023 Test date:15/12/2023

Age: 7 days

Sample Name	**S21**	**S22**	**S23**
Pace rate (kN/s)	2.4	2.4	2.4
Weight (g)	3750	3743	3810
Diameter (mm)	103	103	103
Height (mm)	200	199	201
Density (kg/m^3)	2250.28	2257.37	2274.91
Max Load (kN)	104.1	98.7	101.8
f_{ck} (MPa)	12.50	11.85	12.22
$f_{ck,average}$ (MPa)	12.19		

Casting date: 08/12/2023 Test date:05/01/2024

Age: 28 days

Sample Name	**S24**	**S25**	**S26**
Pace rate (kN/s)	2.4	2.4	2.4
Weight (g)	3588	3610	3648
Diameter (mm)	102	102	102
Height (mm)	200	201	202
Density (kg/m^3)	2195.49	2197.97	2210.11
Max Load (kN)	178.7	194.0	185.2
f_{ck} (MPa)	21.88	23.75	22.68
$f_{ck,average}$ (MPa)	22.77		

Casting date: 08/12/2023 Test date:27/02/2024

Age: 81 days

Sample Name	**S27**	**S28**	**S29**
Pace rate (kN/s)	2.4	2.4	2.4
Weight (g)	3575	3595	3580
Diameter (mm)	102	102	103
Height (mm)	202	201	200
Density (kg/m^3)	2165.88	2188.83	2148.27
Max Load (kN)	185.0	204.5	205.1
f_{ck} (MPa)	22.65	25.04	24.63
$f_{ck,average}$ (MPa)	24.11		

Specimen-3 (EB)

Cylinder compressive test (BS EN 12390-3:2009)

Casting date: 11/12/2023 Test date:18/12/2023

Age: 7 days

Sample Name	**S31**	**S32**	**S33**
Pace rate (kN/s)	2.4	2.4	2.4
Weight (g)	3741	3701	3688
Diameter (mm)	102	102	102
Height (mm)	201	199	197
Density (kg/m^3)	2277.73	2276.02	2291.05
Max Load (kN)	98.7	105.8	104.1
f_{ck} (MPa)	12.09	12.95	12.75
$f_{ck,average}$ (MPa)	12.60		

Casting date: 11/12/2023 Test date:08/01/2024

Age: 28 days

Sample Name	**S34**	**S35**	**S36**
Pace rate (kN/s)	2.4	2.4	2.4
Weight (g)	3510	3490	3568
Diameter (mm)	102	101	102
Height (mm)	195	195	198
Density (kg/m^3)	2202.84	2233.87	2205.31
Max Load (kN)	173.7	176.8	182.8
f_{ck} (MPa)	21.27	22.08	22.38
$f_{ck,average}$ (MPa)	21.91		

Casting date: 11/12/2023 Test date:01/03/2024

Age: 81 days

Sample Name	**S37**	**S38**	**S39**
Pace rate (kN/s)	2.4	2.4	2.4
Weight (g)	3528	3558	3538
Diameter (mm)	102	102	102
Height (mm)	199	201	201
Density (kg/m^3)	2169.63	2166.31	2154.13
Max Load (kN)	183.1	200.6	201.4
f_{ck} (MPa)	22.42	24.56	24.66
$f_{ck,average}$ (MPa)	23.88		

Specimen-4 (Hybrid)

Cylinder compressive test (BS EN 12390-3:2009)

Casting date: 13/12/2023 Test date:20/12/2023

Age: 7 days

Sample Name	**S41**	**S42**	**S43**
Pace rate (kN/s)	2.4	2.4	2.4
Weight (g)	3773	3759	3773
Diameter (mm)	102	103	103
Height (mm)	200	199	200
Density (kg/m^3)	2308.70	2267.02	2264.08
Max Load (kN)	105.7	105.4	100.7
f_{ck} (MPa)	12.94	12.66	12.09
$f_{ck,average}$ (MPa)	12.56		

Casting date: 13/12/2023 Test date:10/01/2024

Age: 28 days

Sample Name	**S44**	**S45**	**S46**
Pace rate (kN/s)	2.4	2.4	2.4
Weight (g)	3532	3531	3555
Diameter (mm)	103	103	102
Height (mm)	193	194	195
Density (kg/m^3)	2196.34	2184.40	2231.08
Max Load (kN)	194.3	202.6	189.1
f_{ck} (MPa)	23.33	24.33	23.15
$f_{ck,average}$ (MPa)	23.60		

Casting date: 13/12/2023 Test date:05/03/2024

Age: 83 days

Sample Name	**S47**	**S48**	**S49**
Pace rate (kN/s)	2.4	2.4	2.4
Weight (g)	3619	3621	3601
Diameter (mm)	102	103	103
Height (mm)	201	202	200
Density (kg/m^3)	2203.45	2151.36	2160.87
Max Load (kN)	202.4	205.0	205.9
f_{ck} (MPa)	24.79	24.62	24.72
$f_{ck,average}$ (MPa)	24.71		

Figure B2 shows the stress-strain curve of concrete.

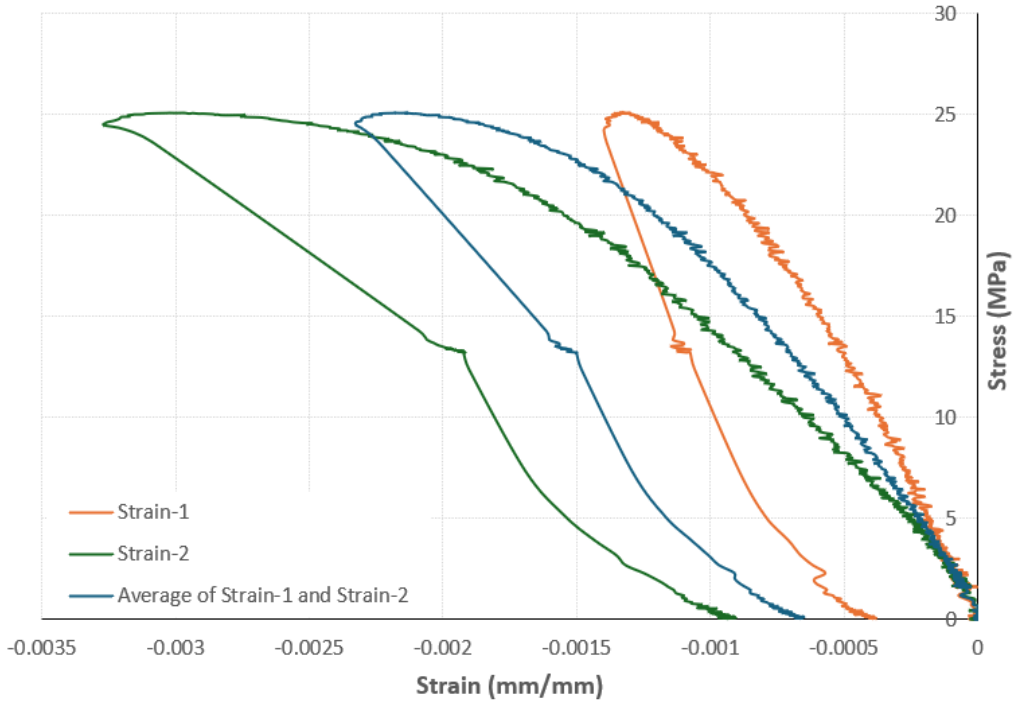

Figure B2. Stress-strain curve of concrete.

Reinforcement Tensile Test

Properties of longitudinal and transverse reinforcement

Tensile test (ISO 15630-1 & ASTM A370)

Test date:31/01/2024

Sample Name	**Sample-1**	**Sample-2**	**Sample-3**	**Average**
Type	Ribbed bar	Ribbed bar	Ribbed bar	Ribbed bar
Class	B 420C	B 420C	B 420C	B 420C
Bar size (mm)	16	16	16	16
Pace rate (mm/min)	10	10	10	10
Weight (g)	1491	1500	1499	1497
Length (mm)	945	948	947	945
Density (kg/m^3)	7847.22	7869.61	7872.67	7863.17
Yield Load (N)	93661.5	95110.2	95455.8	94742.50
f_{sy} (MPa)	465.83	473.04	474.76	471.21
ε_{sy}	0.00236	0.00237	0.00238	0.00237
Ultimate Load (N)	115791.6	117095.5	117271.8	116719.63
f_{su} (MPa)	575.90	582.39	583.26	580.52
ε_{su}	0.118	0.110	0.115	0.114
E_s (MPa)	197387	200017	199478	198963

Test date:31/01/2024

Sample Name	**Sample-1**	**Sample-2**	**Sample-3**	**Average**
Type	Ribbed bar	Ribbed bar	Ribbed bar	Ribbed bar
Class	B 420C	B 420C	B 420C	B 420C
Bar size (mm)	8	8	8	8
Pace rate (mm/min)	10	10	10	10
Weight (g)	393	386	386	388
Length (mm)	1000	1000	1000	1000
Density (kg/m^3)	7818.49	1679.23	7679.23	7725.65
Yield Load (N)	24699.0	25527.9	25452.6	25226.50
f_{sy} (MPa)	491.37	507.86	506.36	501.87
ε_{sy}	0.002425	0.00253	0.002525	0.00249
Ultimate Load (N)	29139.2	29021.8	29058.7	29073.23
f_{su} (MPa)	579.71	577.37	578.10	578.39
ε_{su}	0.11455	0.09736	0.09633	0.103
E_s (MPa)	202627.21	200735.74	200539.96	201283

Appendix-C

Properties of SikaWrap®-930G

Figure C1 shows the SikaWrap®-930G product data sheet.

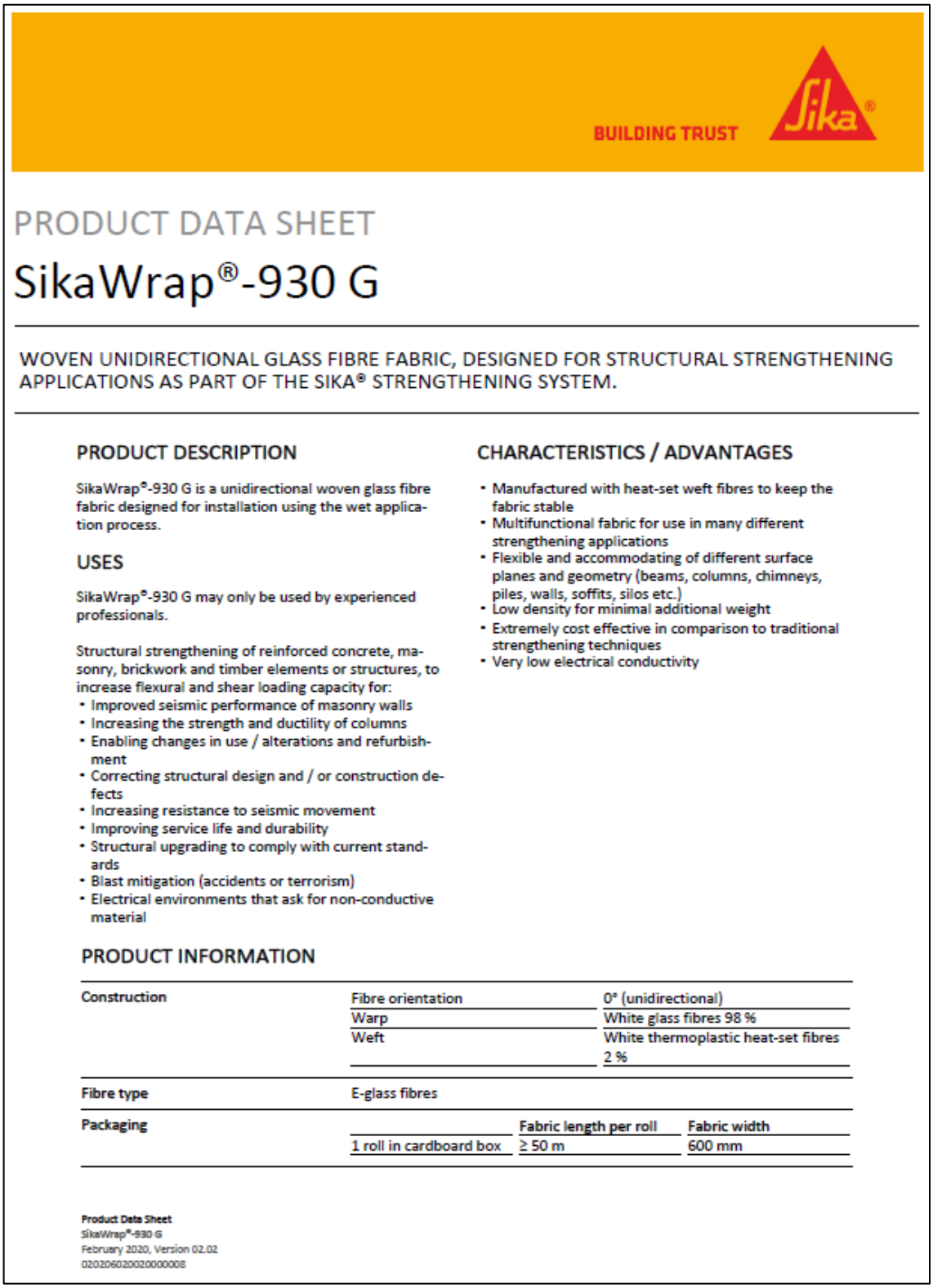

BUILDING TRUST

PRODUCT DATA SHEET

SikaWrap®-930 G

WOVEN UNIDIRECTIONAL GLASS FIBRE FABRIC, DESIGNED FOR STRUCTURAL STRENGTHENING APPLICATIONS AS PART OF THE SIKA® STRENGTHENING SYSTEM.

PRODUCT DESCRIPTION

SikaWrap®-930 G is a unidirectional woven glass fibre fabric designed for installation using the wet application process.

USES

SikaWrap®-930 G may only be used by experienced professionals.

Structural strengthening of reinforced concrete, masonry, brickwork and timber elements or structures, to increase flexural and shear loading capacity for:

- Improved seismic performance of masonry walls
- Increasing the strength and ductility of columns
- Enabling changes in use / alterations and refurbishment
- Correcting structural design and / or construction defects
- Increasing resistance to seismic movement
- Improving service life and durability
- Structural upgrading to comply with current standards
- Blast mitigation (accidents or terrorism)
- Electrical environments that ask for non-conductive material

CHARACTERISTICS / ADVANTAGES

- Manufactured with heat-set weft fibres to keep the fabric stable
- Multifunctional fabric for use in many different strengthening applications
- Flexible and accommodating of different surface planes and geometry (beams, columns, chimneys, piles, walls, soffits, silos etc.)
- Low density for minimal additional weight
- Extremely cost effective in comparison to traditional strengthening techniques
- Very low electrical conductivity

PRODUCT INFORMATION

Construction	Fibre orientation		0° (unidirectional)
	Warp		White glass fibres 98 %
	Weft		White thermoplastic heat-set fibres 2 %
Fibre type	E-glass fibres		
Packaging		Fabric length per roll	Fabric width
	1 roll in cardboard box	≥ 50 m	600 mm

Figure C1. SikaWrap®-930G product data sheet.

Shelf Life	24 months from date of production		
Storage Conditions	Store in undamaged, original sealed packaging, in dry conditions at temperatures between +5 °C and +35 °C. Protect from direct sunlight.		
Dry Fibre Density	2.56 g/cm³		
Dry Fibre Thickness	0.363 mm (based on total glass content)		
Area Density	930 g/m² + 20 g/m² (glass fibres only)		
Dry Fibre Tensile Strength	2 500 N/mm² (measuerd on roving)		(EN 2561)
Dry Fibre Modulus of Elasticity in Tension	72 000 N/mm²		(EN 2561)
Dry Fibre Elongation at Break	2.7 % (measured on roving)		(EN 2561)

TECHNICAL INFORMATION

Laminate Nominal Thickness	0.363 mm		
Laminate Nominal Cross Section	363 mm² per m width		
Laminate Tensile Strength	**Average** 1 500 N/mm²	**Characteristic** 1 200 N/mm²	(EN 2561*)
Laminate Tensile Modulus of Elasticity	**Average** 70 kN/mm²	**Characteristic** 68 kN/mm²	(EN 2561*)
	* modification: sample with 50 mm Values in the longitudinal direction of the fibres Single layer, minimum 27 samples per test series		
Laminate Elongation at Break	Strain 2.14 %		(EN 2561)
Tensile Resistance	**Average** 545 kN/m	**Characteristic** 436 kN/m	(EN 2561)
Tensile Stiffness	**Average** 25.4 MN/m 25.4 kN/m per ‰ elongation	**Characteristic** 24.7 MN/m 24.7 kN/m per ‰ elongation	EN 2561)

SYSTEM INFORMATION

System Structure	The system build-up and configuration as described must be fully complied with and may not be changed.	
	Concrete substrate adhesive primer	Sikadur®-330
	Impregnating / laminating resin	Sikadur®-300
	Structural strengthening fabric	SikaWrap®-930 G
	For detailed information on Sikadur®-330 or Sikadur®-300, together with the resin and fabric application details, refer to the Sikadur®-330 or Sikadur®-300 Product Data Sheet.	

APPLICATION INFORMATION

Consumption	**Wet application with Sikadur®-300, primer Sikadur®-330**	
	Primer layer	0.6–0.8 kg/m²
	Fabric layers	1.0 kg/m²
	Refer to the relevant Technical Information Manual for further information.	

Figure C1. SikaWrap®-930G product data sheet (continue).

Properties of Sikadur®-30

Figure C2 shows the Sikadur®-30 product data sheet.

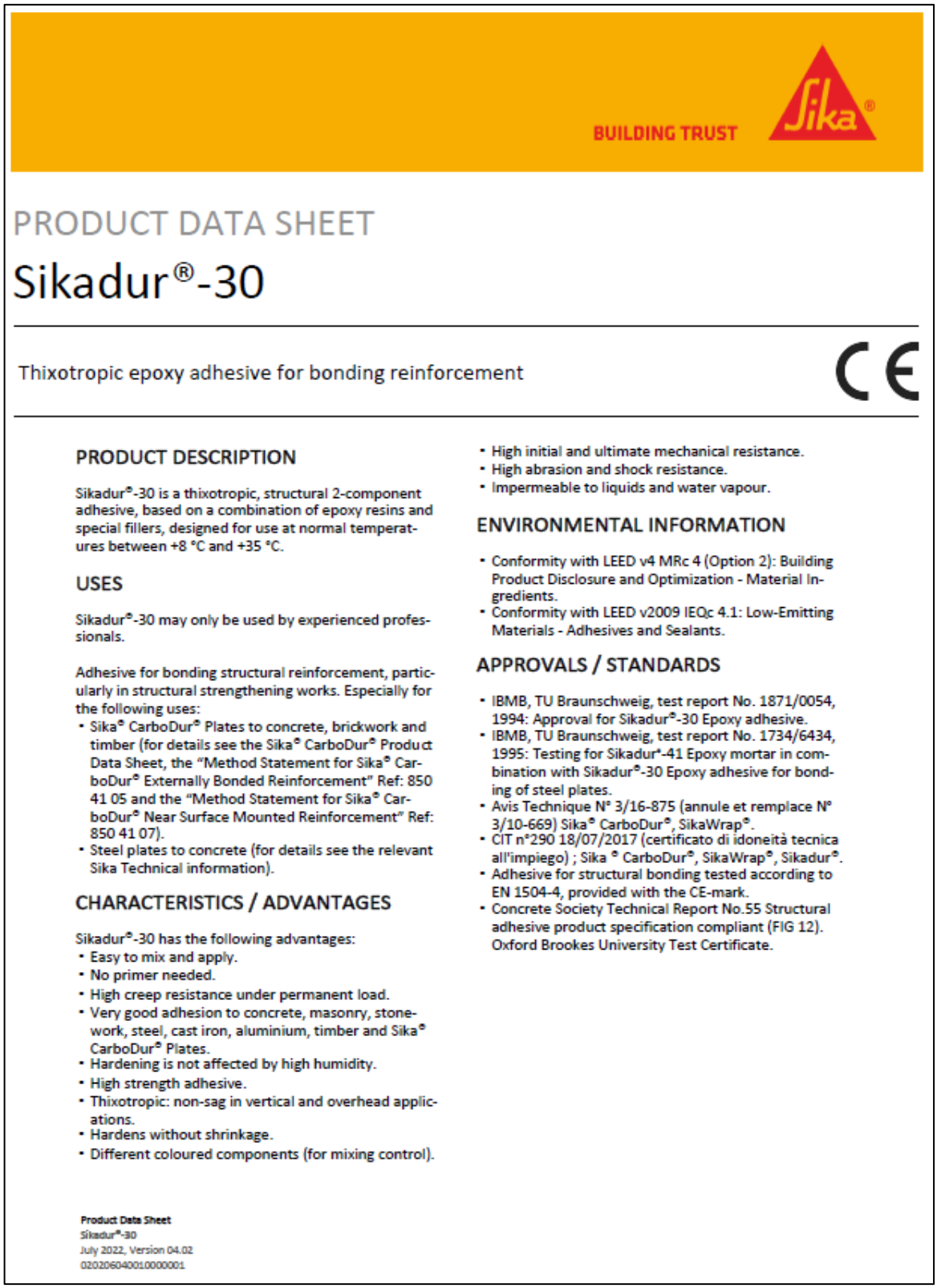

BUILDING TRUST

PRODUCT DATA SHEET

Sikadur®-30

Thixotropic epoxy adhesive for bonding reinforcement

CE

PRODUCT DESCRIPTION

Sikadur®-30 is a thixotropic, structural 2-component adhesive, based on a combination of epoxy resins and special fillers, designed for use at normal temperatures between +8 °C and +35 °C.

USES

Sikadur®-30 may only be used by experienced professionals.

Adhesive for bonding structural reinforcement, particularly in structural strengthening works. Especially for the following uses:

- Sika® CarboDur® Plates to concrete, brickwork and timber (for details see the Sika® CarboDur® Product Data Sheet, the "Method Statement for Sika® CarboDur® Externally Bonded Reinforcement" Ref: 850 41 05 and the "Method Statement for Sika® CarboDur® Near Surface Mounted Reinforcement" Ref: 850 41 07).
- Steel plates to concrete (for details see the relevant Sika Technical information).

CHARACTERISTICS / ADVANTAGES

Sikadur®-30 has the following advantages:

- Easy to mix and apply.
- No primer needed.
- High creep resistance under permanent load.
- Very good adhesion to concrete, masonry, stonework, steel, cast iron, aluminium, timber and Sika® CarboDur® Plates.
- Hardening is not affected by high humidity.
- High strength adhesive.
- Thixotropic: non-sag in vertical and overhead applications.
- Hardens without shrinkage.
- Different coloured components (for mixing control).
- High initial and ultimate mechanical resistance.
- High abrasion and shock resistance.
- Impermeable to liquids and water vapour.

ENVIRONMENTAL INFORMATION

- Conformity with LEED v4 MRc 4 (Option 2): Building Product Disclosure and Optimization - Material Ingredients.
- Conformity with LEED v2009 IEQc 4.1: Low-Emitting Materials - Adhesives and Sealants.

APPROVALS / STANDARDS

- IBMB, TU Braunschweig, test report No. 1871/0054, 1994: Approval for Sikadur®-30 Epoxy adhesive.
- IBMB, TU Braunschweig, test report No. 1734/6434, 1995: Testing for Sikadur®-41 Epoxy mortar in combination with Sikadur®-30 Epoxy adhesive for bonding of steel plates.
- Avis Technique N° 3/16-875 (annule et remplace N° 3/10-669) Sika® CarboDur®, SikaWrap®.
- CIT n°290 18/07/2017 (certificato di idoneità tecnica all'impiego) ; Sika ® CarboDur®, SikaWrap®, Sikadur®.
- Adhesive for structural bonding tested according to EN 1504-4, provided with the CE-mark.
- Concrete Society Technical Report No.55 Structural adhesive product specification compliant (FIG 12). Oxford Brookes University Test Certificate.

Product Data Sheet
Sikadur®-30
July 2022, Version 04.02
020206040010000001

Figure C2. Sikadur®-30 product data sheet.

PRODUCT INFORMATION

Chemical Base	Epoxy resin	
Packaging	6 kg (A+B)	Pre-batched unit pallets of 480 kg (80 x 6 kg)
Shelf Life	24 months from date of production	
Storage Conditions	Store in original, unopened, sealed and undamaged packaging in dry conditions at temperatures between +5 °C and +30 °C. Protect from direct sunlight.	
Colour	Component A: white Component B: black Components A+B mixed: light grey	
Density	1.65 kg/l ±0.1 kg/l (components A+B mixed) (at +23 °C)	

TECHNICAL INFORMATION

Compressive Strength (EN 196)

Curing Time	Curing Temperature	
	+10 °C	+35 °C
12 hours	-	~85 N/mm²
1 day	~55 N/mm²	~90 N/mm²
3 days	~70 N/mm²	~90 N/mm²
7 days	~75 N/mm²	~90 N/mm²

Modulus of Elasticity in Compression ~9 600 N/mm² (at 23 °C) (ASTM D 695)

Tensile Strength (DIN EN ISO 527-3

Curing Time	Curing Temperature	
	+15 °C	+35 °C
1 day	~20 N/mm²	~26 N/mm²
3 days	~23 N/mm²	~27 N/mm²
7 days	~26 N/mm²	~29 N/mm²

Tensile Modulus of Elasticity ~11 200 N/mm² (+23 °C) (ISO 527)

Shear Strength (FIP 5.15)

Curing time	Curing Temperature		
	+15 °C	+23 °C	+35 °C
1 day	~4 N/mm²	-	~17 N/mm²
3 days	~15 N/mm²	-	~18 N/mm²
7 days	~16 N/mm²	~18 N/mm² (1)	~18 N/mm²

Concrete failure (~15 N/mm²)
(1) (DIN EN ISO 4624)

Tensile adhesion strength (EN ISO 4624, EN 1542, EN 12188)

Curing time	Substrate	Curing temperature	Adhesion strength
7 days	Concrete dry	+23 °C	> 4 N/mm² *
7 days	Steel	+23 °C	>21 N/mm²

*100% concrete failure

Shrinkage 0.04 % (FIP: Fédération Internationale de la Précontrainte)

Coefficient of Thermal Expansion 2.5 x 10^{-5} per °C (Temperature range: −20 °C to +40 °C) (EN 1770)

Service Temperature −40 °C to +45 °C (when cured at +23 °C)

Glass transition temperature (EN 12614)

Curing time	Curing temperature	TG
30 days	+30 °C	+52 °C

Figure C2. Sikadur®-30 product data sheet (continue).

Heat deflection temperature	Curing time	Curing temperature	HDT	(ASTM-D 648)
	3 hours	+80 °C	+53 °C	
	6 hours	+60 °C	+53 °C	
	7 days	+35 °C	+53 °C	
	7 days	+10 °C	+36 °C	

APPLICATION INFORMATION

Mixing Ratio	Component A : Component B = 3 : 1 by weight or volume When using bulk material the exact mixing ratio must be safeguarded by accurately weighing and dosing each component.
Consumption	Refer to Sika CarboDur Method Statement.
Layer Thickness	30 mm max.
Sag Flow	On vertical surfaces it is non-sag up to 3–5 mm thickness at 35 °C (FIP: Fédération Internationale de la Précontrainte)
Squeezability	4'000 mm² at +15 °C at 15 kg (FIP: Fédération Internationale de la Précontrainte)
Product Temperature	Sikadur®-30 must be applied at temperatures between +8 °C and +35 °C.
Ambient Air Temperature	+8 °C min. / +35 °C max.
Dew Point	Beware of condensation. Substrate temperature during application must be at least 3 °C above dew point.
Substrate Temperature	+8 °C min. / +35 °C max.
Substrate Moisture Content	Max. 4 % pbw When applied to matt damp concrete, brush the adhesive well into the substrate.

Pot Life (FIP: Fédération Internationale de la Précontrainte)

Temperature	Potlife	Open time
+8 °C	~120 minutes	~150 minutes
+20 °C	~90 minutes	~110 minutes
+35 °C	~20 minutes	~50 minutes

The pot-life begins when the resin and hardener are mixed. It is shorter at high temperatures and longer at low temperatures. The greater the quantity mixed, the shorter the pot-life. To obtain longer workability at high temperatures, the mixed adhesive may be divided into portions. Another method is to chill components A+B before mixing them (although not below +5 °C).

VALUE BASE

All technical data stated in this Product Data Sheet are based on laboratory tests. Actual measured data may vary due to circumstances beyond our control.

LIMITATIONS

Sikadur® resins are formulated to have low creep under permanent loading. However, due to the creep behavior of all polymer materials under load, the long term structural design load must account for creep. Generally the long term structural design load must be lower than 20–25 % of the failure load.
A structural engineer must be consulted for load calculations for the specific application.

ECOLOGY, HEALTH AND SAFETY

User must read the most recent corresponding Safety Data Sheets (SDS) before using any products. The SDS provides information and advice on the safe handling, storage and disposal of chemical products and contains physical, ecological, toxicological and other safety-related data.

APPLICATION INSTRUCTIONS

SUBSTRATE QUALITY

See the Product Data Sheet of Sika® CarboDur® Plates and Sika® CarboDur® BC rods.

SUBSTRATE PREPARATION

See the "Method Statement for Sika® CarboDur® Externally Bonded Reinforcement" Ref: 850 41 05 and the "Method Statement for Sika® CarboDur® Near Surface Mounted Reinforcement" Ref: 850 41 07.

Figure C2. Sikadur®-30 product data sheet (continue).

Properties of Sikadur®-300

Figure C2 shows the Sikadur®-300 product data sheet.

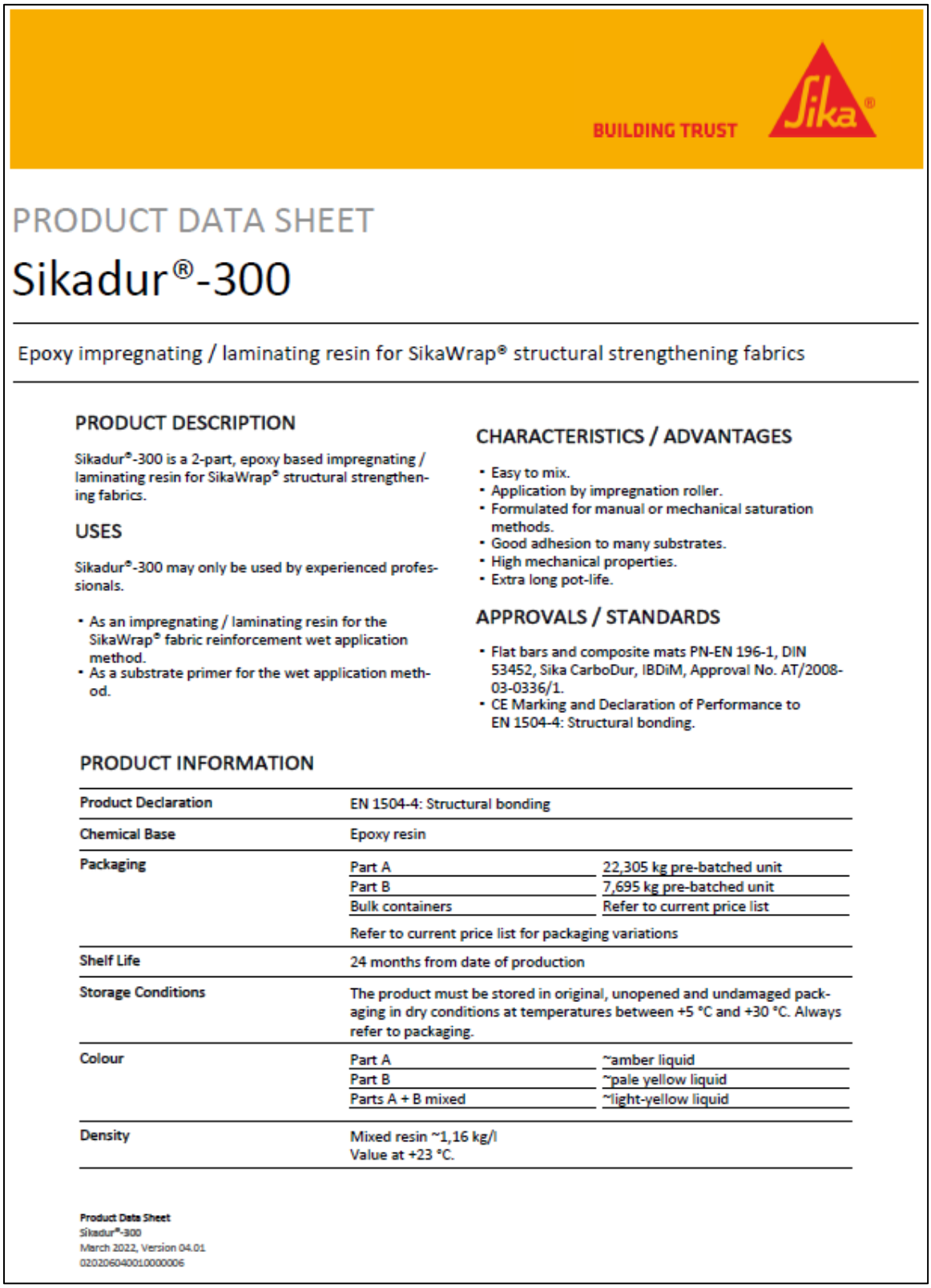

BUILDING TRUST

PRODUCT DATA SHEET

Sikadur®-300

Epoxy impregnating / laminating resin for SikaWrap® structural strengthening fabrics

PRODUCT DESCRIPTION

Sikadur®-300 is a 2-part, epoxy based impregnating / laminating resin for SikaWrap® structural strengthening fabrics.

USES

Sikadur®-300 may only be used by experienced professionals.

- As an impregnating / laminating resin for the SikaWrap® fabric reinforcement wet application method.
- As a substrate primer for the wet application method.

CHARACTERISTICS / ADVANTAGES

- Easy to mix.
- Application by impregnation roller.
- Formulated for manual or mechanical saturation methods.
- Good adhesion to many substrates.
- High mechanical properties.
- Extra long pot-life.

APPROVALS / STANDARDS

- Flat bars and composite mats PN-EN 196-1, DIN 53452, Sika CarboDur, IBDiM, Approval No. AT/2008-03-0336/1.
- CE Marking and Declaration of Performance to EN 1504-4: Structural bonding.

PRODUCT INFORMATION

Product Declaration	EN 1504-4: Structural bonding	
Chemical Base	Epoxy resin	
Packaging	Part A	22,305 kg pre-batched unit
	Part B	7,695 kg pre-batched unit
	Bulk containers	Refer to current price list
	Refer to current price list for packaging variations	
Shelf Life	24 months from date of production	
Storage Conditions	The product must be stored in original, unopened and undamaged packaging in dry conditions at temperatures between +5 °C and +30 °C. Always refer to packaging.	
Colour	Part A	~amber liquid
	Part B	~pale yellow liquid
	Parts A + B mixed	~light-yellow liquid
Density	Mixed resin ~1,16 kg/l Value at +23 °C.	

Figure C3. Sikadur®-300 product data sheet.

Viscosity	Shear rate: 50/s		
	Temperature	**Viscosity**	
	+15 °C	~2000 mPa·s	
	+23 °C	~700 mPa·s	
	+40 °C	~200 mPa·s	

TECHNICAL INFORMATION

Flexural E-Modulus	~2800 N/mm² (7 days at +23 °C)	(DIN EN 1465)
Tensile Strength	~45 N/mm² (7 days at +23 °C)	(ISO 527)
Tensile Modulus of Elasticity	~3500 N/mm² (7 days at +23 °C)	(ISO 527)
Elongation at Break	1,5 % (7 days at +23 °C)	(ISO 527)
Tensile adhesion strength	Concrete fracture (> 4 N/mm²) on sandblasted substrate	(EN ISO 4624)
Coefficient of Thermal Expansion	~6,0 × 10^{-5} (±0,2 × 10^{-5}) 1/K (linear expansion between -20 °C and +40 °C)	(EN 1770)
Service Temperature	–40 °C to +45 °C	

Glass transition temperature (EN 12614)

Curing time	Curing temperature	TG
30 days	+30 °C	+53 °C

Heat deflection temperature (ASTM D 648)

Curing time	Curing temperature	HDT
7 days	+15 °C	+43 °C
7 days	+23 °C	+49 °C
3 days	+40 °C	+60 °C
7 days	+40 °C	+66 °C

Resistant to continuous exposure +45 °C.

SYSTEM INFORMATION

System Structure

- Substrate primer: Sikadur®-300 / Sikadur®-330.
- Impregnating / laminating resin: Sikadur®-300.
- Structural strengthening fabric: SikaWrap® (type to suit requirements).

APPLICATION INFORMATION

Mixing Ratio	Part A : Part B = 100 : 34,5 by weight
Consumption	Guide: ~0,4–1,0 kg/m² Also refer to: • Method Statement: SikaWrap® manual wet application - Ref. 850 41 03. • Method Statement: SikaWrap® saturator machine wet application - Ref. 850 41 04.
Ambient Air Temperature	+15 °C min. / +40 °C max.
Dew Point	Beware of condensation. The substrate and uncured applied resin must be at least +3 °C above dew point to reduce the risk of condensation or blooming on the resin surface.
Substrate Temperature	+15 °C min. / +40 °C max.

Figure C3. Sikadur®-300 product data sheet (continue).

Substrate Moisture Content	≤ 4 % parts by weight The following test methods can be used: Sika®-Tramex meter, CM-measurement or Oven-dry-method. No rising moisture according to ASTM (Polyethylene-sheet).

Pot Life (EN ISO 9514)

Temperature	Pot-life	Open time
+15 °C	~3 hours	~6 hours
+23 °C	-	~4 hours
+40 °C	~60 minutes	~90 minutes

The pot-life begins when Parts A+B are mixed. It is shorter at high temperatures and longer at low temperatures. The greater the quantity mixed, the shorter the pot-life. To obtain longer workability at high temperatures, the mixed adhesive may be divided into smaller quantities. Another method is to chill Parts A+B before mixing (although not below +5 °C).

VALUE BASE

All technical data stated in this Product Data Sheet are based on laboratory tests. Actual measured data may vary due to circumstances beyond our control.

FURTHER DOCUMENTS

- Method Statement: SikaWrap® manual wet application - Ref. 850 41 03.
- Method Statement: SikaWrap® saturator machine wet application - Ref. 850 41 04.

LIMITATIONS

- Sikadur® resins are formulated to have low creep under permanent loading. However due to the creep behaviour of all polymer materials under load, when using adhesive for structural applications, the long term structural design load must account for creep. Generally, the long-term structural design load must be lower than 20–25 % of the failure load. A structural engineer must be consulted for design calculations for specific structural applications.
- Protect from rain for at least 24 hours after application. Ensure placement of fabric and laminating with roller takes place within open time.
- For application in cold or hot conditions, pre-condition material for 24 hours in temperature-controlled storage facilities to improve mixing, application and pot-life limits.

ECOLOGY, HEALTH AND SAFETY

User must read the most recent corresponding Safety Data Sheets (SDS) before using any products. The SDS provides information and advice on the safe handling, storage and disposal of chemical products and contains physical, ecological, toxicological and other safety-related data.

APPLICATION INSTRUCTIONS

SUBSTRATE QUALITY

Substrates must be structurally sound and of sufficient tensile strength to provide a minimum tensile strength of 1,0 N/mm² or as required in the design specification.

Reference must be made to the Sika® Method Statements:

- Method Statement: SikaWrap® manual wet application - Ref. 850 41 03.
- Method Statement: SikaWrap® saturator machine wet application - Ref. 850 41 04.

SUBSTRATE PREPARATION

Reference must be made to the Sika® Method Statements:

- Method Statement: SikaWrap® manual wet application - Ref. 850 41 03.
- Method Statement: SikaWrap® saturator machine wet application - Ref. 850 41 04.

MIXING

Pre-batched unit

Prior to mixing all parts, mix Part A (resin) briefly using an electric single or double paddle mixer (maximum 300 rpm) with a spiral paddle.
Add Part B (hardener) to part A and mix Parts A+B continuously for at least 3 minutes until a uniform mix has been achieved. To ensure thorough mixing, pour materials into a clean container and mix again for approximately 1 minute. Overmixing must be avoided to minimise air entrainment. Mix full units only. Mixing time for A+B = ~4 minutes.

Bulk container

Add both parts in the correct proportion into a suitable clean, dry container and mix in the same way as for the pre-batched unit. Mix only the quantity which can be used within its pot-life.

APPLICATION METHOD / TOOLS

Reference must be made to the Sika® Method Statements:

- Method Statement: SikaWrap® manual wet application - Ref. 850 41 03.
- Method Statement: SikaWrap® saturator machine wet application - Ref. 850 41 04.

CLEANING OF TOOLS

Clean all tools and application equipment with Sika® Thinner C immediately after use. Hardened material can only be mechanically removed.

Figure C3. Sikadur®-300 product data sheet (continue).

Appendix-D

Calculation of the development length

Anchorage is achieved by extending the reinforcing bars a distance of l_b beyond the point of maximum stress in the bar. This length, known as the development length, can be calculated for deformed bars using Equation (D1) in TS 500 (2000).

$$l_b = \left(0.12 \times \frac{f_{yd}}{f_{ctd}} \times \varphi\right) \quad \text{(D1)}$$

When the above equation is applied for φ16 and C20, the development length was calculated as 701 mm, and the calculation steps are below.

In Equation (D1), f_{yd} is the design strength of the reinforcement, f_{ctd} is the design tensile strength of concrete, and φ is the diameter of the reinforcement.

$$f_{ckt} = 0.35 \times \sqrt{f_{ck}} \quad \text{(D2)}$$

$$f_{ckt} = 0.35 \times \sqrt{20} = 1.6 \text{ MPa}$$

where, f_{ckt} is the concrete characteristic tensile strength, f_{ck} is the characteristic compressive strength.

$$f_{ctd} = \frac{f_{ctk}}{1.5\ (safety\ factor\ of\ concrete)} \quad \text{(D3)}$$

$$f_{ctd} = \frac{1.6}{1.5} = 1.0 \text{ MPa}$$

$$f_{yd} = \frac{f_{yk}}{1.15\ (safety\ factor\ of\ steel)} \quad \text{(D4)}$$

where, f_{yk} is the minimum yield strength according to TS 708.

$$f_{yd} = \frac{420}{1.15\ (safety\ factor\ of\ steel)} = 365 \text{ MPa}$$

Using Equation (D1), $l_b$can be calculated below.

$$l_b = \left(0.12 \times \frac{365}{1.0} \times 16\right) = 701 \text{ mm}$$

In addition, the development length can be obtain using Table D1.

Table D1. Development Length for B420C (TS 500, 2000)

Concrete Class	**C20**	C25	C30	C35	C40
Diameter (mm)	Development Length (l_b) (mm)				
10	438	381	350	324	302
12	526	457	420	389	362
14	613	533	491	454	423
16	**701**	609	561	519	483
18	788	686	631	584	544
20	876	762	701	649	604

TEC (1998) regulation was used for the calculation of the anchorage length at the beam-column junction. Formulas for minimum length values are shown in Figure D1. In this study, the anchorage length was used as 754 mm. The calculation of anchorage length is shown below.

$$\text{the anchorage length} = a + b$$

Here, “b” is chosen as 500 mm because it is desired to use the net value during the cutting and bending of the longitudinal reinforcement. “a” is calculated as follows.

$$a = b_{column} - (\text{concrete cover} + \text{diameter of longitudinal rebar of column})$$

where, b_{column} is the length of the column.

$$a = 300\ \text{mm} - (30\ \text{mm} + 16\ \text{mm}) = 254\ \text{mm}$$

$$\text{the anchorage length} = 500\ \text{mm} + 254\ \text{mm} = 754\ \text{mm} \geq 701\ \text{mm}$$

In addition, detail is shown in Figure D2.

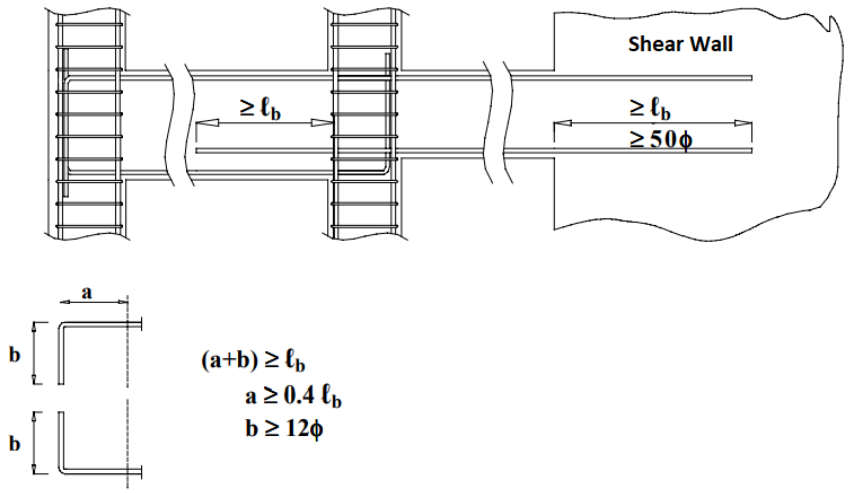

Figure D1. The calculation of the anchorage length at the beam-column joint (TEC, 1998).

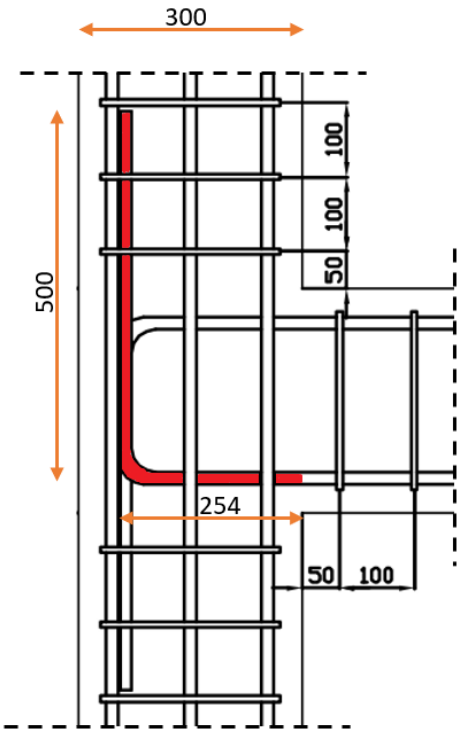

Figure D2. The detail of the anchorage length at the beam-column joint (units are mm).

Shear links design

Beam;

Beam confinement zone requirements as follow;

$s_b \leq h_b/4 = \frac{300}{4} = 75$ mm

$s_b \leq 8 \times \varphi = 8 \times 16 = 128$ mm (φ= min longitudinal rebar diameter)

$s_b \leq 150$ mm

Φ8/100 was selected for this project.

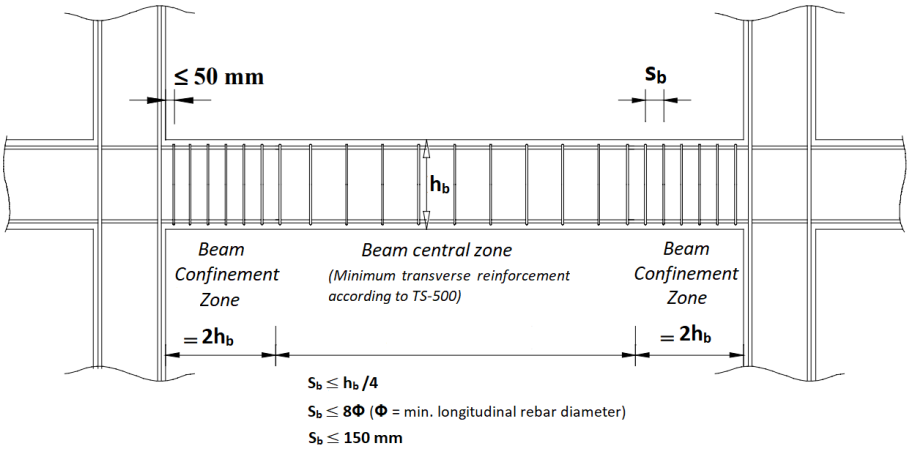

Figure D3. Transverse Reinforcement Requirements for beam (TEC, 1998).

Column;

Column central zone requirements as follow;

$s_o \leq 200$ mm

$s_o \leq \frac{b_{min}}{2} = \frac{250}{2} = 125$ mm

Column confinement zone requirements as follow;

$s_c \geq 50$ mm

$s_c \leq 100$ mm

$s_c \leq \frac{b_{min}}{3} = \frac{250}{3} = 83.33$ mm

Φ8/100 was selected for this project.

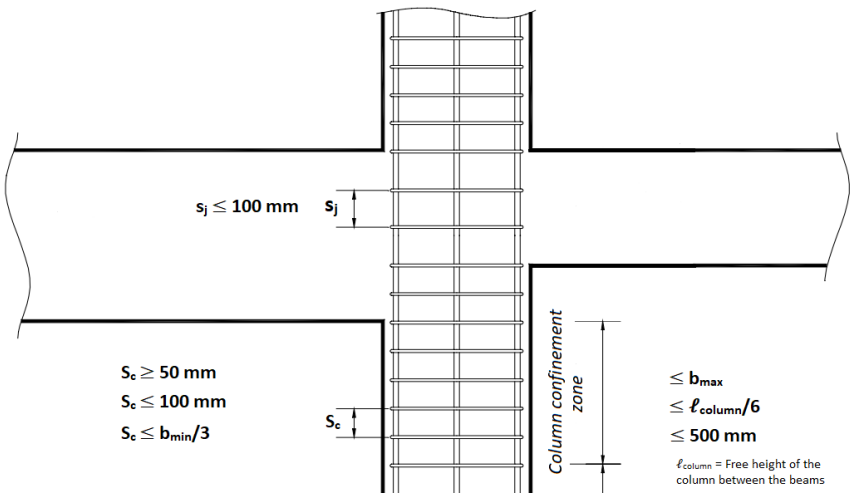

Figure D4. Transverse Reinforcement Requirements for column (TEC, 1998).

Capacity Calculations for Column and Beam Sections

This section calculates the maximum bending moment and shear force values that can be carried by the beam and column sections used to create the joints studied in the experiment. These capacity values will be used to evaluate the results of the experimental investigation. The capacity calculations were performed using the XTRACT software by Chadwell and Imbsen (2004) for moment capacities and the TS-500 (2000) standard for shear capacity. In addition, the concrete and steel models used in the Extract program are given following heading. The shear strength (V_r) of the sections was calculated by Equation (D5).

$$V_r = V_c + V_w \tag{D5}$$

where V_c is the contribution to the shear strength of concrete and V_w denotes the contribution of transverse reinforcement to shear strength. The contribution of concrete to the shear strength was taken as 80% of the cracking strength ($V_c = 0.8V_{cr}$) and the cracking strength (V_{cr}) was calculated by Equation (D6).

$$V_{cr} = (0.65 \times f_{cd} \times b \times d) \times \left(1 + \left(\gamma \times \frac{N}{A_c}\right)\right) \tag{D6}$$

where f_{cd} is the tensile strength of concrete, b is the beam/column section width, d is the useful depth of the beam/column section, N is the amount of axial load, A_c is the cross-sectional area, γ is the coefficient used for the effect of axial force on cracking strength. This coefficient is taken as "0" since there is no axial load on the beam and "0.07" since axial pressure is applied on the column. f_{ctk} and f_{cd} of the concrete can be calculated by Equation (D7) and (D8), respectively.

$$f_{ctk} = 0.35 \times \sqrt{f_{ck}} \tag{D7}$$

$$f_{cd} = \left(\frac{f_{ctk}}{\gamma_c}\right) \tag{D8}$$

where f_{ctk} is the design tensile strength of concrete, and γ_c= 1.5 is the safety factor of concrete (TS 500, 2000). In this calculation, since f_{ckt} is calculated in section 3.2.1, this value is used directly, and the safety factor was not used. The contribution of transverse reinforcement to the shear strength (V_w) is calculated by Equation (D9).

$$V_w = \frac{A_{sw}}{s} \times f_{ywd} \times d \tag{D9}$$

f_{ywd} can be calculated by Equation (D10).

$$f_{ywd} = \left(\frac{f_{ywk}}{\gamma_s}\right) \quad \text{(D10)}$$

where A_{sw} is the total area of transverse reinforcement, s is the spacing of transverse reinforcement, f_{ywk} is the yield strength of transverse reinforcement, f_{ywd} is the design yield strength of transverse reinforcement, and γ_s = 1.15 is the safety factor of steel (TS 500, 2000). In this calculation, since f_{ywk} is measured in section 3.2.2, this value is used directly, and the safety factor was not used.

Geometric details of the column and beam sections and reinforcement details of the specimens in the experimental study are given in Figure D5 and Figure D6, respectively.

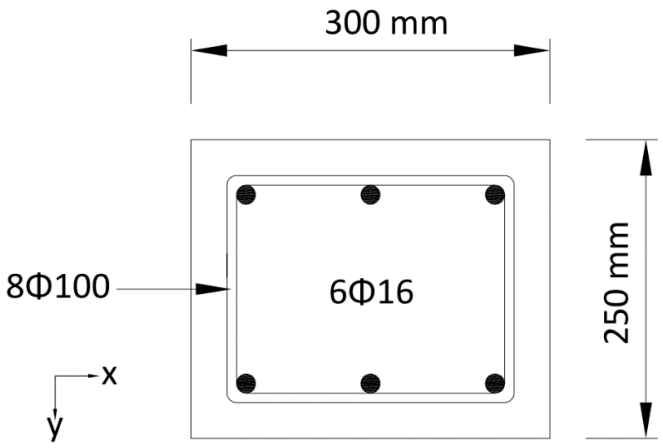

Figure D5. Geometric details of the column section and reinforcement placement.

Column dimensions are 300×250 mm. In the columns, 6 longitudinal reinforcements with a diameter of 16 mm and transverse reinforcements with a diameter of 8 mm were used at 100 mm intervals. In column capacity calculations, an axial load of 9.74% of the column capacity (168 kN) was applied. In the calculations were used the values found as a result of concrete compression-tensile tests and steel tensile tests, and nominal column moments and beam moments are found below. In these calculations, 24.35 MPa, 1.8 MPa, 471 MPa, and 502 MPa were used for f_{ck}, f_{ctk}, f_{yk} and f_{ywk}, respectively.

The moment capacity of the column under this load is M_{ry} = 70.89 kN-m for the strong direction (y-axis) while M_{rx} = 65.96 kN-m for the weak direction (x-axis). In addition, the yield moment of the column for the y-axis and x-axis was found to be $M_{yield,y}$ = 66.22 kN-m and $M_{yield,x}$ = 64.24 kN-m when the first yielding occurred in the longitudinal reinforcement. The shear force capacity of the column is V_r = 196.88 kN for the strong direction. The load required

to be applied to the end of the beam in the experiment to reach the moment capacity of the column for the strong direction (y-axis) was calculated as 109.06 kN and the load required to reach the yield moment was calculated as 101.88 kN.

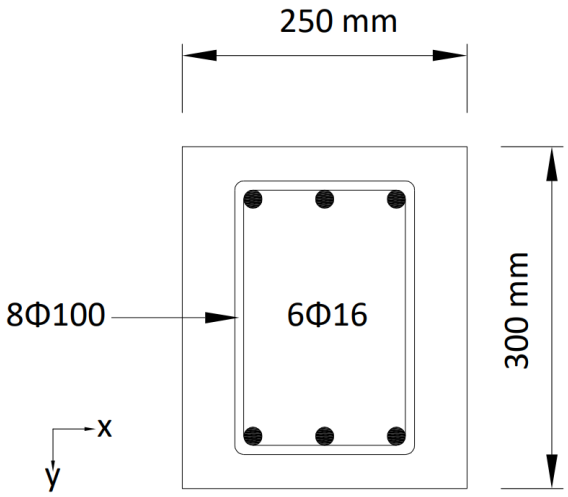

Figure D6. Geometric details of the beam section and reinforcement placement.

The moment capacity of the beam around its strong axis is M_r = 73.26 kN-m. In addition, the yield moment of the beam was found to be M_y = 62.86 kN-m when the first yielding occurred in the longitudinal reinforcement. The shear force capacity of the beam is V_r = 187.56 kN. The load required to be applied to the end of the beam in the experiment to reach the moment capacity of the beam was calculated as 56.35 kN and the load required to reach the yield moment was calculated as 48.35 (62.86 kN-m/ 1.3 m) kN. In addition, moment and shear capacities of the beam and column are given in Table D2 and Table D3.

Table D2. Capacity of beam.

Beam (250×300 mm)	**Moment Capacity**		**Shear Capacity**
	Max Moment (kNm)	**Yield Moment (kNm)**	**Max Shear (kN)**
	M_r	***M_y***	***V_r***
C24.35	73.26	62.86	187.56

Table D3. Capacity of column.

Column (300×250 mm)	**Moment Capacity**				**Shear Capacity**
	Max Moment (kNm)		**Yield Moment (kNm)**		**Max Shear (kN)**
	Strong axis	**Weak axis**	**Strong axis**	**Weak axis**	**Strong axis**
	M_{ry}	***M_{rx}***	***$M_{yield,y}$***	***$M_{yield,x}$***	***V_r***
C24.35	70.89	65.96	66.22	64.24	196.88

Material Models for Concrete and Steel Reinforcement for Analytical Phase

The concrete used during the casting of the specimens for use in the Extract program was defined by taking into account the results obtained from the compressive strength tests, while the steel material model for the reinforcement was defined by taking into account the results of the "tensile" tests performed for the strength of the reinforcement used in the specimens tested. Existing models in the literature were used for material behaviour.

Material Model for Concrete:

For the concrete material in the analytical model, the Mander unconfined concrete model (Mander *et al.*, 1988), which is frequently used in structural analysis and whose stress-strain relationship is presented in Figure D7, was used. This material model is also described in the information annex 7.B of the earthquake code used in Turkey (TEC, 2007).

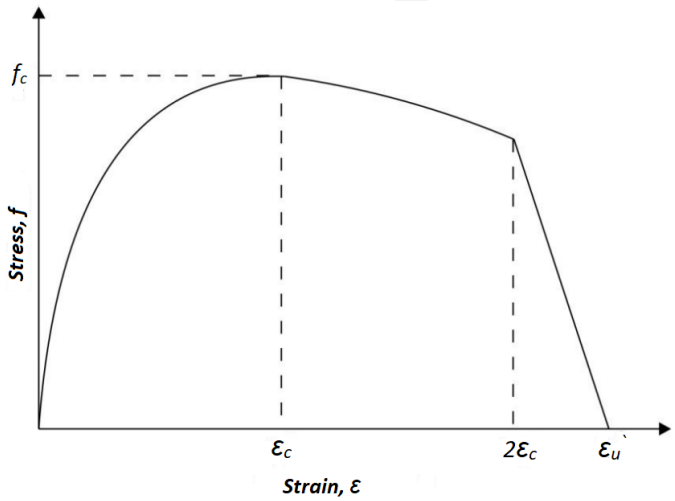

Figure D7. Mander unconfined concrete model (Mander *et al.*, 1988).

According to Mander unconfined concrete model:

- For $\varepsilon \leq (2 \times \varepsilon_c)$

$$f = \frac{f_c \times r \times (\varepsilon/\varepsilon_c)}{r-1+(\varepsilon/\varepsilon_c)^r} \quad \text{(D11)}$$

- For $(2 \times \varepsilon_c) < (2 \times \varepsilon) \leq \varepsilon_u$

$$f = \left(\frac{2 \times f_c \times r}{r-1+2^r}\right) \times \left(\frac{\varepsilon_u - \varepsilon}{\varepsilon_u - (2 \times \varepsilon_c)}\right) \quad \text{(D12)}$$

where, f_c is the compressive strength of concrete, ε_c is the strain corresponding to the compressive strength, f is the stress at any point, ε is the strain at any point. The value of *r* is calculated with the help of the following Equation (D13).

$$r = \left(\frac{E_c}{E_c - (f_c/\varepsilon_c)}\right) \quad \text{(D13)}$$

where, E_c is the initial modulus of elasticity of the concrete. E_c (ACI 318-14 section 19.2.2) can be calculated as follow using Equation (D14).

$$E_c = 4700 \times \sqrt{f_c} \quad \text{(D14)}$$

In this model, concrete values for the compressive strength of unconfined concrete, f_c, is "24.35" MPa, for the modulus of elasticity of concrete, E_c, "21781" MPa, for the strain at compressive strength, ε_c, "0.0024", and for the maximum strain, ε_u, "0.006".

Defined Material Model for Reinforcing Steel:

The stress-strain relationship of reinforcing steel is generally modelled as bi-linear, elasto-plastic. In this study, the bi-linear model considering the effects of yielding plateau given in earthquake code (TEC, 2007) was used. This model consists of three regions. The first region is the "Elastic Region" which reflects the linear behaviour up to the yield strength. In the second region, increasing strain values remain at constant strength (yield strength) until the beginning of the yield plateau zone. The region showing this behaviour is the "Fully Plastic Region". The third zone is the "Hardening Zone", which is expressed by a parabolic curve up to the failure strain and failure strength. This model described for reinforcing steel is presented in Figure D8 Figure . The expression of the curves for this model is given by Equation (D15).

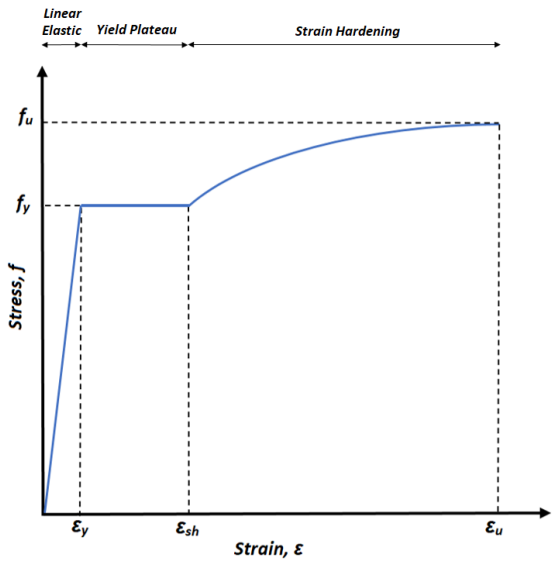

Figure D8. Typical stress-strain curve of reinforcement material model.

$$f_x = \begin{cases} E_s\varepsilon & \longrightarrow \varepsilon < \varepsilon_y \\ f_y & \longrightarrow \varepsilon_y < \varepsilon_y < \varepsilon_{sh} \\ f_y + (f_u - f_y)\sqrt{\dfrac{\varepsilon - \varepsilon_{sh}}{\varepsilon_u - \varepsilon_{sh}}} & \longrightarrow \varepsilon_{sh} < \varepsilon < \varepsilon_u \end{cases} \quad \text{(D15)}$$

where, E_s = the modulus of elasticity of reinforcing steel in the linear region, ε = strain of reinforcing steel at a location on the curve, f_y = yield strength of reinforcement steel, f_u = tensile strength of reinforcement steel, ε_y = yield strain, ε_u = tensile strain, ε_{sh} = strain at the end of the yield plateau.

The material test results (average of three tests) given in section 3.2.2 for ribbed reinforcement. These data were used for calculations.

Results of column and beam capacity calculations for analytical studies using experimental data

Figure D9 shows the moment capacity of the column for the strong axis.

XTRACT Analysis Report -

For use only in an academic or research setting.

Section Name: Column-300x250
Loading Name: MCYY
Analysis Type: Moment Curvature

OYE
PhD
20/05/2025
PhD
Column-300x250-Postexperiment
Page __ of __

Section Details:

X Centroid:	-.3293E-17 m
Y Centroid:	-.9444E-19 m
Section Area:	75.00E-3 m^2

Loading Details:

Constant Load - P:	168.0 kN
Incrementing Loads:	Myy Only
Number of Points:	32
Analysis Strategy:	Displacement Control

Analysis Results:

Failing Material:	Confined1
Failure Strain:	20.00E-3 Compression
Curvature at Initial Load:	.2543E-19 1/m
Curvature at First Yield:	15.40E-3 1/m
Ultimate Curvature:	.2943 1/m
Moment at First Yield:	66.22 kN-m
Ultimate Moment:	70.89 kN-m
Centroid Strain at Yield:	.7655E-3 Ten
Centroid Strain at Ultimate:	12.96E-3 Ten
N.A. at First Yield:	49.71E-3 m
N.A. at Ultimate:	44.04E-3 m
Energy per Length:	20.86 kN
Effective Yield Curvature:	17.46E-3 1/m
Effective Yield Moment:	75.07 kN-m
Over Strength Factor:	.9442
EI Effective:	4.301E+6 N-m^2
Yield EI Effective:	-15.12E+3 N-m^2
Bilinear Harding Slope:	-.3516 %
Curvature Ductility:	16.86

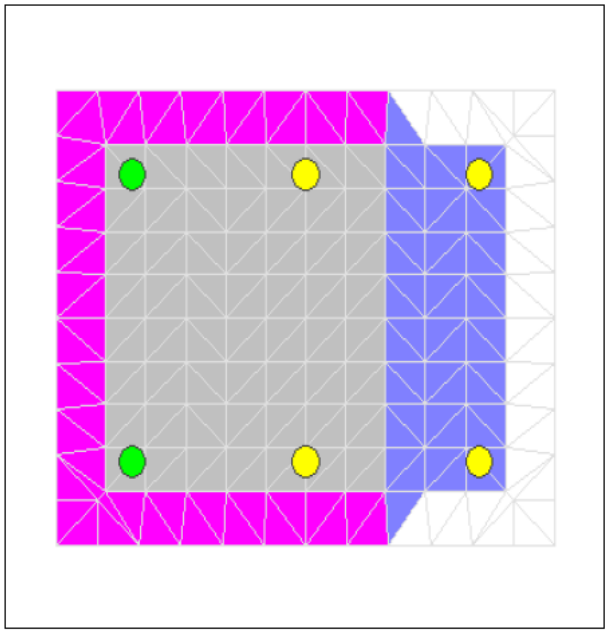

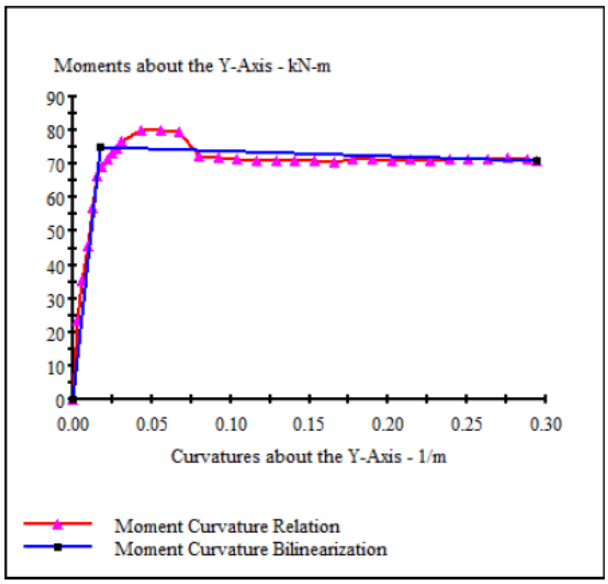

Comments:

User Comments

Figure D9. Moment capacity of the column for the strong axis.

Figure D10 shows the moment capacity of the column for the weak axis.

XTRACT Analysis Report -

For use only in an academic or research setting.

Section Name: Column-300x250

Loading Name: MCXX

Analysis Type: Moment Curvature

OYE
PhD
20/05/2025
PhD
Column-300x250-Postexperiment
Page __ of __

Section Details:

X Centroid:	-.3293E-17 m
Y Centroid:	-.9444E-19 m
Section Area:	75.00E-3 m^2

Loading Details:

Constant Load - P:	168.0 kN
Incrementing Loads:	Mxx Only
Number of Points:	31
Analysis Strategy:	Displacement Control

Analysis Results:

Failing Material:	Confined1
Failure Strain:	20.00E-3 Compression
Curvature at Initial Load:	.2845E-19 1/m
Curvature at First Yield:	19.79E-3 1/m
Ultimate Curvature:	.6258 1/m
Moment at First Yield:	64.24 kN-m
Ultimate Moment:	65.96 kN-m
Centroid Strain at Yield:	.8030E-3 Ten
Centroid Strain at Ultimate:	34.50E-3 Ten
N.A. at First Yield:	40.57E-3 m
N.A. at Ultimate:	55.12E-3 m
Energy per Length:	39.18 kN
Effective Yield Curvature:	18.87E-3 1/m
Effective Yield Moment:	61.24 kN-m
Over Strength Factor:	1.077
EI Effective:	3.245E+6 N-m^2
Yield EI Effective:	7776 N-m^2
Bilinear Harding Slope:	.2396 %
Curvature Ductility:	33.16

Comments:

User Comments

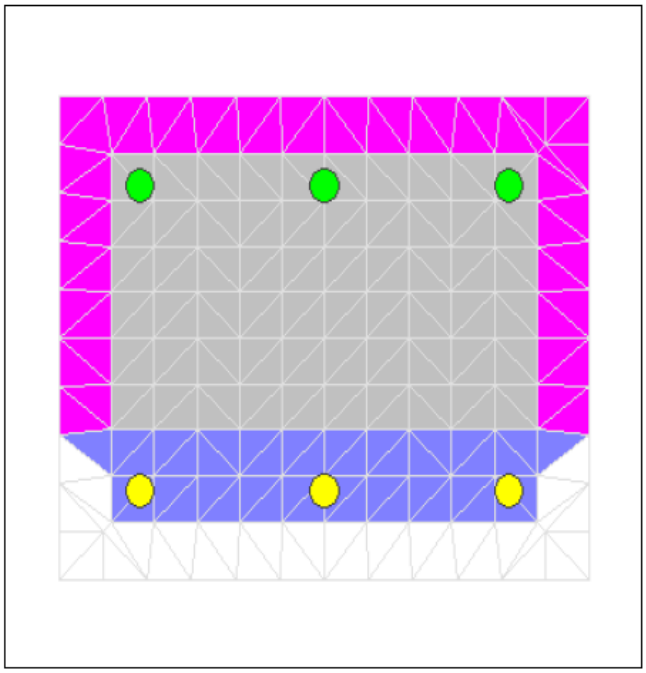

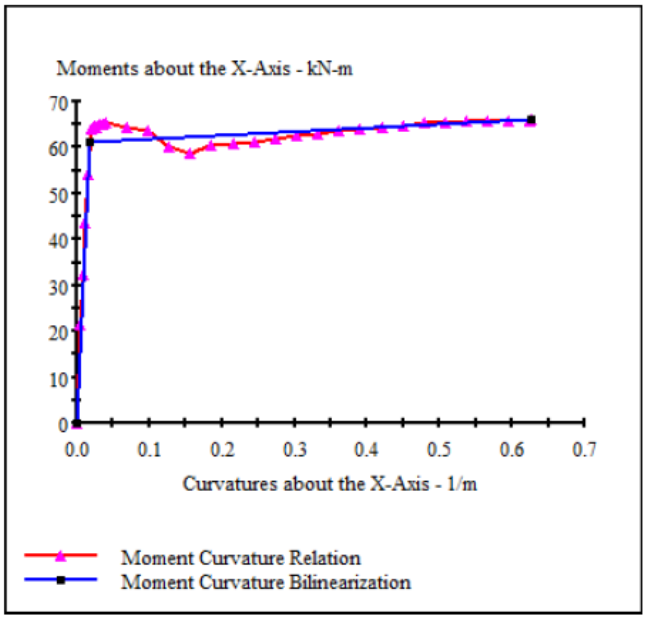

Figure D10. Moment capacity of the column for the weak axis.

Figure D11 shows the moment capacity of the beam for the strong axis.

XTRACT Analysis Report -

For use only in an academic or research setting.

Section Name: Beam-250x300

Loading Name: MXX

Analysis Type: Moment Curvature

OYE
PhD
20/05/2025
PhD
Beam-250x300-Postexperiment
Page __ of __

Section Details:

X Centroid:	-.8713E-18 m
Y Centroid:	-.2848E-17 m
Section Area:	75.00E-3 m^2

Loading Details:

Incrementing Loads:	Mxx Only
Number of Points:	30
Analysis Strategy:	Displacement Control

Analysis Results:

Failing Material:	B420C-Experiment
Failure Strain:	.1140 Tension
Curvature at Initial Load:	0 1/m
Curvature at First Yield:	13.73E-3 1/m
Ultimate Curvature:	.5576 1/m
Moment at First Yield:	62.86 kN-m
Ultimate Moment:	73.26 kN-m
Centroid Strain at Yield:	.9389E-3 Ten
Centroid Strain at Ultimate:	56.01E-3 Ten
N.A. at First Yield:	68.38E-3 m
N.A. at Ultimate:	.1005 m
Energy per Length:	37.60 kN
Effective Yield Curvature:	13.85E-3 1/m
Effective Yield Moment:	63.42 kN-m
Over Strength Factor:	1.155
EI Effective:	4.578E+6 N-m^2
Yield EI Effective:	18.10E+3 N-m^2
Bilinear Harding Slope:	.3954 %
Curvature Ductility:	40.25

Comments:

User Comments

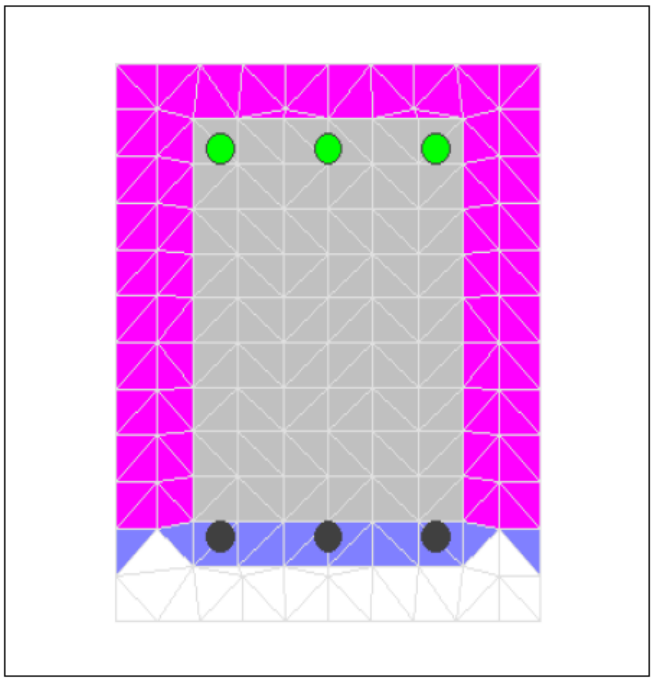

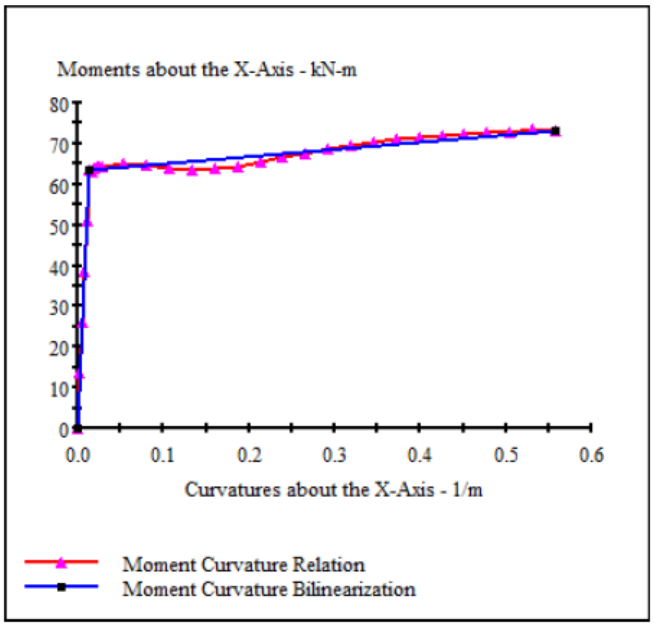

Figure D11. Moment capacity of the beam for the strong axis.

Figure D12 shows the analytical approach for shear force using experimental data for column and beam, respectively.

Column

f_{ck}	24.35	N/mm^2
f_{ctk}	1.80	N/mm^2
b	250	mm
d`	30	mm
φ_w	8	mm
φ	16	mm
h	300	mm
s	100	mm
d	254	mm
N_d	168000	N
A_{sw}	100.48	mm^2

V_{cr}	85.94	kN
V_c	68.76	kN

f_{yw}	502	N/mm^2
b	250	mm
d`	30	mm
φ_w	8	mm
φ	16	mm
h	300	mm
s	100	mm
d	254	mm
A_{sw}	100.48	mm^2

$$V_w = \frac{A_{sw}}{s} \times f_{yw} \times d$$

V_w	128.12	kN

$$V_{cr} = (0.65 \times f_{ctk} \times b \times d) \times \left(1 + \left(0.07 \times \frac{N_d}{A_c}\right)\right)$$

$$V_c = 0.8 \times V_{cr}$$

$$V_r = V_c + V_w$$

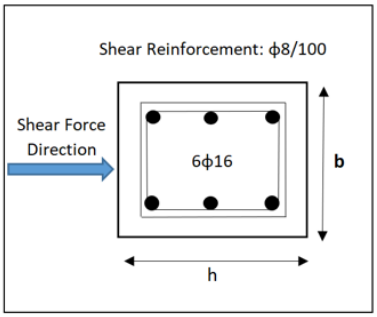

V_r	196.88	kN

(a)

Beam

f_{ck}	24.35	N/mm^2
f_{ctk}	1.800	N/mm^2
b	250	mm
d`	30	mm
φ_w	8	mm
φ	16	mm
h	300	mm
s	100	mm
d	254	mm
N_d	0	N
A_{sw}	100.48	mm^2

V_{cr}	74.30	kN
V_c	59.44	kN

f_{yw}	502	N/mm^2
b	250	mm
d`	30	mm
φ_w	8	mm
φ	16	mm
h	300	mm
s	100	mm
d	254	mm
A_{sw}	100.48	mm^2

$$V_w = \frac{A_{sw}}{s} \times f_{yw} \times d$$

V_w	128.12	kN

$$V_{cr} = (0.65 \times f_{ctk} \times b \times d)$$

$$V_c = 0.8 \times V_{cr}$$

$$V_r = V_c + V_w$$

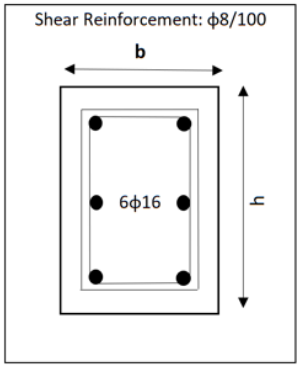

V_r	187.56	kN

(b)

Figure D12. Analytical approach for shear force using experimental data: (a) Column; (b) Beam.

Appendix-E

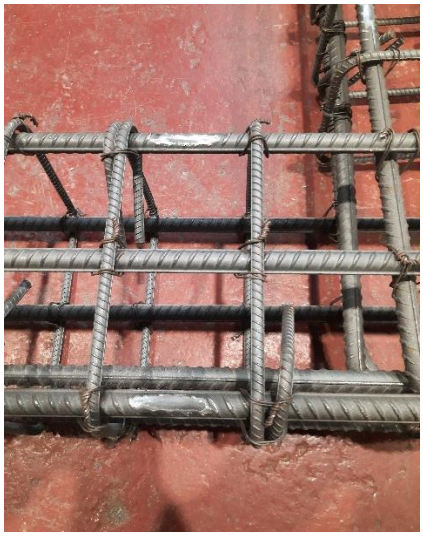

(a)
The surface of the reinforcement rebar is levelled with a sand disc.

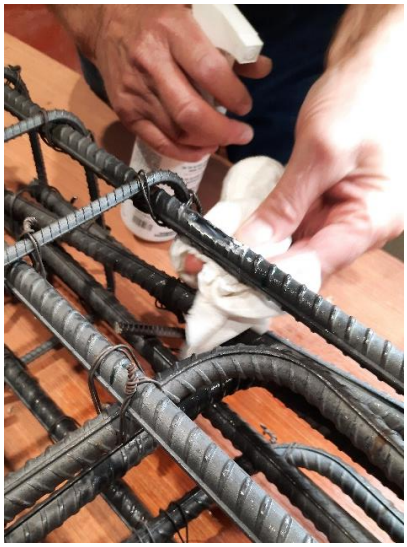

(b)
The reinforcement rebar surface is smoothed with fine sandpaper and cleaned with acetone.

(c)
The surface of the rebar is properly dried using a dryer.

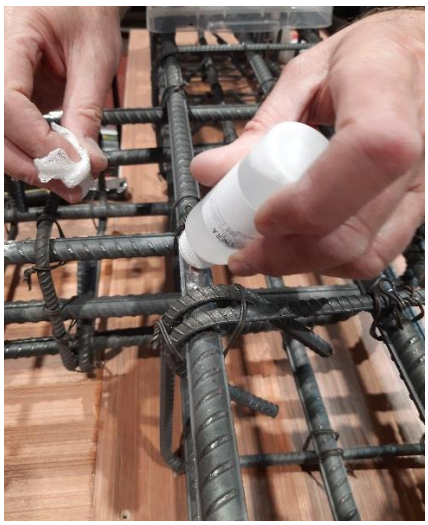

(d)
The surface of the rebar is cleaned by means of M-Prep conditioner A.

Figure E1. The installation process of the strain gauge.

(e)
The surface of the rebar is applied using M-Prep neutralizer 5A.

(f)
To fasten adhesion, an appropriate amount of 200 Catalyst is applied to the back side of the strain gauge before the superglue (M-bond 200 Adhesive) is applied.

(g)
The appropriate amount of superglue on the rebar is applied.

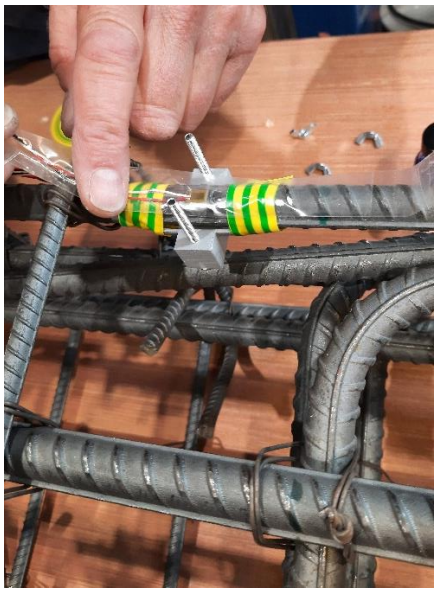

(h)
The strain gauge and superglue are combined.

Figure E1. The installation process of the strain gauge (continue).

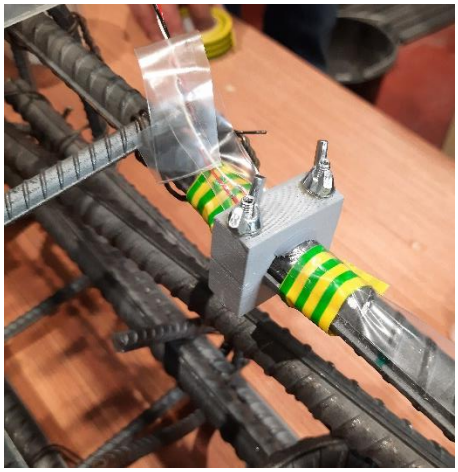

(i)
To ensure effective adhesion of the strain gauges, clamps produced with 3D printers are tightened and left for at least 30 minutes.

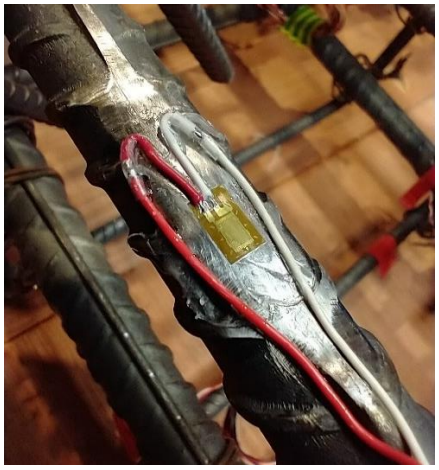

(j)
The clamp and fabric are carefully lifted and checked to see if the gauge is sticking or not.

(k)
The cables on the strain gauge are covered with PTFE tape to cover the bare strain gauge connections as the M-Coat JA is conductive and the cable splices are folded back to fit neatly into the M-Coat JA.

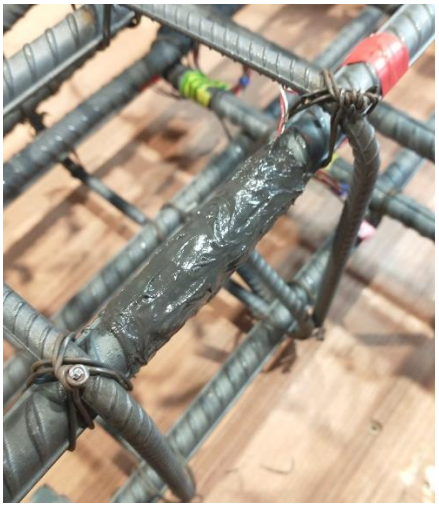

(l)
Completely cover the cables and strain gauge with M-Coat JA.

Figure E1. The installation process of the strain gauge (continue).

Figure E2. M-Prep conditioner A, M-Prep neutralizer 5A, 200 Catalyst, M-bond 200 Adhesive.

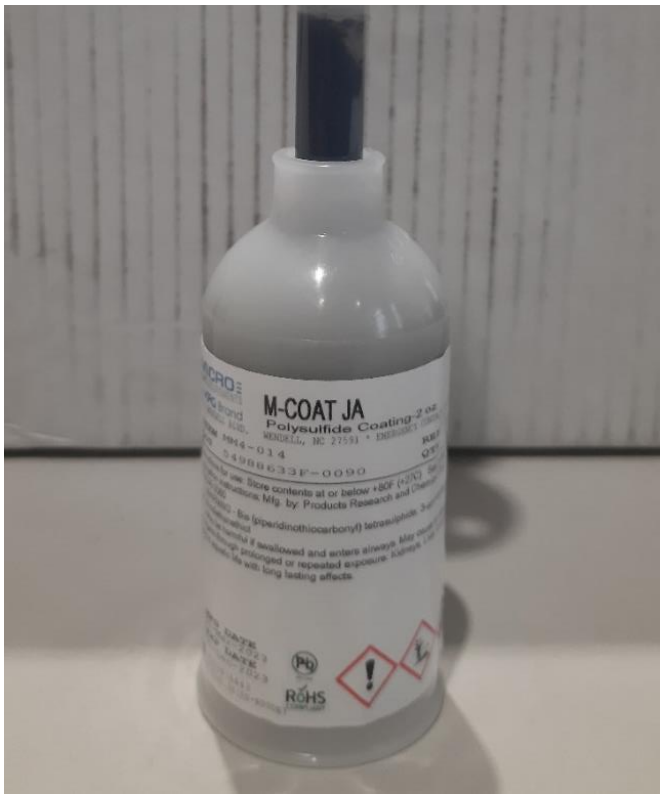

Figure E3. M-Coat JA

GAGE PATTERN DATA – BASED ON ADVANCED SENSORS TECHNOLOGY

actual size

GAGE DESIGNATION (See Note 1)	RESISTANCE (OHMS)	OPTIONS AVAILABLE
C4A-XX-125SL-120-23P	120 ± 0.3%	
C4A-XX-125SL-120-29P	120 ± 0.3%	
C4A-XX-125SL-120-33P	120 ± 0.3%	
C4A-XX-125SL-120-39P	120 ± 0.3%	
C4A-XX-125SL-350-23P	350 ± 0.3%	
C4A-XX-125SL-350-29P	350 ± 0.3%	
C4A-XX-125SL-350-33P	350 ± 0.3%	
C4A-XX-125SL-350-39P	350 ± 0.3%	

DESCRIPTION

Widely used general-purpose gage.

Pb-free RoHS COMPLIANT

GAGE DIMENSIONS

Legend
ES = Each Section
S = Section (S1 = Section 1)
CP = Complete Pattern
M = Matrix

inch
millimeter

Gage Length	Overall Length	Grid Width	Overall Width	Matrix Length	Matrix Width
0.125	0.233	0.100	0.130	0.31	0.19
3.18	5.91	2.54	3.30	8.0	4.9

GAGE SERIES DATA — See Gage Series datasheet for complete specifications

Series	Description	Strain Range	Temperature Range
C4A	C4A encapsulated Constantan alloy gages with pre-attached ready-to-use cables. Length selections: 23P= 2 wires, 3 ft long; 29P= 2 wires, 9 ft long, 33P= 3 wires, 3 ft long; 39P= 3 wires, 9 ft long.	±3%	–60°F to +180°F (–51°C to +80°C)

Figure E4. Properties of the strain gages

Appendix-F

Theoretical Consideration of Shear Strength of Joints

The calculations in this section include calculations at the design stage before the experiments. The effect of the reinforcement methods used is shown analytically below.

Beam shear force (V), column axial force (N), resulting shear (τ_v), and axial stresses (σ_N) in the joint, and corresponding principal stresses (σ_1 and σ_2) in the joint core are given in Figure F1 (a). The Mohr circle (Mohr, 1900) for these stresses is shown in Figure F1 (b). Because there is no shear reinforcement in the joint, for control specimens, shear failure is assumed to correspond to the formation of a diagonal crack in the joint (this assumption may not be valid for cases of high column axial-compression stress) (Ilki *et al.,* 2011).

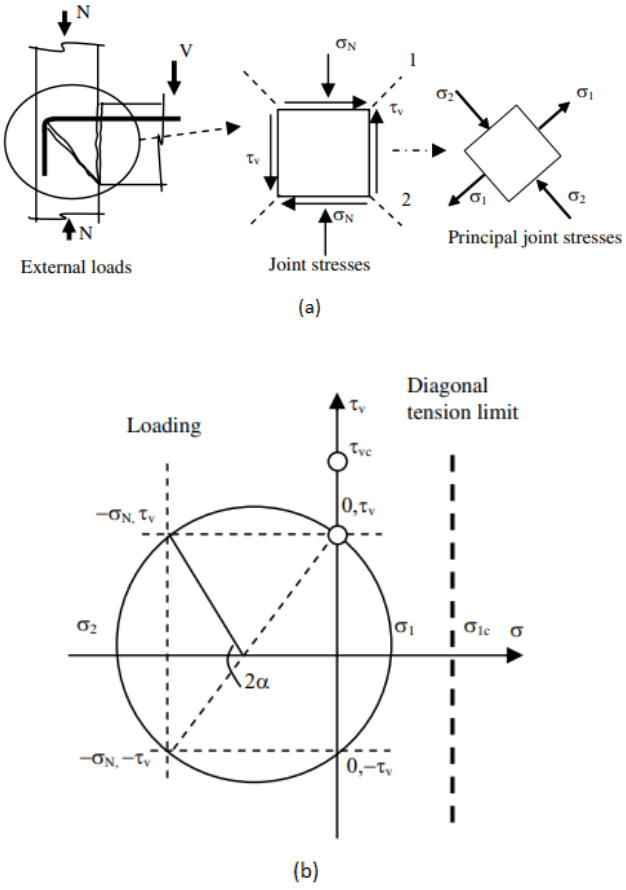

Figure F1. (a) External loads, joint stresses, and principal stresses (Ilki *et al.*, 2011); (b) Mohr's circle (Mohr, 1900).

A diagonal crack is assumed to form when principal tensile stress reaches the tensile strength of concrete. Consequently, shear failure of the joint is a function of the tensile strength of the concrete.

In the 1960s, the American Concrete Institute (ACI)-ASCE Committee 326 (1962) discovered that the tensile strength of concrete, f_{ctk} (= σ_1), is roughly proportional to $\sqrt{f_{ck}}$. Concrete tensile strength is given as $f_{ctk} = C\sqrt{f_{ck}}$, where C is a constant. ACI-318 (2011) recommends a value of "0.5" for the C coefficient. However, this coefficient is given as "0.35" in TEC (2007). In TS-500 (2000), it is stated that the direct tensile strength can be obtained approximately by dividing the value obtained from the splitting tensile strength test by 1.5 and the value obtained from the flexural tensile strength test by 2. By using the compressive strength value calculated in accordance with the material tests of the samples within the scope of the thesis, it was deemed appropriate to use the coefficient of “0.35” for the tensile strength value in the calculations. Principal stresses under normal and shear stresses can be calculated by using Equation (F1), according to Mohr’s theorem (Mohr, 1900):

$$\sigma_{1,2} = \frac{\sigma_x+\sigma_y}{2} \pm \sqrt{\left(\frac{\sigma_x+\sigma_y}{2}\right)^2 + \tau_{xy}^2} \quad \text{(F1)}$$

where σ_x = stress on plane parallel to the longitudinal axis of the member which is equal to the axial stress (σ_N) on the column; σ_y = normal stress on plane perpendicular to the axis of the member, which is zero for the joint; and τ_{xy} = shear stress, which is shown as τ_v in Figure (b). Consequently, for the tested joints, Equation (F1) can be rewritten as Equation (F2). The shear stress is a function of principal tensile stress (σ_1) and can be obtained by Equation (F3) by making use of Equation (F2). Assuming failure occurs when σ_1 reaches the tensile strength of concrete, the shear strength of the joint can be calculated by Equation (F4), where $\sigma_N = N/A_g$ and A_g = gross cross-sectional area of the column, N = column axial force. The contribution of concrete to the shear capacity of the joints of the control specimens can then be calculated by Equation (F5), where d = effective depth of the column. The joint shear strengths of the reference specimens depend only on the contribution of concrete because there is no shear reinforcement in the joint core.

$$\sigma_{1,2} = \frac{\sigma_N}{2} \pm \sqrt{\left(\frac{\sigma_N}{2}\right)^2 + \tau_v^2} \quad \text{(F2)}$$

$$\tau_v = \sigma_1 \times \sqrt{1 - \frac{\sigma_N}{\sigma_1}} \quad \text{(F3)}$$

$$\tau_{vc} = 0.35 \times \sqrt{f_{ck}} \times \sqrt{1 - \frac{N}{0.35 \times \sqrt{f_{ck}} \times A_g}} \quad \text{(F4)}$$

$$V_c = \tau_{vc} \times b_c \times d \quad \text{(F5)}$$

The contribution of concrete to the shear force is 165.2 kN in a shear force direction. Shear capacity of the FRP-retrofitted joints is calculated by using truss analogy (Paulay and Priestley, 1992). The shear capacity of the joint is assumed to be the sum of the contribution of the concrete and the FRP. The shear force, which is resisted by the FRP (F_{FRP}) in the direction of the fibres (diagonal to beam axis) can be calculated by Equation (F6). In this equation, ε_{fe} is the effective strain of the FRP sheets, which is assumed to be the minimum of 0.004 or 0.5 ε_{frpult}, as suggested by different codes Canadian Standards Association (CSA) (2002) and Concrete Society (2004). The effective FRP strain, Ilki *et al.* (2011) found ε_{fe} = 0.004 in his study. Although the ultimate strain value given by the manufacturer is "0.0155", Ilki *et al.* (2011) considering the joint zone tests, it was suggested that 25~30% of the final capacity should be taken into account for the joints strengthened with FRP. E_f, A_f and ε_{frpult} stand for modulus of elasticity, effective cross-sectional area of the FRP sheets in diagonal direction, ultimate strain value given by the manufacturer, respectively. The contribution of FRP sheets to the shear capacity in a horizontal or vertical direction can be calculated by Equation (F7).

$$F_{\mathrm{FRP}} = \varepsilon_{fe} \times E_f \times A_{f,total} \quad \text{(F6)}$$

$$V_{\mathrm{FRP}} = F_{\mathrm{FRP}} \times \sin(90^o) \quad \text{(F7)}$$

When determining the number of FRP layers, the point generally considered is to provide a shear capacity support equal to or more than the calculated concrete capacity value. Within the scope of this thesis, calculations were made by taking 30% (Ilki *et al.* 2011) of the ultimate strain value given by the manufacturer. Using this value, it was calculated how many layers the FRP material will be applied. Accordingly, 4 layers of FRP were wrapped to resist the shear force on the joint area. The contribution of 4 layers of FRP to the shear force is 195.8 kN in a horizontal or vertical direction (see in Figure A18).

The contribution of NSM steel to the shear capacity of the joints of the retrofitted specimen can then be calculated by Equation (F8).

$$V_s = A_{sw} \times \left(\frac{f_{ywk}}{\gamma_s}\right) \times \left(\frac{d}{s}\right) \quad \text{(F8)}$$

where, f_{ywk} is the yield strength of the transverse reinforcement, γ_s is the safety factor of steel, A_{sw} is the cross-sectional area of shear reinforcement, *d* is the effective depth of the column, and *s* is the spacing of NSM-steel reinforcement.

The contribution of NSM steel to the shear force is 170.8 kN in a shear force direction.

The total shear capacity of the retrofitted joint (V_t) can be calculated by Equation (F9).

$$V_t = V_c + V_{FRP} + V_s \quad \text{(F9)}$$

Using Equation (F9), total shear capacity of beam-column joint is 532.8 kN in a shear force direction. Table F1 shows the actual shear force calculation for the beam-column joint using the concrete and steel values obtained from the experiments.

Table F1. Nominal shear force capacities (V_t) of the joint areas of the test specimens.

Specimen Name	V_c (kN)	V_{FRP} (kN)	V_s (kN)	V_t (kN)
S1 (Control)	165.2	-	-	165.2
S2 (NSM)	165.2	-	170.8	336
S3 (EB)	165.2	195.8	-	361
S4 (Hybrid)	165.2	195.8	170.8	531.8

In these calculations, the above steps were repeated and a value of 24.35 MPa for concrete and 502 MPa for transverse reinforcement were used. Since the material values are known with certainty, calculations are made without using safety coefficients.

Calculation Steps in Theoretical Consideration of Shear Strength of Joints

The joint shear strengths of the reference specimens depend only on the contribution of concrete because there is no shear reinforcement in the joint core.

$$\sigma_{1,2} = \frac{\sigma_x+\sigma_y}{2} \pm \sqrt{\left(\frac{\sigma_x+\sigma_y}{2}\right)^2 + \tau_{xy}^2} \quad \text{(F1)}$$

$$\sigma_{1,2} = \frac{\sigma_N}{2} \pm \sqrt{\left(\frac{\sigma_N}{2}\right)^2 + \tau_v^2} \quad \text{(F2)}$$

$$\tau_v = \sigma_1 \times \sqrt{1 - \frac{\sigma_N}{\sigma_1}} \quad \text{(F3)}$$

$$\tau_{vc} = 0.35 \times \sqrt{f_{ck}} \times \sqrt{1 - \frac{N}{0.35 \times \sqrt{f_{ck}} \times A_g}} \quad \text{(F4)}$$

where, A_g is the gross cross-sectional area of the column, N is the column axial force, and f_{ck} is the compressive strength of concrete.

$$\tau_{vc} = 0.35 \times \sqrt{24.35} \times \sqrt{1 - \frac{-168000}{0.35 \times \sqrt{24.35} \times (250 \times 300)}} = 2.6\ N/mm^2$$

$$V_c = \tau_{vc} \times b_c \times d \quad \text{(F5)}$$

$$V_c = 2.6 \times 250 \times 254 = 165.2\ kN$$

The contribution of concrete to the shear force is 165.2 kN in a shear force direction.

The contribution of FRP sheets to the shear capacity in a horizontal or vertical direction can be calculated by Equation (F6).

$$F_{\text{FRP}} = \varepsilon_{fe} \times E_f \times A_{f,total} \quad \text{(F6)}$$

$$\varepsilon_{fe} = \varepsilon_{frpult} \times (30\%)$$

where, ε_{frpult} is the laminate elongation at break, E_f is the laminate tensile modulus of elasticity, A_f is the effective cross-sectional area of the GFRP sheets.

$$\varepsilon_{fe} = 0.0214 \times \left(\frac{30}{100}\right) = 0.00642$$

$$A_f = t_f \times l_f$$

where, t_f is the thickness of the GFRP sheet, l_f is the length of the GFRP sheet.

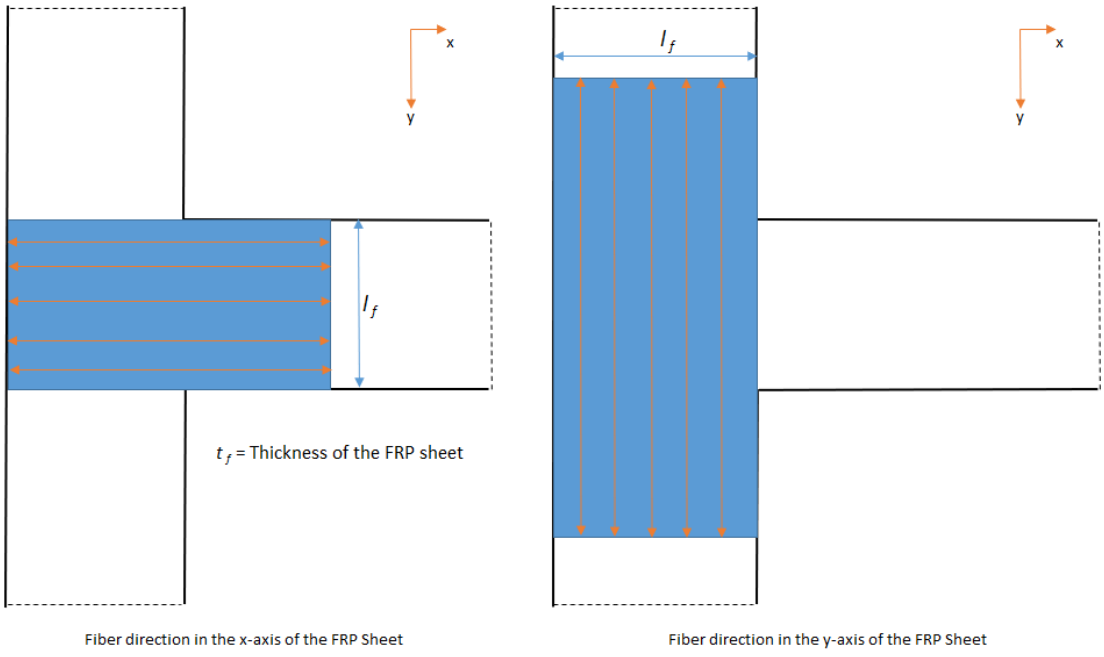

Figure F2. Direction of the fibre on the beam-column joint.

$$A_f = 0.363\ mm \times 300\ mm = 108.9\ mm^2$$

$$A_{f,total} = 108.9\ mm^2 \times 4\ layers = 435.6\ mm^2$$

$$F_{\mathrm{FRP}} = 0.00642 \times 70000\ N/mm^2 \times 435.6\ mm^2 = 195758.6\ N$$

$$F_{\mathrm{FRP}} = 195.8\ kN$$

$$V_{\mathrm{FRP}} = F_{\mathrm{FRP}} \times \sin(90^o) \quad \text{(F7)}$$

$$V_{\mathrm{FRP}} = 195.8 \times 1 = 195.8\ kN$$

The contribution of 4 layers of FRP to the shear force is 195.8 kN in a horizontal or vertical direction.

The contribution of NSM steel to the shear capacity of the joints of the retrofitted specimen can then be calculated by Equation (F8).

$$V_s = A_{sw} \times f_{yw} \times \left(\frac{d}{s}\right) \quad \text{(F8)}$$

where f_{yw} is the yield strength of the transverse reinforcement, A_{sw} is the cross-sectional area of shear reinforcement, *d* is the effective depth of the column, and *s* is the spacing of NSM-steel reinforcement.

$$V_s = 100.5\ mm^2 \times 502\ Nmm^2 \times \left(\frac{254\ mm}{75\ mm}\right)$$

$$V_s = 170826.7\ N = 170.8\ kN$$

The contribution of NSM steel to the shear force is 170.8 kN in a shear force direction.

The total shear capacity of the retrofitted joint (V_t) can be calculated by Equation (F9).

$$V_t = V_c + V_{FRP} + V_s \quad \text{(F9)}$$

Using Equation (F9), total shear capacity of beam-column joint is 531.8 kN in a shear force direction.

Appendix-G

Figure G1 shows the plan of the test frame (units are mm).

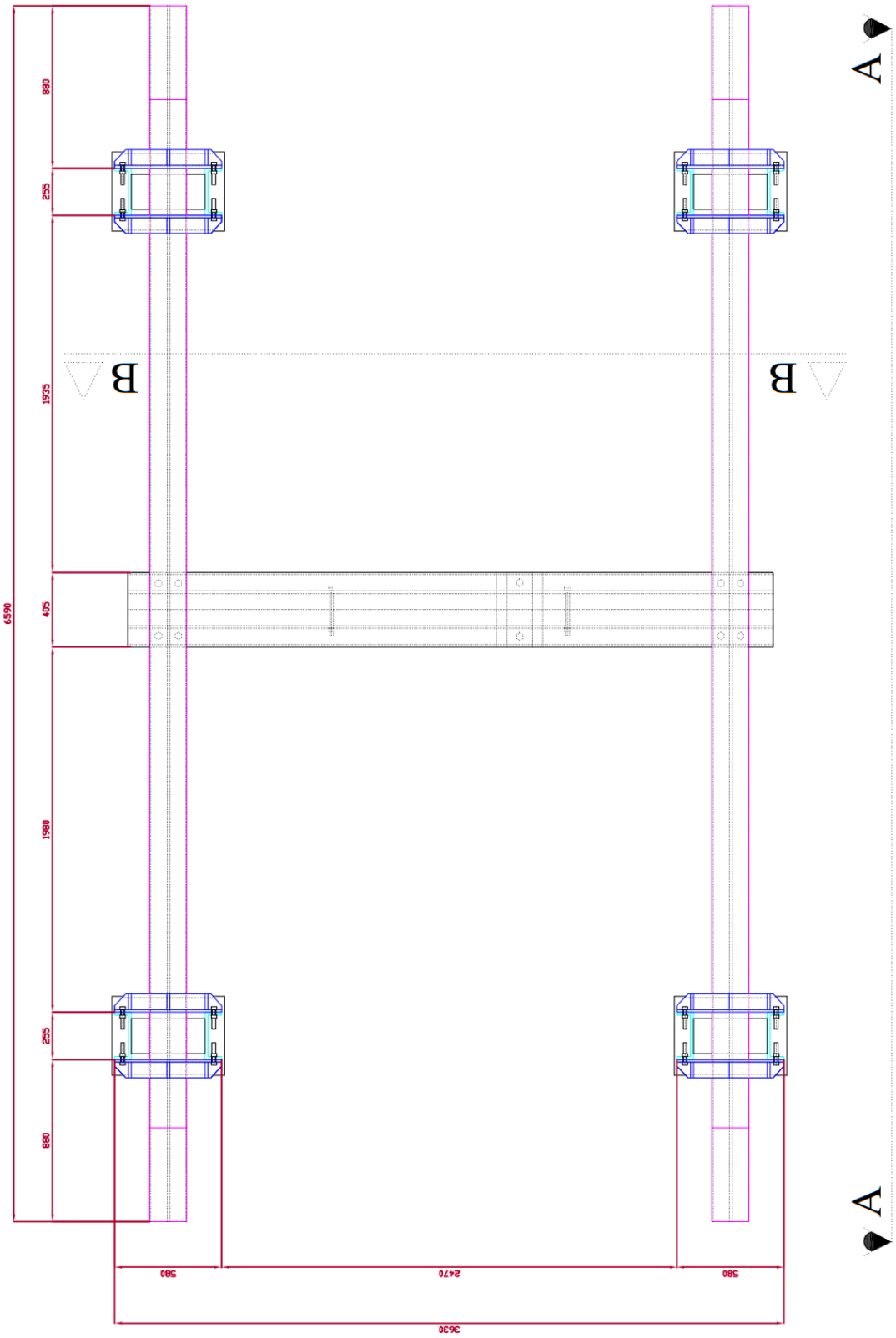

Figure G1. Plan of the test frame (Units are mm).

Figure G2 shows the A-A front view of the test frame (units are mm).

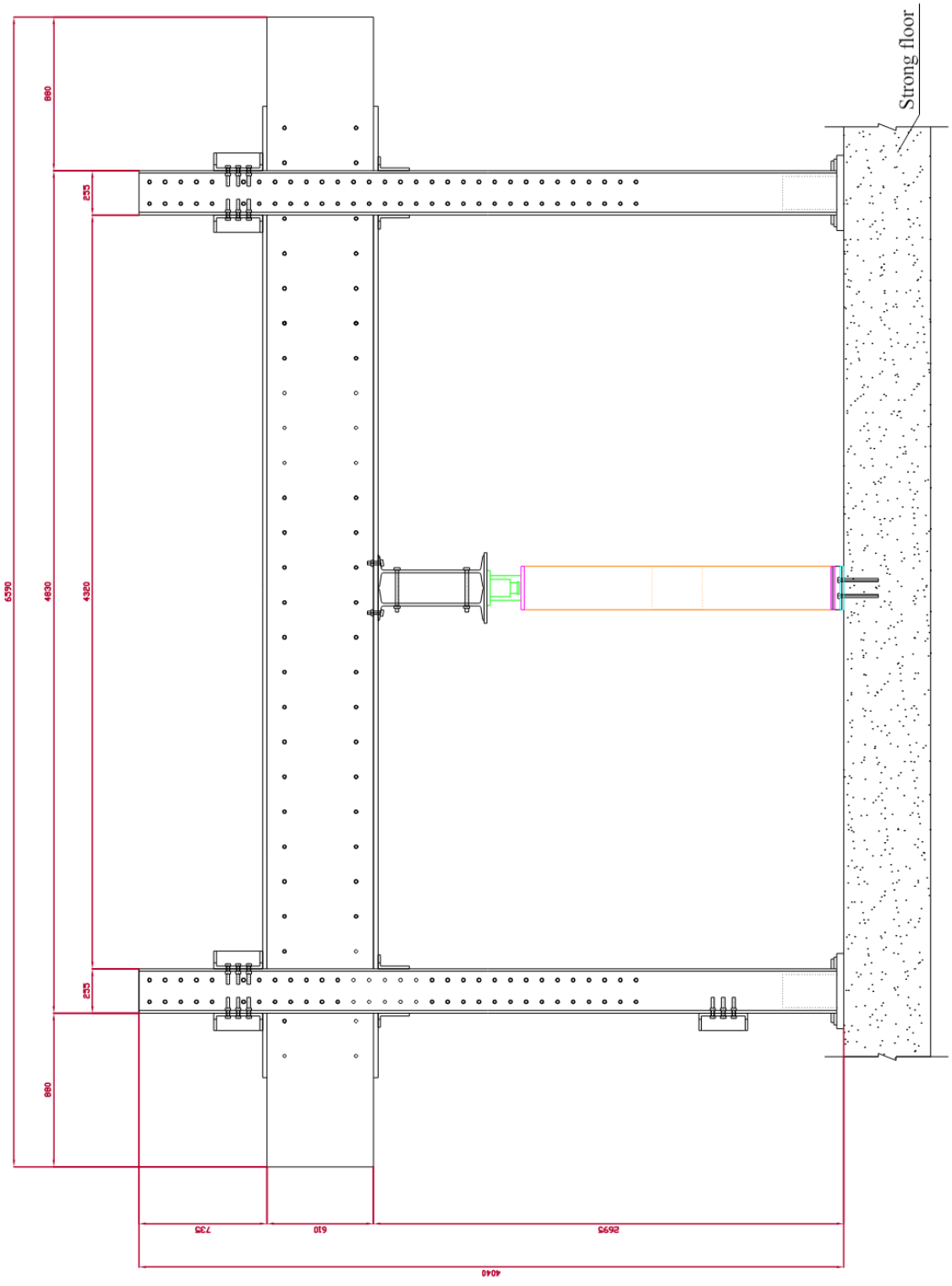

Figure G2. A-A front view of the test frame (Units are mm).

Figure G3 shows the B-B cross-section of the test frame (units are mm).

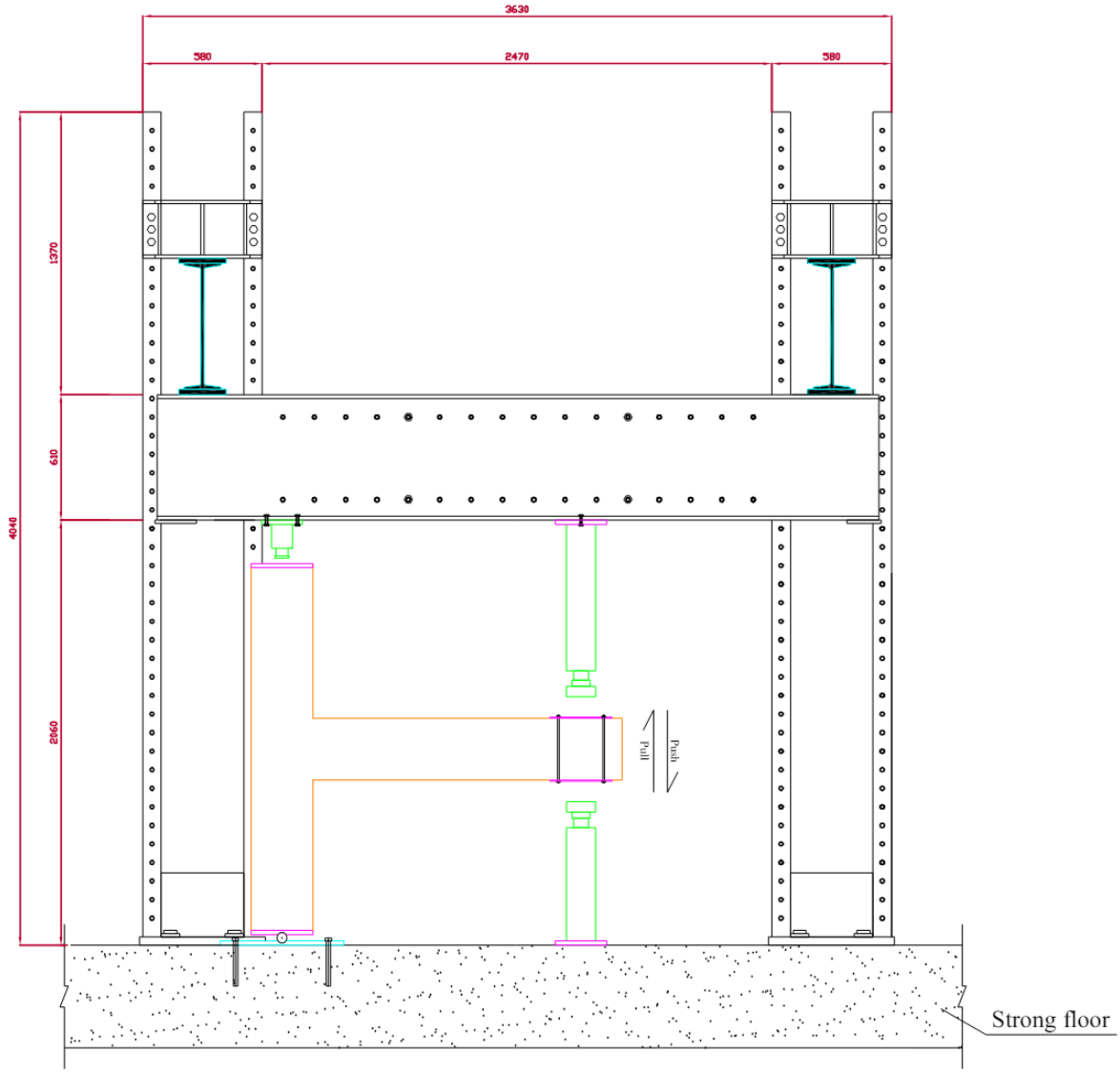

Figure G3. B-B cross-section of the test frame (Units are mm).

Appendix-H

Load-Displacement Response

Specimen-1 (Control)

	Step	Displacement (mm)	Load (kN)
	0	0.000	0.000
Push	1	0.196	2.394
Pull	2	-0.172	-1.474
Push	3	0.120	2.031
Pull	4	-0.144	-1.667
Push	5	0.221	3.359
Pull	6	-0.294	-3.441
Push	7	0.259	3.649
Pull	8	-0.255	-3.346
Push	9	1.188	8.471
Pull	10	-0.964	-9.072
Push	11	1.125	8.331
Pull	12	-1.027	-9.457
Push	13	2.196	12.033
Pull	14	-2.018	-12.817
Push	15	2.255	12.007
Pull	16	-2.086	-12.444
Push	17	3.458	15.624
Pull	18	-3.186	-16.392
Push	19	3.497	14.976
Pull	20	-3.289	-15.983
Push	21	5.316	20.266
Pull	22	-4.947	-22.005
Push	23	5.401	19.631
Pull	24	-5.039	-21.246
Push	25	8.590	27.291
Pull	26	-8.314	-28.609
Push	27	8.795	26.415
Pull	28	-8.378	-27.930

	Step	Displacement (mm)	Load (kN)
Push	29	12.406	32.484
Pull	30	-12.243	-32.909
Push	31	12.734	31.650
Pull	32	-12.468	-32.535
Push	33	18.783	42.690
Pull	34	-19.183	-41.072
Push	35	20.489	39.748
Pull	36	-20.514	-39.860
Push	37	28.580	48.913
Pull	38	-29.264	-46.144
Push	39	29.554	44.964
Pull	40	-29.717	-44.467
Push	41	42.166	50.813
Pull	42	-42.491	-46.764
Push	43	52.005	36.336
Pull	44	-51.543	-37.466
Push	45	62.749	32.637
Pull	46	-60.357	-30.227
Push	47	64.596	24.022
Pull	48	-64.131	-25.768
Push	49	75.340	20.726
Pull	50	-74.736	-23.623
Push	51	76.365	16.155
Pull	52	-75.981	-18.768
Push	53	86.712	14.693
Pull	54	-88.584	-17.481
Push	55	87.640	11.416
Pull	56	-87.556	-14.159
Push	57	0.000	0.000

Specimen-2 (NSM)

	Step	Displacement (mm)	Load (kN)
	0	0.000	0.000
Push	1	0.237	1.740
Pull	2	-0.091	-2.060
Push	3	0.157	1.531
Pull	4	-0.154	1.923
Push	5	0.335	3.264
Pull	6	-0.233	-3.450
Push	7	0.288	3.034
Pull	8	-0.230	-3.375
Push	9	1.083	8.297
Pull	10	-0.964	-9.010
Push	11	1.047	8.210
Pull	12	-0.989	-8.799
Push	13	2.099	12.415
Pull	14	-1.928	-13.056
Push	15	2.142	12.161
Pull	16	-1.969	-12.970
Push	17	3.390	15.695
Pull	18	-3.104	-16.663
Push	19	3.403	15.539
Pull	20	-3.167	-16.427
Push	21	5.244	20.607
Pull	22	-5.389	-22.126
Push	23	5.322	19.864
Pull	24	-5.186	-20.920
Push	25	8.634	27.679
Pull	26	-8.306	-28.472
Push	27	8.666	26.773
Pull	28	-8.477	-28.164

	Step	Displacement (mm)	Load (kN)
Push	29	11.947	34.657
Pull	30	-11.817	-34.550
Push	31	12.820	33.710
Pull	32	-12.141	-33.627
Push	33	18.985	47.372
Pull	34	-19.476	-44.899
Push	35	19.175	45.767
Pull	36	-19.422	-44.464
Push	37	26.942	57.111
Pull	38	-24.236	-51.444
Push	39	28.210	55.975
Pull	40	-28.071	-50.617
Push	41	34.413	57.355
Pull	42	-37.585	-53.932
Push	43	48.860	49.363
Pull	44	-49.323	-47.092
Push	45	56.656	47.246
Pull	46	-57.991	-42.352
Push	47	61.985	38.255
Pull	48	-63.176	-31.517
Push	49	71.818	31.025
Pull	50	-73.669	-25.409
Push	51	75.102	23.028
Pull	52	-75.814	-19.263
Push	53	85.499	20.726
Pull	54	-85.928	-17.899
Push	55	86.358	16.294
Pull	56	-86.911	-14.904
Push	57	0.000	0.000

Specimen-3 (EB)

	Step	Displacement (mm)	Load (kN)
	0	0.000	0.000
Push	1	0.144	1.560
Pull	2	-0.128	-1.674
Push	3	0.134	1.652
Pull	4	-0.216	-2.426
Push	5	0.246	3.171
Pull	6	-0.272	-3.184
Push	7	0.249	3.171
Pull	8	-0.272	-3.202
Push	9	0.966	8.554
Pull	10	-0.886	-9.174
Push	11	0.968	8.514
Pull	12	-0.885	-8.924
Push	13	2.031	12.589
Pull	14	-1.769	-13.712
Push	15	2.090	12.268
Pull	16	-1.805	-13.751
Push	17	3.218	15.898
Pull	18	-2.879	-17.413
Push	19	3.302	15.882
Pull	20	-2.926	-17.198
Push	21	4.989	21.057
Pull	22	-4.643	-22.447
Push	23	5.053	20.702
Pull	24	-4.703	-22.241
Push	25	8.051	29.285
Pull	26	-7.825	-30.116
Push	27	8.184	28.548
Pull	28	-7.912	-29.613
Push	29	11.667	36.619
Pull	30	-11.350	-37.222

	Step	Displacement (mm)	Load (kN)
Push	31	12.025	35.724
Pull	32	-12.044	-35.783
Push	33	17.993	50.637
Pull	34	-19.197	-44.972
Push	35	18.117	49.466
Pull	36	-19.682	-42.154
Push	37	22.898	60.458
Pull	38	-27.149	-54.606
Push	39	26.223	57.917
Pull	40	-27.624	-51.439
Push	41	44.925	64.235
Pull	42	-47.331	-53.603
Push	43	45.952	59.782
Pull	44	-47.475	-53.224
Push	45	55.433	62.129
Pull	46	-57.079	-55.879
Push	47	55.594	62.139
Pull	48	-58.047	-55.867
Push	49	65.258	62.863
Pull	50	-66.846	-56.969
Push	51	65.480	62.893
Pull	52	-66.898	-56.196
Push	53	70.904	62.989
Pull	54	-74.192	-55.819
Push	55	78.536	52.162
Pull	56	-78.710	-49.862
Push	57	89.859	39.663
Pull	58	-90.864	-37.802
Push	59	94.449	26.517
Pull	60	-94.310	-28.589
Push	61	0.000	0.000

Specimen-4 (NSM & EB)

	Step	Displacement (mm)	Load (kN)
	0	0.000	0.000
Push	1	0.227	2.392
Pull	2	-0.136	-1.601
Push	3	0.144	1.650
Pull	4	-0.131	-1.611
Push	5	0.263	3.146
Pull	6	-0.263	-3.287
Push	7	0.270	3.295
Pull	8	-0.269	-3.335
Push	9	0.937	8.685
Pull	10	-0.836	-9.238
Push	11	0.920	8.831
Pull	12	-0.835	-9.246
Push	13	1.926	13.124
Pull	14	-1.658	-14.237
Push	15	1.903	13.259
Pull	16	-1.720	-14.103
Push	17	3.024	16.785
Pull	18	-2.730	-18.059
Push	19	3.129	16.499
Pull	20	-2.800	-17.739
Push	21	4.848	21.833
Pull	22	-4.320	-23.851
Push	23	4.932	21.424
Pull	24	-4.396	-23.698
Push	25	7.925	30.028
Pull	26	-7.028	-33.361

	Step	Displacement (mm)	Load (kN)
Push	27	7.986	29.468
Pull	28	-7.141	-33.163
Push	29	11.101	37.789
Pull	30	-10.106	-41.664
Push	31	12.042	37.150
Pull	32	-10.890	-40.812
Push	33	17.785	52.861
Pull	34	-17.153	-55.137
Push	35	18.640	51.213
Pull	36	-17.882	-53.547
Push	37	21.776	60.155
Pull	38	-22.384	-62.795
Push	39	27.493	57.686
Pull	40	-27.176	-60.687
Push	41	45.068	65.077
Pull	42	-46.068	-59.761
Push	43	46.651	61.019
Pull	44	-46.583	-60.328
Push	45	55.527	62.008
Pull	46	-55.888	-60.782
Push	47	57.072	60.916
Pull	48	-57.365	-61.357
Push	49	67.271	61.272
Pull	50	-65.225	-64.060
Push	51	66.885	59.303
Pull	52	-66.472	-63.406
Push	53	77.941	50.680
Pull	54	78.260	-48.256
Push	55	0.000	0.000

Appendix-I

Strain Measurement: Figure I1 shows the results of strain gauges for S1-Control. Strain measurements of S1-Control are below.

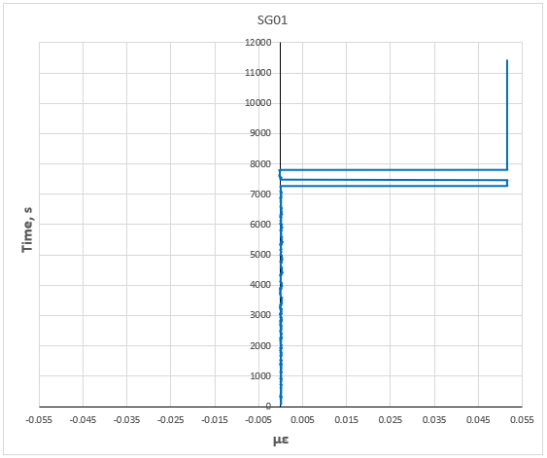

(a) SG01

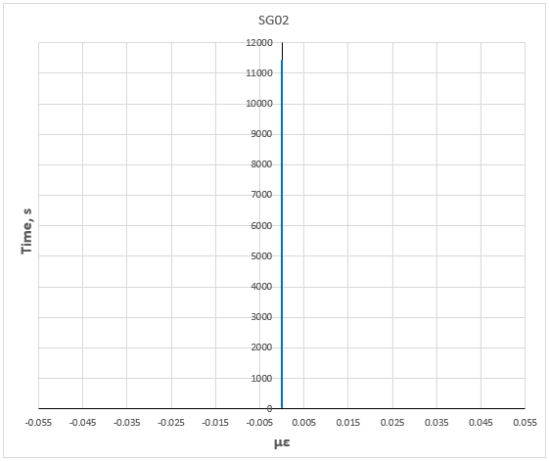

(b) SG02

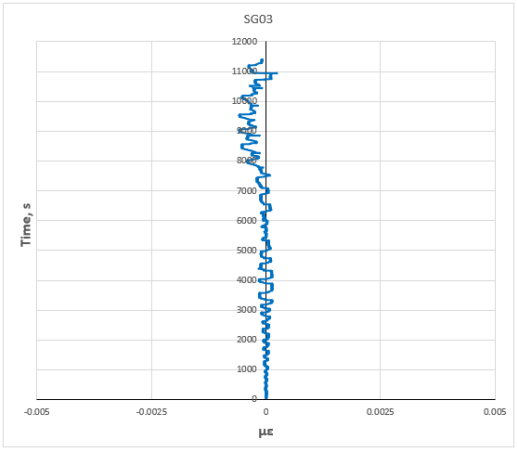

(c) SG03

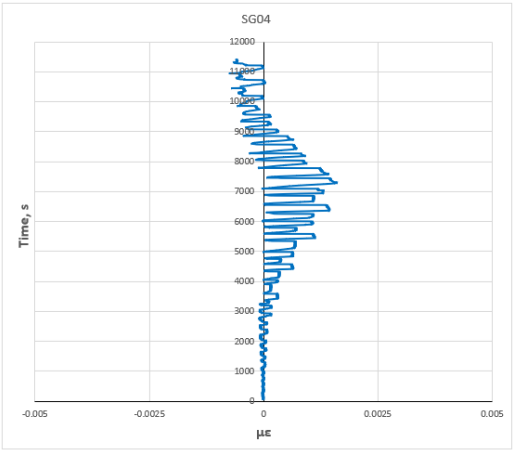

(d) SG04

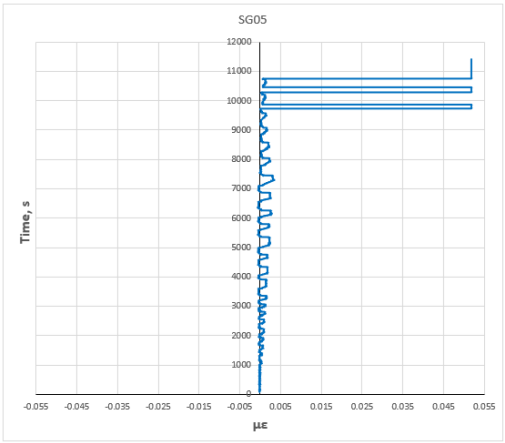

(e) SG05

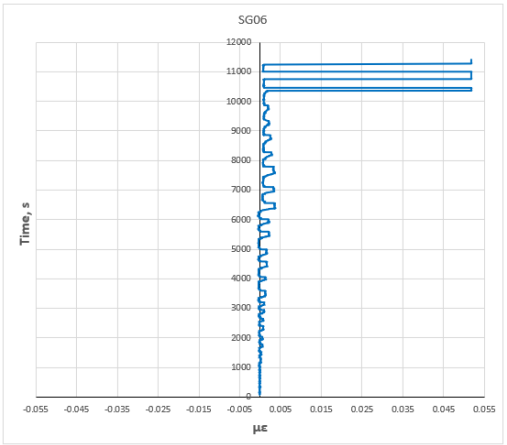

(f) SG06

Figure I1. Results of strain measurements on S1-Control.

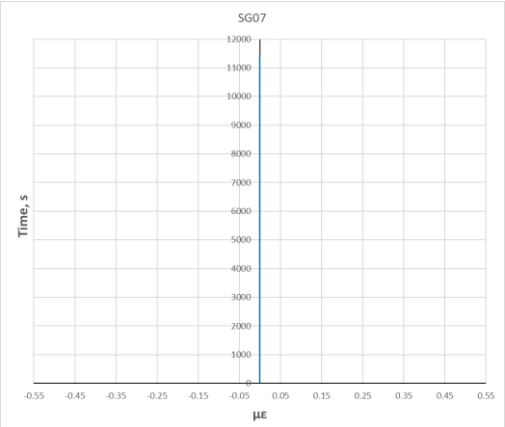

(g) SG07

Figure I1. Results of strain measurements on S1-Control (continue).

Referring to Figure 3.26 in Section 3.8.1, SG01, SG02, SG03 and SG04 represent strain gauges on the column longitudinal reinforcement, while SG05, SG06 and SG07 stand for strain gauges on the beam. This numbering is the same for all specimens and only for the u-shaped reinforcing steel used in specimen S2-NSM, 3 extra strain gauges were applied. The strain gauge SG01 shows that the reinforcement yielded at step 40, i.e., cycle 20. This value corresponds to the second cycle of the 2.31% drift ratio. SG02 was probably damaged, and no data could be obtained. SG03 and SG04 showed no yielding of the reinforcement during the experiment. When strain gauges SG05 and SG06 were analysed, it was found that the reinforcement with strain gauge SG05 yielded at step 50 (5.77% drift ratio in the first cycle at pulling direction), while the reinforcement with strain gauge SG06 yielded at step 52 (5.77% drift ratio in the second cycle at pulling direction). When the strain gauge of SG07 was probably damaged, and no data could be obtained. Figure I2 shows the results of strain gauges for S2-NSM.

Strain measurements of S2-NSM are below.

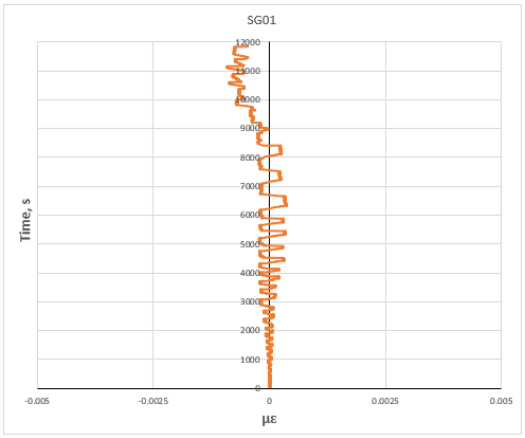

(a) SG01

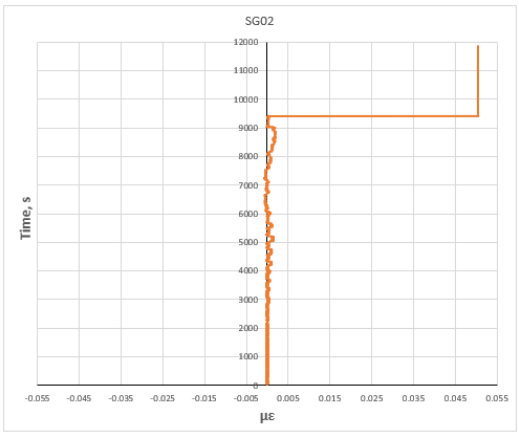

(b) SG02

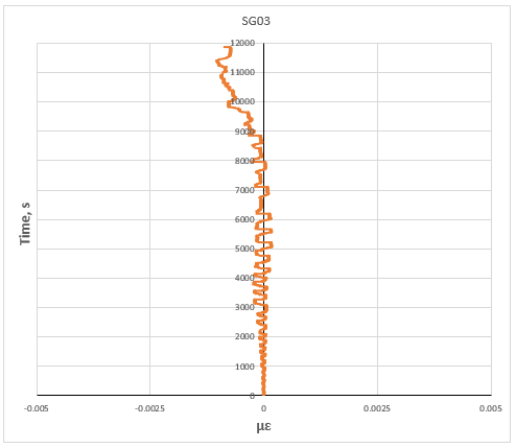

(c) SG03

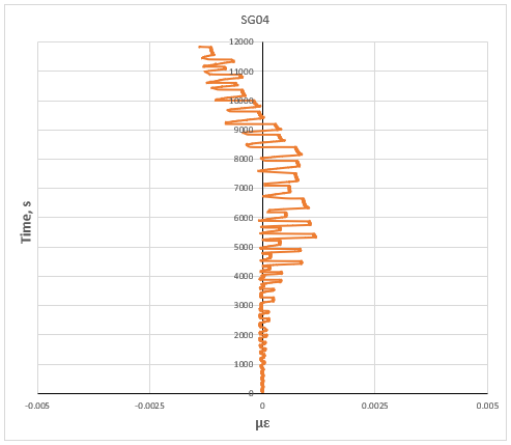

(d) SG04

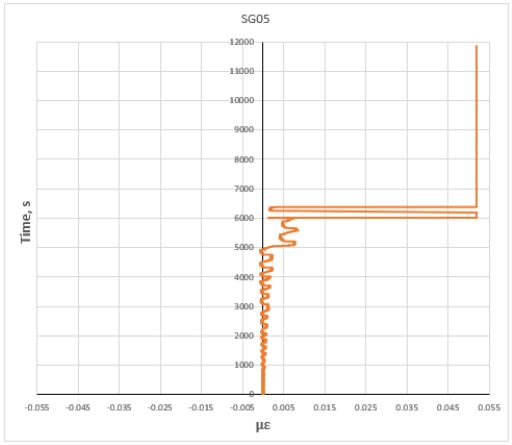

(e) SG05

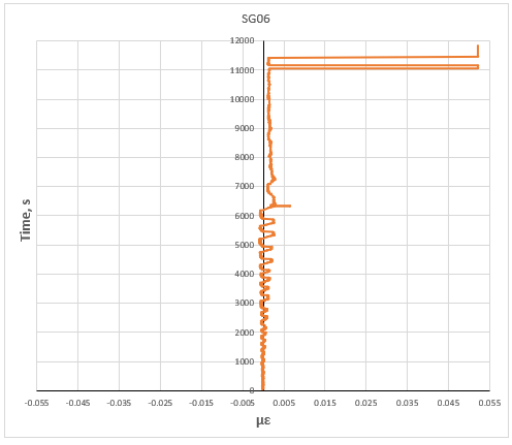

(f) SG06

Figure I2. Results of strain measurements on S2-NSM.

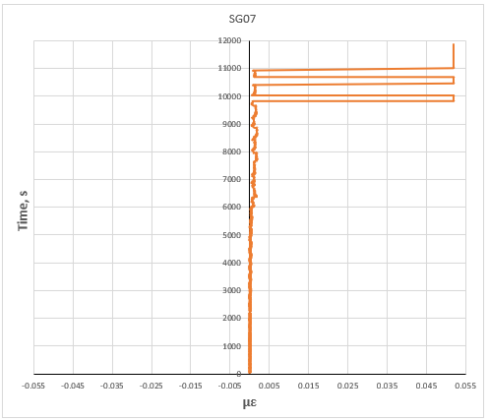

(g) SG07

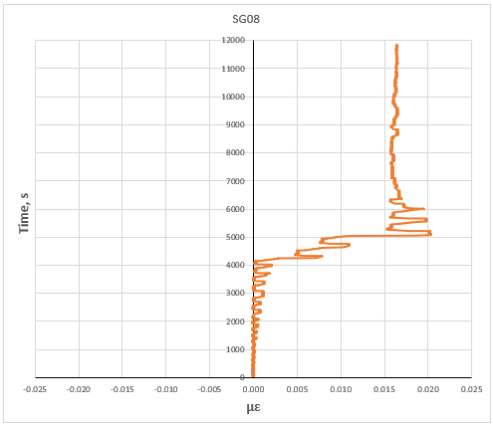

(h) SG08

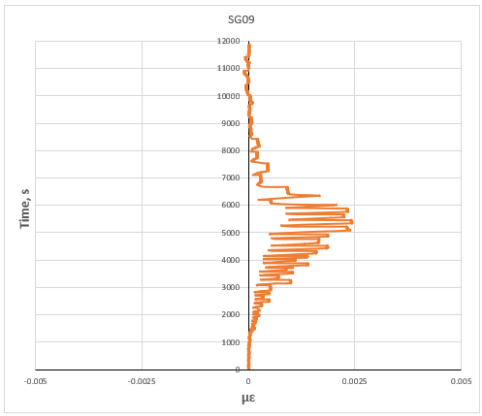

(i) SG09

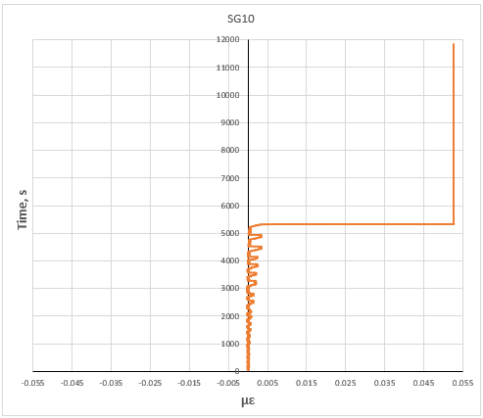

(j) SG10

Figure I2. Results of strain measurements on S2-NSM (continue).

When the strain gauges on the column in the S2-NSM were examined, it was observed that the reinforcements did not yield throughout the experiment in SG01, SG03 and SG04 gauges, but SG02 gauge yielded at step 49, i.e., cycle 25. This value corresponds to the first cycle of the 5.77% drift ratio. When SG05 and SG06 strain gauges on the beam bottom and top reinforcement were analysed, it was found that the reinforcement with strain gauge SG05 yielded at step 37 (2.31% drift ratio in the first cycle at pushing direction), while the reinforcement with strain gauge SG06 yielded at step 38 (2.31% drift ratio in the first cycle at pulling direction). When the strain gauge of SG07 was analysed, it was observed that this reinforcement yielded at step 49 (5.77% drift ratio in the first cycle at pushing direction). When it comes to the results of strain gauges SG08, SG09 and SG10, which were added to the S2-NSM specimen, were examined, it was observed that there was no yielding in the u-shaped reinforcement in the centre of the beam-column joint (strain gauge SG09). However, it was found that the reinforcement with strain gauge SG08 yielded at step 33 (1.54% drift ratio in the first cycle at pushing direction) and strain gauge SG10 yielded at step 34 (1.54% drift ratio in the first cycle at pulling direction). Figure I3 indicates the results of strain gauges for S3-EB.

Strain measurements of S3-EB are below.

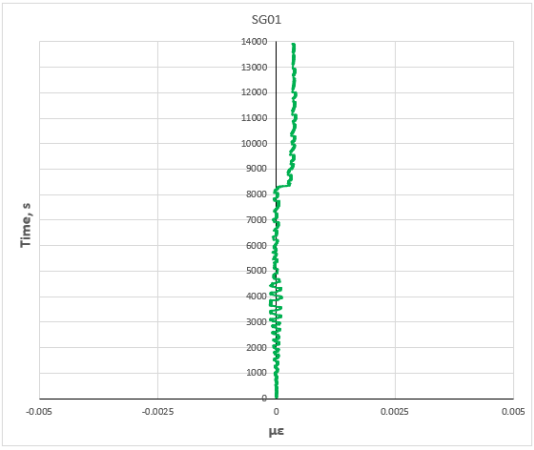

(a) SG01

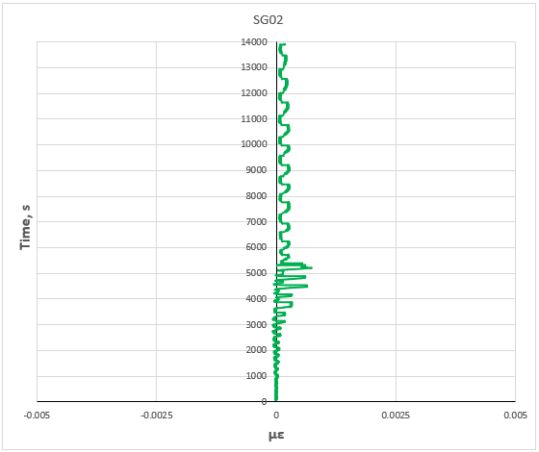

(b) SG02

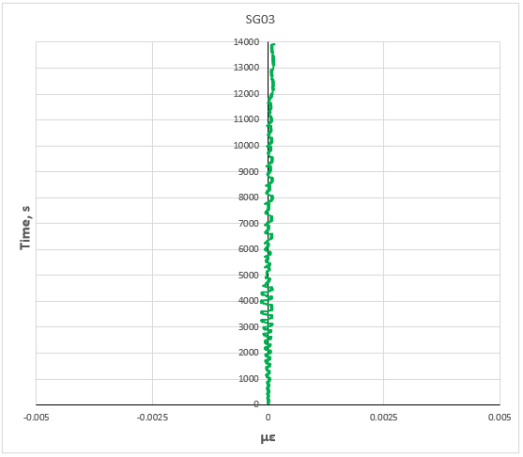

(c) SG03

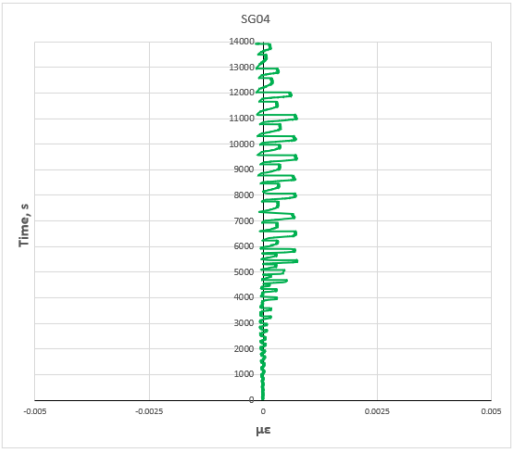

(d) SG04

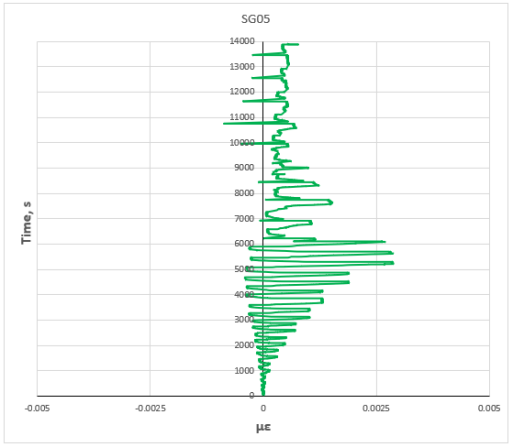

(e) SG05

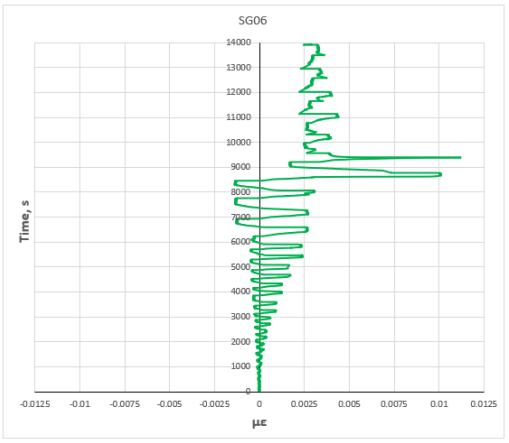

(f) SG06

Figure I3. Results of strain measurements on S3-EB.

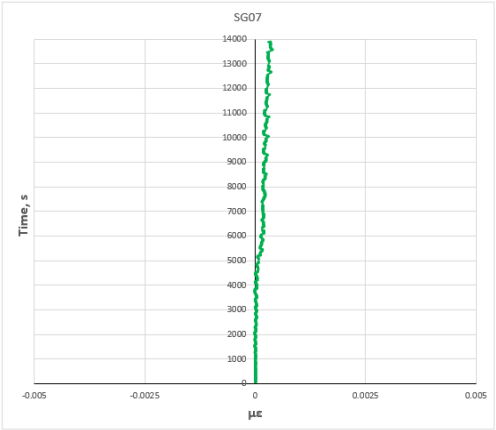

(g) SG07

Figure I3. Results of strain measurements on S3-EB (continue).

Once the strain gauges on the column in the S3-EB were examined, it was observed that the reinforcements did not yield throughout the experiment in SG01, SG02, SG03, and SG04 gauges. In the same way, strain gauge SG07, which was placed on the transverse reinforcement in the beam element, was also found not to yield. When SG05 and SG06 strain gauges on the beam top and bottom reinforcement were analysed, it was found that the reinforcement with strain gauge SG05 yielded at step 37 (2.31% drift ratio in the first cycle at pushing direction), while the reinforcement with strain gauge SG06 yielded at step 42 (3.85% drift ratio in the first cycle at pulling direction). Figure I4 shows the results of strain gauges for S4-Hybrid.

Strain measurements of S4-Hybrid are below.

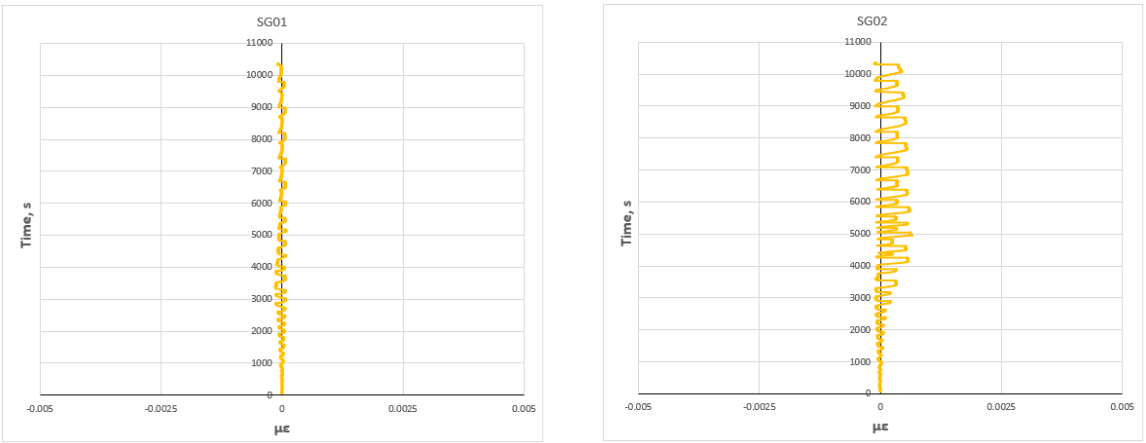

(a) SG01 (b) SG02

Figure I4. Results of strain measurements on S4-Hybrid.

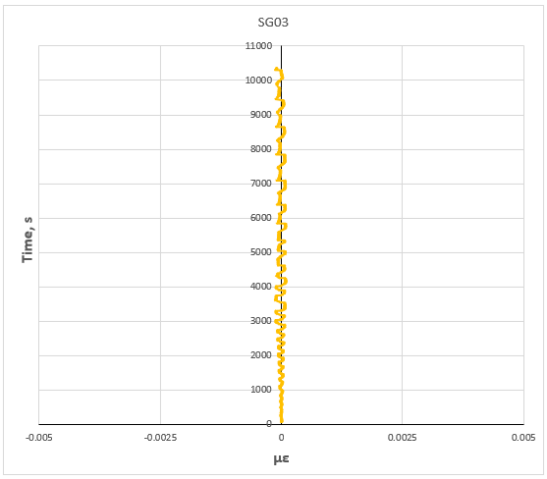

(c) SG03

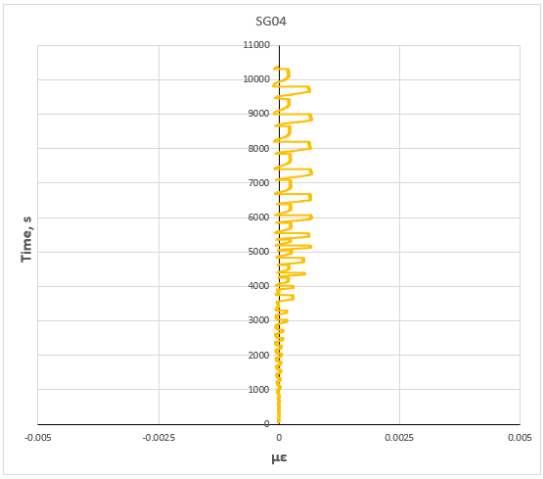

(d) SG04

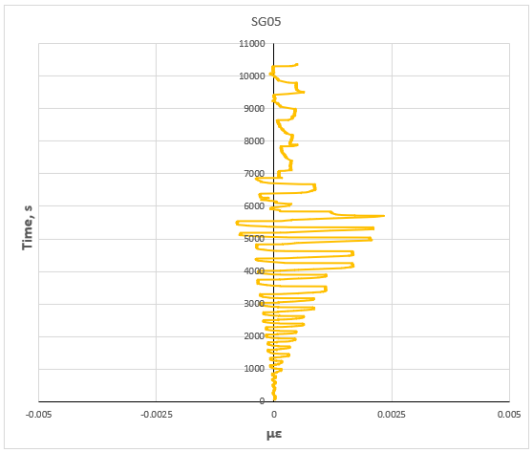

(e) SG05

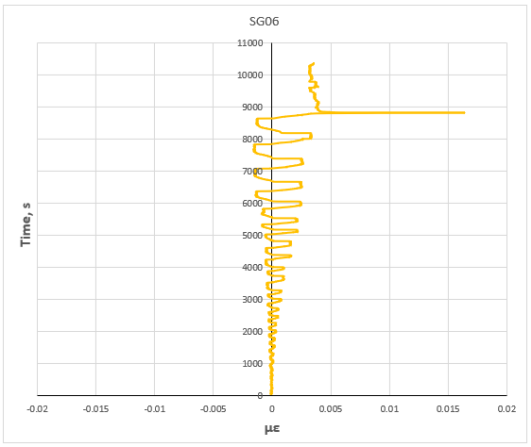

(f) SG06

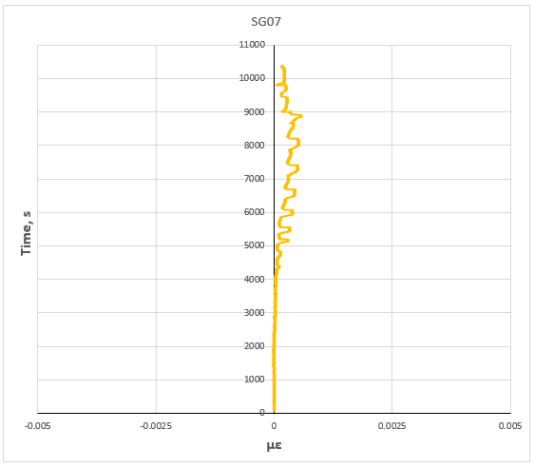

(g) SG07

Figure I4. Results of strain measurements on S4-Hybrid (continue).

When the strain gauges on the column in the S4-Hybrid were examined, it was determined that the reinforcements did not yield throughout the experiment in SG01, SG02, SG03, and SG04 gauges. Likewise, strain gauge SG07, which was placed on the transverse reinforcement in the beam element, was also found not to yield. Once SG05 and SG06 strain gauges on the beam top and bottom reinforcement were analysed, it was found that the reinforcement with strain gauge SG05 did not yield during the experiment while the reinforcement with strain gauge SG06 yielded at step 42 (3.85% drift ratio in the first cycle at pulling direction).

Appendix-J

Table J1 and Table J2 shows the compression and tension part of the concrete model, respectively. In addition, the Concrete Damage Plasticity (CDP) parameters are given in Table J3.

Table J1. Compression part of the concrete model.

Concrete Compression Behaviour		***Concrete Compression Damage***	
Yield Stress (MPa)	***Inelastic Strain***	***Damage Parameter***	***Inelastic Strain***
9.74	0.00000	0	0.00000
9.99	0.00000	0	0.00000
11.66	0.00001	0	0.00001
12.54	0.00002	0	0.00002
15.69	0.00008	0	0.00008
18.24	0.00016	0	0.00016
20.24	0.00027	0	0.00027
21.74	0.00040	0	0.00040
22.83	0.00055	0	0.00055
23.57	0.00072	0	0.00072
24.03	0.00090	0	0.00090
24.28	0.00109	0	0.00109
24.35	0.00128	0	0.00128
24.29	0.00148	0.0025	0.00148
24.13	0.00169	0.0091	0.00169
23.89	0.00190	0.0187	0.00190
23.52	0.00217	0.0340	0.00217
23.10	0.00244	0.0515	0.00244
22.63	0.00271	0.0706	0.00271
22.15	0.00298	0.0904	0.00298
21.66	0.00326	0.1106	0.00326
21.16	0.00353	0.1308	0.00353
20.58	0.00386	0.1548	0.00386
17.17	0.00421	0.2949	0.00421
8.64	0.00510	0.6453	0.00510
0.10	0.00600	0.9959	0.00600

Table J2. Tension part of the concrete model.

Stress-Cracking Displacement (fracture energy criterion)			
Concrete Tension Behaviour		***Concrete Tension Damage***	
Yield Stress (MPa)	***Cracking Displacement***	***Damage Parameter (T)***	***Cracking Displacement***
1.800	0.0000	0.000	0.0000
1.500	0.0089	0.167	0.0089
1.200	0.0178	0.333	0.0178
0.900	0.0267	0.500	0.0267
0.700	0.0327	0.611	0.0327
0.600	0.0356	0.667	0.0356
0.500	0.0564	0.722	0.0564
0.300	0.0980	0.833	0.0980
0.100	0.1396	0.944	0.1396
0.010	0.1583	0.994	0.1583

Table J3. Concrete Damage Plasticity (CDP) parameters.

The material parameters of Concrete Damage Plasticity (CDP) model for concrete class C24.35			
Material's Parameters	*C24.35*	***The Parameters of CDP Model***	
		Dilation Angle (ψ)	32
		Eccentricity (ϵ)	0.1
Concrete Elasticity		***$f=f_{b0}/f_{c0}$***	1.16
E_c (MPa)	21781	***K_c***	0.667
Poisson's ratio	0.2	***Viscosity Parameter***	0.003

Figure J1 shows the fibre direction and thickness of FRP sheets on the joint for the x-axis and the y-axis, respectively. In addition, fibre direction of FRP sheets on the joint is given in Figure J2.

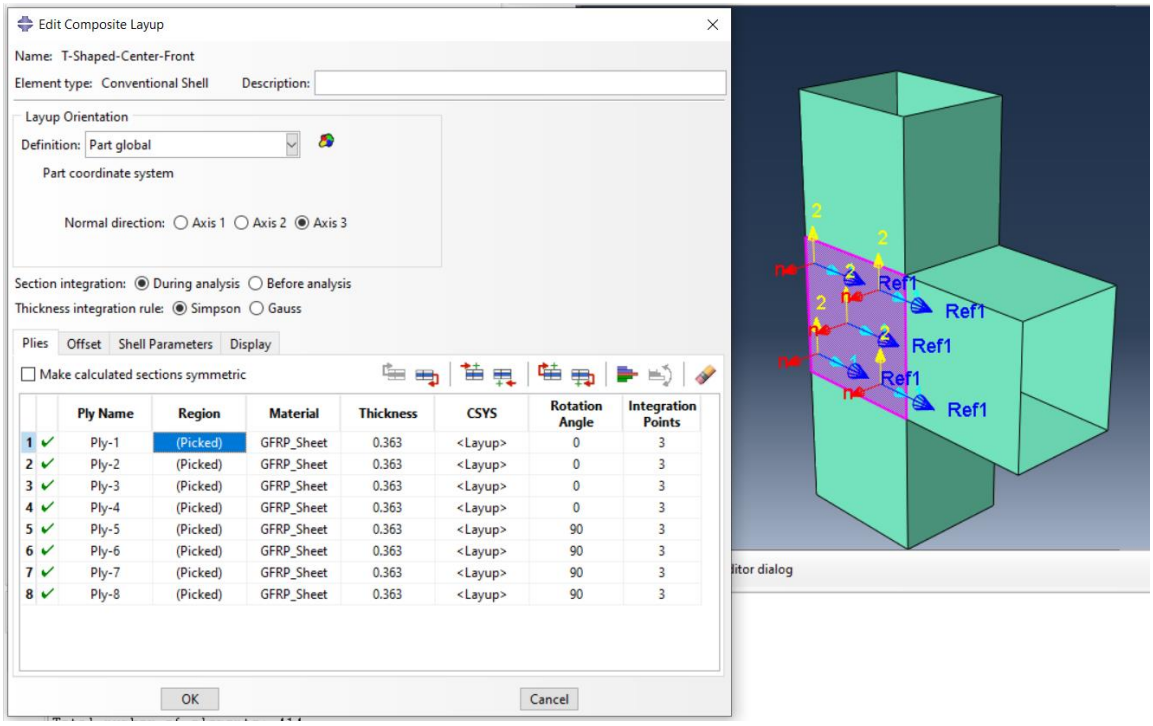

(a)

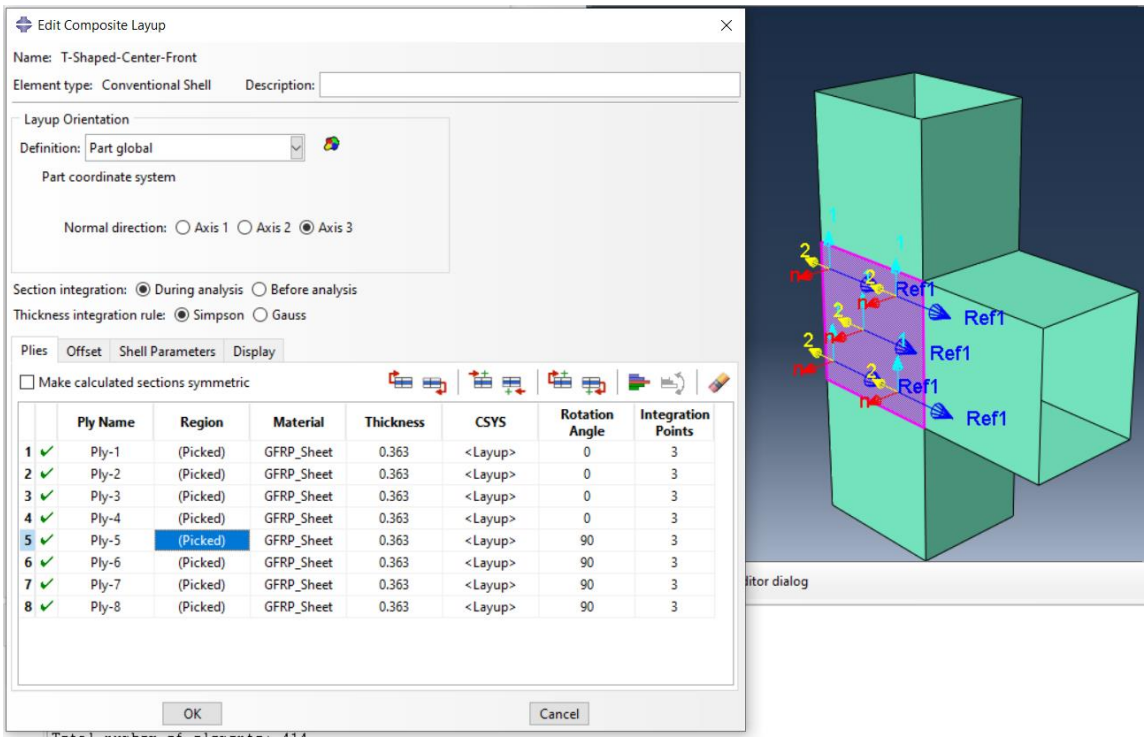

(b)

Figure J1. Showing fibre direction and thickness of FRP sheets on the joint: (a) in the direction of the x-axis; (b) in the direction of the y-axis.

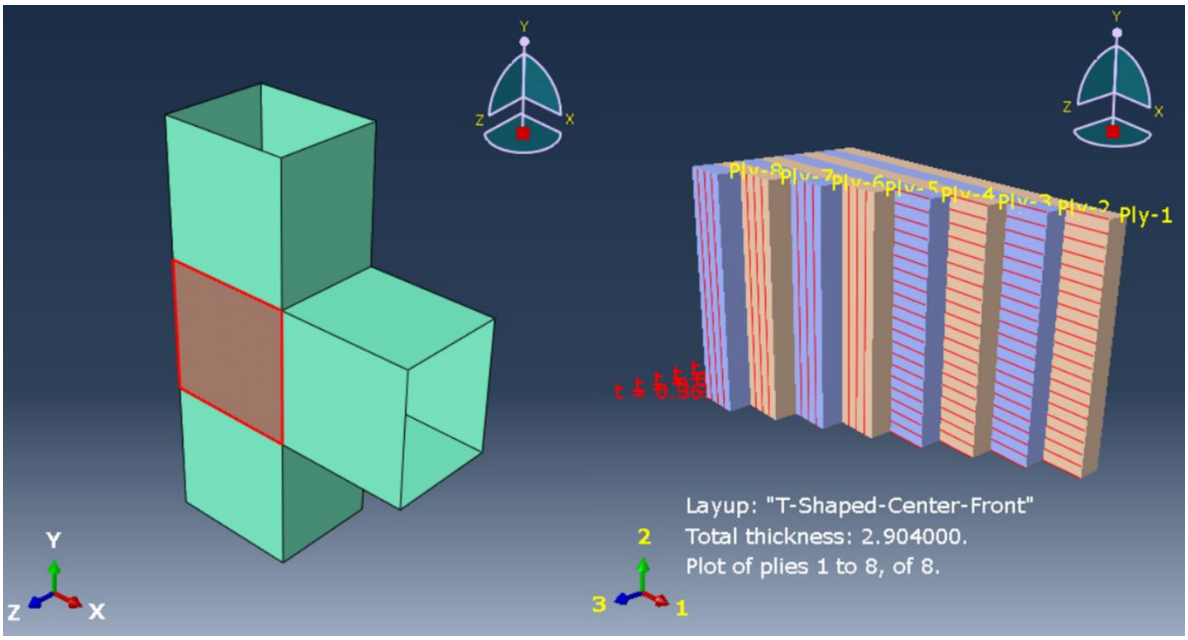

Figure J2. Fiber direction of FRP sheets on the joint.

Figure J3, Figure J4 and Figure J5 show the comparison with numerical model and experimental results for Tensile Damage Evolution for S1-Control, S2-NSM, and S4-Hybrid, respectively.